

TECHNICAL DIGEST

1 9 9 5

PHOTOSENSITIVITY
AND QUADRATIC
NONLINEARITY
IN GLASS
WAVEGUIDES

FUNDAMENTALS
AND APPLICATIONS

SEPTEMBER 9-11, 1995

PORTLAND, OREGON

1995 TECHNICAL DIGEST SERIES
VOLUME 22

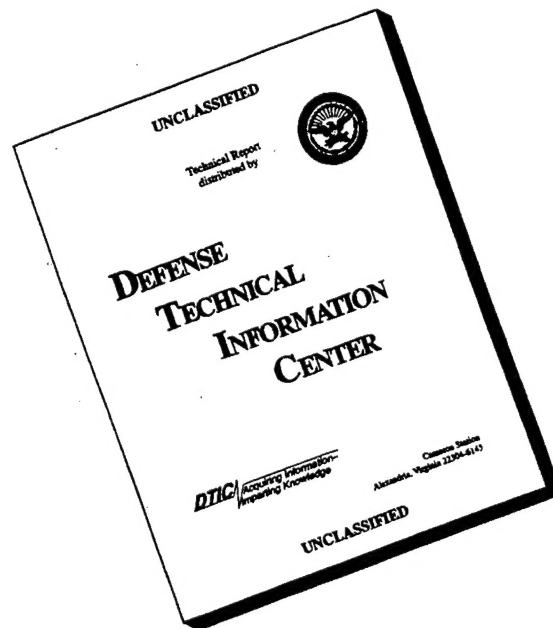


SPONSORED BY
OPTICAL SOCIETY OF AMERICA

DISTRIBUTION STATEMENT A

Approved for public release;
Distribution Unlimited

DISCLAIMER NOTICE



**THIS DOCUMENT IS BEST
QUALITY AVAILABLE. THE
COPY FURNISHED TO DTIC
CONTAINED A SIGNIFICANT
NUMBER OF PAGES WHICH DO
NOT REPRODUCE LEGIBLY.**

CONFERENCE EDITION

1 9 9 5

*Summaries of the papers
presented at the topical meeting*

PHOTOSENSITIVITY
AND QUADRATIC
NONLINEARITY
IN GLASS
WAVEGUIDES

FUNDAMENTALS
AND APPLICATIONS

September 9-11, 1995
Portland, Oregon

1995 Technical Digest Series
Volume 22

SPONSORED AND MANAGED BY
Optical Society of America



IN COOPERATION WITH
IEE—The Institution of Electrical Engineers
IOP—The Institute of Physics

Optical Society of America
2010 Massachusetts Avenue NW
Washington DC 20036-1023

19960325 109

DISTRIBUTION STATEMENT A

Approved for public release;
Distribution Unlimited

DTIC QUALITY INSPECTED 3

Articles in this publication may be cited in other publications. To facilitate access to the original publication source, the following form for the citation is suggested:

Name of Author(s), "Title of Paper," in *Photosensitivity and Quadratic Nonlinearity in Glass Waveguides: Fundamentals and Applications*, Vol. 22, 1995 OSA Technical Digest Series (Optical Society of America, Washington DC, 1995), pp. xx-xx.

Optical Society of America

ISBN

Conference Edition	1-55752-413-0
Postconference Edition	1-55752-414-9
(Note: Postconference Edition includes postdeadline papers.)	
1995 Technical Digest Series	1-55752-368-1

Library of Congress Catalog Card Number

Conference Edition	95-68690
Postconference Edition	95-68691

Copyright © 1995, Optical Society of America

Individual readers of this digest and libraries acting for them are permitted to make fair use of the material in it, such as to copy an article for use in teaching or research, without payment of fee, provided that such copies are not sold. Copying for sale is subject to payment of copying fees. The code 1-55752-368-1/95/\$6.00 gives the per-article copying fee for each copy of the article made beyond the free copying permitted under Sections 107 and 108 of the U.S. Copyright Law. The fee should be paid through the Copyright Clearance Center, Inc., 21 Congress Street, Salem, MA 01970.

Permission is granted to quote excerpts from articles in this digest in scientific works with the customary acknowledgment of the source, including the author's name and the name of the digest, page, year, and name of the Society. Reproduction of figures and tables is likewise permitted in other articles and books provided that the same information is printed with them and notification is given to the Optical Society of America. In addition, the Optical Society may require that permission also be obtained from one of the authors. Address inquiries and notices to Director of Publications, Optical Society of America, 2010 Massachusetts Avenue, NW, Washington, DC 20036-1023. In the case of articles whose authors are employees of the United States Government or its contractors or grantees, the Optical Society of America recognizes the right of the United States Government to retain a nonexclusive, royalty free license to use the author's copyrighted article for United States Government purposes.

Printed in the U.S.A.

Contents

Agenda of Sessions	v
SaA Plenary.....	1
SaB Fiber Gratings in Communications	5
SaC Self-Organized Second-Harmonic Generation	27
SaD Photosensitivity and Planar Waveguides and Mechanisms.....	43
SuA New Materials and Techniques	65
SuB Poster Session	91
SuC Poling I	165
SuD Poling II	179
PMA Materials Studies	195
PMB Sensors and Theory I	215
PMC Sensors and Theory II	233
PMD Fiber Lasers	251
Key to Authors and Presiders	277

**PHOTOSENSITIVITY AND QUADRATIC NONLINEARITY IN
WAVEGUIDES: FUNDAMENTALS AND APPLICATIONS**

TECHNICAL PROGRAM COMMITTEE

Gerry Meltz, *United Technologies Research Center, General Chair*

Philip St. J. Russell, *University of Southampton, UK, General Chair*

Ken O. Hill, *Communications Research Center, Canada, Program Chair*

Dana Z. Anderson, *University of Colorado*

Charles G. Askins, *U. S. Naval Research Laboratory*

Victor N. Bagratashvili, *Russian Academy of Sciences, Russian Federation*

Gary A. Ball, *3M Bragg Grating Technologies*

Steven R. J. Brueck, *University of New Mexico*

Kevin K. Byron, *Bell Northern Research, Ltd., UK*

Eugenii M. Dianov, *Russian Academy of Sciences, Russia*

Marc Douay, *Université des Science Technique, France*

E. Joe Friebele, *U. S. Naval Research Laboratory*

David R. Huber, *Ciena Corporation*

Avais Kamal, *EME College NUST, Pakistan*

Raman Kashyap, *British Telecom Research Laboratories, UK*

Hiroshi Kawazoe, *Tokyo Institute of Technology, Japan*

John J. Kester, *Frank J. Sella Research Laboratory*

Nabil M. Lawandy, *Brown University*

Paul J. Lemaire, *AT&T Bell Laboratories*

Walter Margulis, *Imperial College, UK*

Ulf Österberg, *Dartmouth College*

François Ouellette, *University of Sydney, Australia*

Bertrand Poumellec, *Université de Paris Sud Orsay, France*

Laurence Reekie, *University of Southampton, UK*

R. P. Salathé, *Swiss Federal Institute of Technology, Switzerland*

* **Roger Stolen**, *AT&T Bell Laboratories*

Robert A. Weeks, *Vanderbilt University*

* OSA Technical Council Representative

MULTNOMAH ROOM

8:15am-8:30am

Opening Remarks

8:30am-10:30am

SaA • Plenary SessionKen O. Hill, *Communications Research Center, Canada Presider*

8:30am (Invited)

SaA1 • Optical devices based on photo-induced index changes in silica, A. M. Glass, *AT&T Bell Laboratories*. The discovery of photo-induced index changes in silica has formed the basis for a large number of novel optical devices. This talk reviews both fiber and planar waveguide devices of interest for communications. (p. 2)

9:10am (Invited)

SaA2 • In-fiber Bragg grating devices for telecommunications applications, David R. Huber, *Ciena Corp.* The in-fiber Bragg grating is one of the most important developments in fiber telecommunications in this decade. Fiber gratings have found application in continuous wave and mode locked lasers, fiber dispersion compensation, pulse compression, fixed and tunable optical filters, add-drop filters and as demultiplexing elements. This paper reviews telecommunication devices that have been realized with this key technology. (p. 3)

9:50am (Invited)

SaA3 • Perspectives on glass poling, S. R. J. Brueck, *Univ. New Mexico*. Abstract not available. (p. 4)

LLOYD CENTER BALLROOM

10:30am-11:00am

Coffee Break

MULTNOMAH ROOM

11:00am-12:30pm

SaB • Fiber Gratings in CommunicationsPaul J. Lemaire, *AT&T Bell Laboratories, Presider*

11:00am (Invited)

SaB1 • Fiber Bragg components in filtering and dispersion compensation applications, K. O. Hill, *Communications Research Centre, Canada*. Photosensitivity enables the photoimprinting of Bragg gratings in optical fibers. This paper reviews two important fiber Bragg grating components: optical fiber filters and fiber dispersion compensators. (p. 6)

11:30am

SaB2 • Long-period cladding-mode-coupled fiber gratings: properties and applications, A. M. Vengsarkar, P. J. Lemaire, G. Jacobovitz-Veselka, J. B. Judkins, *AT&T Bell Laboratories*; V. Bhatia, *Virginia Tech*; T. Erdogan, *Univ. Rochester*; J. E. Sipe, *Univ. Toronto, Canada*. Optical properties of UV-induced long-period fiber gratings are described in terms of their dependence on strain, temperature and bends, and key applications are reviewed. (p. 10)

11:45am

SaB3 • Gain spectrum flattening of erbium-doped fiber amplifier using long-period fiber grating, E. M. Dianov, V. I. Karpov, A. S. Kurkov, O. I. Medvedkov, A. M. Prokhorov, V. N. Protopopov, S. A. Vasil'ev, *General Physics Institute, Russia*. For the first time a long-period fiber grating was used to flatten EDFA gain spectrum. A small signal gain as high as 30.8 ± 0.95 dB in the range 1526–1560 nm was obtained. (p. 14)

12:00m

SaB4 • Asymmetrical UV-written fiber Fabry-Perot form WDM soliton frequency-guiding and equalization, I. Riant, S. Borne, P. Sansonetti, *Alcatel Alsthom Recherche, France*. We report the realization of asymmetrical UV-written fiber Fabry-Perot filters suitable for frequency-guiding as well as equalization of WDM soliton transmission. (p. 18)

12:15pm

SaB5 • Optical dark soliton generation using a fiber Bragg grating, R. Kashyap, R. J. Campbell, D. J. Armes, *BT Laboratories, UK*; M. de Lathouwer, Ph. Emplit, M. Haelterman, *Univ. Libre de Bruxelles, Belgium*. We propose a simple technique to directly generate a mode locked train of dark soliton pulses at several GHz repetition rate from a semiconductor/fiber laser using a fiber Bragg grating. We show theoretically how this may be achieved for various fiber grating parameters. (p. 22)

12:30pm-1:30pm

Lunch (on your own)

MULTNOMAH ROOM

1:30pm-3:00pm

SaC • Self-Organized Second-Harmonic GenerationRaman Kashyap, *British Telecom Research Laboratories, UK, Presider*

1:30pm (Invited)

SaC1 • Imaging the frequency doubling grating in optical fibers, I. C. S. Carvalho, D. C. Reigada, F. C. Garcia, E. N. Hering, W. Margulis, *Pontifica Univ. de Rio de Janeiro, Brazil*; F. Laurell, *Royal Institute of Technology, Sweden*; B. Lesche, *Univ. Federal do Rio de Janeiro, Brazil*. Frequency doubling gratings in optical fibers were imaged with micron resolution by chemical etching. Microscopic studies were performed and macroscopic charge separation was inferred. (p. 28)

2:00pm

SaC2 • Optical preparation of polymers for frequency doubling, J. M. Nunzi, C. Fiorini, F. Charra, *LETI (CEA-Technologies Avancées), France*. The nonlinear optical process that permits all-optical preparation of materials for frequency doubling is described in terms of a polar photo-induced orientation occurring in a centrosymmetric distribution of molecules. Permanent poling of polymers is efficiently achieved by seeding-type preparation with a dual frequency laser. (p. 31)

2:15pm

SaC3 • Paper withdrawn.

2:30pm

SaC4 • Efficient photo-induced second-harmonic generation in ternary barium borosilicate and pure binary lead-silicate glasses, Y. Nageno, Jae H. Kyung, N. M. Lawandy, *Brown Univ.* Efficient second harmonic generation is studied in pure lead-silicate and barium borosilicate glasses. Evidence of dispersive transport in photoinduced $\chi^{(2)}$ eff relaxation is discussed. (p. 35)

2:45pm

SaC5 • Modal and polarization properties of SHG in doped-silica waveguides: transverse modulation effects, John J. Kester, Iyad Dajani, Peter Ranon, Thomas Alley, *Frank J. Seiler Research Laboratory.* Waveguide mode combinations and polarization effects are measured and calculated for planar germanium-doped silica waveguides. (p. 39)

LLOYD CENTER BALLROOM

3:00pm–3:30pm

Coffee Break

MULTNOMAH ROOM

3:30pm–5:15pm

SaD • Photosensitivity and Planar Waveguides and Mechanisms

Gerry Meltz, *United Technologies Research Center, Presider*

3:30pm (Invited)

SaD1 • Photosensitivity in planar waveguides, T. Kitagawa, Y. Hibino, M. Abe, *NTT Opto-Electronics Laboratories, Japan.* We discuss the use of the photo-induced refractive index change in silica-based planar lightwave circuits both for tuning the spectral responses of waveguide devices and for fabricating Bragg gratings in waveguide circuits. (p. 44)

4:00pm

SaD2 • Microscopic investigations of Bragg gratings photowritten in germanosilicate fibers, M. Douay, D. Ramecourt, T. Taunay, P. Bernage, P. Niay, *Univ. des Sciences et Technologies de Lille, France;* A. Dacosta, C. Mathieu, *Univ. Artois à Lens, France;* J. F. Bayon, *France Telecom CNET Technopole Anticipa, France;* B. Pommellec, *Univ. Paris Sud, France.* The fiber cladding was etched at the place of the photowritten Bragg grating. Atomic force microscopy reveals corrugations at core-cladding interface and structural or chemical modifications in core at the grating location. (p. 48)

4:15pm

SaD3 • Evidence of densification in UV-written Bragg gratings in fibers, I. Riant, S. Borne, P. Sansonetti, *Alcatel Alsthom Recherche, France;* B. Pommellec, *Univ. Paris Sud, France.* We show that a densification explaining a part of the index change is associated with Bragg grating inscription in optical fibers as in preforms. (p. 52)

4:30pm

SaD4 • UV-induced stress changes in optical fibers, H. G. Limberger, P. Y. Fonjallaz, R. P. Salathé, *Swiss Federal Institute of Technology;* F. Cochet, *Cabloptic SA, Switzerland.* Bragg grating formation increases the tension in the fiber core. The resulting photoelastic index change is countered by the positive contribution due to structural changes. (p. 56)

4:45pm (Invited)

SaD5 • UV-induced photochemical reactions and point defects in photorefractive $\text{SiO}_2\text{:GeO}_2$ and implanted SiO_2 glasses, Hideo Hosono, Hiroshi Kawazoe, *Tokyo Institute of Technology, Japan;* Junji Nishii, *Osaka National Research Institute, Japan.* Photochemical reactions that occur in $\text{SiO}_2\text{:Ge}$ glasses differ strikingly between a Hg lamp and excimer lasers. Band-to-band excitation effects via 2-photon process are dominant for the laser irradiation. (p. 61)

LLOYD CENTER BALLROOM

6:30pm–8:30pm

Conference Reception

MULTNOMAH ROOM

8:30am–10:30am

SuA • New Materials and Techniques

Robert A. Weeks, *Vanderbilt University, Presider*

8:30am (Invited)

SuA1 • Bragg grating photoinscription within various types of fibers and glasses, P. Niay, P. Bernage, M. Douay, T. Taunay, W. X. Xie, G. Martinelli, *Univ. des Sciences et Technologies de Lille, France*; J. F. Bayon, H. Poignant, E. Delevaque, *France Telecom CNET Lannion*. Bragg grating photoinscription within various types of fibers revealed that aluminosilicate fibers are photosensitized by H₂ loading and that germanosilicate fiber type II. A photosensitivity kinetics depends upon fiber stress. (p. 66)

9:00am

SuA2 • Large photo-induced index changes in Sn-co-doped germanosilicate fibers, L. Dong, J. L. Cruz, L. Reekie, M. G. Xu, D. N. Payne, *Univ. Southampton, UK*. Index change ($\sim 1.4 \times 10^{-3}$) of 3 times larger than in germanosilicate fibers is demonstrated. Both fiber loss at 1.55 μ m and high temperature stability of the gratings are much improved compared to those in B-co-doped germanosilicate fibers. (p. 70)

9:15am

SuA3 • Moving fiber/phase mask-scanning beam technique for writing arbitrary profile fiber gratings with a uniform phase mask, M. J. Cole, W. H. Loh, R. I. Laming, M. N. Zervas, *Univ. Southampton, UK*. We demonstrate a new technique for writing in-fiber gratings with a uniform phase mask. By moving the fiber phase mask while the beam is scanning, a range of important grating profiles, such as multiwavelength gratings, 'pure' apodization, and chirped structures, have been produced. (p. 74)

9:30am (Invited)

SuA4 • Hydrogen-enhanced UV photosensitivity of optical fibers: mechanisms and reliability, Paul J. Lemaire, *AT&T Bell Laboratories*; Turan Erdogan, *Univ. Rochester*. UV exposure of fibers sensitized with H₂ causes several types of defects to form. Annealing ensures the long term stability of UV-induced index changes. (p. 78)

10:00am

SuA5 • Growth dynamics of fiber Bragg gratings written with a KrF excimer laser, Glen M. Williams, Martin A. Putnam, Tsung E. Tsai, Charles G. Askins, E. Joseph Friebele, *U.S. Naval Research Laboratory*. We report the growth dynamics of Bragg gratings written in Ge-doped optical fibers under different exposure conditions (0.5 mJ/cm² to 45 mJ/cm² per pulse). (p. 82)

10:15am

SuA6 • Photosensitization of phosphosilicate fiber Bragg gratings, J. Canning, R. Pasman, M. G. Sceats, *Univ. Sydney, Australia*. The characteristics of optical fiber Bragg gratings written in phosphosilicate fibers at 193 nm are reviewed. Enhanced photosensitivity is demonstrated at this wavelength and characterized using side-diffraction. The results suggest a more complex mechanism than a single-photon absorption process. (p. 86)

LLOYD CENTER BALLROOM

10:30am–11:00am

Coffee Break

LLOYD CENTER BALLROOM

11:00am–12:00m

SuB • Poster Session

SuB1 • A large second-order nonlinearity in poled phosphate glass containing mobile protons, Yuichi Watanabe, Naoyuki Takeshita, Toshio Tsuchiya, *Science Univ. Tokyo, Japan*; Hideo Hosono, Hiroshi Kawazoe, *Tokyo Institute of Technology, Japan*. Second-order nonlinearity induced in binary phosphate glass by the electric-field poling process is explained in terms of the nature of proton-contamination in the glass. (p. 92)

SuB2 • Effective indices of the propagating modes in planar waveguides measured with UV-induced Bragg gratings, Jörg Hübner, Christian V. Poulsen, Lars-Ulrik Aaen Andersen, Martin Kristensen, Thomas Rasmussen, *Technical Univ. Denmark*. Bragg gratings, induced with 193 nm light, have been used to characterize the propagation properties and to measure the effective refractive index in planar waveguides. (p. 96)

SuB3 • Thermal stability of direct UV-written channel waveguides, Christian V. Poulsen, *Technical Univ. Denmark*. The thermal stability of direct UV-written germanium-doped silica channel waveguides is investigated. A difference is found between low and high intensity effects. (p. 100)

SuB4 • New sensitive method for measuring induced refractive index change in optical fiber core, E. M. Dianov, A. S. Kurkov, O. I. Medvedkov, S. A. Vasil'ev, *General Physics Institute, Russia*. We present a new sensitive method for determining the induced refractive index change in the fiber core. The method is based upon the measurement of the loss peak displacement during a long-period grating formation. (p. 104)

SuB5 • Photosensitivity of Ge-doped silica films deposited in a PECVD hollow cathode reactor, M. V. Bazylenko, M. Gross, P. L. Chu, *Univ. New South Wales, Australia*; D. Moss, *Univ. Sydney, Australia*. Ge-doped silica films deposited in a PECVD hollow cathode reactor exhibit UV-induced refractive index changes ranging from -0.00355 to +0.00173. (p. 108)

SuB6 • UV-induced densification during Bragg grating writing, B. Poumellec, *Univ. Paris Sud, France*; P. Niay, M. Douay, *Univ. des Sciences et Technologies de Lille, France*; J. F. Bayon, *Technopole Anticipa France Telecom CNET-Lannion, France*. Corrugations appear on surface of a slice of preform core during grating writing. This is due to densification consistent with the observed refractive index change. (p. 112)

SuB7 • Characterization of long-phase masks for writing fiber Bragg gratings, François Ouellette, Peter A. Krug, Remco Pasman, *Univ. Sydney, Australia*. We analyze the effects of periodic phase shifts due to stitching errors in phase masks made by electron beam lithography. Fiber gratings written with these masks show sidebands, the strength of which is used to determine the value of the phase shift. (p. 116)

SuB8 • All-optically-written planar germanosilicate waveguide gratings, D. Moss, F. Ouellette, *Univ. Sydney, Australia*; M. Faith, P. Leech, P. Kemeny, *Telecom Research Laboratories, Australia*; M. Ibsen, O. Leistiko, C. V. Poulsen, *Mikroelektronik Centret, Denmark*; J. D. Love, F. J. Ladouceur, *Australian National Univ., Australia*. We demonstrate all-optically-written buried waveguide grating structures in PECVD grown germanosilicate trilayers without the aid of hydrogen loading using $\lambda = 193$ nm light. (p. 120)

SuB9 • Linear and nonlinear effects in deep gratings superstructures, N. G. R. Broderick, C. Martijn de Sterke, Benjamin J. Eggleton, *Univ. Sydney, Australia*. We implement a new coupled-mode approach for treating grating superstructures. This approach is accurate, fast and leads to novel soliton solutions. (p. 124)

SuB10 • Characterization of UV-induced birefringence in optical fiber rocking filters, D. C. Psaila, C. M. de Sterke, F. Ouellette, *Univ. Sydney, Australia*. The growth of optical fiber rocking filters in both hydrogenated and unhydrogenated fiber is investigated. We also demonstrate the dependence of rocking filter growth on the energy of the UV writing beam. (p. 128)

SuB11 • In-fiber transmission filters with broad stopbands using chirped Bragg gratings, L. Zhang, K. Sugden, J. A. R. Williams, I. Bennion, *Aston Univ., UK*; D. C. J. Reid, C. M. Ragdale, *GEC Marconi Material Technology Limited*. We demonstrate a new approach to in-fiber transmission bandpass filter fabrication enabling a wide range of bandpass filters with independently controllable passband and stopband characteristics. (p. 132)

SuB12 • Dissimilar wavefront technique for linear and quadratic chirps, Kate Sugden, Lin Zhang, John Williams, Ian Bennion, *Aston Univ., UK*. New regimes of operation of the two-beam interference method for UV-grating writing are presented, offering wide flexibility for producing both linear and nonlinear chirps. (p. 136)

SuB13 • Novel actively modelocked dual-wavelength fiber laser using chirped in-fiber Bragg gratings and its application to all-optical memory, D. A. Pattison, P. N. Kean, J. W. D. Gray, I. Bennion, N. J. Doran, *Aston Univ., UK*. We use chirped in-fiber Bragg gratings to demonstrate a novel, actively mode-locked dual-wavelength fiber laser and apply this source to a novel all-optical memory architecture. (p. 140)

SuB14 • First-principles characterization of structure and properties of E' centers in silica glass, Shashi P. Karna, John J. Kester, Frank J. Seiler *Research Laboratory*. Electronic structure and properties of E' center and its precursor in α -SiO₂ have been calculated for the first time by *ab initio* Hartree-Fock method. (p. 144)

SuB15 • Comparison of UV photosensitivity and fluorescence during fiber grating formation, Heather Patrick, Sarah Gilbert, *NIST-Boulder*. We find that the ultraviolet photosensitivity of optical fiber is strongly correlated with the amount of change in the blue fluorescence emitted during the exposure. (p. 148)

SuB16 • Ion implantation induced photosensitivity in silica and Ge-doped silica, M. Essid, M. Verhaegen, L. B. Allard, J. L. Brebner, *Univ. Montréal, Canada*; J. Albert, *Communications Research Center, Canada*. Refractive index changes larger than 10^{-3} are obtained by excimer laser irradiation of silicon implanted silica and germanium-doped silica. (p. 152)

SuB17 • Photochemical start-up of photorefractivity in SiO₂ and SiO₂: GeO₂ glasses, V. M. Marchenko, *General Physics Institute, Russia*. Start-up of photorefractivity in germanosilicate glasses is explained by the reactions of photodissociation of =Si: and =Ge: oxygen-deficient centers and switching of valent bonds. (p. 156)

SuB18 • Dynamics of UV-induced luminescence and fiber Bragg grating formation in the high fluence regime, Mikael Svalgaard, *Technical Univ. Denmark*. We observe strong nonlinearities in the dynamics of Bragg grating formation and correlate these with the dynamics of a UV induced luminescence band at 650 nm. (p. 160)

12:00m–1:30pm

Lunch (on your own)

MULTNOMAH ROOM

1:30pm–3:00pm

SuC • Poling I

Roger H. Stolen, *AT&T Bell Laboratories, Presider*

1:30pm (Invited)

SuC1 • Glass fiber poling and applications, P. G. Kazansky, V. Pruneri, A. R. Smith, O. Sugihara, L. Dong, P. St. J. Russell, *Univ. Southampton, UK*. Recent developments in the application of poled optical fibers to electrooptic light modulation and second harmonic generation are reviewed. (p. 166)

2:00pm

SuC2 • Creation of optical nonlinearity in organic polymer-dye films by asymmetric charge injection, G. Berkovic, R. Cohen, A. Donval, B. Lavi, R. Yam, *Weizmann Institute of Science, Israel*. Asymmetric charge injection can create second-order optical nonlinearity in organic polymer-dye systems. Similarities and differences with glass poling will be discussed. (p. 169)

2:15pm (Invited)

SuC3 • Frequency doubling in thin film waveguides of borate glasses, Keisuke Sasaki, Suguru Horinouchi, *Keio Univ., Japan*. Novel quadratic nonlinearities in multi component glass films on various glass substrates were developed by usual corona poling processing. Phase-matched blue second-harmonic generation (SHG) in a tapered nonlinear glass waveguide was observed using a Ti:sapphire laser 860 nm fundamental input. (p. 172)

2:45pm

SuC4 • Laser-induced pressure pulse probe of charge distribution in thermally poled glass: evidence of dipole polarization? P. G. Kazansky, A. R. Smith, P. St. J. Russell, *Univ. Southampton, UK*; G. M. Yang, G. M. Sessler, *Technical Univ. Darmstadt, Germany*. For the first time charge distributions in thermally poled silica glass are mapped by using laser induced pressure pulse technique. The experimental results may be explained through postulating the formation of both real space charge layers and dipole polarization inside the depletion region. (p. 175)

LLOYD CENTER BALLROOM

3:00pm–3:30pm

Coffee Break

SUNDAY

SEPTEMBER 10, 1995

MULTNOMAH ROOM

3:30pm-4:45pm

SuD • Poling II

Philip St. J. Russell, *University of Southampton, UK, Presider*

3:30pm (Invited)

SuD1 • UV-excited poling of germanosilicate fiber, S. C. Fleming, T. Fujiwara, D. Wong, *Univ. Sydney, Australia*. Practical electro-optic fiber devices are realized using UV-poling of germanosilicate fibers, yielding high electro-optic coefficients. Fiber design, poling (including periodic) conditions and characterization are discussed. (p. 180)

4:00pm

SuD2 • Measurement of photo-induced charge distribution in seeded second-harmonic generation by charge-selective etching in glasses, Jae H. Kyung, N. M. Lawandy, *Brown Univ.* Using a new charge-selective etching process, we measured the charge distribution at high and low encoding intensities responsible for second harmonic generation in glasses. (p. 184)

4:15pm

SuD3 • Second-harmonic generation in low-water fused silica by proton implantation, Leanne J. Henry, Thomas G. Alley, Dennis S. Rand, John J. Kester, *Frank J. Seiler Research Laboratory*. A nonlinear optical layer having a $\chi^{(2)}$ as high as 1.4 pm/V was generated in low-water fused silica by proton implantation. (p. 188)

4:30pm

SuD4 • Charge trapping in metal ion-activated quantum dot-doped silica glasses, Alan L. Huston, Brian L. Justus, *U.S. Naval Research Laboratory*. Metal ion-activated quantum dot-doped silica glasses containing nanocrystalline ZnS exhibit significant charge trapping behavior. Thermally stable photoinduced and photoreversible birefringence is observed in the ZnS:Cu²⁺-doped glass. Trap densities and storage times are estimated from thermoluminescence measurements. (p. 192)

MULTNOMAH ROOM

4:45pm-6:00pm

Postdeadline Papers

R. P. Salathé, *Swiss Federal Institute of Technology, Switzerland, Presider*

MULTNOMAH ROOM

8:30am–10:00am

PMA • Materials Studies

François Ouellette, *University of Sydney, Australia, Presider*

8:30am (Invited)

PMA1 • Formation of nonlinear optical materials by ion implantation, Robert H. Magruder, III, *Vanderbilt Univ.* Ion implantation offers a flexible technique to form nanometer dimension metal particles in dielectrics for nonlinear optical materials. These nanocluster glass composites have some unique properties that may make them viable candidates for all optical switching networks. (p. 196)

9:00am

PMA2 • Direct correlation between UV-excited photo-luminescence and refractive index change in photosensitive Ge-doped and hydrogenated optical fiber, Jean Martin, Michel Têtu, Jean Deslauriers, Michel A. Duguay, *Univ. Laval, Canada*; Graham Atkins, François Ouellette, *Univ. Sydney, Australia*. We report to our knowledge the first direct correlation between the UV ($\lambda = 266$ nm) excited blue photo-luminescence and refractive index change during Bragg grating growth in Ge-doped and hydrogen loaded fiber. (p. 200)

9:15am

PMA3 • Mechanisms of photo-bleaching of 5 eV absorption band in hydrogen loaded Ge-doped SiO₂, Koichi Awazu, Hideo Onuki, *Electrotechnical Laboratory, Japan*; Ken-ichi Muta, *Showa Electrical Wire & Cable Co. Ltd., Japan*. Photo-bleaching of 5 eV absorption band in hydrogen loaded Ge-doped SiO₂ was studied. Photochemical reactions with H₂ molecules in the glass were proposed. (p. 204)

9:30am

PMA4 • UV laser-induced photocurrent in oxygen-deficient silica and germanosilicate glasses, Victor N. Bragatashvili, Svetlana I. Tsykina, Pavel V. Chernov, Aleksey O. Rybaltovskii, Yurly S. Zavorotny, Sergey S. Alimpiev, Yaroslav O. Simanovskii, *Laser Chemistry Research Center, Russia*; Liang Dong, Philip St. J. Russell, *Univ. Southampton, UK*. UV laser-induced excitation and ionization of silicon oxygen deficient centers (SODC) in silica glasses and germanium oxygen deficient centers (GODC) in germanosilicate glasses has been studied by direct displacement photocurrent and photoluminescence measurements. For both SODC and GODC the two-photon nature of photoionization has been established. (p. 208)

9:45am

PMA5 • Characterization of photosensitivity in germanosilicate, Christian V. Poulsen, Søren Haugbølle, Jörg Hübner, *Technical Univ. Denmark*. The photosensitivity of plasma-enhanced chemical vapor deposited germanium doped silica thin films is investigated at UV wavelengths at 193 and 244 nm. (p. 212)

LLOYD CENTER BALLROOM

10:00am–10:30am

Coffee Break

MULTNOMAH ROOM

10:30am–12:30pm

PMB • Sensors and Theory I

Walter Margulis, *Imperial College, UK, Presider*

10:30am (Invited)

PMB1 • Fiber optic Bragg grating sensor systems for multi-point distributed strain monitoring, Alan D. Kersey, *U.S. Naval Research Laboratory*. Fiber Bragg grating (FBG) based sensors represent one of the most exciting developments in the area of fiber sensor technology in recent years. A wide range of sensor types and interrogation techniques is possible, and methods for addressing multiple FBG elements along a fiber have been developed. This presentation reviews this rapidly emerging area of fiber sensing and describes some of the potential applications of the technology. (p. 216)

11:00am

PMB2 • Chirped fiber gratings for temperature-independent strain sensing, M. G. Xu, L. Dong, L. Reekie, J. A. Tucknott, J. L. Cruz, *Univ. Southampton, UK*. A temperature-independent strain sensor using a chirped fiber grating is demonstrated with a strain resolution of 0.1% over the total measurement range. (p. 217)

11:15am (Invited)

PMB3 • Photo-induced birefringence and applications in sensing, V. A. Handerek, S. E. Kanellopoulos, *King's College London, UK*. Abstract not available. (p. 221)

11:45am

PMB4 • Wavelength shifts in fiber Bragg gratings due to changes in the cladding properties, G. Meltz, *United Technologies Research Center*; W. W. Morey, *3M Bragg Grating Technologies*; S. J. Hewlett, J. D. Love, *Australian National Univ., Australia*. Tuning of Bragg grating resonances due to changes in the evanescent field are characterized. Large shifts in birefringence are observed in etched e-core fiber. (p. 225)

12:00m (Invited)

PMB5 • Photosensitive processes in silica glass using 193-nm light, Jacques Albert, *Communications Research Centre, Canada*. The effects of 193-nm ArF excimer laser light on the optical absorption of several silica glasses and on fiber Bragg grating fabrication are reviewed. (p. 229)

12:30pm–2:00pm

Lunch (on your own)

MULTNOMAH ROOM

2:00pm-3:30pm

PMC • Sensors and Theory II

P. Niay, *Laboratoire de Dynamique, France, Presider*

2:00pm (Invited)

PMC1 • Advances in fiber grating sensors, W. W. Morey, G. A. Ball, *3M Bragg Grating Technologies*; G. Meltz, J. R. Dunphy, *United Technologies Research Center*; A. D. Kersey, *U.S. Naval Research Laboratory*. A couple of new decoding schemes for fiber grating sensors use matched gratings and acousto-optic tunable filter in the decoding unit. These systems can measure many grating transducer elements simultaneously with high sensitivity. Short cavity fiber lasers that utilized fiber gratings can also act as sensor transducer elements giving one ultra high sensitivities that are limited by the fundamental noise in the fiber. One fiber laser sensor uses heterodyning to generate a signal that can be measured on an rf spectrum analyzer. New techniques for simultaneous measurement of temperature and strain are also discussed. (p. 234)

2:30pm

PMC2 • Cladding-mode resonances in Bragg fiber gratings: depressed- and matched-cladding index profiles, S. J. Hewlett, J. D. Love, *Australian National Univ., Australia*; G. Meltz, T. J. Bailey, W. W. Morey, *United Technologies Research Center*. Transmission spectra of Bragg gratings in depressed- and matched-cladding fibers are characterized. The fine-structure features arise from power coupling to discrete cladding modes. (p. 235)

2:45pm

PMC3 • Fiber grating filters based on radiation- and cladding-mode coupling, T. Erdogan, *Univ. Rochester*; J. E. Sipe, *Univ. Toronto, Canada*. Measurements and calculations show how grating tilt can control the grating loss spectrum and nullify bound-mode Bragg reflection, and how cladding modes affect the spectrum. (p. 239)

3:00pm

PMC4 • Super coupled mode equations for periodic superstructure Bragg gratings, C. Martijn de Sterke, Neil G. R. Broderick, *Univ. Sydney, Australia*. Periodic superstructure gratings are gratings with periodically varying parameters. We apply a novel coupled mode theory, using the envelopes of the usual envelope functions to these structures. (p. 243)

3:15pm

PMC5 • Chirp, self-chirp and meta-chirp in sampled fiber gratings, François Ouellette, Benjamin J. Eggleton, Peter C. Hill, Peter A. Krug, *Univ. Sydney, Australia*. We show that a chirp applied to a sampled fiber grating broadens all the reflection peaks in the same way. The refractive index change in the exposed regions shifts the envelope. A chirp in the sampling period results in a different chirp for the different reflection peaks. (p. 247)

LLOYD CENTER BALLROOM

3:30pm-4:00pm

Coffee Break

MULTNOMAH ROOM

4:00pm-5:45pm

PMD • Fiber Lasers

Gary A. Ball, *3M Bragg Grating Technologies, Presider*

4:00pm (Invited)

PMD1 • Laser applications of fiber gratings, Laurence Reekie, *Univ. Southampton, UK*. Fiber gratings can be usefully incorporated into the cavities of fiber and semiconductor lasers. This paper describes both past achievements and recent advances in the field. (p. 252)

4:30pm

PMD2 • Hamiltonian approach to propagation in chirped and non-uniform Bragg grating structures, P. St. J. Russell, T. A. Birks, *Univ. Southampton, UK*. The frequency-dependent time delay in chirped Bragg gratings, and the trapping of light at defects in otherwise uniform gratings, are treated and analytically using a Bloch wave Hamiltonian. The approach provides benefits in insight and an appealing physical picture. (p. 257)

4:45pm

PMD3 • Grating Michelson mirrors for optimized fiber laser performance, Kate Sugden, Ian Bennion, *Aston Univ., UK*; Kevin Byron, Howard Rourke, Sandra Davies, *BNR Europe Ltd., UK*. The novel use of fiber grating Michelson reflectors gives reflection tunability and background noise suppression for fiber lasers and FM/AM frequency stabilization for semiconductor lasers. (p. 261)

5:00pm

PMD4 • Fiber ring laser with fiber grating transmission filter, M. C. Farries, D. C. Reid, *GMMT, UK*; L. Zhang, I. Bennion, *Aston Univ., UK*. An erbium-doped ring laser is described in which single-frequency operation below 10 kHz linewidth is achieved by incorporation of a fiber grating transmission filter into a unidirectional ring. (p. 265)

5:15pm

PMD5 • Photo-induced absorption and photo bleaching in thulium-doped fluorozirconate fibers, Pierre Laperle, Alain Chandonnet, *National Optics Institute, Canada*; Réal Vallée, *Univ. Laval, Sainte Foy, Canada*. Photo-induced absorption is observed in thulium-doped fluorozirconate fibers exposed to 1.12- μ m radiation. The fibers are subsequently bleached when exposed to 488 nm radiation. (p. 269)

5:30pm

PMD6 • Photo-darkening in upconversion-pumped thulium-doped fluorozirconate fiber lasers, I. J. Booth, J.-L. Archambault, B. F. Ventrudo, *Seastar Optics Inc., Canada*. Thulium-doped fluorozirconate fiber is observed to undergo photodegradation when pumped at 1130 nm. A multistep upconversion process is shown to occur, generating color center defects. (p. 273)

5:45pm-6:00pm

Closing Remarks

Saturday, September 9, 1995

Plenary

SaA 8:30–10:30am
Multnomah Room

Ken O. Hill, *Presider*
Communications Research Center, Canada

Optical Devices Based on Photo-induced Index Changes in Silica

A. M. Glass
AT&T Bell Laboratories
Murray Hill NJ 07974

The discovery of photo-induced index changes in silica has formed the basis for a large number of novel optical devices. This talk reviews both fiber and planar waveguide devices of interest for communications.

In-Fiber Bragg Grating Devices for Telecommunications Applications

David R. Huber
Ciena Corporation
1340-C Ashton Road
Hanover MD 21076

The in-fiber Bragg grating is one of the most important developments in fiber telecommunications in this decade. Fiber Bragg gratings have been demonstrated that have reflectivity ranging from zero to almost one. Simple gratings have been demonstrated that have bandwidths ranging from a few GHz to many nanometers. Fiber gratings have found application in continuous wave and mode locked lasers, fiber dispersion compensation, pulse compression, fixed and tunable optical filters, add-drop filters and as demultiplexing elements. This paper will review telecommunication devices that have been realized with this key technology.

Perspectives in Glass Poling*

S. R. J. Brueck

Center for High Technology Materials

University of New Mexico

Albuquerque NM 87131

Glass has long been established as the lowest loss and most manufacturable optical material. However, the low third-order nonlinearity of silica glasses and the absence of a second-order nonlinearity, forbidden by the inherent macroscopic inversion symmetry of amorphous materials, have resulted in many material investigations searching for a suitable complimentary nonlinear optical material. To date, no material has been found that combines a strong nonlinearity with the unrivaled optical transparency, manufacturing flexibility, environmental stability, and optoelectronic and microelectronic integrability of glass.

Thus, the discovery of a significant ($\sim \text{pm/V}$) second-order nonlinearity in glass poled by application of an electric field at modest temperatures ($200\text{--}300^\circ\text{C}$) has excited significant interest, both in the physics of this new nonlinearity and in potential applications. Glass poling has been investigated in bulk materials, thin-film waveguides, and optical fibers. Poling techniques including electric field/temperature and electric field/UV exposure, analogous to the photosensitive modification of the linear glass refractive index, have been demonstrated. Present status and outstanding questions of the physics of the poling process will be reviewed.

Emerging applications of poled glass materials for both electro-optic effect and frequency conversion (second-harmonic generation) will also be discussed.

*Funding for this work provided by the Air Force Office of Scientific Research and the C. S. Draper Laboratory.

Saturday, September 9, 1995

Fiber Gratings in Communications

SaB 11:00am–12:30pm
Multnomah Room

Paul J. Lemaire, *Presider*
AT&T Bell Laboratories

Fiber Bragg Components in Filtering and Dispersion Compensation Applications

K. O. Hill

*Communications Research Centre
3701 Carling
P. O. Box 11490, Station "H"
Ottawa, Ontario, Canada
K2H 8S2*

Introduction

The photorefractive effect,^[1] "photosensitivity", has great practical value in that it makes possible a family of novel passive fiber devices that have applications in optical communications and optical sensors.^[2]

In this invited paper, the application of photosensitivity technology to the fabrication of optical fiber filters and dispersion compensators is discussed in the context of work carried out at the Communications Research Centre. It is shown that photosensitivity technology is a flexible fabrication process allowing the manufacture of devices with a wide range of performance parameters.

Bragg grating based optical fiber filters

Bragg reflectors are easily photoimprinted in optical fibers using the phase mask technique.^[3] However, the manufacture of fiber components to predetermined performance parameters requires techniques to control the resonant wavelength, bandwidth and reflectivity of the Bragg reflector. Fortunately, photosensitivity technology offers several methods for controlling these parameters.

Firstly, although standard telecommunication fiber is photosensitive, its inherent photosensitivity is too weak. Only refractive index changes of 10^{-4} are obtainable, whereas index changes of 10^{-3} are needed in the manufacture of practical fiber components. The photosensitivity of standard optical fiber can be enhanced by hydrogen loading^[4] or flame brushing.^[5] Recently, it has also been shown that index changes of 10^{-3} can be obtained in standard optical fiber simply by by photoimprinting the Bragg gratings using 193 nm light with irradiation at high intensity levels.^[6] This result has the practical advantage of avoiding some of the problems associated with hydrogen loading and flame brushing: the drift in the

resonant frequency of a Bragg reflector photoimprinted in hydrogen loaded fiber as the hydrogen diffuses out of the fiber and distortions in the optical waveguide that are sometimes created during the flame brushing photosensitization process.

The bandwidth of Bragg reflectors can be controlled by varying the length of the grating and the strength of the photoinduced index modulation. This method is limited, however, and the fabrication of reflectors with large bandwidths requires a different approach such as chirping the pitch of the photoinduced index gratings.

Chirped gratings can be photoimprinted using a phase mask by including an additional step in the irradiation procedure.^[7] It is also feasible to chirp a uniform pitch Bragg grating by applying a nonuniform strain along the length of the grating.^[8] Using this latter method, optical fiber filters can be made in which the resonant wavelength and the bandwidth are adjustable independently.

Another important performance parameter of Bragg reflectors is the reflection response for wavelengths outside the filter bandwidth. A finite-length Bragg grating with uniform modulation typically has in its reflection response a series of sidelobes on both sides of the main reflection peak. In applications such as wavelength division multiplexing, these sidelobes need to be suppressed in order to reduced the separation (guard space) between the optical carriers. The sidelobes can be suppressed by designing filters that are apodized.^{[9], [10]} Apodized Bragg reflectors have been made using two different techniques.^{[11], [12]} The resulting reflectors are suitable for operation in WDM systems with 100 GHz channel spacings.

The fabrication of transmission filters and wavelength selective taps based on fiber Bragg grating reflectors requires the use of fused optical fiber coupler technology.^{[13], [14]} Even in this part of the filter fabrication process, photosensitivity has proven to be useful for trimming the coupling and balancing the fiber interferometer.^[15]

Dispersion Compensators

The concept that chirped Bragg reflector operating in the reflection mode can be used to compensate the dispersion of an optical fiber has been known for some time.^[9] It is only recently that a demonstration of the concept has been possible.^[16]

The techniques used to fabricate the chirped grating for the compensator is similar to that used in the fabrication of large bandwidth optical filter. A major difference between dispersion compensators and filters is that dispersion compensators have the requirement that the relative delay for optical pulses with different wavelengths is linear across the bandwidth of the compensator. It has been discovered that apodization can be used to obtain a linear relative delay characteristic.

REFERENCES

1. K. O. Hill, Y. Fujii, D. C. Johnson and B. S. Kawasaki, "Photosensitivity in optical fiber waveguides: Application to reflection filter fabrication", *Applied Physics Letters*, Vol. 32, No. 10, pp. 647-649, May 15, 1978.
2. K. O. Hill, B. Malo, F. Bilodeau, and D. C. Johnson, "Photosensitivity in optical fibers", *Annual Review of Material Science*, Vol. 23, pp. 125-157, 1993.
3. K. O. Hill, B. Malo, F. Bilodeau, D. C. Johnson, and J. Albert, "Bragg gratings fabricated in monomode photosensitive optical fiber by UV exposure through a phase mask", *Applied Physics Letters*, Vol. 116: 62, No. 10, pp. 1035-1037, March 8, 1993.
4. P. J. Lemaire, R. M. Atkins, V. Mizrahi and W. A. Reed, "High pressure H_2 loading as a technique for achieving ultrahigh UV photosensitivity and thermal sensitivity in GeO_2 doped optical fibres", *Electronics Letters*, Vol. 29, No. 13, pp. 1191-1193, June 24, 1993.
5. F. Bilodeau, B. Malo, J. Albert, D. C. Johnson, K. O. Hill, Y. Hibino, M. Abe, and M. Kawachi, "Photosensitization of optical fiber and silica-on-silicon/silica waveguides", *Optics Letters*, Vol. 18, No. 12, pp. 953-955, June 15, 1993.
6. B. Malo, J. Albert, K. O. Hill, F. Bilodeau, D. C. Johnson and S. Thériault, "Enhanced photosensitivity in lightly doped standard telecommunications fibre exposed to high fluence ArF excimer laser light", submitted to *Electronic Letters*.
7. K. O. Hill, F. Bilodeau, B. Malo, T. Kitagawa, S. Thériault, D. C. Johnson, J. Albert and K. Takiguchi, "Aperiodic in-fiber Bragg gratings for optical fiber dispersion compensation", *Optical Fiber Communication Conference, OFC'94*, San Jose, California, February 20-25, 1994, Technical Digest, Postdeadline Papers, PD17, pp. 17-20, February 24, 1994.
8. K. O. Hill, B. Malo, F. Bilodeau, S. Thériault, D. C. Johnson, and J. Albert, "Variable Spectral Response Optical Waveguide Bragg Grating Filters for Optical Signal Processing", Paper accepted for publication in *Optics Letters*.
9. K. O. Hill, "Aperiodic Distributed-Parameter Waveguides for Integrated Optics", *Applied Optics*, Vol. 13, pp. 1853-1856, August 1974.
10. M. Matsuhara and K. O. Hill, "Optical-waveguide band-rejection filters: Design", *Applied Optics*, Vol. 13, pp. 2886-2888, December 1974.
11. B. Malo, S. Thériault, D. C. Johnson, F. Bilodeau, J. Albert, and K. O. Hill, "Apodised in-fibre Bragg grating reflectors photoimprinted using a phase mask", *Electronics Letters*, Vol. 31, No. 3, pp. 223-225, February 2, 1995.
12. J. Albert, K. O. Hill, B. Malo, S. Thériault, F. Bilodeau, D. C. Johnson and L. E. Erickson, "Apodisation of the spectral response of fibre Bragg gratings using a phase mask with variable diffraction efficiency", *Electronics Letters*, Vol. 31, No. 3, pp. 222-223, February 2, 1995.
13. K. O. Hill, D. C. Johnson, F. Bilodeau and S. Faucher, "Narrow-bandwidth optical waveguide transmission filters: A new design concept and applications to optical fibre communications", *Electronics Letters*, Vol 23, No. 9, pp. 465-466, April 23, 1987.
14. D. C. Johnson, K. O. Hill, F. Bilodeau and S. Faucher, "New design concept for a narrowband wavelength-selective optical tap and combiner", *Electronics Letters*, Vol. 23, No. 13, pp. 668-669, June 1987.

15. F. Bilodeau, D. C. Johnson, S. Thériault, B. Malo, J. Albert, and K. O. Hill, "An all-fiber dense-wavelength multiplexer/demultiplexer using photoimprinted Bragg gratings", *IEEE Photonics Technology Letters*, Vol. 7, No. 4, pp. 388-390, April, 1995.
16. K. O. Hill, S. Thériault, B. Malo, F. Bilodeau, T. Kitagawa, D. C. Johnson, J. Albert, K. Takiguchi, T. Kataoka, and K. Hagimoto, "Chirped in-fibre Bragg grating dispersion compensators: Linearization of the dispersion characteristic and demonstration of dispersion compensation in a 100 km, 10 Gbit/s optical fibre link", *Electronics Letters*, Vol. 30, No. 21, pp. 1755-1756, October 13, 1994.

Long-period cladding-mode-coupled fiber gratings: properties and applications

A. M. Vengsarkar, P. J. Lemaire, G. Jacobovitz-Veselka, J. B. Judkins,
V. Bhatia,[‡] T. Erdogan*, and J. E. Sipe*

AT&T Bell Laboratories, 600 Mountain Avenue, Murray Hill, NJ 07974

[‡]Virginia Tech, *University of Rochester, and *University of Toronto

Introduction

In a recent paper,¹ we introduced compact, low insertion-loss long-period optical fiber gratings that function as spectrally-selective loss elements. These devices are useful as ASE filters to improve erbium amplifier performance and as band-rejection filters in Raman lasers/amplifiers.² In this paper, we present a detailed description of their properties in terms of their dependence on strain, temperature, recoating and sensitivity to bends. Two new applications, gain-flattening of optical amplifiers and stabilization of errant laser diodes, are described.

The fabrication principle of these devices is based on the ability to induce large index changes in hydrogen loaded germanosilicate fibers by exposing the cores to uv light, typically, in the 242-248 nm range.³ Long-period fiber gratings with periodicities in the hundreds of microns have been used in the past for coupling from one guided mode to another.^{4,5} The grating periodicities in our devices are chosen such that the guided fundamental mode in a single-mode fiber couples out to forward-propagating cladding modes, which in turn, decay rapidly as they propagate along the fiber axis owing to the lossy cladding-coating interface and bends in the fiber. Since the coupling is wavelength-selective, the grating acts as a wavelength-dependent loss element. The wavelength at which the coupling from the guided to cladding modes takes place is dependent on the periodicity, Λ , the photoinduced index change, Δn_{uv} and is related to the phase-matching condition, $\beta_{01} - \beta_{cl}^{(n)} = 2\pi/\Lambda$, where the β 's denote the propagation constants of the respective modes.

Properties

Hydrogen loaded germanosilicate fibers were exposed to a KrF laser through an amplitude mask.

In Fig. 1, we show the transmission spectrum of a strong grating of length 2.54 cm written with a grating period $\Lambda = 402 \mu\text{m}$. The maximum loss is 32 dB at a peak wavelength $\lambda_p = 1517 \text{ nm}$, the 20 dB isolation point is 4 nm wide and the insertion loss is $< 0.20 \text{ dB}$ for wavelengths $< 1480 \text{ nm}$ and $> 1545 \text{ nm}$. This grating can be used as an ASE suppressor, presenting a near-transparent path to the pump and signal wavelengths. An optical coherence domain reflectometer trace shows backreflections typically less than -80 dB. The backreflection numbers are consistent with our estimate of maximum Δn_{uv} of 5×10^{-4} . Measured values of polarization mode dispersion $< 0.01 \text{ ps}$ and polarization dependent loss $< 0.02 \text{ dB}$ indicate minimum sensitivity to polarization effects.

The characteristics of long-period fiber gratings are affected by external perturbations such as strain, temperature and bends. The effect is primarily due to a differential change induced in the two modes. The temperature dependence of the peak wavelength in the transmission spectrum for four different lengths of gratings written in DSFs is shown in Fig. 2. The slope is found to vary from $0.04 - 0.05 \text{ nm/}^\circ\text{C}$. We see that neither the length of the grating nor the peak wavelength significantly affects the temperature sensitivity. By means of comparison, a Bragg grating peak wavelength shifts by about 1.1 nm for a 100°C change (slope $\approx 0.01 \text{ nm/}^\circ\text{C}$). The effect of strain on the grating is more dependent on the type of fiber. The variations in peak wavelengths with strain for two different fibers are plotted in Fig. 3. Grating A exhibits a slope of $-0.7 \text{ nm/m}\epsilon$, while grating B has a slope of $+1.5 \text{ nm/m}\epsilon$. This dramatic dependence on the fiber type is currently being studied. In comparison, Bragg gratings show a strain dependence of $+1.0$ to $+1.8 \text{ nm/m}\epsilon$.

A low-index ($n = 1.38$) polymer coating was applied to a grating whose transmission spectrum had three peaks at $\lambda_1 = 1479.0 \text{ nm}$, $\lambda_2 = 1510.2 \text{ nm}$, and $\lambda_3 = 1564.2 \text{ nm}$, corresponding to the coupling of the $\text{LP}_{01, \text{core}}$ to the $\text{LP}_{01, \text{cl}}$, $\text{LP}_{02, \text{cl}}$ and $\text{LP}_{03, \text{cl}}$ modes, respectively. After recoating, the three peaks shifted by -0.4 , -1.2 , and -2.4 nm , respectively. The relative amplitudes of these shifts are consistent with the relative mode confinement.

Applications

For gain-flattening of erbium doped fiber amplifiers over the entire 1530-1560 nm range, one typically desires a device with an inverted erbium gain spectrum, the losses of the filter corresponding to the difference in the gain peaks. The maximum loss in the transmission spectrum

of a device can be controlled by inducing different levels of Δn_{uv} in the hydrogen-loaded fiber during fabrication. Using this approach, we have fabricated spectral shape-shifters that compensate for the peaks at ~ 1530 and ~ 1560 nm by concatenating two gratings of different periodicities. The transmission spectrum of such a gain-flattening device, fabricated by varying exposure conditions in the range $\Lambda = 474 - 492$ μm , are shown in Fig. 4.

A novel application of these gratings is in countering the band-gap filling effect⁶ seen in Bragg-grating stabilized 980 nm pump-diodes. The laser has a tendency of to split its spectrum and lase at $\lambda > 980$ nm, thus rendering it ineffective for erbium pumping applications. The insertion of a small band-rejection filter at ~ 1 μm can overcome this effect⁷ as shown in Fig. 5.

Conclusion

We have presented properties of long-period gratings that function as spectrally selective loss elements. These all-fiber devices have low insertion losses, low back-reflections and excellent polarization insensitivity, and have been used effectively for gain-flattening of optical amplifiers and in stabilizing semiconductor pump diodes.

References

1. A. M. Vengsarkar *et al.*, Proc. OFC '95, San Diego CA, March 1995, Postdeadline Paper, PD4. Also, J. Lightwave Technol., To be published.
2. S. G. Grubb *et al.*, Proc. Optical Amplifiers Meeting, Breckenridge CO, August 1994, Paper PD3.
3. P. J. Lemaire, R. M. Atkins, V. Mizrahi, and W. A. Reed, *Electron. Lett.* **29**, 1191 (1993).
4. K. O. Hill *et al.*, *Electron. Lett.* **26**, 1270 (1990).
5. K. O. Hill, F. Bilodeau, B. Malo, and D. C. Johnson, *Electron. Lett.* **27**, 1548 (1991).
6. C. R. Giles, T. Erdogan, V. Mizrahi, *IEEE Photon. Technol. Lett.*, **6**, 907 (1994).
7. G. Jacobovitz-Veselka, *et al.*, Proc. Optical Amplifier Meeting, Davos Switzerland, June 1995, Paper FC4.

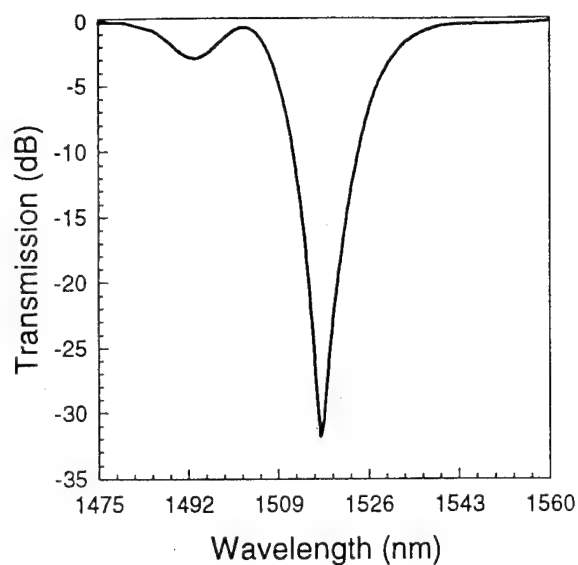


Figure 1. Transmission spectrum of ASE suppression filter.

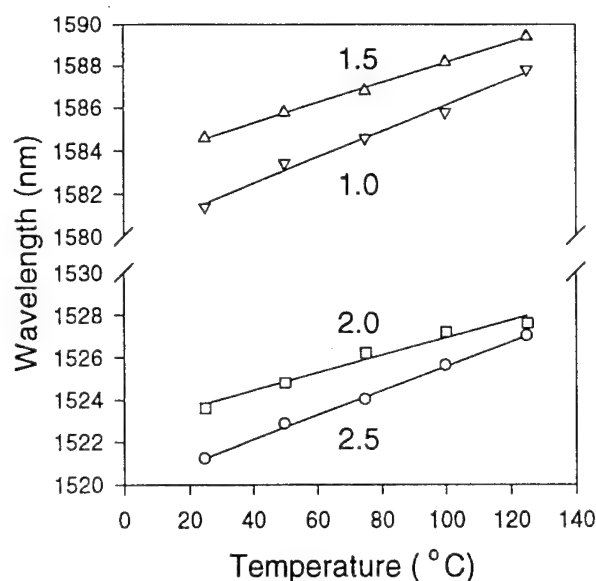


Figure 2. Effect of temperature on peak wavelength for different lengths (cms).

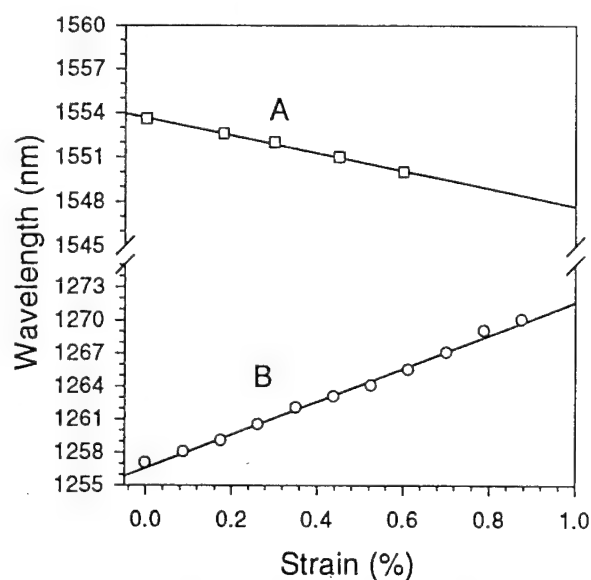


Figure 3. Effect of strain on peak wavelength in two fibers A & B.

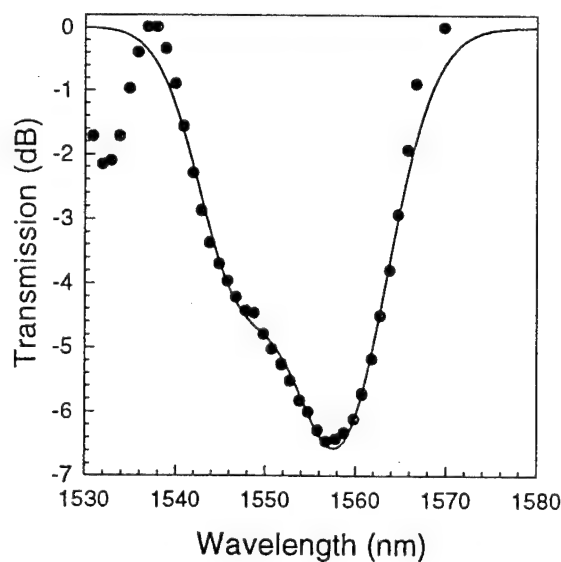


Figure 4. Gain flattening filter data. •: Inverted Er spectrum ; Solid Line: Filter spectrum.

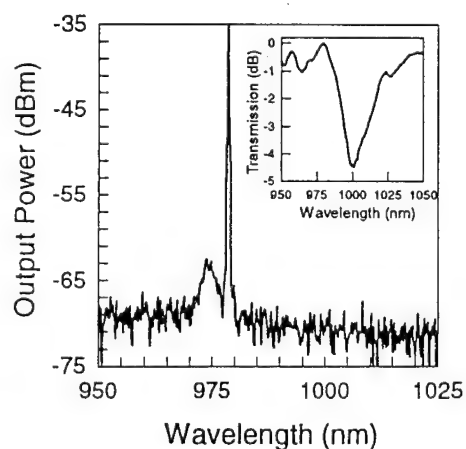
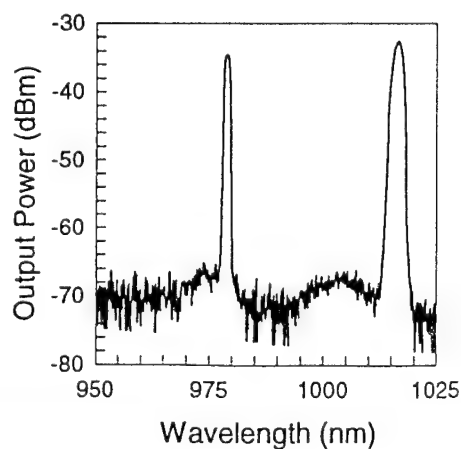


Figure 5. Stabilization of 980 nm laser diode. Inset shows grating transmission spectrum.

GAIN SPECTRUM FLATTENING OF ERBIUM-DOPED FIBER AMPLIFIER USING LONG-PERIOD FIBER GRATING

**E.M. Dianov, V.I. Karpov, A.S. Kurkov, O.I. Medvedkov,
A.M. Prokhorov, V.N. Protopopov, S.A. Vasil'ev**

*Fiber Optics Research Center at the General Physics Institute
of the Russian Academy of Sciences, 38 Vavilov Street, 117942, Moscow, Russia
Fax: (095) 135-8139*

INTRODUCTION

The gain spectrum nonuniformity is one of the most important problems in using erbium-doped fiber amplifiers (EDFA) in wavelength-division-multiplexing transmission systems. Several techniques for the gain spectrum flattening with the use of passive filters have been proposed: mechanical deformation of the fiber to couple fundamental and leaky modes [1], etching of the grating at the surface of a D-fiber [2], utilization of a twin-core fiber filter [3], application of photoinduced fiber Bragg grating [4], application of a Fourier filter based on the incorporation of the glass plate [5] or a tapered fiber filter [6].

The application of photoinduced fiber Bragg gratings appears to be the most suitable filter for the gain control, because it allows one to suppress the sharp narrow gain peak at 1532 nm without affecting the signal at another wavelength and the pumping. However, the application of conventional fiber Bragg gratings demands suppressing the reflected signal power, thereby complicating the gain flattening technique. On the other hand, long-period fiber gratings, described in [7], have similar transmission spectra and do not give rise to the above problem, because these gratings operate using the coupling of propagated and leaky modes. In addition, these gratings are more easy to prepare, as its period is several hundreds of microns. Such fiber gratings also have the following advantages: fiber compatibility, low additional loss. A low insertion loss at the pump wavelength in the vicinity of 980 nm allows one to insert the grating into the middle of an EDFA to suppress the build-up of an amplified spontaneous emission in the region of 1532 nm.

In this report we present for the first time the application of the long-period fiber grating with a transmission dip at 1532 nm to achieve a broad and flat gain spectrum.

FIBER GRATING FABRICATION

Operation of long-period fiber gratings is based on the coupling of fundamental and leaky cladding modes. The wavelengths corresponding to the coupling are described by the

following equation:

$$\beta_{01} - \beta_n^{cl} = 2\pi/\Lambda \quad (1),$$

where β_{01} and β_n^{cl} are the propagation constants of the fundamental and the n^{th} -order cladding mode, Λ is the grating period. For conventional single-mode fibers and for the first cladding modes, condition (1) is satisfied in the 1-1.6 μm wavelength region when the grating period lies in the range 10^2 - 10^3 μm .

The experimental configuration for the long-period grating preparation is shown in Fig.1. We used a germanosilicate core fiber with a 0.018 index difference and a 800 nm cut-off wavelength. The fiber was irradiated through an amplitude mask by 300 mJ/cm^2 pulses at a 248 nm wavelength from KrF laser. The pulse frequency was 20 Hz, and exposure time, 15 min. The mask period was 350 μm , and the grating length was 70 mm. The transmission spectrum was measured during the UV-exposure by an optical spectrum analyser (OSA). The spectrum of the prepared grating in the region of 1550 nm is shown in Fig.2. No additional loss at 980 nm was detected.

EXPERIMENT

We used an erbium-doped fiber based on the aluminosilicate germanium-free host glass. The erbium ion concentration estimated from the absorption spectrum was 500 ppm. The fiber had an effective refractive index difference of 0.02 and a cut-off wavelength of 0.90 μm . The gain spectra were investigated using a pump light at 978 nm from a Ti:Sapphire laser and a signal light from an erbium-doped fiber laser.

The gain spectrum of the 17 m long EDFA measured with an input signal of -30 dBm and an input pump power of 40 mW is shown in Fig.3 (curve 1). The gain of more than 30 dB was obtained in a spectral region broader than 35 nm owing to a high aluminium concentration. Nevertheless, the difference of the gain at 1532 nm and 1555 nm was still ~8 dB.

To flatten the gain spectrum, the grating with a transmission spectrum shown in Fig.2 was spliced into the middle of the EDFA. The gain measurements were carried out under the same conditions as for the reference EDFA. As seen from curve 2 in Fig.3, the gain peak in the vicinity of 1532 nm is completely suppressed. Inside the 1526 - 1560 nm band the average gain was 30.8 ± 0.95 dB. The gain of the EDFA with the grating at 1555 nm exceeds the reference gain by 2 dB. The gain decrease in the region of 1536 - 1538 nm can be connected with the excess width of the dip in the grating transmission spectrum, which can be corrected by optimising the grating length. Moreover, optimising the grating structure must lead to a flatter gain spectrum.

RESUME

Thus we have presented the first realisation of the gain spectrum flattening of erbium-doped fiber amplifier using a long-period fiber grating. In comparison with the other flattening methods, the application of a long-period grating has the following advantages:

- *wide wavelength range of the flattening (~35 nm);*
- *high level of the smoothed gain (more than 30 dB);*
- *ease of preparation;*
- *low insertion loss of the grating at the wavelength beyond the absorption peak and at the pump wavelength.*

These features make this type of the fiber gratings very promising for creating of the all-fiber flat gain spectrum amplifier.

ACKNOWLEDGEMENTS

We are grateful to Dr. A.N.Gur'yanov and Dr. D.D.Gusovskii for the preparation of the erbium-doped fiber.

REFERENCES

1. M.Tachibana et al., IEEE Photonics Technol. Lett., vol.3, no.2, p.118, 1991.
2. M.Wilkinson et al., Electron. Lett., vol 28, no 2, 131, 1992.
3. G.Grasso, in Proc. Conference on Optical Fiber Communications, OFC'91, OSA, Washington, D.C., paper FA3, 1991.
4. R.Kashyap et al., Electron. Lett., vol 29, no 2, p.154, 1993.
5. R.A.Betts, S.J.Frisken, D.Wong, in Proc. Conference on Optical Fiber Communications, OFC'95, OSA, Washington, D.C., vol.8 p.TuP4, 1995.
6. A.V.Belov, E.M.Dianov, V.I.Karpov et al., submitted to Conference on Optical Amplifiers and Their Applications, 1995.
7. A.M.Vemgsarkar et al., Proc. Conference on Optical Fiber Communications, OFC'95, OSA, Washington, D.C., Post deadline paper, PD4, 1995.

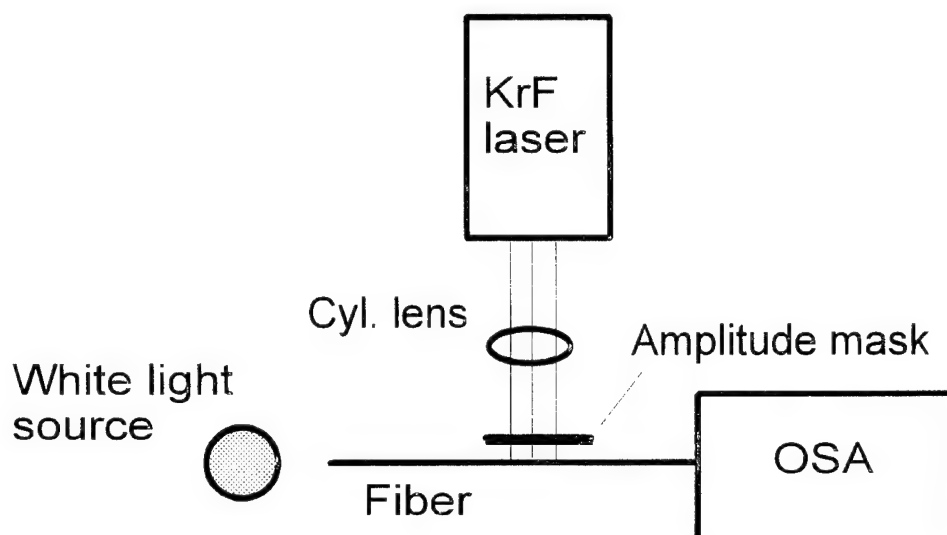


Fig.1. Experimental configuration of the long-period grating preparation

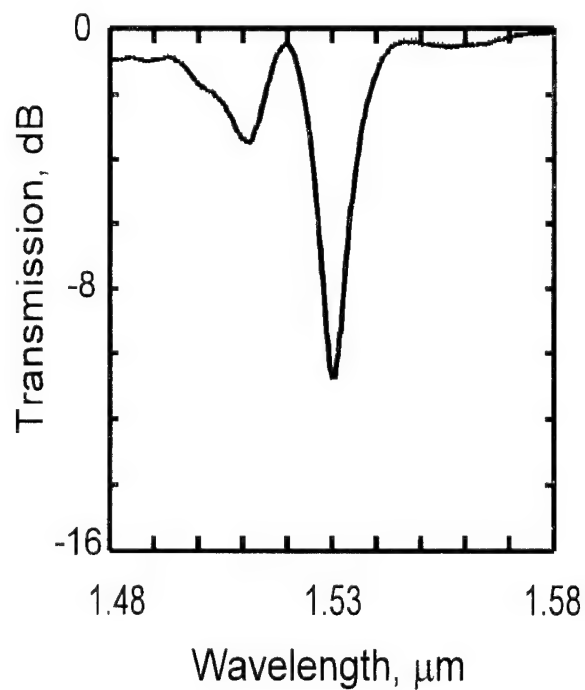


Fig.2. Transmission spectrum of the prepared grating.

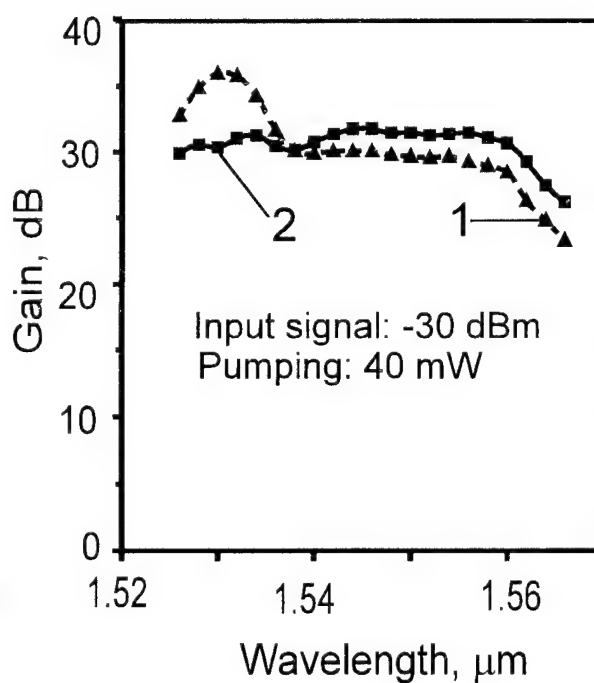


Fig.3. Initial (1) and flattened (2) gain spectra.

**ASYMETRICAL UV-WRITTEN FIBRE FABRY-PÉROT
FOR WDM SOLITON FREQUENCY-GUIDING
AND EQUALIZATION**

I. RIAnt, S. BORNE, P. SANSONETTI

ALCATEL ALSTHOM RECHERCHE, Rte de Nozay, 91460 Marcoussis, France

Tel: 33 16 1 64 49 14 34. Fax: 33 16 1 64 49 15 39

E-mail: riant@aar.alcatel-alsthom.fr

Single mode fibre soliton transmission is of great interest for high bit rate-long haul optically amplified links [1], but requires in-line frequency-guiding filters to decrease temporal jitter of the soliton pulses [2]. We here report the realization of asymmetrical UV-written fibre Fabry-Pérot filter suitable for both frequency-guiding of WDM soliton transmission and equalization, to compensate, for instance, the asymmetries brought between the different channels by the erbium-doped fibre amplifier gain. Such solution offers filter fabrication simplicity, straightforward splicing to other fibres, and extremely low insertion loss.

We have shown previously [3] that a Fabry-Pérot filter implemented with two UV-written fibre Bragg gratings [4] was a potential solution for frequency-guiding WDM solitons. The characteristics of this filter are dictated by simulations on soliton propagation. Considering a bit rate per channel of 5 Gbit/s, the channel spectral separation is about 0.35 nm and the spectral transmission contrast factor about 0.6 dB [5,6].

Soliton pulses of different channels are guided at the Fabry-Pérot filter transmission peaks, equal to unity. They experience about the same transmission loss, but, because the erbium-doped fibre amplifier gain is not spectrally flat, they are not amplified with the same gain. A possibility for compensating the fibre amplifier gain by the filter shape was then studied. A Fabry-Pérot filter implemented with two UV-written fibre Bragg gratings of different length introducing a curvature in the transmission maxima envelope is proposed.

Fabry-Pérot filters were realized using a UV writing set-up based on a pulsed, frequency doubled, excimer pumped dye laser. For spectral response reproductibility, both gratings were not successively written as previously reported [7], but simultaneously written by masking the interference pattern generated by a mirror [8] with a 50 μm nickel mask possessing two slits.

The curvature in the transmission maxima envelope necessary for compensating the erbium-doped fibre amplifier is of the order of 0.01 dB [9], but to demonstrate the principle of this kind of filter, we have realized filters exhibiting higher curvature values.

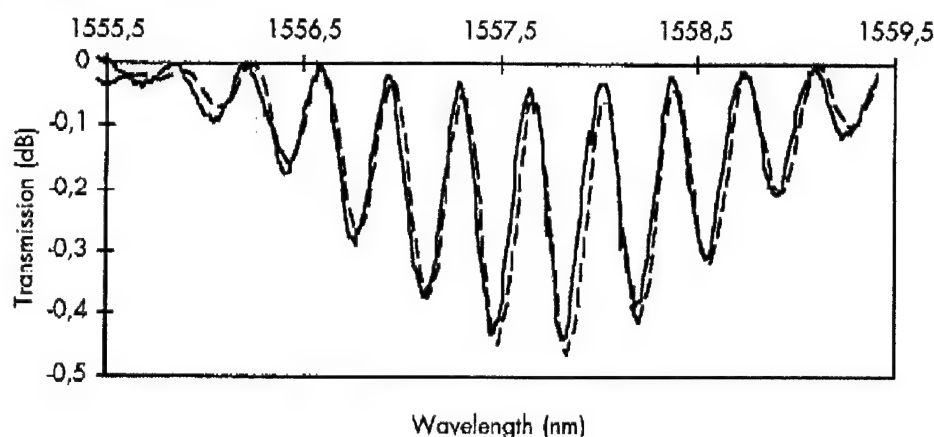


Figure 1: Spectral transmission of Fabry-Pérot filter realized with nickel mask:

Full line: measured

Dashed line: calculated .

A Fabry-Pérot filter, consisting of two Bragg gratings of length respectively equal to 0.2 mm and 0.4 mm, 1.95 mm apart, was realized in a high Germanium content fibre. The fluence per pulse was 0.22 J/cm² with a repetition rate of 10 Hz. The filter insertion loss was measured to be lower than 0.1 dB. Its spectral transmission was measured with a HP 8168A tunable laser source for high spectral resolution 0.01 nm. It is represented with full lines in figure 1, normalized to the source spectral response. Dashed line represents calculated values, using coupled mode formalism [10], and considering the whole filter as being formed of two gratings separated by a length with unmodulated refractive index. The Bragg wavelength shift occurring during inscription was taken into account in the

calculation. The photoinduced index difference is about $4 \cdot 10^{-4}$. It is seen that the different length introduces a curvature of maxima envelope around 0.03 dB.

A second Fabry-Pérot filter was realized exhibiting a higher asymmetry. This filter is formed of a 0.05 mm Bragg grating and a 0.65 mm one, separated by 1.9 mm. The fluence per pulse was 80 mJ/cm^2 with a 10Hz repetition rate. The filter spectral transmission is represented in figure 2 for two different polarization states of the incident light. Insertion loss and polarization sensitivity figures were equivalent to those previously described [3], both lower than 0.1dB. By modelization, the photoinduced index difference was estimated to be $5.5 \cdot 10^{-4}$. The curvature of the maxima envelope is this time very large due to the great difference in length between the gratings.

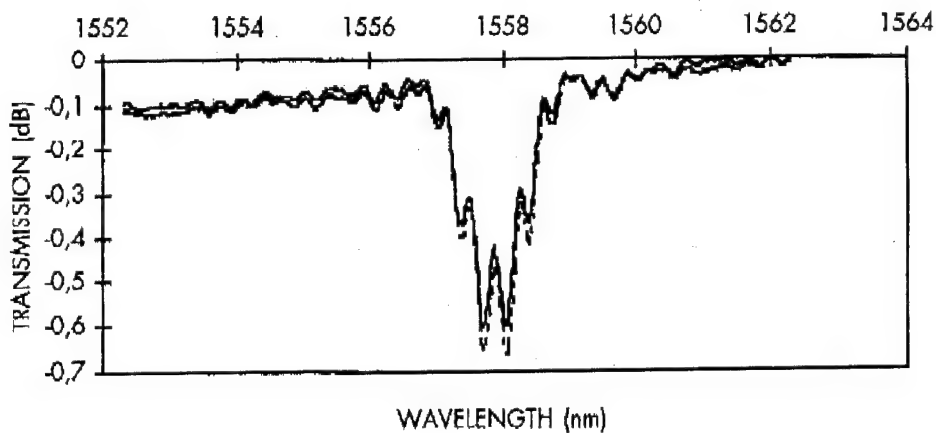


Figure 2: Spectral transmission of Fabry-Pérot filter for two polarization states:
 Full line: maximum transmission
 Dotted line: minimum transmission

We have reported the realization of asymmetrical UV-written fibre Fabry-Pérot filters suitable for both frequency-guiding of WDM soliton transmission and equalization, to compensate, for instance, the asymmetries brought between the different channels by the erbium-doped fibre amplifier gain. They are formed of two short Bragg gratings of different length simultaneously written by UV exposure. Filters insertion loss and polarization sensitivity were measured to be lower than 0.1 dB. This shows the powerful properties offered by UV-written fibre Bragg gratings and

that such a filter is a very good candidate for in line frequency-guiding of WDM soliton transmission.

References:

- [1] GORDON, J. P. and MOLLENAUER, L. F.: 'Effects of Fibre Nonlinearities and Amplifier Spacing on Ultra-Long Distance Transmission', *Journal of Lightwave Technology*, **9**, 2 (1991).
- [2] MECOZZI, A., MOORES, J. D., HAUS, H. A. and LAI, Y.: 'Soliton transmission Control', *Optics Letters*, **16**, 23 (1991).
- [3] RIAnt I., SANSONETTI P.: 'UV-written fibre Fabry-Pérot filter for WDM soliton frequency-guiding', *submitted to Electron. Letters*.
- [4] MELTZ, G., MOREY, W. W. and GLENN, W. H.: 'Formation of Bragg gratings in optical fibres by a transverse holographic method', *Optics Letters*, **14**, 823 (1989).
- [5] AUDOUIN, O., HAMAIDE, J.P., BRUN, E., PRIGENT, L., BRYUERE, F. and BERNARD, J. J.: 'Design of amplified optical transoceanic systems with WDM soliton pulses', *Proceedings of the 2nd International Conference on Optical Fibre Submarine Telecommunication Systems*, paper 61, Versailles, France (1993).
- [6] MOLLENAUER, L. F., LICHTMAN, E., HARVEY, G. T., NEUBELT, M. J. and NYMAN, B. M.: 'Demonstration of error-free soliton transmission over more than 15000 km at 5 Gb/s, single-channel, and over more than 11 000 km at 10 Gb/s in two-channel WDM', *Electron. Letters*, **17**, 1575 (1992).
- [7] TOWN, G. E., SUGDEN, K., WILLIAMS, J. A. R., BENNION, I. and POOLE, S. B.: 'Wide-band Fabry-Pérot-like Filters in Optical Fibre', *IEEE Photonics Technology Letters*, **7**, 1 (1995).
- [8] LIMBERGER H.G., FONJALLAZ P.Y., SALATHE, R.P.: 'Spectral characterization of photoinduced high efficient Bragg gratings in standard telecommunication fibres', *Electron. Letters*, **29**, 1, p 47 (1993).
- [9] DESTHIEUX, B. M., BAYART, D., BEYLAT, J. L.: *OFC'95*, San Diego (1995).
- [10] KOGELNIK, H.: 'Filter Response of Nonuniform Almost-Periodic Structures', *The Bell System Journal* (1976).

Optical dark soliton generation using a fibre Bragg grating

R Kashyap, M de Lathouwer*, Ph Emplit*, M Haelterman*
R J Campbell and D J Armes

BT Laboratories, Martlesham Heath,
Ipswich IP5 7RE, United Kingdom

*Universite Libre de Bruxelles, Service d' Optique et Acoustique,
50 av. F D Roosevelt, CP 194/5, B-1050, Bruxelles, Belgium.

There is currently worldwide interest in the theory and transmission of dark solitons for application in communications. Theoretical techniques have been proposed[1-3] for the generation of CW dark soliton pulse trains. One of them has been recently demonstrated recently[4]. The techniques rely on spectral filtering of a train of mode-locked pulses using both conventional phase and amplitude masks[1,5], or on the adiabatic transformation of a beat frequency from two lasers[3,4]. A third approach[2] is based on the direct modulation of a CW signal from a DFB laser. In another technique, a chirped fibre grating was used to provide the correct sign of dispersion in a Pr:ZBLAN fibre laser to generate dark pulses[6]. In the spectral filtration technique, the frequency content of mode-locked pulses is first spatially dispersed and this allows for the alteration of the amplitude and phases of the spectral components in the Fourier plane[1]. The Fourier transform of the filtered spectrum generates the dark pulse train. These techniques are generally more suitable for the generation of ultra high repetition rate dark pulse train since it is easier to filter larger bandwidths.

In this paper we propose a novel application of a fibre Bragg reflection grating as the spectral and phase imposing filter to generate dark soliton like pulses directly. This technique should be especially useful in the generation of dark soliton pulse trains at rates below 10 GHz.

The spectrum of an ideal mode-locked source is shown in Figure 1a. The electric field of the pulse train may be described as[7]:

$$E(t) = \sum_{m=1}^{\infty} G(m\nu_0) \exp(-i2m\pi\nu_0 t) \quad (1)$$

$G(\nu)$ is the gain bandwidth of the laser, $\nu_0 = c/2L$ is the longitudinal mode spacing in the L metre long laser cavity, while m is the order of the longitudinal mode. We assume that the modes are symmetrically distributed around the carrier frequency.

It has been shown that if a filter, $M(\omega)$ is used which selectively filters the frequencies $\omega_n = (2n+1)\omega_0/2$ in the Fourier plane as:

$$M(\omega) = \frac{1}{2n+1} \quad , \text{ for } n\omega_0 \leq \omega < (n+1)\omega_0 \quad , n = 0, \pm 1, \pm 2, \dots \quad (2)$$

then the resultant output is a train of dark pulses on a constant intensity background. In equation (2) the sign of the index, n represents the phase imparted to the frequency component, such that all frequency components on the low frequency side of the carrier have the opposite phase to those on the higher frequency side. To convert the bright into a dark pulse, it is necessary to introduce a phase transition at the centre of the spectrum. A second requirement of the filter is that it adjust the amplitude ratios of the frequency components according to equation (2) and that the phases of the frequency components within each side-band are identical. The ratios of the amplitudes of the frequency components are fixed as shown in Figure 1b[8]. Here, the frequency components of the lasing modes (shown in Figure 1a) lie half way between the integer values of the detuning. These requirements are usually met by separate amplitude and phase filters[8].

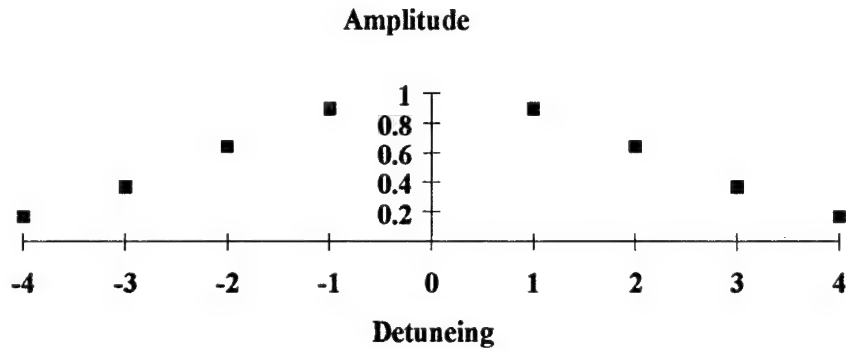


Figure 1a

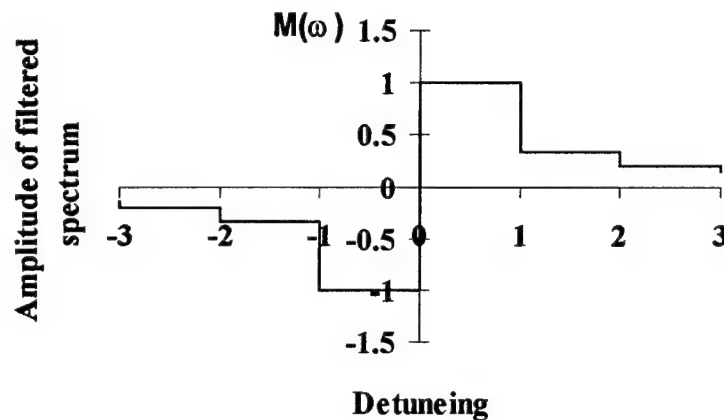


Figure 1b

Figure 1a. The optical spectrum of a mode-locked laser as a function of detuning. The detuning has been normalized to laser cavity mode spacing. Figure 1b shows the transmission filter required for transforming the spectrum in figure 1a to a dark pulse. Note that the frequency spectrum of figure 1a lies at a detuning of $\pm 0.5, 1.5, 2.5, \dots$ in figure 1b.

The principle of how a suitable fibre grating can be used as a filter may be understood by examining the reflection spectrum and phase, shown in Figure 2, of an ideal sinusoidal Bragg grating. From this spectrum it may be seen the reflectivities of the sidelobes on either side of the reflection peak decrease monotonically with detuning from the Bragg wavelength (as is well known), and that the phase change between every other side-lobe peak is 2π . It should be noted that there is only a π phase change across the main reflection peak. The reflectivity of the side-lobes increases with increasing grating coupling constant, κ for a given length, L of the grating. The position of the side lobes' maxima relative to the central peak is strongly affected by the length of the grating (ie bandwidth) for a given κL . In order to make a filter with the appropriate reflectivity, it is necessary to plot the sensitivity of the relative shift between the peaks as a function of the length of the grating.

In designing a fibre Bragg grating filter for use as a frequency selective filter, the appropriate coupling constant must be used so that the reflectivities at the peak of the side-lobes approximately follows $|M|^2$ as per equation (2). The length of the grating must also be such that the frequency difference between every other side-lobe peak matches the mode spacing so that the phase separation is 2π . This results in the modes in the lower and upper side band of the carrier being separated in phase by 2π , so that the main peak of the grating spectrum can be positioned symmetrically around the mode spacing of a laser such that the phase difference is π between the two dominant modes.

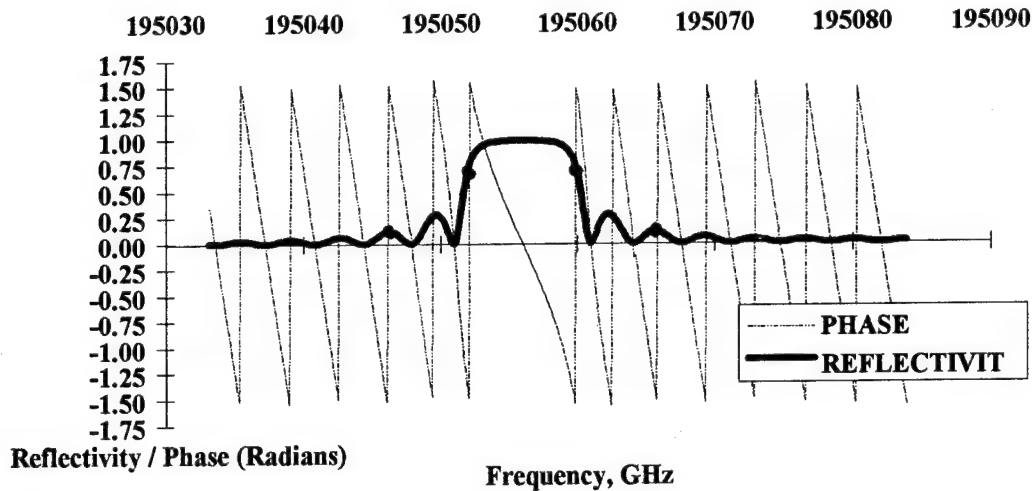


Figure 2. An uniform grating reflection spectrum and phase. Also shown are the positions of the bright pulse spectrum for conversion to a dark pulse.

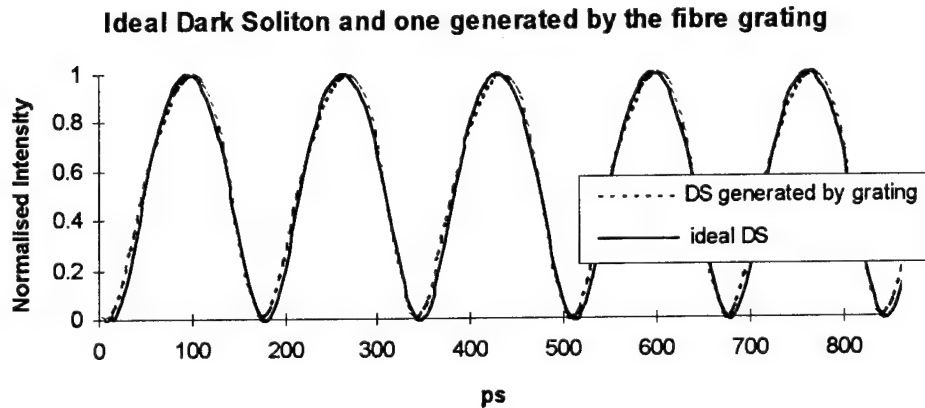


Figure 3. Comparison between dark solitons generated by the grating and an ideal dark soliton. (30mm long grating, $\Delta n = 4 \times 10^{-5}$). The two pulse trains have been shifted slightly to make the shapes clear.

It was found that a theoretical coupling constant, κl of 2.456 gives the correct values for $|M|^2$ (being approximately, 1, 1/9, 1/25...). The full bandwidth of the grating (to the first zeroes), and the difference in the frequencies of the peaks of the side lobes vary linearly with inverse length of the grating, but have different slopes. This dependence was examined to give a matched filter with a length of 30mm for a laser mode spacing of 6 GHz (pulses of ~50ps FWHM, Figure 3).

The cavity round-trip is adjusted to the mode spacing required for the designed grating. However, optimisation of the fibre grating reflection spectrum may need to be optimised to take account of the active cavity. Simulations of using the fibre as a linear filter show that the reflected spectrum will automatically generate a train of dark pulses closely matching the dark soliton shape (hyperbolic tanh Figure 3). The position of the lasing modes are carefully adjusted to lie within the grating spectrum, as shown in Figure 2. The discrepancy between the perfect dark soliton and the one generated by the grating is due to the minor differences in phases from the ideal.

30mm long fibre Bragg gratings have been fabricated using the scanned phase-mask technique[9]. The first result of one such grating is shown in Figure 4. Along with the experimental data is the theoretically calculated reflection spectrum, showing excellent agreement for the band-width and the two adjacent lobes. The peak reflectivity is adjusted by selecting the index of modulation, Δn of the grating; in this case is approximately 15dB ($\Delta n = 0.00004$).

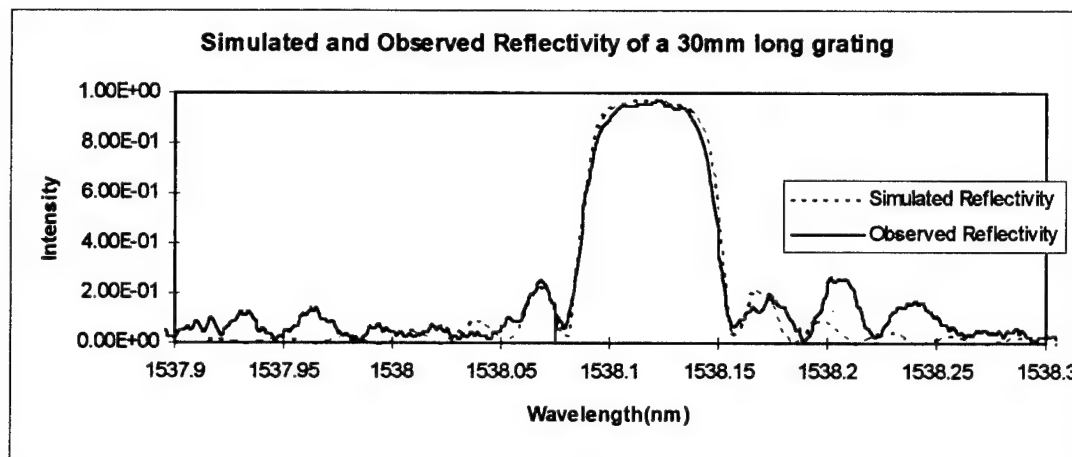


Figure 4. Measured reflection spectrum of a 30mm long grating designed for 6.5Ghz dark pulse generation. The theoretical fit is also shown.

Slight chirp in the grating has caused the deterioration in the subsequent lobes. The $\pm 1,2$ modes of the laser dominate in the formation of the dark pulse. The contribution from larger detuning causes only slight changes in the shape of the pulse. Work is currently in progress to correct for this error to produce ideal gratings for a mode-locked dark soliton source, the results of which will be reported at the meeting.

Acknowledgements

M. De Lathouwer acknowledges BT for providing her a student fellowship. Ph. Emplit and M. Haelterman acknowledge the Belgium OSTC for financial support in the frame of the Interuniversity Attraction Poles program under grant PAI P3-047.

References

1. M Haelterman & Ph Emplit, "Optical dark soliton trains generated by passive spectral filtering technique", *Electron. Lett.* 29(4), 356-357, 1993.
2. W Zhao & E Bourkoff, "Generation, propagation and amplification of dark solitons", *J. Opt. Soc. Am. B* 9, 1134-1144, 1992.
3. A Shipulin, D Fursa, E Golovchenko, & E Dianov, in *Digest of NLGWPM93, Proc. of the Opt. Soc. Am.* 15, 216, 1993.
4. D J Richardson, R P Chamberlain, L Dong and D N Payne, "Experimental demonstration of 100GHz darksoliton generation and propagation using a dispersion decreasing fibre", *Electron. Lett.* 30(16), 1326, 1994.
5. C Froehly, B Colombeau & M Vampouille, "Shaping and analysis of pico-second light pulses", in Wolf (Ed.): *Progress in Optics XX*, (North Holland, Amsterdam, 1983), pp. 65-153.
6. Pataca D M, Rocha M L, Kashyap R & Smith K, "Bright and dark pulse generation in an optically modelocked fibre laser", *Electron. Lett.* 1995.
7. M Haelterman & Ph Emplit, "Generation of odd symmetry pulse train with constant background from a mode locked laser", *IEEE J. of Quant. Electron.* 1994.
8. J Martin & F Ouellette, "Novel writing technique of long and highly reflective in-fibre gratings", *Electron. Lett.* 30(10), 811, 1994.

Saturday, September 9, 1995

Self-Organized Second-Harmonic Generation

SaC 1:30–3:00pm
Multnomah Room

Raman Kashyap, *Presider*
British Telecom Research Laboratories, UK

Imaging the Frequency Doubling Grating in Optical Fibers

I. C. S. Carvalho, D. C. Reigada, F. C. Garcia, E. N. Hering, W. Margulis

Physics Department, Pontificia Universidade Católica do Rio de Janeiro, 22452, RJ, Brazil

e-mail: isabel@fis.puc-rio.br, Phone: (5521) 529 9357, Fax: (5521) 512 3222

F. Laurell

Physics II Department, Royal Institute of Technology, S10044, Stockholm, Sweden

and

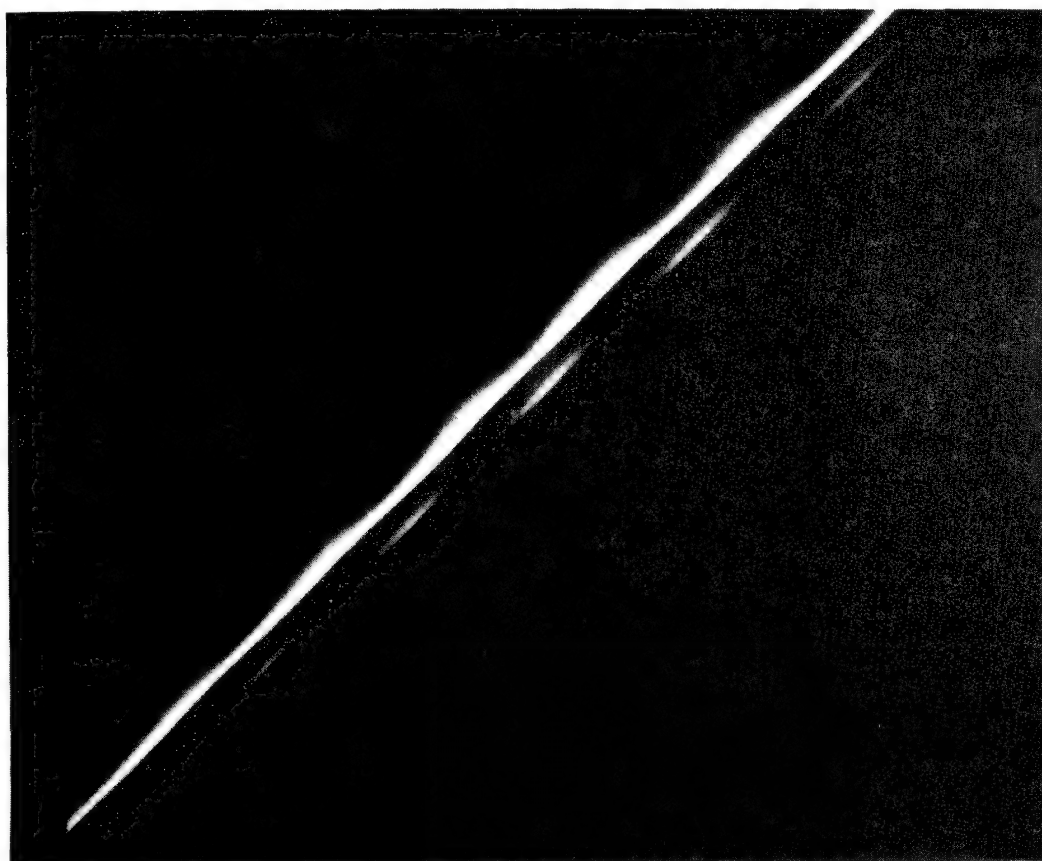
B. Lesche

Physics Institute, Universidade Federal do Rio de Janeiro, P.O.Box 68258, RJ, 21945-970, Brazil

It is now generally believed that second harmonic generation in an optical fiber can be attributed to the creation of a permanent dc electric field grating along the fiber. The grating allows for quasi phase matching and gives rise to high conversion efficiencies. Imaging the grating with micrometer spatial resolution has so far been a difficult task because the cladding of the fiber shields efficiently the core from the environment. Indirect techniques have been employed, such as probing the small changes in the spontaneous Raman spectrum scattered as side-light¹. Besides being of difficult interpretation, such technique gives low signal-to-noise ratio measurements.

In the present work the grating was imaged through of a straightforward etching technique. Preparation of frequency doubling fibers was done with a Q-switched mode-locked Nd:YAG laser, either with external or self-seeding. Etching was carried out at room temperature with 40% HF acid, that both removed the cladding and selectively attacked the core of the prepared fiber. The presence of the high electric field frozen in the fiber is sufficient to attract the cations of the solution to the positive locations and anions to the regions of negative charge. Typical etching times were 58 minutes. The resulting thin fiber (5-10 μm thick) was inspected under a conventional microscope with magnification 40-500 times. The transmission mode with polarized

light gave high contrast images. The spatial resolution of the measurements was approximately one micron. A clear periodicity was found at the grating location, previously known from macroscopic measurements such as the heat scan². Well defined gratings were seen in all three germanium silicate fibers tested, one of which was a standard telecommunications fiber, one was P-codoped and the other B-codoped. The grating period was 35-40 μm , and the effect of alternating sign of the field was also clearly recorded.. The figure below illustrates an example of image obtained of a self-prepared fiber grating (3 mol% Ge doping, 0.5 weight % P doping, cut-off wavelength 1.299 μm , core diameter 8.8 μm , 120 μm outer diameter). The period is 39 μm .



It was expected that if the electric field is created by a distribution of dipoles, removal of the outer layer of the core should leave a high intensity field in the center of the fiber. On the other hand, if the creation of the field is caused by charge separated to the interface core-cladding, etching away the outer layer of the core should remove the source of the field. Therefore, in order to estimate the field distribution, pieces of the fiber above were prepared for SHG and subsequently etched to various discrete thicknesses or tapered. It was found that the image of the grating was

visible for a thickness $<4\ \mu\text{m}$. This result suggests that the electric field in frequency doubling fibers originates from macroscopic charge separation, as in bulk samples³. Furthermore, the grating only appeared when the fiber thickness was $<16\ \mu\text{m}$, and was clearest at a diameter of $8\ \mu\text{m}$. It should be possible to measure in real time (during etching) the second harmonic conversion efficiency, and estimate more accurately the transverse distribution of the electric field in the fiber.

The etching technique can also provide information about the microscopic aspects of gratings prepared varying conditions of temperature, modal distribution, and excitation with optical radiation. Furthermore, details can be revealed about the grating remaining after erasure by heat or by light, and after the introduction of a phase-shift. Grating aspects not previously recorded can also be studied. For example, a superstructure was also observed in one sample with period $0.55\ \text{mm}$ formed by amplitude modulation of the grating. Its origin is not understood at present. The etching technique is a powerful tool to understand SHG in fibers, and some of these studies will be described in the present work.

References:

- [1] A. Kamal, D. A. Weinberger, W. H. Weber: Opt.Lett. 15, 613 (1990)
- [2] M. M. Lacerda, I. C. S. Carvalho, W. Margulis, B. Lesche: Opt. Lett. 19, 948 (1994).
- [3] E. M. Dianov and D. S. Starodubov: Optical Fiber Technology 1, 3-16 (1994), and references therein.

Optical Preparation of Polymers for Frequency Doubling

J.M. Nunzi, C. Fiorini and F. Charra
 Groupe Composants Organiques,
 LETI (CEA - Technologies Avancées)
 CE Saclay, F91191 Gif sur Yvette, France
 phone: 33 1 69086812
 fax: 33 1 69087679
 internet: nunzi@serin.cea.fr

The discovery that combinations of optical fields could exhibit polarity opens up new possibilities for optical handling of molecules [1]. A standard situation in which an optical field exhibits polarity is the coherent superposition of a field E_ω at a fundamental frequency ω with its harmonic $E_{2\omega}$ at frequency 2ω . It is pictured in Figure 1. Polarity of the cubic interferences appears in the non-zero average cube $\langle E^3 \rangle_t$ where the subscript t holds for time average.

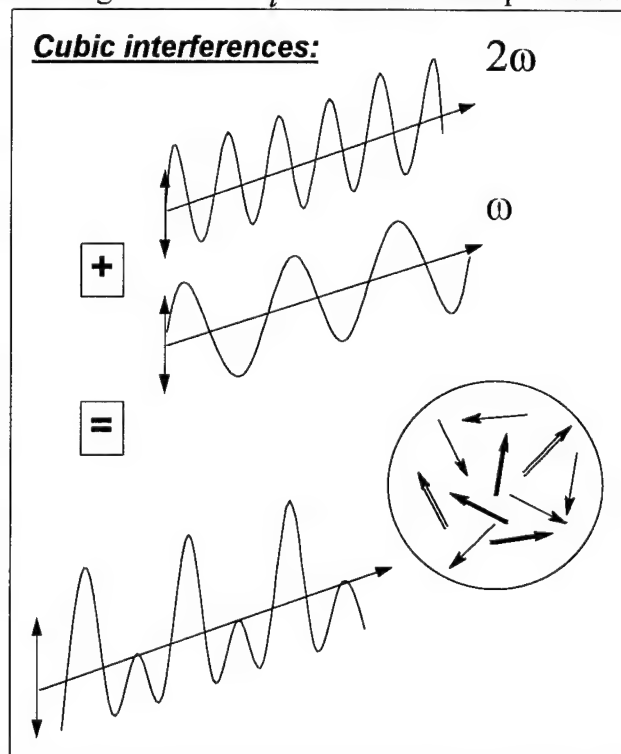


Figure 1: Polar cubic interference between fields at fundamental and harmonic frequencies.

The observation of a second-harmonic generation in optical fibres prepared by an intense light at 1064 nm [2] or with a simultaneous *seeding* light at double frequency (532 nm) [3] revealed the possibility of inducing a noncentrosymmetry using light in a centrosymmetric material. It is the first reported application of a mechanism involving cubic interferences with $\langle E^3 \rangle \neq 0$. In order to build the molecular engineering rules which permit a control of this effect, it is necessary to identify efficient processes by which condensed materials record $\langle E^3 \rangle$.

$\langle E^3 \rangle$ effects find a simple description in the case of a solution of molecules excited under resonant conditions. The origin of the nonlinearity can then be pictured in terms of a hole burning into the distribution of molecular orientations. Let us consider a two-level molecule. Under one-photon excitation at 2ω , the projection of its wave function on the excited state is proportional to $(\vec{\mu}_{01} \cdot \vec{E}_{2\omega})$ where μ_{01} is the transition dipole-moment between ground and excited states. Under two-photon excitation at ω , the projection of its wave function on the excited state is proportional to $(\vec{\mu}_{01} \cdot \vec{E}_{\omega})(\delta\vec{\mu} \cdot \vec{E}_{\omega})/\hbar\omega$ where $\delta\mu$ is the dipole-moment difference between ground and excited states. A molecule which is irradiated at resonance with fields E_{ω} and $E_{2\omega}$, respectively at fundamental and harmonic frequencies, experiences a transition probability to the excited state which contains the one and two-photon interference contribution [4]: $(\vec{\mu}_{01} \cdot \vec{E}_{2\omega})(\vec{\mu}_{01}^* \cdot \vec{E}_{\omega}^*)(\delta\vec{\mu} \cdot \vec{E}_{\omega})/\hbar\omega$. In this expression, brackets represent scalar products between vectors. This interference term which is proportional to E^3 depends on the polar orientation of the molecule via $\delta\vec{\mu}$. The process involves the microscopic polarizability tensor β of the molecule. The average value of this cubic interference over molecule orientations is zero in isotropic mixtures. That means that the cubic interference is not associated with an index grating. However, absorption is preferentially directed towards molecules oriented either upward or downward, as in Figure 1, depending on the phase of the product $E_{2\omega}E_{\omega}^{*2}$. There results a net noncentrosymmetry. The overall process of second harmonic generation can be viewed as a six-wave mixing processes [5]. The process consists in the record and readout of a c(2) grating caused by the $\langle E^3 \rangle$ interference. The grating is a quasi phase-matched one and unlike with usual quasi phase-matching techniques, there is no simultaneous induction of an index grating. Hence, using dual-frequency optical excitation, both polar orientation and phase matching conditions can be achieved in polymers.

The growth and decay dynamics of the efficient susceptibility $d_{33} = \frac{1}{2}\chi_{yyy}^{(2)}$ induced in a random methacrylic copolymer with nonlinear 4-nitro-4'-amino-diazobenzene chromophores grafted as pendant side groups is displayed in Figure 2. The frequency doubling coefficient reaches $d_{33} = 45$ pm/V after 2 hours of preparation. It is as high as what is currently obtained using corona electric-field poling [6]. After seeding-type preparation, the decay dynamics of the induced d_{33} is the same as with the same polymer prepared using the corona-poling technique. This corresponds to an electrooptic coefficient r_{33} close to 10 pm/V at 1.3 μm -wavelength. Molecules are oriented in the plane of the film. Order parameter $\langle \cos^3(\theta) \rangle$ is close to 0.2. Understanding of the fundamental aspects of laser-matter interaction permits optimization of the preparation process.

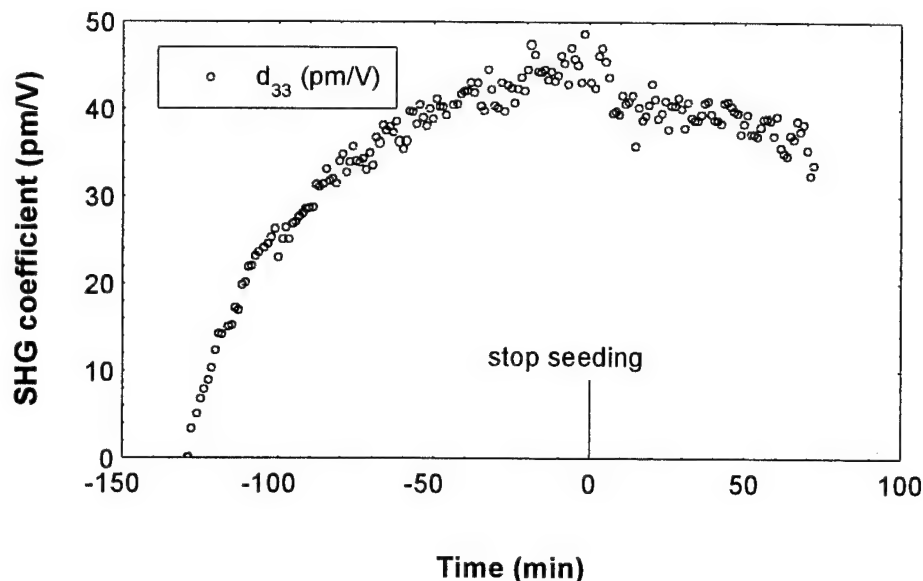


Figure 8: Growth and decay dynamics of the efficient susceptibility d_{33} .

This opens new directions towards the molecular engineering of transparent phase-matched oriented micro-structures for efficient frequency conversion. We give some perspectives on the quasi-phase-matched frequency doubling performances offered by those new optical components.

References

1. Baranova, N.B.; Zel'dovitch, B.Ya; *JETP Lett.*, **1987**, *45*, 716.
2. Osterberg, U.; Margulis, W.; *Opt. Lett.*, **1986**, *11*, 516.
3. Stolen, R.H.; Tom, H.W.K.; *Opt. Lett.*, **1987**, *12*, 585.
4. Charra, F.; Kajzar, F.; Nunzi, J.M.; Raimond, P.; Idiart, E.; *Opt.Lett.*, **1993**, *18*, 941.
5. Charra, F.; Devaux, F.; Nunzi, J.M.; Raimond, P.; *Phys. Rev. Lett.*, **1992**, *68*, 2440.
6. Broussoux, D.; et al.; *Rev. Tech. Thomson-CSF*, **1989**, *20-21*, 151.

Paper withdrawn.

Efficient Photo-induced Second Harmonic Generation in Ternary Barium Borosilicate and Pure Binary Lead-silicate Glasses

Y. Nageno

Division of Engineering, Brown University, Providence, RI 02912

Jae H. Kyung

Department of Physics, Brown University, Providence, RI 02912

N.M. Lawandy

Department of Physics and Division of Engineering, Brown University, Providence, RI 02912

Tel: (401) 863-2755

Fax: (401) 863-1157

Most studies of photo-induced efficient second harmonic generation (SHG) in bulk glass systems are currently being performed with commercial glasses which are highly impure. The existence of impurities, even trace amounts, can significantly affect the photo-induced SHG characteristics in glasses as demonstrated in experiments performed on Ce-doped lead germanate glasses [1]. In fact, it was shown that Ce concentration as low as 0.2% was enough to cause a significant increase in SHG in these glasses. Therefore, it is advantageous to study glass systems that are devoid of impurities and consistent in composition in order to gain a better insight into the role of the glass matrix in photo-induced SHG. In a series of experiments performed by Dianov, et al [2], the effect of PbO concentration on SHG was studied using commercial lead-silicate glasses with different lead-oxide concentrations. They found a peaked correlation between lead concentration and SHG power at approximately 21 mol % PbO. However, the effects due to the presence of impurities and variations in composition in different lead-silicate glasses were not addressed. In this study, we measured compositional dependence on SHG characteristics on pure binary lead-silicate and pure ternary barium borosilicate glass systems.

The samples were prepared using Q-switched (1 KHz), modelocked (76 MHz) Nd:YAG laser pulses emitting at 1.064 μm . Co-propagating second harmonic pulses (532 nm) were generated by frequency doubling in a KTP crystal. A 12.5 cm focal length lens was used to focus the overlapped pulses onto 1 mm thick glass samples. The second harmonic light produced from these samples were measured using a phase-sensitive detection system capable of detecting signals

of less than 1 picowatt of average power. Binary lead-silicate ($x \text{ PbO} - (100-x) \text{ SiO}_2$) glasses with PbO concentrations ranging from 30 to 70 mol % were made using high purity PbO (purity level of 99.999%) and special grade SiO_2 (purity level greater than 99.5%). The composition of these glasses were determined from the batch composition and confirmed by X-ray fluorescence measurement. Similarly, $40 \text{ BaO} - x \text{ B}_2\text{O}_3 - (60-x) \text{ SiO}_2$ glass systems were made using special grade materials with purity exceeding 99.5%.

The lead glass samples were first encoded with peak intensities of 2 GW/cm^2 at $1.064 \mu\text{m}$ and 3.7 GW/cm^2 at 532 nm for 20 minutes to insure saturation. Figure 1 shows the result of the saturated relative $\chi^{(2)}_{\text{eff}}$ at various PbO concentrations. This result confirms the decreasing nature of the SHG signal with increasing PbO content as reported in ref [2]; however, exact comparison with their results could not be made as the SHG is dependent on readout IR ($1.064 \mu\text{m}$) power. Furthermore, at 70 mol % PbO, no photo-induced SHG was observed.

The readout decay of the lead-silicate glasses appears to correlate well with the high conductivity in these materials [2]. We have measured the decay curves of the SHG signal over time for various lead-silicate glasses and found that they fit a stretched exponential function of the form:

$$\chi^{(2)}_{\text{eff}}(t) = \chi^{(2)}_{\text{eff}}(0) e^{-(\frac{t}{\tau})^\beta} \quad (1)$$

The data fits very well indicating that the nature of relaxation of the $\chi^{(2)}_{\text{eff}}$ grating is possibly due to dispersive transport which is characteristic of disordered, amorphous systems. A E_{dc} field induced decay model of the form:

$$\chi^{(2)}_{\text{eff}}(t) = 2 E_c \text{ArcTan}[c_1 e^{-c_2 t}] \quad (2)$$

used to fit thermal erasure of $\chi^{(2)}_{\text{eff}}$ grating in SK5 glass [3] was also used to fit the non-exponential decay curves but failed to fit the data accurately. Figure 2 shows the dependence of the relaxation time τ and β on PbO concentration. Although the $\chi^{(2)}_{\text{eff}}$ grating exhibits increased decay with lead concentration as evident by the decrease in τ , β remained steady at approximately 0.3.

When ternary barium borosilicate glasses were prepared and readout, a peaked correlation between B_2O_3 concentration and relative $\chi^{(2)}_{\text{eff}}$ was observed with optimal SHG signal at approximately 20 mol % B_2O_3 as shown in Figure 3. It is interesting to note that binary systems consisting of a network modifier BaO and glass former SiO_2 and B_2O_3 both show significant photo-induced SHG and saturate at approximately the same level while pure silica does not exhibit seeded SHG. This is consistent with the picture in which an inclusion of network modifiers increases the number of dangling bonds available for carrier excitation.

We also investigated the threshold behavior for 40BaO-60 B_2O_3 , 40BaO-20 B_2O_3 -40 SiO_2 , 40BaO-60 SiO_2 , and 30PbO-70 SiO_2 glass systems and found clear threshold points as shown in Figure 4. The 30 mol % PbO content lead-silicate glass showed strong SHG even at very low IR intensities and significant seeded SHG was detected when the glass was encoded with the Nd:YAG laser operating only in the modelocked mode. Preparation intensities of 9.2 MW/cm² at 1.064 μm and 36.9 KW/cm² at 532 nm were enough to generate several orders of magnitude increase in second harmonic light above the background.

We have measured the dependence of photo-induced second harmonic generation on the variation of specific compositional content of glasses devoid of impurities and inconsistency in their compositions. We have also observed photo-induced decay in pure binary lead-silicate glasses indicative of dispersive transport which may hold clues to the light-induced transport mechanism leading to SHG in glasses [4].

references

- [1] E.M. Dianov, D.S. Starodubov, and A.A. Izyneev, Opt. Lett. **19**, 936 (1994).
- [2] E.M. Dianov, P.G. Kazansky, D.S. Starodubov, D. Yu. Stepanov, and E.R. Taylor, Proc. Soc. Photo-Opt. Instrum. Eng. **2044**, 27 (1993).
- [3] T.J. Driscoll and N.M. Lawandy, J. Opt. Soc. Am. B **11**, 355 (1994).
- [4] S. Li, J.B. Khurgin, and N.M. Lawandy, Opt. Commun. **115**, 466 (1995).

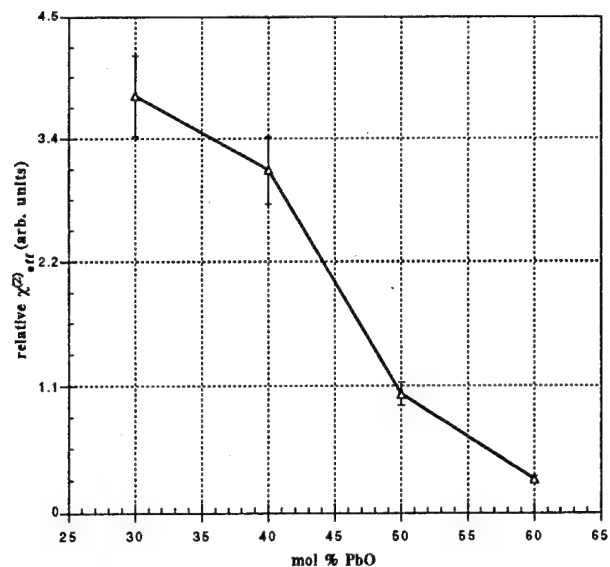


Figure 1. The relative $\chi_{eff}^{(2)}$ dependence on PbO concentration for pure binary lead-silicate glasses.

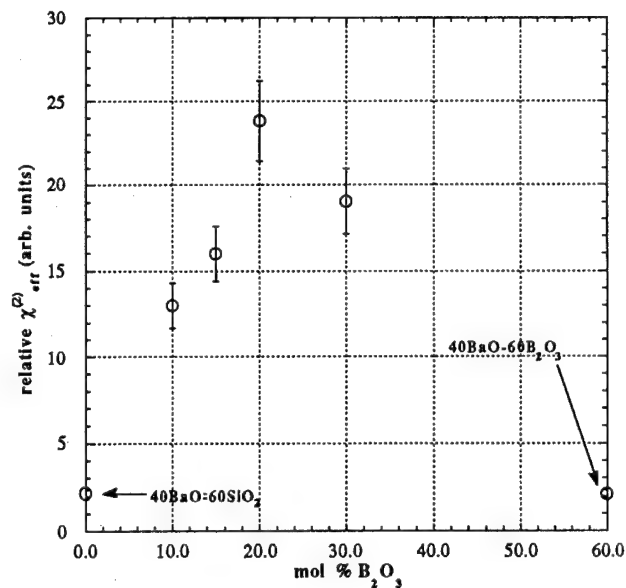


Figure 3. The relative $\chi_{eff}^{(2)}$ dependence on B₂O₃ concentration for pure ternary barium borosilicate glasses. An optimal SHG is obtained at 20 mol % B₂O₃.

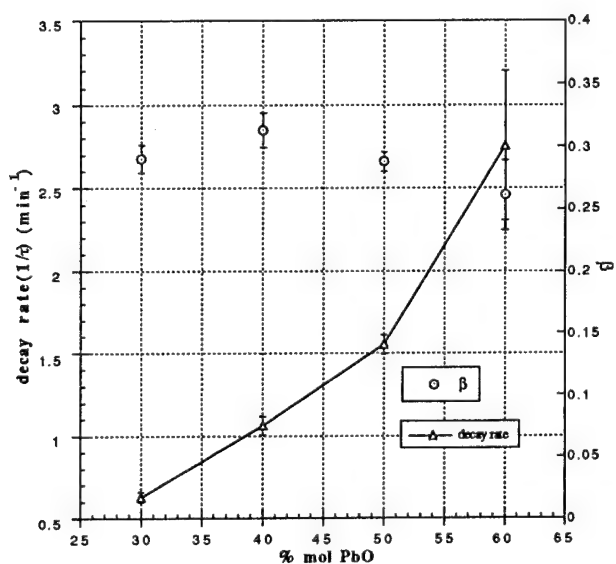


Figure 2. τ^{-1} and β dependence on PbO concentration. The characteristic decay rate increases with PbO content while β remains nearly constant at approximately 0.3.

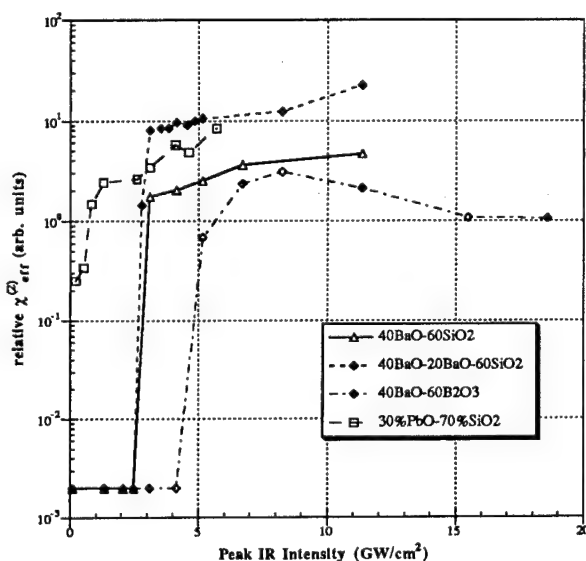


Figure 4. IR intensity dependent threshold measurement of various glass systems. The 532 nm encoding intensity was set constant at 4 GW/cm².

Modal and Polarization Properties of SHG in Doped-Silica Waveguides: Transverse Modulation Effects

John J. Kester, Iyad Dajani, Peter Ranon, and Thomas Alley

Frank J. Seiler Research Laboratory
2354 Vandenberg Dr., Suite 6H79
USAF Academy CO 80840-6272
Tel. (719) 472-3133, FAX (719) 472-3649
e-mail KesterJJ%FJSRL%USAFA@dfmail.usafa.af.mil

The generation of second harmonic light in optically modified fibers¹ and thin films² has been shown to arise from a periodic modulation of the second-order susceptibility, $\chi^{(2)}$, along the direction of propagation.³ This longitudinal modulation allows the phase matching of the generated second harmonic light with the fundamental wave. The efficiency of the second harmonic for different waveguiding modes and different polarizations is governed by an additional modulation in the transverse direction. The overlap of $\chi^{(2)}$ with the transverse profiles of the optical electric fields across the waveguide, as described by the overlap integral, governs the modal response of the waveguide generated light.⁴ Unlike the traditional second harmonic generation (SHG) processes, the overlap integrals describing higher order modal combinations may be on the same order as the overlap integral describing the combination of the lowest order modes. In planar waveguides the difference in the transverse charge density governs the polarization dependence.

Theoretical predictions of second harmonic light from various fiber mode combinations have indicated that relative efficiencies within an order of magnitude are possible for lower order modes.⁵ Furthermore, they found the fiber-generated SHG was produced in the same mode as that used during the seeding process. Recent experimental work with modal combinations in fibers showed that while the seeding was typically carried out with one second harmonic mode, the fiber generated SHG was reported in a number of modes.⁶ In one experiment the SHG was not observed in the second harmonic seeding mode.

We report here on the modal and polarization properties of SHG in germanium-doped planar waveguides. While there has been experimental observation of polarization effects in planar waveguides² no theoretical models have been proposed. The film-generated second harmonic (FGSH) was measured for different modal combinations and polarizations and was compared to the theoretical predictions based on the asymmetric photoionization model. The cause of the variation in the efficiency for different mode combinations is attributed to the confinement of the beams within the waveguide and the overlap integrals. These modal combinations can be used for possible optical switch applications.

The waveguides were produced by ion beam sputtering and consisted of 6M percent of germania in silica. The experimental setup is shown in Fig. 1. A fundamental beam at 1.06 μm was produced by a Q-switched mode-locked Nd:YAG laser. A second harmonic beam, produced by KDP, was separated and recombined with a slight offset to allow prism coupling into specific waveguiding modes of the film with TM or TE polarization. After simultaneous illumination by the fundamental and second harmonic beam, FGSH light was observed by reading the grating with a fundamental beam having a power equal to the power of the writing beam.

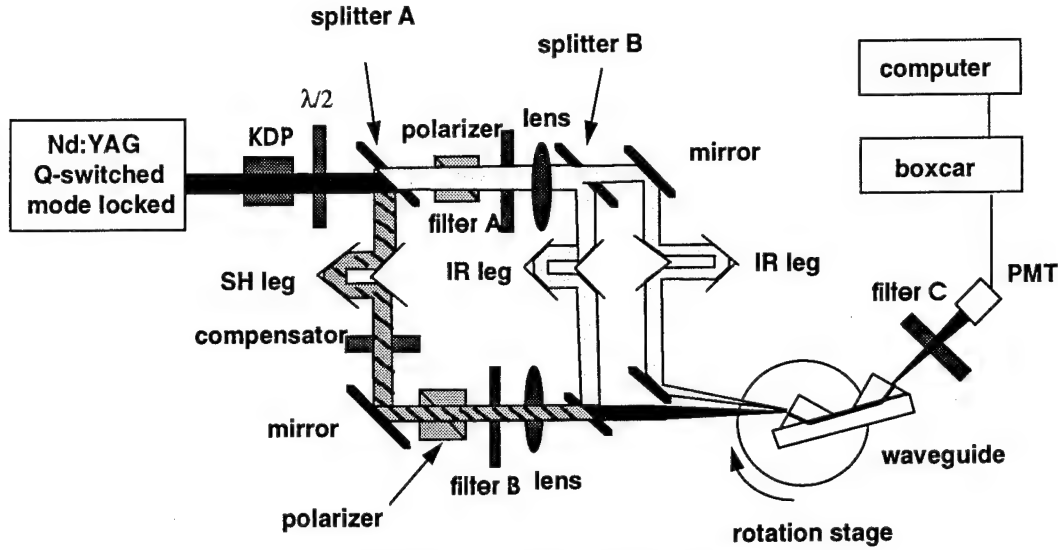


Figure 1. Experimental setup

Films prepared with both beams in either TM or TE polarization show almost three orders of magnitude difference in FGSF light (Fig. 2). This difference is not due to differences in the overlap integral between the two polarizations, but rather to the space charges that arise due to the asymmetric photoionization current⁷, $J_{pi} \propto E_{\omega}^{*2} E_{2\omega}$, and the backfield field current, $J_{bf} = \sigma^{(1)} E_{DC}$, where $\sigma^{(1)}$ is the linear conductivity. At saturation the continuity equation, $\frac{\partial \rho}{\partial t} + \nabla \cdot J = 0$, yields $\nabla \cdot J = 0$. However, the most general solution is not $J_{pi} = -J_{bf}$, but rather, $\nabla \cdot (J_{pi} + J_{bf}) = 0$. Only by adopting the general solution can one explain the difference in FGSF power between the two polarizations. The photoionization current will be the same for either polarization, however, the divergence of the current is much larger for the TM configuration. The larger divergence in the current for the TM polarization will yield a larger charge density and higher effective second order susceptibility. This has been verified through numerical simulations.

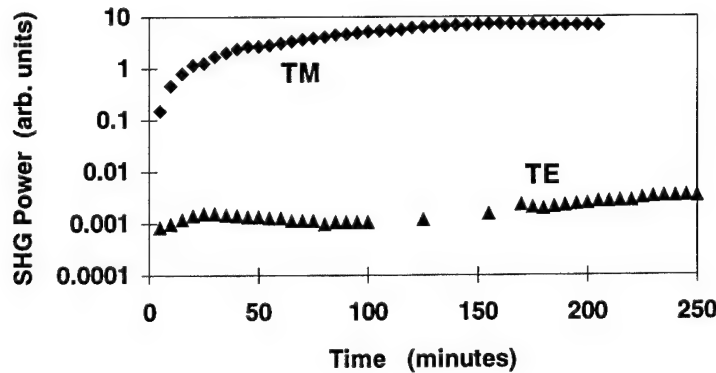


Figure 2. Growth of film generated second harmonic for TM and TE polarizations

Using only TM polarization the planar waveguides were conditioned using the fundamental and second harmonic in various lower order mode combinations. For each

mode combination the FGSH was allowed to grow until saturation. The output FGSH powers were then normalized to the lowest order mode combination and by the factor $1/P_{\omega}^4 P_{2\omega}$ for the seeding beams powers (Table 1.).

When the film was conditioned by seeding in one particular mode, the subsequent FGSH light was observed substantially in the same order mode. Some light was observed in adjacent modes. However, the percentage of FGSH light observed in other modes was in exactly the same percentage ($\pm 0.2\%$) as that observed for scattering of light from one mode to another within the waveguide. Thus, there is no appreciable SHG light generated in other modes that is in excess of the FGSH scattered light from the mode in which it was conditioned.

The relative power generated is calculated for various low order mode combinations by normal mode analysis.⁸ For TM modes, the dominant component of the electric field is in the transverse direction, i.e., normal to the plane of the waveguide. In the case where the writing and reading IR beams are in the same mode, the overlap integral describing the FGSH produced in the same waveguiding mode as the seed green is:

$$G(z) = \int_{-a}^a \int_{-\infty}^{\infty} \chi_{iiii}^{(3)} \left[|\Phi_{1,k}|^4 + (r_1 + 1/3) \Phi_{1,k}^2 \Psi_{1,k}^{*2} + (1/3) r_1 |\Psi_{1,k}|^4 \right] |\Phi_{2,l}|^2 + ((r_2 + 2/3) \times |\Phi_{1,k}|^2 \Phi_{1,k} \Psi_{1,k}^* + (1/3)(2r_1 + r_2) \Phi_{1,k} |\Psi_{1,k}|^2 \Psi_{1,k}^*) \Phi_{2,l} \Psi_{2,l}^* (2/3) r_2 |\Phi_{1,k}|^2 |\Psi_{1,k}|^2 |\Psi_{2,l}|^2] dx dy \quad (1)$$

where the IR beams are assumed to be in mode k , the seed and generated green are assumed to be in the mode l , and where Φ and Ψ represents the transverse profiles of the transverse and longitudinal components of the optical fields. The coefficients r_1 and r_2 are obtained from experimental results.⁹

The predicted FGSH powers are listed in Table 1 with two different normalizations. The column marked *Total Predicted Power* calculates the power in various modes when normalized to the total power propagating in the waveguide for the conditions used in our experimental setup. This column can then be compared with the experimental results observed. A very rough correlation can be observed between the experimental and calculated SHG powers. The difference is primarily attributed to variability among the mode combinations in the temporal and spatial overlap of the fundamental and second harmonic used for conditioning the waveguide. In addition, the input and output prism coupling efficiency varies from one mode combination to another. However, the key point is that SHG can be produced in various mode combinations and that they have been predicted and measured to be within an order of magnitude for lower order modes.

Table 1. Experimental and predicted SHG powers for various mode combinations

Fundamental Mode	Second Harmonic Mode	Measured Power	Total Predicted Power	Waveguide Predicted Power
0	0	1.0	1.0	1.0
0	1	0.39	0.30	0.31
0	2	0.51	0.36	0.38
1	0	0.10	0.13	0.28
1	1	0.34	0.40	0.89
1	2	0.58	0.21	0.48

Contributions from modal confinement and the overlap integral were examined. The column marked *Waveguide Predicted Power* normalizes the output to the power

confined within the waveguide itself. This column excludes power that is outside the waveguide in the evanescent fields. When comparing the calculated total power and waveguide power it is observed that ratios are similar for a specific fundamental waveguide mode. When the fundamental mode increases from zeroth to first order, a large discrepancy is observed due to the increased electric fields outside the waveguide. With better confinement conditions the SHG powers in the $TM_{\omega,1} - TM_{2\omega,1}$ could be up to 90% of the $TM_{\omega,0} - TM_{2\omega,0}$ mode combination.

A waveguide was then modified to produce multiple gratings within the same spatial region of the waveguide. The waveguide was modified by directing a fundamental and second harmonic beam into the film as described above. The FGSH was allowed to grow to a specific level. The same region of the waveguide was then illuminated by directing a fundamental beam into a different waveguide mode along with the second harmonic beam in the same mode used previously. There was no FGSH initially observed with this mode combination. A FGSH signal was allowed to grow from this new mode combination to a level similar to the first mode combination. While some erasure of the original grating occurred during the growth of the second grating, second harmonic light was observed in the same mode (the same mode originally used to condition the film) when illuminated by only the fundamental beams from either of the two waveguiding modes. With proper temporal and spatial overlap the second harmonic beams can be made to interfere, which is the basis of an optical switch.

In conclusion we have found that combining different waveguiding modes produces the same order of magnitude FGSH as the lowest order mode combination. Unlike fibers, the FGSH was produced in the same waveguiding mode as the seed second harmonic wave. Furthermore, we found that TM modes produced many orders of magnitude greater SHG power than the TE modes. This is due primarily to the greater charge density induced with TM polarization, and appears to be consistent with the asymmetric photoionization model.

References

1. U. Osterberg and W. Margulis, *Opt. Lett.* **11**, 516 (1986).
2. J. J. Kester, P. Wolf, and W. R. White, *Opt. Lett.* **17**, 1779 (1992).
3. H. Stolen and H. W. K. Tom, *Opt Lett* **12**, 585 (1987).
4. R. H. Stolen, in *Nonlinear Waves in Solid State Physics*, A. D. Boardman, T. Twardowski, and M. Bertolotti, eds (Plenum, New York), pp 297-324, (1990).
5. P. S. Weitzman and U. Osterberg, *IEEE J Quantum Elec.* **29**, 1437 (1993).
6. B. Pommellec, *Optical Materials* **3**, 169 (1994)
7. E. Dianov, P. Kazansky, and D. Yu Stepanov, *Sov J. Quantum Elect.* **19**, 575 (1990).
8. I. Dajani, *J. Mod. Optics* (accepted for publication).
9. V. Dominic, Ph.D. Thesis, Univ of Southern California (1993).

Saturday, September 9, 1995

Photosensitivity and Planar Waveguides and Mechanisms

SaD 3:30–5:15pm
Multnomah Room

Gerry Meltz, *Presider*
United Technologies Research Center

Photosensitivity in planar waveguides

T. Kitagawa, Y. Hibino, and M. Abe

NTT Opto-Electronics Laboratories

Tokai-Mura, Ibaraki-Ken, 319-11 Japan

Phone: +81-29-287-7401, Facsimile: +81-29-287-7865

Introduction

Silica-based planar lightwave circuits (PLCs) are promising as practical optical circuits with excellent levels of performance [1]. Four generations of PLCs, including the Mach-Zehnder interferometer and arrayed-waveguide grating configurations, have been developed using $\text{GeO}_2\text{-SiO}_2$ waveguides with low propagation and fiber-connection losses fabricated on silicon substrates [2]. The PLCs have been used in feasibility experiments on advanced optical communication systems, such as wavelength division multiplexing (WDM) systems, optical switching systems, and optical access networks. In addition to the family of PLCs, Er^{3+} -doped $\text{P}_2\text{O}_5\text{-SiO}_2$ waveguides have been fabricated in order to achieve optical amplification in PLC devices [3].

Photosensitivity [4], which is observed in silica-based planar waveguides made with glass materials similar to those used for optical fibers, has been applied to silica-based planar waveguide technology. Specifically, it has been used for trimming the spectral response in the PLCs [5-7]. Photo-induced Bragg gratings have been fabricated in PLCs by UV exposure in the same way as used for optical fibers [8-10].

In this paper, we review applications of the photosensitivity in planar waveguides. We discuss techniques for trimming interferometric circuits and fabricating Bragg gratings in PLCs.

Photosensitivity in silica-based planar waveguides

Exposure to UV light induces permanent refractive index changes in silica-based planar waveguides. The $\text{GeO}_2\text{-SiO}_2$ planar waveguides exhibit small index changes (less than 10^{-4}) before sensitization [5]. These are the same as those observed in commercial optical fibers which had not been sensitized before exposure. Photo-induced birefringence has also been observed in these less photosensitive planar waveguides. When exposed to intense UV light, the SiO_2/Si waveguides exhibit a larger increase in the refractive index for the TE mode than in that for the TM mode. This reduces the intrinsic birefringence caused by the difference in the thermal expansion coefficients of a silica-based waveguide and a silicon substrate [1]. As a result, the intrinsic birefringence decreases to a negligible value under a suitable exposure condition [7]. This photo-induced birefringence may be due to stress relief in the waveguides.

The GeO_2 -doped silica waveguides are highly sensitive to UV light at 193 nm and 249 nm after consolidation in a reduced atmosphere [6], flame-brushing [9] or hydrogen loading sensitization [11].

A refractive index increase of more than 10^{-3} has been observed in $\text{GeO}_2\text{-SiO}_2$ planar waveguides. In a similar way, irradiation at 193 nm induces large index increases of more than 10^{-4} in sensitized $\text{P}_2\text{O}_5\text{-SiO}_2$ waveguides while 249 nm exposure induces relatively small index changes of less than 10^{-5} [10]. At least, a part of these index changes are due to the photobleaching of the color centers in the doped silica systems [12]. The induced refractive index changes have been used to control the optical path length in Mach-Zehnder interferometers [5,6] or photo-imprint Bragg gratings in planar waveguides [8-10]. Photo-induced birefringence is not significant in sensitized waveguides because large index changes are induced at low UV doses before the birefringence increases.

Trimming waveguide circuits

It is important to control the phase difference in interferometric circuits in order to obtain desired spectral responses for filter devices. The exposure of one arm in a Mach-Zehnder interferometer to UV or visible light induces a change in the phase difference in the interferometer as a result of the photo-induced refractive index change [5]. In this way, the transmission bands of the filter device are tuned to desired wavelengths after the fabrication. Figure 1 shows the spectral change of the interferometer induced by exposure to 249 nm light from a KrF excimer laser [6]. An index change of 4×10^{-4} , which is larger than that required for a phase change of more than π along a 10 mm-long waveguide, is observed in the waveguide which was consolidated in a reduced atmosphere. This trimming technique can be applied in order to optimize the extinction ratio of a thermo-optic Mach-Zehnder interferometer switch by reducing its phase error.

Photo-induced birefringence is also used in order to compensate for the intrinsic stress-induced birefringence and to obtain a polarization-insensitive silica-based arrayed waveguide grating filter (see Fig. 2) [7]. The photo-induced birefringence of 5×10^{-5} was observed in the planar waveguide after exposure to UV light at 249 nm. The arrayed-waveguide grating exhibited a polarization-insensitive transmission wavelength after trimming, while the grating showed a transmission wavelength shift of 0.2 nm caused by the intrinsic birefringence before the irradiation.

Photo-imprinting Bragg gratings

Bragg gratings have been formed in silica-based waveguides. Strong gratings with reflectivities of more than 97 % have been made in GeO_2 -doped as well as P_2O_5 -doped silica waveguides using exposure to 193 nm ArF excimer laser light through phase masks after photosensitization by the flame-brushing or hydrogen-loading [9,10].

These Bragg gratings have been integrated with an asymmetric Mach-Zehnder interferometer [13]. Figure 3 shows the configuration of the device, which demultiplexes three wavelengths. The device exhibits periodic transmission spectra because of the asymmetric interferometer with a

wavelength period of 10 nm and a Bragg reflection band with a high extinction ratio of 38 dB and a bandwidth of 1 nm (Fig. 4). The integration of thin-film heater thermo-optic phase shifters enables the switching of transmission wavelengths extracted from two transmission output ports as well as the tuning of phase of reflected light for the purpose of improving the return loss of the circuits at the Bragg resonant wavelength.

Bragg gratings have also been integrated with Er^{3+} -doped P_2O_5 - SiO_2 waveguides in order to construct a laser cavity. Single longitudinal mode oscillation at 1543 nm has been demonstrated in a PLC laser with a cavity length of less than 4 cm and with a grating reflectivity of more than 90 % [14]. The oscillation wavelength is tuned in a 0.5 nm wavelength range by controlling the temperature of the silicon substrate, as shown in Fig. 5. Further integration of the waveguide circuits may allow the construction of a light source for WDM transmission systems.

Conclusion

Photosensitivity in planar waveguides has been used to trim the phase and birefringence of PLCs as well as to photo-imprint Bragg gratings in PLCs. Photosensitive PLCs are expected to be used in advanced WDM optical communication systems.

Acknowledgments

The authors thank K. O. Hill, F. Bilodeau, B. Malo, J. Albert, and D. C. Johnson of Communications Research Centre and M. Kawachi, T. Nozawa, and Y. Ohmori of NTT Opto-Electronics Laboratories.

References

1. M. Kawachi, *Opt. Quantum Electron.*, **22**, 391(1990).
2. M. Kawachi and K. Jinguji, *OFC'95*, FB-3.
3. T. Kitagawa, K. Hattori, K. Shuto, M. Yasu, M. Kobayashi, and M. Horiguchi, *OAA'92*, PD-1.
4. K. O. Hill, Y. Fujii, D. C. Johnson, and B. S. Kawasaki, *Appl. Phys. Lett.*, **32**, 647(1978).
5. Y. Hibino, T. Kominato, and Y. Ohmori, *IEEE Photonics Technol. Lett.*, **3**, 640(1991).
6. Y. Hibino, M. Abe, H. Yamada, Y. Ohmori, F. Bilodeau, B. Malo, and K. O. Hill, *Electron. Lett.*, **29**, 621(1993).
7. M. Abe, H. Takahashi, Y. Inoue, Y. Hibino, and Y. Ohmori, *MOC'93*, D4.
8. R. Kashyap, G. D. Maxwell, and B. J. Ainslie, *IEEE Photonics Technol. Lett.*, **5**, 191(1993).
9. F. Bilodeau, B. Malo, J. Albert, D. C. Johnson, K. O. Hill, Y. Hibino, M. Abe, and M. Kawachi, *Opt. Lett.*, **18**, 953(1993).
10. B. Malo, J. Albert, F. Bilodeau, T. Kitagawa, D. C. Johnson, K. O. Hill, Y. Hibino, and K. Hattori, *Appl. Phys. Lett.*, **65**, 394(1994).
11. P. J. Lemaire, R. M. Atkins, V. Mizrahi, and W. A. Reed, *Electron Lett.*, **29**, 1035(1993).
12. D. P. Hand and P. St. J. Russell, *Opt. Lett.*, **15**, 102(1990).
13. Y. Hibino, T. Kitagawa, F. Bilodeau, B. Malo, J. Albert, D. C. Johnson, and K. O. Hill, to be published.
14. T. Kitagawa, F. Bilodeau, B. Malo, S. Theriault, J. Albert, D. C. Johnson, K. O. Hill, K. Hattori, and Y. Hibino, *Electron. Lett.*, **30**, 1311(1994).

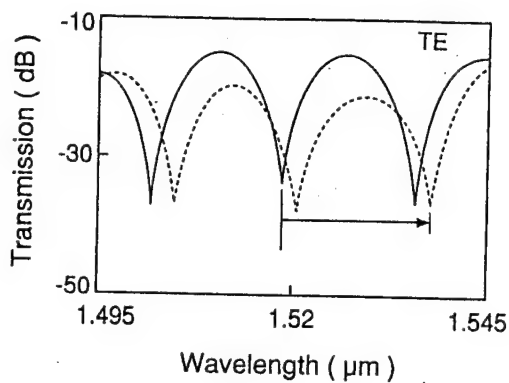


Fig. 1 Spectral change induced by UV exposure in a Mach-Zehnder interferometer. Solid and dashed lines show results before and after irradiation, respectively.

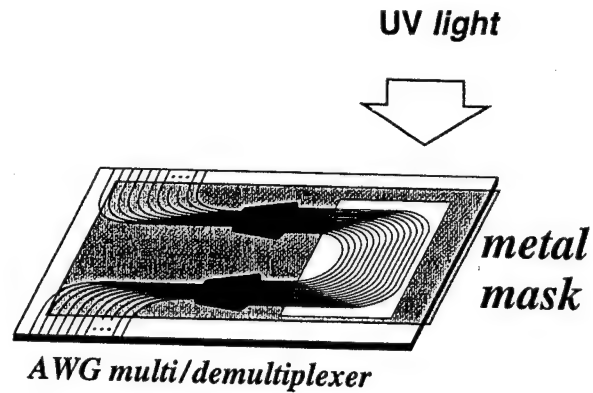


Fig. 2 Trimming birefringence in an arrayed-waveguide grating.

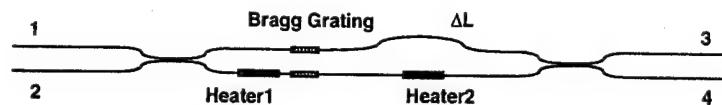


Fig. 3 Multi/demultiplexer composed of Bragg gratings and an asymmetric Mach-Zehnder interferometer.

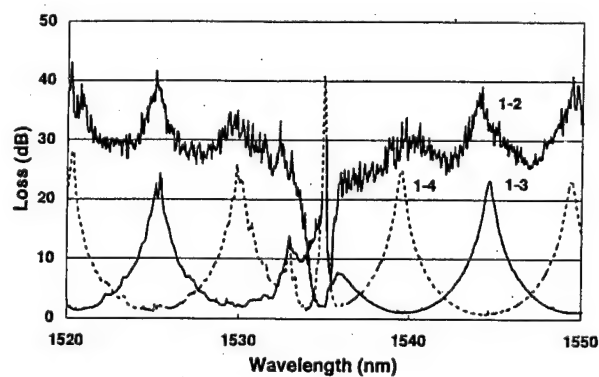


Fig. 4 Loss spectra of the multi/demultiplexer.

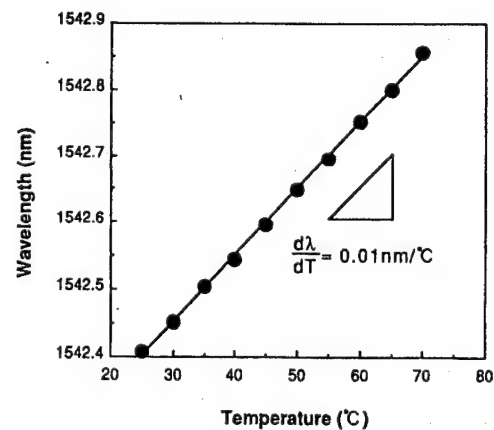


Fig. 5 Wavelength-tuning of a single-longitudinal-mode Er-doped PLC laser.

Microscopic investigations of Bragg gratings photowritten in germanosilicate fibers.

M. Douay, D. Ramecourt, T. Taunay, P. Bernage, P. Niay
Laboratoire de dynamique moléculaire et photonique, URA CNRS 779,
Bât P5, Université des Sciences et Technologies de Lille, 59655 Villeneuve d'Ascq, France,
phone: 20.43.49 82, fax: 20.43.40.84

A. Dacosta, C. Mathieu
Centre de Recherches de l'Université d'Artois à Lens
Faculté J. Perrin, Rue Jean Souvraz, S.P. 18 62307 Lens cedex, France
phone: 33 21 79 17 10, fax: 33 21 79 17 17

J.F. Bayon
LAB/RIO/TSO, France Telecom CNET Technopole Anticipa, 22307 Lannion, France,
phone: 33 96.05.28.28, fax: 33 96.05.13.07

B. Poumellec
Laboratoire CNS, Bâtiment 415, URA CNRS 446
Université de Paris Sud 91405 Orsay France
phone: 331 69 41 63 51, fax: 331 69 85 54 84

Summary:

In 1978, K. O. Hill et al. [1] reported the first observation of photosensitivity in a germanosilicate fiber. Interest in understanding and optimizing this phenomenon was further heightened when Meltz et al. demonstrated that an external exposure method could form a grating for use in telecommunication windows [2]. Three mechanisms have been suggested in order to explain the refractive index changes induced in the fiber core. The first is based on a colour - center model [3]. The bleaching of the UV absorption band at 242nm leads through Kramers - Kronig relationship to a refractive index changes in the visible and infrared part of the spectrum. The second is based on UV induced stress relief of the fiber core [4]. The last model is based on structural modifications which induced compaction in the glass matrix [5]. Such UV induced densification has been already reported in preform plates as a change of volume leading to corrugations at the sample surface [6]. These experiments were performed on bulk sample. Therefore, it is of interest to confirm if compaction is photoinduced or not in photosensitive fibers. The aim of this work is to make microscopic investigations of the fiber core at the Bragg grating place in order to look if the UV exposure changes the structural or chemical properties of the material. The characterization of the grating structure photowritten in the optical fiber was realized by Atomic Force Microscopy on etched fibers.

Bragg gratings were written in the fiber core using the holographic method. The UV fringe pattern was obtained by using a Lloyd's mirror type interferometer. The UV beam at 244nm from a pulsed frequency-doubled, XeCl laser-pumped dye laser (LPD 3002E, LPX 105i LAMBDA Physics) was first expanded through a cylindrical afocal telescope providing an expansion ratio of X10. After a spatial filtering, it was focussed through the interferometer by a cylindrical lens to a spot approximately rectangular in dimensions (10mm wide by 20 μ m in height) onto the fiber. The crossing angle between the UV interfering beams was chosen to get a Bragg wavelength of 1.3 μ m (i.e. a grating pitch Λ of 0.45 μ m). The UV beams were linearly S-polarised. The fiber was an elliptical core fiber manufactured by Andrew Corporation with a D-shaped cross section (type 1300). The germanosilicate fiber had the following characteristics: core/cladding index difference 0.036, core size 2x4 μ m ellipse, normalized birefringence $1.5 \cdot 10^{-4}$.

One way to approach the fiber core (i.e. the grating) is to etch the cladding up to the cladding - core interface at the Bragg grating place. Several types of etching solutions were used. Hydrofluoric acid (HF) solution, diluted to different concentration levels were unsuitable ([HF] close to 1%). Indeed, these solutions etched the doped germanosilicate core faster than the pure silica cladding. Q. Zhong et al. [7] reported that the buffered oxide etch (BOE) solution [3 Ammonium Fluoride (40%): 1 HF (49%)] diluted by 50% with saturated citric acid solution was empirically found to preferentially etch the silica, while suppressing the etching of germanium. Therefore, BOE solution was used to reveal the core and cladding structure at the grating place. The part of the fibre where the Bragg grating was photowritten was set in the etching solution. The etching process was controlled as follows: a He Ne beam was launched into the fiber core at one fiber end using a microscope objective. A detector (set at the other fiber end) allowed the measurement of the optical power transmitted through the fiber. The variation of this optical power as the etching moved towards the core, provided a useful calibration of the etched depth. This process was tried with various combinations of the different etching solutions (BOE or HF). This allows to prepare samples suitable for Atomic Force Microscopy (AFM).

First, BOE solution was used to reveal the core cladding interface at the grating place. The etching was stopped before the core reduction. The as-etched fiber was mounted horizontally on the microscope holder. The AFM is from Park Scientific Instruments. The microscope was operated in the contact mode at a rate of 0.5 Hz. All the images are presented as-acquired without correction. Figure 1 shows a typical record of the surface of the D-shape after etching. The white area represents the highest points in the imaged area, while the black region is the lowest points. Two height profiles are reported on this figure. The height profile 1 was recorded perpendicular to the fiber axis. It shows that the silica surrounding the core was removed until to pull the half cylinder of the core clear. The depth between the top and the bottom is $1.02\mu\text{m}$ (core diameter $2\mu\text{m}$). The height profile 2 was recorded along the fiber axis. The grating pitch appears with a mean peak to valley height of 4 nm close to the core cladding interface.

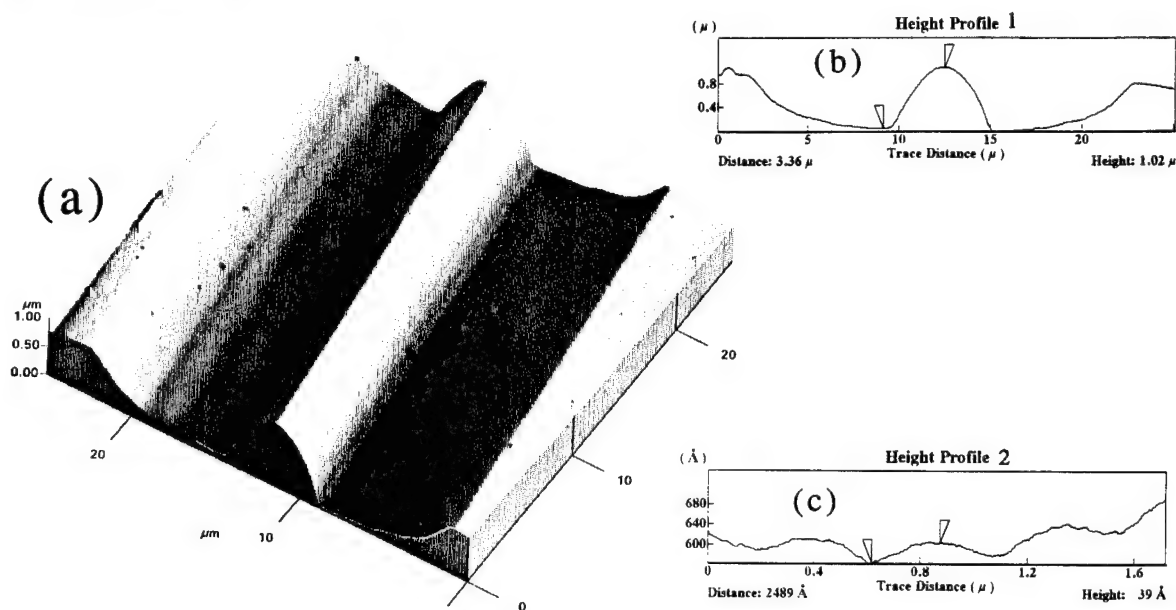


Figure 1: (a) 3-D surface topography of the etched germanosilicate fiber. (b) 2-D height profile taken perpendicular to the fiber axis. (c) 2-D height profile taken along the fiber axis.

Figure 3:
AFM image of the 3-D
surface topography
of etched fiber cladding.

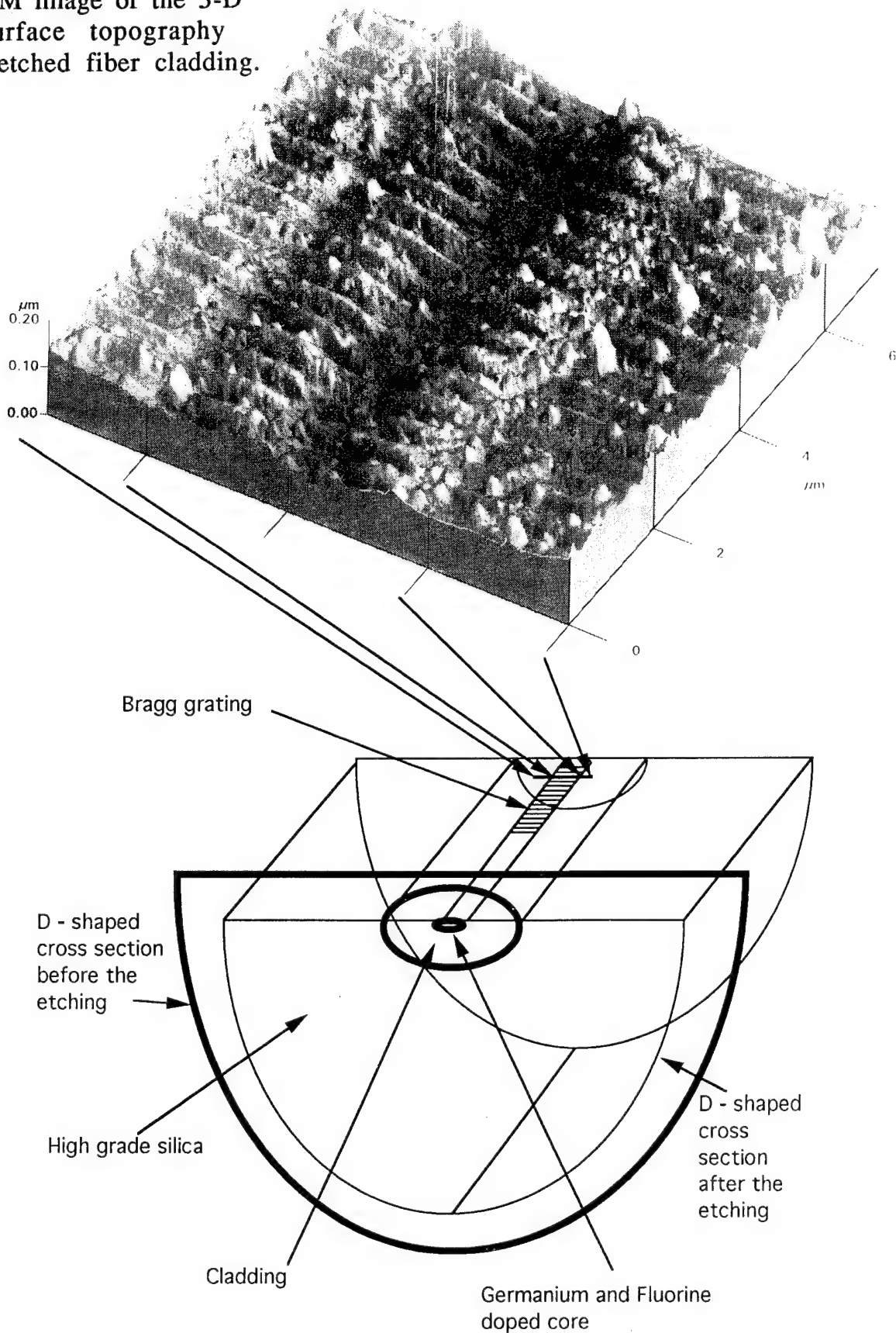
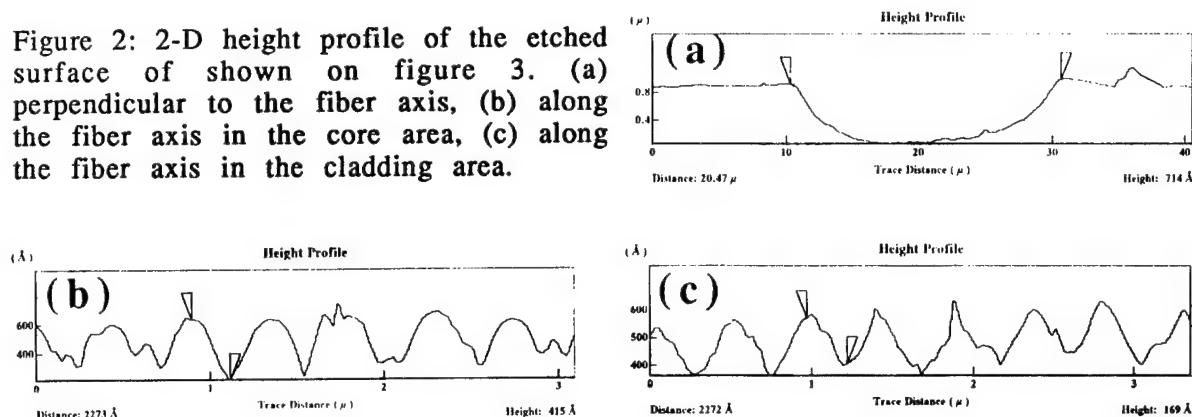


Figure 2: 2-D height profile of the etched surface of shown on figure 3. (a) perpendicular to the fiber axis, (b) along the fiber axis in the core area, (c) along the fiber axis in the cladding area.



Second, 25% of HF solution was added to BOE solution in order to etch cladding and core at the same speed. Records of the surface of the D-shape after the etching using an electronic microscope show that the fiber core can be still recognized on the picture but with a reduced size. Height profile (figure 2a) recorded using AFM shows that the core and the cladding were etched at roughly the same rate. Figure 3 shows a typical record of the grating place on the flat surface of the D-shaped fiber using AFM. The grating pitch is 0.456mm. Two gratings can be observed in the view: one in the core, one in the cladding. The measured depth is close to 41nm (figure 2b) [respectively 17nm (figure 2c)] for the core grating (respectively cladding grating). the core grating has a dephasing of Π (the maxima of the core grating correspond to the minima of the cladding grating).

The corrugation depth is not necessarily a measure of the refractive index change in the fiber core [8]. The depth profile along the core region is indicative of different etching rate. Different etching rates reveal modifications of the glass. Therefore, experimental results indicates that the irradiation of the fiber induced structural or chemical modifications of the silica matrix. This behavior is related to those already observed on preform plates [6]. Further details and comments about these experiments in relation with the different types (I, IIA, II) of photosensitivity will be presented at the conference.

References :

- [1] -K.O Hill, Y. Fujii, D.C. Johnson and B.S. Kawasaki
Appl Phys. 32, 1978, p 647-649
- [2] -G. Meltz, W.W Morey and W.H. Glenn
Opt. Lett 14, 1989, p 823-825
- [3] -D.P. Hand and P. St J. Russell
Opt. Lett. 15, 1990, p102-104
- [4] -M.G. Sceats and S.B. Poole
Australasian Conf. Opt. Fiber Tech. 1991 p 302-305
- [5] -J.P. Bernardin and N.H. Lawandy
Opt. Comm.:79, 1990, p194-199
- [6] -B. Poumellec, P. Guénot, I. Riant, P. Sansonetti, P. Niay, P. Bernage and J.F. Bayon;
Optical Material, 3, 1994, in press
- [7] -Q. Zhong and D. Inniss
J. Light. Tech. 12, 1994, p 1517-1523
- [8] -D. Inniss, Q. Zhong, A.M. Vengsarkar, W.A. Reed, S.G. Kosinski and P.J. Lemaire;
Appl. Phys. Lett., 65(12), 1994, p 1528 - 1530

EVIDENCE OF DENSIFICATION IN UV-WRITTEN BRAGG GRATINGS IN FIBRES

I. RIAnt, S. BORNE, P. SANSONETTI

ALCATEL ALSTHOM RECHERCHE, rte de Nozay, 91460 Marcoussis, France

Tel: 33 16 1 64 49 14 34. Fax: 33 16 1 64 49 15 39.

E-mail: riant@aar.alcatel-alsthom.fr

B. POUMELLEc

Lab. CNS, Bât. 415, URA CNRS 446, Univ. Paris Sud, 91405 Orsay, France

Tel: 33 16 1 64 49 10 21. Fax: 33 16 1 64 49 15 39

Photorefractivity observed in an optical fibre germanium doped core at 240nm, allows the realization of fibre grating devices of great interest for optical telecommunications [1]. To master Bragg grating fabrication or predict the life time of those components, it is necessary to understand the involved physical phenomenons. Several mechanisms are proposed, essentially based on Kramers-Kronig conjugation [2,3]. However, by performing interferometric microscopy measurements at the surface of germanosilicate preforms after Bragg grating inscription, we have pointed out a corrugation. They are accounted for by a model of photoinduced densification grating [4,5]. It explains the major part of photorefractive index change in BPG285 preforms [6]. We generalize here the conclusions by presenting measurements done on a preform made in our laboratories and, for the first time, on the associated optical fibre.

Experiments:

The preform named 2625, used in our experiments, has been elaborated by MCVD process. The core was highly germanium doped. Some slices of thickness 1mm have been cut and polished. A section of this preform has been longitudinally truncated and drawn. The cross section of the resulting fibre has a D-shape with a core diameter of about 3.2 μm . The Bragg gratings were realized in the core of preform slices and on the D-fibre flat surface by side holographic exposure using a pulsed 242 nm laser source. The period of the interference pattern has been chosen to be about 10 μm , that is adequately large for the interferometric microscopy measurements. Different UV laser power densities and irradiation times have been studied.

Results and discussion:

Type I gratings:

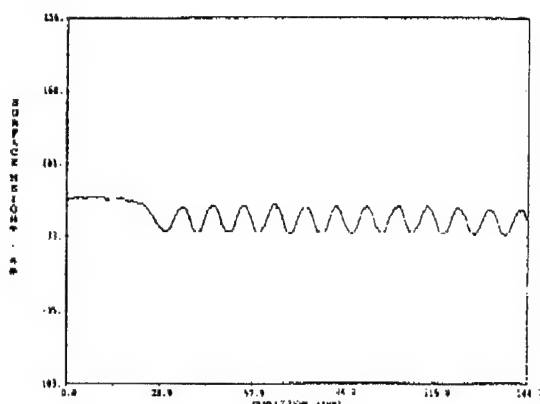


Figure 1: surface along a grating written on a D-shape fibre.

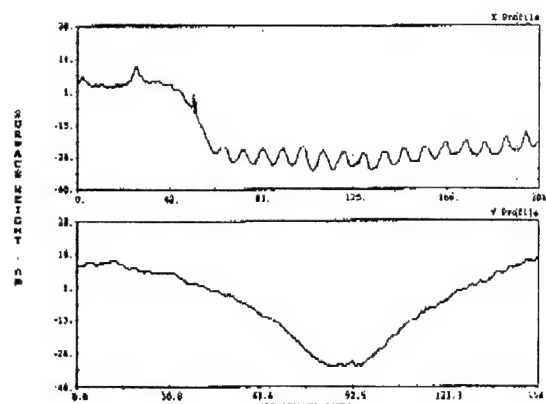


Figure 2: surface of a grating written on preform slice. a: longitudinal view. b: cross section.

Figure 1 presents a longitudinal view of a D-fibre sample that has been irradiated during 30 mn with a power density of 200 mJ/cm² at a 10 Hz repetition rate. We observe, as we already saw in BPG285 preform, a surface modulation embedded in a valley. The depth of the valley is here 17 nm, taken from the normal surface to the mean of the modulation, and the peak to peak modulation is 25 nm. Figures 2a and 2b present respectively a longitudinal view and a cross section of a grating written in the core of a preform from which the D-fibre is issued. This sample has been irradiated during 10 mn with similar exposing conditions as previously described. We found again a surface modulation embedded in a valley but here the valley depth is 31 nm and the modulation is 8 nm. The valley depth values obtained on every D-fibre and preform samples irradiated under different conditions are reported on figure 3. We have added the measurements done on the BPG285 preform given in [4].

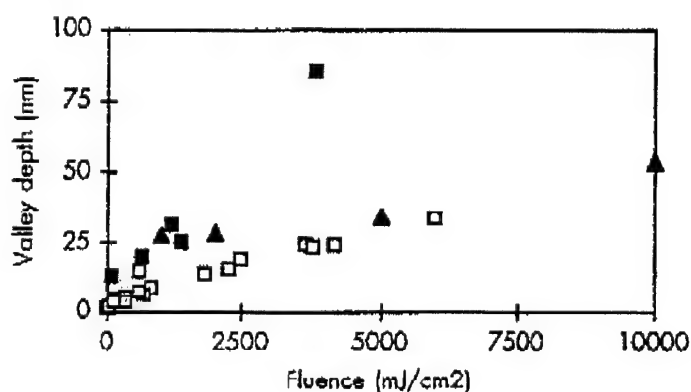


Figure 3: valley depth as a function of fluence. Open squares: D-shape fibre. Black squares: 2625 preform. Black triangles: BPG285 preform.

Plotting the logarithm of the depth as a function of the logarithm of the fluence allows to define a behavior following the law:

$$\text{depth} = A \cdot F^P$$

with F , the total fluence, A , a coefficient and p found to be equal, for each sample, to:

D-fibre:	$p=0.56$	with a regression coefficient of :	0.92
2625 preform:	$p=0.45$		0.81
BPG285 preform:	$p=0.27$		0.86

The 2625 preform and the associated fibre have a p coefficient about equal to $1/2$, implying that the valley depth varies as the square root of the fluence. The p coefficient for the BPG285 preform is closer to $1/4$. Mechanisms involved in UV photorefractivity start with an absorption at 240 nm but seem to evolve differently in these two preforms. A mechanism based on permanent and photoelastic strains is proposed in [9], allowing the calculation of the photoinduced index change in preform. It is possible to use the given equations for the D-shape optical fibre taking into account the effective thickness of the grating, but an adaptation is necessary for the cylindrical fibre because the photoelastic induced strains are different. A study of this adaptation is in progress and will be presented later.

Beyond the type I: the type II gratings ?

When the power density is beyond a threshold, we can observe in the D-shape fibre a fusion then an ablation process. This is shown on figure 4a. This process occurs only where there were both germanium and a bright fringe of the UV interference pattern. We can measure depth of the order of $3\text{ }\mu\text{m}$, implying that the whole core has been etched. We can observe a modulation also in the cladding of the order of several hundred of nanometers, may be due to stresses induced by the core deformation. This threshold is estimated to be about 1 J/cm^2 , value not easily determined because it depends on both power density and germanium concentration. Some samples have only one or two melted periods, probably due to hot spots in the UV profile.

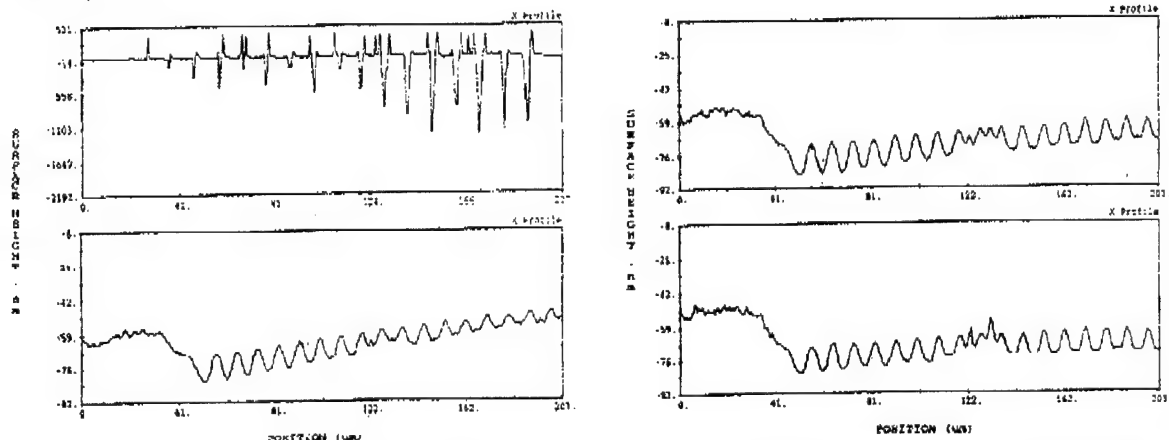


Figure 4: From the top down and from left to right: a Fusion and ablation process on a D-shape fibre grating.

b c d: Transition mechanism on a D-shape fibre grating cross section.

The transition between the sinusoidal corrugation and the fusion is not abrupt, but follows a transition mechanism represented on figure 4b-d. First, the corrugation exhibits saturation and the quasi-sinusoidal modulation becomes square. Then, a

swelling of the corrugation bottom from a few nanometers to several hundred of nanometers appears, followed by a fusion and ablation process, with the emergence of holes where there was swelling. Identical behavior can be seen in the associated preform. We believe that this phenomenon is the transition between the type I grating and the type IIB grating obtained by single pulse excimer laser exposure [10] and that this fusion process is similar to what observed [11]. The swelling, beginning of the transition may be due to oxydation and the intermediate behavior may be related to the type IIA grating observed by [12].

Ageing

For fibre Bragg grating integration in future telecommunication systems, being able to predict their stability in time is of great importance. A study of the decay of UV induced Bragg gratings has been reported [13] and a mechanism, based on carrier distribution, has been proposed. We wanted here to check the stability of the part of the photoinduced index change due to densification. For that, we heated D-fibre samples with Bragg gratings to elevated temperatures in a furnace. A sample with three different gratings possessing valley depths between 6 and 22 nm has been heated to 400°C during 25 mn. When, for equivalent conditions, the reflectivity of a grating written in a cylindrical optical fibre has already decreased, here, modulations and valley depths were not altered, showing a strong resistance of the densification against temperature.

Conclusion

We showed that a densification was associated with the writing of Bragg gratings in fibres and that the densification evolution as a function of the fluence was similar in the optical fibre and in the preform from which it has been issued. We observed a transition mechanism between type I and type II gratings and we showed a strong resistance of the surface modification up to 400°C.

References:

- [1] MELTZ, MOREY and GLENN, Optics Letters, 14, 823 (1989).
- [2] HAND and RUSSEL, Optics Letters, 15, 823 (1990) 102.
- [3] WILLIAMS, DAVEY, KASHYAP, ARMITAGE and AINSLIE, Electron. letters, 28, 369 (1992).
- [4] POUHELLEC, GUENOT, RIAIT, SANSONETTI, NIAY, BERNAGE and BAYON, Optical Materials, 3 (1994).
- [5] POUHELLEC, RIAIT, NIAY, BERNAGE and BAYON, J.F., Submitted to the conference.
- [6] POUHELLEC, RIAIT, NIAY, BERNAGE and BAYON, Optical Materials, 4 (1995).
- [7] ATKINS, Optics Letters, 17, 7, 469 (1992).
- [8] FERTEIN, Thèse (1995).
- [9] POUHELLEC, RIAIT, NIAY, BERNAGE and BAYON, Submitted to Optical Materials.
- [10] ARCHAMBAULT, REEKIE and RUSSEL, Electron. Letters, 29, 453 (1993).
- [11] MIHAILOV and GOWER, Appl. Phys. Letters, 65, 21, 2639 (1994).
- [12] XIE, NIAY, BERNAGE, DOUAY, BAYON, GEORGES, MONERIE, POUHELLEC, Opt. com., 104, (1993).
- [13] ERDOGAN, MIZRAHI, LEMAIRE and MONROE, J. of Appl. Phys. 76, 73 (1994).

UV- induced stress changes in optical fibers

H. G. Limberger, P. Y. Fonjallaz, R. P. Salathé

Laboratory for Applied Optics, Swiss Federal Institute of Technology
CH-1015 Lausanne, Switzerland
Tel: +41 21 6935183
Fax: +41 21 6934916

F. Cochet

Cabloptic SA,
CH-2016 Cortaillod, Switzerland

Photosensitivity in optical fibers has first been observed by Hill et al. in 1978.¹ Recently, the application of Bragg gratings has considerably been increased due to the introduction of side exposure techniques.² Index changes of 10^{-3} have been achieved even in standard telecommunication fibers.³ Reliable fabrication of Bragg gratings depends on the detailed knowledge of the underlying mechanisms of photo-induced index changes. The basis of all proposed mechanisms is the ionization of a GeO deficiency center that exhibits an absorption bands in the UV at 240 nm. A model based on the change of color centers that include 3 or 4 absorption bands,^{4,5} a stress relaxation model,⁶⁻⁸ and structural changes^{9,10} have been proposed as origin of photosensitivity. In the color center model the index changes can be calculated from absorption changes using the Kramers-Kronig relationship. Including 4 absorption bands, an index change of 2×10^{-4} has been calculated.⁵ Higher index changes have been explained using a model based on thermoelastic stress relaxation where the photoelastic effect leads to the index change.⁶⁻⁸ The largest achievable stress and photoelastic index changes would then be determined by the initial thermoelastic stress. Even higher values may be explained by glass densification.^{9,10} Recently, the core stress in fibers with different Ge concentrations before and after UV irradiation with different doses has been measured.^{11,12} Such stress measurements allow directly to test the stress relief model and to correlate stress changes with refractive index changes. Here, we report on extended measurements performed on 3 fibers with Ge concentrations of 9%, 12% and 18% and propose a new model to explain the results.

The Bragg gratings have been fabricated with different irradiation doses using an excimer pumped dye laser system, beam shaping optics, and a Lloyd interferometer¹³ leading to an almost perfect fringe visibility. Beam profiles have been measured using imaging optics and a CCD camera to evaluate the laser fluence. Typical beam diameters were 20 - 40 μm resulting in fluences of 0.17 - 0.58 J/cm² per pulse. The stress measurements were performed using a standard technique to characterize the stress in fibers and preforms.¹⁴⁻¹⁷ A red HeNe laser, linearly polarized at 45° with regard to the fiber axis, is focused transversally on the fiber to about 3 μm . To reduce beam distortions, the fiber is immersed in an index-matching fluid. Due to the stress-induced birefringence, the two polarization components parallel and perpendicular to the fiber axis experience different retardations. The difference in retardation between the two components, Δ , is monitored as a function of distance, y , between the laser beam and the fiber center. The radial distribution of the axial stress, $\sigma_z(r)$, can then be calculated from an Abel integral equation:¹⁶

$$\sigma_z(r) = -\frac{1}{\pi C} \int_r^R \frac{\Delta'(y)}{\sqrt{y^2 - r^2}} dy$$

where $\Delta'(y) = d\Delta/dy$, R the fiber radius and C the stress optic coefficient of silica ($C = 3.46 \times 10^{-5} \text{ mm}^2/\text{kg}$).¹⁶ The sign of $\sigma_z(r)$ is determined from measurements on homogeneous pure silica fibers with and without external tension. The other components of elastic stress, the radial stress, $\sigma_r(r)$, and the circumferential stress, $\sigma_\theta(r)$, can be obtained from the axial stress using the sum rule and the equation of equilibrium.¹⁸

Figure 1 shows the initial radial distributions of axial stress, $\sigma_z(r)$, for three telecommunication fibers doped with 9% (fiber 1), 12% (fiber 2), and 18% Ge (fiber 3). The fibers were fabricated with a modified chemical vapor deposition method. Fiber 1 is a dispersion shifted fiber and fiber 3 is a dispersion compensating fiber. Both have a triangular core index profile. Fiber 2 is a two mode fiber with a step index profile. A positive $\sigma_z(r)$ corresponds to an axial tension, whereas a negative value is related to a compression. The fiber core appears as a peak at the center of the distribution. The stress state in the cladding is not uniform because of compositional variations. Since the thermoelastic stress increases linearly with the germanium concentration, highly doped fibers are more likely to exhibit tensile core stresses,^{14,15} e.g. fiber 2, and 3 which have an initial axial tensile stress of 1.6 kg/mm² and 1.3 kg/mm², respectively. The final stress is the sum of differential thermoelastic stresses and differential mechanical stresses induced by fiber pulling. Therefore, strong

pulling forces can lead to a total negative (compressive) core stress state^{14,16} as in the case of fiber 1 that shows an axial compression of -5.3 kg/mm^2 before irradiation.

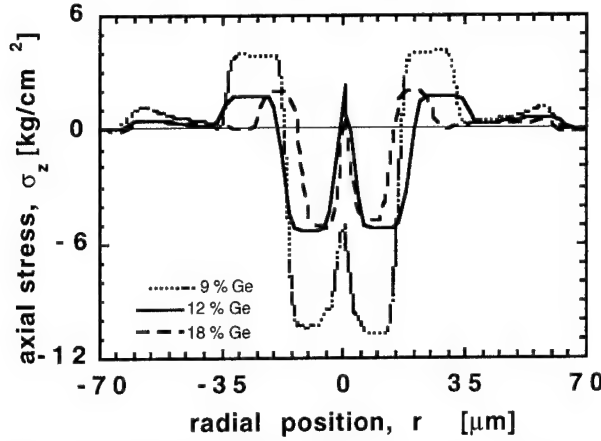


Fig. 1: Radial distribution of axial stress $\sigma_z(r)$ in three fibers with different Ge concentrations drawn with different pulling forces.

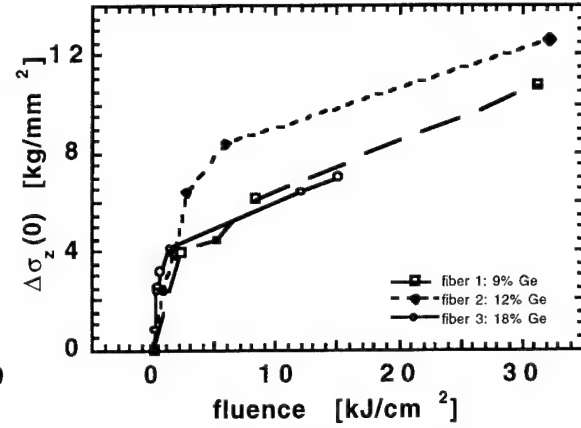


Fig. 2: Axial stress change $\Delta\sigma_z(0)$ in three fibers with different Ge concentrations as a function of laser fluence.

Figure 2 shows the evolution of axial stress change $\Delta\sigma_z(r)$ at the core center ($r=0$) of the three fibers. The UV irradiation of all fibers strongly increases the axial tension within the core, while the cladding remains almost unchanged. In case of fiber 1, an irradiation of 32 kJ/cm^2 leads to a final stress state of 5.5 kg/mm^2 at the core center where the stress has changed by 10.8 kg/mm^2 . Almost the same fluence applied to fiber 2 leads to a very large tensile stress of 14.2 kg/mm^2 where the stress change is 12.6 kg/mm^2 . Fiber 3 shows an important increase of stress at low fluences but its final value of stress change, $\Delta\sigma_z(0)$, stays below that of fiber 1 and 2. The difference in stress change between fiber 1 and 2 is correlated to the fact that fiber 2 is more photosensitive than fiber 1 showing also a higher index change.

The measurements demonstrate that the stress always increases in the fiber core independently of its initial value (negative or positive). These results contradict the stress relief model that considers only the thermal stress contribution and predicts an irradiation induced decrease of an initial tensile core stress towards a zero stress state.

The axial stress changes introduce index changes due to the photoelastic effect. The three cylindrical components of the refractive index depend on the stress components according to the following equations:¹⁸

$$n_r = n_0 - B_2 \sigma_r - B_l (\sigma_\theta + \sigma_z)$$

$$n_\theta = n_0 - B_2 \sigma_\theta - B_l (\sigma_r + \sigma_z)$$

$$n_z = n_0 - B_2 \sigma_z - B_l (\sigma_\theta + \sigma_r)$$

Here, n_0 is the refractive index of the materials without stress and n_r , n_θ , and n_z are the refractive indices of the light rays whose electric vector oscillate in the radial, circumferential and axial directions. B_l and B_2 are the positive stress-optical coefficients, for silica equal to 4.12×10^{-5} and $0.64 \times 10^{-5} \text{ mm}^2/\text{kg}$,¹⁹ respectively. Since $\sigma_r(0) = \sigma_\theta(0) = \sigma_z(0)/2$ ^{15,18} all components of the stress increase and give a negative contribution to the refractive index change. The photoelastic contribution is averaged over several grating periods due to the dimensions of the HeNe laser used for the stress measurements. Therefore we obtain for light polarized perpendicularly to the fiber axis for the mean photoelastic contribution, $\langle \Delta n_\sigma \rangle$, at the core center: $\langle \Delta n_\sigma \rangle = \langle \Delta n_r \rangle = \langle \Delta n_\theta \rangle = -0.65 \times 10^{-4} \times \Delta\sigma_z(0)$ where $\Delta\sigma_z(0)$ is in units of kg/mm^2 . In case of fiber 2 we obtain for $\langle \Delta n_\sigma \rangle$ a value of -8.2×10^{-4} . This value corresponds to the generally induced index changes but has a negative sign.

The index changes of each grating resulting from the irradiations have been evaluated experimentally. The amplitude of refractive index changes Δn^{mod} is obtained by comparing the reflection spectra of the Bragg gratings to a theoretical model based on a sinusoidal index

variation.³ The average change of refractive index $\langle \Delta n \rangle$ is obtained from the Bragg wavelength shift by differentiating the Bragg condition: $\Delta \lambda_B = 2 \Lambda \Delta n_{eff}$, where Λ is the grating period and n_{eff} the effective index. For a constant core radius we have $\Delta n_{eff} = \langle \Delta n \rangle$.

Figure 3 shows as an example the index change Δn^{mod} and the axial stress change $\Delta \sigma_z(r)$ of fiber 2 at the fiber center ($r=0$). Both curves show almost the same fluence dependence. The same behavior has also been observed for fibers 1 and 3. The similarity of index change and axial stress change as a function of laser fluence has recently been reported.^{11,12} A linear relationship with a slope of $(0.8 \pm 0.2) \times 10^{-4} \text{ mm}^2/\text{kg}$ has been observed for all three fibers investigated. Figure 3 shows also the evolution of the mean core index change, $\langle \Delta n \rangle$, of the grating written with the largest dose. $\langle \Delta n \rangle$ is about 30% smaller than the index amplitude and positive since the Bragg wavelength shifts to longer wavelength during the irradiation. This leads to the conclusion that the index change must be negative in the dark regions and that the photoelastic effect is not the dominant mechanism.

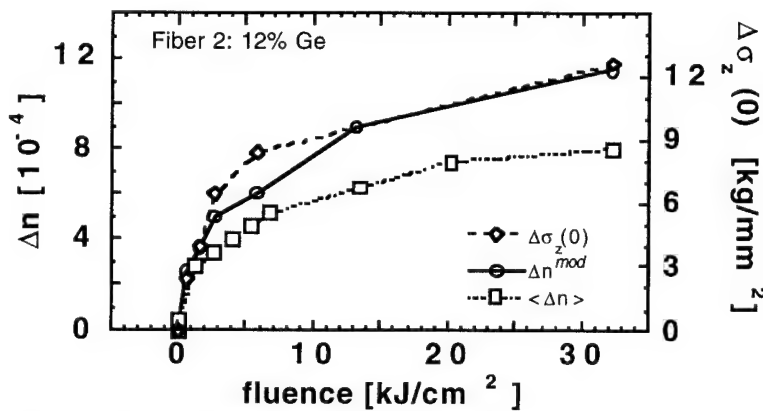


Fig. 3: Index modulation amplitude Δn^{mod} and axial stress change $\Delta \sigma_z(r=0)$ for gratings fabricated in fiber 2 (12% Ge). Evolution of the mean index change $\langle \Delta n \rangle$ of the grating written with the largest dose.

The photoelastic effect has a negative contribution to the index change due to the overall tension increase. Therefore, a totally increased refractive index can only be explained by a structural or plastic modification of the fiber core that contributes more positively to the total index change than the negative part induced by photoelasticity. The structural modifications must be the main contribution to the observed index change, since the color center modifications could never account for index changes of more than 2×10^{-4} .⁵ Such a positive contribution can be obtained from a compaction of the germanosilica network.¹⁰ The results of interferometric microscopy investigations of Bragg gratings written in preforms, have also been interpreted by the combination of compaction and photoelastic induced index changes.²⁰

The total index change Δn of the core after irradiation is the sum of the index change of the stress free material Δn_0 and the photoelastic contribution Δn_σ : $\Delta n = \Delta n_0 + \Delta n_\sigma$. If we assume a sinusoidal variation along the fiber axis, z , for the index modulation induced by compaction and for the photoelastic effect, the total index change is $\Delta n = \langle \Delta n \rangle + \Delta n^{mod} \sin(2\pi z / \Lambda)$, with $\langle \Delta n \rangle$ the mean index change and Δn^{mod} the amplitude. Figure 4a represents the total index change Δn of the grating fabricated with the maximum total fluence in fiber 2, as deduced from the determined values of index amplitude Δn^{mod} and $\langle \Delta n \rangle$.²¹ Figure 4b shows the two contributions to the obtained total refractive index change: the index change of the stress-free material with the amplitude Δn_0^{mod} , and the tension-induced photoelastic index changes with its amplitude Δn_σ^{mod} . Since the observed mean index change $\langle \Delta n \rangle$ is smaller than the modulation amplitude, Δn^{mod} , the index change must be negative in the dark regions. These regions are hence dilated and therefore the bright regions are effectively compacted. The core is attached to the cladding: the bright regions bear tension from all directions (also from the cladding), while the dark regions bear only an axial tension from the compacted bright regions. Therefore, the tension increase in the bright regions is larger than in the dark

regions. From the sum of the mean index values we obtain the mean index of the stress free material: $\langle \Delta n_0 \rangle = \langle \Delta n \rangle - \langle \Delta n_\sigma \rangle$ which amounts to 1.6×10^{-3} . Neglecting a color center contribution and using the Lorentz-Lorenz relation we can calculate a relative volume change of approximately 6 ‰.¹⁰ Due to the almost 100% fringe visibility (no grating erasure was observed) we assume that the amplitude and the mean value of index change of the stress free material are equal. Then we obtain from the sum of the amplitude values the amplitude of the photoelastic contribution: $\Delta n_\sigma^{mod} = \Delta n^{mod} - \Delta n_0^{mod}$ which amounts to -4.3×10^{-4} .

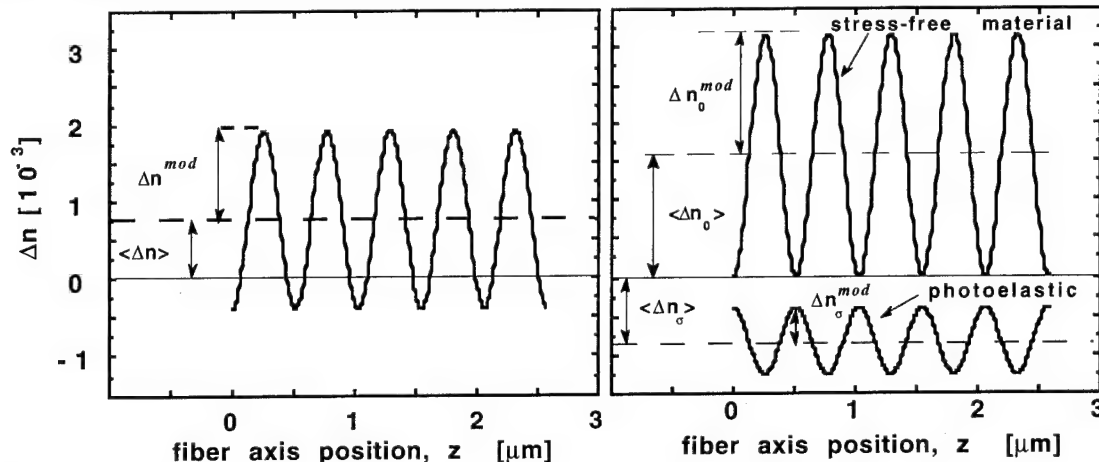


Fig. 4a: Experimentally obtained index change (sinusoidal variation assumed) in fiber 2 (dose = 32 kJ/cm²).

Fig. 4b: Calculated index changes due to the photoelastic effect (Δn_σ) and due to material changes (Δn_0).

In summary, we have shown that the formation of Bragg gratings in single-mode fibers strongly increases the tensile core stress independently of the sign of the initial stress. This is in contradiction with the stress relief model. The increase in tension lowers the refractive index through the photoelastic effect, however the mean effective index is increased since the Bragg resonance is shifted to longer wavelengths during irradiation. The observed mean index change is about 30% smaller than the index modulation amplitude. Both, the tension increase and the overall positive mean index change can be explained by a structural modification of the germanosilicate core network into a more compact configuration. The positive index change of the stress-free materials can be as large as $3.2 \cdot 10^{-3}$ in a 12% Ge fiber.

References:

1. K. O. Hill, Y. Fujii, D. C. Johnson, B. S. Kawasaki, Appl. Phys. Lett. 32, 647, 1978
2. G. Meltz, W. W. Morey, W. H. Glenn, Optics Letters 14, 823, 1989
3. H. G. Limberger, P. Y. Fonjallaz, R. P. Salathé, Electronics Lett. 29 No. 1, 47, 1993
4. D. P. Hand, P. St. J. Russell, Optics Letters 15 (2), 102, 1990
5. L. Dong, J. L. Archambault, P. St. J. Russell, D. Payne, Proc. ECOC 1994, p. 997
6. M. G. Sceats, P. A. Krug, SPIE 2044, 113, 1993
7. D. Wong, S. B. Poole, M. G. Sceats, Integrated Photonics Research 1992, p. 408, paper Pd16 and Optics Letters 24 (17), 1773, 1992
8. M. G. Sceats, G. R. Atkins, S. B. Poole, Annu. Rev. Mater. Sci. 23, 381, 1993
9. J. P. Bernardin, N. M. Lawandy, Optics Comm. 79, 194, 1990
10. C. Fiori, R. A. B. Devine, Materials Research Society Symp. Proc. 61, 187, 1986
11. P. Y. Fonjallaz, H. G. Limberger, R. P. Salathé, F. Cochet, B. Leuenberger, Proc. ECOC 1994, p. 1005
12. P. Y. Fonjallaz, H. G. Limberger, R. P. Salathé, F. Cochet, B. Leuenberger, to be published in Optics Letters.
13. H. G. Limberger, P. Y. Fonjallaz, P. Lambelet, R. P. Salathé, Ch. Zimmer, H. H. Gilgen, Proc. Society of Photo-Optical Instrum. Eng. Vol. 2044, 272, 1993
14. P. K. Bachmann, W. Hermann, H. Wehr, D. U. Wiechert, Appl. Optics 26 (7), 1175, 1987
15. W. Hermann, M. Hutjens, D. U. Wiechert, Appl. Optics 28 (11), 1980, 1989
16. P. L. Chu, T. Whitbread, Applied Optics 21 (23), 4241, 1982
17. P. K. Bachmann, W. Hermann, H. Wehr, D. U. Wiechert, Appl. Optics 25 (7) 1093, 1986
18. G. W. Scherer, Applied Optics, 19, 2000, 1980
19. W. Primak, and D. Post, J. of Applied Physics, 30, 779, 1959
20. B. Poumellec, I. Riant, P. Niay, P. Bernage, J. F. Bayon, to be published in Optical Materials, 1995, 4.
21. P. Y. Fonjallaz, H. G. Limberger, R. P. Salathé, F. Cochet, to be published

UV-induced photochemical reactions and point defects in photorefractive SiO₂:GeO₂ and implanted SiO₂ glasses

Hideo HOSONO, *^{1,2} Junji NISHII ³ and Hiroshi KAWAZOE¹

¹ *Tokyo Institute of Technology, Research Laboratory of Engineering Materials, Nagatsuta, Midori-ku, Yokohama 226, JAPAN*

² *Institute for Molecular Science, Myodaiji, Okazaki 444, JAPAN*

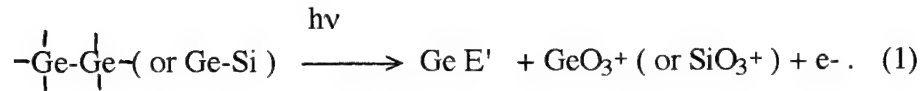
³ *Osaka National Research Institute, AIST, Ikeda, Osaka 563, JAPAN*

* Corresponding author

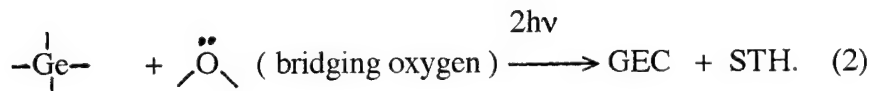
Tel +81-45-924-5359, Fax +81-45-922-5169, E-mail hhosono@nc.titech.ac.jp

SiO₂:Ge(10 %) glasses prepared by the vapor phase deposition were exposed to ultraviolet radiation from a filtered Hg discharge lamp (4.9 eV) and excimer lasers (ArF : 6.4 eV, KrF : 5.0 eV, and XeCl 4.0 eV). Two photochemical reaction channels were ascertained : (1) The exposure to the lamp irradiation (~ 16 mW/cm²) induced Ge E' centers accompanied by bleaching of the absorption component (peaking at 5.06 eV) due to the neutral oxygen monovacancies (NOMV) and emergence of an intense band near 6.4 eV and a shoulder at around 5.7 eV. (2) Irradiation with the excimer lasers (pulse duration; 20 ns) generated two types of paramagnetic defects, electron trapped centers (GEC) ¹ associated with four-fold coordinated two Ge ions or a Ge ion and a Si ion and a self-trapped hole center (STH: bridging oxygen trapping a hole)². The striking difference in induced ESR centers are evident in fig.1. The former and the latter were concluded to be caused via one-photon and two-photon absorption processes (an example indicating 2-photon process is shown for ArF laser in fig.2), respectively. In the case of the lamp irradiation, the neutral oxygen

monovacancy (NOMV) coordinated by two Ge ions is converted into Ge E' center and a planar Ge (or Si)O₃⁺ as shown in eg.1 through a one photon process : ³



The uppermost level of the valence band is composed of the orbitals of lone pair electrons on bridging oxygens and the energy of two photons for each laser exceeds the optical band gap (~7.1 eV), which was determined by the Tauc plot. Thus, we propose that the following reaction path for the excimer laser irradiation:



The schematic energy diagram of relevant defects and photochemical reactions is summarized in Fig.4.

Enormous concentrations of point defects in glasses are produced by implantation and information on chemical interaction of implanted ions with substrate structures can be obtained through the characterization of these defects.⁴ Enhancement of the efficiency of photoeffects is an important issue to realize down-sizing toward optical integrated circuits. Recalling that defects responsible for the photoeffects are the NOMV, we expect a conspicuous concentration enhancement of these defects in Ge-doped SiO₂ glasses by H⁺-implantation as a consequence of chemical interactions of implanted H⁺ and substrate structures.

Formation and photobleaching of optical absorption bands in a 5-ev region were examined in proton-implanted 5GeO₂-95SiO₂ glasses and SiO₂ glasses implanted with Si, Ge, B or P ions. A conspicuous increase in the intensity of the 5-ev band, which are attributed to oxygen vacancies, was seen both in substrates after implantation. However, a distinct difference was observed in bleaching

with 5 ev-light between the H-implanted $\text{SiO}_2\text{:Ge}$ glasses and the implanted SiO_2 glasses. In the former the 5ev-band was bleached and intense absorptions at $> 5\text{eV}$ emerged, whereas in the latter bleaching occurred in the whole uv region. This distinct bleaching nature provides implanted glasses the possibilities of modification of refractive index by uv illumination.

References

- 1) D.L.Griscom, Phys.Rev.B**40**, 4224 (1989).
- 2) H.Kawazoe, J.Non-Cryst.Sol. **71**, 231(1985).
- 3) H.Hosono, Y.Abe, D.L.Kinser, R.A.Weeks, K.Muta and H.Kawazoe, Phys.Rev.B**46**,11445(1992).
- 4) H.Hosono and N.Matsunami, Phys.Rev.B**48**, 13469(1993):
H.Hosono, Phys.Rev.Lett.**74**, 110(1995).

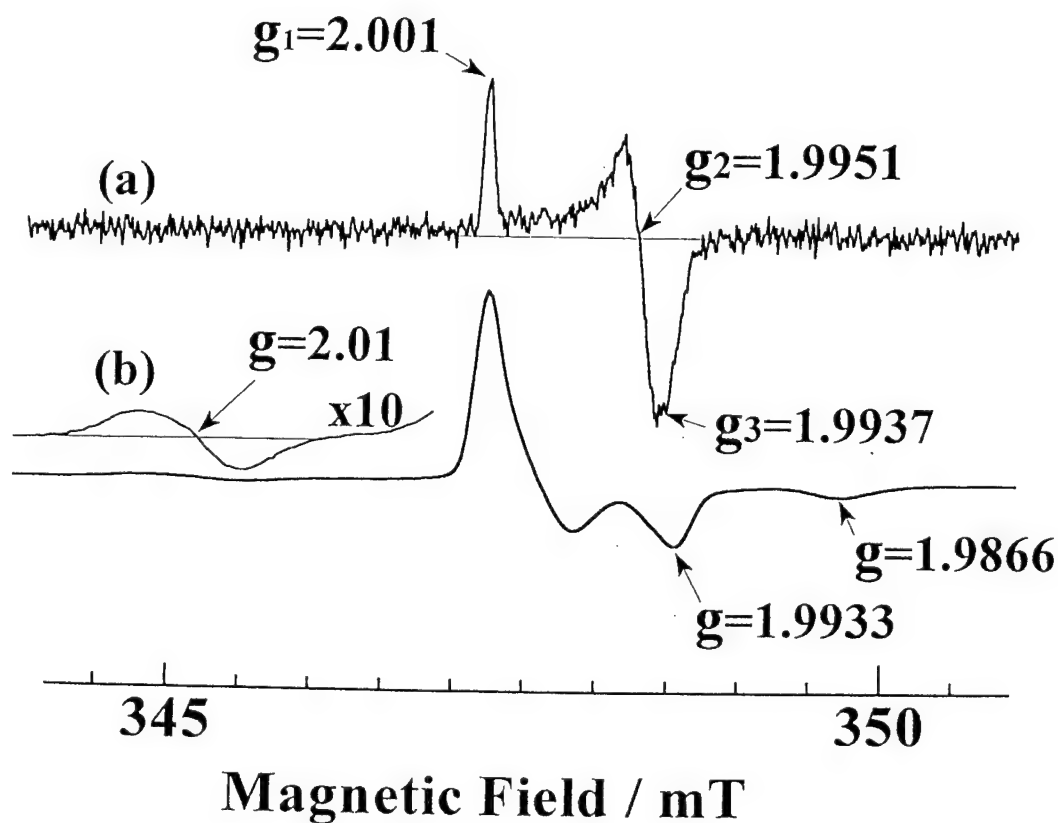


Fig.1. ESR spectra of irradiated $\text{SiO}_2\text{:Ge}$ glasses.

(a) prolonged illuminated with an Hg lamp, (b) irradiated with KrF or ArF laser.

Dominant signals in (a) and (b) are Ge E' center and Ge electron center (GEC), respectively. A resonance centered at $g=2.01$ is tentatively ascribed to a self-trapped hole trapped on an oxygen bonded with Ge.

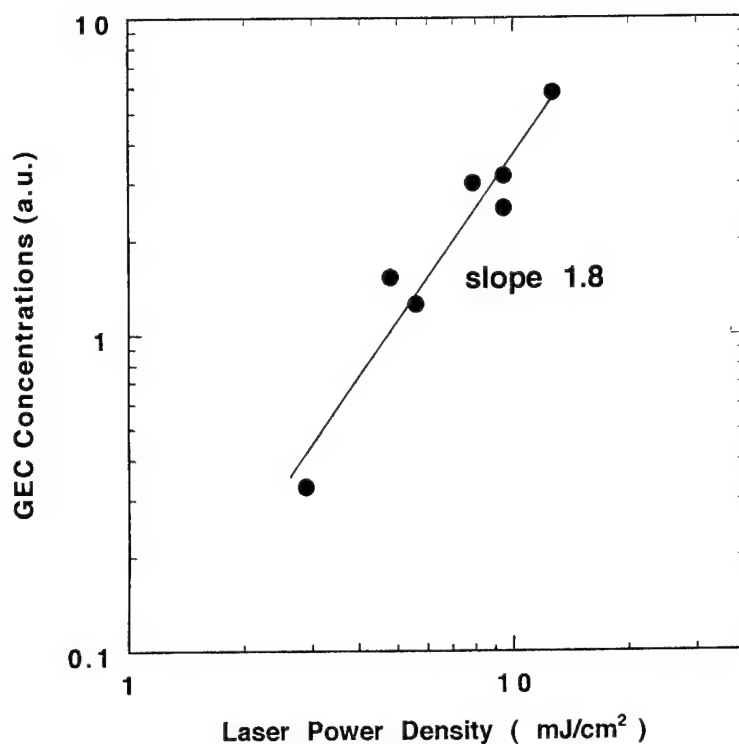


Fig.2 Log-log plots of concentrations of induced Ge electron centers and power density of ArF excimer lasers.

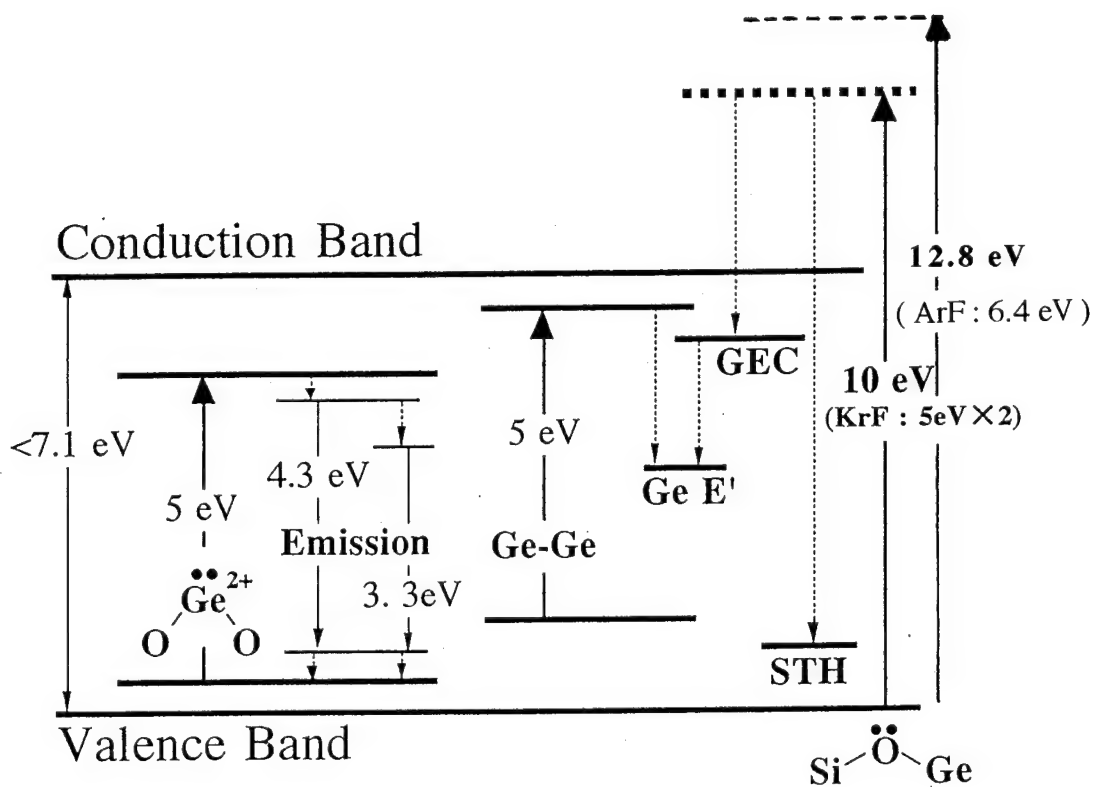


Fig.3. Schematic energy diagram showing relevant defect levels and photochemical reactions.

Sunday, September 10, 1995

New Materials and Techniques

SuA 8:30–10:30am
Multnomah Room

Robert A. Weeks, *Presider*
Vanderbilt University

BRAGG GRATING PHOTOINSCRIPTION WITHIN VARIOUS TYPES OF FIBERS AND GLASSES

P. Niay, P. Bernage, M. Douay, T. Taunay, W.X. Xie, G. Martinelli
 Laboratoire de Dynamique Moléculaire et Photonique, URA CNRS 779,
 Bâtiment P5, Université des Sciences et Technologies de Lille,
 59655 Villeneuve d'Ascq, France,
 phone number : 20.43.47.62, fax number : 20.43.40.84

J.F. Bayon, H. Poignant and E. Delevaque
 LAB/RIO/TSO, France Telecom CNET Lannion, B.P. 40,22301 Lannion, France,
 phone number : 96 05 28 28, fax number : 96.05.13.07

Summary : Optical fiber photosensitivity can be triggered by photochemical processes associated with a large variety of dopants. Thus, photosensitivity in germanosilicate fibers has been related to absorption of light at a germanium defect absorption band located near 5 eV [1] [2]. Photosensitivity in rare-earth doped glasses or optical fibers has been demonstrated by pumping of ion transitions. For example, we have recently reported permanent index changes in Ce^{3+} doped ZBLAN, HBLAN and ZBLALi fluorozirconate glasses or fibers through the pumping of $4f \rightarrow 5d$ Ce^{3+} transitions using a pulsed laser [3] [4]. In most of the experiments dealing with rare-earth or germanium doped glasses or fibers, it was reported that grating inscriptions led to broad absorption changes which were attributed to photoinduced charge transfer from donors to trap sites. This suggests that charge transfer is a common effect involved in grating photoinscription within all the up to now studied insulating glass fibers. Experiments have been carried out with a view to finding other analogies or differences between photosensitive

behaviors of gratings written in various glasses. The aim of the talk is to report results of these experiments with a specific emphasis on the dynamics of grating formation.

To study the effect of H_2 loading on the dynamics of grating inscription, gratings were written for long irradiation time, in standard telecommunication fibers, in small core high numerical aperture Ge doped silica fibers, in Ce^{3+} : Al_2O_3 or in Tb^{3+} : Al_2O_3 doped core silicate fibers and in Ce^{3+} : ZBLALi fluorozirconate fibers by using holographic or phase mask inscription methods. Pulsed or cw UV lasers were used for trying to photoimprint the gratings within either H_2 loaded fibers or within unimpregnated fibers. H_2 loading proved to significantly enhance the photosensitivity of all the above mentioned silicate fibers. It was proving ineffective to increase the efficiency of grating inscription within the fluoride fibers. Some specific experimental conditions didn't lead to a grating inscription. For example, any attempt of grating inscription within the rare earth doped fluoride or silicate fibers was unsuccessful when using 244

nm or 257 nm cw light, whereas pulsed exposure was efficient. In other respects, the photoimprinting could only be made within the Tb^{3+} doped silicate fiber after photosensitization by H_2 loading the fiber. Fig 1 shows the transmission spectra of strong gratings written within the Tb^{3+} doped silicate fiber using pulsed 240 nm light.

FIG1 : TRANSMISSION SPECTRA OF FIBER GRATINGS IN Al_2O_3/Tb^{3+} DOPED OPTICAL FIBER

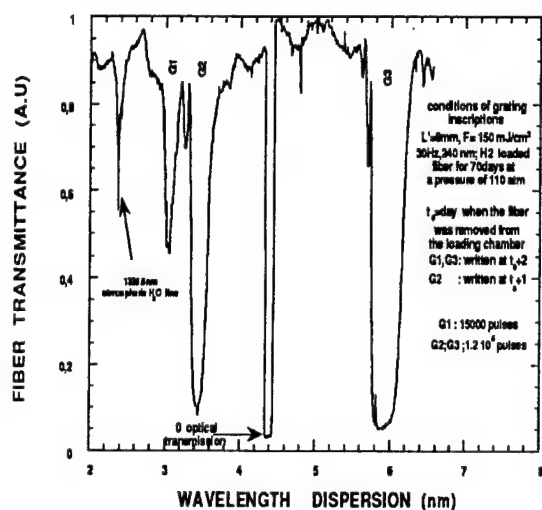
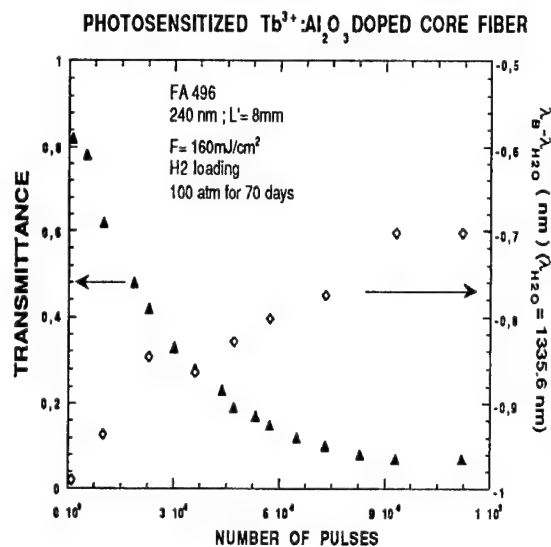


Fig 2 shows the evolution of the grating spectral characteristics as a function of the number of pulses impinging onto the Tb^{3+} doped fiber. To our best knowledge, this is the first report of H_2 photosensitization of germanium and phosphorus free silicate fibers. Unlike P_2O_5 doped fiber, the photosensitization process of the studied Al_2O_3 doped core fibers is efficient when pumping at 244 nm.

The evolutions with time of the refractive index modulation, as calculated from the strengths of gratings, followed monotonous saturating growth behaviors for most fibers.

FIG2: EVOLUTION OF THE SPECTRAL CHARACTERISTICS OF A GRATING BEING WRITTEN IN H_2



However, as previously reported [3], the dynamics of grating inscriptions of high NA GeO_2 doped silica fibers was not monotonous with increasing exposure time. It was first observed a decrease in the fiber transmittance near the first order Bragg wavelength, followed by a complete or partial erasure of the first order spectrum and then by a new spectrum formation. For convenience we distinguish between these two successive spectra by labelling them grating I and grating II A spectra. The inscription of a type I spectrum induced a Bragg wavelength shift towards the red part of the spectrum. This resulted from a photoinduced increase in the fiber effective index. At the time of erasure of the type I spectrum, the Bragg wavelength changed its way. It shifted towards the blue or did not significantly shift in the course of the type II A spectrum inscription. H_2 loading the high NA monomode Ge -doped silica fibers led to complex observations. No type II A photo-

sensitivity could be yet observed when writing grating within these fibers few days after their removal from the pressure vessel [6]. However, grating inscription dynamics recorded by the CNET laboratory team at regular periods of time during the H_2 outgassing didn't only show a recovery of type II A photosensitivity but also an increase in the rate of erasure of type I spectrum and in this of type II A spectrum inscription. These observations show 1) that type II A photosensitivity can be detected at small H_2 residual pressure and 2) that some up to now unknown chemical or physical fiber property governing the dynamics of type II A photosensitivity was modified by the H_2 loading process.

In an attempt to further clarify the origin of the type II A photosensitivity we wrote thick holograms in the cores of highly GeO_2 doped preforms (such as type II A spectrum dynamics can easily be observed in fibers pulled from these preforms). No significant mark of type II A photosensitivity features could be noticed since the growth behavior of the holograms followed a power law time dependence ($\Delta n \propto A t^m$, $m \approx 0.5$). As the distribution of stresses frozen within a fiber core is quite different from this in the core of a preform slice, initial stress distribution within the germanosilicate glass was suspected to be an important parameter to get or not type II A photosensitivity. Accordingly, dynamics of formation of grating spectra were recorded during photoinscription of gratings within high NA germanosilicate fibers put under strains. Fig 3 shows the comparison between the evolutions of grating transmittance as a function of the number of pulses

impinging onto the fibers. The parameter of this experiment was the strain applied to each fiber in the course of the grating inscription.

FIG3: EVOLUTION OF THE TRANSMITTANCE OF GRATINGS WRITTEN IN UNSTRAINED OR STRAINED FIBERS

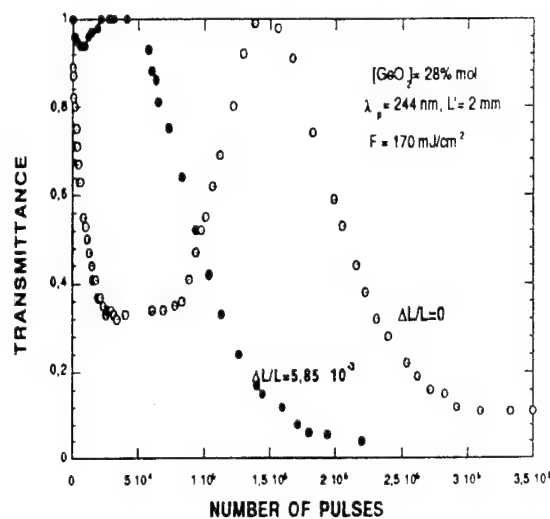
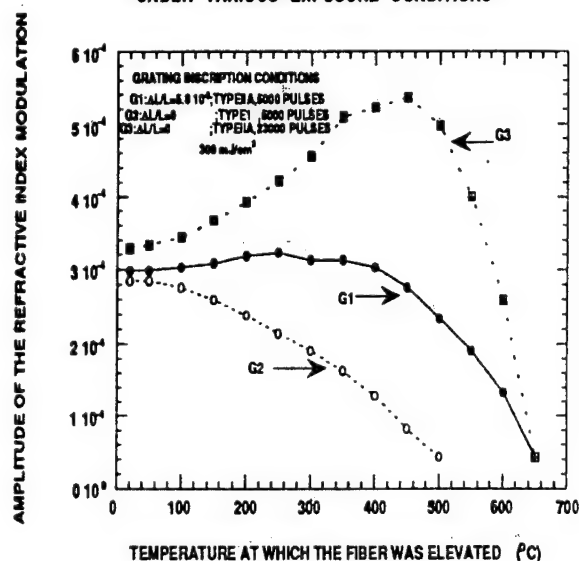


Fig 3 shows that straining the fiber not only reduced the life time of the type I spectrum but also the strength of the grating at this time. Additional measurements performed in the course of grating inscription in strained fibers showed that the shift experienced by the Bragg wavelength moved towards the red during the life time of the type I spectrum and during this of a part of the type II A spectrum. For longer exposure time, the shift changed its direction and moved towards the blue. The order of magnitude of this shift didn't seem to depend on the strain. Fringeless irradiation of a grating at the time of erasure of type I spectrum produced the inscription of a new spectrum. Comparison between the kinetics of thermal bleaching of gratings written in strained or unstrained fibers was performed through 30 mn isochronal thermal

annealing experiments. For this purpose, three gratings G_1 , G_2 and G_3 were written in the high NA fiber at a fluence per pulse of 320 mJ/cm^2 . More specifically, G_1 was written by 5000 pulses within the fiber put in 5.2×10^{-3} strain. This produced a grating of 57 % first order spectrum reflectivity. G_2 and G_3 were written in an unstrained fiber by 5000 pulses and 23 000 pulses respectively. G_2 was a type I grating with a reflectivity of 59 % and G_3 an unsaturated type II A grating of reflectivity 63 %. Fig 4 shows the evolutions of the reflectivities of G_1 , G_2 and G_3 as a function of the temperature at which the fiber was elevated. Spectra were recorded at room temperature.

FIG4: THERMAL ISOCHRONAL BLEACHING OF THREE GRATINGS WRITTEN WITHIN HIGH N.A. GERMANOSILICATE FIBER UNDER VARIOUS EXPOSURE CONDITIONS



Although that the reflectances of G_1 , G_2 and G_3 were nearly equal at the beginning of the experiment and that G_1 and G_2 were written by using the same UV dose, fig 4 shows that their behaviors looked quite different as a function of the temperature rise. This shows that the UV dose but also the

fiber strain (and thus its thermal history) are pertinent parameters when looking at the thermal stabilities of gratings written in these fibers. Further details about these experiments and about properties of the gratings written in the various types of fibers and glasses will be presented at the conference.

References :

- [1] K.O Hill, Y. Fujii, D.C. Johnson and B.S. Kawasaki
Appl Phys. 32, 1978, p 647-649
- [2] G. Meltz, W.W. Morey and W.H. Glenn
Opt. Lett 14, 1989, p 823-825
- [3] T. Taunay, P. Niay, P. Bernage, W.X. Xie, H. Poignant, S. Boj, E. Delevaque and M. Monerie
Opt. Lett. 19, 1994, p 1289-1271
- [4] H. Poignant, S. Boj, E. Delevaque, M. Monerie, T. Taunay, P. Niay, P. Bernage and W. X. Xie
Elect Lett, 30, 1994, p 1339-1340
- [5] W.X. Xie, P. Niay, P. Bernage, M. Douay, J.F. Bayon, T. Georges and M. Monerie
Opt. Com. 104, 1993 p 185-195
- [6] This behavior was first pointed out to our attention by P. Sansonnetti and I. Riant.

Large Photo-Induced Index Changes in Sn-codoped Germanosilicate Fibres

L. Dong, J.L. Cruz*, L. Reekie, M.G. Xu and D.N. Payne
 Optoelectronics Research Centre, The University of Southampton,
 Southampton SO17 1BJ, U.K., Tel: +44 1703 593163,
 Fax: +44 1703 593149, Email: LD@ORC.SOTON.AC.UK

*On leave from Departamento Física Aplicada,
 Universidad de Valencia, Dr. Moliner 50,
 Burjassot, 46100, Valencia, Spain.

Background: There has been a surge of interests in photosensitive fibre gratings in recent years chiefly due to their ease of fabrication and numerous application. Although very large photo-induced index changes have been achieved in pure germanosilicate fibres, an enhanced photosensitivity is desirable to enable gratings to be written with ease and with much cheaper laser source. Stronger photosensitivity also opens up many new applications. Boron-codoping in germanosilicate fibres has been reported to give a much enhanced photosensitivity comparing to that in pure germanosilicate fibres [1], but gratings in those fibres have a much poorer high temperature stability and the B-codoping can also give rise to excessive loss at the important telecommunication window of $1.55\ \mu\text{m}$. Some post-fabrication techniques have also been devised, i.e. H_2/O_2 flame-brushing of a germanium doped fibre [2] and Low-temperature hydrogen loading [3], but they are very time-consuming and there are also large induced losses [3]. In this paper, we report on enhanced photosensitivity in Sn-codoped germanosilicate fibres. The gratings in the Sn-doped fibres also have a much improved high temperature stability than those in B-codoped fibres. Unlike B-codoping, Sn-codoping does not introduce significant loss at the important telecommunication window of $1.55\ \mu\text{m}$.

Experiments: Two Sn-codoped germanosilicate fibres were fabricated for this experiment by introducing SnCl_4 vapour during a MCVD process. The first fibre (fibre I) had a NA of 0.20, first-order mode cut-off wavelength of $1.25\ \mu\text{m}$ and loss of 2 dB/km at $1.55\ \mu\text{m}$. The second fibre (fibre II) had a NA of 0.29, first-order mode cut-off wavelength of $1.32\ \mu\text{m}$, and loss of 25 dB/km at $1.55\ \mu\text{m}$.

The absorption of the core glass in the first preform (preform I) was measured with the technique described in [4] before and after an exposure to a line-narrowed pulsed KrF excimer laser operating at 248.5 nm. The pulse duration was 20 ns and pulse repetition rate was 20 Hz. The original absorption of the preform core shows an tail of an absorption band centred below 190 nm with a peak at $\sim 250\ \text{nm}$. (see fig.1). The 248 nm exposure caused a general increase of the absorption, in contrast to that in pure germanosilicate fibres where a reduction of the 240 nm band is observed. The excimer laser induced loss at infrared was also measured in fibre I after a 5 minute exposure. There was a relatively strong induced loss in the near visible ($\sim 0.44\ \text{dB/mm}$ at 600 nm), but virtually no induced loss above $0.9\ \mu\text{m}$. A slightly stronger temporary induced loss was also noted during exposure, but only a smaller permanent induced loss remained after the exposure.

Fibre gratings were then imprinted in sections of the fibres using an interferometric set-up. The pulse fluence was set at $\sim 0.25 \text{ J/cm}^2$ for the grating writing. The grating length was $\sim 15 \text{ mm}$ in length. The grating in fibre I reached $\sim 100\%$ reflectivity within $\sim 1 \text{ mins}$ (i.e. $\sim 0.3 \text{ kJ/cm}^2$). After 30 minutes, the FWHM bandwidth attained a saturation level of $\sim 0.75 \text{ nm}$ (see fig.2). An index change of $\sim 1.4 \times 10^{-3}$ can be deduced from the grating. Fig.3 gives a comparison between saturated photo-induced index changes deduced from gratings written by the interferometric set-up in fibres of the following core compositions, A) $\text{SiO}_2/\text{GeO}_2$, B) $\text{SiO}_2/\text{GeO}_2/\text{B}_2\text{O}_3$, C) $\text{SiO}_2/\text{GeO}_2/\text{SnO}_2$. The saturated photo-induced index changes in the Sn-codoped germanosilicate fibre are comparable with those in B-codoped germanosilicate fibres and are several times larger than those in pure germanosilicate fibres. Although index change of $\sim 1.2 \times 10^{-3}$ has been reported in a pure germanosilicate fibre (depressed cladding PCVD fibre) [5], similar result has not been repeated by other groups in very similar fibres. It must be pointed out that the B-codoped fibre in which $\sim 1.2 \times 10^{-3}$ index change was achieved had a very high loss of $\sim 100 \text{ dB/km}$ at $1.55 \mu\text{m}$. The results of high-temperature stability tests for gratings in fibres with the three core compositions A) $\text{SiO}_2/\text{GeO}_2$, B) $\text{SiO}_2/\text{GeO}_2/\text{B}_2\text{O}_3$, C) $\text{SiO}_2/\text{GeO}_2/\text{SnO}_2$ are shown in fig.4. The grating in a Sn-codoped germanosilicate fibre (fibre I) is much more stable than that in a B-codoped germanosilicate fibre.

Conclusions: A factor of ~ 3 larger photo-induced index changes have been demonstrated, a result comparable to B-codoping. The gratings in the Sn-doped fibres also have a much improved high temperature stability than those in B-codoped fibres. Unlike B-codoping, Sn-codoping does not introduce significant loss at the important telecommunication window of $1.55 \mu\text{m}$. Tin can also be easily introduced in the vapour phase as SnCl_4 into the state of art optical fibre fabrication process using vapour-phase deposition.

References:

1. D.L. Williams, B.J. Ainslie, J.R. Armitage, R. Kashyap and R. Campbell: "Enhance UV photosensitivity in boron codoped germanosilicate fibres", *Elect. Lett.*, **29**, 1993, pp.45-47.
2. F. Bilodeau, B. Malo, J. Albert, D.C. Johnson and K.O. Hill: "Photosensitization of optical fibre and silica-on-silicon/silica waveguides", *Opt. Lett.*, **18**, 1993, pp.953-955.
3. P.J. Lemaire, R.M. Atkins, V. Mizrahi and W.A. Reed: "High pressure H_2 loading as a technique for achieving ultrahigh UV photosensitivity and thermal sensitivity in GeO_2 doped optical fibres", *Elect. Lett.*, **29**, 1993, pp.1191-1193.
4. L. Dong, J. Pinkstone, P.St.J. Russell and D.N. Payne: "Ultraviolet absorption in modified chemical vapour deposition preforms", *J. Opt. Soc. Am. B*, **11**, 1994, pp.2106-2111.
5. H.G. Limberger, P.Y. Fonjallaz and R.P. Salathé: "Spectral characterisation of photoinduced high efficient Bragg gratings in standard telecommunication fibres", *Elect. Lett.*, **29**, 1993, pp.47-48.

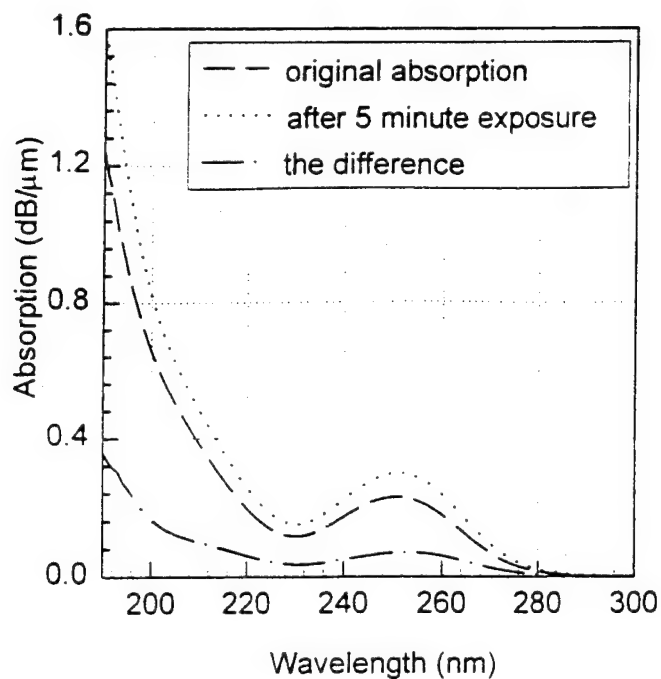


Fig. 1

The UV absorption spectra measured in the Sn-codoped germanosilicate preform before and after exposure to a KrF excimer laser beam for 5 mins. The pulse fluence was set at $\sim 50 \text{ mJ/cm}^2$ for this exposure.

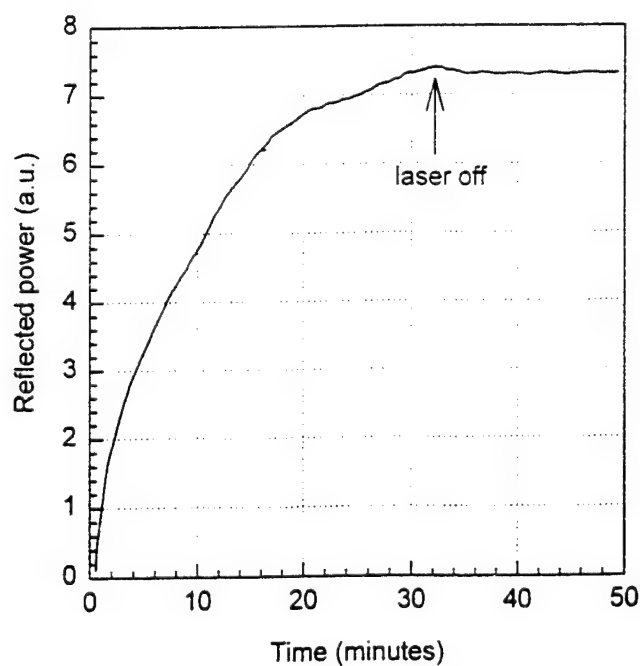


Fig. 2

Growth of a grating in fibre I when writing with a KrF excimer laser at 20 Hz with a pulse fluence of 0.25 J/cm^2 .

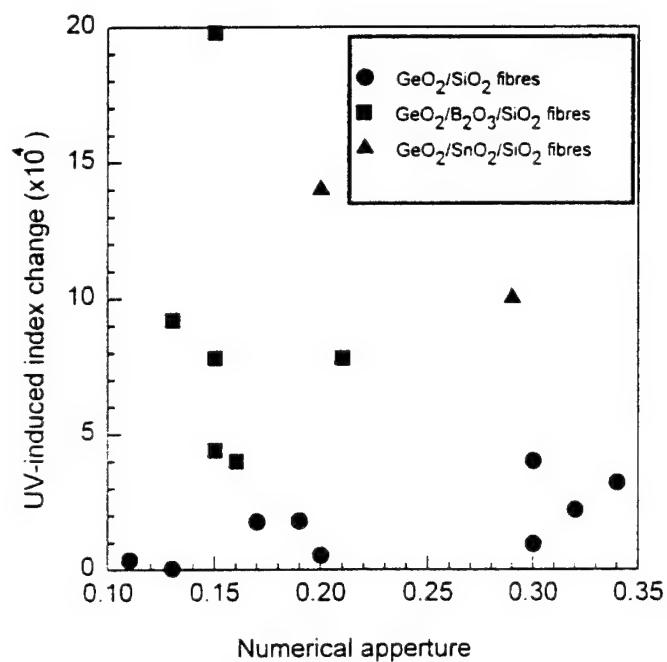


Fig.3 248 nm-induced refractive index changes in three types of fibres A) $\text{SiO}_2/\text{GeO}_2$, B) $\text{SiO}_2/\text{GeO}_2/\text{B}_2\text{O}_3$ and C) $\text{SiO}_2/\text{GeO}_2/\text{SnO}_2$.

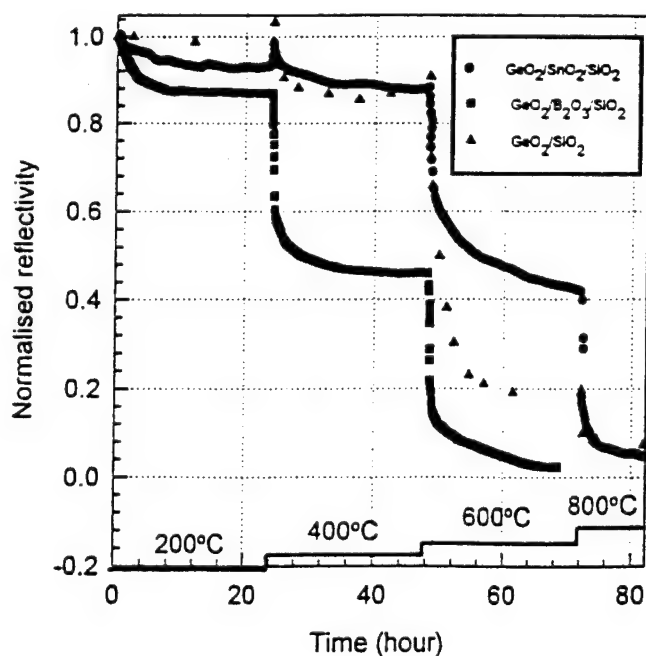


Fig.4 Decay of the UV-induced index changes at elevated temperatures in fibres containing A) $\text{SiO}_2/\text{GeO}_2$, B) $\text{SiO}_2/\text{GeO}_2/\text{B}_2\text{O}_3$ and C) $\text{SiO}_2/\text{GeO}_2/\text{SnO}_2$.

Moving fibre/phase mask-scanning beam technique for writing arbitrary profile fibre gratings with a uniform phase mask

M. J. Cole, W. H. Loh, R. I. Laming and M. N. Zervas

*Optoelectronics Research Centre
University of Southampton
Southampton SO17 1BJ
United Kingdom*

Tel: (44) 1703 592693 Fax: (44) 1703 593142

Introduction

Fibre Bragg gratings are by now well-recognised as key components for many fibre optic and laser systems, but ways for improving their characteristics and ease of fabrication continue to be a subject of considerable research interest. In particular, much of the recent activity has centred on the use of phase masks for grating production[1,2].

The phase mask approach is attractive for it allows fibre gratings to be written with much relaxed tolerances on the coherence of the writing beam, as well as providing greater repeatability than was previously possible. However, a major drawback has been that the grating wavelength is dictated by the period of the phase mask, and separate masks would be required for different wavelengths. Considerable effort has gone into making the phase mask approach more flexible, e.g. by incorporating a magnifying lens to alter the fibre Bragg wavelength[3]. The introduction of a scanning writing beam was a further advance which enabled the fabrication of long fibre gratings without requiring a large beam magnification, as well as allowing more complex structures to be directly written by modulating the writing beam as it scans across the mask[4,5].

The ability to create more complex structures, such as apodised and/or controllably chirped gratings, is of great importance for many applications. While apodisation can be approximated by modulation of the scanning beam cited above, the accompanying variation in the average refractive index imparts an induced chirp to the grating which is often undesirable. 'Pure' apodisation has recently been reported, but at the expense of either requiring a specially designed phase mask[6], or with double exposure to two different masks[7]. Considerable effort has also gone into writing controllable chirp characteristics into the grating, via a double-exposure technique[8], specially designed 'step-chirp' phase masks[9], or by straining the fibre[10].

In this paper, we demonstrate a simple technique which involves slowly moving the fibre, or alternatively the phase mask, as the writing beam is scanning, and show that this is effective in overcoming many of the limitations which are currently associated with phase masks. With this approach, we can produce multi-wavelength gratings, 'pure' apodisation, as well as a variety of dispersive structures.

Experiment

Fig. 1 shows the experimental setup. The UV writing beam (100 mW cw at 244 nm) from a frequency-doubled argon laser is steadily scanned across a zero-order nulled phase mask, while the fibre is slowly moved relative to the mask, causing a gradual phase shift to be added to the fibre grating being written. For uniform motion, this results in a simple shift of the Bragg wavelength. If λ_0 is the unshifted Bragg wavelength, and v_f and v_{sc} are the fibre and scanning beam velocities

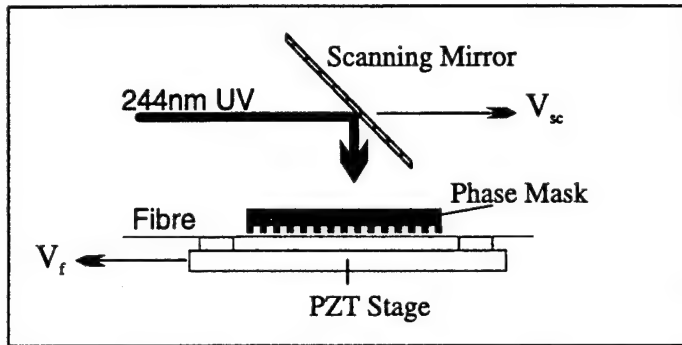


Fig. 1 Experimental configuration

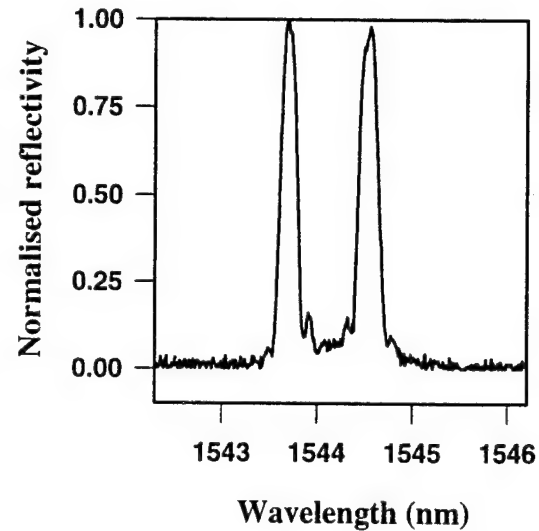


Fig. 2 Reflection spectrum of dual wavelength grating. Peak reflectivity is 67%.

respectively, with $v_f \ll v_{sc}$ (the case of interest here), it is easy to show that the wavelength shift is given by $\Delta\lambda = \lambda_0 v_f / v_{sc}$. Thus for a shift of ~ 1 nm, the fibre has only to move at 0.1% of the scanning speed. Fig. 2 shows a dual wavelength grating written using a boron-germania photosensitive fibre. The scanning beam speed was $37 \mu\text{m/s}$, and the fibre speed was $0.01 \mu\text{m/s}$ for the first half of the writing time, switching to $-0.01 \mu\text{m/s}$ for the second half (total length of grating was 1 cm).

For large wavelength shifts, the grating strength would decrease as the index modulation gets averaged or 'washed out' when the fibre moves too quickly through the interference pattern formed by the phase mask. It can be shown that the refractive index modulation Δn has the following dependence on v_f :

$$\Delta n = \sin(\pi D v_f / \Lambda v_{sc}) / (\pi D v_f / \Lambda v_{sc}) = \sin(2 n_{\text{eff}} \pi D \Delta \lambda / \lambda_o^2) / (2 n_{\text{eff}} \pi D \Delta \lambda / \lambda_o^2)$$

where D is the writing beam diameter, Λ is the fibre grating pitch and n_{eff} is the effective refractive index ($2 n_{\text{eff}} \Lambda = \lambda_o$).

The above relation was verified by writing weak (<20% reflectivity) gratings with different wavelength shifts, and recording their reflectivities R , which will have a Δn^2 dependence. Fig. 3 shows that the experimental reflection data fits well to the above relationship for the (measured) beam diameter $D \approx 350 \mu\text{m}$. It is also worth noting from the above equation that Δn vanishes when $v_f = \Lambda v_{sc} / D$, or $\Delta \Lambda = \Lambda^2 / D$ (where $\Delta \Lambda / \Lambda = \Delta \lambda / \lambda_o$). The maximum achievable wavelength shift is thus only dependent on the beam diameter D . Physically, this condition simply corresponds to the case where a point in the fibre moves by one grating pitch during the time D / v_{sc} that the scanning beam passes over it, resulting in a

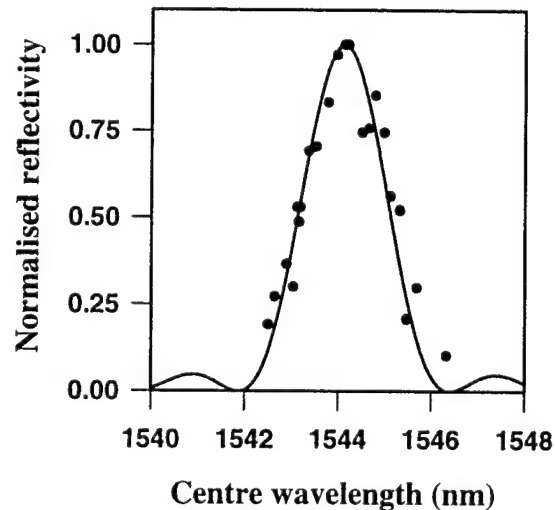


Fig. 3 Dependence of reflectivity with wavelength. Solid trace: sinc^2 function from text.

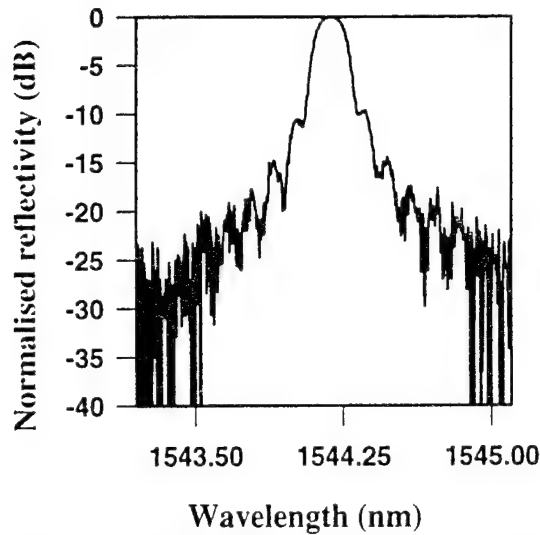


Fig. 4 Reflection spectrum for 1 cm long uniform grating. Peak reflectivity is 82%, bandwidth 0.18 nm.

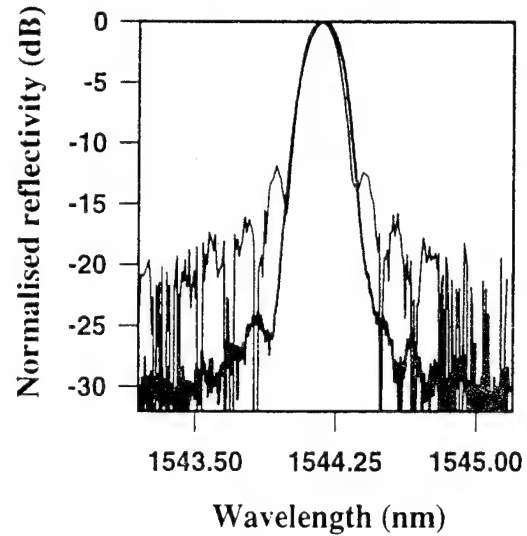


Fig. 5 Reflection spectra for 1 cm long apodised grating (thick trace). Peak reflectivity: 50%, bandwidth: 0.19 nm. Thin trace: uniform grating, same peak reflectivity and bandwidth.

spatial averaging out of the index variation. On the other hand, larger wavelength excursions of several nm should be achievable by simply reducing the writing beam diameter.

Apodisation

Apart from shifting the Bragg resonance wavelength, 'pure' apodisation can also be applied to the grating simply by dithering the fibre back and forth as the writing beam is scanning. In our case, the magnitude of the dither was set to decrease linearly, from $\frac{1}{2}$ grating pitch at the ends to zero at the centre of the grating. It is easy to show that this will produce a cosinusoidal apodisation profile. Since the average UV fluence reaching the fibre is the same for the entire length of the grating, the average refractive index will be independent of length, and only the index modulation will vary, i.e. only Δn is modulated, thus producing a 'pure' apodisation effect. Fig. 4 shows the reflection spectrum for a uniform grating, and Fig. 5 the corresponding spectrum obtained with the apodisation present, showing its effectiveness in reducing the side-lobe levels. With apodisation, the reflectivity is weaker (since the effective grating length is less), so for a fairer comparison, a uniform grating written to have the same peak reflectivity and bandwidth as the apodised one is also shown (Fig. 5, thin trace). It can be seen that the side-lobes of the apodised spectrum are more than 25 dB below the main peak, and 13 dB below those of the uniform grating, comparable to the results by Albert et. al.[6] achieved with a specialised variable diffraction efficiency phase mask.

Chirped Gratings

Finally, instead of applying a constant velocity to the fibre to create a wavelength shift, it is also possible to produce chirped gratings by varying the speed of the fibre relative to the mask. In particular, by simply ramping the velocity of the fibre during the scanning time, a linearly chirped grating can be produced. Fig. 6 shows the reflection spectrum of a 1.5 cm long apodised chirped grating made in this manner. In addition to linearly chirped gratings, it should also be clear that other nonlinear chirp functions can be easily imposed on the grating simply by changing the velocity profile of the fibre during scanning. Indeed, one should in principle be able to compensate for an imperfect phase mask with this method and still produce good quality gratings, provided the imperfections are characterised beforehand. Also, implementing discrete phase shifts for, say, DFB-type structures can be achieved just by shifting the fibre/phase mask by the desired amount at the appropriate time.

In conclusion, we have shown that the moving fibre/phase mask-scanning beam technique for producing gratings from a uniform phase mask imparts a considerable flexibility to the phase mask approach, enabling complex grating structures to be easily written simply by moving the fibre relative to the mask in the appropriate manner. Multiwavelength gratings, 'pure' apodisation and controlled chirp have all been successfully demonstrated.

The authors acknowledge P. St. J. Russell and D. N. Payne for useful discussions, and S. Barcelos for characterising some of the devices made. This work was funded in part by Pirelli Cavi S.p.A. The Optoelectronics Research Centre is an EPSRC-funded Interdisciplinary Research Centre.

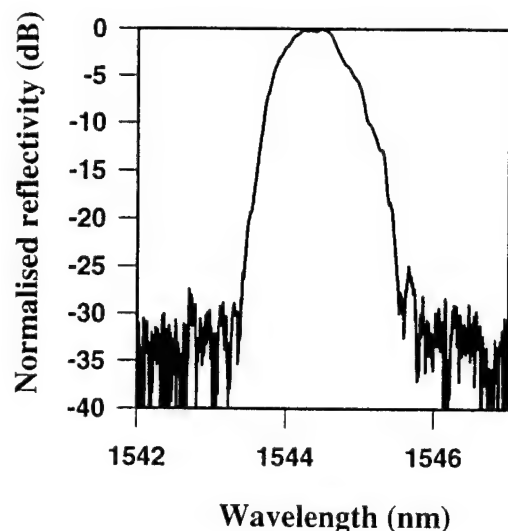


Fig. 6 Reflection spectrum for apodised chirped grating. Bandwidth: 0.82 nm, peak reflectivity: 40%.

References

1. K. O. Hill et. al., Appl. Phys. Lett., **62**, 1993, pp 1035-1037.
2. D. Z. Anderson et. al., Electron. Lett., **29**, 1993, pp. 566-567.
3. J. D. Prohaska et. al., Electron. Lett., **29**, 1993, pp. 1614-1615.
4. J. Martin et. al., Electron. Lett., **30**, 1994, pp. 811-812.
5. H. N. Rourke et. al., Electron. Lett., **30**, 1994, pp. 1341-1342.
6. J. Albert et. al., Electron. Lett., **31**, 1995, pp. 222-223.
7. B. Malo et. al., Electron. Lett., **31**, 1995, pp. 223-224.
8. K. O. Hill et. al., Opt. Lett., **19**, 1994, pp. 1314-1316.
9. R. Kashyap et. al., Electron. Lett., **30**, 1994, pp. 996-997.
10. K. C. Byron et. al., Electron. Lett., **31**, 1995, pp. 60-61.

Hydrogen-enhanced UV photosensitivity of optical fibers: Mechanisms and reliability

Paul J. Lemaire
AT&T Bell Laboratories
600 Mountain Avenue, 6C326
Murray Hill, NJ 07979-0636
908-582-5639 Tel. 908-582-2913 FAX

Turan Erdogan
Institute of Optics
Wilmot Building W303
University of Rochester
Rochester, NY 14627
716-275-7227 Tel. 716-244-4936 FAX

Introduction

The use of optical fiber gratings¹ has rapidly increased in recent years, due to the invention of the side-writing technique,² and to the availability of fibers with enhanced photosensitivity. Enhanced photosensitivity has been achieved in various ways, most of which serve to increase the concentration of "native" defects in the fibers.^{3,4,5,6} More recently the UV photosensitivity of optical fibers has been greatly enhanced by "loading" the fibers with molecular H₂ or D₂ at high pressure.⁷ Subsequent exposure of the sensitized fiber to intense UV light at wavelengths less than about 248nm causes the physically dissolved H₂ to react with cation dopants resulting in the formation of defects which cause large increases in the refractive index of the glass. This high pressure H₂ sensitization technique has been used to great advantage in the UV writing of gratings in optical fibers, and has also been used to sensitize planar waveguides for the UV patterning of waveguide devices,⁸ and in bulk glasses for demonstration of holographic data storage.⁹ The UV induced index changes can readily exceed the initial core-to-cladding index difference in GeO₂ doped fibers, permitting the UV writing of strong gratings in virtually any GeO₂ doped optical fiber. The enhanced photosensitivity is sufficient to allow strong gratings to be written in several minutes using pulsed laser systems (~10-30Hz) at typical irradiances of several 100's mJ/cm². For instance, in standard single mode fiber (3.5% GeO₂) index changes of $\Delta n = 5 \times 10^{-3}$ can be easily achieved and Δn 's of 0.011 have been attained with longer exposures. Recent results have shown that H₂ sensitization can also be used to advantage in P₂O₅ doped waveguides and fibers, either by using 193nm excimer irradiation¹⁰ or by using simultaneous heating and UV exposure at 248nm.¹¹ One advantage of using H₂ sensitization is that any existing fiber (that is either Ge or P doped) can be sensitized after it has been drawn and coated. Hydrogen molecules readily diffuse through polymer coatings and silica claddings at low temperatures, allowing the loading to be done at temperatures as low as 22-75°C, without degradation of polymer coatings. Figure 1 shows the transmission spectrum for a strong grating written in a standard (3.5% GeO₂) single mode fiber that was H₂ sensitized with 3.3% H₂.

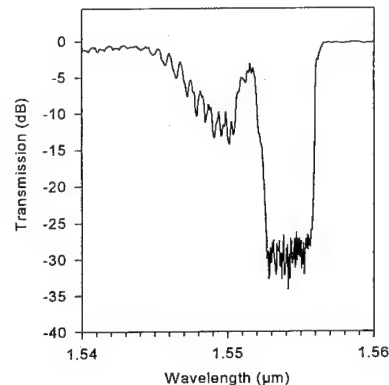


Figure 1. Transmission spectrum for grating written in H₂ sensitized single mode fiber.

Mechanism

The large UV induced index changes that occur when a H₂ sensitized fiber is exposed to UV are due to the creation of large concentrations of defects at cation dopant sites (Ge or P). The UV induced index changes have been observed to occur only in doped sections of fibers, typically in the cores, but also in doped cladding regions. There do not appear to be any significant index changes in undoped SiO₂ that is H₂ loaded, a factor that allows one to form a grating that

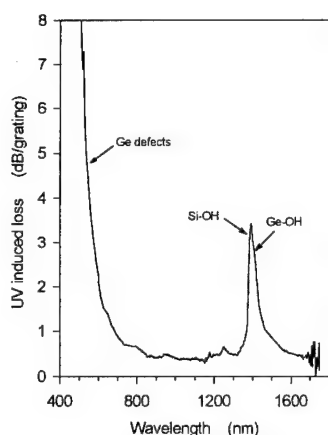


Figure 2. UV induced losses in a 9% GeO₂ doped fiber sensitized with 4.1% H₂.

is confined to the central doped region of a fiber. Figure 2 shows the UV induced loss changes that occurred during the writing of a grating in a GeO₂ doped fiber that was loaded with 4.1% H₂. The prominent OH overtone peak at 1.39μm is due primarily to creation of about 8 mole % of Si-OH defects. (Substituting D₂ for H₂ is advantageous in that it shifts the overtone to 1.9μm, where it does not contribute to the loss.) The strong short wavelength loss edge is related to the formation of Ge defects. Other experimental results have indicated that the saturation value of the Si-OH absorption (i.e. the limiting value seen after long exposure) is approximately equal to the GeO₂ content of the glass. These results suggest that the H₂ (or D₂) molecules tend to react at the bridging bond between a Ge and a normal bridging oxygen, ≡Si-O-Ge≡, forming an ≡Si-OH site and a Ge defect, perhaps ≡Ge-H. The failure to obtain an analogous reaction at a ≡Si-O-Si≡ site is not surprising in view of the greater thermodynamic stability of SiO₂ bonds compared to those in GeO₂. In highly doped samples there is a significant concentration of Ge-O-Ge bonds. H₂ reaction at such a site results in the formation of Ge-OH, which absorbs at 1.41μm, accounting for the subtle shoulder on the main 1.39μm Si-OH peak in Fig. 2.

Raman spectra have indicated that various Ge defect species exist in H₂ sensitized fibers after thermal or UV processing. Germanium monohydrides, ≡Ge-H, have been seen in samples that were rapidly heated, while evidence for the dihydride species, ≡GeH₂, have been obtained for UV irradiated samples.¹² Ab-initio theoretical studies have also been used to investigate the various Ge and Si defects than might exist in hydrogenated germanosilicates, and have also supported the idea that several types of defects can exist.^{13,14} These studies have calculated the activation barriers for various reaction paths, for instance showing that hydrogen reactions at Ge sites are much more likely than at Si sites.¹³

Thermal reliability

Early investigations of thermal decay of UV written gratings showed that there were several decay mechanisms for gratings written in H₂ loaded fibers.¹⁵ Different phases of grating decay correlated with reduction in losses associated with color center defects, OH sites, and oxygen deficient sites. This multiplicity of decay mechanisms is understandable in view of the different types of defects that are formed during the UV writing process. For instance, it is possible that defects may form pairwise during UV writing, e.g. H₂ + Si-O-Ge → Si-OH + Ge-H, but that each type of defect may decay independently during a thermal anneal. The possibility that there is more than one decay mechanism must be recognized when analyzing accelerated test data.

Accelerated test data on gratings written in both hydrogenated and non-hydrogenated fibers show that there are a finite number of UV induced defects that are not thermally stable at typical operating temperatures. The existence of a range of activation energies for each *type* of defect is a fundamental consequence of the amorphous nature of glass. For any given *type* of defect there will be a range of decay time constants, with some fraction decaying rapidly. These unstable sites can be removed by annealing at conditions (time and temperature) that are determined by the distribution of activation energies for the UV created defects. There are at least two approaches to analyzing accelerated aging data, both of which are based on the same physical assumptions.¹⁶ In one approach it can be shown that for a single distribution of activation energies the aging data can be described by an equation of the form,

$$\eta = \frac{1}{1 + A(t/t_1)^\alpha} \quad (1)$$

where η is the UV induced index change, normalized to the initial value. The exponent, α , is predicted to be proportional

to the temperature, and A should vary exponentially with the temperature. Data for gratings in non-hydrogenated fibers have successfully been analyzed by this technique.¹⁶ In an alternative approach¹⁶ it can be shown that an aging parameter (or demarcation energy), $E_d = kT \ln(\nu_0 t)$, can be used to describe the extent of the aging, where ν_0 is a frequency term that is determined from accelerated test data, and $N_d(E)$ describes the distribution of sites having activation energies, E .

$$\eta = \int_{E_d}^{\infty} N_d(E) dE = f[kT \ln(\nu_0 t)] \quad (2)$$

The same aging should be seen for a grating as long as E_d is constant. Therefore aging behavior at long times and low temperatures can be assessed based on short term experiments at high temperatures. Furthermore, the same approach can be used to determine the appropriate anneal conditions required to stabilize a grating. When there are multiple decay paths with different ν_0 's the data analysis is more complicated, but a reasonable approach is to confine the accelerated testing to a moderately low temperature regime where a single decay mechanism dominates the behavior.

Figure 3 shows aging data for strong gratings (2-4nm spectral width) written in standard single mode fibers (3.5% GeO₂) that were H₂ loaded. A value of $\nu_0 = 2.8 \times 10^{14} \text{ sec}^{-1}$ was determined. The decays in η for *unannealed* gratings are rather large. Predictions range from less than 2% to about 15% for temperatures from 10 to 65°C, over a period of 25 years. While some devices (e.g. Er amplifier pump reflectors) may tolerate such changes, others, (e.g. fiber lasers) will not. However, excellent thermal stability can be ensured by simply annealing the gratings at 140°C for 1 day. During the anneal the unstable sites are eliminated and consequently the predicted long term decays are minimal, as shown in Figure 4. For instance less than 1% change is predicted even at 65°C over a period of 25 years for an annealed grating. The act of stabilizing these gratings at 140°C causes about a 14% reduction in the UV induced Δn , a factor that must be anticipated during the grating writing.

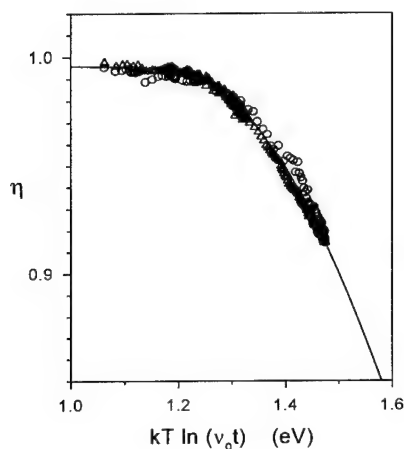


Figure 3. Accelerated anneal data for strong gratings written in H₂ sensitized single mode fibers. Value of ν_0 is determined to be $2.8 \times 10^{14} \text{ sec}^{-1}$.

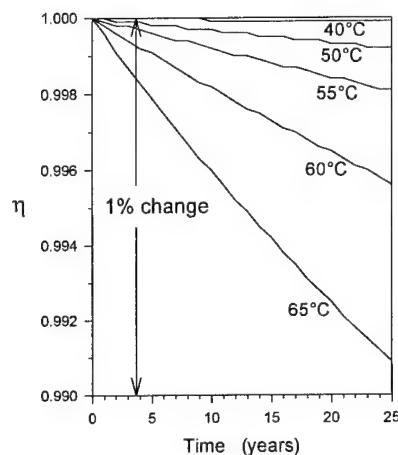


Figure 4. Predicted decay for gratings annealed at 140°C for 24 hours.

Discussion and Conclusions

High pressure hydrogen loading offers major advantages in that it greatly enhances the UV photosensitivity of both GeO₂ and P₂O₅ doped fibers, allowing large index changes to be achieved quickly using short writing times and

"normal" UV irradiances. Gratings can be readily written in any fiber, without having to compromise other properties in order to achieve the required photosensitivity. In many fiber types it is not possible to form strong gratings without the use of H_2 sensitization. While molecular H_2 does have an absorption spectrum, its effects on loss are temporary since any unreacted H_2 can be readily out-diffused once a grating is written. This is highly desirable since the fiber properties are changed only in the grating region, minimizing the overall loss of the device. The same UV-created species that cause the desired index increases also have the potential for increasing the transmission loss. However these loss changes are small at 1.31 and 1.55 μm , and further, the portion of the losses due to OH formation can be greatly reduced by using D_2 in place of H_2 for sensitizing the fibers.

In H_2 sensitized fibers the UV exposure can create large concentrations of defects, resulting in desirable large index changes, and causing major changes in the the glass network. Essentially any cation dopant site (e.g. Ge site) is susceptible to a H_2 reaction, in contrast to non- H_2 loaded fibers where UV induced changes only occur at the small fraction of preexisting defect sites. Several types of UV created defects have been identified in H_2 sensitized fibers, and while some of these (e.g. Si-OH) are very stable, there is evidence that significant numbers of the sites may have low activation energies, a factor which must be addressed in assessing long term thermal stability.

For any UV written grating there is the potential for thermal degradation, whether or not H_2 is used to sensitize the fiber. In large part this is due to the disorder that is inherent in a glass, and the resultant distribution in decay rates. In general it will not be acceptable to use *as-written* grating in any but the least demanding applications. Rather, almost all gratings will have to be annealed prior to use, in order to remove the inevitable population of unstable UV induced sites. Fortunately the required anneal conditions are not extreme, and long term reliability can be assured once suitable accelerated test data have been obtained.

1. K.O. Hill, Y. Fujii, D.C. Johnson, and B.S. Kawasaki, **Appl. Phys. Lett.**, **32**, 647 (1978).
2. G. Meltz, W.W. Morey, and W.H. Glenn, **Opt. Lett.**, **14**, 823 (1989).
3. G.D. Maxwell, B.J. Ainslie, D.L. Williams, and R. Kashyap, **Electron. Lett.**, **29**, 425 (1993).
4. D.L. Williams, B.J. Ainslie, J.R. Armitage, R. Kashyap, and R. Campbell, **Electron. Lett.**, **29**, 45 (1993).
5. F. Bilodeau, B. Malo, J. Albert, D.C. Johnson, K.O. Hill, Y. Hibino, M. Abe, and M. Kawachi, **Opt. Lett.**, **18**, 953 (1993).
6. G. Meltz and W.W. Morey, **Proc. SPIE** **1516**, 185 (1991).
7. P.J. Lemaire, R.M. Atkins, V. Mizrahi, and W.A. Reed, **Electron. Lett.**, **29**, 1191 (1993).
8. V. Mizrahi, P.J. Lemaire, T. Erdogan, W.A. Reed, D.J. DiGiovanni, and R.M. Atkins, **Appl. Phys. Lett.**, **63**, 1727 (1993).
9. A. Partovi, T. Erdogan, V. Mizrahi, P.J. Lemaire, A.M. Glass, and J.W. Fleming, **Appl. Phys. Lett.**, **64**, 821 (1994).
10. B. Malo, J. Albert, F. Bilodeau, T. Kitagawa, D.C. Johnson, K.O. Hill, K. Hattori, Y. Hibino, and S. Gujrathi, **Appl. Phys. Lett.**, **65**, 394 (1994).
11. P.J. Lemaire, A.M. Vengsarkar, W.A. Reed, and D.J. DiGiovanni, **Appl. Phys. Lett.**, **66**, 2034 (1995).
12. B.I. Greene, D.M. Krol, S.G. Kosinski, P.J. Lemaire, and P.N. Saeta, **J. Non-Cryst. Solids**, **168**, 195 (1994).
13. K. Raghavachari and B. Zhang, **J. Non-Cryst. Solids**, **180**, 80 (1994).
14. B. Zhang and K. Raghavachari, **J. Non-Cryst. Solids**, **51**, 7946 (1995).
15. P.J. Lemaire, V. Mizrahi, R.M. Atkins, and K.S. Kranz, **Tech. Digest of OFC'93**, Paper FA7, San Jose (1993).
16. T. Erdogan, V. Mizrahi, P.J. Lemaire, and D.P. Monroe, **J. Appl. Phys.**, **76**, 73 (1994).

Growth Dynamics of Fiber Bragg Gratings Written with a KrF Excimer Laser

Glen M. Williams*, Martin A. Putnam, Tsung E. Tsai*, Charles G. Askins, and E. Joseph Friebele

Optical Sciences Division
Naval Research Laboratory
Washington, DC., 20375

For the production of single shot fiber Bragg gratings¹⁻³ in-line during the fiber drawing process, a knowledge of the effects of exposure conditions and material composition of fiber can be of crucial importance. During in-line production, one is not afforded the possibility of exposing the fiber incrementally to repeated laser shots until the correct grating reflectivity is achieved. Single shot writing of gratings in many different types of fibers indicates that the maximum index change in the Type I regime ($<1 \text{ J/cm}^2$, yielding a spectrally narrow and smooth reflectivity) from a single shot is on the order 10^{-5} . For many applications (*ie* sensor arrays) this index change produces reflectivities that are more than adequate for good system performance. However, for certain applications greater reflectivities are required. In an effort to better control and possibly improve the photosensitivity of optical fibers at 248 nm we studied the growth dynamics of fiber Bragg gratings in various fibers under various exposure conditions.

Previous studies^{4,5} of the growth dynamics of fiber Bragg gratings written using 245 nm light have shown that the photoinduced index change can be modeled most simply as a sublinear power law of the total light fluence. In Reference [4] the gratings were written using a CW laser source with exposure intensities ranging from $1\text{--}50 \text{ W/cm}^2$ and exposures times of seconds to tens of minutes. In Reference [5] the fiber was exposed to a pulsed laser system (pulse width approximately 10 ns) with fluences per pulse on the order of 300 mJ/cm^2 . The fiber was exposed to integrated fluences as great as $10,000 \text{ J/cm}^2$. In this paper we report the growth dynamics of fiber Bragg gratings for the exposure regime in which the single pulse fluences are varied from 0.3 mJ/cm^2 to 40 mJ/cm^2 . The results indicate that there exist two distinct (but possibly coupled) growth behaviors.

Optical fibers were exposed through a Laseris phase mask (period= $1.064 \mu\text{m}$, $<5\%$ zero order transmission) by 248 nm light from a Lambda Physik EMG 150 MSC master oscillator-power amplifier system with the back reflector on the amplifier replaced by a phase conjugate mirror⁶. The laser was run during all experiments at a 1 Hz repetition rate. The writing intensity was varied through a combination of defocussing along the axis parallel to phase mask grooves and the use of partial reflectors. All five fibers used in the study were produced and characterized at NRL. The grating reflectivity was monitored using a tunable Er-doped fiber laser source. Tuning of the laser was achieved by stretching a fiber Bragg grating used for one of the end reflectors of laser.

Displayed in Figure 1 is the photoinduced index change (computed from grating reflectivity) for a given fiber (NRL A) as a function of total exposure fluence for different fluences-per-pulse. The growth curves can not be described by a simple power law growth. This is particularly true for the data from the lower fluence-per-pulse exposures. The low fluence-per-pulse curves show distinctly an early growth which appears to saturate followed by the type of power law behavior observed in the previous studies^{4,5}. It is interesting to note that for the higher fluence per pulse curve, 45 mJ/cm^2 (and also for data taken with 23 mJ/cm^2 and 30 mJ/cm^2 per pulse), only the power law growth section of the curve is clearly visible. In addition, the curves indicate that the growth dynamics are not just a function of the total fluence but also depend on the fluence per pulse. A fit of the data to the sum of a saturated exponential function of the form, $\alpha(1 - \exp(-\beta F))$ (where F is the total fluence and α and β are fitting parameters), and a power law function of the form, $(\kappa F)^{0.3}$ (where κ is a fitting parameter)⁷ helps to further elucidate the fluence-per-pulse dependence of the growth. A functional

form of this type fits the data well with the parameters β and κ varying between curves and the parameter α remaining fairly constant. The parameter β increases nearly linearly as a function of fluence per pulse, indicating that the saturated exponential is describing the generation or bleaching of a defect by a two photon process. The process saturates quickly because of a limited supply (described by parameter α) of defect or defect precursor. The parameter κ also depends on fluence per pulse, but in a sublinear fashion. This is in agreement with the results of Reference [4].

Tsai et al⁸ have studied the effect of 248 nm radiation on intrinsic Ge E' centers in telecommunication fiber preforms. They found that in the exposure regime of 2.5-50 mJ/cm² per pulse Ge E' defects are bleached. For the 2.5 mJ/cm² per pulse exposure, the intrinsic defects are bleached by 60 shots while for the 50 mJ/cm² per pulse exposure, only one shot is required. The bleaching dynamic is best described by a two photon process. This evidence suggests the Ge E' center is responsible, either directly or indirectly, for the index change described by the saturated exponential.

Shown in Figure 2 is the growth dynamics for Bragg gratings written in several different types of fibers at approximately 10 mJ/cm² per pulse. Some properties of these fibers are listed in Table 1. The properties listed are approximate Ge content of the core (proportional to the fiber delta), loss at 240 nm⁹, and Ge E' concentration as measured by electron spin resonance. The Ge E' concentration has been computed assuming all the Ge E' defects are located in the core. This assumption is somewhat questionable considering that the cladding on these fibers does contain Ge. Additional experiments are underway to further elucidate the distribution of Ge E' defects in the fiber. The curves were fit to a function similar to the one used to fit the curves in Figure 1. One adjustment was made to account for the dip observed in fibers NRL B, NRL C, and NRL D. We are uncertain at this point whether the dip represents the true behavior of the defect populations in the glass or is just an artifact associated with the use of phase mask to write the gratings. If the photoinduced response of the system saturates, then even though the zeroth order (or DC component) of the light hitting the fiber is small, it will eventually serve to erase the grating by filling in the valleys between the index modulations. In the fit, this can be dealt with by the addition of a second saturated exponential (with a proportionally scaled down β coefficient) competing with the first.

The result of such a fit yields the following correlations between fiber properties and fitting parameters: The α coefficient increases with increasing Ge E' concentration (assuming all the Ge E' is in the core) for all fibers except for NRL C. NRL C is measured to have the highest Ge E' concentration but only has the second highest α parameter. The parameter β is linearly related to the amount of absorption at 240 nm. This absorption has been associated with an oxygen vacancy or so-called "wrong bond". Thus, apparently the presence of the defect associated with the 240 nm absorption is required to bleach the defect associated with the parameter α . The parameter κ is most strongly correlated with the product of the absorption at 240 nm and the Ge concentration of the core. Thus, both the high oxygen vacancy and high Ge content are needed for good long term growth.

Fiber I.D.	Fiber Δ	Ge E' (normalized)	Absorption @240 nm (dB/mm)
NRL A	0.023	0.44	125
NRL B	0.0075	1.0	165
NRL C	0.01	1.8	85
NRL D	0.003	0.27	40
NRL E	0.012	0.12	20

Table 1. Parameters for various sample fibers.

REFERENCES

1. C.G. Askins, T. Tsai, G.M. Williams, M.A. Putnam, M. Bashkansky, and E.J. Friebele, *Opt. Lett.* **17**, pg. 833 (1992).
2. L. Dong, J.-L. Archambault, L. Reekie, P. St. J. Russell, and D.N. Payne, *Elec. Lett.* **29**, pg. 1577 (1993).
3. C. G. Askins, M.A. Putnam, G.M. Williams, and E.J. Friebele, *Opt. Lett.* **19**, pg. 147 (1994).
4. H. Patrick and S.L. Gilbert, *Opt. Lett.* **18**, pg. 1484 (1993).
5. D.Z. Anderson, V. Mizrahi, T. Ergodan, and A.E. White, *Elec. Lett.* **29**, pg. 566 (1993).
6. M. A. Putnam, C.G. Askins, G.M. Williams, E.J. Friebele, M. Bashkansky, and J. Reintjes, *SPIE Proceedings, Smart Sensing, Processing, and Instrumentation*, **2444**, pg. 403 (1995).
7. The power of 0.3 was selected in accordance with the results of Reference [4].
8. T.E. Tsai, C.G. Askins, and E.J. Friebele, *Appl. Phys. Lett.* **61**, pg. 390 (1992).
9. M.A. Putnam *et al*, to be published.

* Also with Department of Electrical Engineering, Virginia Tech., Blacksburg, VA

FIGURES

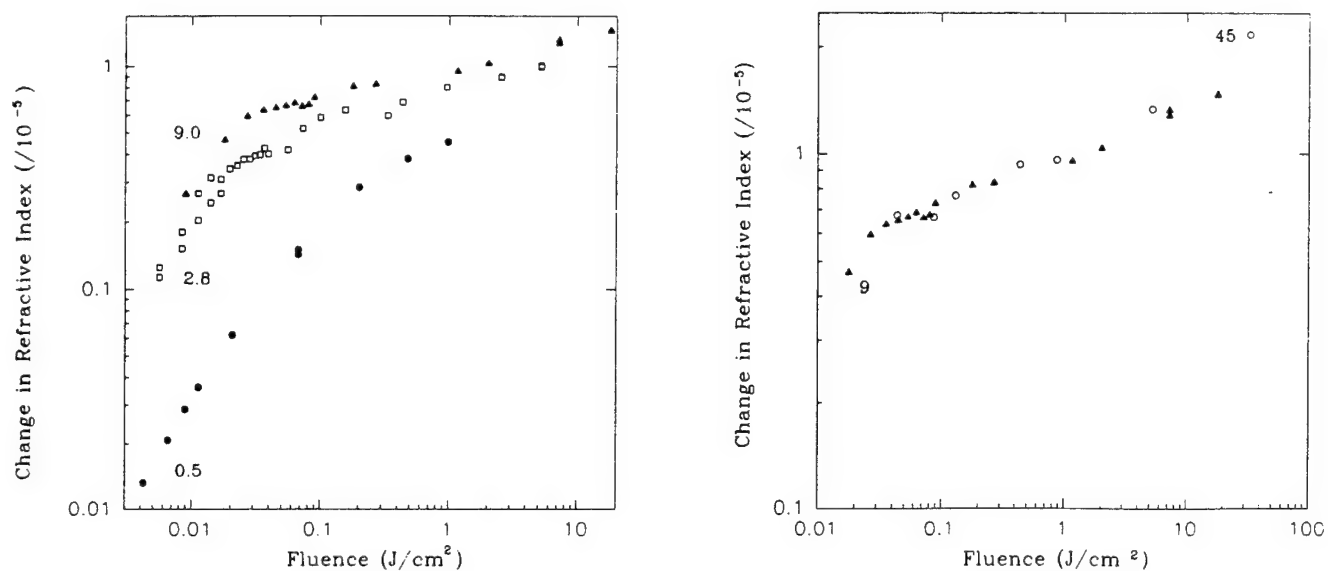


Figure 1. Growth of index change as a function of total fluence for fiber NRL A using different fluences per pulse (0.5, 2.8, 9.0 and 45 mJ/cm² per pulse).

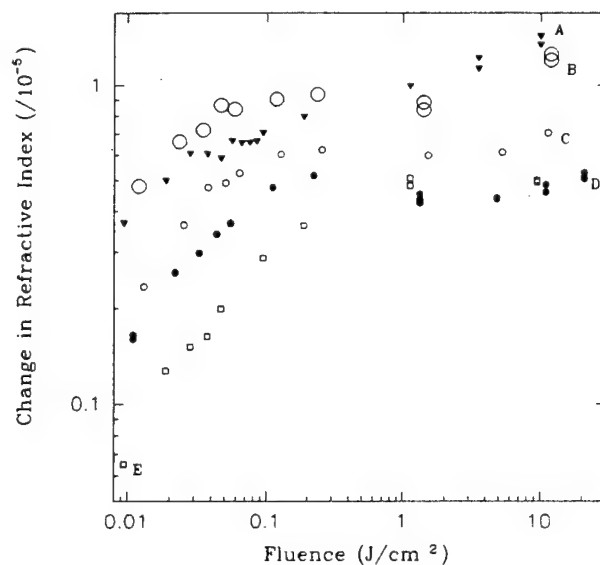


Figure 2. Growth of index change as a function of total fluence for different fibers. In all cases the fluence per pulse is approximately 10 mJ/cm².

Photosensitisation of Phosphosilicate Fibre Bragg Gratings

J. Canning, R. Pasman, M.G. Sceats

Optical Fibre Technology Centre, University of Sydney, Sydney, NSW 2006, Australia

tel: 61 2 335 0940

fax: 61 2 335 0910

Photolytic grating writing in phosphorous doped waveguides has recently been possible only with substantial hydrogen loading [1-3]. In [1] this has been demonstrated for phosphosilicate planar waveguides using 193nm whilst for aluminophosphosilicate fibres the writing wavelength was the 248nm KrF line [2]. We have recently demonstrated photosensitivity at 193nm in phosphosilicate fibres [3] fabricated by the flash condensation technique [4]. This technique appears unique in that it has pre-existing phase separation within the fibre [5] which assists in the incorporation of up to 14wt% of rare-earth ions. In addition to showing significantly better performance than at 240nm under similar irradiation conditions the induced photosensitivity was found to be dependent on slow chemical sensitisation with hydrogen prior to irradiation. Fig. 1 is a comparison between the expected diffusion profile for hydrogen loading at 373K and 40atm and the saturated reflectivities obtained for various loading times. The importance of hydrogen loading is accentuated with the observation of only transient gratings (Fig 2) without loading. The decay profile of these gratings cannot be accounted for by a single relaxation process. Instead, we propose that (1) there are several contributions to the index change in which one mechanism promotes the next, and (2) the role of hydrogen is to quench the back reactions. A two step process suggests that memory effects, such as presensitisation, may be observed. In this paper, we use a novel side diffraction technique [6] for measuring the index contrast to demonstrate that these phosphosilicate glass fibres exhibit large photolytic presensitisation.

A standard grating was written in phosphosilicate fibre over 3cm using the output of an ArF laser (193nm, 20Hz, 6.5mJ/cm², 10 000shots) through a phase mask. The phase mask was removed and this grating was post-processed in the centre over 3 sections each 0.2mm long. Using identical irradiation conditions the first section (A) was exposed for ~70000 shots, the second exposure (B) ~6800 shots and for section (C), which was approximately 1mm further along, ~30000 shots. The grating was then scanned using the side diffraction technique [6] illustrated in Fig 3. A HeNe laser probes a portion of the grating (resolution up to 20µm) from the side at an angle such that it is diffracted into two beams which have intensities dependent on the depth of index induced into the grating. The region where post-processing took place is shown in Fig. 4. At low post processing fluences (B,C) the index contrast has increased by up to a factor

of four. The side diffraction showed no evidence of a strong imprinted grating on the surface of the fibre, which could have acted as a replica diffraction source for the post-processing uv light. Therefore we conclude that the enhancement of the grating arises from a presensitisation memory effect, i.e. areas exposed by the initial uv light have an increased photosensitivity than unexposed areas. Phase structures which are weakly imprinted by exposure through the phase mask can be later developed by exposure to uv light from an incoherent source. At high post-processing fluence (C) the available index change saturated and the index contrast drops below the initial values. These results are similar to that reported for germanosilicate fibre exposed to 193nm [7] where we believe a two step process can also be inferred

In conclusion we have demonstrated enhanced photosensitivity at 193nm in hydrogen loaded phosphosilicate fibres which supports a two step mechanism where initial 193nm absorption results in an increase in the number of defects which enables local structural rearrangement [8] and hence further index change.

References:

- [1] B. Malo, J. Albert, F. Bilodeau, T. Kitagawa, D.C. Johnson, K.O. Hill, Appl. Phys. Lett., 65, (4), 394-396, 1994
- [2] J.-L. Archambault, L.Reekie, L. Dong, P.st.J. Russell, Conference on Lasers and Electro-Optics, Vol. 8 of 1994 OSA Technical Digest Series (Optical Society of Amerisa, Washington D.C., 1994), paper CWK3
- [3] J. Canning, M.G. Sceats, H.G. Inglis, P.Hill, Submitted to Opt. Lett.
- [4] A.L.G. Carter, M.G. Sceats, S.B. Poole, Elec. Lett., 28, (21), 2009-2011, (1992)
- [5] A. L. G. Carter, M. G. Sceats, S. B. Poole, J. V. Hanna, Proceedings of Optical Fibre Conference, (San Jose, California, USA, 1994), p4
- [6] P.A. Krug, R. Stoltz, U. Reinhardt, Submitted to Opt. lett.
- [7] P.E. Dyer, R.J. Farley, R. Giedl, K.C. Byron, Elec. Lett., 30, (14), 1133-1134, (1994)
- [8] M. G. Sceats, P.A. Krug, SPIE Proceedings on Photosensitivity and Self-Organisation in Optical Fibres and Waveguides, F. Oullette, ed. (SPIE-International Society for Optical Engineering, Quebec, Canada, 1994), 2044, 113-120

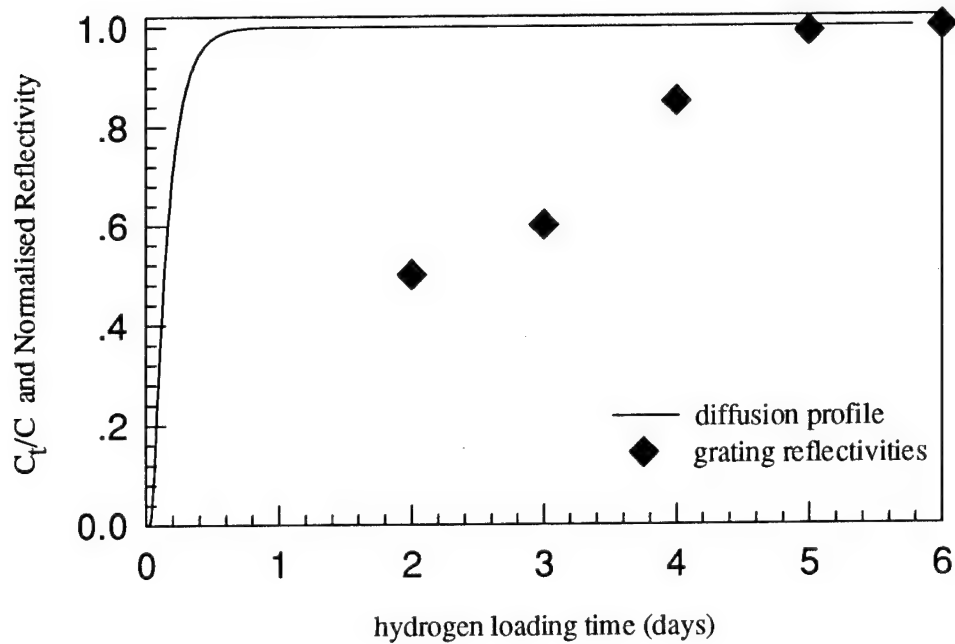
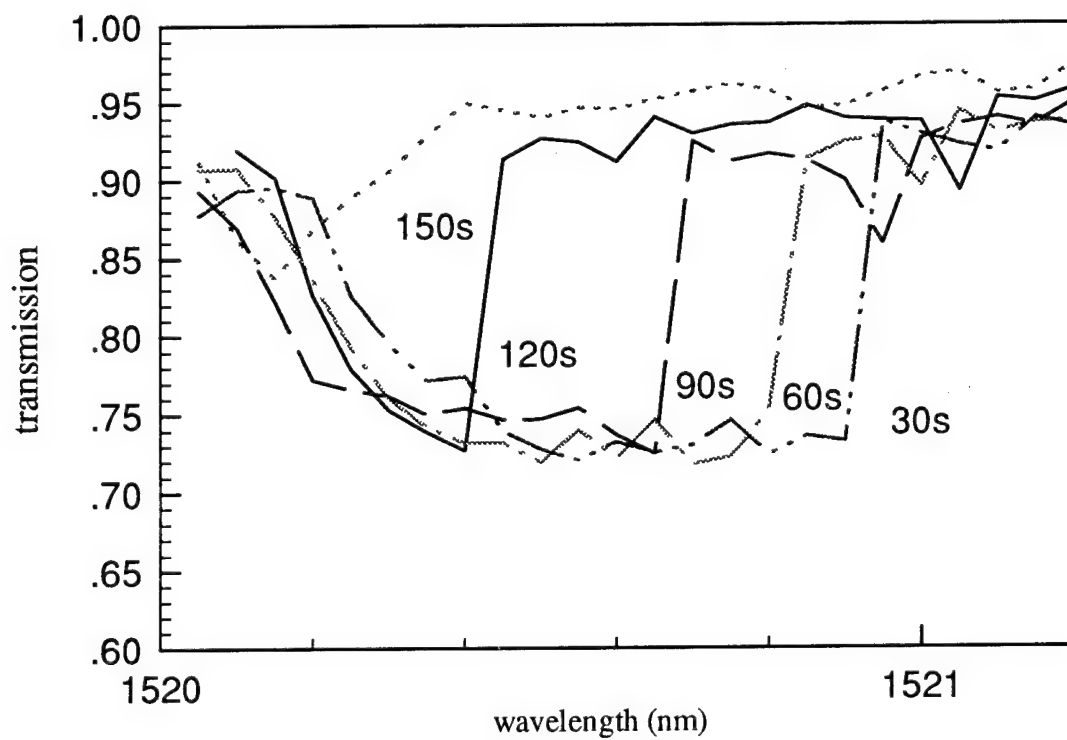
Fig 1. Comparison between hydrogen diffusion and grating reflectivity**Fig 2. Decay of transient phosphosilicate gratings**

Fig 3. Side diffraction of HeNe laser through side of fibre

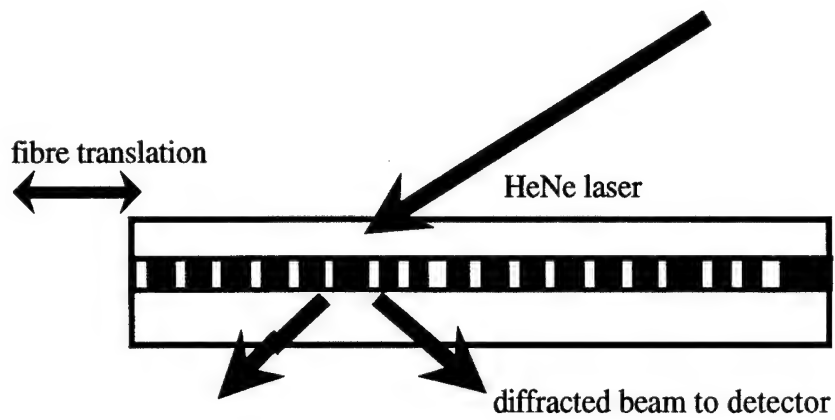
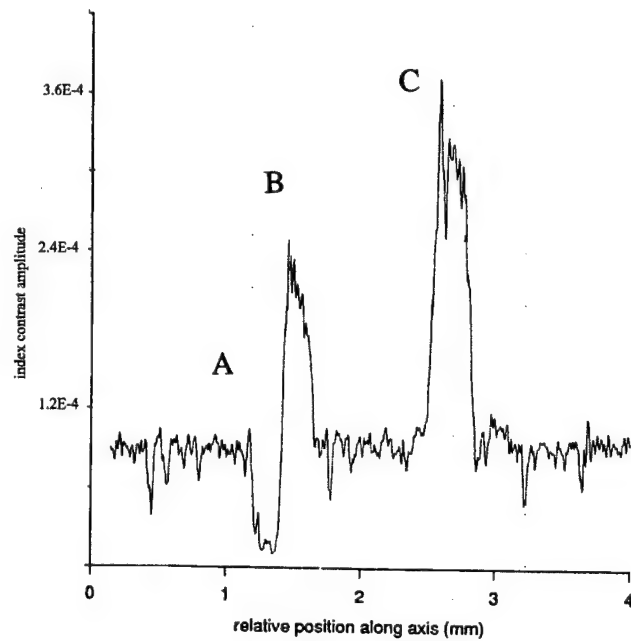


Fig 4. Index contrast profile along 4mm centre portion of grating



Sunday, September 10, 1995

Poster Session

SuB 11:00am–12:00m
Lloyd Center Ballroom

A large second-order nonlinearity in poled phosphate glass containing mobile protons

Yuichi Watanabe*, Naoyuki Takeshita, Toshio Tsuchiya

Department of Materials Science and Technology,

Faculty of Industrial Science and Technology,

Science University of Tokyo

2641 Yamazaki, Noda-shi, Chiba 278 JAPAN / TEL. +81-471-24-1501 FAX. +81-471-23-9362

Hideo Hosono and Hiroshi Kawazoe

Research Laboratory of Engineering Materials, Tokyo Institute of Technology,

Nagatsuta, Midori-ku, Yokohama 226 JAPAN

* corresponding author

Recently, Myers et al. reported that a large second-order nonlinearity [$\chi^{(2)} \sim 1 \text{ pm/V}$] was induced in the near surface region ($\sim 4 \mu\text{m}$) of commercial fused silica by electric-field ($5 \times 10^4 \text{ V/cm}$) poling process at 300°C ¹. Since the large nonlinearity that they observed were remarkable in the glass containing a small amount of alkali (Na^+) impurity, they proposed a model, based on the formation of space-charge layer due to drift of Na^+ during poling process, that could explain the nonlinearity. Here we report second-order nonlinearity in poled phosphate glass. The observed nonlinearity is explained tentatively by considering the drift of protons in the poled glasses.

Phosphate glasses of $\text{RO}:\text{P}_2\text{O}_5$ ($\text{R}=\text{Mg}$ or Ca) were prepared from reagent-grade respective alkaline-earth carbonate and H_3PO_4 liquid by the conventional melt-quenching method. The glass plate of 1mm thick was heated in air ambient to 300°C with a d. c. bias of 5kV across the plate. After 30min at this temperature, the sample was removed from an electric furnace to be cooled to room temperature with biasing. The poled sample was subjected to measurement of second-harmonic generation (SHG) by using a Nd:YAG laser beam at $1.06 \mu\text{m}$.

Figure 1 shows the SHG signal in a poled $\text{MgO}:\text{P}_2\text{O}_5$ and $\text{CaO}:\text{P}_2\text{O}_5$ glass, respectively, versus the angle of incidence of pumping beam. One can notice two distinct features in the figure: (1) A fringe pattern can be observed clearly in $\text{MgO}:\text{P}_2\text{O}_5$ glass whereas no fringe is observed in $\text{CaO}:\text{P}_2\text{O}_5$ glass. (2) The maximum SHG intensity is larger in the latter glass than that in the former glass by a factor of ~ 3000 . The first feature indicates that the thickness of SHG active region in the $\text{CaO}:\text{P}_2\text{O}_5$ glass is less than or comparable to the coherent length (about $20 \mu\text{m}$)

predicted from the linear index of refraction of the glass, while that in the $\text{MgO:P}_2\text{O}_5$ glass is much larger than the coherent length. By using a procedure described in Ref. 2, thickness of the SHG active layer was evaluated to be $\sim 3\mu\text{m}$ in the $\text{CaO:P}_2\text{O}_5$ and $\sim 800\mu\text{m}$ in the $\text{MgO:P}_2\text{O}_5$ glass, respectively. The effective nonlinear coefficient d_{33} of the poled glass was approximately $2 \times 10^{-2} \text{ pm/V}$ for the $\text{CaO:P}_2\text{O}_5$ glass and $3.6 \times 10^{-4} \text{ pm/V}$ for the $\text{MgO:P}_2\text{O}_5$ glass, respectively, by comparing the SHG intensity with that in 1mm-thick quartz.

Here we tentatively explain the present observations as follows. It should be noted that the large nonlinearity within the thin surface layer in poled $\text{CaO:P}_2\text{O}_5$ glass was quite similar to those observed in fused silica^{1,2}. The nonlinearity in fused silica has been explained as a field-induced third-order process similar to that proposed for the fiber experiment³. The large d. c. field induced in poled silica was considered to be a space-charge region near the anode side which was formed by the drift of mobile cation (Na^+ impurity) to cathode side under application of external electric field. The formation of thin space-charge layer in multi-component oxide glass had been confirmed experimentally by Proctor et al.⁴. Therefore, it can be expected that a small amount of mobile cations contaminated in the phosphate glass plays a similar role for the appearance of nonlinearity.

Alkali impurity in the sample glass might be a possible candidate for the mobile cation. However, since both the amount and drift-mobility of alkali impurity in the sample glasses should not differ significantly from each other, it was difficult to explain the large difference in d_{33} and/or thickness of SHG-active region between $\text{MgO:P}_2\text{O}_5$ and $\text{CaO:P}_2\text{O}_5$ glass in terms of alkali impurities. Another candidate for the mobile ion is proton in these glasses. It should be noted that the protonic conductivity in phosphate glass is exceptionally high among many kinds of oxide glasses⁵. For example, proton mobility in $\text{CaO:P}_2\text{O}_5$ glass is larger than that in SiO_2 glass by a factor of 10^7 . It had been already confirmed that the dominant charge carrier for ionic conduction in phosphate glass was proton even when the glass contained a several percent of alkali ion⁶. In contrast to this case, the mobility of Na^+ in silica glass was found to be 10^4 times as large as that of proton in the glass⁷. Thus, it is reasonable to consider that the drift of proton plays an important role upon the formation of SHG-active layer in phosphate glass, as well as the role of alkali impurity in fused silica glass.

The amount of mobile proton was semi-quantitatively evaluated to be 0.1mol% in both phosphate glasses by observing the infra-red absorption band due to hydroxyl group. According to the systematic study on the protonic conduction in phosphate glass by Abe et al.⁵, the

conductivity of proton in the $\text{CaO:P}_2\text{O}_5$ glass was larger than that in the $\text{MgO:P}_2\text{O}_5$ glass by a factor of $\sim 10^3$. Thereby the drift of protons is expected to take place easily in the former glass, which in turn results in the formation of space-charge layer within the glass, while the drift is hard in the latter glass under the same poling condition.

It should be noted that the thickness of SHG-active region was almost the same with the sample thickness of $\text{MgO:P}_2\text{O}_5$ glass. A similar phenomenon has been observed in poled silica glass. Nasu et al. reported weak second-order nonlinearity in alkali-free synthesized silica glass containing hydroxyl group of $\sim 1000\text{ppm}^8$: the thickness of SHG-active region deduced from an analysis of the Maker's fringe pattern was $\sim 700\mu\text{m}$, being comparable to the thickness of the glass. By comparing this with that in the present observation, we suppose that the formation of SHG-active region through whole thickness of the glass might be independent from the drift of proton or mobile cation in the glass. Further quantitative investigation is ongoing now to examine the origin of the appearance of second-order nonlinearity in poled phosphate glass.

References

1. R. A. Myers, N. Mukherjee, and S. R. J. Brueck, *Opt. Lett.*, **16**, 1732(1991).
2. R. Kashyap, G. J. Veldhuis, D. C. Rogers, and P. F. Mackee, *Appl. Phys. Lett.*, **64**, 1332(1994).
3. R. H. Stolen and H. W. K. Tom, *Opt. Lett.*, **12**, 585(1987).
4. T. M. Proctor and P. M. Sutton, *J. Am. Ceram. Soc.*, **43**, 173(1960).
5. Y. Abe, H. Hosono, Y. Ohta, and L. L. Hench, *Phys. Rev. B*, **14**, 10166(1988).
6. Y. Abe, H. Hosono, O. Akita, and L. L. Hench, *J. Electrochem. Soc.*, **141**, L64(1994).
7. R. H. Doremus, *J. Electrochem. Soc.*, **115**, 181(1968).
8. H. Nasu, H. Okamoto, A. Mito, J. Matsuoka, and K. Kamiya, *Jpn. J. Appl. Phys.*, **32**, L406(1993).

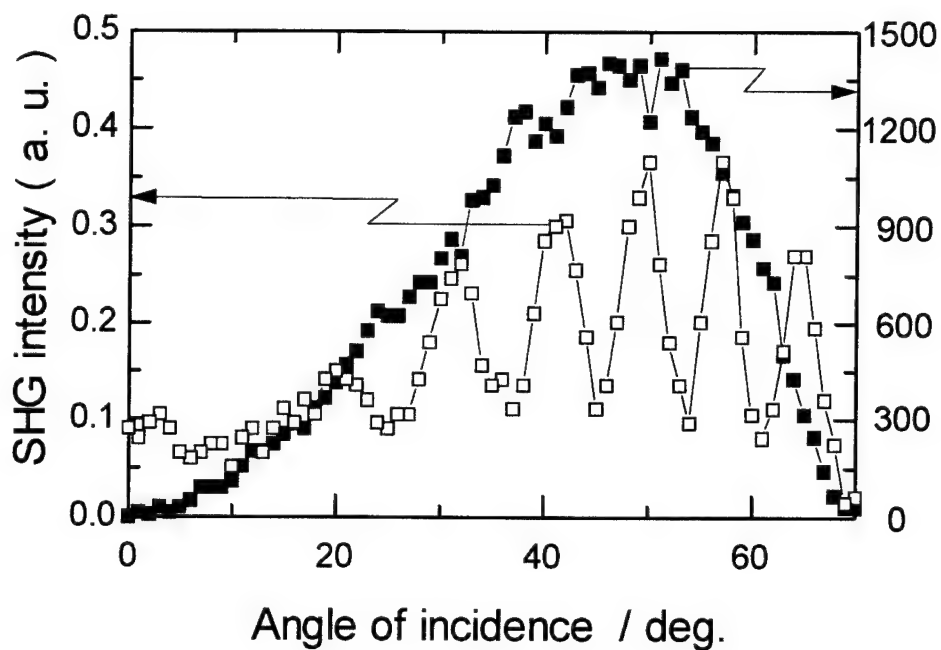


Fig.1 SHG signals from poled $\text{MgO:P}_2\text{O}_5$ (□) and $\text{CaO:P}_2\text{O}_5$ (■) glass versus the angle of incidence for a fundamental beam at $1.06\mu\text{m}$.

Effective Indices of the Propagating Modes in Planar Waveguides Measured with UV-Induced Bragg Gratings

Jörg Hübner, Christian V. Poulsen, Thomas Rasmussen*, Lars-Ulrik Aaen Andersen
and Martin Kristensen

Mikroelektronik Centret, DTU, Bldg. 345 East, DK-2800 Lyngby, Denmark

*Electromagnetics Institute, DTU, Bldg. 348, DK-2800 Lyngby, Denmark

Phone: +45 4525 5760 Fax: +45 887762

Email johu@novell.mic.dtu.dk

Introduction: The design and development of integrated optical components require precise information about the propagating modes in the planar waveguides and their effective refractive indices (n_{eff}). Most of the standard telecommunication waveguides and fibers produced today contain germanium in the core and are therefore photosensitive. A long Bragg-Grating with very low refractive index change can be used to characterize the mode propagation in a waveguide because each mode will have a different effective refractive index and thus the corresponding transmission dip of the grating will be located at a characteristic centre wavelength.

Experimental setup: Ten waveguides were illuminated simultaneously by 193nm ArF laser light via a phasemask. The beam was focused to about a third of its original size perpendicular to the waveguides by using a cylindrical lens. With 50 mJ per puls and 1800 pulses the total exposure fluence was kept as low as 120J/cm² in order not to change the refractive index significantly. With a grating length of 15 mm the total index change was estimated to be around $4 \cdot 10^{-5}$.

Waveguide Geometry: The buried channel waveguides were produced by plasma enhanced chemical vapor deposition and reactive ion etching. One set consisted of 10 different waveguides with a nominal (mask) width from 3 μm to 15 μm separated by 200 μm . The process of making these waveguides includes a reflow of the core glass where the sharp edges of the rectangular shape of the waveguides cross sections are smoothened. The waveguide core consists of germanium/phosphorous doped silica. Figure 1 shows the measured height of the waveguides as a function of their nominal width. Precise knowledge about the waveguide cross section is important, as the effective refractive index depends on both the core area and shape.

The strength of the grating corresponds to the power travelling in the mode. By adding the fractions of the intensity in the TE and TM modes the dip corresponding to the fundamental mode in figure 2 is around 35% whereas the first order mode dip is about 22%.

Figure 3 shows the center wavelength of the first, second and third order modes. On the right axis the corresponding effective refractive index is written. Waveguides with less than 8 μm nominal width are single moded whereas waveguides with more than 10 μm seem to be at least triple moded.

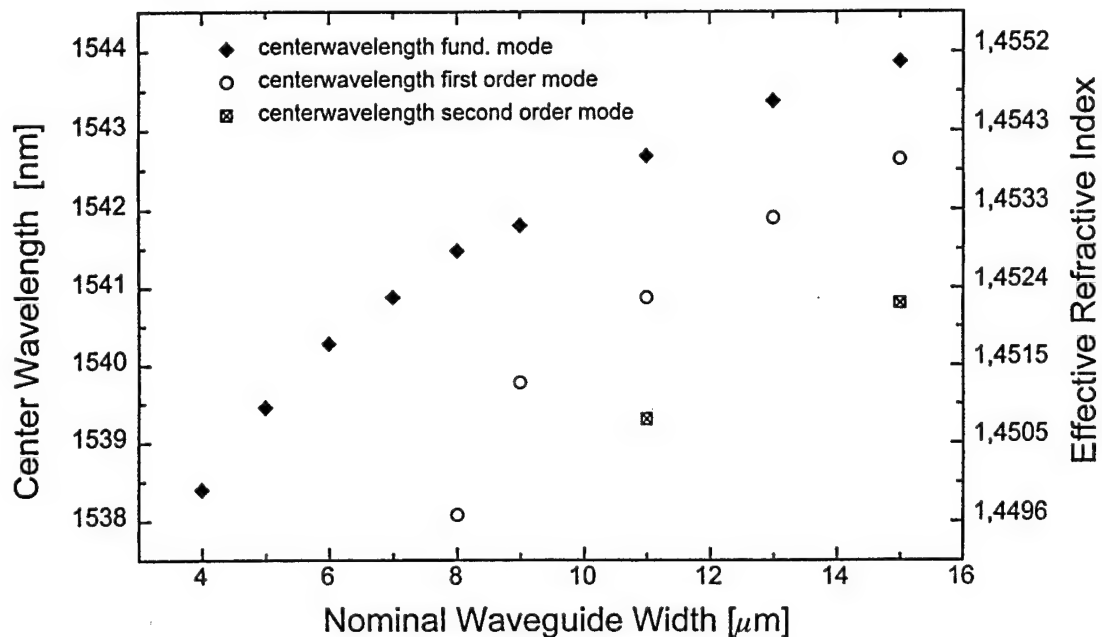


Fig. 3. Center wavelength and effective refractive index as function of the nom. waveguide width.

We have calculated the dispersion curves with the optimised effective index method [5] for a rectangular core waveguide with the width and heights equal to the measured values. As mentioned earlier the core shape after the reflow is smoothend. The difference in effective index between a strictly rectangular and a more realistic parabolic core shape has been calculated to be in the order of $2 \cdot 10^{-3}$. The measured effective indices are within the uncertainty of these theoretical values.

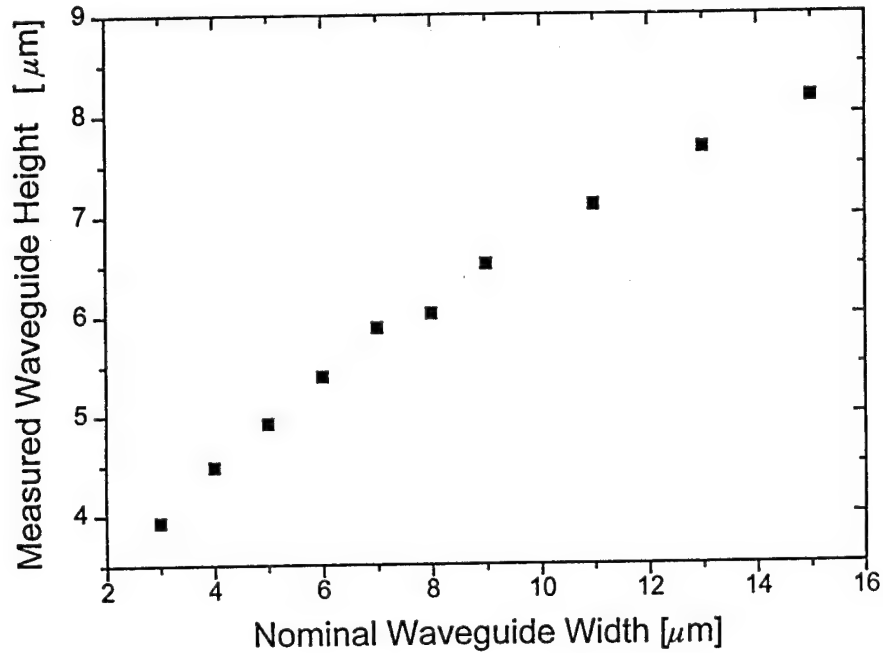


Fig. 1. Waveguide dimensions of the illuminated set of 10 waveguides.

Results: The transmission spectrum of a 13 μm broad waveguide is shown in figure 2. The fundamental mode is centred around 1543.5 nm whereas the first order mode is located around 1542 nm. The modes are split in TE and TM due to the birefringence of the waveguides which is partly stress induced (silica on silicon) and partly due to the waveguide geometry.

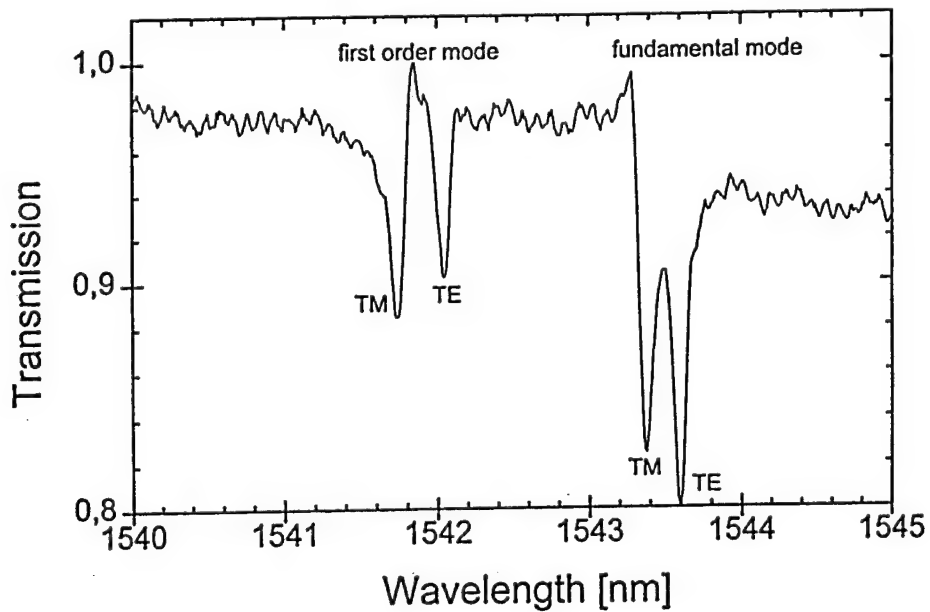


Fig. 2. Transmission spectrum of the 13 μm broad waveguide.

Conclusion: By writing low index difference, long Bragg Gratings simultaneously in 10 different germanium doped buried channel waveguides, we demonstrated a very accurate and simple method to determine the effective refractive index of each propagating mode in a planar waveguide. The method is suitable for all germanium doped waveguides and independent of the shape of their core cross sections.

References:

- [1] G.Meltz and W.W. Morey "Photoinduced Refractivity in Germanosilicate Waveguides" ,Integrated Photonics Research PD6-2 Feb.94
- [2] P. E. Dyer, R. J. Farley, R. Giedl, K. C. Byron and D. Reid: "High reflectivity fibre gratings produced by incubated damage using 193 nm ArF laser", Electronic Letters, 1994, Vol. 30, No. 11, pp. 860-862.
- [3] T. Kitagawa, K. O. Hill, D. C. Johnson, B. Malo, J. Albert, S. Theriault, F. Bilodeau, K. Hatori and Y. Hibino: "Photosensitivity in P_2O_5 - SiO_2 waveguides and its application to Bragg reflectors in single-frequency Er^{3+} -doped planar waveguide laser", 1994, OFC-94, PD-17.
- [4] D. Moss, M. Ibsen, F. Oullette, P. Leech, M. Faith, P. Kemeny, O. Leistiko and C. V. Poulsen: "Photo-Induced Planar Germanosilicate Waveguides", ACOFT, 1994, pp. 333-336.
- [5] T. Rasmussen, J. M. Poulsen, A. Bjarklev, O. Lumholt, B. Pedersen and K. Rowitt:"Detailed Comparison of two Approximate Methods for the Solution of the Scalar Wave Equation for Rectangular Waveguides" , J. Lightwave Technol., Vol.11,No. 3, 1993, pp. 429-433.

Thermal stability of direct UV-written channel waveguides

Christian V. Poulsen

Mikroelektronik Centret

Technical University of Denmark, bldg. 345 E, DK-2800 Lyngby, Denmark

Phone: (+45) 45 25 57 60, Fax: (+45) 45 88 77 62

E-mail: cvp@mic.dtu.dk

Introduction: An important issue of the UV-induced effects in germanium doped silica glasses is the long term stability. Investigations concerning the thermal stability show a major difference between effects induced by low and high intensity [1] (type I and type II). In this paper, the thermal response of UV-induced waveguides in germanium doped silica glass is investigated, as a function of UV-intensity.

The silica glass is grown with plasma enhanced chemical vapor deposition (PECVD) on silicon wafers. PECVD offers an excellent control of the glass structure due to the low deposition temperature. The glass is deposited in a gas mixture of silane, germane and nitrous oxide. A film waveguide is deposited with germanium doped silica (6 mole %) in the core layer surrounded by a silica buffer layer. The core layer is 2.5 μm thick which ensures support of only a single mode in the vertical plane.

UV-writing: A CW frequency doubled Ar-ion laser emitting 100 mW of 244 nm UV-light was focused in the film waveguide, which was mounted on a translation stage. Direct point to point waveguides were written with beam diameters from 5 μm to 50 μm and scan speeds from 20 $\mu\text{m/s}$ to 500 $\mu\text{m/s}$. These exposure conditions give intensities from 5 kW/cm^2 to 500 kW/cm^2 . More details are described in [2]. The visibility of the waveguides increased with the applied UV-intensity suggesting that type II effects were becoming important at the highest intensities.

Thermal stability: To investigate the thermal stability, the direct written waveguides were exposed to increasing temperatures. For each temperature the full width at half maximum (FWHM) of the propagating modes was measured with a microscope objective projecting the pattern on to a CCD camera. The direct written waveguides were annealed for ten minutes at temperatures starting from 100°C and continued to 800°C in steps of 100°C. In figure 1 the FWHM of the propagating modes of the waveguides induced with the highest intensity is shown as function of the annealing temperature for three different exposure times.

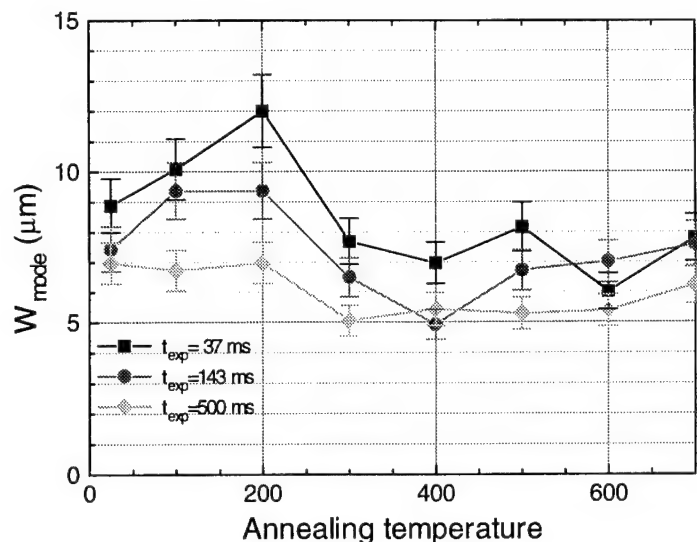


Fig. 1: The FWHM of the propagating modes shown as function of increasing annealing temperatures for three different exposure times.

The effects may be divided in four different temperature-regimes; the first up to 200°C, the second between 200°C and 300°C, the third between 300°C and 700°C and the fourth between 700°C and 800°C.

Up to 200°C the FWHM of the propagating mode is getting wider in the waveguides induced with low exposures fluences. This may be caused by a thermal diffusion of the UV-induced effects like observed in [4]. The longer exposure time the higher is the total fluence. When annealed at 200°C in short time the UV-induced effects diffuse and the refractive index step is getting wider.

Above 300°C the FWHM of the propagating modes get more narrow, showing that either the refractive index increases or the waveguide gets more narrow. Type I effects have been observed to disappear at temperatures around 250°C [3]. The UV-induced refractive index increase, surviving beyond 300°C is probably due to Type II induced effects, which endures much higher temperatures [3]. The reason why the FWHM of the propagating mode is reduced may be understood by considering the UV-beam profile shown in figure 2.

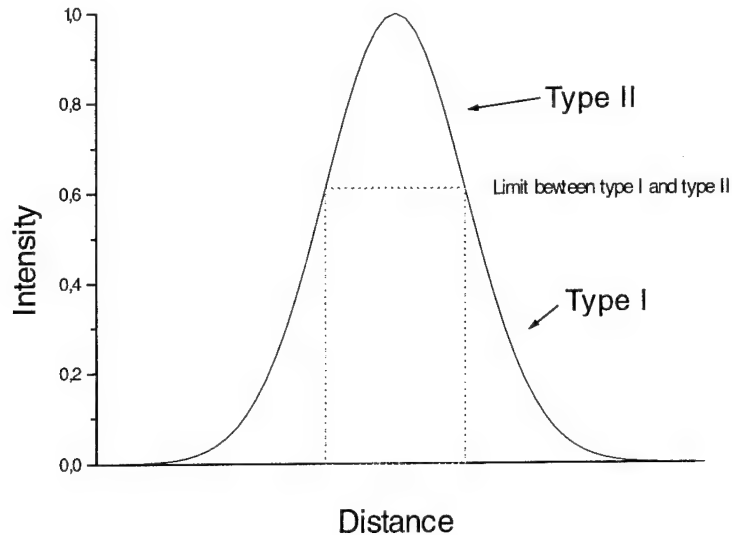


Fig. 2: The 244 nm UV-beam mode profile used for inducing the channel waveguides. Above a certain level type II effects occur.

Type II effects appear above a certain intensity. This limit will slightly depend on the exposure time but is mostly decided by the intensity. When exposing with a Gaussian like beam profile, the center part has a higher intensity than the wings. The type I effects disappear at 300°C, meaning the waveguides have become more narrow resulting in a smaller FWHM of the propagating mode.

Between 300°C and 700°C no significant change is observed, indicating that all type I induced effects totally disappeared at 300°C. By annealing UV-induced refractive index changes, which contain type II effects, at 300°C, the remaining UV-induced refractive index increases will be stable up to well above this temperature. Until 700°C, the waveguides were visible.

Beyond 800°C the waveguides disappeared and no guiding was observed indicating, that all the UV-induced effects had been annealed away.

Conclusion: UV-induced refractive index changes in germanium doped silica glasses have been investigated in direct written channel waveguides. The consequence of successive annealing has been characterized showing the difference between type I and type II effects. Type I effects disappear totally around 300°C and type II effects at ~700-800°C. Highly stable UV-induced effect may be created by a post-annealing after UV-exposure at 300°C, when type II effects are involved.

References:

- [1] T.E.Tsai, E.J.Friebele, D.L.Griscom: "Thermal stability of photoinduced gratings and paramagnetic centers in Ge- and Ge/P-doped silica optical fibers", *Optics Letters*, Vol. 18, pp 935-937, 1993.
- [2] M.Svalggard, C.V.Poulsen, A.Bjarklev and O. Poulsen: "Direct UV writing of buried singlemode channel waveguides in Ge-doped silica films", *Electronics Letters*, Vol. 30, No. 17, pp 1401-1420, Aug 1994.
- [3] T.Erdogan, V.Mizrahi, P.J.Lemaire and D.Monroe: "Decay of ultraviolet-induced fiber Bragg gratings", *Journal of Applied Physics*, Vol. 76, pp 73-80, 1994.

A NEW SENSITIVE METHOD FOR MEASURING INDUCED REFRACTIVE INDEX CHANGE IN OPTICAL FIBER CORE

E.M. Dianov, A.S. Kurkov, O.I. Medvedkov, S.A.Vasil'ev

*Fiber Optics Research Center at the General Physics Institute
of the Russian Academy of Sciences, 38 Vavilov Street, 117942, Moscow, Russia
Fax: (095) 135-8139*

INTRODUCTION

It is well known that germanium-doped silica and a number of other fiber materials exhibit photorefractivity; that is, their refractive index changes in the process of exposure to ultraviolet or blue light. This phenomenon gives an opportunity to produce different types of in-fiber gratings, which are successfully used in many optical devices [1-3].

In choosing a specific glass for the grating writing, it is important to assess the refractive index change during the UV-irradiation. There are several methods to do this [2]. Unfortunately, the most sensitive methods (the change in the output response of Mach Zehnder interferometer, the change in the far-field pattern) are difficult to perform.

We present a new sensitive method for measuring UV-induced refractive index in the fiber core. It is based on the determination of the loss peak wavelength displacement during the formation of a long-period grating, a new type of grating that has been recently suggested [3]. This technique is easy to realize and makes it possible to detect very small refractive index changes.

THEORY

As in the case of short-period gratings, during the long-period grating creation the effective refractive index of the fundamental mode n_{ef}^{core} increases. This is accompanied by a displacement of the resonance wavelength λ_r to the long wavelength region. The phase matching condition between the guided mode and a forward propagating cladding mode is given by:

$$(n_{ef}^{core} - n_{ef}^{cl})\Lambda = \lambda_r, \quad (1)$$

where Λ is the grating period required to couple the fundamental mode to the cladding mode and n_{ef}^{cl} is the effective refractive index of the cladding mode. Assuming that the n_{ef}^{cl} change during the UV-irradiation is negligible, one can obtain a relation between the UV-induced

effective refractive index change Δn_{ef}^{core} and the displacement of the resonance wavelength $\Delta \lambda_r$:

$$\Delta n_{ef}^{core} \approx (n_{ef}^{core} - n_{ef}^{cl}) \Delta \lambda_r / \lambda_r. \quad (2)$$

In the case of a conventional Bragg grating, Δn_{ef}^{core} and $\Delta \lambda_r$ are related by the following equation:

$$\Delta n_{ef}^{core} \approx n_{ef}^{core} \Delta \lambda_r / \lambda_r. \quad (3)$$

Equations (2) and (3) show that during the long-period grating formation the resonance wavelength shift is by a factor of $n_{ef}^{core} / (n_{ef}^{core} - n_{ef}^{cl}) \approx 10^2$ greater than the same value for the Bragg grating and can be equal to several tens of nanometers.

Now let us assume that Δn_{ef}^{core} is mainly due to the UV-induced refractive index change in the fiber core Δn^{UV} . From (2), as a rough estimate, we obtain

$$\Delta n^{UV} \approx \Delta n \frac{\Lambda}{d} \frac{\Delta \lambda_r}{\lambda_r}, \quad (4)$$

where Δn is the core-cladding index difference and d is the width of the open part of the mask period. Thus, by measuring $\Delta \lambda_r$, the UV-induced change of the core refractive index can be easily calculated. For a typical value $\Delta n \approx 10^{-2}$, and for the measurement accuracy $\Delta \lambda_r \approx 0.5$ nm ($\lambda_r \approx 1500$ nm, $\Lambda/d=2$), we have from (4) $\Delta n^{UV} \approx 7 \cdot 10^{-6}$. This accuracy is comparable to that of the interferometric method.

It should be noted that the UV-induced index change can be measured by this method, if a weak grating has been written; that is, if some initial index has been induced. This value can be estimated, for example, with the aid of extrapolation of the peak loss dependence on Δn^{UV} to zero (see fig.3).

Our method has the following strong points:

- simplicity;
- high sensitivity ($\Delta n^{UV} \leq 10^{-5}$);
- no rigid requirements on the spectrometer resolution;
- applicability of the sources with low spatial and temporal coherence;
- high mechanical and thermal stability.

Note that there are also some weak points:

- it is necessary to have accurate data of the waveguiding properties of the fiber;

- high sensitivity to the fiber bending;
- the refractive index of the medium surrounding the fiber must be smaller than that of silica and must not change during the measurement.

EXPERIMENT

To demonstrate the possibilities of the technique described, we measured the writing dynamics of a long-period grating. The experimental setup for the grating fabrication was the same as in [3]. We used a step-index germanosilicate fiber with 12 mol.% of GeO_2 in the fiber core. The fiber was exposed to a KrF laser radiation ($\approx 300 \text{ mJ/cm}^2/\text{pulse}$, 20 Hz) through an amplitude mask. Fig.1 shows changes in the transmission spectrum of a 3 cm long grating written with a period of $360 \mu\text{m}$ during the UV-irradiation.

The induced refractive index was calculated by the technique based on the numerical solution of the scalar wave equation for the measured refractive index profile [4]. Fig.2 presents the temporal dependencies of the calculated Δn^{UV} and the peak value of the loss spectrum. Thus, after 20 minutes' irradiation we obtained $\Delta n \approx 6 \cdot 10^{-4}$.

This value is in a good agreement with that of [5] which was obtained in similar experimental conditions. The dependence of peak value of the loss spectrum on the induced refractive index change is plotted in Fig.3. This dependence is well approximated by a straight line.

CONCLUSIONS

The writing dynamics of a long-period grating has been investigated experimentally. A new sensitive method for the determination of the photoinduced refractive index change in fibers has been developed. It is easy to perform and may become a useful tool in assessing glass photorefractivity.

REFERENCES

1. Kashyap R. Optical Fiber Technology, 1, 1, 17-34, 1994.
2. Williams D.L., Ainslie B.J., Kashyap R. et al, SPIE'93, Vol.2044, 55-68, 1993.
3. Vengsarkar A.M., Lemaire P.J., Judkins J.B. et al, OFC'95, PD4, 1995.
4. Belov A.V., Kurkov A.S., Chicolini A.V., Kvantovaya Elektronika (Sov. J. Quantum Electronics), 16, 2, 354-356, 1989.
5. Hill K.O., Bilodeau F., Malo B. et al, OFC'93, PD15, 1993.

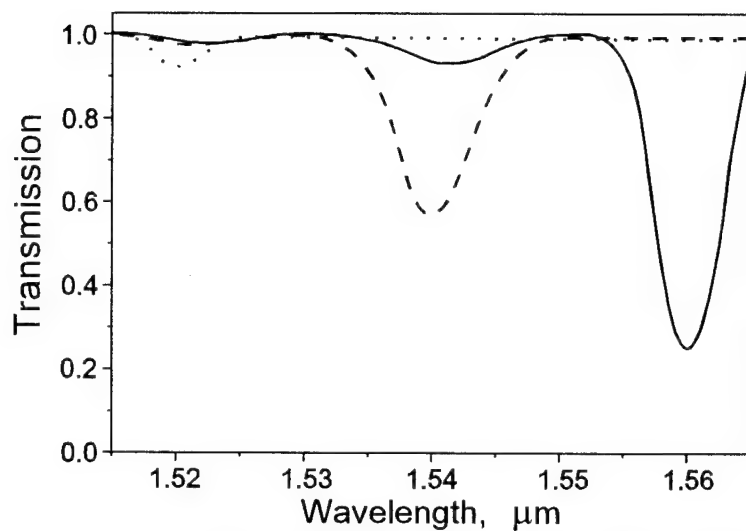


Fig.1. Transmission spectra of a long-period grating after 0.25 (· · · · ·), 4 (— — —), 20 (—) minutes' UV-irradiation

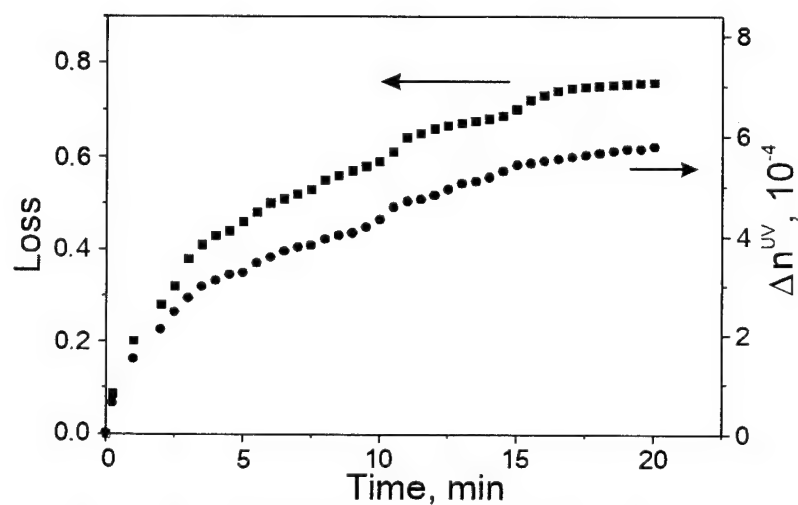


Fig.2. Time dependence of the normalized peak loss and UV-induced refractive index change

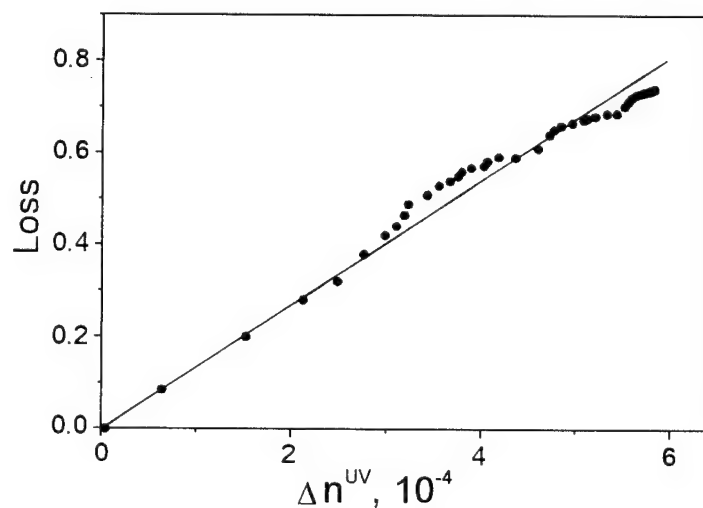


Fig.3. Dependence of the normalized peak loss of the long-period grating on UV-induced refractive index change

Photosensitivity of Ge-doped silica films deposited in a PECVD hollow cathode reactor.

M. V. Bazylenko, M. Gross and P.L. Chu

Electrical Engineering, University of New South Wales, Sydney, NSW, 2052, Australia.
(ph: Int-61-2-385-4027, fax: Int-61-2-385-5993)

D. Moss

Optical Fibre Technology Centre, University of Sydney, Sydney, NSW, 2006, Australia.
(ph: Int-61-2-335-0936, fax: Int-61-2-335-0910)

Introduction.

In recent years there has been a considerable research effort directed towards the process and applications of the UV induced refractive index change in germanosilicate glasses. Most of the germanium doped planar structures reported in previous work were formed by flame hydrolysis and need to be hydrogen loaded for up to 2 weeks [1] to become reasonably photosensitive. An alternative deposition technique, which is able to produce photosensitive films without hydrogen loading is Plasma Enhanced Chemical Vapour Deposition (PECVD). A UV induced refractive index change of 0.0025 has been reported for germanium doped PECVD silica films without use of hydrogen loading [2].

In this paper we present the results of an on-going investigation into the photosensitivity of germanium doped silica films deposited in a high density hollow cathode PECVD reactor [3]. Exposure of the films at both 193 nm and 248 nm wavelengths has so far resulted in refractive index changes ranging from -0.00355 to +0.00173.

Experimental

Silica films with varying germanium content were deposited on 2" silicon substrates in a high plasma density hollow cathode reactor from mixtures of silane (SiH_4), germane (GeH_4) and oxygen. The hollow cathode reactor consists of two opposing radio frequency (13.56 MHz) powered electrodes located inside a grounded chamber. A conventional, low density diode discharge is generated between each of the electrodes and the grounded chamber, but between the two electrodes a very intense hollow cathode discharge region is created due to so called "electron mirror" effect [3].

Table 1. Gas flow conditions

Run	Gas flow rates, sccm		
	O_2	SiH_4	GeH_4
1	130	20	---
2	130	20	2.9
3	130	20	5.5
4	130	20	5.5
5	130	20	8.9
6	130	20	15.5

A series of deposition runs with varying gas mixtures were carried out at a fixed rf power density of 1.95 W/cm^2 and a process pressure of 2 Pa. The gas mixtures are listed below in Table 1.

In runs 1, 2, 3, 5 and 6, the film was deposited on one wafer clamped in the "face down" position to the top electrode. In run 4 two wafers (4a and 4b) were deposited simultaneously. Wafer 4a was clamped to the top electrode in the normal manner, while wafer 4b was placed on the bottom electrode, but supported slightly above it on three small ceramic spacers. The purpose of this was to

reduce the level of ion bombardment on this wafer by reducing its voltage from the bias voltage of the electrode to the floating potential of plasma glow.

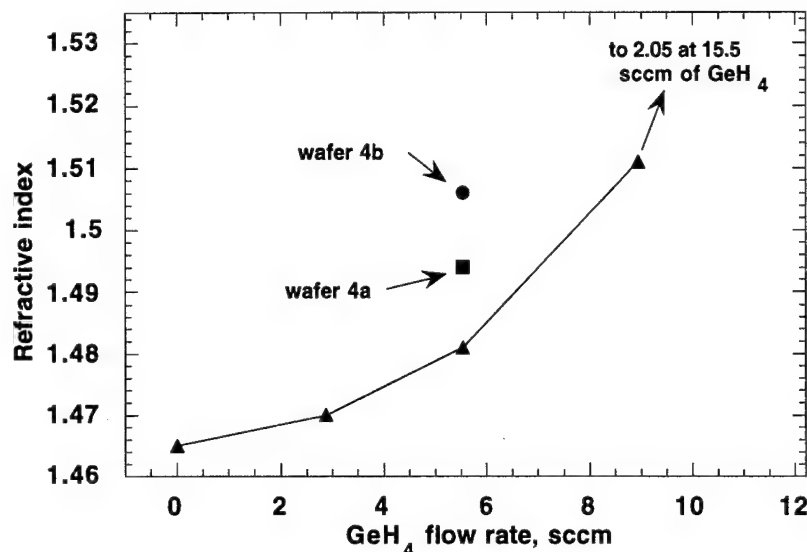


Fig. 1. Refractive index versus GeH_4 flow rate.

technique at 633 nm wavelength with measurement repeatability within ± 0.00015 . During the exposure the samples were partially masked and the refractive index changes were obtained as a difference between the averages of three measurements in the exposed and unexposed areas near the edge of the mask. The differences were then compared with the maximum deviation in the refractive index for exposed and unexposed areas in order to confirm the significance of the refractive index change.

Results.

Figure 1 show the refractive index as a function of GeH_4 flow rate. The refractive index at first increases gradually with the GeH_4 flow rate and then rises very sharply to a value of 2.05 at the maximum flow rate. This last index value was measured using an ellipsometer at 633 nm wavelength, since the value was outside the range of the prism coupler setup.

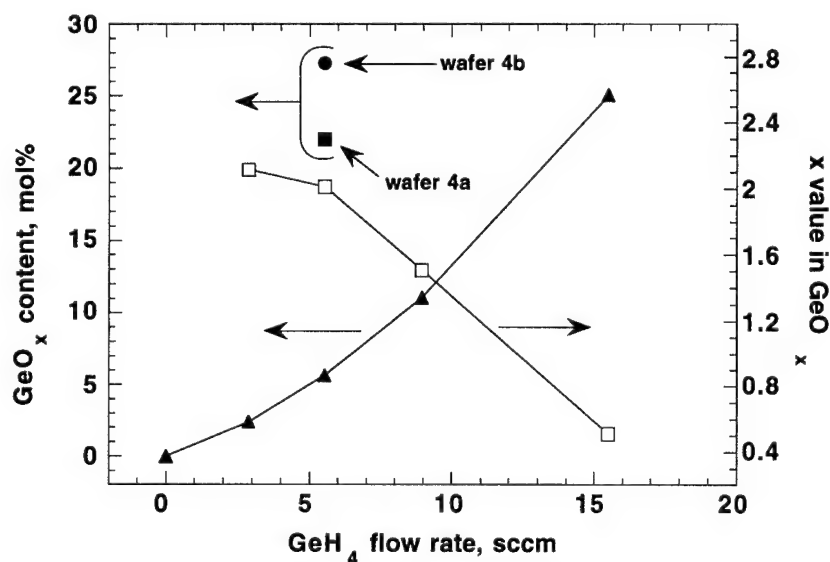


Fig. 2. GeO_x content and calculated x value versus GeH_4 flow rate. The x value for wafers 4a and 4b is 1.8.

The deposited films were characterized for their hydrogen content and bond structure by Fourier Transform Infrared Spectroscopy (FTIR), and the film composition, including Ge, Si and O content was determined by Wavelength Dispersive X-ray Spectroscopy (WDS). The deposited films were UV exposed using an excimer laser with a fluence of 10 kJ/cm^2 at both 193 nm and 248 nm wavelengths. The film refractive index, both before and after UV exposure, was measured by the prism coupling

The GeO_x content in the deposited films is shown in Fig.2. Also shown in Fig. 2 is the x value in GeO_x , which was calculated from the oxygen and silicon content data, assuming that oxygen is first consumed by silicon because of a more energetic Si-O bond compared with the Ge-O bond [4]. It is seen that at higher GeH_4 flow rates the films become Ge-rich, which is most likely caused by the discharge becoming increasingly oxygen

deficient, since the oxygen flow is kept constant while increasing the GeH_4 flow rate.

The refractive indices and GeO_x content for wafers 4a and 4b are also shown in Figs. 1 and 2. For the same GeH_4 flow rate they have 4 to 5 times higher GeO_x content and a higher refractive index.

The OH content in the deposited films is plotted in Fig. 3. It is seen that OH content decreases to below the FTIR detection limit (0.1-0.2 at. %) with increasing GeH_4 flow and then increases slightly in the Ge-rich film.

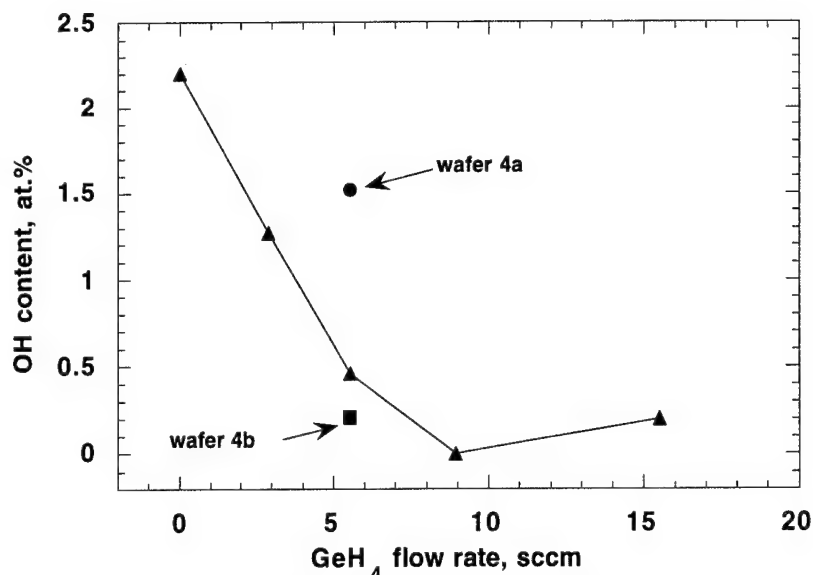


Fig. 3. OH content versus GeH_4 flow rate.

The refractive indices measured in the exposed and unexposed areas for all samples except sample 6, which could not be measured by the prism coupling technique, are shown in Table 2.

The maximum deviations ($[\text{max-min}]/2$) listed under each averaged refractive index value allows us to judge the significance of the appropriate UV induced refractive index change. It can be seen that the index changes ranges from -0.00355 for wafer 4a to +0.00173 for wafer 4b, both exposed at 193 nm.

Discussion.

In an attempt to explain the variety of the UV induced refractive index changes obtained we shall try to correlate them with other observed film properties and the appropriate deposition conditions used.

Table 2. UV induced refractive index changes.

Wafer	193nm			248nm		
	exposed	unexposed	change	exposed	unexposed	change
1	1.46553 (± 0.00016)	1.46551 (± 0.00014)	+0.00002*	1.46574 (± 0.00008)	1.46567 (± 0.00014)	+0.00007*
2	1.47064 (± 0.0001)	1.4703 (± 0.00008)	+0.00034	1.47078 (± 0.00006)	1.47064 (± 0.00003)	+0.00014*
3	1.48219 (± 0.00016)	1.48169 (± 0.00005)	+0.00050	1.48189 (± 0.00002)	1.48119 (± 0.00002)	+0.00070
4a	1.49117 (± 0.00022)	1.49472 (± 0.00028)	-0.00355	1.49445 (± 0.00026)	1.49724 (± 0.00019)	-0.00279
4b	1.50801 (± 0.00016)	1.50628 (± 0.00025)	+0.00173	1.50714 (± 0.00007)	1.50682 (± 0.00004)	+0.00042
5	1.51190 (± 0.00007)	1.5120 (± 0.00016)	+0.0001*	1.51247 (± 0.00040)	1.51253 (± 0.00021)	-0.00006*

* These values are less than the appropriate deviations and are therefore considered insignificant.

For runs 1, 2, 3 and 5, the UV induced refractive index change at both wavelengths appears first to increase with GeH_4 flow rate, then goes through a maximum and then returns to zero. This behaviour can be explained by referring to Figs. 3 and 4, where it is seen that the Ge content increases while the OH content decreases with GeH_4 flow rate. As is well known, the presence of hydrogen enhances the photosensitive effect and so the reduction in the UV induced refractive index change as OH content is reduced seems reasonable, despite the increase in Ge content. In addition, no photosensitivity is observed in either the Ge doped but OH free film (wafer 5) or in the OH containing but Ge-free pure silica film (wafer 1).

The observation of both negative and positive UV induced refractive index changes on wafers 4a and 4b, which were deposited in the same run is rather interesting. While one would expect different film properties from a sample deposited with reduced ion bombardment (wafer 4b), the completely different behaviour (large negative index change) for wafer 4a, which was clamped to the top electrode as in all the other runs, is rather surprising. Apparently the bottom wafer, which is separated from the bottom electrode by the ceramic supports, has altered the deposition conditions of the top wafer. Thermocouple measurements of the temperature of the top wafer in similar experiments showed that its temperature can be reduced by 100-150° C when the bottom floating wafer is present. Thus it may be possible that the observed negative UV induced refractive index change is a result of the combined effects of substrate temperature and ion bombardment. Work is currently in progress to separate these temperature and ion bombardment effects.

Conclusions

UV induced refractive index changes in PECVD Ge-doped silica films ranging from -0.00355 to +0.00173 have been demonstrated at 193 nm. The mechanism of photosensitivity is likely to involve a dependence on the OH content as well as a combined effect of ion bombardment and wafer temperature during the deposition.

Acknowledgements

The authors would like to thank J. Arkwright for helpful discussions. This work has been supported by the Australian Photonics Cooperative Research Centre (APCRC) of which the University of NSW and the Optical Fibre Technology Centre (OFTC) are members.

References

1. G. D. Maxwell and B. J. Ainslie: "Demonstration of a directly written directional coupler using UV-induced photosensitivity in a planar silica waveguide". *Electron. Lett.*, 1995, **31**(2), pp. 95-96.
2. M. Svalgaard, C. V. Poulsen, A. Bjarklev and O. Poulsen: "Direct UV writing of buried singlemode channel waveguides in Ge-doped silica films". *Electron. Lett.*, 1994, **30**(17), pp. 1401-1403.
3. C.M. Horwitz, S. Boronkay, M. Gross and K.E. Davies: "Hollow cathode etching and deposition", *J. Vac. Sci. Technol.*, 1988, **A6**, pp. 1837-1844.
4. CRC handbook of chemistry and physics. 64th edition 1983-1984, CRC Press, Inc. Boca Raton, Florida, p. D110.

U. V. induced densification during Bragg grating writing.

B. Poumellec, Lab. CNS, Bât. 415, URA CNRS 446, Université Paris Sud, 91405 Orsay, France. Tel.: 33 1 69 41 63 51. Fax.: 33 1 69 85 54 84.

P. Niay, M. Douay, Lab. LDMP, Bât. P5, URA CNRS 779, Université des Sciences et Technologies de Lille, 59655 Villeneuve d'Ascq Cedex, France. Tel.: 33 20 43 47 62. Fax.: 33 20 43 40 84.

J. F. Bayon, LAB/RIO/TSO, Technopole Anticipa France Telecom CNET-Lannion, B.P.40, 22301 Lannion Cedex, France. Tel.: 33 96 05 28 28 Fax. 33 96 05 13 07

It was expected that the bleaching of the 240-260 nm absorption band and creation of others were sufficient to explain all part of the index change through Kramers-Kronig conjugation. However, Williams et al. [1] taking into account the UV absorption change showed that at most 20% of the index change can be accounted for by this effect. This statement was confirmed also by Eric Fertein [2] in various type of fibers and in taking into account the VUV absorption change. In addition, some recent experiments by Albert et al. [3] using 193 nm light indicates that the bleaching of absorption bands near 242 nm is not essential to induce refractive index changes. A second phase of the process may be that transformed defects lead to a change in the microstructure of the silica. The first idea is a change of volume and so we can expect to see corrugations at the surface of irradiated flat substrate close as the ones of preform slices.

Experimental proof of densification.

Preforms used were preforms for Telecoms or specially made for with few % to 11% of Germanium in the core. One exempla of observations made by interferometric microscopy is shown in fig. 1. The 3D image has been inverted in order to show clearly the corrugations. They appear embedded in a valley, i.e. the surface is depressed not only at the places of irradiation but also between the fringes and all around the gratings. This means that a non-local effect is associated with the direct effect of irradiation.

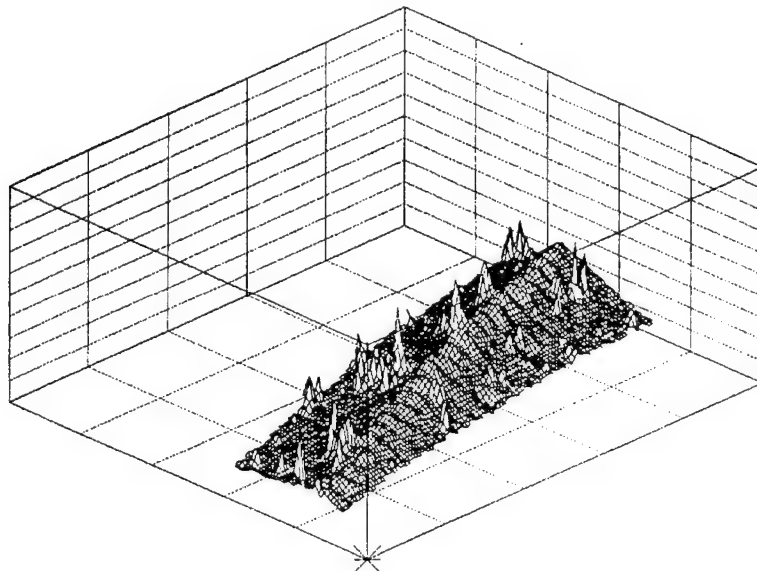


Fig. 1: 3D view of the grating 285d-R2. The image has been z inverted in order to show clearly the corrugations in the bottom of a valley.

Furthermore, the depressed surface corresponds to a decrease of volume of material but without loss of matter. This is not obvious when one use a pulsed laser to write the grating but the

same effect has been observed with a much lower power density like a CW laser. All results versus the dose are collected in the following table.

Gratings	Peak power density (W/cm ²)	Cumulated fluence (kJ/cm ²)	Δn_{mod} (by diffraction efficiency) grating period (μm)	depth of the valley (mean value in nm)	peak to peak modulation (nm)	period of the grating (μm)
CW irradiations						
285c-R4	21	9	unknown 8.15 ± 0.15	-8.7 ± 0.7	< 1	unknown
285c-R3	22	20	$1.9 \cdot 10^{-4}$ 8.15 ± 0.15	-18 ± 2	< 1.4	unknown
285c-R2	23	41	$5.5 \cdot 10^{-4}$ 8.15 ± 0.15	-27.3 ± 2.6	2 ± 1	7.8 ± 0.2
285c-R1	18	60	$8.8 \cdot 10^{-4}$ 8.15 ± 0.15	-37 ± 1	6.0 ± 0.6	8.4 ± 0.1
285d-R1	135	243	$2.1 \cdot 10^{-4}$ 5.9 ± 0.2	-59 ± 5	10 ± 1	5.87 ± 0.08
285d-R2	135	486	$2.1 \cdot 10^{-3}$ 5.9 ± 0.2	-69 ± 5	13 ± 6	6.1 ± 0.1
285d-R3	135	972	$1.5 \cdot 10^{-3}$ 5.9 ± 0.2	-78 ± 6	6 ± 2	6.2 ± 0.1 (3.1)
Pulsed irradiations						
285b-R4	MW/cm ² 4	1	$4.2 \cdot 10^{-4}$ 8.3 ± 0.1	-27.5 ± 0.5	3.9 ± 0.2	8.0 ± 0.1
285b-R3	4	2	$6.4 \cdot 10^{-4}$ 8.3 ± 0.1	-29 ± 1	7.6 ± 0.5	8.1 ± 0.1
285b-R2	4	5	$8.2 \cdot 10^{-4}$ 8.3 ± 0.1	-34.5 ± 1	6.2 ± 0.9	8.0 ± 0.1
285b-R1	4	10	$9.8 \cdot 10^{-4}$ 8.3 ± 0.1	-53 ± 2	12 ± 0.6	8.1 ± 0.1

The sample 285d, 285c, and 285b are respectively 100 μm , 140 μm , and 134 μm thick.

Strain-densification model

The decrease of volume at the place of irradiation corresponds to a densification of the material. It is accompanied by an elastic deformation all around the irradiated regions. Hence, let us state that densification takes place periodically in a Ge-SiO₂ substrate to form a grating (see fig. 2). We will have region I with no densification because no irradiation and region II with densification. This is exemplified in the fig. 2a showing the permanent displacement in the z direction i.e. the direction of observation. This occurs also in the other directions x, y but not necessary with the same extend. This depends on the importance of polarization in this matter.

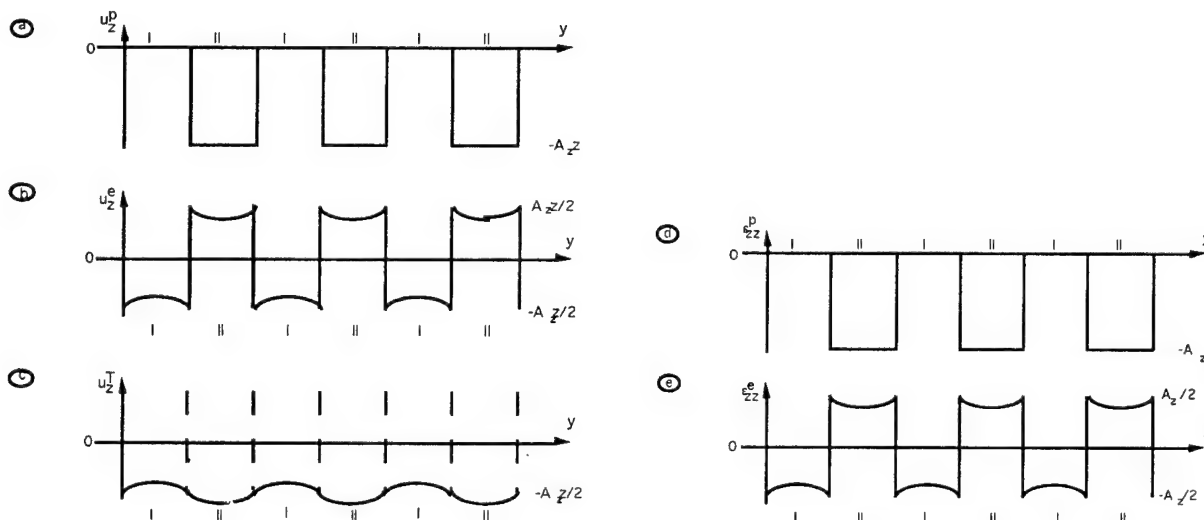


Fig. 2: Model for the surface displacement following the direction z of observation (a-b-c). d-e are for the deduced strains.

For continuity reason, the permanent strain is accommodated by an elastic strain. We can consider that region I and II are of the same thickness and that the elastic strain is equally distributed in both regions. We get fig. 2b showing that non-irradiated region are compressed following z and region II in tension. The total deformation throughout the solid must be continue. So, the amplitude of the discontinuity of the permanent deformation must be opposite to the discontinuity of the elastic one. We get fig. 2c finally. Two points are noticeable.

- 1) The mean displacement is non zero and equal to the half of the one related to densification i.e. $u_m = -A_z z/2$. As the origin is taken at the center of the sample, the corrugations are symmetrical and $2z$ is the sample thickness. We get $A_z = -2 \epsilon_m$ where $\epsilon_m = u_m/z$ the normalized depth of the valley.
- 2) The modulation is connected to the magnitude of densification through the elastic properties of the material. If it is hard the amplitude will be weak, whereas when it is soft the amplitude will approach $A_z z$.

We explain thus why a grating embedded in a valley is observed at the surface of Ge doped silicas validating in the same time the elasto-densification process. Now, since the strain tensor is described, we can turn to the calculation of the connected change of index.

Calculation of the index change

Assuming a constant polarization, we have $\Delta n = -\frac{(n^2-1)(n^2+2)}{6n} \Delta v/v$ with $\frac{(n^2-1)(n^2+2)}{6n} = 0.59$ (1)

This relation can be expressed also in term of density and we obtain with $\rho=2.2$, $\Delta n=0.267 \Delta \rho$ with ρ in cgs system. We find in ref. [4] an empirical law for SiO₂ rather close to the one above: $\Delta n=0.25 \Delta \rho$.

For strained material, the polarizability is no longer constant. In this case, the index change is relevant of photoelastic relations. Because of the symmetry of the problem and assuming that anisotropy appears only in the index change, we have:

$$\Delta n_\alpha = -\frac{n^3}{2} (p_{11} \epsilon_{\alpha\alpha} + p_{12} (\epsilon_{\beta\beta} + \epsilon_{\gamma\gamma})) \quad (2)$$

where β, γ are the two other directions differing from α .
where p_{11} and p_{12} are the photoelastic coefficients [5].

Noting that (1) acts equally on all directions and that $\Delta v/v = \text{Tr}(\epsilon)$, combining (1) and (2) and putting the relevant superscript, we get:

$$\Delta n_\alpha = -\frac{n^3}{2} (p_{11} \epsilon_{\alpha\alpha}^e + p_{12} (\epsilon_{\beta\beta}^e + \epsilon_{\gamma\gamma}^e)) - \frac{(n^2-1)(n^2+2)}{6n} \text{Tr}(\epsilon^p) \quad (3)$$

For sake of simplicity, we can ignore the corrugations (hard limit). To further simplify, we can assume an isotropic densification i.e. $A_x=A_y=A_z=A$ (these quantities appear in fig. 2). We get the following results replacing coefficients by numerical values:

$$I \begin{cases} \Delta n_x = 0.093 \times A \\ \Delta n_y = -0.51 \times A \\ \Delta n_z = 0.093 \times A \end{cases} \quad II \begin{cases} \Delta n_x = 1.26 \times A \\ \Delta n_y = 1.26 \times A \\ \Delta n_z = 1.26 \times A \end{cases} \quad \text{For the mean index change and the index modulation we get:}$$

$$\begin{cases} \langle \Delta n_x \rangle = 0.67 \times A \\ \langle \Delta n_y \rangle = 0.38 \times A \\ \langle \Delta n_z \rangle = 0.67 \times A \end{cases} \quad \begin{cases} \Delta n_x^{\text{mod}} = 0.59 \times A \\ \Delta n_y^{\text{mod}} = 0.89 \times A \\ \Delta n_z^{\text{mod}} = 0.59 \times A \end{cases}$$

Let us examine at once the magnitude of the calculated index change. Let us take the 285d-R3 grating with $A \approx 3 \cdot 10^{-3}$ for that purpose. The diffraction efficiency measurements have been made with in-plane polarization, so the relevant axis is x. We get $\Delta n_x^{\text{mod}} = 1.8 \cdot 10^{-3}$ which is close to the experimental value: $1.3 \cdot 10^{-3}$.

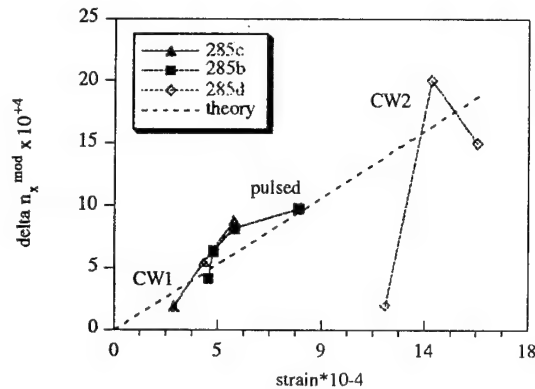


Fig. 3: Refractive index modulation versus strain. The former is either measured or from theory developed above, the latter is computed from the depth of the valley.

In fig. 3, Δn_{mod} is plotted against ϵ_m , the normalized depth of the valley. Experimental data are compared with the theoretical ones. It can be noticed that our model is able to explain the formation of a refractive index grating. Note that the theoretical curve cross the axis origin that it is not actually the case as we have to take into account some index modulation coming from the change of the absorption spectrum (Kramers-Kronig process).

On the other hand, from the model developed here, we can explain the appearance of birefringence between the axis of the grating and the perpendicular direction.

The birefringence is $\Delta n_y - \Delta n_{x,z} = -0.603A$ in region I (non - irradiated)
 $\Delta n_y - \Delta n_{x,z} = 0$ in region II (irradiated)

It is worth noticing that the birefringence is quite high in non-irradiated region and of the same magnitude that the mean index change. On contrast, assuming an isotropic densification, the birefringence is weak in the irradiated region. This is in good agreement with the experiment.

Conclusion

We have shown that the use of CW or pulsed irradiation for elaborating refractive index grating yields similar observations i.e. corrugations embedded in a valley. We have interpreted these surface effects by a model invoking densification and elastic strain. The implications on refractive index change is in good agreement with the experimental observations.

References

- 1-D. L. Williams, S. T. Davey, R. Kashyap, J. R. Armitage and B. J. Ainslie., Appl. Phys. Lett. **59** 7 (1991) 762.
- 2-E. Fertein, *Contribution à l'étude des mécanismes de la photoréfractivité dans des fibres optiques dopées à l'oxyde de germanium*. 1994, Lille/Flandres:
- 3-J. Albert, B. Malo, F. Bilodeau, D. C. Johnson, K. O. Hill, Y. Hibino and M. Kawachi, Optics Letters **19** 6 (1994) 387.
- 4-C. Fiori and R. A. B. Devine. *Ultraviolet irradiation induced compaction and photoetching in amorphous, thermal SiO₂*. in Mat. Res. Soc. Symp. 1986. MRS Pittsburg Pennsylvania.
- 5-L. B. Jeunhomme, *Single-mode fiber optics: Principles and applications*. Vol. Second Edition, Revised and expanded. 1990, Marcel Dekker, Inc., Marly le Roi, France.

CHARACTERISATION OF LONG PHASE MASKS FOR WRITING FIBRE BRAGG GRATINGS

François Ouellette, Peter A. Krug, Remco Pasman

Optical Fibre Technology Centre, University of Sydney, Bldg. GO5, Maze Crescent,
NSW 2006, Australia, tel. +61-2-335-0919, fax +61-2-335-0910

The use of phase masks for writing fibre Bragg gratings was first demonstrated by Anderson et al.[1]. These masks are etched in silica (for high transmission at the writing wavelength), and can be fabricated by either photolithographic techniques or electron beam lithography. It was demonstrated afterwards that long gratings can be written by scanning a narrow beam along a phase mask-fibre assembly [2]. The length of gratings is then limited by the length of the mask. Since very long gratings are useful for dispersion compensation, as well as very narrow reflection filters, there is a strong interest in the fabrication of very long phase masks. While in principle there is no limit to photolithographic techniques, the size of the optics required sets a practical limit, and masks greater than 5 cm diameter are prohibitively expensive. On the other hand, to date electron beam lithography can fabricate masks up to 14 cm in length. In this process, the pattern is divided into fields, and parallel lines are scanned with the electron beam in the photoresist across the width of the field. The process is then repeated at a new position until the whole mask is written. Sometimes, this process results in a phase jump between the fields of the grating, called a "stitching error". In this paper, we analyse the consequences of this stitching error, and present experimental characterization of gratings written with long phase masks fabricated by electron beam lithography.

A uniform grating written in the fibre with such a mask will have a periodic phase shift in it. This phase shift could either vary randomly from field to field, or have the same value. Fig.1 (a) shows the simulated reflection spectrum of an 8 cm long grating with random phase shifts every 1mm. The value of the phase shift is made to vary randomly between 0 and 1.2π . As can be seen, the resultant spectrum is very noisy, and much broader than what is expected from a perfectly uniform grating of the same length and strength.

If the phase shift has the same value for each field, there is an analytical expression for the resulting spectrum. The grating is then a "sampled grating" [3], and shows sidebands separated

by $\lambda^2/2nP$, where P is the period and n the refractive index. The strength of the sidebands can be determined by the Fourier decomposition of the sampling function. We get effective coupling coefficients κ_m of the m^{th} term of the Fourier series:

$$\kappa_m = \frac{\pi \delta n}{\Lambda n_o} \frac{2}{P} \left[\int_{-P/2}^{P/2} \exp \left[-2i \left(m\pi + \frac{\phi}{2} \right) \frac{z}{P} \right] dz \right]$$

where δn is the index modulation, Λ is the grating period, n_o is the core effective index, z is the axial coordinate and ϕ is the phase shift. The solution is:

$$\kappa_m = \frac{\pi \delta n}{\Lambda n_o} \text{sinc} \left[\pi m + \frac{\phi}{2} \right]$$

For $\phi=0$, only κ_0 has a non-zero value. For other values of the phase shift, however, multiple reflection peaks appear, whose relative strengths depend on the phase shift value. For $\phi=\pi$, the $m = 0$ and $m = -1$ peaks have equal strength. Fig. 1(b) shows simulated spectra of 8 cm long gratings with a phase shift every 1 mm, for three different values of phase shift (0.4π , 0.8π , π).

Fig. 2 shows the measured transmission spectrum of a 12 cm long uniform grating written with a phase mask, showing a central peak and two sidebands (further sidebands are not shown). The multiple reflection peaks are indicative of a periodic phase shift. It is clear that the phase shift has a constant value, and is not random. From the relative strengths of the central peak and two sidelobes, the phase shift is estimated to be $\phi=1.3\pi$. This means that the field stitching system in the electron beam machine used to fabricate the mask has only a systematic error.

To further characterise the gratings, we measured their local strengths using a recently developed external diffraction technique [4]. In this technique, a HeNe laser beam is incident on the side of the fibre at the Bragg angle, and is diffracted by the grating. The diffracted intensity is proportional to the square of the amplitude of the refractive index modulation. Thus the strength of a grating along its length can be mapped.

In our setup, the fibre was placed on a translation stage. The HeNe beam was focused at the appropriate Bragg angle, and the diffracted light was collected by a lens, and measured by a

silicon photodiode. Fig. 3(a) shows the diffracted intensity as a function of z (with a spatial resolution of about $10\text{ }\mu\text{m}$) for a 1 cm long uniformly exposed grating. The phase shifts are readily detectable by the "blips" in the diffracted light intensity, every 1 mm . There is, however, also a periodic amplitude modulation of the diffracted intensity. This modulation is of the order of 10% of the total diffracted light. Since the diffracted light is proportional to the square of the grating strength [4], the modulation of the grating amplitude is only about 5% and is too small to give significant sidelobes. To find out the origin of this modulation, we also measured the diffracted intensity as a function of z for the phase mask itself. The result is shown in Fig. 3(b). It is indeed found that the diffracted intensity varies periodically, however in a saw tooth fashion. The phase shifts are also apparent there. We hypothesise that the modulation results from a variation of electron beam intensity or focusing across each field.

In conclusion, we have characterized gratings written with long phase masks fabricated by electron beam lithography. We found that even though there is a stitching error, it is constant for all the fields, and results in reflection sidebands whose intensities depend on the value of the phase shift between the fields. The phase mask also shows a periodic variation in diffracted intensity, that transfers to the fibre grating, but does not contribute significantly to the creation of reflection sidebands.

Acknowledgments

The OFTC is a partner of the Australian Photonics Cooperative Research Centre.

References

- [1] D.Z. Anderson, V. Mizrahi, T. Erdogan, A.E. White, 'Production of in-fibre grating using a diffractive element', *Electron. Lett.* **29**, pp. 566-568 (1993).
- [2] J. Martin, and F. Ouellette, 'Novel writing technique of long and highly reflective in-fibre gratings', *Electron. Lett.* **30**, pp.811-812 (1994).
- [3] B. J. Eggleton, P. A. Krug, L. Poladian, F. Ouellette, 'Long periodic superstructure Bragg gratings in optical fibres', *Electron. Lett.* **30**, pp.1620-1622 (1994).
- [4] P. A. Krug, R. Ulrich, R. Stolte, 'Measurement of axial distribution of refractive index modulation along a fibre grating by Bragg reflection of an external probe beam', *OFC'95 proceedings*, paper W15, p. 136.

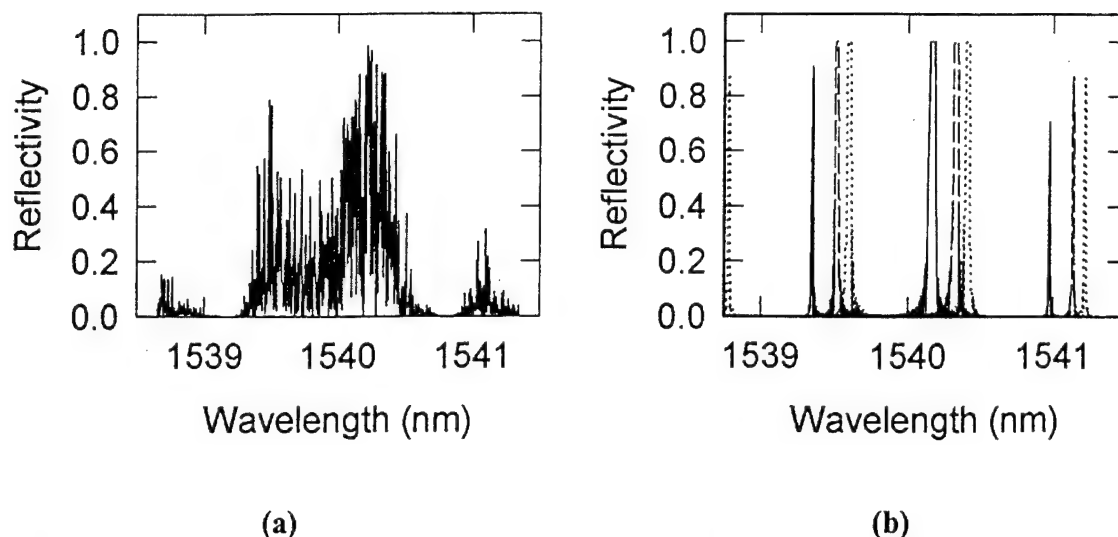


Fig.1: (a) Calculated reflection spectrum of an 8 cm long grating, with 1mm periodic phase shift having random value between 0 and 1.2π (b) Calculated reflection spectra for 8 cm long gratings with 1mm periodic phase shifts of values: 0.4π (solid), 0.8π (short dash), π (dotted).

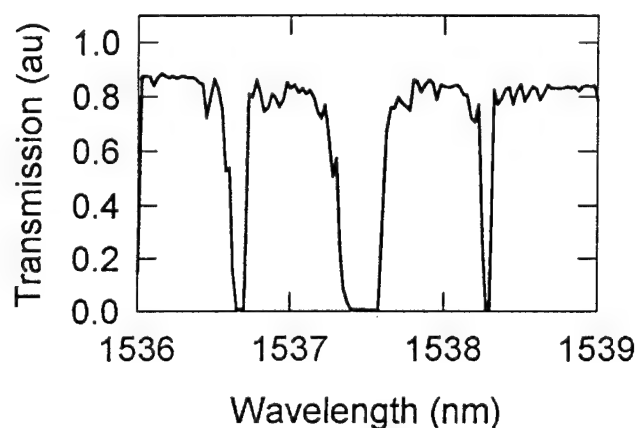


Fig.2 Experimental transmission spectrum of 12 cm long grating.

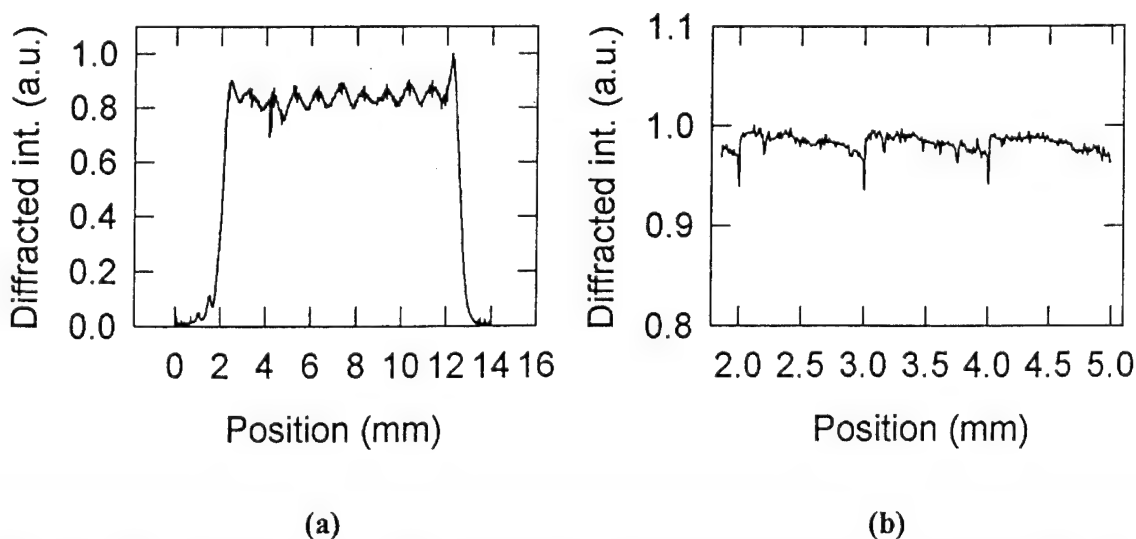


Fig.3 (a) Diffracted intensity vs position for a 1cm long uniformly exposed grating; (b) Diffracted intensity vs position for the phase mask used to write the grating.

All Optically Written Planar Germanosilicate Waveguide Gratings

D. Moss and F.Ouellette

Optical Fibre Technology Centre, University of Sydney, Sydney, NSW 2006, Australia
Telephone: +61-2-335-0936, Fax: +61-2-335-0910.

M. Faith, P. Leech, and P. Kemeny

Telecom Research Laboratories, Clayton 3168, Victoria, Australia

M. Ibsen, O. Leistiko, C.V.Poulsen

Mikroelektronik Centret, DTU, Bldg.345e, DK-2800 Lyngby, Denmark

J.D. Love and F. J. Ladouceur

Australian National University, Canberra, ACT, Australia

Photo-induced index changes in germanosilicate glass is a well known effect and has provided the basis for much recent activity on photoinduced refractive index gratings in fibres¹. Since then, very large ($>10^{-3}$) index changes in hydrogen loaded waveguide structures have been observed and used as the basis for patterning channel waveguides² and directional couplers³. Recently, we have demonstrated waveguide structures patterned in PECVD grown material without the aid of hydrogen loading^{4,5}, and in this paper we report the fabrication of all optically patterned buried waveguide grating structures, again without the aid of hydrogen loading. This demonstrates that the achievable index changes (without hydrogen loading) in this material is large enough to simultaneously support both waveguide and grating structures. The elimination of hydrogen loading is an important practical issue because, unlike fibres, planar waveguides need anomalously large overcladding layers to prevent rapid out diffusion of hydrogen during writing.

Figure 1 shows the layer structure, consisting of a 2.4 μm thick 10% Ge germanosilicate core and 6 μm thick silica cladding layers, grown on a silicon substrate. Details of the growth process are described elsewhere⁵. Waveguides were

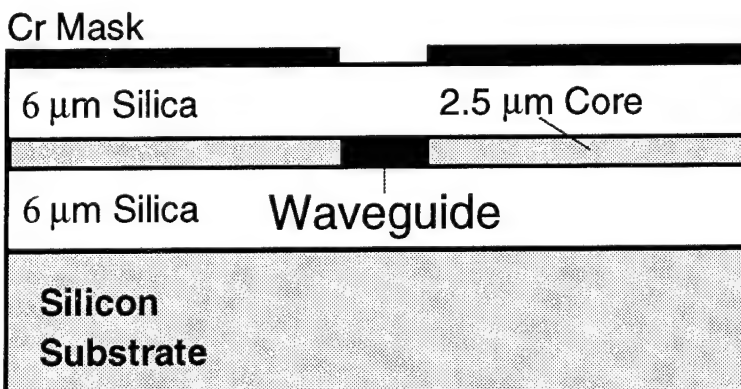


Figure 1. Trilayer structure. The core consists of 10% Ge doped silica.

patterned using 1000Å thick chrome masks having optical window widths of 3 to 7 microns. The samples were then exposed to light from an unfocused ArF excimer laser ($\lambda=193\text{nm}$) operating with pulsewidths of 10ns, pulse energies of 50mJ/pulse at 50Hz, and a total fluence of 3500 J/cm². The wafers were then cut, the end facets polished, and some had the chrome removed. In addition, a number of 2cm long waveguides were further exposed to 193nm light by cylindrically focusing the output of the ArF laser onto the waveguides through a 2cm long phase mask (beam spot size 0.5 x 2cm) designed to produce a grating at $\lambda=1557\text{nm}$. The total fluence in this case was comparable to the initial exposure of 3500J/cm²

Figure 2 shows the results of fibre-to-fibre loss and cleave-back measurements at $\lambda=1.3\mu\text{m}$, for samples with the chrome removed, as a function of waveguide width. We obtained residual losses of about 1.5 dB/facet for both TE and TM polarizations, and minimum coupling losses of about 0.3 dB/facet. The losses for samples with chrome still present were substantially higher, implying that perhaps some of the residual 1.5dB/cm loss could be due to leakage into the Si substrate, since the upper and lower cladding layers have the same thickness.

Figure 3 shows the optical transmission spectra for the grating structures, obtained by fibre-to-fibre coupling the amplified spontaneous emission output of an erbium doped fibre amplifier (EDFA) into the waveguide, and looking at the resulting transmission spectra on an optical spectrum analyser. The four spectra were taken from different waveguides along the UV beam waist, having different exposure levels, and show a uniform shift to longer wavelength of

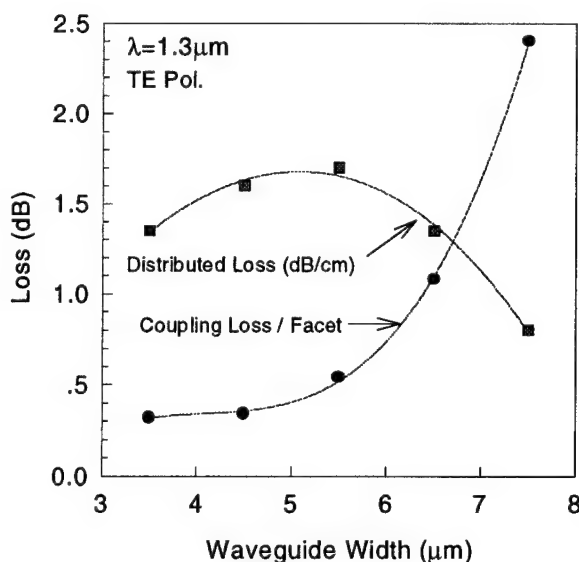


Figure 2. Coupling and propagation loss versus waveguide width for direct written buried waveguides with no grating structure.

2nm with increasing exposure. This is consistent with the waveguide effective index increasing with UV exposure. The shift of 2nm implies an effective index change of 2×10^{-3} , in addition to the original index change used to form the waveguide to begin with. Since both exposures were comparable, we estimate that the total induced index change (to pattern the waveguide and write the grating) is about 5×10^{-3} , taking into account the fact that the peak index change will be larger than the average effective index change, as well as possible saturation effects. This is a significant increase over the previously reported⁴ maximum induced index change in this material of 2.4×10^{-3} using $\lambda = 240\text{nm}$ light. The grating peaks for the waveguides with the highest exposure in Figure 3 are broadened substantially and we suggest that this is due to index saturation. Finally, we point out that the resolution of the spectrum analyser was 0.05nm, and is of the order of the grating width. This means that the transmission peak depths observed are limited by the spectrometer resolution.

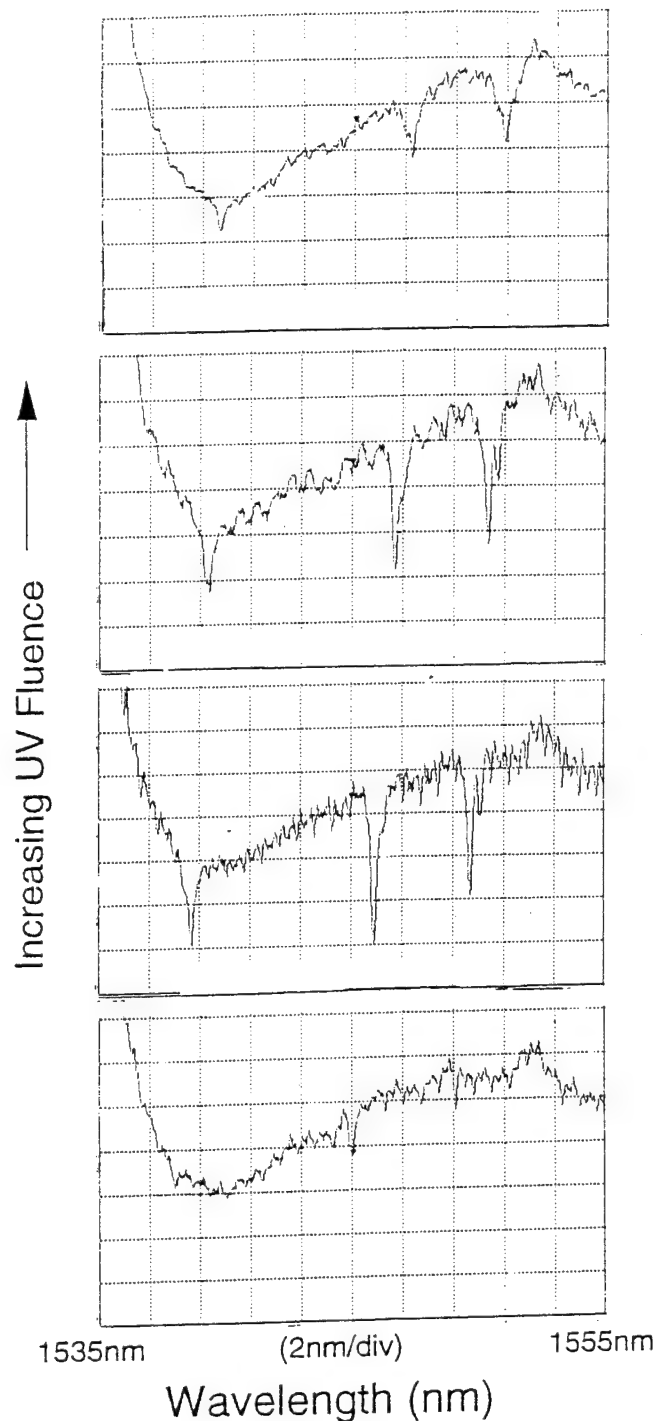


Figure 3. Unpolarized transmission spectra for various waveguide gratings (with chrome removed) as a function of increasing UV fluence.

It still remains, however, to explain the appearance of three separate peaks in the transmission spectra of Figure 3. While the presence of multiple peaks usually indicates multimode behaviour, calculations and observations of near field patterns both verify that the waveguide is single moded in both the vertical and lateral directions. We note that the overall peak separation of almost 12nm implies a modal index difference comparable to the core/cladding index step, ruling out any lateral effects. Although birefringence could possibly explain two of the three peaks, since the EDFA source we used was unpolarized, it seems unlikely to us since we observed the same spectra in samples with the chrome mask present, where the differential TE/TM losses were very large. Also, some peaks did display a barely resolvable double structure, which could be birefringence splitting. Our current work suggests that the multiple peaks might be due to cladding modes of the waveguide.

In conclusion, we report all optically written waveguide gratings in PECVD grown Ge doped silica trilayers, without the use of hydrogen loading. The shift in grating peaks suggests that the induced index changes in this material is substantially larger at 193nm than at 240nm.

Acknowledgments:

The Optical Fibre Technology Centre, the Australian National University, and Telstra Research Laboratories, are members of the Australian Photonics Cooperative Research Centre which supported this work. The permission of the Director, Telstra Research Laboratories to publish this paper is acknowledged. Assistance with the fabrication of waveguides was provided by F. Gigliotti and R. Tarran.

1. F.Ouellette, D.Gagnon, S.Larochelle and M.Poirer, SPIE proc. Intl. Wkshp. on Photoinduced Self-Organization Effects in Optical Fiber, **1516** Quebec, May 1991 p2.
2. V. Mizrahi, P.J.Lemaire, T.Erdogan, W.Reed, D.J. DiGiovanni, and R.M. Atkins, Applied Physics Letters **63** 1727 (1993).
3. G.D.Maxwell and B.J.Ainslie, Electronic Letters **31** 95 (1995).
4. M.Svalgaard, C.V.Poulsen, A.Bjarklev, and O.Poulsen, Electronic Letters **30** 1401 (1994).
5. D. Moss, M.Ibsen, F.Ouellette, P.Leech, M.Faith, P.Kemeny, O.Leistiko, and C.V.Poulsen, Australian Conf. on Optical Fibre Tech., Melbourne, Dec. 1994, p. 333.

Linear and nonlinear effects in deep gratings superstructures

N. G. R. Broderick, C. Martijn de Sterke and Benjamin J. Eggleton

School of Physics and Optical Fibre Technology Centre, University of Sydney, New South Wales 2006, Australia.

Phone: (612) 351 3241, Fax: (612) 660 2903, email: neilb@physics.usyd.edu.au

1. Introduction

Recent developments in fibre grating writing techniques have lead to the fabrication of gratings whose parameters vary periodically along the optical fibre.^{1,2} Such *grating superstructures* may have significant applications in fibre lasers, as they can be designed to have a reflection spectrum spanning the entire Erbium gain bandwidth². Grating superstructures have earlier been investigated in semiconductor geometries,³⁻⁵ and have also been studied theoretically.^{6,7} Much of the previous analysis is applicable to *weak* gratings superstructures; in contrast we present here a general approach which is suitable for *deep* grating superstructures as well. Such a general description is pertinent for grating superstructures in optical fibre,¹ where, although the refractive index modulation is small, the variations in the modulation can be large.

2. Coupled Mode Theory

The standard coupled mode equations used to describe nonlinear light propagation in a Bragg grating are:⁸

$$\begin{aligned} i\frac{\partial \mathcal{F}_+}{\partial x} + \frac{i}{v_g} \frac{\partial \mathcal{F}_+}{\partial t} + \kappa(x)\mathcal{F}_- + \delta(x)\mathcal{F}_+ + 2\Gamma|\mathcal{F}_-|^2\mathcal{F}_+ + \Gamma|\mathcal{F}_+|^2\mathcal{F}_+ &= 0, \\ -i\frac{\partial \mathcal{F}_-}{\partial x} + \frac{i}{v_g} \frac{\partial \mathcal{F}_-}{\partial t} + \kappa(x)\mathcal{F}_+ + \delta(x)\mathcal{F}_- + 2\Gamma|\mathcal{F}_+|^2\mathcal{F}_- + \Gamma|\mathcal{F}_-|^2\mathcal{F}_- &= 0, \end{aligned} \quad (1)$$

where \mathcal{F}_+ and \mathcal{F}_- are the slowly varying envelopes of the forward and backward modes, and v_g is the group velocity in the absence of the grating. The position-dependent strength of the grating is given by $\kappa(x)$, while the *self-chirp* $\delta(x)$ gives the position-dependent Bragg condition. We note that for gratings written in optical fibre, δ and κ are related by $\delta(x) = 2\kappa(x)$, and we assume this relation to be true here. The terms proportional to Γ represent the nonlinear phase modulation. Though Γ is in general also a function of position, we here take it to be constant for simplicity. We note however, that the procedure described below is applicable to either case.

In a grating superstructure with period Λ , the functions $\kappa(x)$, and thus also $\delta(x)$, are periodic with the same period. Since in general the coupled mode equations (1) cannot be solved exactly for finite gratings, it is informative to consider infinite periodic gratings. By analysing the photonic band diagrams of these structures, and locating the positions of the photonic band gaps the locations of the high-reflection regions for finite structures can be predicted.

In an infinite periodic structure the general harmonically varying solutions to the linear coupled mode equations [Eqs. (1)] can be written in terms of the *Bloch functions* $\varphi_{\ell,k}(x)$ of the structure:

$$\hat{\mathcal{F}}_{\ell,k}(x) = \left(e^{ikx} u_{\ell,k}(x) \right) e^{-i\Delta t} \equiv \varphi_{\ell,k}(x) e^{-i\Delta t}, \quad (2)$$

where $\hat{\mathcal{F}}$ and the Bloch functions are two-component column vectors with components \mathcal{F}_{\pm} . The function $u_{\ell,k}(x)$ is periodic with the superstructure; the integer ℓ labels the photonic bands, while k , crystal momentum, is taken to be in the first Brillouin zone, $-\pi/\Lambda < k \leq +\pi/\Lambda$.

A typical photonic band structure of a grating superstructure is shown in Fig. 1. In this example $\kappa(x) = 2\cos^2(2\pi x/\Lambda) \text{ cm}^{-1}$, with $\Lambda = 1 \text{ cm}$; the grating strength thus varies sinusoidally with position. Δ_u and Δ_l label the top and bottom of a typical gap. Note the photonic band gaps which have opened in the centre and at the edges of the Brillouin zone. These give rise to strongly reflective behavior in finite structures.

3. Meta-Coupled Mode Equations

It is well known that for each value of k , the associated Bloch functions labeled by an integer ℓ form a complete orthogonal set. In the linear limit, therefore, any field can be written as a superposition of these Bloch functions with constant coefficients. Here we deviate from this ideal situation in two ways. The first of these is that we assume that the spectrum of the field we are considering is concentrated near one of the photonic band gaps of the structure, and we thus limit the number of terms in the expansion. The second deviation is that we take the structure to be slightly nonlinear. These effects have the consequence that the expansion coefficients are no longer constant, but are slowly varying functions in space and time, and, as discussed in more detail below, they are thus *envelope functions*. Here we limit the number of terms in the expansion of the field to two; one each for the upper and lower edge of the band gap we are considering. We therefore use the following *ansatz* for the field (c.f. Eq. (2))

$$\mathcal{F}(x, t) = \left(f_u(x, t)\varphi_u(x) + f_l(x, t)\varphi_l(x) \right) e^{-i\Delta_0 t}, \quad (3)$$

where φ_u and φ_l are the Bloch functions at the top and bottom of the gap of interest respectively while f_u and f_l are the associated envelope functions. Finally, $\Delta_0 = (\Delta_u + \Delta_l)/2$ is the frequency at the centre of the band gap we are considering. Fig. 1 shows the position of Δ_u and Δ_l for a typical gap in the photonic band diagram.

Using a procedure very similar to that described by Salinas *et al*⁹ it can be shown that the superpositions

$$f_{\pm} = f_l \pm f_u \quad (4)$$

satisfy the *super coupled mode equations*

$$\begin{aligned} i\frac{\partial f_+}{\partial x} + \frac{i}{V}\frac{\partial f_+}{\partial t} + \tilde{\kappa}f_- + 2\tilde{\Gamma}|f_-|^2f_+ + \tilde{\Gamma}|f_+|^2f_+ \\ + \Gamma_1(|f_-|^2 + |f_+|^2)f_- + \Gamma_1(f_+f_-^* + f_-f_+^*)f_+ + \Gamma_2f_-^2f_+^* = 0, \\ -i\frac{\partial f_-}{\partial x} + \frac{i}{V}\frac{\partial f_-}{\partial t} + \tilde{\kappa}f_+ + 2\tilde{\Gamma}|f_+|^2f_- + \tilde{\Gamma}|f_-|^2f_- \\ + \Gamma_1(|f_-|^2 + |f_+|^2)f_+ + \Gamma_1(f_+f_-^* + f_-f_+^*)f_- + \Gamma_2f_+^2f_-^* = 0, \end{aligned} \quad (5)$$

which are very similar to the original coupled mode equations (1). Note however that, in contrast to Eqs. (1), for a periodic superstructure the grating strength $\tilde{\kappa}$ is *constant*, and that the self-chirp terms in δ are totally absent, as they reside now in the details of the Bloch functions. However, the nonlinear coefficients in the super coupled mode equations (5) appear to be more complicated than in Eqs. (1), though, as we discuss in Section 5, this poses no significant problem.

We note that in general the coefficients in Eqs. (5) depend on the details of the Bloch functions of the superstructure. In particular, the coefficients $\tilde{\Gamma}$ and Γ_i are linear combinations of nonlinear overlap integrals of the various Bloch functions and the nonlinearity. However, when the superstructure is shallow, $\tilde{\kappa}$ reduces to one of the Fourier components of $\kappa(x)$, and $\Gamma_1 = \Gamma_2 = 0$, though in general this cannot be assumed to be true¹⁰. The three new nonlinear terms have been grouped so that each term conserves energy. The first new term describes a nonlinear change to the grating strength, while the second term gives rise to a shift in the band gap. The last term is a phase conjugate term.

4. Implementation of the linear super coupled mode equations

Here we consider the solutions to linearized super coupled mode equations (5). Unlike the original coupled mode equations (1), the new equations can be solved trivially in terms of exponential functions. However the relationship between the super envelopes and the actual fields inside the grating is complicated since it involves the Bloch functions of the superstructure [Eq. (3)]. In addition the natural boundary conditions involve the original envelopes themselves and not the super envelopes. Hence to implement the boundary conditions it is necessary to know the Bloch functions. For a uniform grating superstructure the approximate solution to the coupled mode equations using this approach can symbolically be written as:

$$\begin{pmatrix} \mathcal{F}_+(x) \\ \mathcal{F}_-(x) \end{pmatrix} = U(x) T U(0)^{-1} \begin{pmatrix} \mathcal{F}_+(0) \\ \mathcal{F}_-(0) \end{pmatrix}. \quad (6)$$

Where T is the transfer matrix for the super coupled mode equations (5) and $U(x)$ is a 2×2 unitary matrix which incorporates the effect of the Bloch functions at a position x . Once the Bloch functions are known the matrix $U(x)$ can be found by inverting Eqs. (4) and Eqs. (3) to express the fields \mathcal{F}_\pm in terms of f_+ and f_- .

Fig. 2 shows the exact and approximate reflection spectra near the gap centred at $\Delta = 1.4 \text{ cm}^{-1}$ in Fig. 1 for a 10 cm long grating with $\kappa(x) = 2 \cos^2(2\pi x) \text{ cm}^{-1}$. The solid line shows the exact reflection spectrum obtained by integrating the full coupled mode equations, while the dotted line shows the approximate result. The dashed line shows the approximate reflection if we assumed that the grating was shallow¹⁰. The asymmetry in the approximate spectrum is due entirely to the Bloch functions as the transfer matrix T is symmetric w.r.t. the centre of the gap.

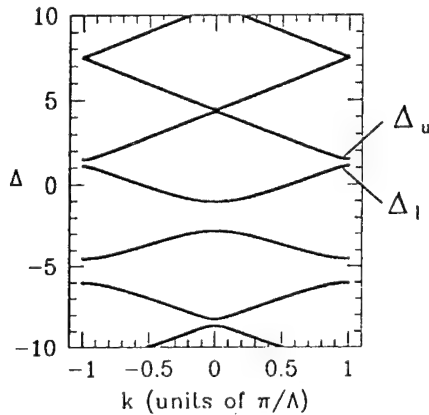


Fig. 1. The photonic band diagram for a deep cosine squared grating with $\kappa(x) = 2 \cos^2(2\pi x) \text{ cm}^{-1}$. The wavenumber k has units of π/Λ .

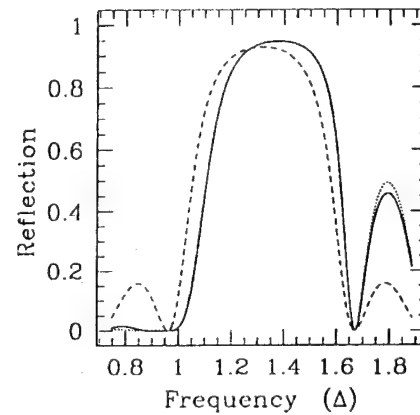


Fig. 2. Shows the reflection spectrum for the grating superstructure described in Fig. 1 near one of the gaps. The solid line is the exact result and the dotted line the approximate one. The dashed line shows the results for a weak superstructure.

5. Nonlinear Meta-Gratings

Numerical investigations of nonlinear propagation in grating superstructures using Eqs. (1) have indicated that nonlinear pulses can move coherently through the grating superstructure at frequencies inside a band gap of the structure. In the case of a uniform grating such *gap soliton* solutions are well known⁸, but for a super grating they have not previously been reported. However, we have not been able to solve the original nonlinear coupled mode equations (1) for a nonlinear grating superstructure.

However we have derived evolution equations [Eqs. (5)] for the envelopes of the Bloch functions near a photonic band gap. Compared to the original coupled mode equations (1) Eqs. (5) appear more complicated as they have more nonlinear terms. However these new equations have a constant linear coupling term and no chirp. For weak grating superstructures these new terms are insignificant and the new equations are then identical to the old equations. The importance of these new equations (5) is that solitary wave solutions are known to exist and thus the nonlinear pulses we have observed in these grating superstructures are expected to be gap soliton solutions of the super coupled mode equations (5). The running wave solutions can be found using a generalisation of a procedure outlined by Feng and Kneubühl.¹¹ Fig. 2 shows the intensity profile for such a stationary gap soliton with centre frequency $\Delta \approx -5.26$ in the same units as in Fig. 1. for an infinite grating superstructure with linear parameters as in Fig. 1, and with $\Gamma = 1$. The envelope of the intensity profile is a solution to the super coupled mode equations (5) with vanishing velocity and with $\tilde{\Gamma} = 0.521 \Gamma_1 = -2.7 \times 10^{-2}$, $\Gamma_2 = -5.9 \times 10^{-3}$.

The stability of these new gap solitons has not yet been fully investigated. However our numerical simulations suggest that for a large range of parameters these solitons can propagate over distances large compared to their width without significantly altering their shape. These gap solitons can be created at an interface by an incident Gaussian pulse and propagate over distances longer than the length of most currently feasible gratings. Hence these gap solitons could be observed in future experiments. In

addition these gap solitons contain energy at spatial frequencies corresponding to the other band gaps of the grating unlike conventional solitons which have a frequency range centered round a single spatial frequency.

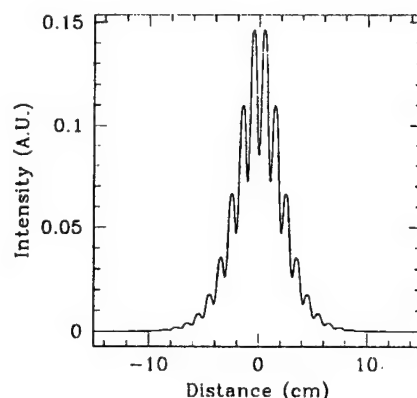


Fig. 3. Intensity profile for a super gap soliton. The intensity is normalised such that $\Gamma = 1$ while the distance is measured in cm.

6. Conclusion

We have presented an overview of linear and nonlinear effects in *deep* grating superstructures. In order to analyse such structures it is necessary to consider slowly varying envelopes of the Bloch functions. This analysis leads to new equations which are formally identical to the old equations and thus the knowledge which we have developed for gratings can be applied to grating superstructures. The advantage of the new equations is that the coefficients are constant and so the equations can be solved exactly instead of resorting to lengthly computer simulations for the original equations.

We have also found soliton solutions to the super coupled mode equations (5). These correspond to the pulses appearing in our numerical simulations of the full nonlinear coupled mode equations (1); they represent a new class of nonlinear solutions to the original nonlinear coupled mode equations (1). These solutions are characterised by the fact that they contain energy at a variety of spatial frequencies, unlike most ordinary solitons where the energy is concentrated around a single spatial frequency.

-
1. B.J. Eggleton *et al*, Electron. Lett. **30**, 1621-1622 (1994).
 2. M. Ibsen *et al* Electron. Lett. **31**, 37-38 (1995).
 3. D. C. V. Jayaraman and L. Coldren, Appl. Phys. Lett **60**, 2321 (1992).
 4. D. C. V. Jayaraman and L. Coldren, IEEE J. Quantum Electron. **29**, 1824 (1993).
 5. Y. Tohmori *et al*, IEEE J. Quantum Electron. **29**, 1817-1823 (1993).
 6. P. St. J. Russell, Phys. Rev. Lett. **56**, 596-599 (1986).
 7. P. St. J. Russell, J. Appl. Phys. **59**, 3344-3355 (1986).
 8. C. M. de Sterke and J. E. Sipe, in *Progress in Optics*, edited by E. Wolf (North Holland, Amsterdam, 1994), Vol. XXXIII, Chap. III Gap Solitons, pp. 203-260.
 9. D. G. Salinas *et al* Optics Comm. **11**, 105 (1994).
 10. C.M. de Sterke and N.G.R. Broderick, submitted to the "Photosensitivity and Quadratic Nonlinearity in Glass Waveguides: Fundamentals and Applications" Topical Meeting.
 11. J. Feng and F. K. Kneubühl, IEEE J. Quantum Electron. **29** 590-597 (1993)

Characterisation of UV-induced Birefringence in Optical Fibre Rocking Filters

D.C. Psaila*, C.M. de Sterke* and F. Ouellette†

* *School of Physics and Optical Fibre Technology Centre, University of Sydney, NSW, 2006, Australia.*

† *Optical Fibre Technology Centre, University of Sydney, NSW 2006, Australia.*

Introduction

In single-mode birefringent fibre, a mode launched along a principal polarisation axis maintains that polarisation state. Optical fibre rocking filters (or polarisation mode converters) are structures that rotate the polarisation state of the optical field. To achieve this, the fibre's principal axes are periodically rocked through a small angle θ by either oscillating the preform during the draw process [1] or by using UV light to externally irradiate the fibre periodically [2]. Since the birefringence beat length is wavelength dependent, there is a resonant wavelength at which the beat length is equal to the rocking filter twisting period. At this wavelength there is complete coupling from one polarisation mode to the other, while at other wavelengths, there is only partial coupling. At resonance, the state of polarisation is rotated by an angle 2θ per period and thus for complete power transfer, $\pi/(4\theta)$ coupling steps are required.

In this paper, we describe the results of experiments that quantitatively determine the dependence of rocking filter growth and the rocking angle θ , with UV beam exposure. This is investigated in both hydrogen loaded and unhydrogenated Ge-doped birefringent optical fibres. We also show the dependence of rocking filter growth in hydrogenated fibre on the UV writing beam's energy.

Experimental Technique

The rocking filters in this experiment were written by an external point-by-point technique that differs from that described in Ref. [2] in that the fibre is held fixed while the UV beam is traversed along the fibre via a steering mirror mounted onto a long-travel (1200 mm) precision translation stage controlled by a personal computer. The incident UV light was passed through a narrow slit (~ 0.5 mm) situated 2 cm above the fibre and traversed along the fibre at a velocity of 2.4 mm/s. The growth of the rocking filter was monitored throughout the writing process by launching white-light polarised along one of the birefringent axes of the fibre and then monitoring the signal after passing through a second polariser (oriented at 90° to the first) at the output of the fibre with an optical spectrum analyser (Fig. 1).

The UV source used in these experiments was a frequency-doubled excimer-pumped dye laser (Lambda Physik) operating at 240 nm with a repetition rate set to 10 Hz. The unfocussed beam energy density was attenuated to approximately 0.2 mJ and focussed to a spot size of $0.5 \text{ mm} \times 1 \text{ mm}$. The polarisation of the beam was set to be perpendicular to the fibre axis. The UV beam was incident on the fibre at 45° to the birefringent principal axes as this is known to maximise the induced birefringence and hence the rocking angle, θ [2,3].

The fibre consisted of a high NA (0.254) Ge-doped elliptical core fibre with core dimensions of $2.8 \times 9.8 \text{ } \mu\text{m}$ and a beat length $L_b = 14.4 \text{ mm}$ at $\lambda = 1257 \text{ nm}$ and thus a

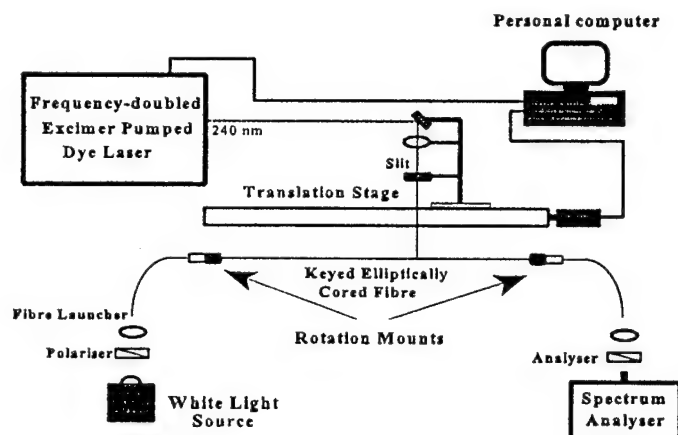


Figure 1. Schematic diagram of the experimental set-up.

birefringence of $B = 8.7 \times 10^{-5}$. The fibre was "keyed" by machining a small flat surface onto the preform before it was drawn. This surface is used to determine the orientation of the birefringent axes of the fibre and to ensure that the fibre was not twisted when mounted on to the rotatable fibre chucks. For the purpose of these experiments, the fibre was treated in one of three ways:

- A) hydrogenated for 24 hours at 100°C at 100 atmospheres;
- B) after hydrogen loading, heated at high temperature for a few minutes to induce reactions with the core and then left to stand at 100°C for 24 hours to drive off any unreacted hydrogen;
- C) left unhydrogenated.

To obtain the results presented in this paper, a short rocking filter consisting of twenty coupling steps was written into the fibre with a burst of thirty laser shots per step. The amount of optical signal coupled into the orthogonal polarisation and the photoinduced loss was then recorded. This procedure then repeated over the same twenty steps. The rocking angle measured in degrees was then determined by the relation $\theta = \alpha(90^\circ/2N)$ where α is the measured coupling ratio between polarisation states and N is the number of coupling steps.

Experimental Results

The results of the measured UV-induced rocking filter growth for the fibres treated as above are shown in Fig. 2. It is clear that loading the fibre with molecular hydrogen substantially

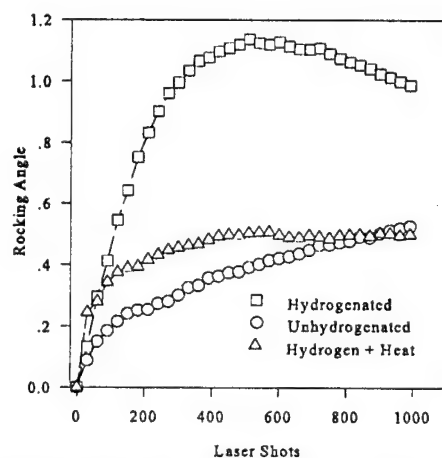


Figure 2. Diagram showing the change of rocking angle in degrees versus the number of laser shots per step for a UV energy of 0.2 mJ.

increases the strength of rocking filters written with this fibre, however, increasing the number of laser shots results in the eventual erasure of the rocking filter. No appreciable difference was noted with fibre B. We suspect that this may be due to incomplete reactions with the hydrogen in the core.

The photoinduced loss for the three fibres was also measured and found to be a minimum for the unhydrogenated fibre (<0.0025 dB/cm at 1257 nm) and reached a maximum for the heated/hydrogenated fibre (0.025 dB/cm at 1275 nm).

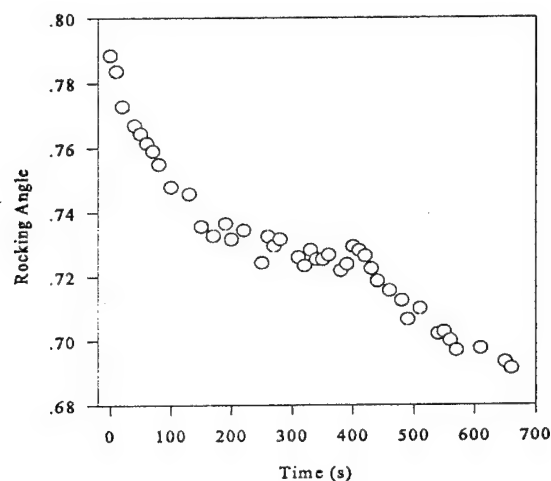


Figure 3. Decay of the UV induced birefringence displayed as a rocking angle for an unhydrogenated fibre.

We have also recorded a decay in the birefringence (rocking angle) to a steady state value after the UV beam is switched off (Fig. 3) similar to that reported by Erdogan *et. al.*[3] for circular-cored fibres during Bragg grating formation. The reason for this decay is not clearly understood but it appears to be related to the relaxation of the UV induced change in refractive index of the fibre.

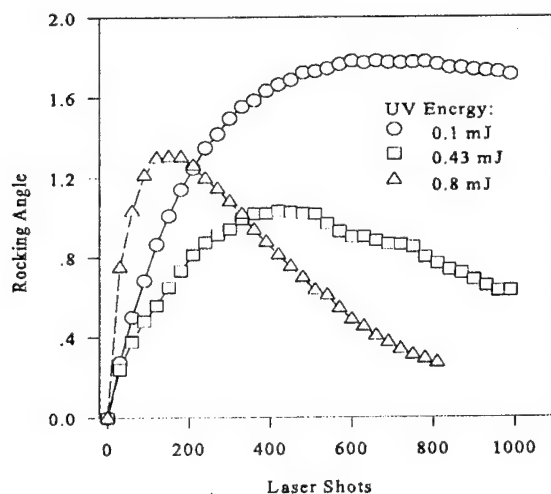


Figure 4. Diagram showing rocking angle versus laser shots per step at various UV beam energies for a hydrogenated fibre.

In order to maximise the rocking angle in our rocking filters, we further investigated the effects of the UV writing energy on hydrogen loaded fibres. The results reported in Fig. 4 indicate that at high pulse energies, the rocking filter strength quickly reaches a maximum but begins to decay with further exposure. We have found that applying more laser shots will completely erase the rocking filter. In fact, writing rocking filters with low pulse energies (of the order of 0.1 mJ) appears to be the most efficient method with a maximum measured rocking angle of 1.78° . This corresponds to a value of 3.36×10^{-6} for the off-diagonal terms in the refractive index tensor. The rocking angle can be effectively doubled if alternate sections of the fibre's core are illuminated from opposite sides [4]. Subsequently, we have written very short rocking filters with 100% coupling efficiency in as a few as 13 coupling steps (Fig. 5).

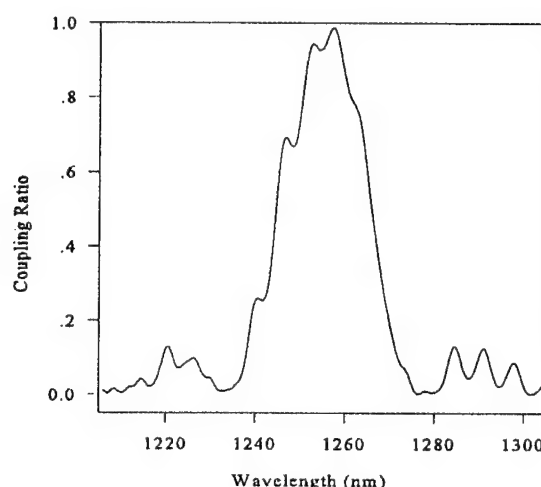


Figure 5. Polarisation coupling spectrum for a rocking filter written in hydrogenated fibre with only 13 coupling steps.

Conclusion

We have presented the results of a systematic study into the growth dynamics of optical fibre rocking filters. We have shown that by using fibres loaded with molecular hydrogen that the coupling efficiency can be improved by more than a factor of three from our previous results. We have further shown that at high UV energies, rocking filters may be erased as they are written and that an optimum UV beam energy exists for writing rocking filters. These results should prove useful in designing components that rely on UV written rocking filters.

References

1. R.H. Stolen, A. Ashkin, W. Pleibel and J.M Dziedzic, *Opt. Lett.*, **9**, 300, (1984).
2. K.O. Hill, F. Bilodeau, B. Malo and D.C. Johnson, *Electron. Lett.*, **27**, 1548, (1991).
3. T. Erdogan and V. Mizrahi, *J. Opt. Soc. Am. B*, **11**, 2100, (1994).
4. D.C. Psaila, C. Martijn de Sterke and F. Ouellette, Submitted to *Electron. Lett.* (1995).

In-Fiber Transmission Filters with Broad Stopbands using Chirped Bragg Gratings

L. Zhang, K. Sugden, J. A. R. Williams and I. Bennion
Department of Electronic Engineering & Applied Physics,
Aston University, Birmingham, B4 7ET, UK
Tel: 0121 359 3621 x 4961. Fax: 0121 359 0156

D. C. J. Reid and C. M. Ragdale
GEC Marconi Material Technology Limited,
Caswell, Towcester, Northampton, NN12 8EQ, UK

Many optical fiber applications, such as wavelength division multiplexing/ demultiplexing, frequency-guiding in soliton systems, and the filtering out of spontaneous emission noise from fiber amplifiers require transmission band-pass filters with a wide range of finesses and free spectral ranges. Bragg gratings written directly into the optical fiber by direct UV exposure [1] show particular promise in this area and there have been many reported techniques to date proposed for fabricating fiber grating transmission filters (e.g. [2–7]). Most of these techniques however do not allow independent arbitrary selection of the pass and stop band characteristics thus limiting their usefulness for many applications. While the recently reported wide stop band transmission filters based on resonant chirped grating Moiré and Fabry-Perot designs [2,3] do allow a large degree of control of the pass and stop band characteristics, in practice the parameters of the filter including transmissivity, transmission wavelength and linewidth are difficult to tailor during fabrication. Where multiple pass bands are required the number of passbands and the free spectral range are inherently fixed by the phase shift between the two interacting gratings.

The technique of performing post-fabrication UV exposure on standard in-fiber gratings was first described in reference [4]. It involves using a focused UV beam exposure to raise the refractive index at a selected region in an existing in-fiber grating. In a linear (unchirped) fiber grating this produces a Fabry-Perot resonator inside the grating giving rise to the pass-band characteristic. A high finesse transmission filter with a linewidth as narrow as 100MHz has been produced in this way [4]. However in unchirped gratings the stop-band width is limited (for high reflectivity's) to less than a nm limiting the usefulness of such filters in many applications. Another problem with resonant type in-fiber transmission filters is that the wavelength of the passband depends critically on the optical length of the resonator. Therefore very precise control is required during fabrication to obtain a specified wavelength, and the filters are sensitive to environmental changes which may change this effective optical length.

In this paper we present a new technique for fabricating efficient and selective in-fiber transmission filters using a secondary UV exposure to modify the stop band of broadly chirped fiber gratings. In contrast to the previous work the passband does not arise from a resonant Fabry-Perot effect but instead from the removal or modification of that part of the chirped grating which is resonant at a specific wavelength. Therefore the wavelength at which the passband is opened depends on which physical part of the original grating is reexposed and not on the precise exposure conditions. The transmission linewidth is determined by the spot size of the post-exposing UV beam and the grating chirp gradient. Multiple independent passbands are easily obtained by exposing several different parts of the original grating.

The chirped fiber gratings used in this work were manufactured using a two-beam UV holographic exposure technique with dissimilar wavefront curvatures in the two beams providing a linear chirp in the period along the grating length [8]. Both standard communication and B/Ge co-doped fiber were used, and each was hydrogen-soaked at 150 atmospheres pressure at room temperature for a week. The maximum reflection bandwidths achieved for chirped gratings were, in hydrogenated standard communication fiber $\sim 15\text{nm}$ with 95% reflectivity, and in hydrogenated B/Ge fiber $\sim 140\text{nm}$ with $\sim 80\%$ reflectivity.

Figure 1 shows the principle of this new technique. In this instance the original chirped grating with $\approx 100\%$ reflectivity and 11.3nm bandwidth was fabricated in a hydrogenated B/Ge co-doped fiber. A UV beam was then focused on the center of the grating using a cylindrical UV lens of focal length of 20cm . The growth of the passband was monitored *in situ* and the exposure halted when it stopped. This gave rise to a 0.185nm narrow passband with a peak transmissivity of $\sim 70\%$ after an exposure of 3 minutes duration. The finesse achieved, here defined as the ratio of passband to stopband width, was 60.

Figure 2 shows the reflection and transmission spectra for a single 1.2nm passband filter at 1546nm fabricated in a 50nm stopband broadly chirped fiber designed to cover the fluorescence spectrum of Er-doped fiber. The stop band reflectivity is $\sim 90\%$ and the passband transmissivity is $\sim 60\%$. It is apparent that there are some oscillations arising in the stop-band response of the device. These are also observed in numerical simulations of these devices and arise from interference caused by some residual overlap in the reflection spectra of the two halves of the grating either side of the gap. They are worse for gratings with a larger chirp and wider stopband, and therefore can be minimized if the stopband is not made too wide. To minimize this effect while still maintaining a broad stop band the grating concatenation technique [2] was applied. Figure 3 shows the transmission spectrum of a concatenated fiber-grating bandpass filter. The pass band of 0.16nm bandwidth was written into a 11nm reflection bandwidth chirped grating fabricated in hydrogenated B/Ge co-doped fiber. Two

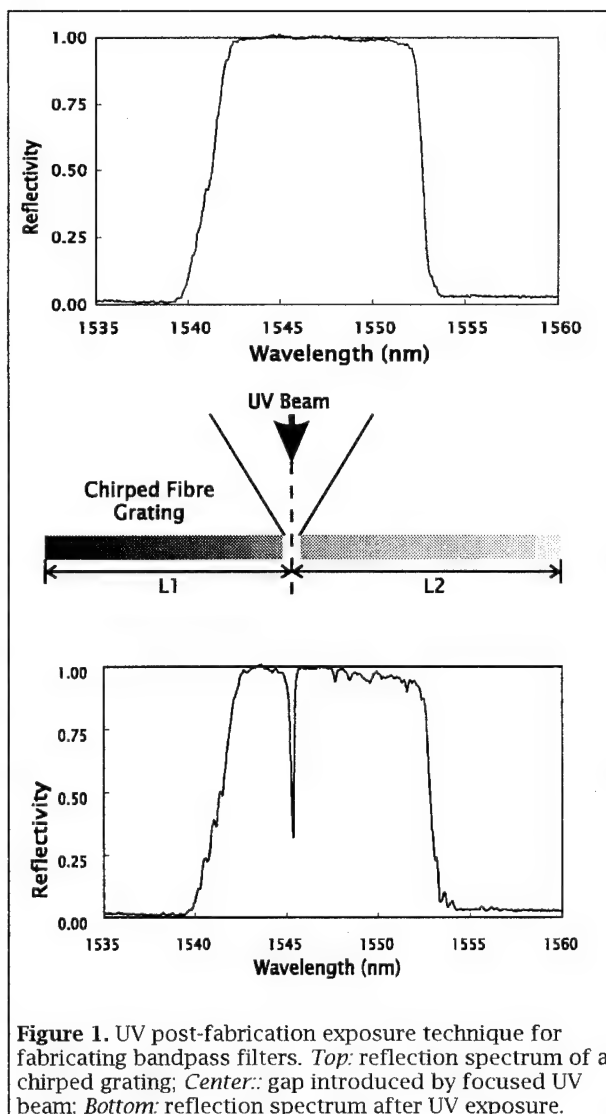


Figure 1. UV post-fabrication exposure technique for fabricating bandpass filters. *Top:* reflection spectrum of a chirped grating; *Center:* gap introduced by focused UV beam; *Bottom:* reflection spectrum after UV exposure.

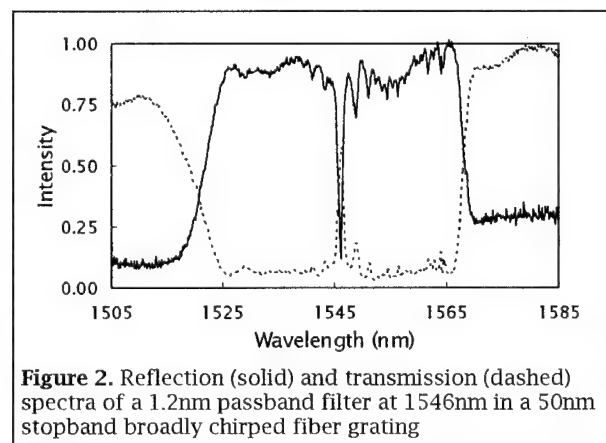


Figure 2. Reflection (solid) and transmission (dashed) spectra of a 1.2nm passband filter at 1546nm in a 50nm stopband broadly chirped fiber grating

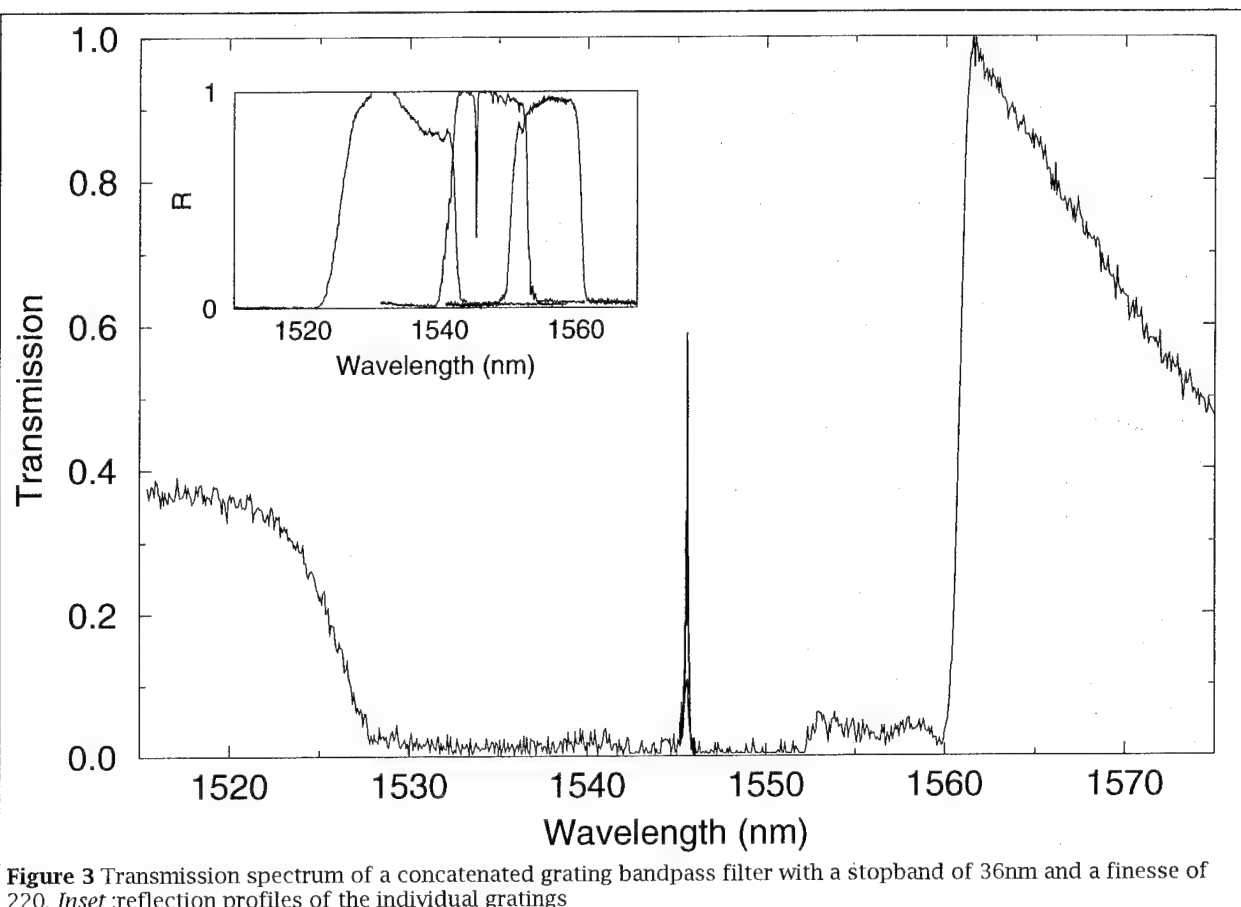


Figure 3 Transmission spectrum of a concatenated grating bandpass filter with a stopband of 36nm and a finesse of 220. *Inset* reflection profiles of the individual gratings

additional chirped gratings with reflection profiles on each side of but overlapping that of the initial grating were concatenated with it. The total stopband was $\sim 35\text{nm}$ giving an effective finesse for the whole device of 220, the largest achieved for a multi-nanometer stopband filter to date. Concatenation of chirped stopband filters with other bandpass filter types having a narrower stopband would not so easily produce this performance enhancement due to residual overlap in the reflection spectra of the edge reject filters with the central transmission band.

To demonstrate the ease with which independent passband could be fabricated inside of a single chirped grating a multi-passband filter with four channels evenly spaced inside a 50nm stopband covering the Er doped fiber fluorescence was fabricated. Figure 4 shows the transmission spectrum of this device. The four channels were written at selected positions along the fiber grating by simply translating the grating along the direction perpendicular to the UV writing beam successively between four equal duration ($\sim 2.5\text{min}$) UV exposures.

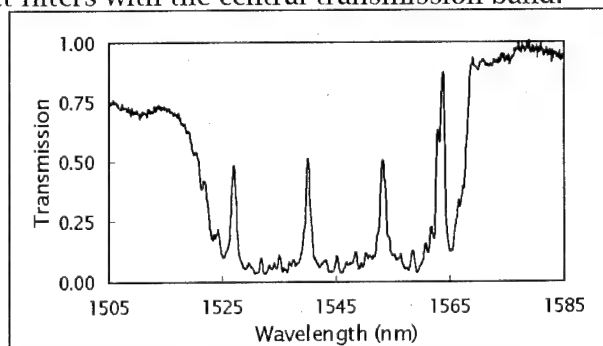


Figure 4 A four channel multiple passband filter

Characterization of the growth of the grating passband with UV exposure time has been carried out. The transmissivity of the passband was measured every 30 seconds while the focused UV gap writing beam was applied to a chirped grating which had a 15 nm stop band. Figure 5 shows these results. The growth rate slows down during the exposure and, in this case, saturates with a maximum transmissivity of $\sim 60\%$. The maximum transmissivity typically

achieved is about 80%, and it is not currently fully understood why higher transmissivities are not obtained. In these band-pass devices the intensity and spot size of the UV writing beam and the fiber photosensitivity are clearly important parameters. Further systematic investigation of the limiting parameters is currently underway. The short wavelength loss caused by coupling of the light from the fiber core to non-guiding modes clearly plays a limiting role on maximum transmissivity [9]. This effect is most detrimental for broad bandwidth chirped gratings and low numerical aperture fibers. Concatenation of gratings allows the use of chirped gratings with smaller bandwidths and thus allows a significant reduction of the short wavelength loss.

In conclusion then we have used a new technique, employing a secondary UV exposure to modify the stop band of broadly chirped fiber gratings, to fabricate practical effective in-fiber transmission filters. We have demonstrated a single 1.2nm bandwidth bandpass filter with a 50nm stopband covering the whole Er-doped fiber fluorescence spectrum. We have also demonstrated that using concatenation allows us to overcome some of the limitations and problems of using individual filters made in this way and has allowed the fabrication of a single 0.16nm linewidth transmission filter within a 36nm stopband. Multiple independent passband filters have also been demonstrated with this technique.

Compared with resonant Fabry-Perot filters this new approach allows the fabrication of high finesse transmission filters with a broad stop band and is more practical in terms of controlling precisely the transmission wavelength and linewidth. It also allows the arbitrary positioning of one or more passbands inside the chirped grating stopband. These new filters have a sufficiently wide stopband that they can easily be concatenated with other chirped fiber gratings to improve the overall filter performance.

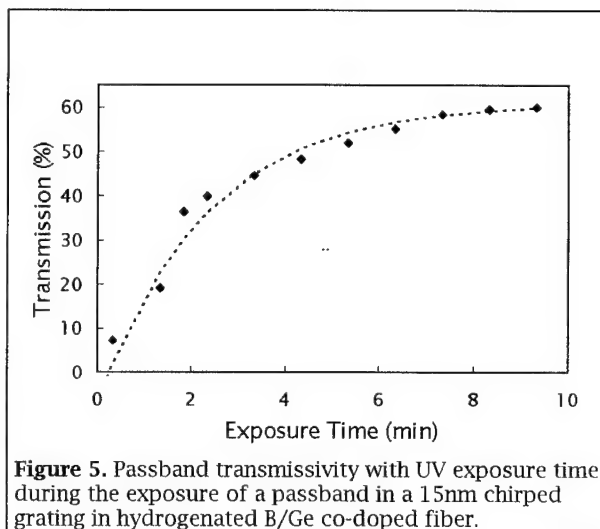


Figure 5. Passband transmissivity with UV exposure time during the exposure of a passband in a 15nm chirped grating in hydrogenated B/Ge co-doped fiber.

- 1 G.Meltz, W. W. Morey, and W. H. Glenn. *Opt. Lett.*, 14(15):823—825, August 1989.
- 2 L. Zhang, K. Sugden, I. Bennion, and A. Moloney. *Electron. Lett.*, 31(6):477—479, March 1995.
- 3 G.Town, C.Sugden, J.A.R. Williams, S.Poole, and I.Bennion. *IEEE Photonics Tech. Lett.*, 7(1), January 1995.
- 4 J. Canning and M. G. Sceats. *Electron. Lett.*, 30(16):1344—1345, August 1994.
- 5 F. Bilodeau, K. O. Hill, B. Malo, D. C. Johnson, and J. Albert. *IEEE Photonics Tech. Lett.*, 6(1):80—82, January 1994.
- 6 R. Kashyap, P. F. McKee, and D. Armes. *Electron. Lett.*, 30(23):1977—1979, November 1994.
- 7 W. W. Morey, T. J. Bailey, W. H. Glenn, and G. Meltz. In *OFC '92 Technical Digest*, volume 5, page 96, Washington D.C., February 1992.
- 8 M.C. Farries, K.Sugden, D.C.J. Reid, I.Bennion, A.Molony, and M.J. Goodwin. *Electron. Lett.*, 30(11):891—892, 1994.
- 9 Victor Mizrahi and J.E. Sipe. *J. Lightwave Technol.*, 11(10):1513—1517, October 1993.

Dissimilar wavefront technique for linear and quadratic chirps.

Kate Sugden, Lin Zhang, John Williams, Ian Bennion

*Electronic Engineering and Applied Physics, Aston University, Aston Triangle,
Birmingham B4 7ET, UK. Tel: 44 121 359 3611, fax: 44 121 359 0156*

In this paper, we discuss and characterise two variations on the dissimilar wavefront technique¹ that give near-linearly and quadratically chirped gratings. This technique is advantageous over others that have been proposed for the fabrication of chirped gratings because of its simplicity and flexibility. A high level of bandwidth control is demonstrated for gratings of bandwidths in the range of 0.5-23nm.

First order dispersion compensation and pulse compression require linearly chirped gratings of narrow bandwidth and linear chirp². Both of these applications have been demonstrated with gratings fabricated by the dissimilar wavefront technique³, and by phase mask imprinting⁴. Although beam quality and alignment are both critical factors in the reproducibility of gratings when using the dissimilar wavefronts, the technique offers certain advantages over phase masks. Flexibility, cost and a fast turnaround time for new one-off orders make this method attractive to establishments that are either without phase mask fabrication facilities or where a large number of widely varying gratings are required for research purposes. The technique described here enables a vast range of narrow to wide bandwidth gratings to be made with high precision.

Phase mask fabrication offers the advantages of stability and reproducibility and has become the method of choice for grating writing at a known Bragg wavelength. However, as we have previously described and demonstrate further here, free-space two-beam interference is particularly useful for its flexibility at the exploratory stages of device assessment, and permits complex, often multiply-exposed structures to be produced with relative ease^{5,6}.

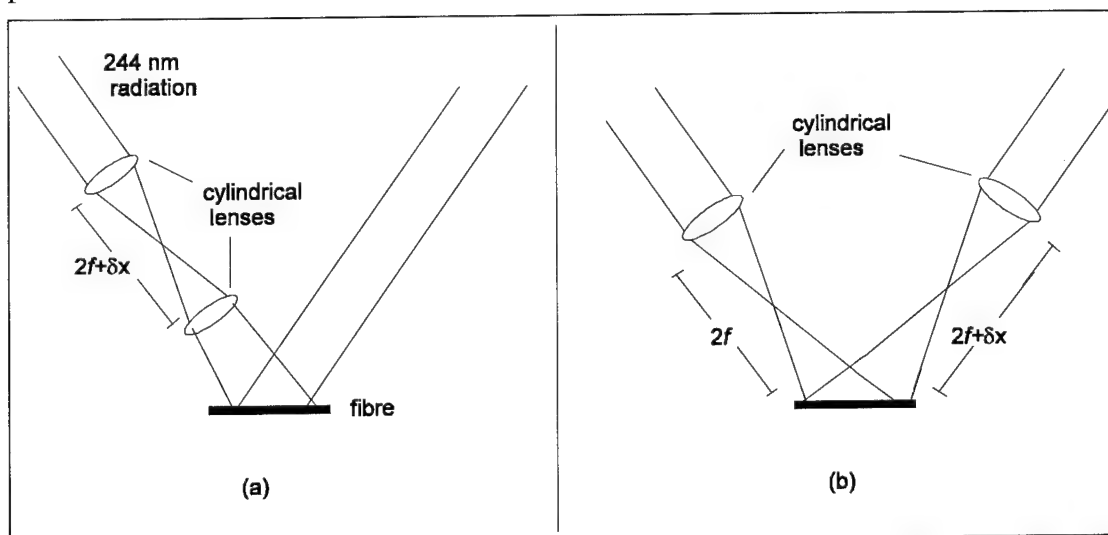
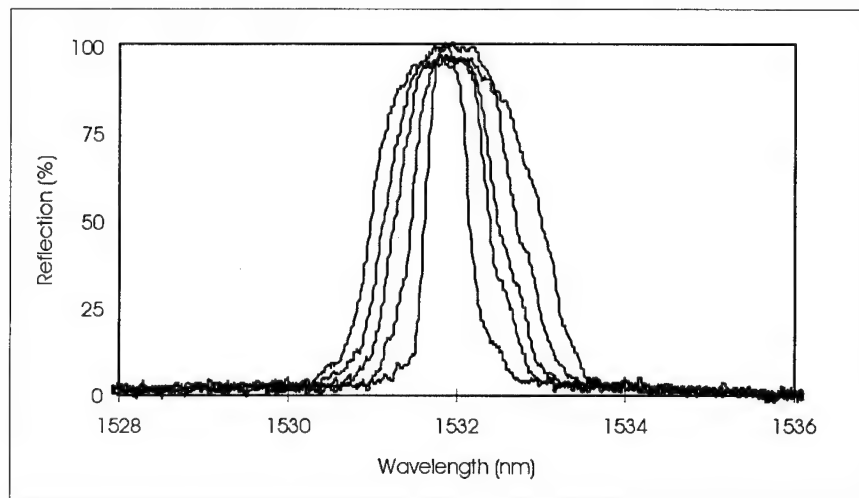


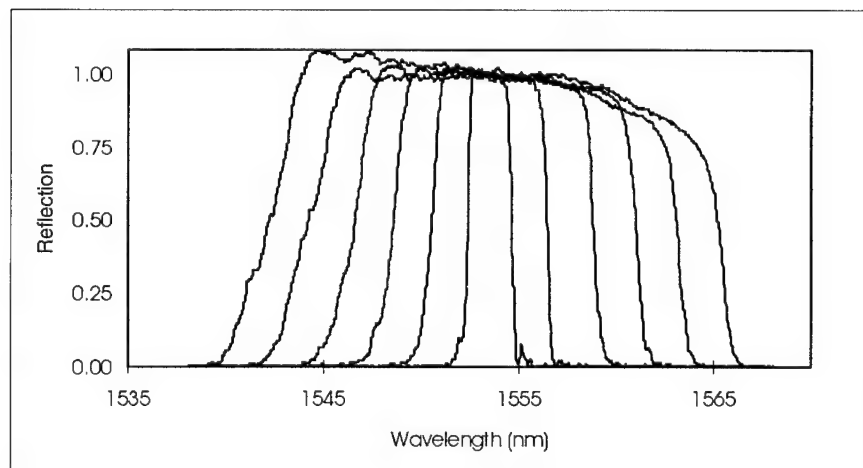
Figure 1: (a) the telescope lens arrangement for producing quasi-linearly chirped gratings, (b) two lens approach for quadratically chirped gratings.

Linearly chirped gratings: near-linearly chirped gratings can be made using two cylindrical lenses in-line to produce a telescopic system. This can be slightly detuned to give either a slowly diverging or slowly converging beam. The telescope mimics the effect of introducing a very wide selection of very long focal length lenses into the interferometer where the chirp produced is a function of the focal lengths; the difference being, that it physically fits into the space available.

Two cylindrical lenses of equal focal length, aligned in one arm of the interferometer at a distance of twice their focal length apart, give a 1x telescope configuration, figure 1(a). The front lens should be approximately one focal length away from the fibre to minimise the incident beam width variation. Gratings made with the lenses exactly in this position are effectively linear in nature. To introduce a chirp, the back lens is moved a small distance δx towards or away from the other lens. An effective focal length, f_{eff} , can be defined for the system as being twice the virtual image distance that is coincident with the front lens. The effective focal length, f_{eff} , is then variable and depends on the lens separation and hence, there is very fine control over the chirp rates and resultant bandwidths.



(a)



(b)

Figure 2: Reflection profiles of successively fabricated gratings with linear chirp with bandwidths in the ranges (a) 0.5-2.1nm, (b) 2.2-22.9nm.

Gratings with dispersions measuring in excess of 100 ps/nm, over a bandwidth of 0.4nm, have been fabricated in this way. This technique is highly flexible in being able to produce a continuum of small to medium bandwidth gratings. Figures 2(a) and (b) illustrates how easy it becomes to make a range of chirped gratings using this technique. The reflection profiles of eleven gratings, made consecutively with a progressively broadening wavelength response, are shown. Calculations and initial dispersion measurement indicate that the linearity of these gratings is good. The solid lines in figure 3 show the calculated variation of wavelength along the length of a 4mm grating. The lenses were taken to have focal lengths of 9cm. With a total lens movement of less than 1cm, along the beam axis, it is possible to fabricate chirped gratings with bandwidths that range from being barely wider than a linear grating to those that exceed 20nm.

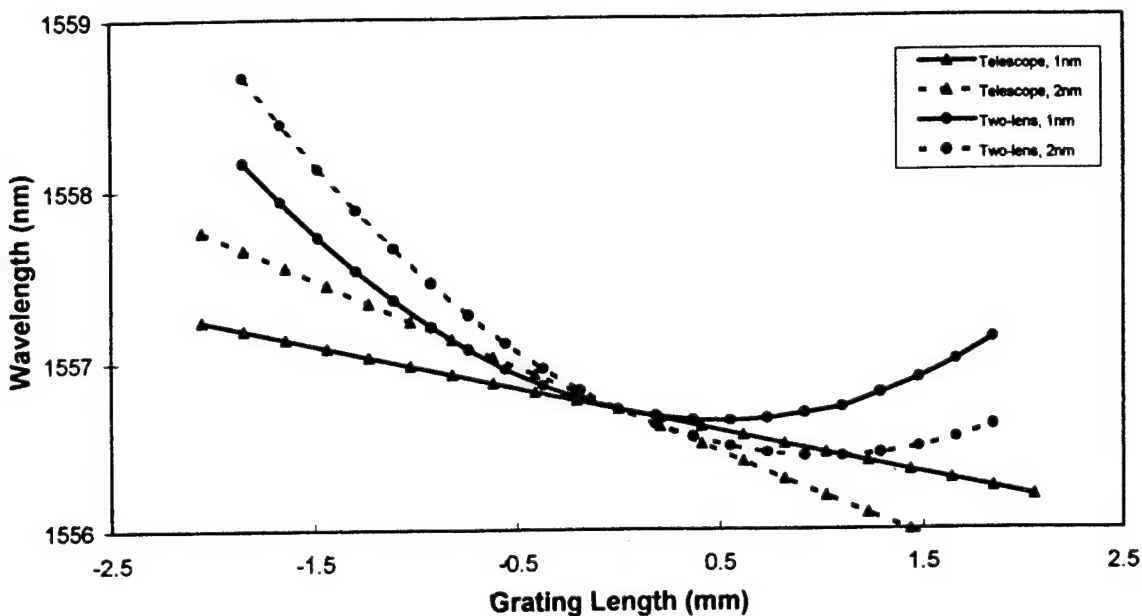


Figure 3 : Calculated wavelength profiles along the grating length for the telescopic method (solid lines) and the two lens method (dashed lines).

Quadratically chirped gratings: In some situations, a linear wavelength change along the length of the grating may not be necessary or, indeed, a non-linear response may be desirable^{7,8}. The lens arrangement described in this section produces gratings where the chirp is nonlinear along the length of the grating. Contrary to phase mask imprinted gratings, the chirped gratings from this arrangement can be made to vary in a continuously quadratic nature rather than in a stepped form.

If single cylindrical lenses are positioned one in each arm of the interferometer, figure 1(b), at twice their focal length from the fibre, then a narrow bandwidth grating ~1nm wide will be formed, where the lowest wavelength reflected will come from the centre of the grating and, moving outward, the reflected wavelengths will increase symmetrically. This produces a resonator structure and resonances are observed on the reflected spectrum. Moving one of the lenses away from the $2f$ position increases the bandwidth of the grating formed. As the bandwidth increases, an asymmetry in the profile of the chirp occurs around the centre point. Eventually, the chirp gradient

acquires the same sign across the length of the grating; this is indicated by the disappearance of resonances on the reflection spectrum. As the bandwidth broadens the chirp gradient remains quadratic, however, it does become noticeably more linear as the gratings start to exceed 10nm. The grating bandwidth is again determined by the lens focal lengths, f_1 and f_2 , and their distance from the fibre, x_1 and x_2 . The dashed lines on figure 3 show the calculated variation in wavelength for two narrowly chirped gratings fabricated by this method. Lenses of 9cm focal lengths were assumed for the calculation. Initial characterisation of these gratings is under way and the results of these will be presented.

In conclusion, dissimilar wavefront techniques provide a highly flexible approach to chirped fibre grating fabrication. We have shown how two different lens arrangements can be used to produce linear and quadratically chirped gratings. A wide range of consecutively made, chirped gratings, with bandwidths in the range of 0.5-20 nm, have been illustrated. It is possible to produce gratings with high linear dispersion characteristics, over 100 ps/nm. We believe that the techniques described represent important and flexible methods for fabricating gratings over a very wide parameter range.

-
1. A C Livanos, A Katzir, A Yariv, 'Fabrication of grating structures with variable period', *Opt Comm*, **20**, 1977, 179-182.
 2. F Ouellette, 'All-fibre filter for efficient dispersion compensation', *Opt Lett*, **16**, 1991, 303-305.
 3. J A R Williams, I Bennion, K Sugden, N J Doran, 'Fibre dispersion compensation using a chirped in-fibre Bragg grating', *Electron Lett*, **30**, 1994, 985-986.
 4. K O Hill, B Malo, F Bilodeau, D C Johnson, J Albert, 'Bragg gratings fabricated in monomode photosensitive optical fibre by UV exposure through a phase mask', *Appl Phys Lett*, **62**, 1993, 1035-1037.
 5. G Town, K Sugden, J Williams, I Bennion, S Poole, 'Wide-band Fabry-Perot-like Filters in Optical Fibre', *IEEE Photon Technol Lett*, **17**, 1994, 78-80.
 6. L Zhang, K Sugden, I Bennion, A Molony, 'Wide stopband chirped fibre Moiré grating transmission filters', *Electron Lett*, 1995, **31**, 477-478.
 7. J A R Williams, K Sugden, L Zhang, I Bennion, N J Doran, 'In-fibre grating systems for pulse compression and complete dispersion compensation', *IEE Colloq*, Optical fibre gratings and their applications. 1995.
 8. A Galvanauskas, M E Fermann, D Harter, K Sugden, I Bennion, 'All-fibre femtosecond pulse amplification circuit using chirped Bragg gratings', *Appl Phys Lett*, **66**, 1995, 1053-1055.

Novel Actively-Modelocked Dual-Wavelength Fibre Laser Using Chirped In-Fibre Bragg Gratings and its Application to All-Optical Memory

D.A. Pattison, P.N. Kean, J.W.D. Gray, I. Bennion and N.J. Doran

Dept. Electronic Engineering & Applied Physics

Aston University, Aston Triangle, Birmingham B4 7ET, UK

Telephone +44 121 359 3611

Fax +44 121 359 0156

Introduction

Ultrafast switching devices and high level processing architectures place two fundamental constraints on picosecond-regime data sources. The narrow spectral ranges of all-optical components for WDM [1] require multi-wavelength sources with output characteristics which are both arbitrarily and accurately definable over a wide wavelength range. In addition, use of the nonlinear-optical loop mirror (NOLM) in higher level functional systems [2], in which pulse-streams symmetrically straddle the zero-dispersion wavelength, necessitates low levels of inter-pulse-stream jitter [3, 4].

Multi-wavelength sources have been demonstrated in both active [5, 6] and passively mode-locked [7] configurations. The flexibility of both implementations, which are based on a single amplifier, is restricted, however, by the need to overcome the mode competition inherent in largely homogeneously broadened erbium doped fibre amplifiers (EDFA's).

In this paper we present a novel, all-fibre, actively mode-locked, dual-wavelength laser in which a NOLM modulator is used to simultaneously modelock two cavities which use chirped in-fibre Bragg gratings as end mirrors. The use of chirped gratings produces a configuration in which the operating wavelengths may be chosen across the entire erbium gain band and which may be independently dispersion-tuned across the reflection bandwidth of each grating. We show that this configuration has a very low level of inter-pulse-stream jitter, and present results from its application to a novel all-optical memory architecture.

Experiment

The experimental setup is shown in Fig.1 and is based on that in ref. [8]. The NOLM was built using a 40m standard fibre phase modulator section and was switched by a train of 90ps pulses at a repetition rate of 76MHz from a mode-locked Nd:YAG laser. The laser operating wavelengths were set using two 4mm length, linearly chirped, Bragg reflectors with bandwidths of 3.5nm and centre wavelengths of 1539nm and 1556nm respectively. Intracavity gain was provided by two 980nm pumped EDFA's, producing average mode-locked powers of 6.9mW and 3.4mW at 1539nm and 1556nm respectively. The intracavity dispersions, which were largely dominated by the gratings, were measured to be +13ps/nm

at 1556nm and +11.2ps/nm at 1539nm. An additional grating, centred at 1543nm with a measured short wavelength loss of 7.4dB at 1539nm, was used to increase the intercavity decoupling.

Fig.2(i) shows an autocorrelation and sech² fit for the 1539nm pulse train. The cavity generates transform limited sech² pulses of duration $\tau=6.6$ ps (time-bandwidth product, $\Delta\nu\Delta\tau=0.32$). Fig.2(ii) shows the corresponding results for the 1556nm cavity. The measured pulse width was $\tau=11.5$ ps with $\Delta\nu\Delta\tau=0.54$. The high value of time-bandwidth product is due to the fact that the laser operating point is close to the grating edge where the pulses receive excess chirp. When tuned to the centre of the grating the cavity produces transform limited pulses of 8ps duration, however the intracavity power is not high enough to maintain a full train in this operating region. This may be overcome by increasing the intracavity gain or by increasing the cavity pulse width. Since the latter is dependent on intracavity dispersion [9] this may be achieved by appropriate grating design.

The inter-pulse-stream jitter performance of this dual-wavelength configuration was compared with that of a mode-locked F-centre laser, synchronously pumped by the same Nd:YAG source, using the statistics package of a 50GHz sampling oscilloscope. The scope was triggered using the 1539nm pulse train while the 1556nm and F-centre trains were viewed on infinite persist. Fig.3(i) and (ii) show the resultant traces after 2000 samples. The measured standard deviation jitter levels were 900fs and 2.6ps respectively thus demonstrating the excellent jitter performance of this laser configuration.

We utilise the low jitter level of this source to implement a novel ultrafast all-optical memory architecture based on two control pulse switched NOLM's configured with a feedback path. Fig.4 shows a schematic of the memory configuration and a summary of its functionality in truth table form. The power supply consists of two continuous clock streams at wavelengths λ_1 and λ_2 which straddle the NOLM zero-dispersion wavelength. If an input word W1 is followed by a word W2 with all-zeroes W1 is stored. Unlike the previous memory implementation of Avramopolous and Whitaker [10], the word is not inverted on alternate round trips. If W2 is all-ones then the word W1 is logically inverted and stored, otherwise the device performs and stores the exclusive OR of W1 and W2.

Conclusion

In conclusion, we have demonstrated a novel, dual-wavelength, mode-locked erbium fibre laser configuration based on a single NOLM modulator with two cavities. The laser produces stable pulse trains at wavelengths which are arbitrarily definable by the choice of chirped grating end mirrors used and which may be independently dispersion-tuned across each grating reflection-band. We have shown that the inter-pulse-stream jitter of this configuration is extremely low (standard deviation=900fs) and present results from a novel all-optical memory architecture based on two NOLM modulators configured with feedback.

References

- [1] D.A. Pattison et al., *Opt. Lett.*, 1995, **20**, pp362-365.
- [2] J.K. Lucek and K. Smith, *IEEE Phot. Tech. Lett.*, 1995, **7**, pp59-61.

- [3] D.M. Patrick et al., *Elect. Lett.*, 1993, **29**, pp702-703.
- [4] M. Jinno, *Opt. Lett.*, 1993, **18**, pp1409-1411.
- [5] J.B. Schlager et al., *Elect. Lett.*, 1991, **27**, pp2072-2073.
- [6] H. Takara et al., *Elect. Lett.*, 1992, **28**, pp2274-2275.
- [7] D.U. Noske et al., *Opt. Comm.*, 1994, **108**, pp297-301.
- [8] P.N. Kean et al., *Elect. Lett.*, 1994, **30**, pp2133-2135.
- [9] M.L. Dennis and I.N. Duling III, *Appl. Phys. Lett.*, 1993, **62**, pp2911-2913.
- [10] H. Avramopolous and N.A. Whitaker *Opt. Lett.*, 1993, **18**, pp22-24.

Figures

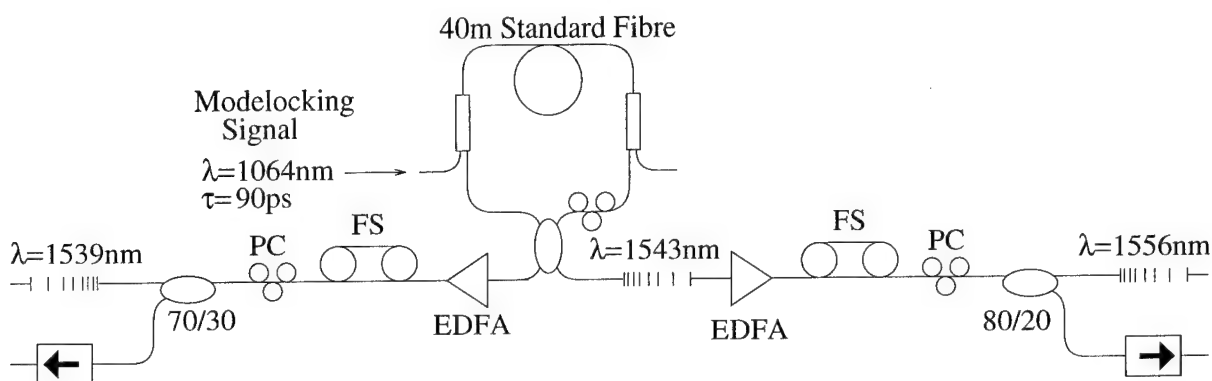


Figure 1: Experimental configuration. PC, polarisation controller. FS, fibre stretcher.

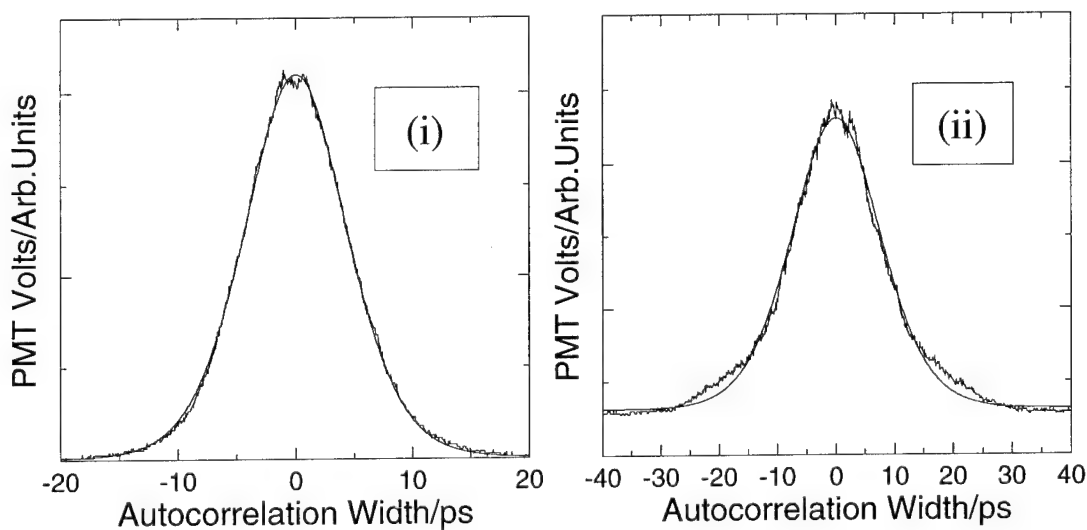


Figure 2: (i) 1539nm autocorrelation and sech^2 fit, $\Delta\tau=6.6\text{ps}$, $\lambda=1540.3\text{nm}$. (ii) 1556nm autocorrelation and sech^2 fit, $\Delta\tau=11.5\text{ps}$, $\lambda=1554.9\text{nm}$.

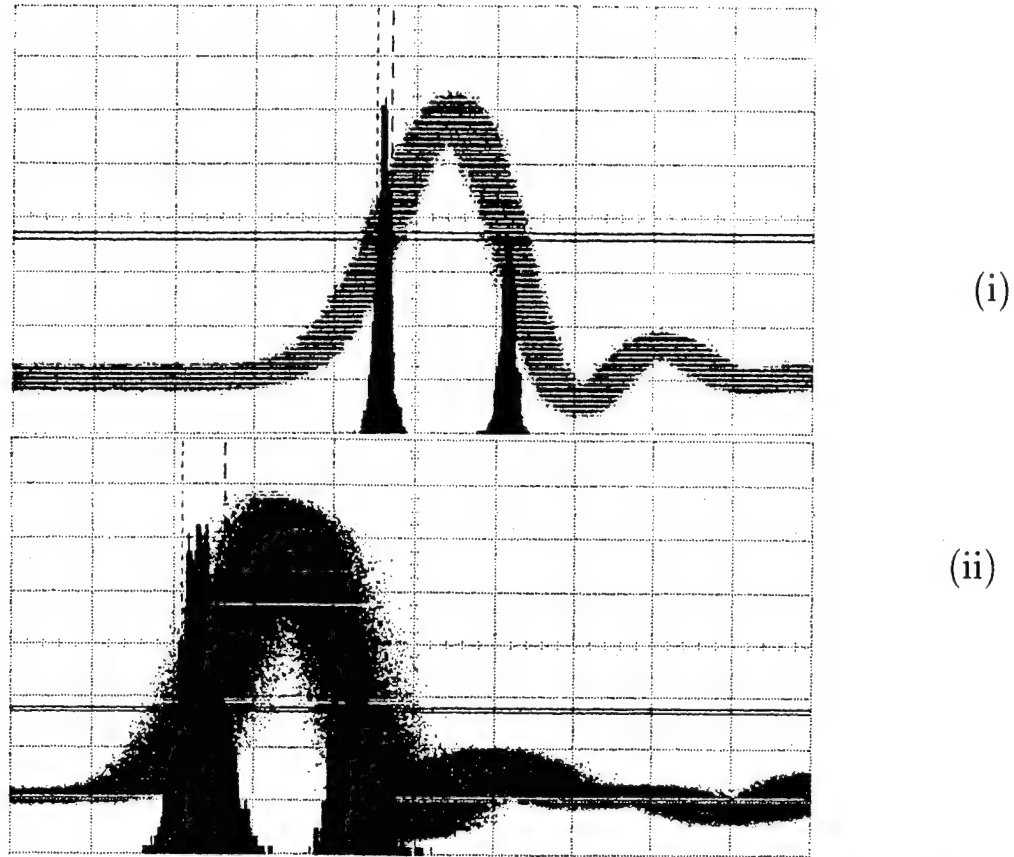


Figure 3: Jitter performance evaluation. Horizontal scale - 10ps/div (i) Trigger - 1539nm pulse train, signal - 1556nm pulse train. (ii) Trigger - 1539nm pulse train, signal - F-centre laser.

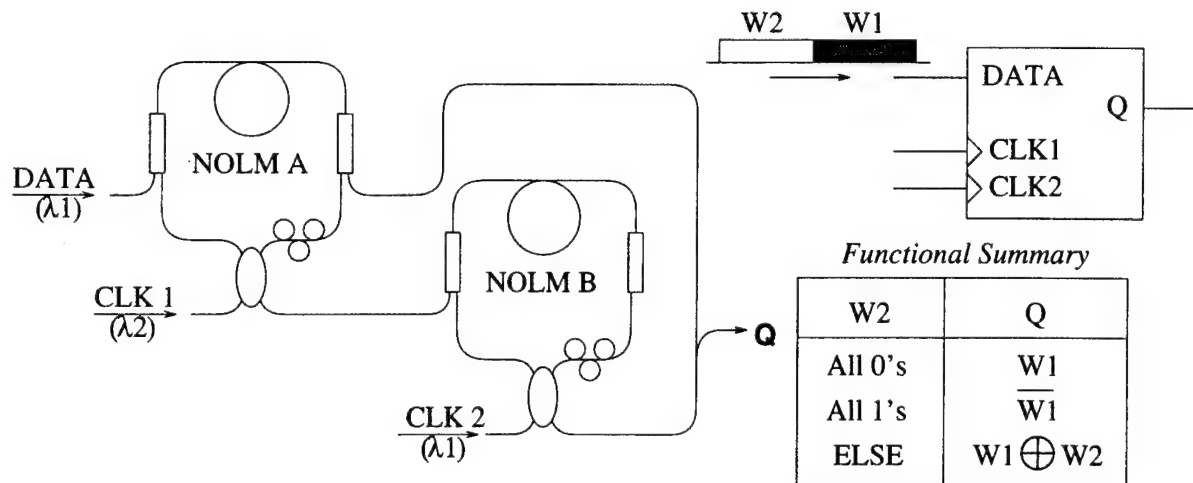


Figure 4: Schematic of memory configuration and functional summary.

First-Principles Characterization of Structure and Properties of E' Centers in Silica Glass

Shashi P. Karna and John J. Kester
Frank J. Seiler Research Laboratory
2354 Vandenberg Dr., Ste 2A35
U.S. Air Force Academy CO 80840-6272
Phone: (719) 472-2655
FAX: (719) 472-3649

The recent observations of second harmonic generation (SHG) of the infrared (IR) light in doped silica glass fibers,^{1,2} planar waveguides,^{3,4} and poled silica glass⁵ have attracted a great deal of attention in understanding the mechanism and origin of nonlinear optical (NLO) processes in a -SiO₂. A number of possible mechanisms have been proposed^{6,7} to explain the experimental observations. However, in so far as these phenomenological models describe the observed SHG in fibers and waveguides, they do not address the microscopic mechanism of optical nonlinearity in silica glass. An understanding of the atomic-scale mechanism of NLO properties in a -SiO₂ is important, not only for increasing our fundamental knowledge, but also for modeling new materials with yet enhanced optical susceptibility and faster response time for device applications. Here we present the results of first-ever *ab initio* studies of microscopic structure-NLO property relationships in systems containing free spin electrons, such as a -SiO₂.

Considering the structure of a -SiO₂ as a continuous random network of Si-O,⁸ its second order NLO coefficient, $\chi^{(2)}$, should vanish by virtue of symmetry. The possibility of observing SHG in silica glass based materials, therefore, requires a non-centrosymmetric structure created either by intrinsic defects or by external dopants. In this work, we concentrate on characterizing the *intrinsic* defect and its possible contribution to the observed NLO properties of a -SiO₂.

Among the various intrinsic defects identified to date, the E' centers constitute the single most important paramagnetic point defect in amorphous silica.⁹ From the similarity of the electron spin resonance (esr) spectrum of the γ -ray irradiated silica glass with that observed in radiation induced α -quartz,¹⁰ Griscom concluded¹¹ that the atomic-scale structure of the paramagnetic center in a -SiO₂ was similar to that of E_1' . The current accepted structure of the E_1' centers in α -quartz is based on the Feigl, Fowler and Yip model.¹² According to this model, the E_1' center in irradiated quartz is produced by asymmetric relaxation of $\equiv\text{Si}-\text{Si}\equiv$ created by an O⁻ vacancy. The unpaired electron spin is located on a tetrahedral Si atom in the Si-O (sp³ hybridized) bond and the 'hole' containing Si (Si⁺ ion) relaxes to sp² hybridization, containing its three SiO bonds in the same plane. The two types of Si centers in E' in this model are characterized by the two distinct (423 G and 8G) hyperfine splitting observed in the esr spectrum and both attributed to ²⁹Si nuclei ($I=1/2$).

The extensive work of Griscom,^{9,11} aided by the quantum mechanical studies of Fowler and coworkers^{12,13} in the past several years have recognized the E_γ' the E_1' equivalent in silica glass. It is now also believed the E_γ' centers constitute the intrinsic Frenkel defects (vacancy-interstitial pairs) in amorphous silica created by melt quenching and/or the action of ionizing particle irradiations.⁹

In order to establish the structure-NLO property relationship of E_γ' , we have calculated the geometry, one-electron properties, and linear and nonlinear optical properties of four model systems by the *ab initio* Hartree-Fock method. The model systems selected (Fig. 1) for our study, though smaller in dimension than one would consider adequate for modeling purposes, contain all the essential structural features of the proposed E_γ' center⁹ and its precursor. The

technical advantage of selecting the four model systems of the present study is that it allowed us to perform accurate calculations by the first-principles quantum mechanical method.

The oxygen vacancies (II-IV) will be designated as follows: Structure II will be denoted as V_O^0 , structure III will be denoted as V_O^{+1} , and structure IV will be denoted as V_O^{-1} . The notation is such that V_O denotes an oxygen vacancy and the superscript indicates the charge on the vacancy. Accordingly, a positive charge indicates a 'hole' and a negative charge indicates an 'electron'. The precursor, (structure I) will be denoted as P. The geometry of P and the three vacancies, V_O^0 , V_O^{+1} , and V_O^{-1} were optimized by the *ab initio* Hartree-Fock method using a double zeta plus polarization (DZP) Gaussian type basis set. For the property calculations, the DZP basis was further augmented by adding a set of diffuse p (0.025) and d(0.025) functions on Si, diffuse p(0.05) and d(0.05) functions on O, and a diffuse p(0.1) function on H. The numbers in parentheses are the orbital exponents.

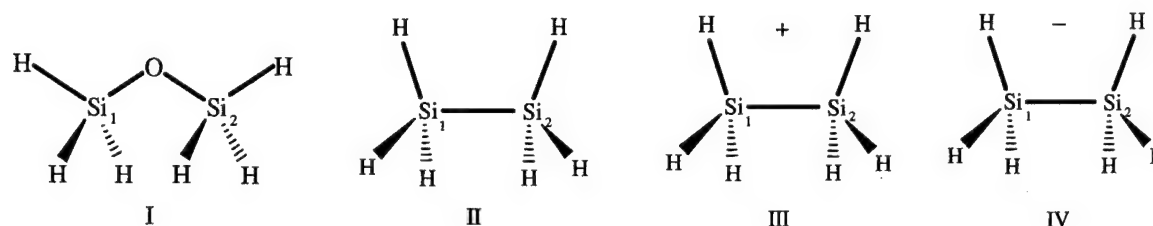


Figure 1.

The geometry optimization and the calculation of one-electron properties were performed by the HONDO-8 suite of programs.¹⁴ The linear and the nonlinear optical properties were calculated using the recently developed XNLOP program.¹⁵ The XNLOP program is a general purpose computer code for calculating the static (dc field) and dynamic (frequency-dependent) linear and NLO properties of molecules within the framework of the time-dependent coupled perturbed Hartree-Fock (TDCPHF) theory. The details of the TDCPHF method for the closed shell systems are described in the works of Karna and Dupuis,¹⁶ Karna,¹⁷ and those for the open-shell systems have been given in a recent work by Karna.¹⁵

The calculated bond distance and bond angles of the systems were in reasonable agreement with the available experimental^{18,19} and the most recent theoretical values²⁰ For example, the $R_{Si-O}=1.633$ Å, $R_{Si-H}=1.474$ Å, $\angle SiOSi=150$ degrees, and $\angle HSiO=109.5$ degrees obtained for P (structure I) in the present study, agrees well with the corresponding values obtained recently in a similar calculation²⁰ and also with the experimental data.¹⁹ We believe the calculated geometries of other structures (II-IV) also have similar accuracy. During the geometry optimization, no attempt was made to force the symmetry on the structures. This had the effect that in the systems where symmetry would cause the dipole moment to vanish, e.g. in V_O^0 , the relaxed geometry leads to a nonzero value of the dipole moment.

Table 1. Calculated values of R_{Si-Si} (Å) and dipole moment (D)

Structure	I	II	III	IV
R_{Si-Si}	3.164	2.367	2.786	3.370
μ_x	-0.00258	0.01344	0.00262	0.14997
μ_y	-0.30653	0.11267	0.02290	0.14714
μ_z	0.05827	0.00923	-0.00109	0.02770
$ \mu $	0.31204	0.11384	0.02307	0.14997

In order to examine the geometry relaxation and its effect on calculated properties, the calculated Si-Si distance and the dipole moment of structure I - IV are listed in Table 1. It is noted that a neutral O vacancy brings the two Si atoms much closer by about 0.08 Å with respect to the precursor (P). A negative O vacancy (O^-) creating the V_O^{+1} structure also brings the two Si atoms closer with respect to P, but the decrease in the Si-Si bond length is now smaller than that in V_O^0 . On the other hand, a positive O vacancy (O^+) that leaves behind an electron, thus creating V_O^{-1} , considerably elongates the Si-Si distance with respect to P.

The calculated changes in the Si-Si distance is consistent with the composition of the highest occupied molecular orbital (HOMO). In the case of P, the HOMO is a *nonbonding* p_z orbital situated on the oxygen atom. In the case of V_O^0 the HOMO is a σ -type (sp^3) *bonding* MO and the lowest unoccupied molecular orbital (LUMO) is its *antibonding* complement, a σ -type (sp^3) orbital. In the case of V_O^{+1} , an electron is removed from the σ bonding MO of the neutral vacancy which leads to the weakening of the binding between the Si atoms and elongation of the Si-Si bond. In the case of V_O^{-1} , an electron is added in the antibonding (σ^*) MO of the neutral vacancy which destabilizes the bonding between the Si atoms, resulting in a large R_{Si-Si} .

The components of the linear polarizability tensor, $\alpha(-\omega;\omega)$, and first-hyperpolarizability tensor, $\beta(-2\omega;\omega,\omega)$, for the two neutral species, P (structure I) and V_O^0 (structure II), calculated at a fundamental wavelength, $\lambda=1.064 \mu m$ are listed in Table 2. It is noted that whereas the linear polarizabilities of the precursor and the neutral oxygen vacancy are very similar, the NLO polarizability tensor is vastly different for the two structures. In fact, the observable vector quantity, $\beta_i (= \sum_j (\beta_{ijj} + \beta_{jij} + \beta_{jji})/5)$ for the V_O^0 structure is vanishingly small because of its nearly centrosymmetric structure.

Table 2. Components of $\alpha(-\omega;\omega)$ (10^{-24} esu) and $\beta(-2\omega;\omega,\omega)$ (10^{-32} esu) for P (structure I) and V_O^0 (structure II) calculated at $\lambda=1.064 \mu m$

Struct.	α_{aa}	α_{bb}	α_{cc}	β_{aab}	β_{bbb}	β_{bbc}	β_{bcc}	β_{ccc}
I	8.27	7.35	7.40	5.85	6.71	-0.02	11.86	0.03
II	10.65	7.68	7.67	-0.24	-7.13	10.27	7.75	-10.27

Even if the V_O^0 had a completely non-centrosymmetric structure, as would be expected in silica glass, its NLO coefficient is expected to be quite small due to the fact that the outermost electrons in its valence space occupy a strongly bonded σ MO.

Table 3. The hyperfine coupling constants, a_{iso} (G), and T_{ii} (G) for V_O^{+1} and V_O^{-1}

Struct.	Center	a_{iso}	T_{xx}	T_{yy}	T_{zz}
III	Si ₁	-17.77	15.84	15.68	-31.52
	Si ₂	-17.75	15.83	15.67	-31.50
IV	Si ₁	-323.21	13.64	12.55	-26.19
	Si ₂	-323.74	13.75	12.55	-26.30

The ^{29}Si hyperfine coupling constants of the two paramagnetic species, V_O^{+1} (structure III) and V_O^{-1} (structure IV), calculated by spin-unrestricted Hartree-Fock method are listed in Table 3. It is immediately clear that the 420 G spectrum observed by Griscom¹¹ could not be

due to a V_O^{+1} center. Such a large hyperfine splitting, according to the present calculation would require excess electron spin on the Si nuclei, as may be possible by an 'electron' trapping, resulting in a V_O^{-1} (structure IV) type structure. Of course, the smaller hyperfine splitting of 8G observed by Griscom¹¹ could very well be due to a V_O^{+1} center as the present calculation does yield a small a_{iso} value for this species. In fact, the value of a_{iso} for V_O^{+1} calculated after removing the lowest contaminating component from the spin density matrix, reduces to ~ 11 G, in much closer agreement with the experiment. An important implication of these results is that it does not fully support the hitherto accepted structure of the E' center.^{9,12,13} Rather, the present study indicates an 'electron'-'hole' pair having two ^{29}Si nuclei with distinct electronic environments as the source of the observed esr spectra. A more detailed analysis of the electronic and NLO properties of the model E' systems, presently underway in our laboratory, will be able to provide additional information about the structure of this important defect in silica glass.

References

1. U. Österberg and W. Margulis, *Opt. Lett.* **11**, 516 (1986)
2. R. H. Stolen and H. W. K. Tom, *Opt. Lett.* **12**, 585 (1987)
3. J. J. Kester, P. W. Wolf, and W. R. White, *Opt. Lett.* **17**, 1779 (1986).
4. P. S. Weitzman, J. J. Kester, and U. Österberg, *Electron. Lett.* **30**, 697 (1994).
5. R.A. Myers, N. Mukherjee, and S.R.J. Brueck, *Opt. Lett.* **16**, 1732 (1991).
6. V. Dominic and J. Feinberg, *Phys. Rev. Lett.* **71**, 3446 (1993).
7. M. L. Brauer, I. Dajani, and J. J. Kester, *Electron. Lett.* **30**, 297 (1994).
8. W. H. Zachareisen, *J. Am. Chem. Soc.* **54**, 3841 (1932).
9. D. L. Griscom, *Proc. Mat. Res. Soc.* **61**, 213 (1986).
10. R. H. Silsbee, *J. Appl. Phys.* **32**, 1459 (1961).
11. D. L. Griscom, *Phys. Rev. B* **20**, 1823 (1979); *ibid.* **22**, 4192 (1980).
12. F. J. Feigl, W. B. Fowler, and K. L. Yip, *Solid State Commun.* **14**, 225 (1974).
13. K. L. Yip and W. B. Fowler, *Phys. Rev. B* **11**, 2327 (1975); J. K. Rudra and W. B. 14 Fowler, *Phys. Rev. B* **35**, 8223 (1987) and references therein.
14. M. Dupuis, A. Farazdel, S. P. Karna and S. Maluendes, *Modern Techniques in Computational Chemistry*, Ed. E. Clementi (ESCOM, Leiden, 1990), p. 277.
15. S. P. Karna, *J. Chem. Phys.*, submitted for publication.
16. S. P. Karna and M. Dupuis, *J. Comp. Chem.* **12**, 487 (1991).
17. S. P. Karna, *Chem. Phys. Lett.* **214**, 186 (1993).
18. J. A. Aronson, R. C. Lord, and D. W. Robinson, *J. Chem. Phys.* **33**, 1004 (1960).
19. M. J. Barrow, E. A. V. Ebsworth, and M. M. Harding, *Acta. Crystall. B* **35**, 2093 (1979).
20. M. R. Bär and J. Sauer, *Chem. Phys. Lett.* **226**, 405 (1994), and references therein.

Comparison of UV Photosensitivity and Fluorescence During Fiber Grating Formation

Heather Patrick and Sarah Gilbert
National Institute of Standards and Technology
M/S 815.03, 325 Broadway, Boulder, CO 80303
Tel. (303) 497-3120, Fax (303) 497-7621

We have conducted a comparison of the UV photosensitivity of optical fiber with the blue fluorescence emitted during the exposure. In a survey of ten non-hydrogen-loaded germanium-doped fibers, we measured the UV photosensitivity and monitored the blue fluorescence during the growth of fiber gratings. Our goal was to determine whether the initial fluorescence, or the change in the fluorescence during exposure, is correlated with the index change. This provides insight into the underlying physical mechanism of UV-induced index change and also determines whether the blue fluorescence can be used as an indicator of the photosensitivity of a fiber.

Gratings were written in ten types of fiber using cw 244 nm UV light and a prism interferometer.¹ Each grating was exposed for 5 min to the full power of the UV beam at an intensity of $I_{uv} = 50 \text{ W/cm}^2$. During the exposure, we detected the UV-induced fluorescence emitted from the side of the fiber as described in our previous work.² For all fibers studied, the fluorescence level always dropped during the UV exposure. We also monitored the grating reflectance during the exposure using a LED source and an optical spectrum analyzer. The data for fluorescence and reflectance versus time were transferred to a computer.

We converted the reflectance data to refractive index modulation Δn . The results for Δn and fluorescence after a 5 min exposure are given in Table I. The fiber core composition is shown in the "Dopants" column, and the approximate mol % concentration of germanium is shown if it was known. In many cases, the exact composition of commercial fiber is proprietary. However, the index difference between core and cladding of the fiber is mostly determined by the germanium content, so if the germanium content was not known, it could be estimated from this difference.³ Figure 1 compares the total change in fluorescence signal $1 - FL_f/FL_0$ from the Table with the final index modulation Δn_f .

We found that the grating growth in all the fiber types could be characterized well by the power law $\Delta n(t) = Ct^b$. The parameter C was highly fiber dependent and ranged from about 1×10^{-5} for fiber C2 to 1×10^{-4} in fiber EB (with t in minutes). The parameter b was roughly constant for all the fibers except EB and C1. For twenty-three data sets in the non-boron-doped fibers (and excluding C1), we found $b = 0.31 \pm 0.03$, whereas for three data sets in the boron-codoped fiber EB we found $b = 0.42 \pm 0.03$. A particularly interesting comparison is between fiber E2 and fiber EB, which are very similar except for the boron doping in fiber EB. In fiber E2 we found $C = 5.0 \times 10^{-5}$ and $b = 0.32$, whereas $C = 1.0 \times 10^{-4}$ and $b = 0.42$ for fiber EB. Finally, for fiber C1 with 3 mol % germanium, b was higher than in the other germanium-doped fibers, at $b = 0.39 \pm 0.02$, although the photosensitivity was quite low.

Table I. Comparison of index change and fluorescence in ten fibers; three gratings were written in each fiber. FL_0 is the fluorescence signal in volts recorded at the start of the measurement. R_f and Δn_f refer to the grating reflectance and corresponding index modulation at the end of the exposure. Because the fluorescence is dropping very quickly at the start of the exposure, there is a variation in the value of FL_0 measured for the same fiber due to the 0.3 s resolution of the recording apparatus. FL_f is the fluorescence signal in volts at the end of the exposure, and $1 - FL_f/FL_0$ is the fractional drop in fluorescence over the exposure.

Symbol	Fiber	Dopants [Ge concentration]	R_f	Δn_f	FL_0	$1-FL_f/FL_0$
▲	A1	Ge [9 mol %]	0.58	6.9×10^{-5}	1.6	0.60
			0.55	6.6×10^{-5}	1.8	0.53
			0.53	6.4×10^{-5}	2.3	0.60
●	E1	Ge [7 mol % (Ref. 3)]	0.78	9.6×10^{-5}	1.1	0.72
			0.79	9.8×10^{-5}	1.1	0.71
			0.82	1.0×10^{-4}	1.9	0.74
◆	A2	Ge [9 mol %]	0.34	4.6×10^{-5}	2.4	0.35
			0.35	4.7×10^{-5}	2.4	0.32
			0.32	4.4×10^{-5}	2.2	0.34
+	E2	Ge [9 mol % (Ref. 3)]	0.61	7.2×10^{-5}	1.6	0.65
			0.77	9.4×10^{-5}	1.5	0.65
			0.69	8.2×10^{-5}	-	-
○	L1	Ge, Al, Er [9 mol % (Ref. 3)]	0.59	7.0×10^{-5}	0.63	0.65
			0.63	7.4×10^{-5}	0.48	0.57
			0.55	6.6×10^{-5}	0.50	0.56
□	L2	Ge, Er [6 mol % (Ref. 3)]	0.25	3.8×10^{-5}	0.42	0.57
			0.25	3.8×10^{-5}	0.46	0.59
			0.28	4.1×10^{-5}	0.54	0.67
△	EB	Ge, B [9 mol %]	0.98	1.8×10^{-4}	1.4	0.79
			0.98	1.8×10^{-4}	1.6	0.75
			0.98	1.8×10^{-4}	2.3	0.78
x	C1	Ge [3 mol % (Ref. 3)]	0.05	1.6×10^{-5}	0.67	0.32
			0.05	1.6×10^{-5}	0.57	0.43
			0.05	1.6×10^{-5}	0.61	0.40
*	C2	Ge [7 mol % (Ref. 3)]	0.03	1.2×10^{-5}	0.19	0.41
			0.05	1.6×10^{-5}	0.16	0.28
			0.04	1.4×10^{-5}	0.12	0.33
◇	N1	Ge, Al, P, Er [7 mol % (Ref. 3)]	0.57	6.8×10^{-5}	0.83	0.52
			0.60	7.1×10^{-5}	0.74	0.49
			0.63	7.5×10^{-5}	0.64	0.48

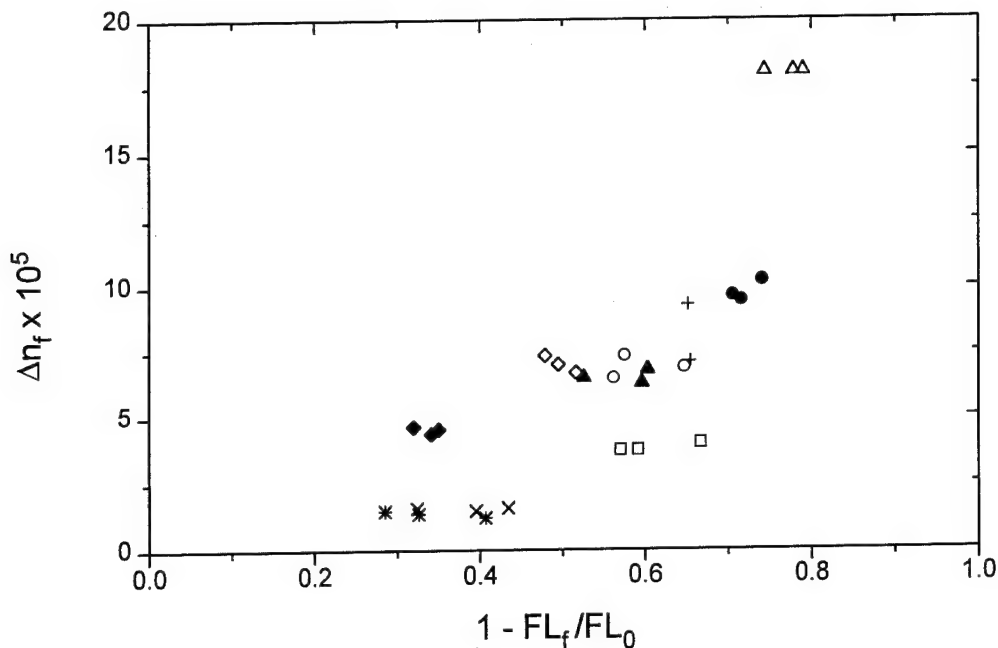


Figure 1. Comparison of the total change in fluorescence signal $1 - FL_f/FL_0$ from Table I with the final index modulation Δn_f . The fibers are represented by the symbols in the Table.

We also fitted the normalized fluorescence to the power law $FL(t)/FL_0 = 1 - Jt^h$. Although this function allows the nonphysical result of negative fluorescence (it does not account for saturation), in all cases the fluorescence is far from saturation, and it allows a direct comparison of the parameters J and h with the parameters C and b from the Δn fits. Although the fluorescence and Δn change over the same time scale, in general the fluorescence changes more slowly than Δn , with h smaller than b for all the fibers studied. The most dramatic difference was for fiber EB, with h typically 0.2 and b typically 0.4.

As seen in the figure, index change is correlated with the amount of drop in the fluorescence. Fibers with the largest change in fluorescence ($> 70\%$) showed the largest index changes ($R > 78\%$ and $\Delta n > 10^{-4}$); those with the smallest change in fluorescence ($< 40\%$) gave gratings of $R < 35\%$. The exception was L2, where the fluorescence changed by 60% but the grating was only $R = 25\%$. Among the fibers which contain no dopants other than germanium, the change in index was very well correlated with the change in fluorescence. The linear correlation coefficient for Δn_f and $1 - FL_f/FL_0$ was 0.8, indicating less than 0.1 % probability that the two are not correlated.⁴ This change in fluorescence could be a useful diagnostic when designing germanium-doped fiber for photosensitivity.

The change in fluorescence, however, does not have the same time dependence as the index change. Although both Δn and the normalized fluorescence could be fitted to a power law, the time exponent h for the fluorescence was consistently lower than the exponent b for the index change. In addition, our previous work^{1,2} showed that the fractional change in fluorescence was only a function of fluence $I_{uv} \times t$, whereas the index change was a stronger function of I_{uv} than of t .

The initial fluorescence and the germanium concentration were only very rough predictors of photosensitivity. In the case of the germanium concentration, this may be due to the difficulty in estimating the actual concentration from the refractive index difference. In particular, if other dopants are present in the core, they also raise (in the case of Al, P) or lower (in the case of B) the refractive index. The statements of concentration in mol % when the concentration was calculated from the refractive index difference (using Ref. 3) should be taken as accurate to only $\pm 15\%$. Also, the defect concentration depends both on the germanium concentration and on the processing conditions (particularly oxygen concentration and temperature) when the fiber preform is made. This may explain conflicting reports of photosensitivity in fibers with low germanium content (around 3 mol %). For the most part, fibers with low germanium content have been reported to have low photosensitivity.⁵ However, there has been one report of high photosensitivity in a 3 mol % germanium-doped fiber.⁶

As observed by other researchers, the addition of boron enhanced the photosensitivity. The germanium doping of fiber EB was about the same as that of fiber E2, but the UV-induced index change was more than twice as large in the boron-codoped fiber. However, the difference in the fluorescence behavior between the two fibers was not as dramatic, with a 65% change in fluorescence in fiber E2 and a 77% change in fluorescence in fiber EB. Also, the addition of boron did not significantly change the initial value of the fluorescence. Assuming that the initial fluorescence is linearly related to the 240 nm absorption, this is consistent with the observation that adding boron does not change the size of the absorption.⁵

In conclusion, we found that the fast decrease in the blue fluorescence emitted during UV exposure of optical fiber is a good predictor of photosensitivity. However, the temporal behavior of the fluorescence does not match that of the UV-induced index change, suggesting that these phenomena may not be due to the same excitation, but are both products of a particular fiber manufacturing process.

References

1. H. Patrick and S. L. Gilbert, *Opt. Lett.* **18**, pp. 1484-1486 (1993).
2. H. Patrick, S. L. Gilbert, and A. Lidgard, *Optical Materials* **3**, pp. 209-216 (1994).
3. The germanium concentration was estimated from the core-cladding refractive index difference using a formula from J.P. Pocholle, *Revue Technique Thomson - CSF* **15**, 881 (1983). The information came through private communication, Anne Lidgard.
4. John R. Taylor, *An Introduction to Error Analysis*, (University Science Books, Mill Valley, California, 1982), pp. 180-184.
5. D.L. Williams, B.J. Ainslie, J.R. Armitage, R. Kashyap, and R. Campbell, *Electron. Lett.* **29**, 45 (1993).
6. H.G. Limberger, P.Y. Fonjallaz, and R.P. Salathé, *Electron. Lett.* **29**, 47 (1993).

Ion Implantation Induced Photosensitivity in Silica and Ge-Doped Silica

M. Essid, M. Verhaegen, L.B. Allard, and J.L. Brebner

Groupe de recherche en physique et technologie des couches minces, Physics department, Université de Montréal, P.O. Box 6128, Station "Centre-ville", Montréal, Québec, H3C 3J7, CANADA.

Tel : (514) 343 6614 Fax : (514) 343 2071

J. Albert

Communications Research Centre, P.O. Box 11490, Station H, Ottawa, Ontario, K2H 8S2, CANADA

Tel : (613) 990 7690 Fax : (613) 993 7139

INTRODUCTION

Photosensitivity can be induced in silica¹ and Ge-doped silica² by high energy ion implantation. The optical absorption induced in the ultraviolet region by the implantation can be substantially reduced by exposure to excimer laser light resulting in a polarisation dependent³ change in the refractive index at longer wavelengths. This refractive index change can be related to the variation in the absorption by Kramers-Kronig analysis^{4,5}. We describe here, the result of a series of experiments undertaken to determine the effects of ion implantation on the photosensitivity of silica and Ge-doped silica planar waveguide structures.

II EXPERIMENTAL METHODS

Two different samples were used in these experiments. 0.5 mm thick high-purity silica substrates (Suprasil-2, Heraeus Amersil Inc) and Ge-doped silica glass from PIRI, prepared by the deposition of a 20 μm thick film of Ge-doped silica film ($\sim 7\%$ Ge) on a silica substrate, using the flame hydrolysis process. Samples were implanted with 5 MeV Si^{2+} ions at a dose of 1×10^{15} ions cm^{-2} . TRIM simulations indicate that the implantation induced damage lies in a layer approximately 3.2 μm beneath the surface

and that the concentration of silicon implanted ions is of the order of 0.045 mol.%. The implantations were carried out using the Université de Montréal 6 MV Tandem accelerator. The beam current of Si^{2+} ions was typically 150 nA with a beam spot of 3 mm in diameter scanned over an area of 1 cm^2 on the sample. The implantation were carried out at room temperature. After implantation, optical transmission spectra were measured on the samples between 200 and 400 nm using a UV-Visible Cary-5 spectrophotometer.

Implantation of ions in silica and Ge-doped silica forms optical waveguides by increases the refractive index locally through compaction of the implanted region and, to a lesser extent, through an increase in polarisability. The refractive index change in the samples was estimated by measuring the guided modes with an Abbe refractometer with an accuracy of 2×10^{-4} . This measurement yields the effective index for the guided mode and also provides a lower bound for the refractive index in the ion implanted layer. Bleaching experiments were carried out using a Lumonics excimer laser model 500 operating on a KrF (248 nm) or ArF (193 nm) gas mixtures. The pulse duration was 20 ns and the energy density 100 mJ/cm^2 pulse.

III RESULTS AND DISCUSSION

Strong absorption bands in the ultraviolet appear in both silica and Ge-doped silica after implantation. In silica, the prominent features of the implantation-induced optical absorption spectrum (Fig. 1), are the so called B_2 band (244 nm), the silica E band (212 nm) and the low energy tail of the E band (163 nm). In Ge-doped silica, we observe a GeO band (240 nm) and the low energy tail of the GeE band (175 nm) (Fig. 2), both of which have substantially higher intensity than the bands induced in silica. Following implantation, the Ge-doped sample was irradiated with 600 J/cm^2 total energy delivered by a KrF excimer laser and the silica sample was irradiated by both KrF and ArF Laser with 600 J/cm^2 and 20 J/cm^2 respectively. This illumination bleached

most of the absorption bands in both silica and Ge-doped silica leaving only some residual absorption in the E, E and GeE bands.

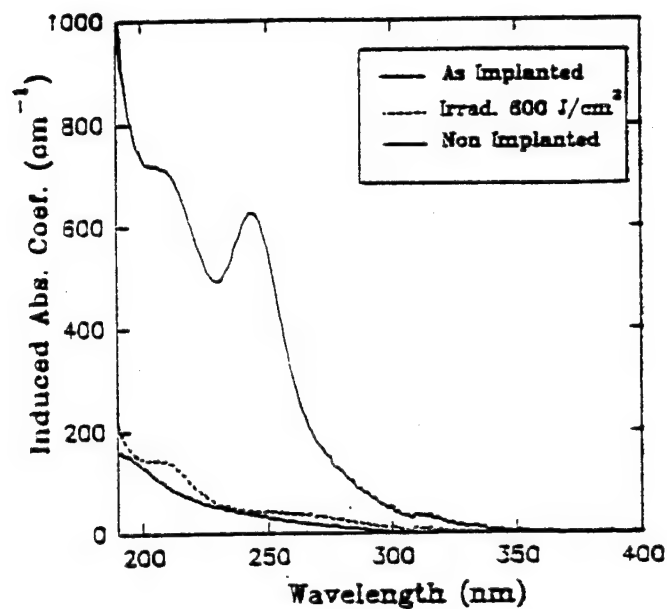


Fig.1. UV absorption spectra induced by the implantation of silica and after optical bleaching with 100 mJ/cm² pulses at 20 pulses/s.

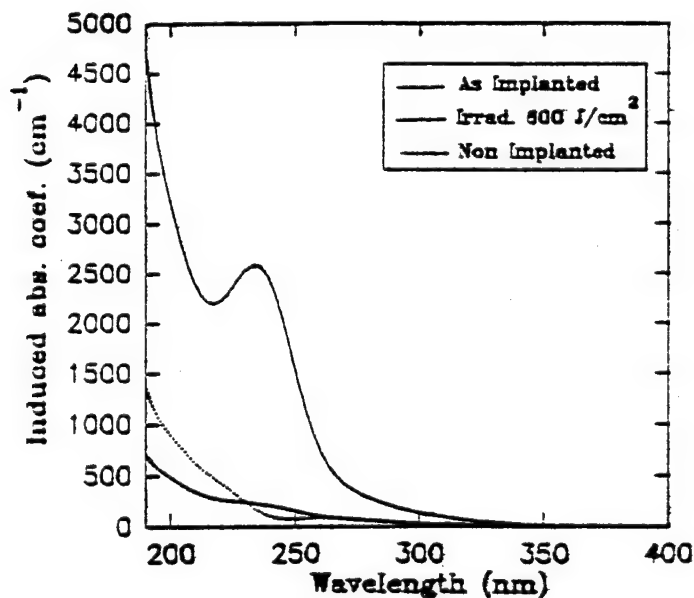


Fig.2. UV absorption spectra induced by the implantation of Ge-doped silica and after optical bleaching with 100 mJ/cm² pulses at 20 pulses/s

The refractive index changes in both materials following implantation and UV bleaching are reported in table 1.

Table 1. Summary of Measurements

Samples	(Δn) Implantation	UV dose KrF(J/cm ²)	(Δn) KrF bleaching	UV dose ArF(J/cm ²)	(Δn) ArF bleaching
SiO ₂	+14.8x10 ⁻³	600	-1.3x10 ⁻³	20	-1.7x10 ⁻³
SiO ₂ :GeO ₂	+25.8 10 ⁻³	600	-3.8x10 ⁻³	-	-

CONCLUSION

In summary, we have compared the photosensitivity induced by high energy ion implantation in silica and in Ge-doped silica. Both the implantation induced and the photoinduced refractive index changes obtained are significantly higher in Ge-doped silica than in silica.

REFERENCES

- [1] J. Albert, K. O. Hill, B. Malo, D.C. Johnson, J. L. Brebner, Y. B Trudeau, and G. Kajrys, Appl. Phys. Lett. 60 (2) (1991) 148.
- [2] D. L. Kyle, B. L. Weiss, and G. D. Maxwell, J. Appl. Phys, 77 (3), (1995) 1207.
- [3] J. Albert, B. Malo, D.C. Johnson, F. Bilodeau, K. O. Hill, J. L. Brebner, and G. Kajrys, Opt. Lett. 18 (14), (1993) 1126.
- [4] J. Albert, B. Malo, K. O. Hill, D.C. Johnson, J. L. Brebner, and R. Leonelli, Opt. Lett. 17 (23), (1992) 1652.
- [5] M. Verhaegen, L. B Allard, J.L. Brebner, M. Essid, S. Roorda and J. Albert, Nucl. Instr. and Meth. B, in Press.

PHOTOCHEMICAL START-UP OF PHOTOREFRACTIVITY IN SiO_2 AND $\text{SiO}_2:\text{GeO}_2$ GLASSES

V.M. Marchenko

General Physics Institute, 38 Vavilov St., 117333 Moscow,
Russia. Tel: (095) 135-3437, Fax: (095) 135-0270

Introduction

Progress in applications of photosensitivity of silica glasses for fabrication of reflection optical fiber gratings is restrained by an obscurity of nature of photorefractivity of the glasses. There is a lot of inconsistent interpretations of spectral properties of oxygen deficient centers (ODC) responsible of UV absorbance of the glasses. Photoinduced refractive index variations of the glasses are in accordance with Kramers-Kronig relation due to the absorbance changes. As much as $\sim 10^{-4}$ photoinduced index variation of Ge-doped silica at $1.5 \mu\text{m}$ is for instance explained by photobleaching of 5.1 eV spectral band and increasing of absorptivity of 6.5 eV band [1]. However experimentally obtained index changes larger than 10^{-3} are probably caused by changes of the absorbance at shorter wavelengths corresponding to energy gap transitions and consequently accompanied by modification and compaction of glass matrix [2]. In this work, the interpretation of ODC optical spectra of SiO_2 and $\text{SiO}_2:\text{GeO}_2$ glasses is discussed and model of the solid-state photoinduced chemical reactions is proposed to explain the start-up of physical and chemical processes of varying of ODC concentrations and macroscopic parameters of the glasses which is confirmed by the analysis of ODC preparation technique.

Optical spectroscopy of ODC

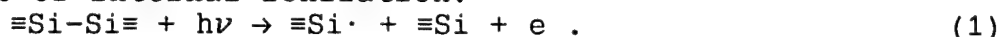
The most probable interpretation of ODC optical spectra of SiO_2 and $\text{SiO}_2:\text{GeO}_2$ glasses based on analysis of spectroscopic data [3,4] is following. ODC in silica glasses are characterized by $\equiv\text{Si}-\text{Si}\equiv$ absorption band of 7.6 eV (163 nm), by $\equiv\text{Si}:\text{B}_2\alpha$ absorption transition $S_0 \rightarrow S_1$ of 5.0 eV (248 nm) and luminescence transitions $S_1 \rightarrow S_0$ of 4.45 eV (280 nm) with decay time $\tau_{ss} \approx 5$ ns at UV exposure dose of $< 10^{-3} \text{ J/cm}^2$ and $\tau_r \approx 10 \mu\text{s}$ at the dose of $> 10^{-2} \text{ J/cm}^2$ [5] and $T_1 \rightarrow S_0$ of 2.7 eV (460 nm) with $\tau_{TS} = 10$ ms and by $\equiv\text{Si}\cdot$ absorption band of 5.8 eV (215 nm). In germanosilicate glasses ODC are also characterized by $\equiv\text{Ge}:\text{B}_2\beta$ absorption transition $S_0 \rightarrow S_1$ of 5.1 eV (242 nm) and luminescence transitions $S_1 \rightarrow S_0$ of 4.3 eV (290 nm) with $\tau_{ss} < 50$ ns and $T_1 \rightarrow S_0$ of 3.1 eV (400 nm) with $\tau_{TS} = 0.1$ ms and by $\equiv\text{Ge}\cdot$ absorption band of 6.5 eV (191 nm) [6,7]. Calculated energies of spectral bands are in disagreement with registered ones [8]. It is necessary to point out that 5 eV band of germanosilicate glass has a complex structure and two

photobleaching times [6,9]. Taking also into account transformations of absorption and luminescence bands of Ge-doped silica samples prepared by laser distillation [10] one can recognize that the band appears to be a superposition of $B_2\alpha$ and $B_2\beta$ bands.

Photochemical transformations of ODC

Photobleaching of $B_2\alpha$ and $B_2\beta$ bands produces increasing of optical density of 5.8 eV and 6.5 eV absorption bands and creation of $E'(Si)$ and $E'(Ge)$ centers accordingly [3-7]. Illumination of silica glass by 6.5 eV laser radiation is followed by creation of $E'(Si)$ [11]. Long time excitation of 7.6 eV $\equiv Si-Si \equiv$ absorption band at 80 K produces increasing of 4.4 eV $\equiv Si:$ luminescence intensity [12]. Photoinduced transformations of ODC are accompanied by a change of refraction index, nonlinear susceptibility, birefringence and density.

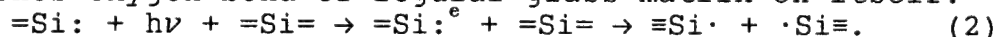
It is supposed [4] that $\equiv Si-Si \equiv$, unrelaxed oxygen vacancy $\equiv Si/\backslash Si \equiv$ and $\equiv Si:$ models are reasonable for $B_2\alpha$ center but conversion of $B_2\alpha$ to $E'(Si)$ would require to be a precursor one of two first corresponding to photobleaching reaction by means of internal ionization:



In a similar reaction $\equiv Si:$ seems unlikely to be the precursor because a paramagnetic center $\equiv Si\cdot$ is not revealed.

Reaction (1) does not explain low intensity photoionization by quanta of $h\nu = 5 \text{ eV} < E_g = 9 \text{ eV}$, photoinduced birefringence and density change. Electron conductivity and explanation of relaxation times are to be proved.

Interpretation of photobleaching may be grounded on the basis of the assumption of photochemical rearrangement of a microstructure of ODC. In particular photobleaching of $B_2\alpha$ band by UV excitation occurs in consequence of a local disturbance of thermodynamic equilibrium of electron-vibration subsystem and dissociation and may be considered as chemical reaction in solid glass during which excited $\equiv Si:$ switches oxygen bond of regular glass matrix on itself:



Neighboring $E'-$ centers form oxygen monovacancy:



The scheme of structural transformations is presented in Fig.1. Si-O valent bond dissociation energy $E_d = 3.82 \text{ eV} < h\nu = 5 \text{ eV}$ [13]. Kinetic investigations of photobleaching and photoconductivity [5] indicate that characteristic lifetime of the reaction is of $\tau_r \approx 50 \mu s$.

Photoexcitation of $\equiv Si:$ has to be followed by characteristic transitions as of $\equiv Si\cdot$ as of $\equiv Si-Si \equiv$. Reversibility of reactions (2,3) is confirmed by lifetime of $\equiv Si:$ recombination luminescence $\tau_r \gg \tau_{ss}$ [5], by photobleaching of $E'-$ centers and by photolysis of $\equiv Si-Si \equiv$

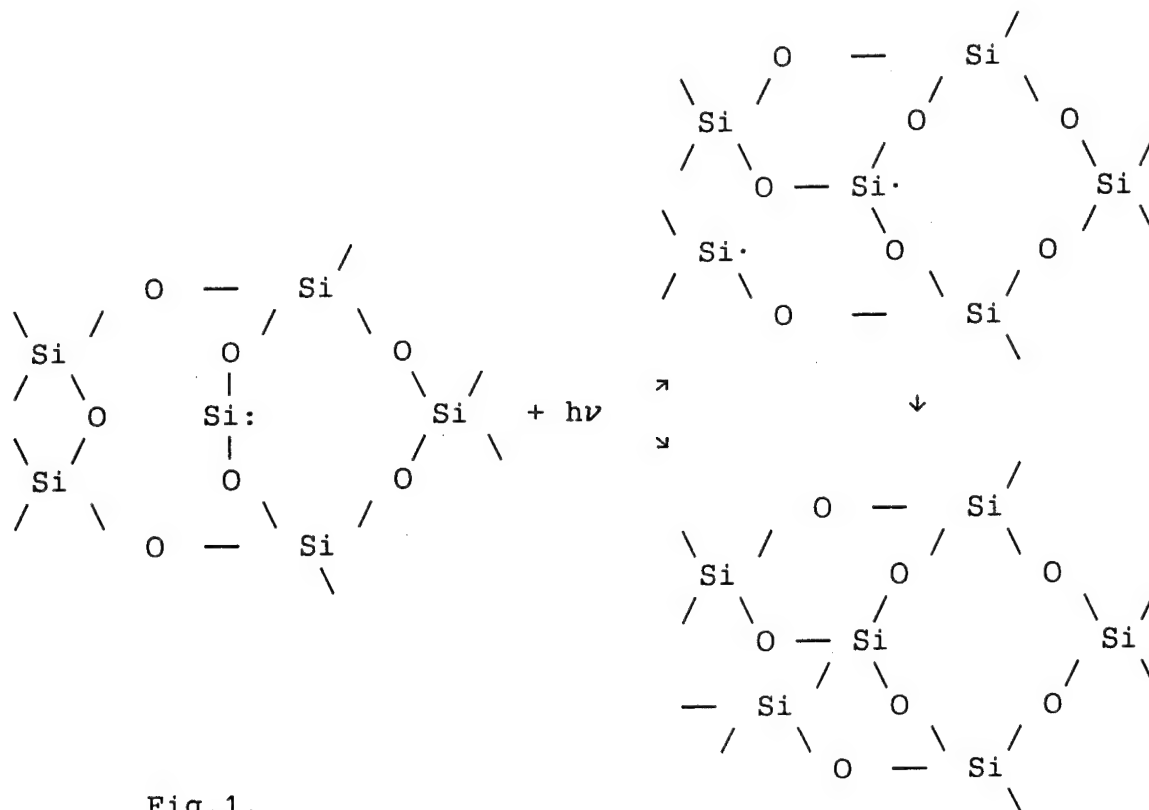
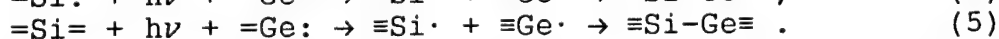
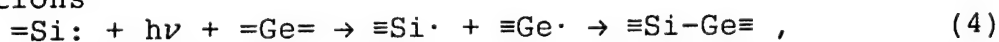


Fig.1.

absorption band 7.6 eV. Relatively slow dissipation rate of photoexcitation has naturally to be accounted for a charge transfer during the rearrangement of microstructure instead for thermalization of electrons at electron traps.

Photobleaching of the most photosensitive $B_2\alpha$ and of $B_2\beta$ bands in $\text{SiO}_2\text{:GeO}_2$ glasses is accordingly described by reactions

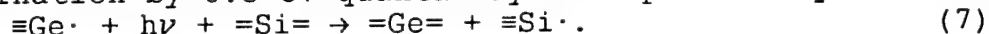


E' -centers $=\text{Si}\cdot$ unlike $=\text{Ge}\cdot$ in the glass were not observed [9] and the reason was apparently in high probability of reaction



because of binding energy of Si-O is higher of Ge-O. Structural formula of the rearrangement is shown in Fig.2.

However an appearance of 5.8 eV absorption band after illumination by 6.5 eV quanta may be explained by reaction



Conclusion

Photosensitivity of ODC doped silica glasses is governed by photochemical reactions of ODC. Photosensitivity of $=\text{Si}: \text{ODC}$ at 5.0 eV in germanosilicate glasses is higher than that of $=\text{Ge}: \text{ODC}$ at 5.1 eV. Room temperature photoinduced solid-state chemical reactions appear to be thermodynamically nonequilibrium owing to local quenching. Such a conception is confirmed by analysis of ODC doping technique. Thermal heating of the glasses up to ≈ 2 kK gives rise to ODC concentrations of $10^{16} - 10^{18} \text{ cm}^{-3}$ [13] and created ODC can be frozen by

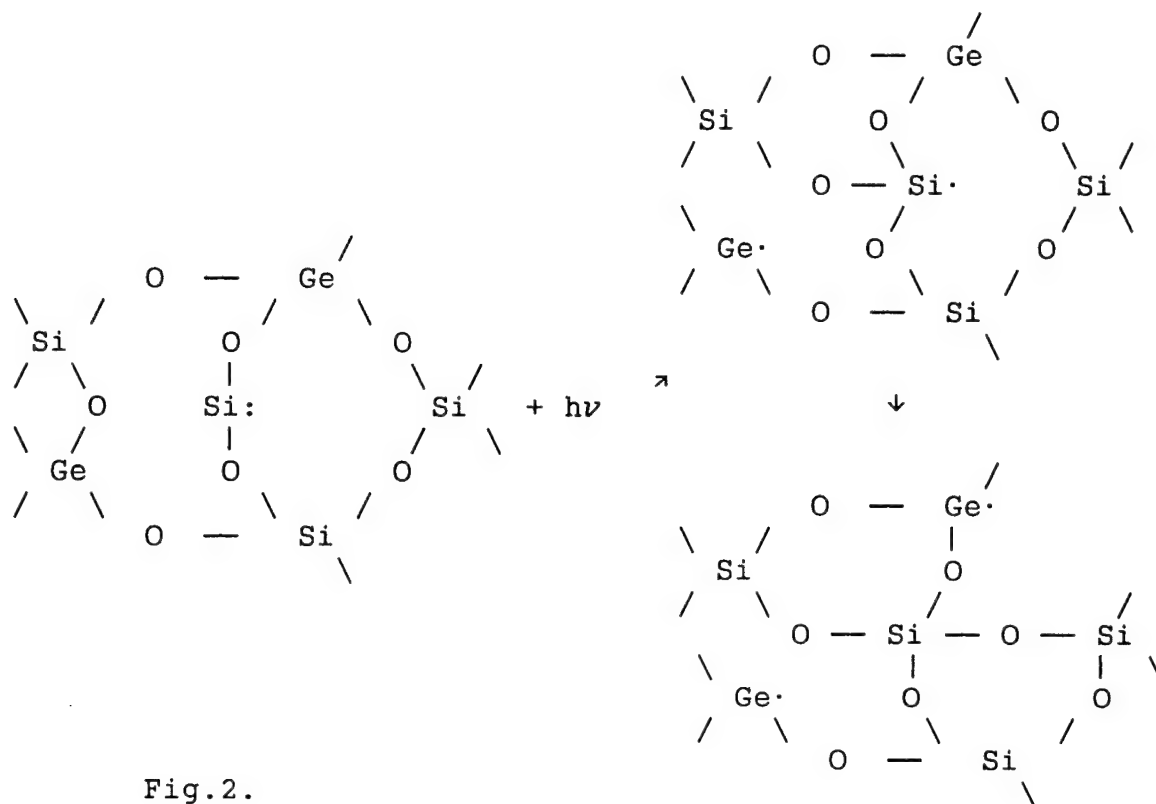


Fig.2.

quenching [10]. Concentration of ODC was reduced by annealing. Two orders higher magnitudes have reached by low temperature chemical H_2 treatment [9]. The highest ODC concentrations of $\sim 10^{20}$ - 10^{21} cm^{-3} obtained by e-irradiation [14] and ion implantation [15] are probably due to combination of switching and quenching of valent bonds. Microstructural nonequilibrium after UV illumination looks like a reason of internal stresses revealed by the birefringence and by the change of glass density accompanied by increasing of refraction index.

References

1. Dong L. et al. Proc. ECOC'94, 1994, v.2, 997-1000.
2. Fonjallaz P.Y. et al. Proc. ECOC'94, 1994, v.2, 1005-1008.
3. Skuja L. J.Non-Cryst.Solids, 1992, v.149, No.1,2, 77-95.
4. Griscom D.L. J.Ceram.Soc.Japan, 1991, v.99, 899-916.
5. Bagratashvili V.N. et al., XVI Intern. Congr. on Glass, Proc., Madrid, S. E. de Ceramica y Vidreo, 1992, v.4, 539-545.
6. Neustrujev V.B. J.Phys.: Cond.Matt., 1994, v.6, 6901-6936.
7. Williams D.L. et al. Proc. SPIE, 1993, v.2044, 55-68.
8. Sokolov V.O. et al. Phys.Stat.Sol.B, 1994, v.186, 185-198.
9. Awazu K. et al. Proc. SPIE, 1993, v.2044, 78-87.
10. Lebedev V.F. et al. Quantum electr., 1994, v.24, 1020-1022.
11. Rothschild M. et al. Appl.Phys.Lett., 1989, v.55, 1276-1278.
12. Trukhin A.N. et al. J.Non-Cryst.Solids, 1992, v.149, 96-101.
13. Silin A.R. et al. J.Non-Cryst.Solids, 1992, v.149, 54-61.
14. Pfeiffer R.L. J.Appl.Phys., 1985, v.57, 5176-5180.
15. Hosono H. et al. In: XVI Intern. congr. on glass, v.3, S.E.de Ceramica y Vidrio, Madrid, 1992, 33-34.

Dynamics of ultraviolet induced luminescence and fiber Bragg grating formation in the high fluence regime.

Mikael Svalgaard
Microelectronics Center,
Technical University of Denmark,
Bld. 345 east, DK-2800 Lyngby, Denmark
Tel. +45 4525 5711, Fax +45 4588 7762

Germanosilicate glass exhibits a strong absorption band at 240 nm which can be bleached upon excitation with UV radiation. Simultaneously, a permanent increase of the refractive index at longer wavelengths is seen. Experimental results indicate that the UV absorption band is due to germanium related oxygen deficient centers (GODC's). Excitation and bleaching of these defects triggers a range of not fully understood processes which are responsible for the UV induced index change. Photoluminescence (PL) bands at 290 nm and 400 nm have also been associated with GODC excitation and a correlation between the 400 nm PL dynamics and the dynamics of the index change has been reported ¹. Other experiments indicate increased concentrations of Ge-related drawing induced defects (Ge-DID), associated with 650 nm luminescence, following UV irradiation of germanosilicate fiber preforms ². Recent experiments have shown that UV induced index changes can be strongly non-linear as a function of the exposure time, with several maxima occurring during one UV exposure ³. In this paper we report results indicating that these non-linearities may be associated with a corresponding behavior of the UV induced luminescence.

The investigation is limited to three single mode germanosilicate optical fibers, provided by LYCOM, containing 3.2, 21 and 25 mol % Ge with core diameters of 8.8, 2.9 and 2.0 μm , respectively. The fibers were irradiated with a continuous wave frequency doubled Ar^+ laser producing up to 150 mW of 244 nm radiation with an approximately Gaussian intensity distribution. Two UV irradiation schemes were applied: one using a cylindrical lens and a phase mask and another using a single focusing lens without the phase mask.

Fiber Bragg gratings were produced by focusing the laser to a $\sim 20 \times 3000 \mu\text{m}^2$ (FWHM) spot size and irradiating a fiber placed 1 mm behind the silica phase mask. The mask period was 1.06 μm with <5% of the transmitted power in the zero order diffraction, about 75% in the ± 1 st orders and the remaining power in higher orders. Grating transmission spectra could be monitored with a broad band LED on a spectrum analyser placed at the fiber end. Luminescence was also monitored on the spectrum analyser during grating exposures, however, these measurements should be interpreted with caution since photodarkening effects⁴ could not be avoided, due to the long length of irradiated fiber.

Effects of time- and wavelength dependent photodarkening were reduced by using a plano convex lens to achieve a circular UV spot with a diameter of $\sim 40 \mu\text{m}$ (FWHM). A weak 442 nm probe signal transmitted through the fiber during some UV exposures was used to verify that effects of photodarkening on the luminescence signal were reduced below the noise level (<5%).

The UV laser and LED were continuously monitored to ensure that any instabilities were insignificant. Furthermore, very stable mounting of the phase mask and optics was performed.

Spectral luminescence measurements generally revealed the bands reported by others at 650 nm and 400 nm. Avoiding effects of photodarkening we investigated the band dynamics for UV intensities ranging from 10^2 - 10^4 W/cm^2 . A typical measurement is shown in figure 1 where

the 400 nm and 650 nm luminescence signals were monitored for the 3.2 mol% fiber with a UV intensity of 6 kW/cm². The 400 nm signal exhibits a rapid initial decay, gradually slows down and finally reaches a constant level at ~5% of the initial value. The 650 nm signal showed a more complicated behavior with multiple periods of growth and saturation, slowing down as time increases. With exposure times of several hours we observed five (possibly six) such periods in the 650 nm dynamics with the 3.2 mol % fiber. Decreasing the UV intensity resulted in slower - but not qualitatively different - evolutions. The fibers with 25 and 21 mol % Ge showed a similar behavior. However, the overall PL intensity was about one order of magnitude lower. At ~100 W/cm² the 400 nm signal bleached about twice as fast in the Ge rich fibers. A much more dramatic difference was seen with the 650 nm signal which, at a similar UV intensity, evolved 15-20 times faster.

Typical results obtained during 6 hours of grating enscription at 100 W/cm² with the 25 mol% fiber are shown in figure 2. Although photodarkening effects could not be separated from the PL measurements, the qualitative dynamical features were the same as before. The 650 nm signal reached two plateaus and approached a third while the 400 nm signal decayed smoothly to 20% of its initial value. The Bragg grating evolution is complex with several periods consisting of increasing reflectivity followed by saturation and decrease. Two such periods have been fully observed while a third period of growth begins after $\sim 1 \times 10^4$ sec. The third period occurred too slowly for us to observe saturation. The peak reflectivity of the second period is 93% and thus higher than the 75% reached during the first period. The Bragg wavelength also experienced a complex evolution, increasing during the first growth period and saturating after a positive change of 0.5 nm, corresponding to a index change of 5×10^{-4} . During the second period the Bragg wavelength experienced a small (reproducible) *negative* change, corresponding to a negative index change. Note the correlation between the 650 nm PL intensity and the grating characteristics, illustrated by horizontal and vertical bars in figure 2. Horizontal bars indicate three time periods, each one corresponding to a growth and saturation cycle of the 650 nm signal, while the vertical bars illustrate that transitions between 650 nm PL periods correlate with occurrences of reflectivity and Bragg wavelength saturation.

Similar grating experiments with the 21 mol % Ge fiber with exposure times of 10 hours yielded results similar to those described above. However, the time evolution of the grating and luminescence occurred somewhat slower, so that only two periods of 650 nm and grating growth dynamics were observed. A correlation between the 650 nm PL periods and periods of grating growth was also noted for this fiber. Experiments with the 3.2 mol % Ge fiber showed the slowest rate of evolution, with the Bragg grating exhibiting the dynamics often reported by others; i.e. a fast initial increase followed by decelerating rate of reflectivity change. The Bragg wavelength increased by 0.58 nm during 8.5 hours of UV exposure with 150 W/cm² and did not show any sign of saturation. The more 'ordinary' grating dynamics observed with this fiber show that the complex behavior observed with other fibers is a fiber intrinsic effect and not due to peculiarities of the enscription method.

When comparing dynamics of the effective index change (deduced from the Bragg wavelength evolution) with the 400 nm PL, our results imply that a correlation between 400 nm PL bleaching and index change, as suggested by Duval et al., does not hold in general for large fluences. For fluences in the range of several MJ/cm² the 400 nm PL approaches a constant level while the index change shows no sign of saturating. However, our results support the notion that faster evolution of the index change is associated with faster initial luminescence bleaching.

Other workers⁵ have shown that UV irradiation of pure silica gives rise to a 650 nm PL band due to excitation of non bridging oxygen hole centers (NBOHC; structure $\equiv \text{Si}-\text{O}^\bullet$). Our observation of 650 nm PL during UV exposure suggests the NBOHC as being the source of luminescence via a similar process. We observed that the luminescence originated from the Ge doped core and not the silica cladding, thus the presence of Ge must somehow also be involved

in the process. The final observation to note, is that the 650 nm PL intensity generally increases during UV exposure. To explain these features we suggest that the GeO defect (a twofold coordinated Ge atom in the Ge^{2+} valence state, $\equiv\text{Si-O-Ge}^{2+}\text{-O-Si}\equiv$) is not photo-chemically stable. The GeO defect is known to give rise to a absorption band at 240 nm, and the electronic excitation could result in breakage of the bond to one of the two neighboring oxygen atoms. This would yield one free electron while the oxygen atom involved would form a NBOHC. This hypothesis could explain why 650 nm luminescence is seen only where Ge is present and also that the band intensity increases during UV exposure.

In conclusion, we have investigated the dynamics of UV induced luminescence and index change in germanosilicate fibers with a continuous wave laser for fluences up to $\sim 10^7 \text{ W/cm}^2$. In general two luminescence bands at 400 nm and 650 nm were observed. We have shown that the 400 nm band is photobleached and reaches a steady state at 5-10% of the initial level, while the refractive index continues to increase. Therefore the degree of 400 nm PL bleaching cannot in general be associated with a given index change. The 650 nm PL band was found to increase during UV exposure and has been associated with NBOHC production that we suggest arises from UV induced GeO defect ionization. The 650 nm band and Bragg grating dynamics were shown to be correlated and followed a complicated evolution with multiple periods of growth and saturation that cannot be explained at this time.

References:

1. Y. Duval, R. Kashyap, S. Fleming, F. Ouellette, Appl. Phys. Lett. 61(25), 2955 (1992)
2. J Canning, M.G. Sceats, Opt. Lett. 19(15), 1119 (1994)
3. W.X. Xie, P. Niay, P. Bernage, M. Douay, Opt. Comm. 104, 185 (1993)
4. H. Patrick, S.L. Gilbert, A. Lidgard, Opt. Mat. 3, 209 (1994)
5. R. Tohmon, Y. Shimogaichi, S. MuneKuni, Y. Ohki, Y. Hama, Appl. Phys. Lett. 54(17), 1650 (1989)

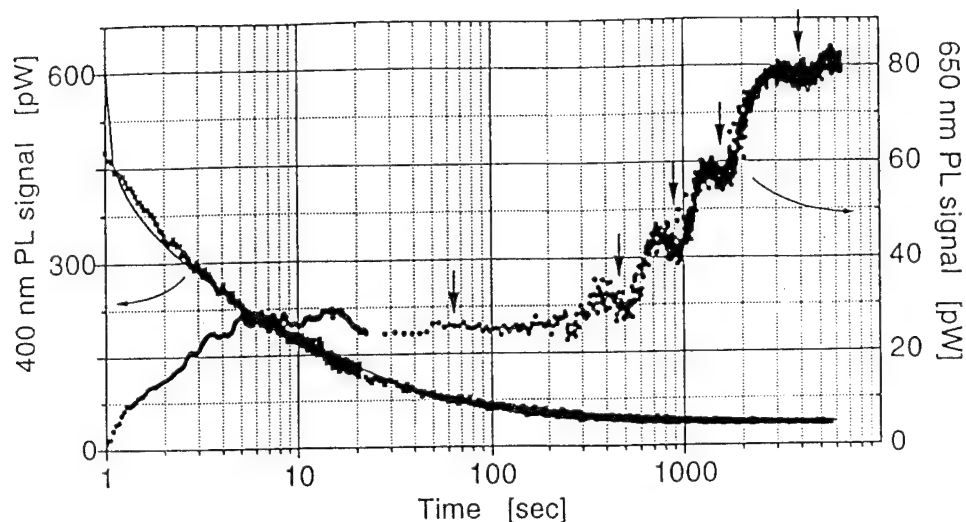


Figure 1: Dynamics of the 400 nm and 650 nm luminescence bands during UV exposure (3.2 mol% Ge fiber, $I_{UV} = 6 \text{ kW/cm}^2$, UV on at $t = 1 \text{ sec}$). Note the multi-period structure of the 650 nm dynamics, as indicated by the small arrows.

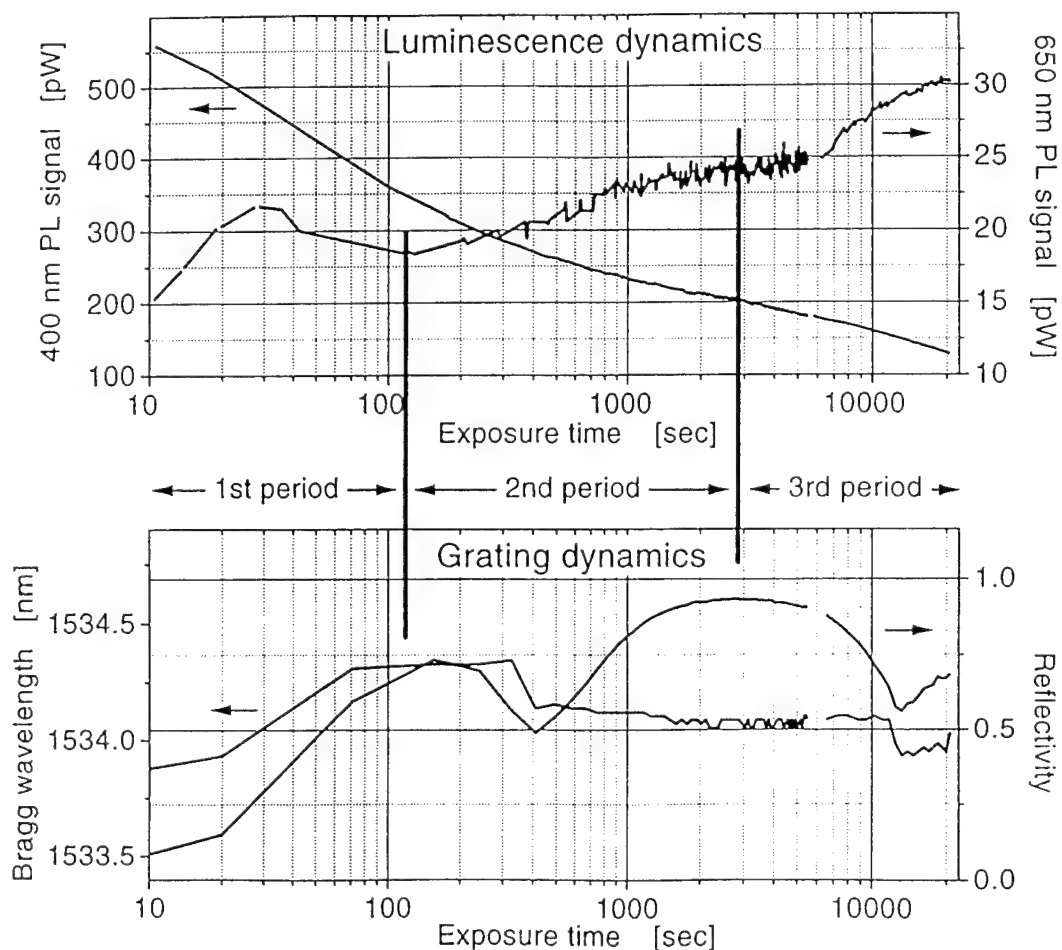


Figure 2: Time evolution of luminescence bands, grating reflectivity and Bragg wavelength during UV exposure (25 mol% Ge fiber, $I_{UV} = 100 \text{ W/cm}^2$, UV on at $t = 1 \text{ sec}$). Horizontal bars indicate three periods of 650 nm luminescence dynamics, while the vertical bars illustrate that these periods are correlated with saturation of grating reflectivity and Bragg wavelength.

Sunday, September 10, 1995

Poling I

SuC 1:30–3:00pm
Multnomah Room

Roger H. Stolen, *Presider*
AT&T Bell Laboratories

GLASS FIBRE POLING AND APPLICATIONS

P.G. Kazansky, V. Pruneri, A.R Smith, O. Sugihara, L. Dong and P.St. J. Russell

Optoelectronics Research Centre, University of Southampton,
Southampton S017 1BJ, United Kingdom

Glass is a dominant material in fibre-optics technology. Recently, the discovery that dopants such as Ge and Ce render silica glass photosensitive has made possible the routine fabrication of important passive components such as fibre Bragg gratings. The absence of a second-order nonlinearity in glass however makes impossible the fabrication of active components such as modulators, switches, parametric frequency converters and frequency doublers. Thus, when efficient photoinduced second-harmonic generation was first discovered in fused silica fibres, wide-ranging studies ensued into the mechanism and properties of this unexpected phenomenon. Nonetheless, until fairly recently second harmonic generation in specially treated glasses and glass fibres has been of more scientific than practical interest, owing to levels of nonlinearity that were typically 3-4 orders of magnitude less than in the best nonlinear crystals¹⁻³.

During the past several years, however, second-order nonlinearities ~ 1 pm/V have been achieved in glasses using a variety of different techniques: thermal poling⁴, corona poling⁵ and electron implantation^{6,7}. These observations have excited considerable interest because they offer the prospect of linear electro-optic modulators and frequency converters monolithically integrated into optical fibres or planar glass waveguides⁸⁻¹⁵.

To date the thermal poling technique is the most promising. The nonlinearity is extremely stable and shows no degradation under illumination with intense visible and infrared light.

Electro-optic phase modulation has been demonstrated in a thermally poled fused silica channel waveguide made by electron implantation¹⁶ and an electrooptic coefficient of about 0.3 pm/V has been measured in thermally poled silica glass¹⁷. Quasi-phase-matched frequency doubling of Q-switched Nd:YAG laser light at 1064 nm has been demonstrated in thermally poled silica glass¹⁸. The nonlinear coefficients, especially for electrooptic effect, are still small, and so require long interaction lengths. This is not a significant problem in fibre applications where the issues are cost, integrability and packaging, not length.

We now review recent developments in the application of poled optical fibre to electrooptic light modulation and second harmonic generation.

The first successful thermal poling of optical fibre was reported in 1994¹⁹ and substantial improvements in the reproducibility and quality of the induced nonlinearity were obtained by vacuum poling²⁰. The effective value of second order nonlinearity was about 0.2 pm/V.

The linear electrooptic effect has also been measured in poled silica fibres²¹⁻²³ and an electrooptic coefficient of 0.05 pm/V obtained.

Recently, periodically patterned second-order nonlinearities were created using thermal poling in vacuum and cw quasi-phase-matched frequency conversion to the blue in thermally poled

silica fibres was demonstrated²⁴. The bandwidth measured was 0.78 nm·cm, which is an order of magnitude larger than in an equal length of periodically poled bulk lithium niobate (0.06 nm·cm). Moreover, the group velocity mismatch at 860 nm is about 130 fs/mm in silica, compared to 1.8 ps/mm in lithium niobate. This may be of importance in short pulse work, where large acceptance bandwidths and long interaction lengths are desirable.

The effective nonlinear coefficients in poled fibres are still small. Considerable improvements are expected by optimizing the poling process, in particular by improving the overlap of the fibre modes and the poled layer and improving the fibre poling technology.

Last but not least, an electrooptic coefficient of about ~ 6 pm/V has been reported in germanosilicate fibre poled via internal electrodes²⁵. Although UV excitation was used, it seems that this is not the major factor responsible for the high value measured. Indeed, even without UV excitation the measured coefficient is comparable to the one obtained in thermally poled fibres, and two to three orders of magnitude higher than in prior experiments made in fibres with internal electrodes³. The structure of the fibre used, in particular high Ge concentration, may be responsible. Further experiments are necessary to clarify the mechanism behind this excited result.

In conclusion, better understanding of the physical mechanisms behind glass poling²⁶⁻²⁷ may lead to even higher values of nonlinearity and thence to the development of a range of new fibre devices.

References

1. U. Österberg and W. Margulis, *Opt. Lett.* **11**, 516 (1986).
2. M.-V. Bergot, M.C. Farries, M.E. Fermann, L. Li, L.J. Poyntz-Wright, P.St.J. Russell and A. Smithson, *Opt. Lett.* **13**, 592 (1988).
3. L. Li and D.N. Payne in *Digest of Conference on Integrated and Guided Wave Optics* (Optical Society of America, Washington, D.C., 1989), paper TuAA2-1.
4. R.A. Myers, N. Mukherjee and S.R.J. Brueck, *Opt. Lett.* **16**, 1732 (1991).
5. A. Okada, K. Ishii, K. Mito and K. Sasaki, *Appl. Phys. Lett.* **60**, 2853 (1992).
6. P.G. Kazansky, A. Kamal and P.St.J. Russell, *Opt. Lett.* **18**, 693 (1993).
7. P.St.J. Russell, P.G. Kazansky and A. Kamal, *SPIE* **2044**, 192 (1993).
8. K. Tanaka, K. Kashima, K. Hirao, N. Soga, A. Mito and H. Nasu, *Jap.J.Appl.Phys.*, **32**, 843 (1993).
9. H. Nasu, H. Okamoto, K. Kurachi, J. Matsuoka, K. Kamiya, A. Mito and H. Hosono, *J. Opt. Soc. Am.* **B**, **12**, 644 (1995).
10. P.G. Kazansky, A. Kamal and P.St.J. Russell, *Opt. Lett.* **19**, 1141 (1993).
11. K. Tanaka, K. Kashima, K. Hirao, N. Soga, S. Yamagata, A. Mito and H. Nasu, *Jpn. J. Appl. Phys.*, **34**, 173 (1995).
12. K. Tanaka, K. Kashima, K. Hirao, N. Soga, S. Yamagata, A. Mito and H. Nasu, *Jpn. J. Appl. Phys.*, **34**, 175 (1995).
13. L.J. Henry, A.D. DeVilbiss, T.E. Tsai and D.L. Griscom, to be published in *J. Opt. Soc. Am.* **B** (1995).
14. J.M. Dell and M.J. Joyce, *Australian Optical Society* (1993).
15. Y. Zhao, G. Town and M. Sceats, *Opt. Comm.*, **115**, 129 (1995).
16. A.C. Liu, M.J.F. Digonnet and G.S. Kino, *Opt. Lett.*, 1994, **19**, 466 (1994).
17. X-C. Long, R.A. Myers, and S.R.J. Brueck, *Opt. Lett.*, **19**, 1819 (1994).
18. R. Kashyap, G.J. Veldhuis, D.C. Rogers and P.F. McKee, *Appl. Phys. Lett.*, **64**, 1332 (1994).
19. P.G. Kazansky, L. Dong and P.St.J. Russell, *Opt.Lett.*, **19**, 701 (1994).
20. P.G. Kazansky, L. Dong and P.St.J. Russell, *Electron. Lett.*, **30**, 1345 (1994).
21. P.G. Kazansky, P.St.J. Russell and C.N. Pannell, *Electron. Lett.*, **30**, 1436 (1994).

22. X.-C. Long, R.A. Myers and S.R.J. Brueck, *Electron. Lett.*, **30**, 25 (1994).
23. P.G. Kazansky, P.St.J. Russell, L. Dong and C.N. Pannell, *Electron. Lett.*, **31**, 62 (1995).
24. P.G. Kazansky, V. Pruneri and P.St.J. Russell, *Opt. Lett.*, **20**, 843, (1995).
25. T. Fujiwara, D. Wong, Y. Zhao, S. Fleming, S. Poole and M. Sceats, *Electron. Lett.*, **31**, 573 (1995).
26. N. Mukherjee, R.A. Myers and S.R.J. Brueck, *J. Opt. Soc. Am.* **B**, 665 (1994).
27. P.G. Kazansky and P.St.J. Russell, *Opt. Comm.*, **101**, 611 (1994).

CREATION OF OPTICAL NONLINEARITY IN ORGANIC POLYMER-DYE FILMS BY ASYMMETRIC CHARGE INJECTION

G. Berkovic, R. Cohen, A. Donval, B. Lavi and R. Yam

Department of Materials and Interfaces

Weizmann Institute of Science

Rehovot 76100 Israel

Tel : + 972-8343423 Fax: + 972-8344138 e-mail : csberk@weizmann.weizmann.ac.il

Bulk second order optical nonlinearity in organic polymers containing hyperpolarizable dye molecules is normally created by electrostatic field poling at elevated temperature, where the electric field induces a polar alignment of the dyes. In contrast to this approach, we have used asymmetric injection of electric charge into the polymer to create bulk nonlinearity in the polymer [1]. We show that the charge injection mechanism is fundamentally different from dipole alignment of the dye, and has both similarities and differences to poling of glass.

Charge injection effects are best exhibited when electric fields are applied to polymers films in an 'in-plane' geometry - see Figure 1. Using high voltages but only moderate fields (2000 V across 2mm) charge injection effects can be significant, especially at room temperature. Figure 2 shows how charges injected from the electrodes can break the bulk symmetry of the polymeric medium by setting up a charge gradient along the sample z direction (normal to the film plane). Second-order nonlinear optical effects are observed along the z-direction e.g. optical second harmonic generation (SHG) via the $\chi_{zzz}^{(2)}$ coefficient, even though the externally applied electric field is along the x-direction.

Studies have been carried out in poly-(methyl methacrylate) host polymers doped with optically nonlinear stilbene and azo dyes such as DANS and Disperse Red. Application of 2000 V across the Al electrodes leads to charge injection and current flows of several microamps through the polymer. The symmetry breaking can lead to SHG coefficient as high as $\chi_{zzz}^{(2)} = 10^{-8}$ esu. The current flow and resulting nonlinearity can be varied significantly by changing the substrate, metal electrode material, etc.

The spatial distribution of the resultant optical nonlinearity in the sample has been probed along both the x and z directions. The distribution along x is probed by measuring SHG using a laser focused at various positions between the electrodes [2]. In the first few seconds after charge injection begins, optical nonlinearity is created only near the positive electrode, indicating that hole injection is dominant. However after several minutes almost uniform nonlinearity is created across the entire sample. Polarization along the z-direction has been probed by pyroelectric depth profiling [3], and reveals the anisotropic distribution shown in Figure 2, which has been fitted to an exponentially decaying distribution along z.

This method for inducing $\chi^{(2)}$ in polymers bears some resemblance to poling of glass, as both mechanisms depend *macroscopically* on injection and trapping of (primarily positive) charges into the host. However, on the *microscopic* level there are significant differences to both regular polymer poling and glass poling. Since charge injection can induce $\chi^{(2)}$ at room temperature the nonlinearity is not created by dipolar alignment of dyes. Furthermore, the observed $\chi^{(2)}$ values are much too high to have been created via the $\chi^{(3)}$ properties of the polymer-dye film and the induced (space charge) field.

Consequently, we have proposed a model whereby charged dye dimers and quadrupolar nonlinearities are responsible for the nonlinearity in a charge gradient [1]. This model has been supported by spectroscopic and theoretical studies [4] which will be discussed.

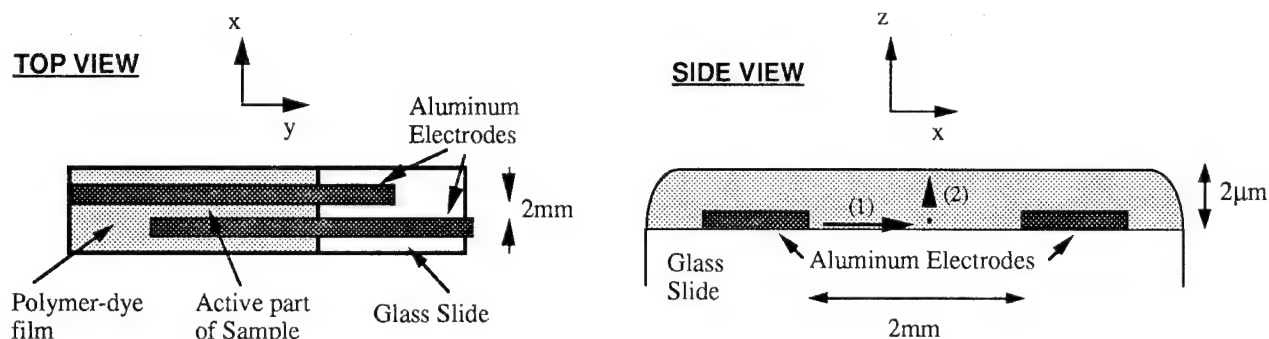


Figure 1. Geometry of samples used for generating optical nonlinearity by asymmetric charge injection. When voltage is applied across the electrodes some current flows {shown by arrow (1) in the side view}. Some of the injected charges will diffuse in the perpendicular direction {broken arrow (2)} and be trapped in the polymer.

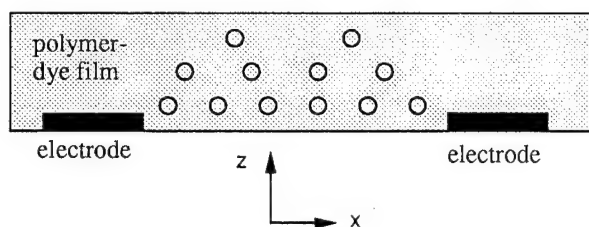


Figure 2. Resultant distribution of charges (circles) in the polymer-dye film resulting from charge injection in the geometry shown in Figure 1. Trapped charges are distributed anisotropically along the z-direction, and approximately uniformly along the x-direction.

References

- [1] S. Yitzchaik, G. Berkovic and V. Krongauz, *Nonlinear Optics* 4 (1993) 265.
- [2] R. Cohen, G. Berkovic, S. Yitzchaik and V. Krongauz, *Mol. Cryst. Liq. Cryst.* 240 (1994) 169.
- [3] S. Bauer, *J. Appl. Phys.* 75 (1994) 5306.
- [4] P. M. Lundquist, S. Yitzchaik, T.J. Marks, G.K. Wong, R. Cohen, G. Berkovic and S. DiBella, paper QMA3, CLEO/QELS '95, Baltimore 1995.

Frequency Doubling in Thin Film Waveguides of Borate Glasses

Keisuke Sasaki and Suguru Horinouchi

Faculty of Science and Technology ,Keio University

3-14-1 Hiyoshi Yokohama 223 Japan

1. Introduction

Rf sputtered multi-component glass films on pyrex substrates exhibited novel quadratic optical nonlinearity by corona poling which was applied for the second harmonic generation in blue-green range^{1),2)}. Maker fringe method proved that d_{33} values of the films was up to 0.6 pm/V at appropriate sample preparation condition. Resistivities of substrate glasses remarkably related to efficient poling. Borate component of multi-component glasses gave some effects to establish the quadratic nonlinearity coming from macroscopically noncentrosymmetric structure of the films. Also boundary situations and combinations of each layers gave influences to decay of the nonlinearity.

2. Sample Preparations

Four types of glass plates which had different volume resistivities as tabulated in Table 1 were tried as substrates of rf sputtered glass film waveguides.

	SiO ₂	B ₂ O ₃	BaO	Al ₂ O ₃	d_{33} (pm/V)
Corning7059	62.64	12.52	16.54	7.53	0.6
Asahi-AN	59.28	15.9	16.4	8.41	0.6
fused quartz	>99.9	-	-	-	0.2

Table 1

Pyrex substrate was best for the sample preparation. Also three types of sputtering target glass plates were tried to prepare the waveguide films as tabulated in Table 2.

	d_{33} (pm/V)	volume resistivities (Ωm)
Pyrex glass	0.6	10^{13}
Fused silica	~ 0	10^{17}
Corning 7059	~ 0	10^{20}
Soda-lime glass	0.05	10^{10}

Table 2

Typical corona poling was carried out by DC. 10 kV for 10 mm spacing distance, at room temperature for 12 hours.

3. Experiments and discussions

d_{33} values were saturated over about ten hours of poling period for Corning 7059/pyrex as shown in Fig 1. Thickness-dependent d values also is shown in Fig.2. Two curves correspond to Maker fringe measurements of just after poling and after a hundred hours respectively.

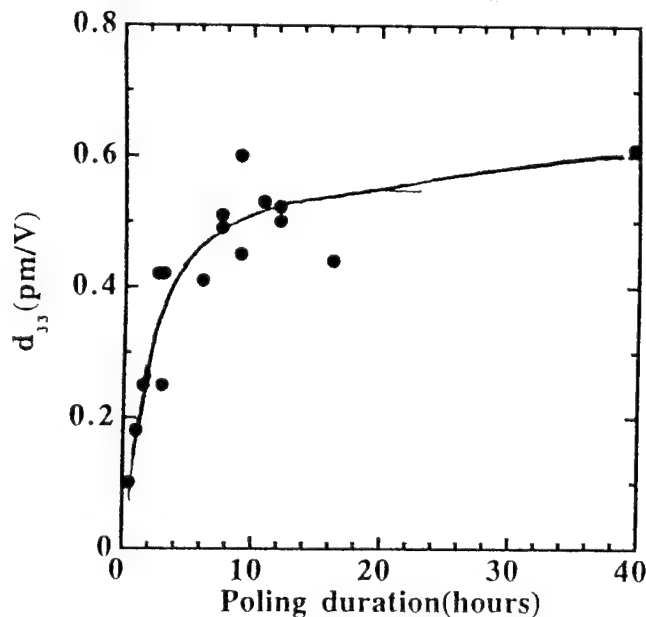


Fig 1

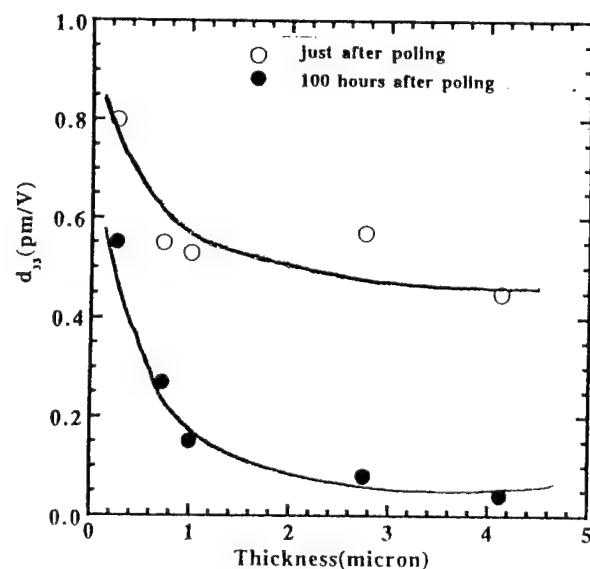


Fig 2

Thinner films exhibited large d values and their slow relaxations. Three types of glass film waveguides which were rf sputtered on pyrex substrates and corona-poled showed relaxation characteristics as shown in Fig 3. Corning 7059 and Asahi-AN films exhibited quick saturations of d values in spite of very steep

decay at the initial stage. On the other hand, d value of fused quartz film went down to zero within a week. This difference is due to existences of components, BaO and B₂O₃ in the former two glasses.

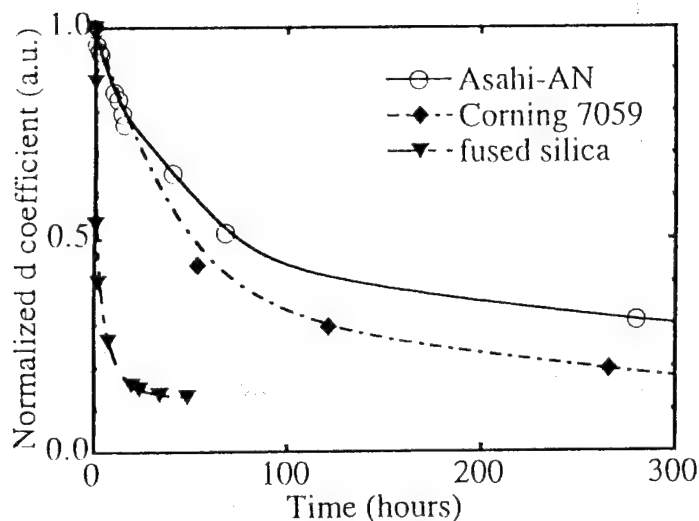


Fig 3

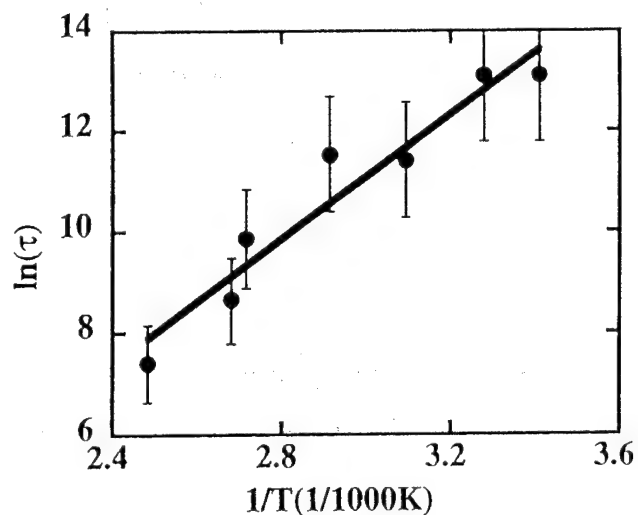


Fig 4

The authors like to infer that one of the main origine of the novel quadratic nonlinearity is related to anisotropic distributions of deeply trapped electrons concentrating near surface boudary of the films. And the multi-components in the glass films contribute to establishing distributed deep traps.

Curve fitting by the stretched exponential function³⁾ gives an averaged activation energy, 0.5 eV as shown in Fig 4.

Acknowledgements

The authors would like to express of their appreciations to their colleagues in Keio University, H.Yamazaki, H.Imai, K.Fukao, G.Zhang, K.Mito and K.Hirashima.

References

- 1) A.Okada, K.Ishii, K.Mito and K.Sasaki: Appl. Phys. Lett. 60 2825 (1992).
- 2) A.Okada, K.Ishii, K.Mito and K.Sasaki: J. Appl. Phys. 74 531 (1993).
- 3) K.D.Singer and L.A.King: J. Appl. Phys. 70 3251 (1991).

LASER INDUCED PRESSURE PULSE PROBE OF CHARGE DISTRIBUTION IN THERMALLY POLED GLASS: EVIDENCE OF DIPOLE POLARIZATION?

P.G. Kazansky, A.R. Smith and P.St.J. Russell

Optoelectronics Research Centre, University of Southampton,
Southampton SO17 2BJ, United Kingdom

G. M. Yang and G. M. Sessler
Institute for Electroacoustics, Technical University of Darmstadt,
Darmstadt D-64293, Germany

In recent years, thermal poling of silica-based glasses has been shown to create permanent second-order nonlinearities (SON) of the order of 1 pm/V in bulk glass [1] and 0.2 pm/V in thermally poled optical fibre [2]. Despite the reproducibility and stability of the effect, the underlying mechanism has still not been fully elucidated.

In thermal poling of fused silica, samples 1-3 mm thick are heated to about 280°C with an applied voltage of about 5 kV, the second-order nonlinearity being observed near the anodic surface [1] and in the whole volume of the glass sample [3]. It has been suggested that a high electrostatic field, appearing in a thin depletion region near the anodic surface, is responsible for the anodic poling phenomenon. Indeed, under the action of the applied field, cations (such as Na⁺ and H⁺) will drift to the cathode leaving behind a *negatively* charged layer near the anodic surface. A high electrostatic field will then appear in this layer, peaking at the interface between the *negatively* charged layer and the anode.

In one scenario, this field creates a permanent $\chi^{(2)}$ by orientation of dipoles (or bonds) [4]. In another scenario [5], the very high field at the glass/anode boundary causes ionization of the glass (or perhaps the air gap), leading to the creation of a *positively* charged layer at the anodic surface. A high field then appears between this layer and the remaining *negatively* charged depletion layer deeper in the glass.

Experimental support for the second mechanism was obtained by testing the ratio of nonlinear tensor components and the spatial distribution of the induced $\chi^{(2)}$. These do not, however, disprove the dipole polarization mechanism [5]. Therefore, other experiments which yield further information about the charge distribution inside the glass are necessary for clarification of the mechanism. An example is the Laser Induced Pressure Pulse (LIPP) method, which is widely used for characterisation of the charge distribution in electrets [6,7]. In this paper we report for the first time the use of this method to map the charge profiles in thermally poled silica glass samples.

Fused silica glass samples were poled at 280°C at 5 kV applied voltage in an air atmosphere. During poling, the thinner samples I, II and III (~100 μ m thick) were placed on top of a ~3 mm thick supporting substrate of Herasil 1 (this avoided electrical breakdown of the sample). They were then poled for 45 min, 15 min and 5 min respectively. Samples IV and V (~1 mm thick) were poled for 15 min. Samples I, II, III and IV were poled via a pressed-on electrode, and sample V was poled via a sputtered aluminium anodic electrode about 300 nm thick. Similar aluminium electrodes were sputtered (*after* poling) on to the cathode side

of each of the samples I, II, III and IV. Sputtered aluminium electrodes were used as front electrodes in all our LIPP studies (Fig.1).

In the LIPP measurements, single laser pulses of about 70 ps duration and 50 mJ energy, generated by a Nd:YAG laser, were used. These pulses were incident on an absorbing layer coated on to the front electrode of the samples. This excites acoustic pulses of < 500 ps duration in the samples (Fig.1). The resulting pressure pulse causes any free charge to move, giving rise to an electrical current proportional to the sum of space-charge density and dipole-polarization gradient. The time axis can be transformed into a depth scale via the longitudinal sound velocity, which is approximately 5.95 km/s in fused silica (Fig.2). With these pulses, the spatial resolution of the LIPP technique turns out to be of about $3 \mu\text{m}$. No LIPP signal was observed near the cathodic side of the samples. The cathodic side in sample I corresponds to positions 1, 3 and 5 of the pressure pulse (Fig.2a).

The first group of LIPP signals is generated after a single pass of the pressure pulse along the sample. The second group of signals is generated by the pressure pulse after one reflection from the rear (anodic) surface and one reflection from the front (cathodic) surface of the sample. And the third group of signals is generated by the pressure pulse after two reflections from the rear (anodic) surface and two reflections from the front (cathodic) surface of the sample. The positive signal spikes in positions 2, 4 and 5 correspond to a positive charge on the anodic surface and the two symmetrical spikes on both sides of the positive spike correspond to a negative charge at a depth of about $5.5 \mu\text{m}$ below the anodic surface. The first negative spike is caused by the incident acoustic pulse and the closely spaced second negative spike by the reflected pulse. The measured ratio of LIPP signals in samples I, II and III poled for different times is about 9:3:1.

We were surprised to observe that the LIPP scans of the samples IV and V revealed completely the opposite charge distribution (Fig.2b and Fig.2c). Notice that only the single pass LIPP signals are measured in these thick samples and that the front electrode is located at the anodic surface of sample V. Under these conditions a negative LIPP spike corresponds to a negative charge at the anodic surface, the two symmetric positive spikes (caused by incident and reflected pressure pulses) to a positive charge at a depth of about $10 \mu\text{m}$ below the anodic surface, and the two small symmetric negative LIPP signals to a small negative charge at a depth of about $20 \mu\text{m}$ below the anodic surface of sample IV (Fig.2b). In sample V the first LIPP spike (positive) corresponds to a positive charge at the front electrode, the second spike (negative) to a negative charge at a depth of about $5 \mu\text{m}$ below the anodic surface, the third spike (positive) to a positive charge at a depth of about $10 \mu\text{m}$ and finally the fourth spike (negative) to a negative charge at a depth of about $30 \mu\text{m}$ below the anodic surface (Fig.2c).

These measurements were carried out 5 days after poling. Repeating them on samples I, II and III 26 days after poling, the LIPP signals were reduced and the charge distribution had changed to look similar to that first observed in sample IV (Fig.2d). However, no significant change in the LIPP signals was observed after repeated measurements in samples IV and V. Notice that the LIPP signal is inversely proportional to the gap between the electrodes (sample thickness). Therefore the initial normalised LIPP signals, and their corresponding charge densities in thin samples I, II and III, were about 3, 9 and 27 times smaller than in samples IV and V, which showed a stable charge distribution.

These experimental results may be interpreted as follows. A positive layer at the surface of the samples (caused either by high field ionization in the sample or by attraction of positively charged ions from the air) and a negatively charged layer deeper in the samples (caused by depletion of cations) are the "real" space charge layers. However, the reversed charge distributions are difficult to explain using "real" space charge. The most logical interpretation of these anomalous distributions is as bound charge caused by the gradient of the dipole polarization at the edges of the depletion region. It is possible to explain the observed transformation of the charge distributions in the thin samples by low stability of the poled layer in these not sufficiently poled samples where the space charge field is not compensated by the field of the bound charges. Indeed, in these samples the space charge field is initially higher than the electric field caused by dipole polarization, but it decays with time, revealing the dipole polarisation.

In conclusion, the charge distribution in thermally poled glass can be successfully characterised by the LIPP technique. The experimental results may be explained through postulating the formation of both real space charge layers and *dipole polarization* inside the the depletion region.

References

1. R. A. Myers, N. Mukherjee, and S. R. J. Brueck, Opt. Lett. **16**, 1732 (1991).
2. P. G. Kazansky, L. Dong, and P. St. J. Russell, Opt. Lett. **19**, 701 (1994).
3. H. Nasu, H. Okamoto, A. Mito, J. Matsuoka, and K. Kamiya, Jpn. J. Appl. Phys. **32**, L406 (1993).
4. N. Mukherjee, R. A. Myers, and S. R. J. Brueck, J. Opt. Soc. Am. **B**, 665 (1994).
5. P.G. Kazansky and P. St. J. Russell, Opt. Comm. **110**, 611 (1994).
6. G. M. Sessler, J. E. West, and G. Gerhard, Phys. Rev. Lett. **48**, 563 (1982).
7. G. M. Yang, S. Bauer-Gogonea, G. M. Sessler, S. Bauer, R. Ren, W. Wirges, and R. Gerhard-Multhaupt, Appl. Phys. Lett. **64**, 22 (1994).

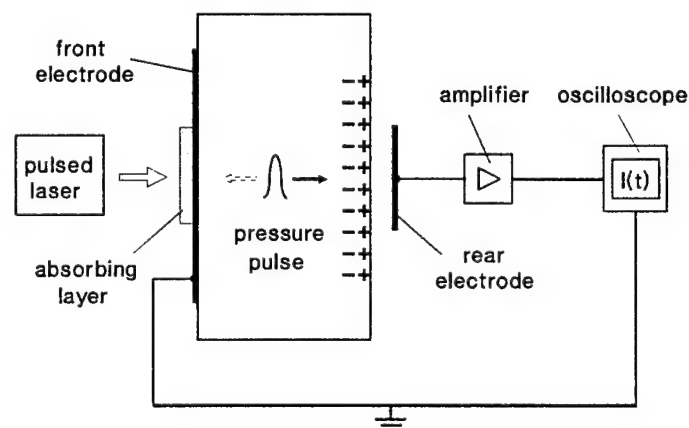


Fig.1 Experimental setup for the LIPP method

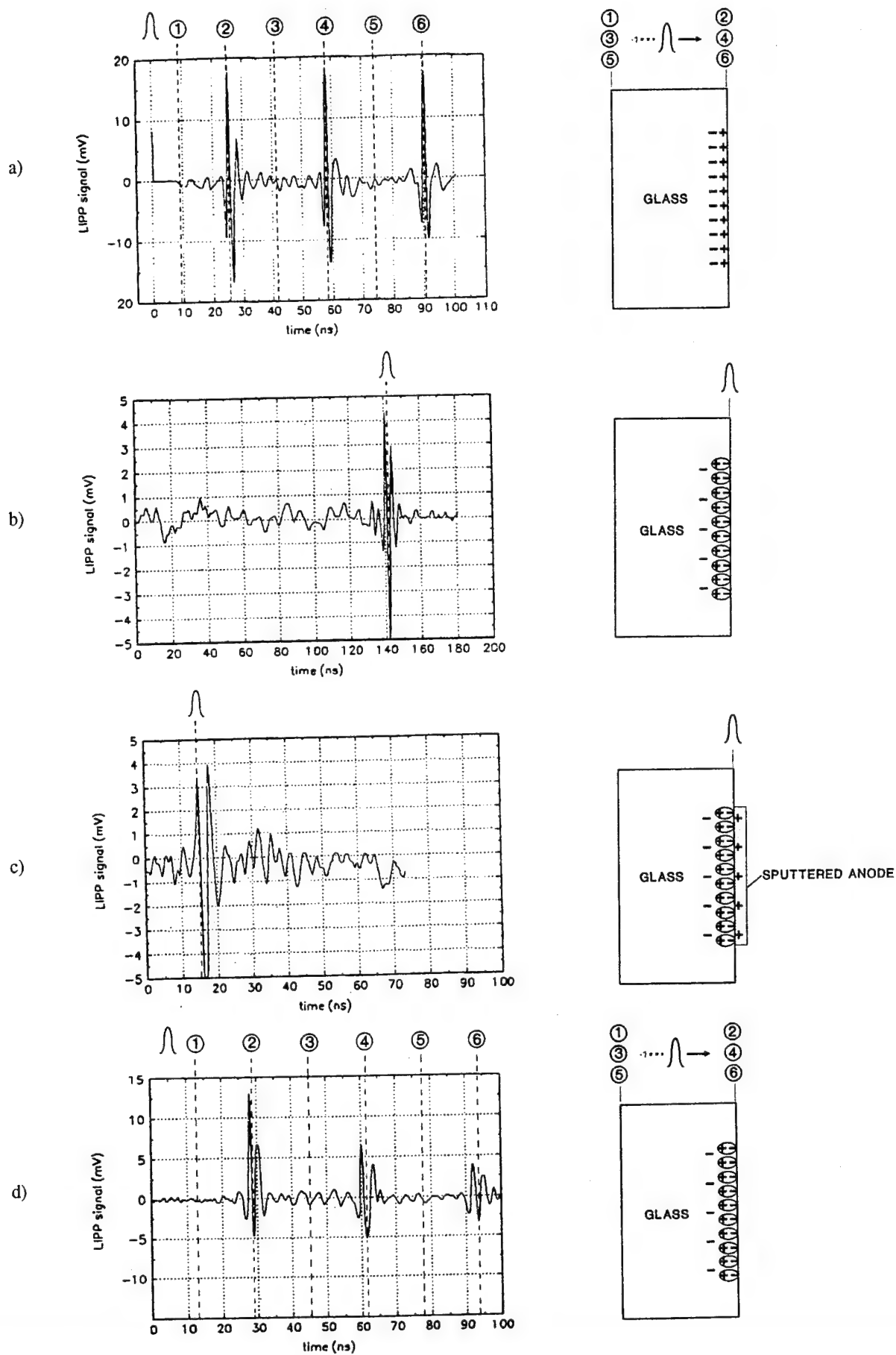


Fig.2 LIPP scans and corresponding charge profiles 5 days after poling in samples I (a), IV (b), V (c) and 26 days after poling in sample I (d).

Sunday, September 10, 1995

Poling II

SuD 3:30–4:45pm
Multnomah Room

Phillip St. J. Russell, *Presider*
University of Southampton, UK

UV Excited Poling of Germanosilicate Fibre

S.C.Fleming, T.Fujiwara & D.Wong

Optical Fibre Technology Centre, University of Sydney, NSW 2006, Australia,
Tel: +61 (0)2 335 0926, Fax: +61 (0)2 335 0910, Email: s.fleming@oftc.usyd.edu.au

Lithium niobate is well known as a material with a high electro-optic coefficient which makes it well suited to applications as an electro-optic modulator or a non-linear optical element. However it has a number of drawbacks, particularly high coupling losses to standard fibre and low photorefractive damage threshold, which have prompted the investigation of electro-optic effects in glassy materials, most notably silica.

Thermally assisted poling of silica [1] has been known for some time to induce abnormally high electro-optic coefficients (up to 0.3pm/V [2]) in both bulk silica and optical fibres. However, for practical devices, this was still too low by about an order of magnitude. We have recently described [3] UV excited poling of germanosilicate fibre which produces electro-optic coefficients comparable to those of the best crystal materials such as lithium niobate. The UV poling technique has the significant further advantage over thermal poling that it permits the writing of poled gratings [4] and other high spatial resolution poled structures. This paper describes the design of fibre suitable for poling, the details of the poling conditions and experimental results for both uniformly and periodically poled fibre devices.

Fibre was fabricated with internal electrodes (Fig. 1) by milling a pair of holes into the endface of a preform close to the core and positioned diametrically across the core with respect to each other. The preform was then drawn into fibre in the standard manner, taking care that the holes did not become too elliptical. Various fibres have been drawn using this technique of which short sections were cut and fine wire electrodes inserted into the holes in the fibre. The important parameters of the different fibres are presented in table 1. This in-fibre electrode geometry has the significant advantage over previous fibre poling geometries that the electrode spacing is very small,

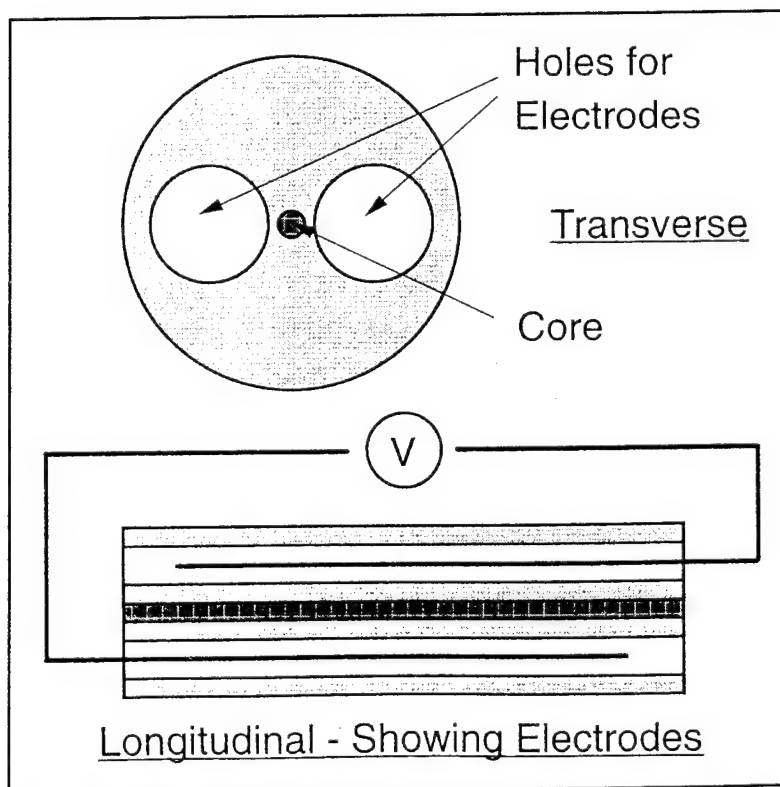


Figure 1 - Poled Fibre Device Geometry

Fibre	# 1	# 2
Core Diameter	5 μm	8 μm
Hole Spacing	10 μm	18 μm
Core Eccentricity	2 μm	~ 0 μm
Hole Diameter	40 μm	70 μm
Electrode Diameter	25 μm	50 μm
Electrode Length	2 cm	6 cm

Table 1- Fibre Device Parameters

preferential poling occurs near the anode [5], but may be disadvantageous in a device where any evanescent coupling to the electrode would increase loss.

These devices have been poled with both thermal excitation (at room temperature and 250°C [6]) and UV excitation (at 193nm with pulse energies $\sim 40\text{mJ}/\text{cm}^2$, repetition rates $\sim 10\text{Hz}$ and durations of around 10 minutes). The applied field strengths were around $100\text{V}/\mu\text{m}$. In the case fibre #1 the anode was closest to the core. Periodic poling was performed using the phase mask technique [7]. Of the work reported here, all the uniform poling was performed on fibre #1 and all the periodic poling on fibre #2, however the poling conditions remained essentially unchanged between fibres.

The electro-optic coefficients induced in the uniformly poled devices were measured using a free-space interferometer at 633nm with and without a DC voltage applied to the electrodes. The fibre was firmly fixed to a silica substrate to reduce the effects of vibration but was not clamped to reduce piezo-electric effects. The V_π voltage was determined from the sinusoidal output of the interferometer; from which the $V_\pi L$ parameter for the device was calculated. The measured $V_\pi L$ saturated with poling duration in all cases (room and elevated temperature and UV excited) and was also found to be polarisation dependent, with the effect being strongest for the polarisation parallel to the applied field. The saturated $V_\pi L$ values for the two devices thermally poled at different temperatures were very similar, at around 200Vcm [6], however the poling rate was found to increase with temperature. Assuming that the measured phase change is predominantly due to the electro-optic effect, the electro-optic coefficient calculated from this measured $V_\pi L$ value is around $1\text{pm}/\text{V}$, which is comparable to the best results achieved in bulk silica [5]. Furthermore, this is the largest reported thermally induced electro-optic coefficient in silica fibre or waveguide. Whilst this is a significant advance, it is still not sufficient for a practical device, since for instance a 5V drive signal would necessitate a 40cm long device to achieve full on-off modulation.

UV excited poling produced nearly an order of magnitude decrease in the $V_\pi L$ value which was measured to be 32Vcm for the polarisation aligned with the applied field. The calculated electro-optic coefficient was $5.8\text{pm}/\text{V}$ for this polarisation and $1.7\text{pm}/\text{V}$ for the orthogonal polarisation. The value of $5.8\text{pm}/\text{V}$ is very close to the r_{22} of lithium niobate, used to fabricate most currently available electro-optic modulators. It is interesting to note that these values for the two

permitting very high field strengths. Furthermore, the electrodes are surrounded by an excellent insulator so the field can be significantly greater than when poling in air. Indeed, in this work we have used field strengths approaching that of dielectric breakdown strength of the glass. The very high field strengths, significantly more than has been used in elevated temperature thermal poling, may be important in inducing an electro-optic effect. It is certainly important for practical devices, as the applied voltage required to produce a π phase shift is reduced with this close electrode spacing. Also the core of the fibre can be arranged to be very close to an electrode with this geometry. This may be advantageous in poling, if

polarisations are almost in the ratio 3:1 as would be expected for an induced $\chi^{(2)}$. However it is not possible to rule out the influence of piezoelectric effects. Hence, the measurements of the UV poled fibre device were repeated at 5MHz [4], well outside the range of likely acoustic resonances [8] (which indeed were observed in the few tens of kilohertz region). The measured $V_{\pi}L$ at 5MHz agreed within a few percent with that at DC, indicating that the measured effects are unlikely to be due to acoustic resonance enhanced piezoelectric effects.

Whilst these results for uniformly poled devices are exciting and significant in their own right, it is possible to produce periodically-poled fibres which incorporate a Bragg grating comprising regions of exposed and un-exposed fibre. This was demonstrated by poling a sample of fibre #2 with the UV irradiation passing through a phase mask designed to write a grating in the core at $\sim 1530\text{nm}$ [4].

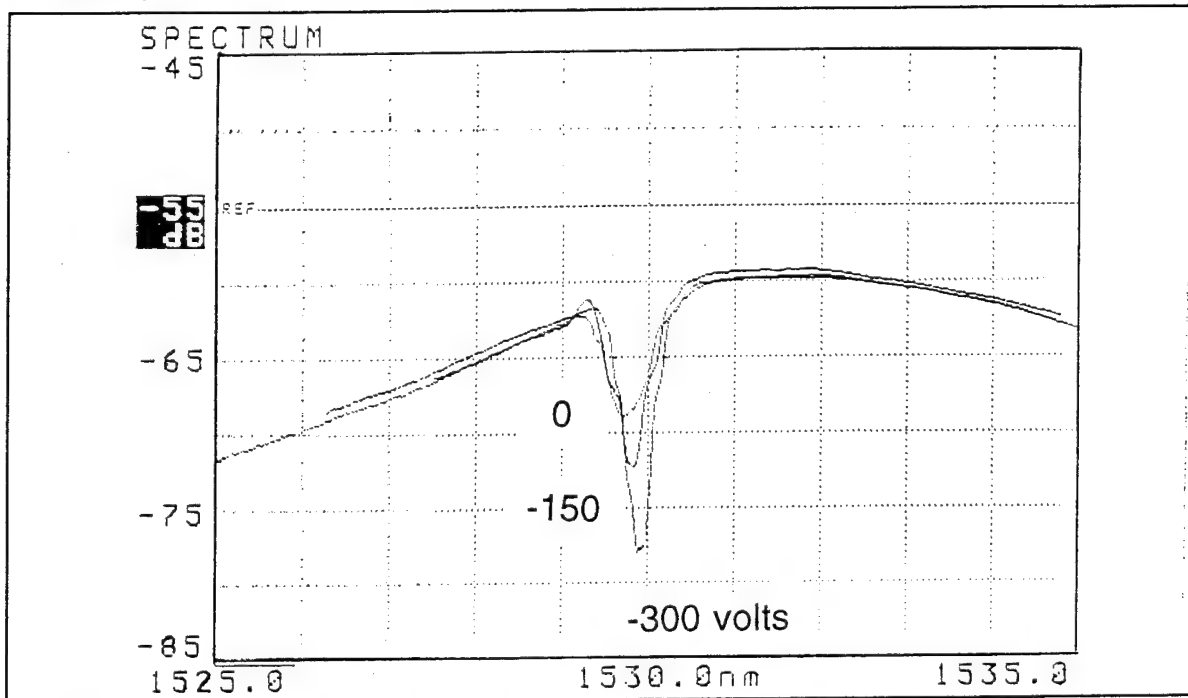


Figure 2 - Poled Grating Transmission Spectra

Figure 2 shows experimentally measured, uncorrected, transmission spectra for the resulting poled grating device with differing applied modulating voltages. The sign of these applied voltages is defined with respect to the poling voltage. Three voltage dependent effects are apparent. Firstly, with increasing negative voltage the reflectivity increases. This is as would be expected with an electro-optic effect since the increasing voltage causes an increase in the refractive index only in the UV exposed regions, thus increasing the depth of the Bragg grating and hence the reflectivity. Secondly, with increasing negative voltage the Bragg reflection shifts to longer wavelengths. This is also as would be expected with an electro-optic effect since the increase in the refractive index of the poled sections results in an effective increase in the average index of the whole device and hence a longer Bragg wavelength. Thirdly, and for reasons which are not yet clear, the optical bandwidth decreases with increasing negative voltage.

Both the periodic poling results and those for uniform poling are exciting in terms of the significant changes that can be induced in the properties of germanosilicate glasses and especially in terms of the practicality of devices that such an induced electro-optic effect provides.

In summary, uniformly UV poled silica fibre devices can be fabricated which have electro-optic coefficients similar to those of lithium niobate and can be used to realise practical amplitude, phase and polarisation modulators. Poled grating devices, as electrically controllable amplitude or reflection modulators, offer even more opportunities in telecommunications and other applications. Other possibilities include electrically controllable chirped gratings for adaptive dispersion compensation, non-interferometric amplitude modulators and quasi-phase matched second harmonic generation.

Acknowledgements

The authors wish to thank M.Sceats, S.Poole, G.Town, Y.Zhao, D.Stepanov and V.Grishina for useful discussions. The authors acknowledge the support of IBM Australia through an Australian Commonwealth Government DIST GIRD grant and the Australian Photonics Cooperative Research Centre, in which the OFTC is a partner.

References

- 1 L.Li & D.N.Payne, "Permanently-Induced Linear Electro-Optic Effect in Silica Optical Fibres", Dig. Conf. Integrated and Guided Wave Optics, 1989, OSA, Paper TuAA2-1 (1989)
- 2 X.-C.Long, R.A.Myers & S.R.J.Brueck, "Measurement of the Linear Electro-Optic in Poled Amorphous Silica", Opt. Lett., 19, 22, pp.1819-21 (15 Nov '94)
- 3 T.Fujiwara, D.Wong, Y.Zhao, S.Fleming, V.Grishina & S.Poole, "UV-Excited Poling and Electrically Tunable Bragg Gratings in a Germanosilicate Fiber", Postdeadline Paper, OFC '95 (Feb '95)
- 4 T.Fujiwara, D.Wong, Y.Zhao, S.Fleming, S.Poole, M.Sceats, "Electro-Optic Modulation in a Germanosilicate Fibre with UV-Excited Poling", Elect. Lett., 31, 7, pp.573-5 (Mar '95)
- 5 R.A.Myers, N.Mukherjee & S.R.J.Brueck, "Large Second-Order Nonlinearity in Poled Fused Silica", Opt. Lett., 16, 22, pp.1732-4 (1991)
- 6 T.Fujiwara, D.Wong, Y.Zhao, S.Fleming, S.Poole & M.Sceats, "Comparison of Linear Electro-Optic Coefficient Induced by UV-Excited and Thermal Poling in a Germanosilicate Fibre" Accepted for CLEO PacRim '95.
- 7 K.O.Hill, B.Malo, F.Bilodeau, D.C.Johnson & J.Albert, "Bragg Gratings Fabricated in Monomode Photosensitive Optical Fibre by UV Exposure Through a Phase Mask", Appl. Phys. Lett., 62, p.1035 (1993)
- 8 X.-C.Long, R.A.Myers & S.R.J.Brueck, "Measurement of Linear Electro-Optic Effect in Temperature/Electric-Field Poled Optical Fibres", Elect. Lett., 30, 25, pp.2162-3 (Dec '94)

Measurement of Photo-induced Charge Distribution in Seeded Second Harmonic Generation by Charge-Selective Etching in Glasses

Jae H. Kyung

Department of Physics, Brown University, Providence, RI 02912

N.M. Lawandy

Department of Physics and Division of Engineering, Brown University, Providence, RI 02912

Tel: (401) 863-2755

Fax: (401) 863-1157

Ever since the discovery of efficient second harmonic generation (SHG) in centrosymmetric optical fibers [1-4] and bulk glasses [5,6], many researchers, through experimental and theoretical work, have investigated this problem in the hopes of developing models to explain the mechanism behind this unexpected effect. Much of the work focused on the mechanism responsible for producing a quasi-phase matched effective $\chi^{(2)}$ in these materials. Models such as the creation of a semi-permanent dc electric field via optical rectification field [7], charge organization by light controlled transport effects [8], and most recently, directional photo-ionization [9] were proposed to explain this phenomenon. Although these models were successful in explaining the mode symmetries of the radiated second harmonic light at high encoding intensity regimes, no one had been successful in directly measuring the charge distribution responsible for second harmonic generation in glasses. Work by Dominic and Feinberg [10] used an SHG mapping technique where they focused a probe beam onto a seeded area of a SK5 glass sample and inferred its charge distribution from the radiated SHG power. Their study supported the dipolar distribution predicted by directional photo-ionization model at high encoding intensities, but did not address the strong mode symmetry violation at low encoding intensities previously reported by Driscoll and Lawandy [11].

In this work, we present a direct and unambiguous measurement of the photo-induced charge distribution at both high and low encoding intensities responsible for SHG in glasses using a new charge-selective etching process.

The experiments were performed on Schott SK5 borosilicate glass samples which were encoded using Q-switched (1 KHz), modelocked (76 MHz) Nd:YAG laser pulses. The 1.064 μm pulses were frequency doubled in a KTP crystal to generate co-propagating 532 nm pulses. The temporally overlapped pulses were focused by a 12.5 cm focal length lens onto the sample. After exposing for 20 minutes, the sample was etched in 12% aqueous hydrofluoric acid (HF) solution for 10 minutes, and the resulting etch patterns were analyzed using contact atomic force microscopy (AFM).

Recent work on the same glasses has shown that after exposing borosilicate glass samples to intense 532 nm pulses and subsequently etching them in 12% HF solution, a post-exposure selective etching takes place [12]. The selectively etched pattern resulting from exposure to the lowest order Gaussian mode of 532 nm light resembled that of a doughnut and is shown in Figure 1. This pattern directly measures the excess negative charge distribution produced from the differential charge diffusion and recombination processes of the photo-generated electrons and holes via multiphoton absorption. Thermal annealing studies have shown that the sites responsible for selective etching are boron E' centers.

Using this simple technique, we were able to selectively etch away the regions where excess negative charges reside after the sample has been prepared with the fundamental and second harmonic beams. We studied the photo-induced charge distribution created at both low and high encoding intensity regimes. Figure 2b shows the etched pattern after exposing the sample to collinearly polarized fundamental and second harmonic beams having peak intensities of 4 GW/cm^2 and 1 GW/cm^2 , respectively. With the inclusion of an immobile positive background, the resulting charge distribution produces the correct $\chi^{(2)}$ symmetry to couple a solid Gaussian mode beam to generate a TEM_{01} -like far-field second harmonic radiation mode as shown in Figure 3b. Moreover, at higher encoding intensities of 8.3 GW/cm^2 for the 1.064 μm beam and 1 GW/cm^2 for the 532 nm beam, the resulting etch pattern (Figure 2a) is a contracted and shifted two-lobe pattern approximately the size of one of the lobes shown in Figure 2b. Once a positive immobile charge background is included in this negative charge distribution, the overall

distribution is nearly dipolar in this encoding regime and basically agrees with the measurements of reference [10] where intensities of the order of 100 GW/cm^2 were used. Figure 3a shows the far-field radiated second harmonic pattern at this high encoding condition.

We have also found that the etched patterns are aligned along the direction of polarization of the encoding beams and rotate as the polarization axis is rotated. When orthogonally polarized beams were used to prepare the sample, the radiated SHG was a double-lobed mode that rotated as the readout beam polarization was rotated suggesting a symmetric charge distribution. The resulting etched pattern was a solid spot.

Through a new charge-selective etching process, we have directly measured the charge distribution responsible for second harmonic generation in glasses for both high and low preparation intensities. The results obtained from this technique show clearly the existence of a non-dipolar charge distribution and cast doubts on the validity of the directional photo-ionization and other single directed flux models. The results suggest that the creation of internal electric field involves a new type of light-induced transport in these glasses [13].

references

- [1] Y. Sasaki and Y. Ohmori, *Appl. Phys. Lett.* **39**, 466 (1981).
- [2] Y. Ohmori and Y. Sasaki, *IEEE Quantum Electron.* **QE-18**, 758 (1982).
- [3] U. Osterberg and W. Margulis, *Opt. Lett.* **11**, 516 (1986).
- [4] D.M. Krol, J.R. Simpson, and D.J. DiGiovanni, in *Annul Meeting*, Vol. 17 of 1991 OSA Technical Digest Series (Optical Society of America, Washington, D.C., 1991), paper **MSS2**.
- [5] M.D. Selker and N.M. Lawandy, *Opt. Commun.* **77**, 339 (1991).
- [6] M.D. Selker and N.M. Lawandy, *Opt. Commun.* **81**, 38 (1991).
- [7] R.H. Stolen and H.W.K. Tom, *Opt. Lett.* **12**, 585 (1987).
- [8] N.M. Lawandy, *Phys. Rev. Lett.* **65**, 1745 (1990).
- [9] D.Z. Anderson, V. Mizrahi, and J.E. Sipe, *Opt. Lett.* **16**, 796 (1991).
- [10] V. Dominic and J. Feinberg, *Phys. Rev. Lett.* **71**, 3446 (1993).
- [11] T.J. Driscoll and N.M. Lawandy, *J. Opt. Soc. Am. B* **11**, 355 (1994).
- [12] E. Sauvain, J.H. Kyung, and N.M. Lawandy, *Opt. Lett.* **20**, 243 (1995).
- [13] S. Li, J.B. Khurgin, and N.M. Lawandy, *Opt. Commun.* **115**, 466 (1995).

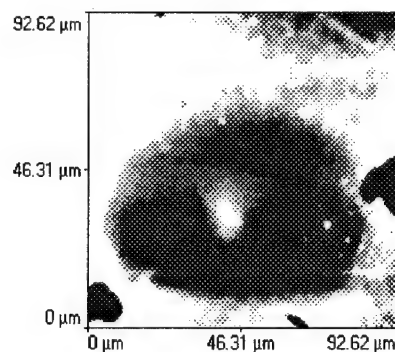


Figure 1. AFM image of the etched pattern from exposure of the glass to a solid Gaussian beam at 532 nm light.

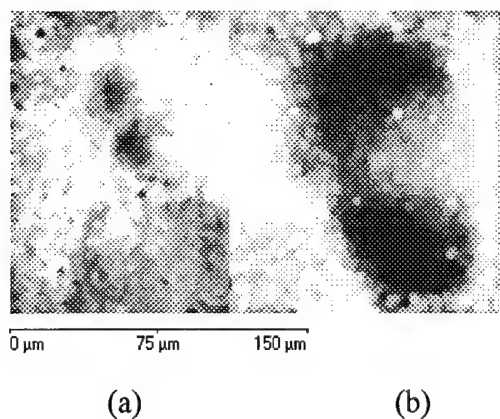


Figure 2. AFM images of the etched pattern in the high encoding intensity regime (a) and in the low encoding intensity regime (b).

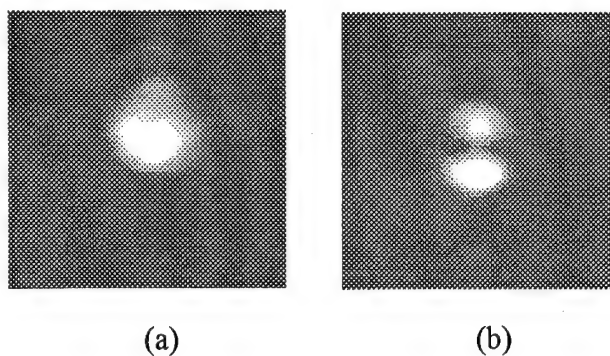


Figure 3. CCD images of the far-field radiated second harmonic patterns at high encoding intensities (a) and at low encoding intensities (b).

Second Harmonic Generation in Low-Water Fused Silica by Proton Implantation

Leanne J. Henry, Thomas G. Alley, Dennis S. Rand and John J. Kester

Frank J. Seiler Research Laboratory
2354 Vandenberg Drive, Suite 6H79
USAF Academy CO 80840-6272
Tel. (719) 472-3502, FAX (719) 472-3649
e-mail - henrylj%fsrl%usafa@dfmail.usafa.af.mil

Second harmonic generation (SHG) in poled fused silica, which was first reported by Myers, Mukherjee and Brueck⁽¹⁾ in 1991, has increased in importance because of a multitude of potential device applications. Such applications include electro-optic switching, frequency doubling crystals, parametric amplification, parametric oscillation, and linear electro-optic modulation/frequency conversion which can be monolithically integrated into optical fibers and planar integrated circuit geometries. Because of these potential applications, much work has been done to understand the phenomenon of SHG in poled fused silica.

In the past, a second-order nonlinearity has been induced in fused silica by either parallel plate⁽¹⁾ or corona poling.⁽²⁾ Through parallel plate poling, Myers et al.⁽¹⁾ were able to induce an optically active region of thickness 5-10 μm on the positively biased face of a sample. The second-order nonlinearity, $\chi^{(2)}$, associated with this region in natural fused quartz was found to be on the order of 1 pm/V. But, for the higher purity UV grade synthetic fused silica having only 10 percent as many impurities as natural fused quartz, the magnitude of the nonlinearity was found to be an order of magnitude lower.⁽¹⁾ Based on this data, Myers proposed that the SHG originated from a space charge region created by migrating impurity ions and electrons. This was further supported by the ratio of electro-optical coefficients, r_{33}/r_{31} , which was found by Long et al.⁽³⁾ to have a value of 3.0. This is consistent with ∞_{mm} symmetry and a space charge region.

Besides parallel plate and corona poling, nonlinearity has also been induced in various glasses by electron implantation. Kazansky et al.⁽⁴⁾ reported second-order nonlinearities as large as 0.7 pm/V upon implantation of lead silicate glass with electrons. Russell et al.⁽⁵⁾ also reported the generation of nonlinearity in lead glass, Ge doped silica glass, Nb doped silica glass, Ti+Zr doped silica glass, lead germanate glass and phosphate glass by electron implantation. Although nonlinearity was induced in the above mentioned materials, attempts to induce nonlinearity in fused silica by electron implantation have failed. In fact, Kazansky et al.⁽⁶⁾ reported the erasure of nonlinearity induced by thermal poling upon electron implantation.

Because of the apparent role of the space charge region in the generation of a second order nonlinearity, fused silica with a low-water content was implanted with protons in an attempt to break the centrosymmetry and produce a space charge region. Protons were implanted using a pelletron at energies ranging from 200 to 725 keV and dosages ranging from 0.25 to 3.0 mC. The depth of the implanted region increased from approximately 1.5 μm to 8.0 μm at proton energies of 200 and 725 keV, respectively. The level of SHG was studied in two ways: (1) as a function of proton implantation energy at a constant dosage of 2 mC (approximately 5×10^{16} protons/cm²),

and (2) as a function of dosage (0.25 to 3.0 mC) at a fixed proton energy of 526 keV. Upon implantation of the desired dosage of protons, the SHG profile was obtained by scanning a polarized 1.06 μm Q-switched Nd/YAG laser beam at an incident angle of 60° across a diameter of the irradiated region of the sample. Prior to striking the sample, the beam was reduced to between 10 and 60 mW of power and was filtered to remove 532 nm radiation. After traversing the sample and generating second harmonic, the beam was filtered to remove all radiation except wavelengths of 530 ± 10 nm. After measurement of the strength of the frequency doubled radiation with a PMT, the absolute level of d_{33} ($d_{33} = \frac{1}{2}\chi^{(2)}$) obtained by comparison with a y-cut quartz standard.

To evaluate the distribution of optical activity in the irradiated region of the sample, linear scans were performed across a diameter of the irradiated area, and each point recorded was the time averaged response of a photomultiplier tube to the SHG signal. For a proton implantation energy of 253 keV, Figure 1a, we found the distribution of nonlinearity induced within the irradiated area to be a maximum at the center of the region, falling off on either side. But, as the proton implantation energy increased, the strong central region became an optically active annulus of increasing diameter (Figure 1b). The central region which had no visible damage, showed very little nonlinearity. The annular region, on the other hand, was quite optically active. The peaks in Figure 1b correspond to the linear scan passing through opposite sides of the annulus. The optically active annulus and less optically active central region are believed to originate from an accelerator beam profile which became annular with increasing diameter as the implantation energy increased. As a result, the portion of the sample corresponding to the beam center probably received very little irradiation and, therefore, had much less optical activity. Kazansky et al.⁽⁵⁾ observed a similar distribution of nonlinearity in lead silicate glass that had undergone electron beam irradiation. A second harmonic signal was observed at the edges of the irradiated region which was twice that in the center.

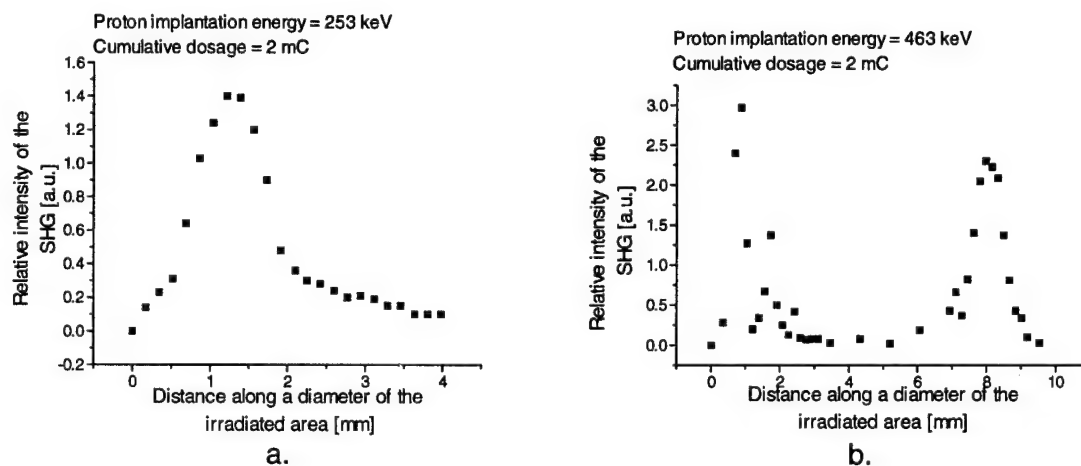


Figure 1 - Relative intensity of the SHG [a.u.] vs distance [mm] along the sample surface for a cumulative proton dosage of 2 mC. Proton implantation energies are: a. 250 keV, b. 463 keV.

The strength of the nonlinear optical signal was first evaluated as a function of the proton implantation energy which ranged from 200 keV to 725 keV at a constant dosage of 2 mC. Upon evaluation of the nonlinear optical coefficient, d_{33} , for the various proton energies (Figure 2) d_{33} was found to be dependent on the proton energy. Each

point in Figure 2 represents a different sample. Each d_{33} value was calculated from the maximum SHG signal found along a single linear scan through the implanted region of the sample. Because a linear scan through a different line of the implanted area might produce a slightly different result, these values are believed to be good within ± 0.1 pm/V. Saturation of d_{33} in the range 0.5 to 0.6 pm/V appeared to occur for proton energies in excess of 410 keV. One exception was found to occur for a sample of fused silica implanted with 568 keV protons where a d_{33} value of 0.68 was generated. Finally, from Figure 2, a minimum proton implantation energy of approximately 350 keV was found to be necessary to generate substantial nonlinearity in fused silica.

One conclusion that can be drawn based on the above data is that proton implantation of fused silica is capable of creating a nonlinear optical region exhibiting a value of d_{33} at least as large as obtainable from parallel plate poling (i.e., approximately 0.5 pm/V). In addition, the potential exists for even larger nonlinearities as evidenced by the d_{33} value of 0.68 pm/V generated by a proton implantation energy of 568 keV.

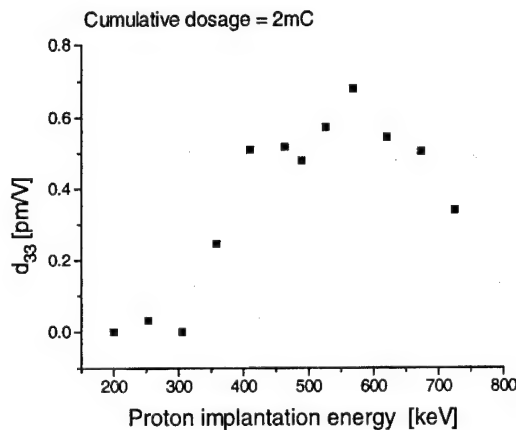


Figure 2 - Maximum d_{33} [pm/V] vs proton implantation energy [keV].

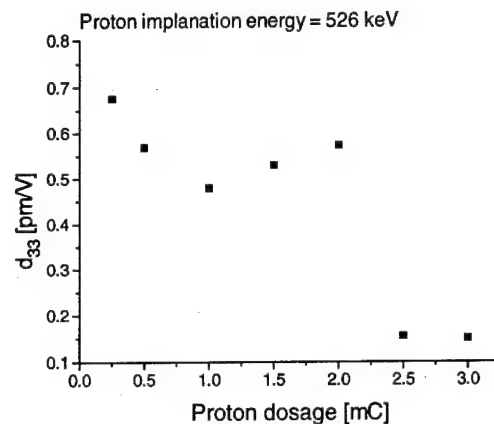


Figure 3 - Max. d_{33} [pm/V] vs dosage [mC] for a proton implantation energy of 526 keV.

The effect of proton dosage at a fixed implantation energy of 526 keV was studied next. This particular proton energy was selected because of its relatively large nonlinear response at a dose of 2 mC. The dosages studied ranged from 0.25 mC to 3.0 mC. As is apparent from Figure 3, values of the nonlinear optical coefficient, d_{33} , ranging from 0.48 to 0.68 pm/V were obtained at dosage levels between 0.5 and 2.0 mC. When compared to the nonlinear optical coefficient, d_{33} , produced by parallel plate poling, the values of d_{33} produced by proton implantation using these parameters are up to 36 percent greater. Another observation apparent from Figure 3 was that as the dosage level increased, the level of d_{33} achieved decreased after a certain point. This was most likely due to extensive lattice damage brought about from prolonged proton bombardment.

In conclusion, the distribution of SHG on the surface of a sample of irradiated fused silica was found to become an annulus of increasing diameter as the energy of the proton beam increased. This damage pattern was most likely the result of an annular beam profile brought about by repulsion of the positively charged protons. By smoothing out the beam profile or moving the sample during irradiation, it should be

possible to induce a uniform area of nonlinearity stronger than that achievable through traditional parallel plate poling.

In addition, for a constant dosage of 2 mC, a threshold proton implantation energy of 400 keV was found to be necessary to generate a nonlinear region in a sample of fused silica. As the proton implantation energy increased above 358 keV, $\chi^{(2)}$ (where $\chi^{(2)} = 2d_{33}$) appeared to generally saturate between 1.0 and 1.2 pm/V for proton implantation energies greater than 400 keV. One exception was found for a proton energy of 568 keV which produced a value of $\chi^{(2)}$ of 1.4 pm/V. For a proton implantation energy of 526 keV, the optimum dosage level was found to be between 0.25 and 2.0 mC. At these levels, values of $\chi^{(2)}$ between 1.0 and 1.4 pm/V were found to occur. Finally, values of $\chi^{(2)}$ larger than 1.4 may be achievable by finding the optimal combination of proton implantation energy and dosage.

References

1. R. A. Myers, N. Mukherjee and S. R. J. Brueck, Opt. Lett. **16** 1732 (1991).
2. A. Okada, K. Ishii, K. Mito and K. Sasaki, Appl. Phys. Lett. **60** 2853 (1992).
3. X. -C. Long, R. A. Myers and S. R. J. Brueck, Opt. Lett. **19**(22) 1819-1821 (1994).
4. P. G. Kazansky, A. Kamal and P. St. J. Russell, Opt. Lett. **18**(9) 693-695 (1993).
5. P. St. J. Russell, P. G. Kazansky and A. Kamal, SPIE (Photosensitivity and self-organization in optical fibers and waveguides) **2044**, August 1993, Quebec, Canada.
6. P. G. Kazansky, A. Kamal and P. St. J. Russell, Opt. Lett. **18**(14) 1141-1142 (1993).

Charge Trapping in Metal Ion-Activated Quantum Dot-Doped Silica Glasses

Alan L. Huston and Brian L. Justus

Optical Sciences Division Code 5611

Naval Research Laboratory

Washington, D.C. 20375

Ph. (202)767-9470 FAX (202)404-8114

Photosensitive glasses containing metal-ion-activated, quantum dot semiconductors such as $\text{ZnS}:\text{Cu}^+$ have been developed. Exposure to UV or ionizing radiation (γ -ray) results in the generation of trapped electrons with a trap density of approximately $10^{18}/\text{cm}^3$. The presence of such a high density of trapped charges in a transparent glass suggests a number of possible applications including optical storage and electro-optic modulation.

Polarized UV excitation produces an anisotropic distribution of trapped charges that leads to photoinduced birefringence. A schematic of the experimental arrangement used to generate and measure photoinduced birefringence is shown in figure 1. The induced birefringence can be reversed by rotating the polarization of the UV source and after more than 1000 write-erase cycles no apparent degradation in the performance was observed. The birefringence is stable at room temperature and can be completely removed by heating the glass to a temperature of 250 C. Photoinduced birefringence can be used for optical data storage applications. The light line in figure 2 shows a series of data

bits written with a spacing of 0.025 inches. The dark line in figure 2. shows the same trace with selected bits erased .

Figure 1.

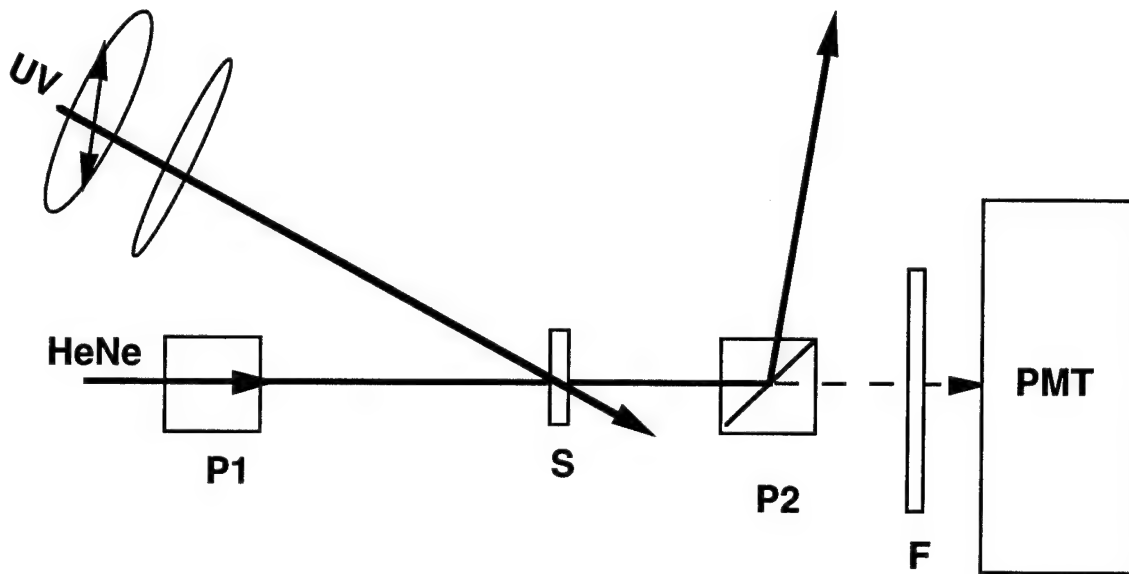
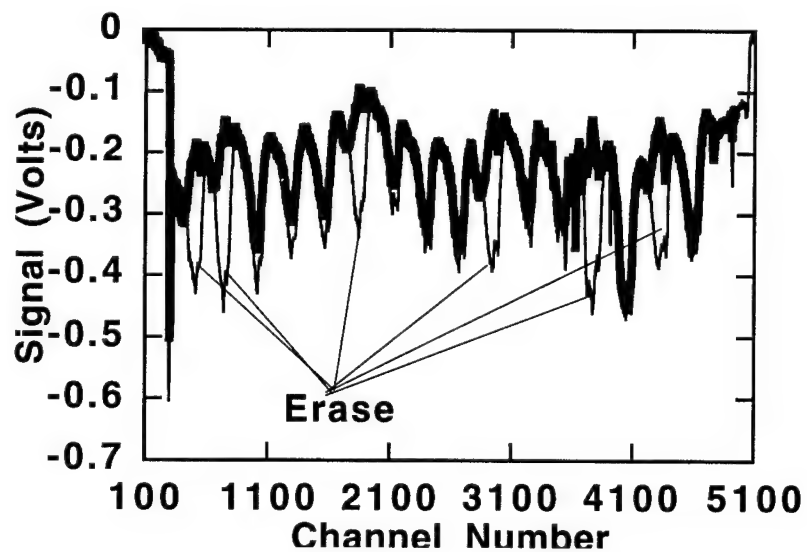


Figure 2.



In a second series of experiments, a sample was placed between electrodes with a spacing of 2 mm as shown in figure 3. Photoinduced birefringence was written into the sample and the transmission of a HeNe laser was monitored through crossed polarizers as a function of applied voltage. The plot in figure 4 shows the signal obtained using a function generator to generate a sine wave, a triangle wave and finally a square wave. Modulation up to a frequency of approximately 1 kHz was observed with this arrangement although much higher frequencies should be possible with a narrower electrode gap.

Figure 3.

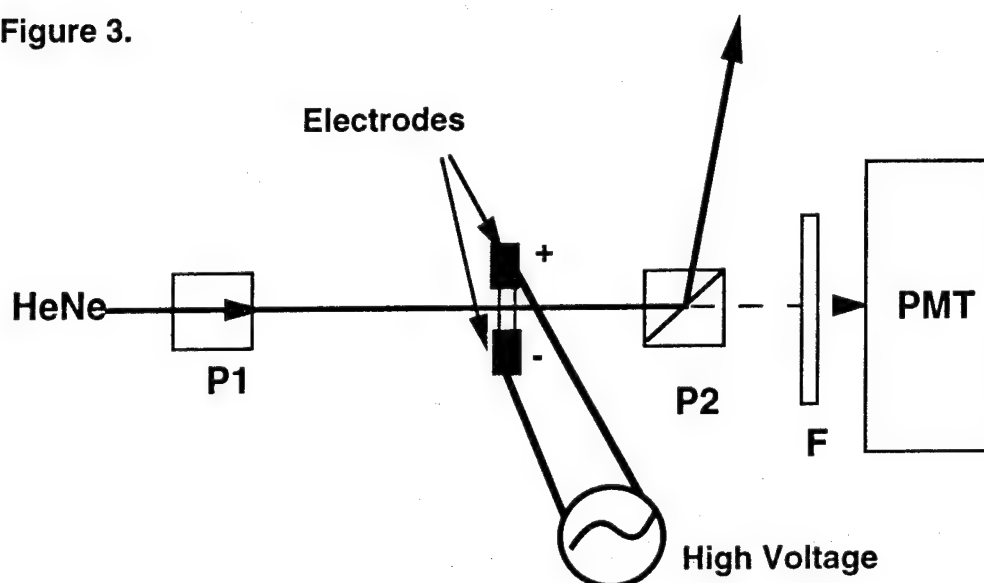
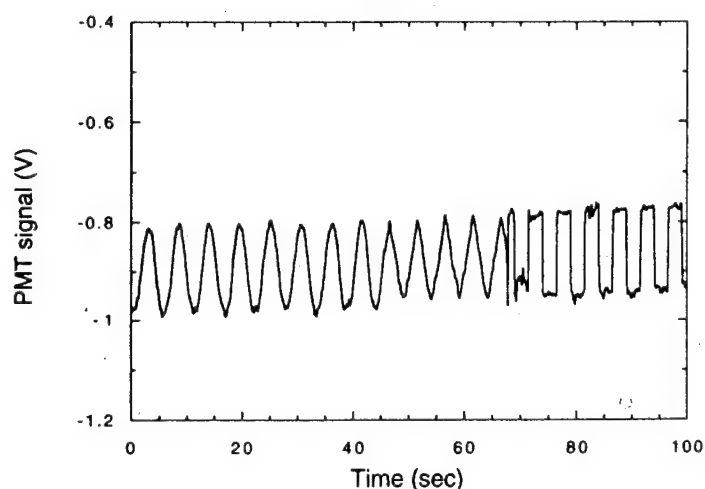


Figure 4



Monday, September 11, 1995

Materials Studies

PMA 8:30–10:00am
Multnomah Room

François Ouellette, *Presider*
University of Sydney, Australia

The Formation of Nonlinear Optical Materials by Ion Implantation
 Robert H. Magruder, III
 Department of Applied and Engineering Physics
 Vanderbilt University, Nashville TN 37240

Introduction:

There are several potential candidate systems for nonlinear optical materials including resonant and non-resonant semiconductor quantum dots, organic materials and glass systems. Two of the glass systems are based on glasses containing transition metal ions. The first system exploits the polarization of the transition metal ions (Ti, V, Nb) incorporated in the glass matrix, while the second is based on glasses with metallic nanoclusters of the transition ions (Cu, Ag, Au). While both systems have been shown to have desirable properties for nonlinear media each system has different nonlinear properties.

While there are stringent performance criteria nanometer dimension metal colloid-glass composites have some unique properties that may make them viable candidates for all optical switching networks including large third order nonlinear response, picosecond switching time and relaxation times, thermal and chemical stability, and low two photon absorption. Moreover the metal nanocluster morphology as well as the structure of the host can be photosensitive to excimer irradiation.¹

There are two principal effects that determine the optical response of nanometer dimension metal particle-glass composites: quantum confinement effects and dielectric confinement effects.^{2,3} Quantum confinement effects arise when de-localized electrons are confined to regions smaller than their de-localized length. The result of this confinement is the modification of their quantum response when exposed to optical frequencies. Quantum confinement effects are usually observed for particles of $< 5\text{-}10$ nm in diameter. As most of the nanoclusters discussed in this work are larger than 5 nm we do not anticipate significant quantum confinement effects. Dielectric confinement effects occur when the wavelength of the applied optical field is larger than the particle, resulting in the field acting on and polarizing the electrons of the particle very differently than the surrounding medium. This polarization of the particles results in modification of the dielectric response of the composite. This latter effect gives rise to the coloration effects in glasses by small metal particles and results from absorption at the surface plasmon resonance frequency of electrons in the metal particles.

The optical response due to dielectric confinement of the metal particles is related to the shape, size and dielectric function, $\epsilon(\lambda)$, of the particles. The surface plasmon resonance depends implicitly on particle size through the dielectric function of the metal particles. The free-electron contribution of the dielectric function will be modified if the mean free path of the electron in the colloid is greater than the size of the colloid.³ As a consequence $\epsilon(\lambda)$ is a function of colloid size for nanometer dimension metal colloids. Effective medium theory for small non interacting particles in a dielectric^{2,4} predicts substantial enhancements of the nonlinear response of the composite for optical frequencies near the surface plasmon resonance (SPR) frequency. This enhancement is due to local field effects and results from the dielectric confinement effects.

A significant problem with metal colloid-glass composites for device applications is that both the linear and nonlinear absorption in general increase near the surface plasmon resonance frequency. This increase in absorption has potentially deleterious effects on the relative merit of these materials for devices operating at or near these SPR frequencies. The ability to increase the nonlinear response off the SPR and decrease the linear and nonlinear absorption could significantly enhance the prospect of these materials for use in devices.

Formation of nanometer dimension metal colloids in glass by ion implantation is of significant interest because of the possibility of forming thin films in dielectrics containing a high volume fraction ($> 1\%$) of metal colloids using a technique compatible with present waveguide technology.^{2,5,6} We have employed three techniques to modify the optical properties of the metal colloid glass composite:

- Modification of the dielectric function of the metal colloids by sequential implantation
- Modification of the host substrate by implantation of polarizable ions
- Modification of the composite by excimer irradiation

All three of these avenues of modification affect both the linear and nonlinear properties.

Sequential ion implantation can be used to extend the ion implantation method of forming metal nanocluster glass composites by allowing the formation of multicomponent nanometer dimension metal particles in glass.^{7,8,9} This technique has been demonstrated to significantly alter the composition of the metal particles formed. Composition changes engender changes in the electronic structure of the colloids present. As a consequence the formation of multicomponent nanoclusters results in changes in both linear and nonlinear optical properties of the composite that are not possible with single element composition colloids. The ability to form these "alloy" metal-glass composites could significantly improve the feasibility of these materials as optical devices by enhancing the nonlinear response and by changing the character of that response.¹⁰ A second use of sequential ion implantation is the modification of the host with polarizable ions before metal nanocluster formation. Effective medium theory predicts that the linear and nonlinear optical response of the composite can be significantly altered by modifying the properties of the host. The third technique uses the photosensitivity of the composite for alteration of its optical properties. The photosensitive response of the composite may arise from modifications to the nanocluster morphology or the structure of the host substrate itself. In either case the optical properties of the composite will be affected.

Experimental:

Implantation energies for all ion species were chosen from calculations using TRIM 89¹¹ to target energies that would overlay the depths of implantation for each metal ion in the sequentially implanted samples. A group of samples consisting of single element implantations were made for comparison for each ion species using of the same nominal dose used in the sequential implantations.

Ion backscattering techniques with 2 MeV He⁺ ions were used to measure the ion depth profiles. Optical measurements were made at room temperature in air from 900 to 200 nm using a Cary 5 dual beam spectrometer. All samples were measured using an unimplanted sample in the reference beam. The spectra are reported as optical density. The absorption spectra were measured at three different positions on each sample. The scatter in the absorption due to these different positions is less than 2%.

The nonlinear index of refraction was measured for the samples using the Z-scan method.⁷ The Z-scan measures the normalized transmission as a function of laser intensity as the sample is moved through the focal plane of a long focal length lens (150 mm in these experiments). The laser used for these experiments was a cavity dumped tunable dye laser with a ~ 6 picosecond pulse duration. The laser was operated at 3.8 MHz. The average power was 200 mW in the TEM₀₀ mode. The peak irradiance for a focal spot of 25μm in radius was ~ 4.4x10⁸ W/cm².

Modification of the Dielectric function

Sequentially implanted samples consisting of the Ag and Sb and Ag and Cu were made by implanting Ag first then Sb or Cu in Corning 7940 UV grade silica. The optical properties of the nanometer dimension metal colloids were characterized as a function of the relative concentrations of Ag and Sb or Cu implanted. The doses used were in ratios, Ag to Sb or Cu, of 9:3, 6:6 and 3:9. Energy of implantation was 305 keV for the Ag, 320 keV for the Sb and 160 keV for the Cu ions. Nominal total doses as determined by current integration for these samples were 12x10¹⁶

(Ag+Sb) or (Ag+Cu) ions/cm². Single element implantations were also made using the same doses as the sequentially implanted samples.

For the single element implanted samples, the Ag and Cu implanted glasses show the absorption characteristic of metal nanoclusters with a surface plasmon resonance absorption. The Sb implanted samples show a $1/\lambda$ dependence for the optical absorption however there is no indication of any surface plasmon resonance absorption. For the sequentially implanted samples we don't observe any definitive SPR resonance peaks in the sequentially implanted Ag/Sb samples but do observe them in the Ag/Cu samples. In the Ag/Cu samples the wavelength and the magnitude of the SPR is significantly different compared with the single element implanted samples and was a function of relative dose. We attribute these changes in the sequentially implanted samples to modifications of the dielectric function of the Ag particles by the formation of multicomponent colloids whose dielectric function depends on composition. We expect the volume fraction of the metal colloids to have an impact on the absorption. In the case of single element implantations of Ag, Sb and Cu this is observed in a general fashion. However for some of the sequentially implanted samples there is a greater volume fraction of metal than the single element implantations but less optical density.

As the total nominal dose is the same for the sequentially implanted samples in both series, the volume fraction of the metal is similar. As a result changes observed must be associated with other effects. These results indicate that changes in the optical absorption are due to presence of the two different metal elements in the colloids. These multicomponent nanoclusters formed are expected to have different dielectric properties than those exhibited by the single element implantations and manifest those difference in the linear and nonlinear properties of the composite.¹² The results observed for the nonlinear measurements suggest that it may be possible to enhance the nonlinear response of one metal colloid near its surface plasmon resonance frequency by the presence of a second element.

Modification of the host substrate

The second method employed was to modify the response of the metal colloids by first modifying the host substrate by implanting Ti and oxygen and then by sequentially implanting Ag or Au. The implantation of Ti and O results in the modification of the host with polarizable Ti ions. They are incorporated with the O in the network to form a Ti-O-silicate layer. Subsequent implantation of Ag or Au into this layer results in the formation of Ag or Au nanometer dimension colloids with significantly modified optical properties compared to sample without the Ti ions, including enhanced nonlinear response and changes in the position of the surface plasmon resonance in accordance with effective medium theory.

For the series involving modification of the host the Ti was implanted first at an energy of 320 keV. The Ti was implanted with nominal doses of 1.2 and 2×10^{17} ions/cm². The samples were implanted with oxygen to the same nominal dose as the Ti. Au was then implanted with a nominal dose of 6×10^{16} ions/cm² in all samples. The samples were subsequently annealed in oxygen at 900 °C for two hours. In the case of the Ti and Ag series the Ti was implanted at 160 keV to a nominal dose of 1.2×10^{17} ions/cm². Oxygen was then implanted to the same dose as the Ti at an energy of 65 keV. The samples were annealed at 900 C for 2 hours in oxygen and then implanted with Ag ions at 305 keV to a nominal dose of 4.5×10^{16} Ag ions/cm².

The incorporation of the Ti gives rise to an effective change in the index of refraction, n_d , of the host substrate resulting in the observed shift in the wavelength of the surface plasmon resonance of the Au and the Ag colloids. Accompanying this shift is a change in the magnitude of the surface plasmon resonance absorption and an increase in the nonlinear response of the composite off the SPR. We attribute the increase in n_2 to the formation of a more polarizable medium in the silica with increasing Ti concentration resulting in the enhanced n_2 response as well as changes in the linear optical properties.

Photosensitivity

The Ti, O and Ag sequentially implanted samples as well as the single element implanted samples of Ag were subsequently exposed to 100 pulses of ArF irradiation. The pulse power was 40 mJ/cm^2 at a frequency of 10 Hz and pulse width of 20 nanoseconds. The irradiation resulted in visible changes in the color of the glass. Absorption measurements in the sequentially implanted samples show a blue shift in peak position of the surface plasmon resonances of the Ag colloids. Smaller effects were observed in the glasses implanted only with Ag. The nature of the nonlinear response in the irradiated composites was not significantly from the non irradiated samples.

A series of samples of high purity silica (Spectrosil A) were implanted with Bi ions at an energy of 320 keV with nominal doses ranging from $1 \times 10^{16} \text{ ions/cm}^2$ to $12 \times 10^{16} \text{ ions/cm}^2$. Samples were exposed to 5 eV KrF irradiation for pulse totals of 10, 40, 100 and 200. The pulse power was 150 mJ/cm^2 at a frequency of 10 Hz and pulse width of 20 nanoseconds. The photosensitive response of these samples was strongly dependent on the total dose of Bi implanted. For the highest concentrations of Bi there was substantial diffusion of the Bi with irradiation as observed from RBS measurements accompanied by a substantial loss of the Bi ions from the surface. In the lower dose samples it was possible to alter the structure of the implanted glass without the loss of Bi ions.

Summary

Ion implantation offers a flexible technique to form nanometer dimension metal particles in dielectrics. Sequential implantation of different metal ion species may become a viable way to significantly alter the optical properties of nanometer dimension metal particle glass composites by altering the dielectric function of the nanoclusters or by altering the host substrate. Moreover the photosensitive response of these composites to excimer irradiation may make possible new ways to control their optical properties and form devices.

The author acknowledge the support of the Army Research Office under grant DAAH04-93-G-0123.

1. R.A. Wood, P.D. Townsend, N.D. Skelland, D.E. Hole, J. Barton and C. N. Afonso, J. Appl. Phys. 74 (1993) 5754.
2. C. Flytzanis, F. Hache, M.C. Klein, D. Ricard and Ph. Roussignol, Progress in Optics, **29**, (1991) 321 and references there in.
3. C. F. Bohren and D.R. Huffman, Absorption and Scattering of Light by Small Particles, New York, John Wiley & Sons, Inc., 1983.
4. J.W. Haus, N.Kalyaniwalla, R. Inguva, M. Bloemer and C. M. Bowden, J. Opt. Soc. Am. **B6** (1989) 787.
5. J.W. Haus, N.Kalyaniwalla, R. Inguva, M. Bloemer and C. M. Bowden, J. Opt. Soc. Am. **B6** (1989) 787.
6. R.H. Magruder, III, R.F. Haglund, L. Yang, C.W. White, Lina Yang, R. Dorsinville and R.R. Alfano. J. Appl. Phys. Lett. **62** (1993) 465.
7. R. H. Magruder, III, J.E. Wittig and R.A. Zuhr, J. Non Cryst. Solids, **163** (1993) 162.
8. R.A. Zuhr, R.H. Magruder, III and J.E. Wittig, Mat. Res. Soc. Sym. Proc., **316** (1994) 457.
9. R.H. Magruder, III, R.A. Zuhr and D. O. Osborne in press Nucl. Instr. and Meth. B.
10. R.H. Magruder, III, D.O. Osborne and R.A. Zuhr, J. Non Cryst. Solids, in press.
11. J.P. Biersack and L.G. Haggmark, Nucl. Inst. Methods B **174** (1980) 257.
12. R. E. Hummel, Electronic Properties of Materials, 2nd Ed., Springer - Verlag, Berlin (1993).

**DIRECT CORRELATION BETWEEN UV-EXCITED PHOTO-
LUMINESCENCE AND REFRACTIVE INDEX CHANGE
IN PHOTOSENSITIVE Ge-DOPED AND
HYDROGENATED OPTICAL FIBRE.**

Jean Martin[†], Graham Atkins[‡], François Ouellette[‡], Michel Têtu[†], Jean Deslauriers[†] and Michel A. Duguay[†].

[†]Centre d'Optique, Photonique et Laser, Département de Génie électrique, Université Laval, Ste-Foy, Québec, Canada G1K 7P4.

[‡]Optical Fibre Technology Centre, University of Sydney, NSW 2006, Australia.

Many studies have been devoted to the origin of photosensitivity since its discovery in the 70's [1]. The time dependence of the UV-excited blue photoluminescence (PL) has been related to photosensitivity, but up to now the only correlation reported [2] is the relation between the decrease of the blue PL and the refractive index change. In this paper we intend to show a direct correlation between the increase of the blue PL and the refractive index change.

The setup used in this experiment is based on the work of Patrick *et al.* [3] and is shown in figure 1. The UV source is a mode-locked Nd:YAG laser that is doubled twice by LBO and BBO crystal in series, giving a train of 50 ps pulses with a repetition rate of 80 MHz and a wavelength of 266 nm. Bragg gratings are side-written by focusing the UV beam with a cylindrical lens through the phase mask onto the core of the fibre. The beam size at the focal point is 0.5 mm by approximately 2 microns, with 100 mW average UV power; that gives a peak intensity of 2.5 MW/cm². The PL signal is collected from one end of the fibre by a Newport silicon photodetector. The reflectivity of the Bragg grating is measured with a 1550 nm LED coupled in the fibre by a 3 dB coupler. The grating was recorded by an optical spectrum analyser. The fourth port of the 3 dB coupler is index matched with glycerin to avoid undesirable reflection. The reflectivity signal is calibrated with a transmission spectrum of the resulting grating.

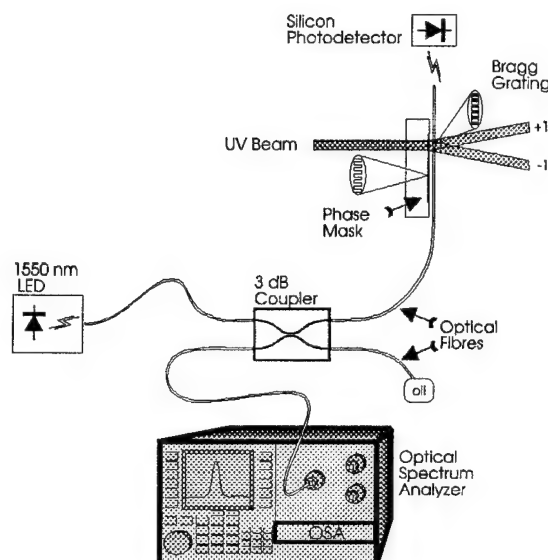
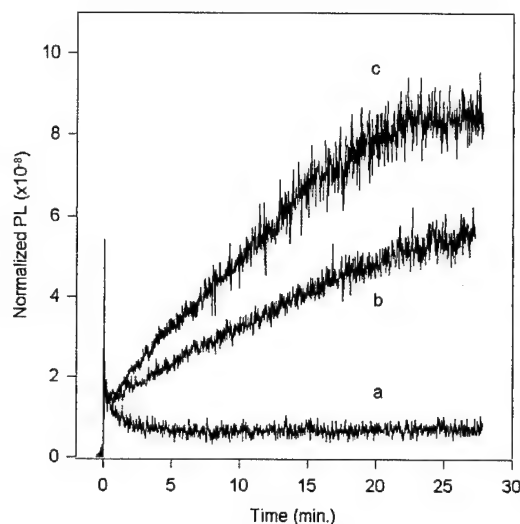


Figure 1: Experimental setup.

Figure 2: Normalized PL power vs time: a) $P_{UV} = 15$ mW, b) $P_{UV} = 60$ mW and c) $P_{UV} = 90$ mW.

The fibre used in this experiment was a Corning SMF-28 fibre containing 4.3% mol. of germanium in the core, soaked in a pressure chamber with 100 atm. of H_2 at room temperature for at least 2 weeks. Figure 2 shows the time evolution of the normalized blue PL (*i.e.* P_{PL}/P_{UV}). At low average UV power ($P_{UV}=15$ mW), we observe the same pattern as when the fibre is not hydrogenated (see also Poirier *et al.*[4]). For higher UV powers, however, the PL intensity increases after the usual decrease, a

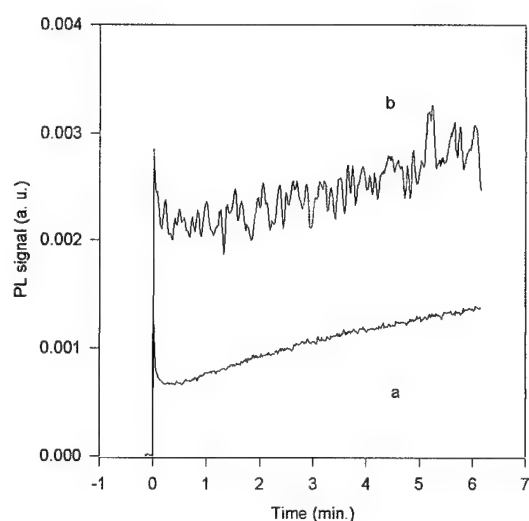
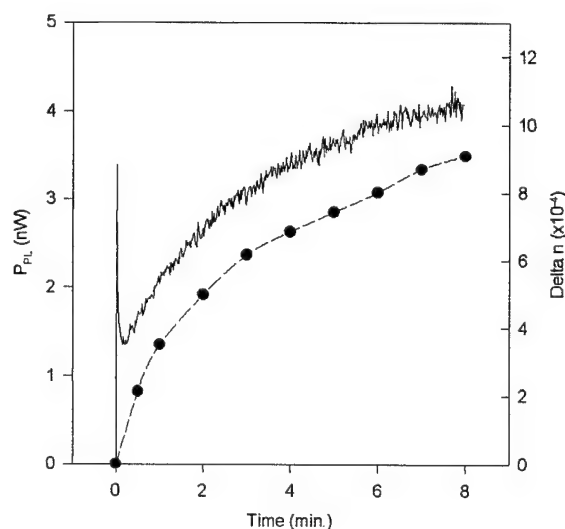


Figure 3: PL signals vs time measured from a) one end and b) the side of the fibre.

Figure 4: PL power (line) and Δn (dot) vs time.

previously unreported phenomenon suggesting that H_2 catalyses a new cycle in the UV absorption and PL emission processes. Patrick *et al.* [5] have pointed out that photodarkening can mask the temporal behaviour of a PL signal. To verify this effect we compare (see figure 3) the time evolution of two PL signals recorded simultaneously a) from one end of the fibre and b) from the side (as in ref. 5) using a lens and blue filters. In curve b) the background is due to remaining 532 nm light. Photodarkening effect does not play an important role in our experiment because only a short length (0.5 mm) of the core was exposed.

In figure 4, we show the correlation between the PL intensity and the refractive index change (Δn) associated with the growth of the Bragg grating. The Δn values were obtained by fitting the actual Bragg grating spectrum with the simulated spectral response of a uniform Bragg grating. The computer program is based on the work of Yamada and Sakuda [6]. The Bragg grating length obtained by the simulation is 0.5 mm. The Δn values are obtained by assuming a 100% overlap between the fibre mode and the transverse index distribution of the grating. The Δn curve does not superpose the PL curve because of the constant level of PL arising from the unhydrogenated response of the fibre (see curve *a* in figure 2: after a few minutes there is a constant PL level) suggesting the superposition of two phenomena.

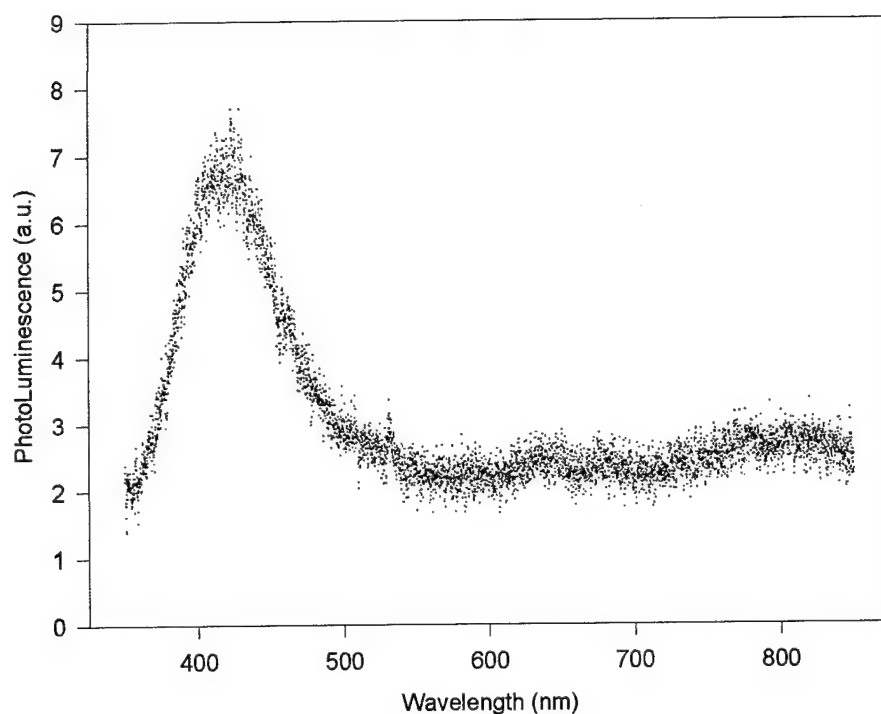


Figure 5: Photoluminescence spectrum.

Figure 5 shows the spectrum of the steady state PL obtained by replacing the photodetector by a monochromator and a photomultiplier tube (after more than 30 min.) with high incident UV power. The DC level is due to noise, and the weakness of the signal prevents us from resolving peaks other than the well known blue band. The absence of other major peaks suggest that the defect responsible for the blue PL is both created and destroyed by the UV radiation. New defect sites could be created by a reaction between H_2 and the glass, catalysed by local heating [7] due to high UV power absorption. The observed increase in PL intensity at higher UV power suggests that the creation process could involve two-photon absorption ($2h\nu = 9.3$ eV), in competition with a one-photon bleaching process. While two 266 nm photons can bridge the 9 eV silica band gap [8] in a similar manner to the commonly used 248 nm wavelength, 266 nm light is further from the centre of the 240 nm absorption band [9] and is not expected to be as efficient at bleaching the defects. An enhancement of the defect creation process relative to the bleaching process for 266 nm light could explain why the competitive increase in PL intensity has not been reported with exposure to 248 nm light. Post-writing thermal treatments will be performed in order to investigate the binding energy of the present defect(s).

In conclusion, we have reported results showing a direct correlation between 266 nm-induced blue photoluminescence and refractive index change during Bragg grating growth in Ge-doped, H_2 loaded optical fibre. The time evolution of the PL was found to depend on the UV power, and the behaviour at higher UV power appears indicative of competing processes of defect creation and bleaching of the defect responsible for the PL.

References:

- [1] K. O. Hill, Y. Fujii, D. C. Johnson and B. S. Kawasaki, *Appl. Phys.*, **32**, 647 (1978).
- [2] Y. Duval, R. Kashyap, S. Fleming and F. Ouellette, *Appl. Phys. Lett.*, **61**, 2955 (1992).
- [3] H. Patrick and S. L. Gilbert, *Opt. Lett.*, **18**, 1484 (1993).
- [4] M. Poirier, S. Thibault, J. Lauzon and F. Ouellette, *Opt. Lett.*, **18**, 870 (1993).
- [5] H. Patrick, S. L. Gilbert and A. Lidgard, *Opt. Mat.*, **3**, 209 (1994).
- [6] M. Yamada and K. Sakuda, *Appl. Opt.*, **26**, 16 (1987).
- [7] R. M. Atkins, P. J. Lemaire, T. Erdogan and V. Mizrahi, *Elect. Lett.*, **29**, 1234 (1993).
- [8] T. H. DiStephano and D. E. Eastman, *Solid State Comm.*, **9**, 2259 (1971).
- [9] R. M. Atkins and V. Mizrahi, *Elect. Lett.*, **28**, 1743 (1992).

Mechanisms of Photo-bleaching of 5eV Absorption Band in Hydrogen Loaded Ge-doped SiO₂

Koichi Awazu and Hideo Onuki

Optical Radiation Section, Electrotechnical Laboratory

Umezono, Tsukuba 305, Japan

Tel 81-298-58-5650, Fax 81-298-58-5657

Ken-ichi Muta

Showa Electrical Wire & Cable Co.Ltd.

Minami-Hashimoto, Sagamihara, Japan

Tel 81-427-74-8208, Fax 81-427-73-6904

INTRODUCTION

It has been well known that the optical absorption band at 5eV exists in Ge doped a-SiO₂. Some origins of photosensitivity are proposed [1] and undoubtedly one of them is related to the origin of 5eV band [2]. Two kinds of different defects have responsibility on the absorption band at 5eV, one is a neutral oxygen vacancy (NOV) peaking at 5.06eV and the other is a Ge lone pair center (GLPC) at 5.14eV [3]. Hosono et al. reported that the NOV was photochemically converted into Ge E' center [2]. Recently, a maximum refractive-index change Δ of 1% has been reported in hydrogen-loaded germanosilicate fibers. In this article, photochemical reactions in H₂ loaded Ge-doped a-SiO₂ were examined [4].

EXPERIMENTAL

10GeO₂:90SiO₂ glass was prepared by the vapor-phase axial deposition (VAD) method. All sample rods were cut into disks having 0.5mm thickness and polished for the optical measurement. Sample disks were loaded with molecular hydrogen at pressure of 200atm and at room temperature. Diffusing depth of H₂ was estimated as about 0.15mm from each surfaces under the condition.

UV illumination was carried out with the 300W Xe/Hg lamp. A cell filled with H₂O and with a-SiO₂ windows was used to remove the deep UV and IR emission from the Xe/Hg lamp. Photon numbers in 5eV region can be estimated as $4 \times 10^{19} \text{cm}^{-2} \text{hr}^{-1}$. Optical absorption, photoluminescence, and ESR spectra were measured.

RESULTS & DISCUSSION

Figure 1 shows changes of optical-absorption spectra of $10\text{GeO}_2:90\text{SiO}_2$ glass before and after UV illumination. Solid lines show the spectra of the as-received sample and H_2 loaded one. Both line shapes of the samples with and without high pressured H_2 loading are almost same before illumination. In case of as-received sample, intensity of the 5.14eV band decreased from 24cm^{-1} to 19cm^{-1} with illumination. Intensity of the 5.14eV band in H_2 loaded one dramatically decreased from 24cm^{-1} to 5.5cm^{-1} with illumination.

Figure 2 shows the photoluminescence spectra excited at 5.14eV . Solid line denotes the spectra of the as-prepared sample and H_2 loaded one without illumination. Again, no obvious change was observed between them. There are two photoluminescence bands peaking at 3.2eV and 4.3eV . Kohketsu et al. reported that absorptions at 5.06eV and 5.14eV , which are assigned to NOV and GLPC, respectively, gave photoluminescence bands at 4.3eV and 3.2eV , respectively [3]. Dotted and dashed lines denote the spectra of as-prepared sample and H_2 loaded one with illumination, respectively. In case of as-received sample, intensity of the 4.3eV band decreased in contrast no change was observed in the band at 3.2eV with illumination. In case of H_2 loaded one, on the other hand, intensities of not only the 4.3eV band but also the 3.2eV one dramatically decreased with illumination. These results mean that only NOV is bleached in as-prepared sample, in contrast, both NOV and GLPC are bleached in H_2 loaded sample with UV illumination.

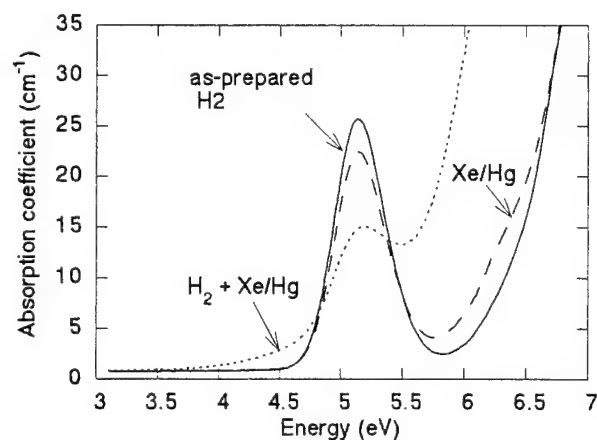


Figure 1 Changes of optical-absorption spectra of $10\text{GeO}_2:90\text{SiO}_2$ glass before and after illumination. Solid lines show the spectra of the as-received sample and H_2 loaded one. Both line shapes are almost same in this scale. Long dashed line and dotted line show the spectra of as-received sample and H_2 loaded one before the 7hr illumination, respectively. Illumination was carried out with Xe/Hg discharged lamp at room temperature.

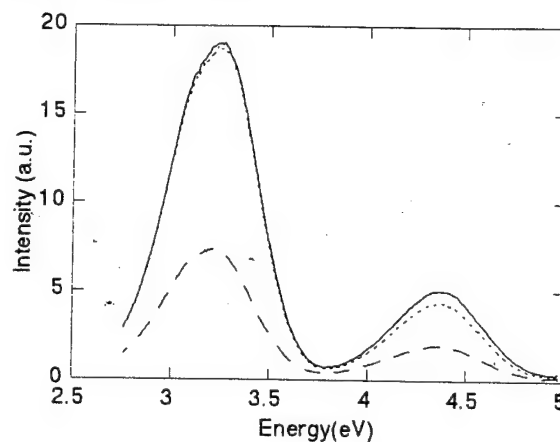


Figure 2 Photoluminescence spectra excited at 5.18eV . Solid lines denote the spectra before and after H_2 loading. No change was observed on the sample with H_2 loading. Spectra with dotted and dashed lines denote the as-received and H_2 loaded samples with illumination, respectively.

Relationship between absorption coefficient at 5eV and concentration of Ge E' center in 10GeO₂:90SiO₂ was shown in figure 3. Open squares and closed circles denote the data of as-received samples and H₂ loaded ones with duration of illumination, respectively. Open squares are on the straight line through the origin. Hosono et al. proposed that the Ge E' center was generated under illumination from NOV as equation (1) in figure 4. Linear relations between band intensity and UV-induced Ge E' center concentrations in figure 3 provide a basis for attributing the 5eV band to the precursor site of the Ge E' center. Concentration of NOV in as-prepared sample can be estimated from the absorption coefficient at 5eV using the oscillator strength of NOV ($f = 0.4$). Concentration of the bleached NOV was almost the same as that of the generated Ge E' center.

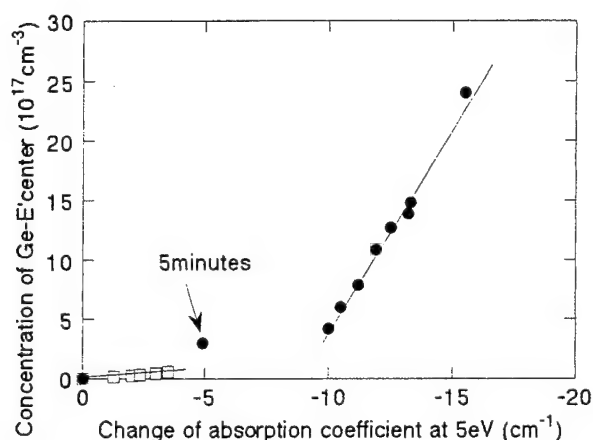


Figure 3 Relationship between absorption coefficient at 5eV and concentration of Ge E' center with duration of illumination. Squares and circles denote the data of as-prepared samples and H₂ loaded ones.

In case of H₂ loaded sample, one circle which is the data of five minutes illumination is very close to the straight line composed of open squares, yet the others are not on the extended line of open squares but on the other straight line in figure 3. The results mean that there are two kinds of photochemical reactions in H₂ loaded sample. As we mentioned previously, both NOV and GLPC are bleached with UV illumination. Here, we proposed that GLPC was also the precursor of Ge E' center as in equation (3) in figure 4. GLPC is photochemically converted into the NOV with help of H₂ molecules in the glass. The reaction of which one Ge-O bond in GeO₂ network breaks to form another Ge-O bond with Ge in GLPC equals to the photochemical conversion of GLPC into NOV (equations (2) and (3) in figure 4). We assumed that H₂ molecules trapped in the glass would be an essential species in the photochemical process, because this reaction was never observed in as prepared sample.

Heated H₂ treatments of the sample at 400°C or 600°C were also examined. Actually, intensity of the 5eV band reduced with illumination, yet the effect of the heating in H₂ is less effective than that of the H₂ loading at room temperature. Solubility of H₂ in SiO₂ or Ge-doped SiO₂ has been reported as $4.2 \times 10^{20} \text{ cm}^{-3}$ (2mol%), $3.3 \times 10^{17} \text{ cm}^{-3}$, and $2.5 \times 10^{17} \text{ cm}^{-3}$ at room temperature,

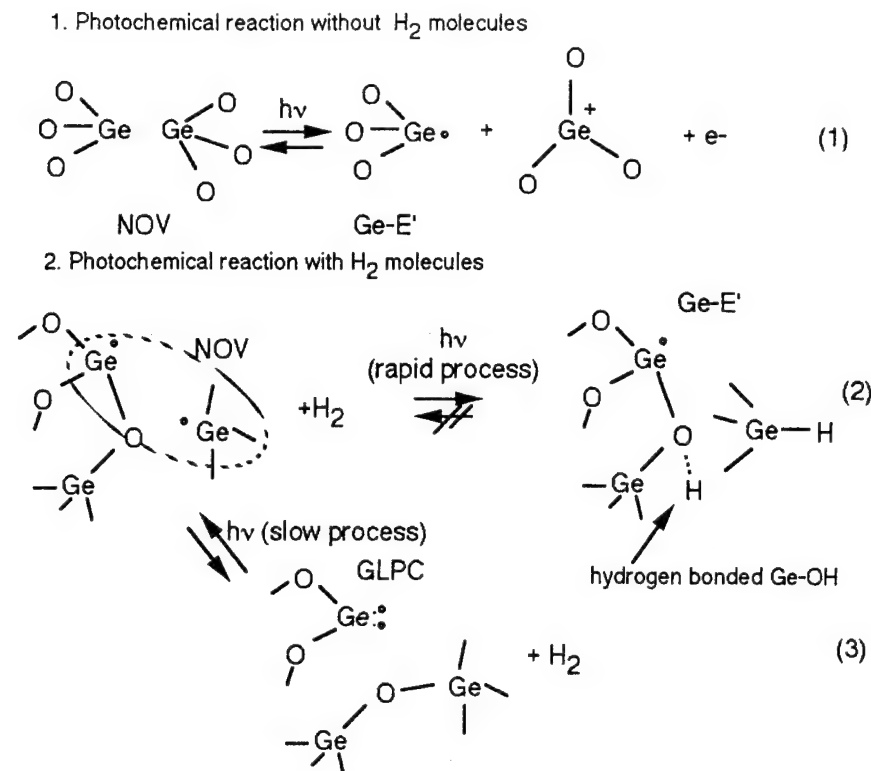


Figure 4 model of photochemical reactions in Ge doped a-SiO₂ glass

(1) denotes the reaction model without H_2 molecules in glass
 (2) and (3) denote the reaction model under the existence of H_2 molecules in the glass.

400°C and 600°C, respectively. Therefore, we proposed the photochemical reaction between 10GeO₂:90SiO₂ glass and H_2 molecules trapped in the glass network. Remarkable photo-bleaching of H_2 loaded sample originated from the high solubility of H_2 in Ge-doped SiO₂ glass.

SUMMARY

In this article, photochemical reactions of Ge doped a-SiO₂ loading H_2 were proposed.

- (1) Only neutral oxygen vacancy (NOV) in Ge doped a-SiO₂ without H_2 treatment is converted into Ge E' center photochemically.
- (2) In case of H_2 loaded Ge doped a-SiO₂, not only NOV but Ge lone pair center (GLPC) which is coordinated with two oxygens are converted into Ge E' center, photochemically.

REFERENCES

- [1] B.Malo et al., Appl.Phys.Lett., 65, 394 (1994).
- [2] H.Hosono, Y.Abe, D.Kinser, R.Weeks, K.Muta, and H.Kawazoe, Phys.Rev.B, 46, 11445 (1992).
- [3] M.Kohketsu, K.Awazu, H.Kawazoe, and M.Yamane, J.Non-Cryst.Solids, 95 & 96, 679 (1987).
- [4] A.Vengsarkar, P.Lemaire, W.Reed, and K.Quoi, in Conference on Opt. Fiber Commun., 1994 Technical Digest Series, 48 (Optical Society of America, San Jose, United States), paper Th13
- [5] J.Shackelford, P.Studt, and R.Fulrath, J.Appl.Phys., 43, 1619 (1972). H_2 solubility at RT and high temperature.

UV Laser Induced Photocurrent in Oxygen Deficient Silica and Germanosilicate Glasses

Victor N. Bagratashvili, Svetlana I. Tsypina, Pavel V. Chernov, Aleksey O. Rybaltovskii,
Yuriy S. Zavorotny, Sergey S. Alimpiev, and Yaroslav O. Simanovskii
Laser Chemistry Research Center, Pionerskaya 2, Troitsk, Moscow Region,
142092 Russia, tel/fax: +7 (095) 3340342,
E-mail: bagrat@laschem.msk.su

Liang Dong, and Philip St.J. Russell
Optoelectronics Research Centre, University of Southampton, Southampton
SO17 1BJ, U.K., tel: +441703583083, fax: +441703533149,
E-mail: PSJR@orc.southampton.ac.uk

Germanium and silicon oxygen deficient centers (GODC and SODC) play a key role in the phenomenon of photosensitivity of glasses.¹⁻⁴ The study of GODC and SODC and their photoreactions is proceeding vigorously,⁵⁻⁸ but the mechanisms of their phototransformations are far from being understood. The most popular mechanism of primary photoreaction of GODC and SODC is their photoionization.^{5,9,10} For SODC the two-step ionization channel was established,^{9,10} but for GODC the situation is more complicated. Unfortunately, up to this point there are only a few direct measurements of UV laser induced photocurrent in oxygen deficient glasses,^{9,11} which allow clarification of the mechanism of UV photoionization and its real part in the photodecomposition of GODC. We report the results of our direct photocurrent and photoluminescence studies of UV laser excitation and decomposition of defect centers in germanosilicate and silicate glasses.

The experiments were performed with 5 different types of silica (N4 and N5) and germanosilicate (N1, 2 and 3) samples (see Table 1). The samples N1, 2, 4 and 5 had a rectangular shape with polished sides, a 5x5 mm² cross-section and different lengths (along the axis of laser beam) to avoid the effect of thick optical layer. The sample N3 was a germanosilicate film deposited on a silica substrate. The concentration of SODC and GODC was determined from UV absorption bands measured with a UV/vis absorption spectrometer (Specord M40),

Table 1. Parameters of samples.

Sample	N1	N2	N3	N4	N5
Parameters					
Type of glass	II	II	IV	IV	III
Impurities content, %	OH - 0.02 Al, Na ~ 0.001 Ge ~ 0.01	OH - 0.02 Al, Na ~ 0.001 Ge ~ 0.05	OH - 10 ⁻⁴ Al, Na ~ 10 ⁻⁵ Ge - 10	Cl ~ 0.01 OH ~ 10 ⁻⁴ Al, Na ≤ 10 ⁻⁴	OH - 10 ⁻⁴ Al, Na ~ 10 ⁻⁵
λ_{max} , nm	242	242	242	248	-
Thickens, cm	1.4	0.1	4×10 ⁻³	0.8	0.6
Concentration of GODC and SODC N_{ODC} , cm ⁻³	GODC 4×10 ¹⁶	GODC 1.2×10 ¹⁸	GODC 10 ²⁰	SODC 2.5×10 ¹⁶	SODC < 10 ¹⁴
*Amplitude of photocurrent, P, mV	50	60	6	150	<1
*Density of displaced charge, q, coulombs/cm ²	2.8×10 ⁻⁹	2.8×10 ⁻⁸	2.3×10 ⁻⁷	1.4×10 ⁻⁸	-

* $\Phi = 0.18$ J/cm²

using the Smacula formula and known oscillator strength: for GODC¹² $f=0.03$ and for SODC¹³ $f=0.14$. Also, we used a high purity silica sample (N5) with no detectable concentration of oxygen deficient centers.

A KrF excimer laser ($\lambda=248$ nm, $\tau=25$ ns) was used in our experiments. The UV laser beam was collimated into the sample (see Fig.1). The sample was placed between metal electrodes, which were slightly narrower than the samples, to minimize the background photocurrent signal caused by photoionization of the air around the sample. Also there is a time-

of-flight separation between this background signal and the signal to be measured. Simultaneously, the laser induced luminescence signal was collected into the monochromator, and

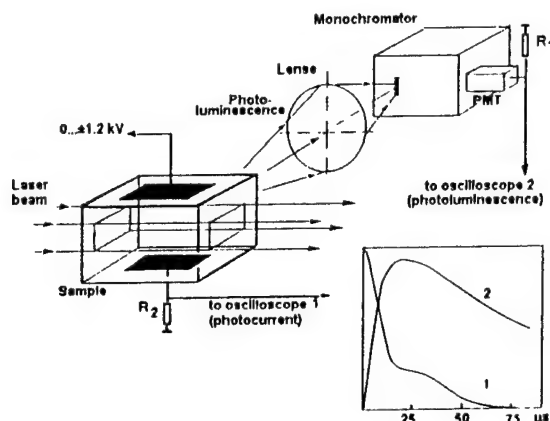


Fig.1. Experimental arrangement for synchronous measurements of UV laser induced photocurrent and photoluminescence. $R_1 = 10^3 \Omega$, $R_2 = 10^6 \Omega$. The inset are the oscillograms: 1 - photocurrent signals (the tail is due to background signal); 2 - photoluminescence signals from germanosilicate samples N1, 2 and 3 ($\lambda_{\max} = 396 \text{ nm}$).

recorded by a photomultiplier and then by a digital oscilloscope. Since the temporal resolution of our photocurrent measurements (10^{-5} sec) was much longer than the lifetime of free carriers ($10^{-9}-10^{-11} \text{ sec}$), the amplitude of the photocurrent $P \sim \delta Q$ (the total number of elementary charges displaced across the UV irradiated sample). The density of charges $q = \delta Q/S$ (S - area of electrodes) for our samples is given in Table 1. The rise of the GODC concentration results in an increase in q . In sample N5 (free of ODC) the q value was about 1% of the signal observed for sample N4. Thus, the observed displacement photocurrent signals in samples N1, 2, 3 and 4 are really induced by photoionization of GODC or SODC. Figure 2 shows rapid pulse-to-pulse degradation of the photocurrent amplitude during the first few pulses. However, the changing the applied voltage polarity resulted in the appearance of an intense photocurrent pulse, opposite in sign. Even with the applied voltage off and the electrodes shorted out, the photocurrent pulse is still observed, having a lower initial amplitude, being opposite in sign, and degrading at about the same rate, as with the applied voltage. In addition, the amplitude of the first pulse after switching the external voltage being off (point D) is equal exactly to the difference in maximal amplitude of the signal (points B or C) and the signal in the first laser pulse (point A). It should also be noted that with the applied voltage being on, the residual (background) signal is about 20% of the initial signal. At the same time, with the applied voltage being off, there is no background photocurrent signal. It is clear, that the observed pulse-to-pulse degradation of P is not caused by a decrease in the GODC concentration. Simultaneously we measured the pulse-to-pulse behaviour of the signal from the triplet luminescence ($\lambda_{\max} = 396 \text{ nm}$), that corresponds to the pulse-to-pulse degradation in the GODC concentration due to their decomposition. The measured decrease of GODC content was no more than 20% throughout our photocurrent measurements presented on Fig.2 (about 40 pulses). This is also supported by equal values of photocurrent amplitudes at the points B and C. Thus, the main reason for the observed pulse-to-pulse degradation of the photocurrent signal is the effect of screening of the external field by the internal field. This internal field is created by UV laser induced ionization of GODC and drift of released charges in the external electric field.

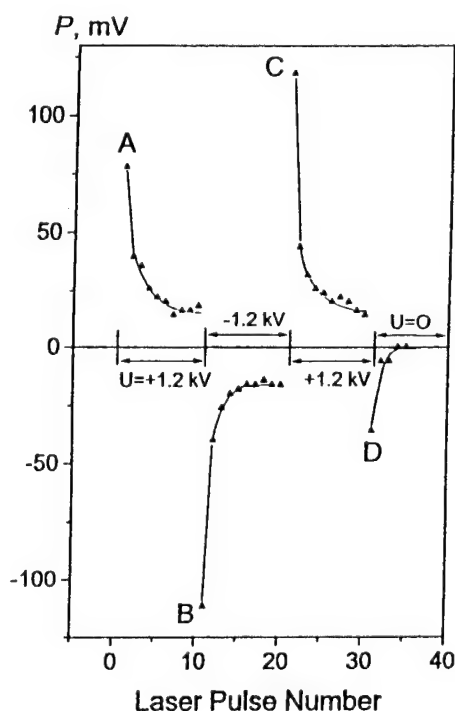


Fig.2. Pulse-to-pulse degradation of the photocurrent amplitude of the sample N2, $\Phi = 0.4 \text{ J/cm}^2$.

For the oxygen deficient silica sample (N4) there is quite a good correlation between the measured $P(\Phi)$ plot and the fluence dependence of yield of SODC decomposition per one pulse $\beta(\Phi)$ (Fig.3a). The square low dependencies of the plots of $P(\Phi)$ and $\beta(\Phi)$ at $\Phi < 0.3 \text{ J/cm}^2$ support the conclusion,⁶ that two-photon $S_0-S_1-S_n$ excitation and ionization is the dominant channel of UV laser induced decomposition of SODC in high purity silica glass. In this case the yield of two-step ionization of SODC can be described by the following formula⁶

$$\frac{N_i}{N_{\text{SODC}}} = \frac{\sigma_{01} \cdot \sigma_{12} \Phi^2}{(h\nu)^2 \tau_{UV} \left[\frac{1}{\tau_S} + \frac{1}{\tau_{ic}} + \frac{\sigma_{12} \Phi}{h\nu \cdot \tau_{UV}} \right]} \quad (1)$$

The parameters of eq.1 (see inset in Fig. 3a) are taken from [6]. The saturation of the plots of $P(\Phi)$ and $\beta(\Phi)$ at $\Phi > 0.3 \text{ J/cm}^2$ gives the cross-section of the S_1-S_n transition $\sigma_{12} = 6 \times 10^{-18} \text{ cm}^2$. The slope of the $P(\Phi)$ plot (in double logarithmic scale) for GODC (sample N1) is about 2, when $\Phi < 0.1 \text{ J/cm}^2$. When $\Phi > 0.2 \text{ J/cm}^2$, P depends nearly linearly on Φ . As for the laser induced luminescence signal, this linearly depends on Φ at low fluences, and tends to saturate at $\Phi > 0.2 \text{ J/cm}^2$. At higher fluences $\Phi > 0.5 \text{ J/cm}^2$ there is even some decrease in the luminescence signal.

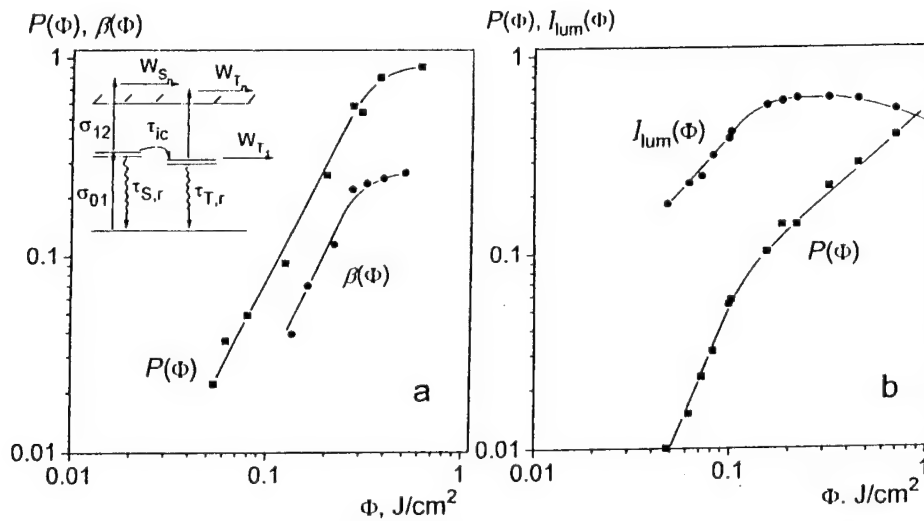


Fig.3. (a) Fluence dependencies of photocurrent signals $P(\Phi)$ and observed yield of SODC decomposition per one pulse $\beta(\Phi)$ (sample N4). The inset is the kinetic scheme of photoprocesses involving SODC or GODC. For SODC $\sigma_{01}=3.2 \cdot 10^{-17} \text{ cm}^2$, $\tau_{S,r}=8.3 \text{ ns}$ - radiative lifetime of S_1 state; $\tau_{T,r}=9.8 \text{ ms}$ - radiative lifetime of T_1 state; $\tau_{ic}=104 \text{ ns}$ - time of intersystem crossing⁸; W_i - the rates of reactions from subsequent excited states.

(b) Fluence dependencies of photocurrent signals $P(\Phi)$ and photoluminescence $I(\Phi)$ for germanosilicate sample (N1). The kinetic parameters for GODC (see inset in Fig.3a) are: $\sigma_{01}=5 \times 10^{-18} \text{ cm}^2$, $\tau_{S,r}=44 \text{ ns}$; $\tau_{T,r}=10^{-4} \text{ s}$; $\tau_{ic}=5.3 \text{ ns}$.¹²

Our synchronous photocurrent and photoluminescence studies of UV laser excitation of GODC also give evidence for their two-step ionization. The change of slope of the $P(\Phi)$ plot from 2 to 1 and the saturation of the one-quantum excitation takes place in the same fluence range $\Phi=0.1-0.2 \text{ J/cm}^2$. At higher Φ the ground state is completely depopulated, and the excitation probability of ionizable states becomes linearly dependent on the laser fluence. Further increases in Φ result in a depopulation of the T_1 state caused by the transition to an ionizable state. From the observed decrease of triplet luminescence one can obtain the following estimate for the transition cross-section from the first to the upper electronic states $\sigma_{12}=(0.5-1) \times 10^{-19} \text{ cm}^2$. Unfortunately, from these experiments it is difficult to decide, which transition (S_1-S_n or T_1-T_n) plays the dominant role for the photoionization of GODC. The two-photon character of the observed GODC photoionization process is, however, beyond question.

The screening effect allows estimation of the concentration of laser induced free charges. The pulse-to-pulse dependence of the photocurrent signal can be written

$$P(n) = P(1) \left[\exp \left(\frac{N_i \tau_i \mu \cdot e}{\varepsilon} \right) \right]^{n-1} \quad (2)$$

where n is the sequential number of the laser pulse, N_i is the concentration of UV laser induced carriers, e is the electronic charge, $\mu = 20 \text{ cm}^2/\text{V}\cdot\text{sec}$ is the carrier mobility,¹⁵ $\varepsilon = 3.8$ is dielectric constant, and τ_i is the carrier lifetime. From $P(n)$ for SODC (sample N4) at $\Phi = 0.18 \text{ J/cm}^2$, we have $N_i \mu \tau_i / \varepsilon = 0.6$. To estimate τ_i and $x = \mu \tau_i E$ one should know the N_i value. In the case of SODC this value can be determined from the $P(\Phi)$ plot under the conditions that $N_i = N_{\text{SODC}}$ when $\Phi > 0.3 \text{ J/cm}^2$. At $\Phi = 0.18 \text{ J/cm}^2$ we have $N_i = 0.8 \times 10^{16} \text{ charge/cm}^3$, $\tau_i = 10^{-10} \text{ sec}$ and $x = 480 \text{ \AA}$. This value is nearly the same as the average distance between ionized SODC $l = 1/\sqrt{N_i} = 500 \text{ \AA}$. Thus one can conclude, that ionized SODC play a key role in electron trapping. This is why the observed yield of the SODC photodecomposition process is much less than 1 (see Fig.3a), and why most of the free charges are recombined with E' centers giving the initial SODC.

For the GODC case it is difficult to make a similar estimate, since the saturation of the $P(\Phi)$ has not been reached, and there is no reference point. However, the higher is the GODC content, the shorter is x . It should be also noted, that in germanosilicate samples both ionized GODC and Ge atoms can play the role of electron traps, so that quantitative estimations are more complicated in this case. Anyway, a rise in GODC concentration can lead to a decrease in the ratio of the two-photon ionization channel to the total yield of GODC decomposition, if no other charge traps are introduced into the glass network.

At low laser fluences $\Phi \ll 0.18 \text{ J/cm}^2$ the role of the two-photon channel is minor, and one-photon photoreaction of GODC from the long-lived triplet ($\tau_i = 10^{-4} \text{ s}$) T_1 state is the dominant process. The specific mechanism of this one-quantum photoreaction is not well understood, but in our opinion it may be the tunneling of electrons from the T_1 state of the GODC to impurity states.⁶ The results of our detailed studies of competition of one- and two-photon reaction channels and of the role of impurities for GODC photodecomposition will be reported in [14].

¹ K. O. Hill, B. Malo, F. Bilodeau, and D. C. Johnson, *Ann. Rev. of Mat. Sci.* **23**, 125 (1993).

² P. St. J. Russell, J.-L. Archambault, and L. Reekie, *Physics World*, 41 October (1993).

³ R. Kashyap, *Opt. Fiber Technology* **1**, 17 (1994).

⁴ W. W. Morey, G. Meltz, and W. H. Glenn, *Optics & Photonics News*, 14, July (1990).

⁵ V. B. Neustruev, *J. Phys.: Condens. Matter* **6**, 6901 (1994).

⁶ V. N. Bagratashvili, A. O. Rybaltovskii, Ya. O. Simanovskii and S. I. Tsykina, *SPIE Proc.* **1856**, 69 (1993).

⁷ V. A. Radzig, V. N. Bagratashvili, S. I. Tsykina, P. V. Chernov, and A. O. Rybaltovskii, *J. Phys. Chem.* **99**, 6640 (1995).

⁸ V. N. Bagratashvili, S. I. Tsykina, V. A. Radtsig, A. O. Rybaltovskii, P. V. Chernov, S. S. Alimpiev, Ya. O. Simanovskii, *J. Non-Cryst. Sol.* **180**, 221 (1995).

⁹ V. N. Bagratashvili, S. I. Tsykina, S. S. Alimpiev, Ya. O. Simanovskii, A. M. Prokhorov, A. O. Rybaltovskii, *Laser Chem.* **12**, 211 (1992).

¹⁰ K. Arai, H. Imai, H. Hosono, J. Abe, and H. Imagawa, *Appl. Phys. Lett.* **53**, 189 (1988).

¹¹ R. Kashyap, G. D. Maxwell, and D. L. Williams, *Appl. Phys. Lett.* **62**, 214 (1993).

¹² V. N. Bagratashvili, V. K. Popov, S. I. Tsykina, P. V. Chernov and A. O. Rybaltovskii, *Opt. Lett.* (submitted).

¹³ L. Skuja, *J. Non-Cryst. Solids* **149**, 77 (1992).

¹⁴ V. N. Bagratashvili, S. I. Tsykina, P. V. Chernov, A. O. Rybaltovskii, P. St. J. Russell, L. Dong, *J. Appl. Phys.* (to be published).

¹⁵ R. G. Hughes, *Rad. Effects* **26**, 225 (1975).

Characterization of photosensitivity in germanosilicate

Christian V. Poulsen, Søren Haugbølle and Jörg Hübner

Mikroelektronik Centret

Technical University of Denmark, bldg. 345 E, DK-2800 Lyngby, Denmark

Phone: (+45) 45 25 57 60, Fax: (+45) 45 88 77 62

E-mail: cvp@mic.dtu.dk

Introduction: Permanent UV-induced refractive index changes in germanium doped silica glasses have been a subject of intense investigation for the last decade [1]. In optical fibers UV-induced Bragg-gratings have many possible applications. In planar waveguides less work has been carried out, partly because the technology is not yet developed to the same maturity as for optical fibers. UV-induced refractive index changes in planar structures offer great possibilities as a new way of producing diffractive elements such as Bragg-gratings in existing waveguides [2] and writing buried channel waveguides directly [3,4]. The performance of the technique highly depends on the photosensitivity of the glasses used, making an investigation of the different glass types important. In this work we describe a characterization of the photosensitivity of germania doped silica glasses deposited by plasma enhanced chemical vapor deposition (PECVD). The degree of refractive index change is measured after UV-exposures at 193 nm and 244 nm.

PECVD is well suited for developing germanium doped silica glasses with high photosensitivity, due to the relatively cold deposition temperature of $\sim 300^\circ\text{C}$ followed by annealing at $\sim 800^\circ\text{C}$. This means an excellent control of the glass matrix may be achieved without melting as for sintering in flame hydrolysis. High photosensitivity has already been demonstrated without any hydrogen loading in PECVD glasses [5].

For directly UV-written waveguides the induced refractive index changes must be in the order of $5 \cdot 10^{-3}$ to match standard optical telecommunication fibers and allow curved structures. This can be obtained by hydrogen-loading, but a significant extra contribution to the propagation loss will be introduced. Deuterium may be used instead of hydrogen to move the absorption peak away from the third optical window. However, this method is relatively expensive. Preferably the high index increase should be obtained in non sensitized glass.

Experiments and discussion: To investigate and compare the photosensitivity, we illuminated limited regions of glass films with 193 nm and 244 nm UV-radiation in two different setups. In the first setup we used an intra cavity frequency-doubled CW Ar-ion laser producing ~ 100 mW of 244 nm UV-radiation. With this source we illuminated a

circular area with a diameter of 3 mm on nine different films for one hour. The results are listed for different mole concentrations of germanium in table 1a.

Mole % GeO ₂	0	2.9	5.9	8.6	10.5	11.8	14.3	22.7	10.5
Comments	SiO ₂	no co-doping						fast growth	B-doped
$\Delta n [10^{-4}]$	0	0	0	2	2.5	5	14	25	3

Table 1a: Photosensitivity on germanosilicates induced by 244 nm CW radiation.

A prism coupler setup, with a resolution of $\sim 5 \cdot 10^{-5}$, was used to measure the refractive index variation at 633 nm within a $15 \times 15 \text{ mm}^2$ region around the exposed area. As expected the photosensitivity increases with the germanium content. In spite of a relatively weak UV-intensity of 1.5 W/cm^2 considerable refractive index changes are measured.

The second setup includes an ArF excimer laser @193 nm with repetition rate up to 20 Hz and pulse energy of up to 100 mJ giving an intensity of $\sim 10 \text{ MW/cm}^2$. The pulses used for this experiment had a rectangular shape of $2 \times 20 \text{ mm}^2$. To investigate the dynamics of the refractive index increase the germanium doped silica thin films were exposed to 500, 1000 and 2000 pulses with this rectangular shape at different locations spaced by 5 -10 mm. The refractive index variation was again measured with the prism coupler, this time by a linear scan across the center of the exposed areas. An example of an exposed boron/germanium doped silica thin film is shown in figure 1:

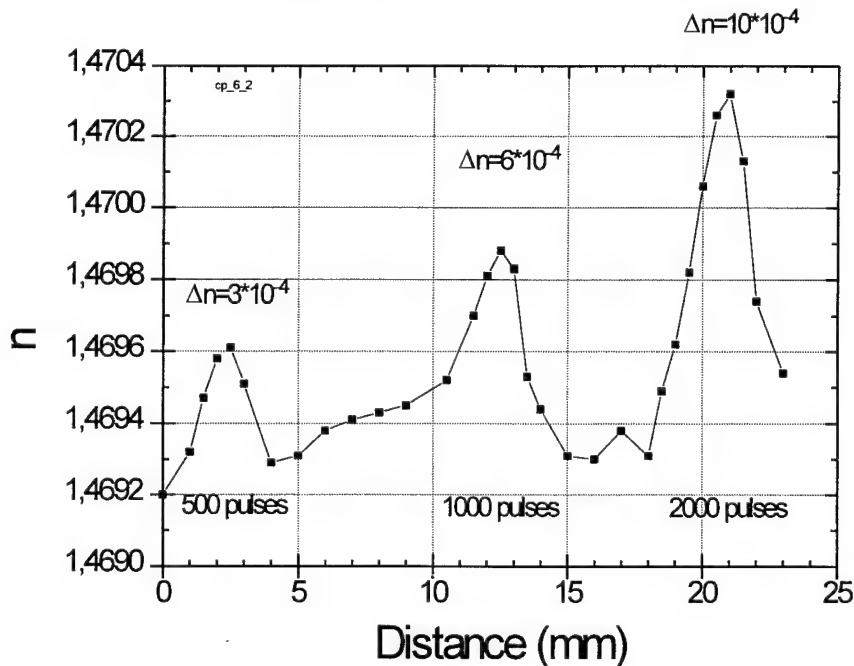


Fig. 1: Prism coupler measurement of refractive index in Germanium/boron doped silica thin film

An overview of the results from the 193 nm exposures are shown in table 1b:

Mole % GeO ₂	0	2.9	5.9	11.8	17.6	23.5	0	5.0	6.6	8.1
Comments	SiO ₂			B-doped	O-deficiency		Phosphor-doped			
$\Delta n [10^{-4}]$	0	0	2.2	10	19.5	32.5	<0.5	<0.5	<1	2.8

Table 1b: Photosensitivity on germanosilicates induced to 193 nm pulsed radiation

As for 244 nm, the photosensitivity increases with the germanium content. The films grown in an atmosphere with low oxygen content show a particularly high photosensitivity possibly caused by an increased number of defects in the glass. The high photosensitivity ensures possibilities for direct writing of channel waveguides.

The phosphor/germanium doped films, which are frequently used for passive waveguides, generally show a lower photosensitivity. Nevertheless, it is sufficient for inducing strong Bragg gratings when the concentration of GeO₂ is more than ~5 mole %.

Conclusion: PECVD offers possibilities for growing highly photosensitive germanosilicates due to the low temperature deposition. Various germanium doped silica thin films have been investigated at 193 nm and 244 nm. Effects of oxygen deficiency are demonstrated to enhance the photosensitivity. UV-induced refractive index increases up to $3.5 \cdot 10^{-3}$ are observed making direct written waveguides possible without hydrogen-loading.

References:

- [1] K.O.Hill, Y.Fujii, D.C.Johnson, B.S.Kawasaki: "Photosensitivity in optical fibre waveguides: Applications to reflection filter fabrication", Applied Physics Letters, Vol. 32, pp 647-649, 1978.
- [2] R.Kashyap, G.D.Maxwell, and B.J.Ainslie: "Laser-Trimmed Four-Port Bandpass Filter Fabricated in Single-Mode Photosensitive Ge-Doped Planar Waveguide", IEEE Photonics Technology Letters, Vol. 6, pp 191-194, 1993.
- [3] G.D.Maxwell and B.J.Ainslie: "Demonstration of a directly written directional coupler using UV-induced photosensitivity in a planar silica waveguide", Electronics Letters, Vol. 31, pp 95-96, 1995.
- [4] M.Svalgaard, C.V.Poulsen, A.Bjarklev and O. Poulsen: "Direct UV writing of buried singlemode channel waveguides in Ge-doped silica films", Electronics Letters, Vol. 30, No. 17, pp 1401-1420, Aug 1994.
- [5] C.V.Poulsen, M.Svalgaard and O.Poulsen: "Photosensitivity in germania- doped silica films", CLEO@Europe 1994, CMM5.

Monday, September 11, 1995

Sensors and Theory I

PMB 10:30am–12:30pm
Multnomah Room

Walter Margulis, *Presider*
Imperial College, U.K..

**Fiber Optic Bragg Grating Sensor Systems for Multi-point
Distributed Strain Monitoring**

Alan D. Kersey
Code 5673, Optical Sciences Division
Naval Research Laboratory
Washington DC 20375

Fiber Bragg grating (FBG) based sensors represent one of the most exciting developments in the area of fiber sensor technology in recent years. A wide range of sensor types and interrogation techniques is possible, and methods for addressing multiple FBG elements along a fiber have been developed. This presentation will review this rapidly emerging area of fiber sensing and describe some of the potential applications of the technology.

Chirped fibre gratings for temperature-independent strain sensing

M.G.Xu, L.Dong, L.Reekie, J.A. Tucknott and J.L.Cruz*

Optoelectronics Research Centre, University of Southampton
Southampton SO17 1BJ, United Kingdom

Tel: +44 1703 594530

Fax: +44 1703 593149

*On leave from:

Departamento Física Aplicada, Universidad de Valencia

Dr. Moliner 50, Burjassot, 46100

Valencia, Spain.

Fibre Bragg grating sensors are of considerable interest for a number of sensing applications [1-6]. More recently, chirped Bragg gratings are attracting research interest for strain sensing [2,3]. However, undesirable temperature sensitivity of the fibre grating sensor may complicate its use as a strain gauge. Morey *et. al.* have suggested that the temperature can be measured and compensated for using a second grating element contained within a different material and placed in series with the first grating [4]. We have also demonstrated that the problem can be resolved by arranging for the simultaneous measurement of strain and temperature [5], or by arranging for the thermal response to be cancelled [6]. Nevertheless, all of the above methods are difficult to implement when a large number of fibre gratings are involved in a multiplexed sensing system. In this paper we describe a novel temperature-independent strain sensor based on the use of a chirped fibre grating in a tapered optical fibre.

In an unchirped fibre grating, both strain and temperature cause a shift in the Bragg wavelength, while the effective bandwidth remains essentially unaffected. As a result, on a single measurement of the Bragg wavelength shift, it is impossible to discriminate between the effects of strain and temperature. However, the bandwidth can be made to be strain-dependent if a strain gradient is introduced along the grating length [2]. Using this singular dependence of bandwidth on strain gradient, temperature-independent strain sensing is now possible. Employing a technique reported recently [7], a chirped grating can be written in a tapered fibre by differential etching. The taper profile can be designed such that the grating becomes linearly chirped when tension is applied thus creating a strain gradient along the grating. The average strain, defined as the integral of local strain over the grating length, is measured by the change in the effective bandwidth. Although both average strain and temperature still induce a shift in the Bragg wavelength, the effective bandwidth variation will only depend on the strain rather than the temperature.

The experimental system is shown in Fig.1. Light from a 1550nm ELED, having a FWHM bandwidth of $\sim 96\text{nm}$, was split via a fibre coupler to illuminate the chirped fibre grating and to provide reference. The ratio of reflected power over reference power provides the

strain information and serves to eliminate the effect of intensity variation due to power fluctuations in the source. The sensing element was the linearly chirped grating described above, with nominal central Bragg wavelength of 1554nm, FWHM bandwidth of 2nm, and peak reflectivity of $\sim 100\%$. The length of the grating was 20mm, in a 25mm taper. The taper diameter varied from $125\mu\text{m}$ - $78\mu\text{m}$. Strain was applied by directly stretching the fibre using different weights to ensure good strain transfer, and temperature was accurately set by using a temperature controlled Peltier heat pump. When the grating simultaneously experiences changes in both strain and temperature, the back-reflected light intensity alters only if the strain changes, provided that attenuation due to microbending in the lead is insignificant and the splitting ratio of the coupler is constant. We assume that a strong grating is used, such that the reflectivity over most of the grating bandwidth is $\sim 100\%$ even under strain.

Fig.2 shows the ratio of the reflected to reference light was measured as a function of temperature from 10°C to 50°C for three different strain levels, showing excellent temperature-independent behaviour as predicted. For a shot-noise-limited system, a strain resolution of $0.8\mu\epsilon$ normalised to a 1Hz bandwidth was expected for the interrogation system used. The measured strain resolution was $4.4\mu\epsilon$, corresponding to a strain resolution of 1% over the full measurement range. The grating used in this experiment was fabricated under tension, resulting in significant pre-chirp. Thus the grating bandwidth decreased as tension was applied, and above a certain value of tension, equal to that at which the grating was written, the bandwidth would increase. By writing the grating without applying tension, the bandwidth would increase monotonically with increasing stress. Fig.3 shows the time response of the sensor. The output is monitored over 10 minutes as the strain of $928.13\mu\epsilon$ and $2108.34\mu\epsilon$ was applied, respectively.

If the sensor is to be embedded directly in a composite material, under conditions of no applied tension, the problem of thermally-induced apparent strain could occur due to the difference in the coefficient of thermal expansion between the host material and the fibre grating sensor. Therefore, to maintain the temperature-independent nature, it is an inherent requirement of this technique that the sensing element be kept in free space. A major source of error can be attributed to microbending loss in the lead. This uncertainty can be eliminated by monitoring the transmission loss in the lead at the far end of the fibre containing the grating at a wavelength different from that of the grating. The strain responsivity of the experimental system is limited by the characteristics of the chirped fibre grating used. The responsivity, and hence strain resolution can be enhanced by varying the taper profile, however a trade-off has to be made between the strain responsivity and the measurement range determined by the taper strength.

In summary, we have demonstrated a temperature-independent strain sensor using a chirped Bragg grating in a tapered fibre. The system developed provides a compact, rugged, low-cost and true strain measurement. A strain resolution of $4.4\mu\epsilon$ over a total measurement range of $4066\mu\epsilon$ has been demonstrated, which can be improved by optimising the design of the fibre taper. In addition, temperature can also be measured simultaneously by monitoring the wavelength shift of the grating if desired. However, more work will be needed if the sensor is to be embedded in or surface-mounted on practical structures.

References

1. Morey, W.W., Meltz, G., and Glenn, W.H.: "Fibre optic Bragg grating sensors", 1989, *Proc. SPIE*, **1169**, pp.98-107.
2. Huang, S., Ohn, M.M., LeBlanc, M., Lee, R., and Measures, R.M.: "Fibre optic intra-grating distributed strain sensor", 1994, *Proc. SPIE.*, **2294**, pp.81-92.
3. Kersey, A.D. and Davis, M.A.: "Interferometric fibre sensor with a chirped Bragg grating sensing element", 1994, *Proc. OFS'94*, pp.319-322, Glasgow, UK.
4. Morey, W.W., Meltz, G., and Weiss, J.M.: "Evaluation of a fibre Bragg grating hydrostatic pressure sensor", 1992, *Proc. OFS'8*, Monterey, USA, Postdeadline Paper PD-4.4
5. Xu, M.G., Archambault, J.L., Reekie, L., and Dakin, J.P.: "Discrimination between strain and temperature effects using dual-wavelength fibre grating sensors", 1994, *Electron. Lett.*, **30**, pp.1085-1087.
6. Xu, M.G., Archambault, J.L., Reekie, L., and Dakin, J.P.: "Thermally-compensated bending gauge using surface mounted fibre gratings", 1994, *Int. J. Optoelectronics.*, **9**, pp.281-283.
7. Putnam, M.A., Williams, G.M. and Friebele, E.J.: "Fabrication of tapered, strain-gradient chirped fibre Bragg gratings", *Electron. Lett.*, 1995, **31**, pp.309-310.

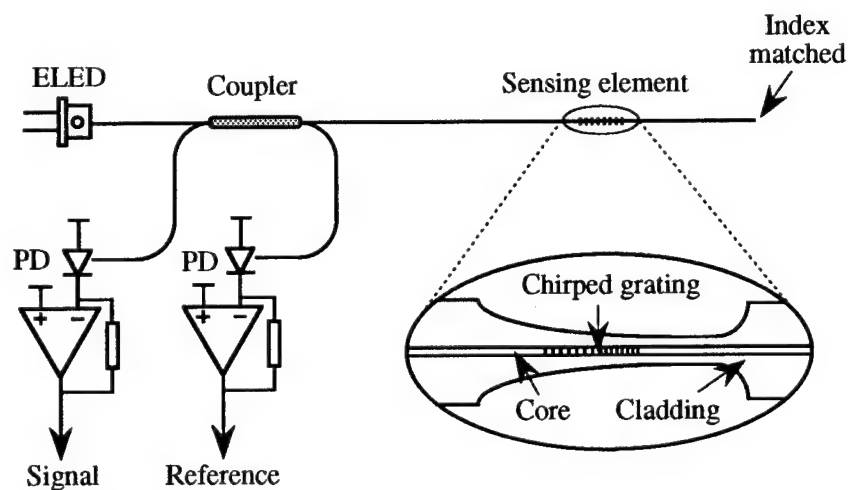


Fig.1 Schematic of temperature-independent strain sensor using a chirped Bragg grating in a tapered fibre.

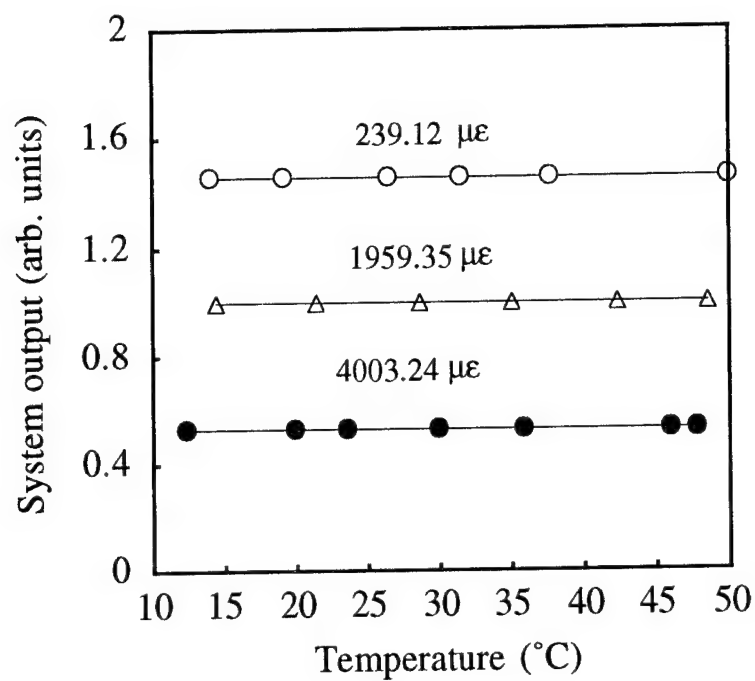


Fig.2 System output versus temperature at three different static strain levels.

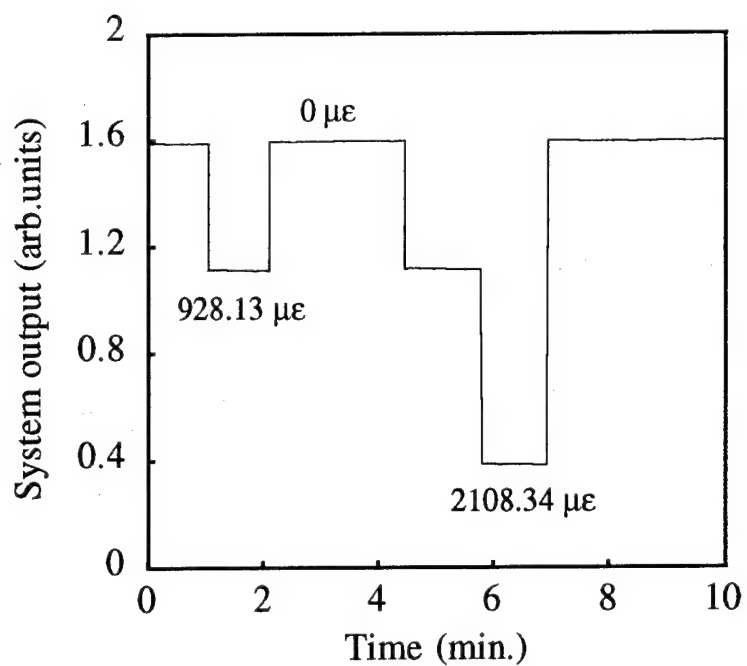


Fig.3 Time response of the sensor as the strain of $923.13 \mu\epsilon$ and $2108.34 \mu\epsilon$ was applied.

Photo-induced birefringence and applications in sensing

V. A. Handerek and S. E. Kanellopoulos

*Department of Electronic and Electrical Engineering
King's College London, Strand, London WC2R 2LS, U. K.*

1. INTRODUCTION

In the last few years optical fibre photosensitivity has been noticed to be anisotropic; that is the photoinduced index change is birefringent.[1] The photoinduced anisotropy of germanium doped silica fibres has allowed the fabrication of polarisation converting gratings analogous to mechanically produced periodic birefringent fibre structures made in the past.[2-8] Such gratings are known as polarisation couplers or rocking filters when they couple forward-travelling fibre modes and as Bragg exchange gratings when backward travelling light is produced.

Birefringent gratings have recently found applications in sensing, where they have been used for combined strain and temperature, and pressure measurements.[9-13] Demonstrations of birefringent gratings have also been presented for possible application in communications as components in nonlinear switching schemes.[14-16] Furthermore, it has also been proposed that birefringent gratings can have a stabilising effect in various fibre resonator configurations.[17-18]

In early experiments carried out with guided, linearly polarised, green/blue light, the photoinduced birefringence was written by two-photon absorption with a circularly symmetric writing field generating refractive index changes throughout the core of the fibre.[1,4,5,19-23] Shortly after these experiments, photoinduced birefringence in fibres and in ion implanted silica was written far more efficiently by using linearly polarised UV light at 240 nm with the aim of directly bleaching the absorption band of oxygen-deficient sites by single-photon absorption.[6,21,24-27] (The fibres were necessarily exposed transversely with respect to the guide axis in these experiments, breaking the axial symmetry of the earlier exposure method.) Similar photoinduced anisotropy had also been observed in amorphous silica.[28] Initially, the peak powers used in experiments with UV light were low and the index changes were attributed to a type I process.[29] Recently, however, photoinduced birefringence has been written externally in hydrogen loaded fibres by intense UV light causing damage localised at the core-cladding interface on the side exposed to the UV radiation. It is believed that the asymmetry in the refractive index change ($\sim 4 \times 10^{-5}$) is the result of transient heating due to UV absorption while a photolytic process increases the index across the entire core.[30-32]

A defect depletion model has been proposed by Kamal and Russell to explain the photoinduced birefringence changes in optical fibres.[33] According to this model, the photoinduced birefringence changes are explained as a result of a reduction or depletion of the dipoles orientated in the direction of polarisation of the driving field, giving rise to negative birefringence variations with a concomitant positive index change.

Highly birefringent fibres have been shown to exhibit different photoinduced refractive index changes along their two optical axes. Stress birefringent fibres are reported to favour the slow axis for large negative photoinduced birefringence changes ($\sim 10^{-5}$)[20] while there are contradictory reports on the photosensitive behaviour of geometrically birefringent fibres. In one study it was reported that the fast axis of an elliptical-core fibre was 3 times more photosensitive than the slow axis [22], whereas in another study with the same fibre no significant difference in photosensitivity was recorded.[24] A balanced photoinduced index change along both axes in elliptical-core fibres can explain the high efficiency of rocking filters written in this type of fibre.[5] More work is needed to properly characterise the behaviour of these types of fibre.

Efficient rocking filters have been reported so far only in one type of elliptical-core fibre. We have recently examined various stress induced birefringent fibres by writing rocking filters for comparison purposes. This work is described in the next section.

A reflective rocking filter or exchange Bragg reflection grating acts as a distributed-feedback (DFB) polarisation state converter that reflects light into the orthogonal polarisation mode within a narrow wavelength range.[7] In this case the pitch of the rocking birefringence is such that light, scattered into the orthogonal polarisation state by each twist in birefringence, couples in phase into the counter-propagating direction instead of the co-propagating direction. To date, only low conversion efficiencies have been reported for this type of component.

There is currently considerable interest in photogenerated fibre gratings for strain and temperature sensing. We have recently shown that photogenerated polarisation couplers or rocking filters which rely on a photoinduced periodic rocking of the birefringence axes of elliptically cored polarisation maintaining fibre can be used for strain and temperature sensing. These two variables can be separately and simultaneously measured by extracting two, independent optical signals from the sensor. This can be achieved in several ways, including the use of superposed Bragg reflection gratings and polarisation couplers, or by using polarisation couplers alone in a fibre supporting a few low-order modes.[11,12] Strain and temperature can be determined by solving a system of linear equations provided that the matrix of the system is well conditioned and can be inverted. The information in these sensors is provided in the frequency domain avoiding the problem of limited unambiguous signal range associated with the use of competing interferometers.

2. EXPERIMENT

Perhaps because of the earlier reported asymmetry in the photosensitivity of fibres having large strain-induced birefringence, there seems to have been very little use of these fibres in rocking filter fabrication. The only work which we are aware of is contained in reference 20. We felt that it would be worthwhile to examine more fibres of this type in order to explore the range of behaviour possible with these fibres. We have found that we can obtain better repeatability of polarisation coupler fabrication in elliptically-cored fibres using the internal writing method than when using the external technique. The internal method was therefore used in all of the experiments described below, using light from a CW Argon ion laser. Some fibres were multimode at the wavelengths used, and this will tend to reduce the attainable coupling efficiency in these fibres but will not prevent the formation of a measurable polarisation coupler.

Two different Panda-type birefringent fibres (made by Fujikura) were first used in our experiments. In a first experiment 1 m of fibre single mode at 514.5 nm and with a polarisation beatlength L_b of 1 mm was exposed to 240 mW for 30 minutes. In a second experiment 60 cm of a fibre with a higher order mode cutoff wavelength λ_c of 1400 nm was exposed to 600 mW for 15 minutes. No rocking filter formed in either of the above fibres.

Three different bow tie fibres were then tried. First a bow-tie fibre (made by Fibrecore) with index matched stress regions ($NA=0.14$, $L_b=1.82$ mm) was exposed with 514.5 nm light (where the fibre was single mode) in order to make a rocking filter. No filter was formed in any sample of this type of fibre for guided powers in the range of 200-300 mW and exposure times ranging from 15 to 45 minutes.

Second, a different bow-tie fibre (Fibercore HB600, $\lambda_c=590$ nm, $L_b=0.8$ mm, $NA=0.17$) was tried. An 86 cm long rocking filter was made after exposing the fibre for 75 minutes with 200 mW. The rocking filter had a peak coupling efficiency of 4.5% at 514.35 nm and a full-width-half-maximum bandwidth $\delta\lambda$ of 0.3 nm.

Finally, a bow-tie fibre (Fibercore HB500, single mode at 514.5 nm, $L_b=0.8$ mm, $NA=0.17$, core diameter 3.5 μm) was tried. An 86 cm long rocking filter was made after exposing the fibre for 30 minutes with 200 mW. The filter had a peak coupling efficiency of 16.6% at 514.3 nm and a $\delta\lambda$ of 0.45 nm. The temperature dependence of the peak resonant wavelength for this fibre was measured at -0.4 nm/ $^{\circ}\text{C}$. The filter was cut in half and the two sections were measured. The results are shown in the following table.

Filter length (cm)	Coupling efficiency (%)	$\delta\lambda$ (nm)
86.5	16.6 %	0.45
0-43	4.3 %	0.6
43-86	3.7 %	0.675

These results show that the rocking filter written in the HB500 bow-tie fibre was effective throughout the entire length of the fibre used. The filter does not appear to have a significant taper in the coupling coefficient since both halves of the filter have almost equal strength which is close to the value predicted by theory (4.3%) for a uniform

coupler. This is quite different from the behaviour of filters formed in elliptical-core fibres by the internal method. These are normally strongly tapered.

The index change along both axes of the fibre can be determined by monitoring the shift of the resonant wavelength of the filters from the writing wavelength. The small shift of the resonant wavelength of the filter from the writing wavelength (-0.225 nm) shows that there is very little asymmetry in the photosensitivity of the two optical axes for this type of fibre. This is contrary to the previous report about a stress birefringent fibre.[20]

3. CONCLUSION

As a conclusion, our recent experiments with internally written rocking filters at 514.5 nm show that stress-induced birefringent fibres exhibit poor anisotropic photosensitivity compared to elliptical-core highly-birefringent fibres and in some cases no observable photosensitivity under the conditions of our experiments. The justification given in the past for the formation of weak rocking filters written in these fibres was that there was a strong asymmetry in the photosensitivity of the two optical axes. This is not borne out from our experiments since the results show clearly that wide variations in behaviour are possible. Our experiments have shown that it can be misleading to draw a sharp distinction between the two types of highly birefringent fibre, since stress-induced birefringent fibres can show no noticeable difference in the photosensitivity of the two axes, whereas geometrically-induced birefringent fibres can exhibit slightly different photosensitivity along the two axes.

4. REFERENCES

- 1 M. Parent, J. Bures, S. Lacroix, J. Lapierre, "Proprietes de polarisation des reflecteurs de Bragg induits par photosensibilite dans les fibres optique monomodes", *Appl. Opt.* 24, 354 (1985).
- 2 Y. Yen, R. Ulrich, "Birefringent optical filters in single-mode fibre", *Opt. Lett.* 6, 278 (1981).
- 3 R. H. Stolen, A. Ashkin, W. Pleibel, J. M. Dziedzic, "In-line fibre-polarisation-rocking rotator and filter", *Opt. Lett.* 9, 300 (1984).
- 4 P. St. J. Russell, D. P. Hand, "Rocking filter formation in photosensitive high birefringence optical fibres", *Electron. Lett.* 26, 1846 (1990).
- 5 S. E. Kanellopoulos, L. C. G. Valente, V. A. Handerek, A. J. Rogers, "Comparison of photorefractive effects and photogenerated components in polarisation maintaining fibres", *SPIE Vol. 1516 International Workshop on Photo-induced Self-Organisation in Optical Fibres*, 200-210 (May, 1991) ; "Photorefractive polarisation couplers in elliptical core fibres", *IEEE Phot. Tech. Lett.* 3, 806 (1991).
- 6 K. O. Hill, F. Bilodeau, B. Malo, D. C. Johnson, "Birefringent photosensitivity in monomode optical fibre : Application to external writing of rocking filters", *Electron. Lett.* 27, 1548 (1991).
- 7 A. Kamal, S. E. Kanellopoulos, J.-L. Archambault, P. St. J. Russell, V. A. Handerek and A. J. Rogers, "Holographically written reflective polarisation filter in single-mode optical fibres", *Opt. Lett.* 17, 1189 (1992).
- 8 D. C. Johnson, F. Bilodeau, B. Malo, K. O. Hill, P. G. J. Wigley, G. I. Stegeman, "Long-length, long-period rocking filters fabricated from conventional monomode telecommunications optical fibre", *Opt. Lett.* 17, 1635 (1992).
- 9 J. J. Guerin, J. M. Mailard, P. Sansonetti, "Polarisation mode couplers made by photoinduced grating for white light quasi distributed polarimetric sensors", *Proceedings of the Eighth Optical Fibre Sensors Conference*, TH2.4, p. 288 (Monterey, 1992).
- 10 S. E. Kanellopoulos, V. A. Handerek and A. J. Rogers, "Compact Mach-Zehnder fibre interferometer incorporating photoinduced gratings in elliptical-core fibres", *Opt. Lett.* 18, 1013 (1993).
- 11 S. E. Kanellopoulos, V. A. Handerek, A. J. Rogers, "Simultaneous strain and temperature sensing employing photogenerated in-fibre gratings", *Opt. Lett.* 20, 333 (1995).
- 12 S. E. Kanellopoulos, V. A. Handerek, A. J. Rogers, "Simultaneous strain and temperature sensing employing a photogenerated polarisation coupler and low-order modes in an elliptically cored optical fibre", *Electron. Lett.* 30, 1787 (1994).
- 13 R. Kaul, "Pressure sensitivity of rocking filters fabricated in an elliptical core optical fibre", *Opt. Lett.* 20, 1000 (1995).
- 14 C. G. Krautschik, G. I. Stegeman, R. H. Stolen, "Phase controlled all-optical switching in rocking filter fibres", *Appl. Phys. Lett.* 61, 1751 (1992).

- 15 C. G. Krautschik, P. Wigley, G. I. Stegeman, R. H. Stolen, "Demonstration of demultiplexing with a rocking filter fibre", *Appl. Phys. Lett.* 63, 860 (1993).
- 16 C. G. Krautschik, G. I. Stegeman, R. H. Stolen, "Asymmetric response of nonlinear coupled-mode devices: all-optical logic gates with a rocking-filter fibre", *Opt. Lett.* 18, 1050 (1993).
- 17 C. X. Shi, K. Hotate, "Polarisation-maintaining fibre ring resonator with a photoinduced birefringent grating", *IEEE Phot. Tech. Lett.* 5, 954 (1993).
- 18 C. X. Shi, "Fabry-Perot resonator composed of a photoinduced birefringent fibre grating", *Appl. Opt.* 33, 7002 (1994).
- 19 F. Ouellette, D. Gagnon, M. Poirier, "Permanent photoinduced birefringence in a Ge-doped fibre", *Appl. Phys. Lett.* 58, 1813 (1991).
- 20 S. Bardal, A. Kamal, P. St. J. Russell, "Photoinduced birefringence in optical fibres: a comparative study of low birefringence and high birefringence fibres", *Opt. Lett.* 17, 411 (1992).
- 21 S. E. Kanellopoulos, V. A. Handerek and A. J. Rogers, "Photoinduced polarisation couplers in elliptical core optical fibres written using 532 and 266 nm sources", *Electron. Lett.* 28, 1558 (1992).
- 22 J. Lauzon, D. Gagnon, S. LaRochelle, A. Blouin, F. Ouellette, "Dynamic polarisation coupling in elliptical-core photosensitive optical fibre", *Opt. Lett.* 17, 1664 (1992).
- 23 A. Wang, S. Zhou, K. Murphy, R. Claus, "Photoinduced birefringence rotation in germanosilicate glass optical fibre", *Opt. Lett.* 19, 460 (1994).
- 24 M. Poirier, S. Thibault, J. Lauzon, F. Ouellette, "Dynamic and orientational behaviour of UV-induced luminescence bleaching in Ge-doped silica optical fibre", *Opt. Lett.* 18, 870 (1993).
- 25 D. Wong, S. B. Poole, M. G. Sceats, "Stress-birefringence reduction in elliptical-core fibres under ultraviolet irradiation", *Opt. Lett.* 17, 1773 (1992).
- 26 K. S. Chiang, M. G. Sceats, D. Wong, "Ultraviolet photolytic-induced changes in optical fibres: the thermal expansion coefficient", *Opt. Lett.* 18, 965 (1993).
- 27 J. Albert, B. Malo, D. C. Johnson, F. Bilodeau, K. O. Hill, J. L. Brebner, G. Kajrys, "Dichroism in the absorption spectrum of photobleached ion-implanted silica", *Opt. Lett.* 18, 1126 (1993).
- 28 J. H. Stathis, "Selective generation of oriented defects in glasses: Application to SiO₂", *Phys. Rev. Lett.* 58, 1448 (1987).
- 29 J-L Archambault, L. Reekie, P. St. J. Russell, "100% reflectivity Bragg reflectors produced in optical fibres by single excimer laser pulses", *Electron. Lett.* 29, 453 (1993).
- 30 T. Erdogan and V. Mizrahi, "Characterisation of UV-induced birefringence in photosensitive Ge-doped silica optical fibres", *J. Opt. Soc. Am. B* 11, 2100 (1994).
- 31 D. Inniss, Q. Zhong, A. M. Vengsarkar, W. A. Reed, S. G. Kosinski, P. J. Lemaire, "Atomic force microscopy study of uv-induced anisotropy in hydrogen-loaded germanosilicate fibres", *Appl. Phys. Lett.* 65, 1528 (1994).
- 32 A. M. Vengsarkar, Q. Zhong, D. Inniss, W. A. Reed, P. J. Lemaire, S. G. Kosinski, "Birefringence reduction in side-written photoinduced fibre devices by a dual-exposure method", *Opt. Lett.* 19, 1260 (1994).
- 33 A. Kamal and P. St. J. Russell, "Physical origins and general dielectric tensor of photoinduced anisotropy in optical fibres and bulk glasses", *J. Opt. Soc. Am. B* 11, 1577 (1994).

Wavelength Shifts in Fiber Bragg Gratings due to Changes in the Cladding Properties.

G. Meltz

United Technologies Research Center
411 Silver Lane, East Hartford,
CT 06108, USA
Tel: 203 727 7486 Fax: 203 727 7909

W.W. Morey

3M Bragg Grating Technologies
Bloomfield, CT

S. J. Hewlett and J. D. Love

Optical Sciences Centre
The Australian National University
Canberra, ACT 0200, Australia

Introduction

Fiber Bragg grating (FBG) devices have received wide attention because they are useful in a variety of passive and active WDM network components and for sensing various measurands. These applications take advantage of either the broad- or narrow-band spectral characteristics of the Bragg resonance and its sensitivity to extrinsic perturbations. In this paper, we examine FBG tuning by controlling the effective index of the optical waveguide through modification of the cladding. This causes a change in the evanescent field which is reflected in a proportional shift in the Bragg wavelength. If the change is large enough then it can be detected by measuring the shift in the resonance line or equivalently by determining phase-path imbalances in an auxiliary interferometer. Very small wavelength changes are more easily measured by forming a compound FBG transmission filter, such as a three-grating Fabry-Perot interferometer, and using a tuneable laser to determine the transmission or reflection spectrum.

The evanescent component of the optical field is easily changed by deeply etching or polishing away the glass cladding layer. We show, both through experiment and by modeling, how this affects the fundamental Bragg lines in elliptical core fiber. The birefringence is also changed by etching because the TE and TM fields decay at different rates into the cladding or superstrate layers. We also present results on tuning a FBG Fabry-Perot filter by removing the cladding and replacing it by a layer with a different index of refraction.

Experimental results

Bragg gratings were written in D-shaped (Andrew Co.), elliptical core fiber, by using a phase mask¹ or a split-beam interferometer² to form the UV fringe pattern. The fiber was subsequently etched to reduce the thickness of the cladding layer. Nearly all of the silica could be removed by applying a dilute solution of HF to the surface of the fiber for 3 to 4 hours. The thickness of layer above the grating was controlled by determining the etch rate from polarimetric measurements of birefringence and quenching the reaction by neutralizing the acid bath.

The goal was to reduce the layer to about 2 microns (a typical result is shown in the photograph of the fiber crosssection in Figure 1) from the original thickness of 16 microns.

In the first series of experiments, we measured the changes in the transmittance spectra due to the etching and with a water layer applied to the etched region of the fiber. An optical spectrum analyzer was used with a broadband source and a polarizer to excite both polarization modes. Prior to the etch, the measured wavelength separation (Fig. 2a) of the vertically and horizontally-polarized eigenmodes was 0.268 nm. This value gives a normalized birefringence of 2.5×10^{-4} compared with a calculated value for a step-index model of 1.9×10^{-4} . Reducing the cladding layer to about 2 microns, blue-shifts both resonance lines and markedly increases the birefringence (Fig. 2b). A water layer above the grating, decreases the wavelength shift (Fig. 2c) somewhat, but still causes a large increase in the local fiber birefringence. These changes, due to modification of the evanescent field and thus the modal index, are easily measurable. If the etch leaves a smooth surface and the fluid applied to the fiber is not highly-absorbing then this technique can be used for sensitive refractometer measurements of the superstrate layer.

An improvement in the minimum resolvable change in the layer properties requires a more sensitive means to observe the shift in the Bragg lines. One way to achieve this, is to generate a narrow feature in the filter spectrum by fabricating a three-grating Fabry-Perot filter with a large free spectral range. To do this, we use a phase mask exposure to write a long grating and then reexpose, an annealed, short section of the grating to form a three-section interferometer³. The second exposure is stopped when the Fabry-Perot maximum moves to the center of the grating spectrum. For example, Figure 3 shows the transmittance of 10 mm grating in a depressed cladding fiber which has been reexposed to a uniform 2 mm UV beam. The spectrum has a narrow peak, about 0.05 nm FWHM, within the Bragg stop band. A similar grating was written in a D-shaped e-core fiber and etched to observe the shift in the wavelength of the transmission peak. In the example shown in Figure 4, the etch was not as smooth or as deep as in the first fiber (Figure 2); consequently, the signal level is reduced and the wavelength shift is smaller, although the change in the location of the peak, 0.28 nm, is clearly observable.

Theoretical analysis

The spectrum of a compound grating, such as a Fabry-Perot filter, can be calculated by using a T-matrix formulation in conjunction with the coupled-mode solutions for each section of the device⁴. It's a technique commonly employed in dielectric layer filter design. We assume that the reexposed section of the grating is partly erased (contrast is reduced) and the average core index is increased. Figure 5 is the spectrum of a three-grating filter in which the 2 mm center section has been reexposed to produce an effective phase jump between the two equal adjacent sections. For simplicity, we use uniform amplitude gratings in each length, although it is easy to model an arbitrary profile grating.

To characterize the affect of changing the evanescent field, we must also model an e-core, D-fiber with a superstrate layer. A suitable method for analyzing this geometry is the recently developed Modified Fourier Decomposition Method (FDM)⁵. This technique is well-suited to computing the change in the modal index of the e-core fiber due to

etching the flat face of the D. Theoretical estimates of the shift in Bragg wavelengths with layer thickness and superstrate index will be presented and compared with the experimental values.

Summary

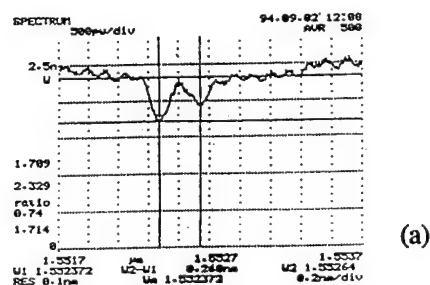
Changes in the resonance spectrum of a fiber Bragg grating occur when the evanescent field is modified through a change in the cladding properties or by the presence of a superstrate layer in contact with a thinned cladding region. These effects have been investigated in etched e-core D-shaped fiber. Large increases in birefringence are observed when the cladding is reduced to about 2 microns. Similar effects are also seen in three-grating Fabry-Perot filters that have been fabricated in D-shaped elliptical core fiber by reexposure techniques.

References

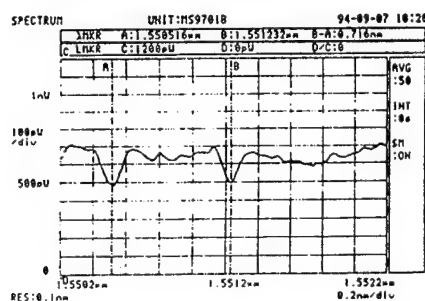
1. K. O. Hill et al, *Appl.Phys.Lett.*, **62**, pp.1035-1037, 1993.
2. G. Meltz, W.W. Morey and W. H. Glenn, *Opt. Lett.*, **14**, pp. 823-825, 1989.
3. J.Canning and M.G.Skeats, *Electron.Lett.*, **30**, pp. 1244-, 1994.
4. M.Yamada and K.Sakuda, *Appl. Opt.*, **26**, pp.3474-3478, 1987.
5. S. J.Hewlett and F.Ladouceur, *J. Lightwave Tech.*, **13**, pp. 375-383, 1995.



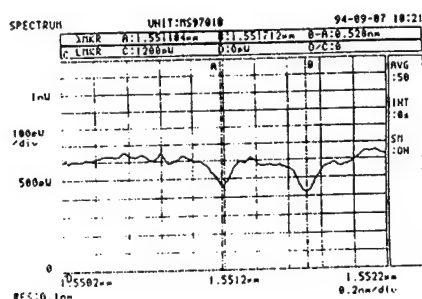
Figure 1: Cross-section of etched elliptical core D-shaped fiber. The cladding thickness has been reduced to less than $3\ \mu\text{m}$.



(a)



(b)



(c)

Figure 2: Optical spectra of a fiber Bragg grating in e-core fiber (a) before etching, $\Delta\lambda = 0.268\text{nm}$, (b) after etching, $\Delta\lambda = 0.716\text{nm}$ and (c) with a water layer above the grating, $\Delta\lambda = 0.528\text{nm}$.

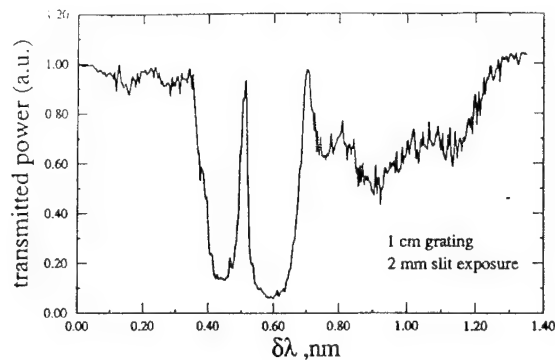


Figure 3: Transmittance of a three grating, FBG Fabry-Perot interferometer written in a depressed cladding fiber.

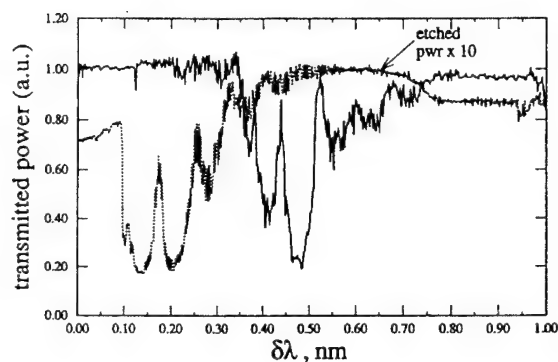


Figure 4: Transmission spectra of a three grating FBG Fabry-Perot filler in D-shaped e-core fiber (a) prior to etching and (b) after etching to remove most of the cladding layer above the grating.

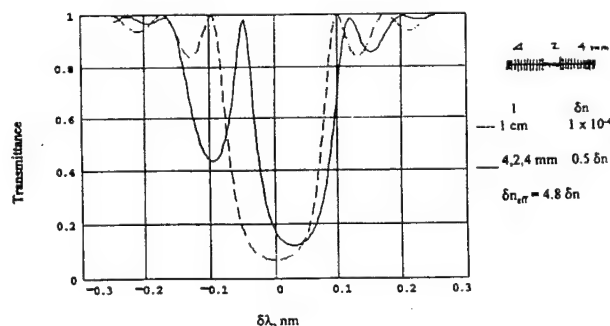


Figure 5: Computed transmission spectra of a uniform grating and a three grating Fabry-Perot filter.

Photosensitive processes in silica glass using 193 nm light

Jacques Albert
Communications Research Centre
P.O.Box 11490, Station H
Ottawa (Ontario) CANADA K2H 8S2
Phone: (613)990-7690 Fax: (613)993-7139

Introduction

The name "Photosensitivity" is associated with the process by which the refractive index of certain types of silica glasses is permanently modified by exposure to short wavelength optical radiation [1]. The process was discovered in germano-silicate optical fibers exposed to intense blue light ($\lambda=488$ nm) from an Argon ion laser [2] but further experiments revealed that the photoinduced index change grows as the square of the laser intensity, indicating a two-photon process[3]. It was eventually found that the photosensitivity was due to an absorption band with a maximum near 242 nm [4], similar to the absorption observed in oxygen deficient germania (i.e. GeO sites in GeO₂)[5]. With direct excitation from intense UV light in the absorption band, the refractive index change in standard optical fibers reaches 10^{-4} and the process becomes sufficiently efficient for writing Bragg gratings in fibers by side exposure [4],[6]. These advances have led to the development of several important applications [7]. Finally, apart from using special fibers with enhanced photosensitivity (from higher germanium concentration, co-dopants, or processing in reducing atmospheres), two methods have been proposed to increase the photosensitivity of standard fibers: flame brushing [8] and low temperature hydrogen (H₂) loading [9]. With these techniques, refractive index changes in the 10^{-3} - 10^{-2} range have been reached, extending the variety of useful fiber devices and allowing other applications to become practical [10-12].

As will be described below, photosensitivity in germanium-doped glasses appears to be linked unequivocally to a 242 nm absorption band of such glasses. However, it was demonstrated recently that the photosensitivity obtained with shorter wavelength light at 193 nm is at least as efficient as when 240-248 nm light is used, and in some cases much more efficient [13-15]. For instance, the photosensitivity of phosphorus-doped silica is an order of magnitude higher at 193 nm than it is at 248 nm.

Following a brief overview of the standard models of photosensitivity, the results of our spectroscopic and photosensitivity experiments using 193 laser irradiations will be reviewed and compared with results obtained using 248 nm light in the same conditions.

Photosensitive mechanisms

Photosensitivity is conventionally explained by the presence of an absorption band near 242 nm due to an oxygen deficiency in germanium-doped silica, as reviewed recently by Sceats et al.[16]. Basically, the oxygen deficiency is thought to manifest itself by the presence of Ge-Si wrong bonds which can be ionized by the UV light. If deep electron traps or strain relief prevent the recombination of the wrong bond, the polarizability of the glass is 'permanently' modified, thereby changing the absorption and refractive index. By extension, the enhanced photosensitivity obtained with flame brushing is explained by the reducing effect of the hydrogen rich flame on the germano-silicate glass [8]. On the other hand, the origin of the enhancement obtained with low temperature H₂ loading is less clear since there is no apparent absorption increase following loading alone. One explanation is that hydrogen molecules in the glass react efficiently with wrong bonds while the bonds are excited by the UV light. The reaction produces X-OH (X=Ge or Si) and prevents the recombination of the Ge-Si bond. In fact, by measuring the induced OH content, hydrogen loading followed by UV exposure has been shown to produce as many defect sites as there are germanium atoms in the glass [9]!

Photosensitivity using 193 nm light

This explanation of the effect of H₂ loading still brings into play a bond ionization by the UV light. However, experiments carried out at CRC have shown that H₂ loading also causes a large enhancement of the photosensitivity in oxygen-rich germanium-doped silica in which there is *no initial optical absorption in the 200-400 nm range* (no wrong bonds initially). Therefore, the presence of wrong bond absorption at 242 nm does not appear to be a necessary condition for photosensitivity: Ultraviolet light somehow catalyzes a reaction between the H₂ and a defect involving germanium atoms. Given this result, we decided to attempt using a shorter wavelength source (with higher photon energy), the 193 nm ArF excimer laser. It turns out that the photosensitive changes obtained using 193 nm light in H₂-loaded germano-silicate glasses and fibers are similar with those obtained under 248 nm exposure, only they occur at a faster rate [13]. This confirms that in this case at least, there is no fundamental relationship between photosensitivity and wrong bond absorption at 242 nm; another band located in the 185-190 nm region [5] may be involved however.

Further experiments show that large absorption changes (several hundred cm⁻¹ and more) are obtained in the ultraviolet for several types of silica glasses under 193 nm exposure, with and without flame brushing or H₂ loading. Refractive index increases in the 10⁻³-10⁻² range have been measured in such cases [14-15]. The spectrum of

absorption changes depends strongly on the materials but in most cases there appears to be a strong correlation between the magnitude of the absorption increase measured near 190 nm and the size of the refractive index changes.

More recently we have identified a different photosensitive mechanism using 193 nm light which allows the fabrication of Bragg gratings with enhanced refractive index increases in non-treated standard optical fibers [17]. The growth rate of the refractive index modulation in terms of the fluence per pulse will be discussed for various cases of interest. Finally the results of preliminary comparative thermal stability tests on Bragg gratings written using both excimer laser transitions (ArF and KrF) will be presented.

REFERENCES

1. HILL, K. O., MALO, B., BILODEAU, F., and JOHNSON, D.C., "Photosensitivity in Optical Fibers", *Annu. Rev. Mater. Sci.* **23**, 125-157 (1993)
2. HILL, K. O., FUJII, Y., JOHNSON, D. C., and KAWASAKI, B. S., "Photosensitivity in optical fiber waveguides: application to reflection filter fabrication", *Appl. Phys. Lett.* **32**, 647-649 (1978)
3. LAM, D. K. W, and GARSIDE, B. K., "Characterization of single-mode optical fibre filters", *Appl. Opt.* **20**, 440-445 (1981)
4. MELTZ, G., MOREY, W. W., and GLENN, W. H., "Formation of Bragg gratings in optical fibers by a transverse holographic method", *Opt. Lett.* **14**, 823-825 (1989)
5. GARINO-CANINA, V., "Quelques propriétés physiques dépendant de défauts de structure dans l'oxyde de germanium pur et vitreux", *J. Phys. Chem. Solids* **20**, 110-121 (1961)
6. HILL, K. O., BILODEAU, F., MALO, B., and JOHNSON, D. C., "Birefringent photosensitivity in monomode optical fibre: application to external writing of rocking filters", *Electron. Lett.* **27**, 1548-1549 (1991)
7. HILL, K. O., "Photosensitivity and its application for optical fiber communications", *Proceedings of the 1995 Optical Fiber Communication Conference (OFC'95), Tutorial Sessions* pp.146-193 (1995)

8. BILODEAU, F., MALO, B., ALBERT, J., JOHNSON, D. C., HILL, K. O., HIBINO, Y., ABE, M., and KAWACHI, M., "Photosensitization of optical fibre and silica-on-silicon/silica waveguides", *Opt. Lett.* **18**, 953-955 (1993)
9. LEMAIRE, P. J., ATKINS, R. M., MIZRAHI, V., and REED, W. A., "High pressure H₂ loading as a technique for achieving ultrahigh UV photosensitivity and thermal sensitivity in GeO₂ doped optical fibres", *Electron. Lett.* **29**, 1191-1193 (1993)
10. PARTOVI, A., ERDOGAN, T., MIZRAHI, V., LEMAIRE, P. J., GLASS, A. M., and FLEMING, J. W., "Volume holographic storage in hydrogen treated germano-silicate glass", *Appl. Phys. Lett.* **64**, 821-823 (1994)
11. SVAALGARD, M., POULSEN, C. V., BJARKLEV, A., and POULSEN, O., "Direct UV writing of buried singlemode channel waveguides in Ge-doped silica films", *Electron. Lett.* **30**, 1401-1403 (1994)
12. ALBERT, J., HUTTUNEN, J., and SAARINEN, J., "Planar Fresnel lens photoimprinted in a germanium-doped silica optical waveguide", to be published in *Opt. Lett.* **20**, 15 May 1995
13. ALBERT, J., MALO, B., BILODEAU, F., JOHNSON, D. C., HILL, K. O., HIBINO, Y., and KAWACHI, M., "Photosensitivity in Germanium-doped silica optical waveguides and fibers using 193 nm light from an ArF excimer laser", *Opt. Lett.* **19**, 387-389 (1994)
14. MALO, B., ALBERT, J., BILODEAU, F., KITAGAWA, T., JOHNSON, D. C., HILL, K. O., HATTORI, K., HIBINO, Y., and GUJRATHI, S., "Photosensitivity in phosphorus doped silica glass and optical waveguides", *Appl. Phys. Lett.* **65**, 394-396 (1994)
15. VERHAEGEN, M., ALLARD, L. B., BREBNER, J. L., ESSID, M., ROORDA, S., and ALBERT, J., "Photorefractive waveguides produced by ion implantation of fused silica", to be published in *Nucl. Inst. Meth. B*, 1995
16. SCEATS, M. G., ATKINS, G. R., and POOLE, S. B., "Photolytic index changes in optical fibers", *Annu. Rev. Mater. Sci.* **23**, 381-410 (1993)
17. MALO, B., ALBERT, J., HILL, K. O., BILODEAU, F., JOHNSON, D. C., and THÉRIAULT, S., "Enhanced photosensitivity in lightly doped standard telecommunication fibre exposed to high fluence ArF excimer laser light", To be published in *Electronics Letters*, June 1995

Monday, September 11, 1995

Sensors and Theory II

PMC 2:00–3:30pm
Multnomah Room

P. Niay, *Presider*
Laboratoire de Dynamique, France

Advances in Fiber Grating Sensors

W. W. Morey, G. A. Ball
3M Bragg Grating Technologies

G. Meltz, J.R. Dunphy
United Technologies Research Center
and
A.D. Kersey
Naval Research Laboratory

Properly annealed fiber gratings can be used as sensor transducer elements at temperatures of 400° C over long periods of time without measurable changes. At 650° C, however, a problem was observed with creep or hysteresis of the grating response. At even higher temperatures diffusion of the core material will become a problem for long term operation. A couple new decoding schemes for fiber grating sensors use matched gratings and acousto-optic tunable filter in the decoding unit. These systems can measure many grating transducer elements simultaneously with high sensitivity. Short cavity fiber lasers that utilized fiber gratings can also act as sensor transducer elements giving one ultra high sensitivities that are limited by the fundamental noise in the fiber. One fiber laser sensor uses heterodyning to generate a signal that can be measured on an RF spectrum analyzer. New techniques for simultaneous measurement of temperature and strain will also be discussed.

Cladding-mode Resonances in Bragg Fibre Gratings: Depressed- and Matched-cladding Index Profiles

S. J. Hewlett and J. D. Love

Optical Sciences Centre,
The Australian National University,
Canberra, ACT 0200, Australia.

Tel: +61 6 249 5129, Fax: +61 6 249 5184

G. Meltz, T. J. Bailey and W. W. Morey

United Technologies Research Center,
411 Silver Lane, East Hartford,
CT 06108, USA.

Tel: 203 727 7486, Fax: 203 727 7909

Experimental observations

A series of blazed, or tilted gratings were fabricated in both depressed-cladding (AT&T Accutether) and matched-cladding (Corning SMF-28) single-mode fibre. In each case, a phase mask was orientated to set the nominal blaze angle (i.e., the complement of the angle between the fibre axis and the etched lines in the mask) from 0° to 3° . The fibres were soaked in hydrogen at 2120 psi and 97.6°C for 15 hours to enhance their photosensitivity. Gratings were formed by exposing the fibre core to a 248 nm KrF laser for 5 minutes with a fluence of $130 \text{ mJ/cm}^2/\text{pulse}$ at a rate of 20 pulses/s.

The transmission spectra of all gratings showed a series of fine-structure features on the short-wavelength side of the fundamental Bragg line. Figures 1(a) and 1(b) show, respectively, the spectra obtained in depressed-cladding fibre with effective blaze angles of $\theta = 0^\circ$ and 4.36° . These values correspond to respective fringe tilts of 0° and 3° and account for the refraction of the UV writing beam at the glass-air interface. In each case, the fundamental Bragg line is labelled as resonance #1. A pronounced 'ghost'-grating reflection becomes immediately apparent in depressed-cladding fibre as the blaze angle increases from $\theta = 0^\circ$, as illustrated by resonance #1a in Figure 1(b) [1]. This is separated from the fundamental, or LP_{01} - LP_{01} Bragg line by approximately 5 nm. Analogous spectra obtained using matched-cladding fibre do not exhibit the 'ghost'-grating transmission notch, as will be discussed further at the meeting.

In this paper, we show that the 'ghost'-grating reflection and the remaining fine-structure features in the transmission spectra are attributable to higher-order cladding-mode resonances [1]. A single set of cladding-mode resonances is observed in the transmission spectra of unblazed ($\theta = 0^\circ$) gratings, as illustrated by resonances #2-11 in Figure 1(a). In contrast, two distinct series of cladding-mode resonances are identifiable when the grating is blazed. These are labelled as resonances #2-15 and #1b-15a in Figure 1(b), respectively. The relative strength and location of these higher-order Bragg lines change as the blaze angle is increased.

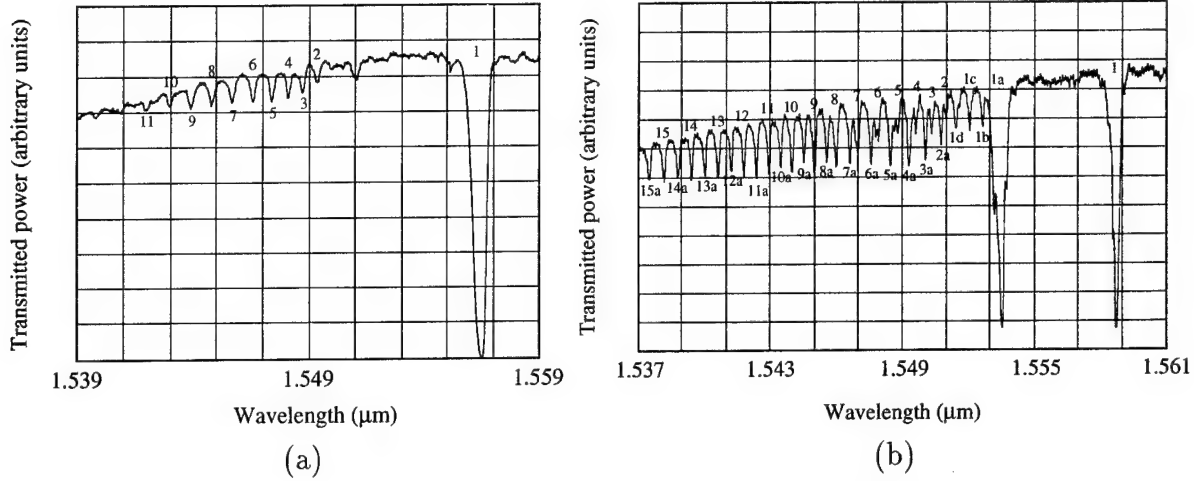


Figure 1: Experimental transmission spectra obtained in depressed-cladding fibre for (a) an unblazed grating with $\theta = 0^\circ$ and (b) a blazed grating with $\theta = 4.36^\circ$. Each resonance position has been numbered for identification purposes.

Theoretical analysis

In addition to the bound fundamental mode, which is guided by the core-cladding interface, the finite extent of the fibre cross-section permits a *discrete* set of higher-order cladding modes to be supported. These modes are guided by the cladding-air interface in the vicinity of the grating; elsewhere, they become attenuated by the external jacket surrounding the cladding. It is, however, their *discrete* nature which holds the key to interpreting the fine-structure features in the transmission spectra presented in Figure 1.

In the presence of a Bragg grating, the forward-propagating fundamental, or LP_{01} mode of a finite-clad, single-mode fibre can couple to either the backward-propagating LP_{01} mode, or to a discrete, backward-propagating cladding mode at some wavelength, λ , provided that (i) the respective propagation constants, $\beta_{LP_{01}}$ and β , satisfy the Bragg phase-matching condition [2]:

$$\beta_{LP_{01}}(\lambda) + \beta(\lambda) = \Omega_z = \Omega \cos \theta, \quad (1)$$

where Ω denotes the grating wavenumber and θ is the effective blazing angle, and (ii) the symmetry of the reflected modal field matches that of the incident mode and the grating. According to coupled mode theory [2, Chapter 27], the strength of the coupling between two discrete modes is then governed by the coupling coefficient, C , which involves an overlap between the modal field distributions and the grating profile.

In the case of an unblazed ($\theta = 0^\circ$) grating, the forward-propagating LP_{01} mode can couple *only* to radially symmetric, backward-propagating LP_{0n} modes. Using the experimentally measured refractive-index profile of the fibre and a shooting technique to solve the scalar wave equation [3], the 20 lowest-order LP_{0n} modal fields and propagation constants were calculated numerically at each of the resonance wavelengths labelled #1–11 in Figure 1(a). The constant, Ω_z , in Equation 1 can then be calculated from the LP_{01} – LP_{01} reflection (resonance #1) and the n -values corresponding to each of the higher-order Bragg lines follow. By numerically evaluating the coupling coefficient, C , and normalising the data to the LP_{01} – LP_{01} mode overlap, the coupling strength at each resonance position

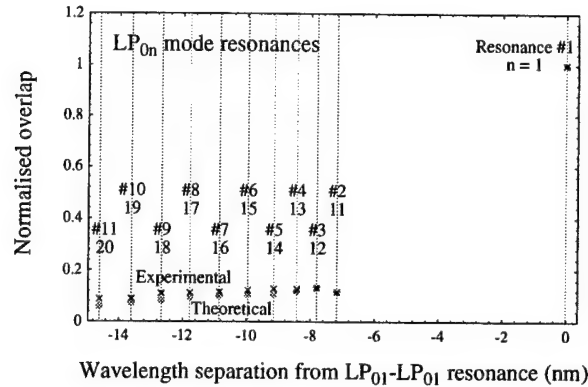


Figure 2: Experimental (crosses) and theoretical (circles) normalised overlap integrals for the LP_{0n} mode set. The results are for the unblazed ($\theta = 0^\circ$) grating in depressed-cladding fibre. Each resonance position is indicated by a light vertical line and is labelled with the notation used in Figure 1(a).

is readily calculated. Figure 2 plots the normalised overlaps as a function of wavelength separation from the fundamental Bragg line. Also shown are the experimentally measured overlaps, as determined by estimating the reflectivity directly from Figure 1(a) and using $R = \tanh^2(CL)$, where L is the grating length, to determine the normalised ratio of coupling coefficients.

In the case of a blazed grating, the inherent asymmetry allows the forward-propagating LP_{01} mode to couple to backward-propagating LP_{0n} and LP_{1n} modes. By analogy with Figure 2, the overlap integrals for the LP_{0n} and LP_{1n} mode sets are plotted as a function of wavelength separation from the fundamental Bragg line in Figures 3(a) and 3(b), respectively. In each case, the data are normalised to the LP_{01} - LP_{01} mode overlap and agree favourably with the experimentally measured values.

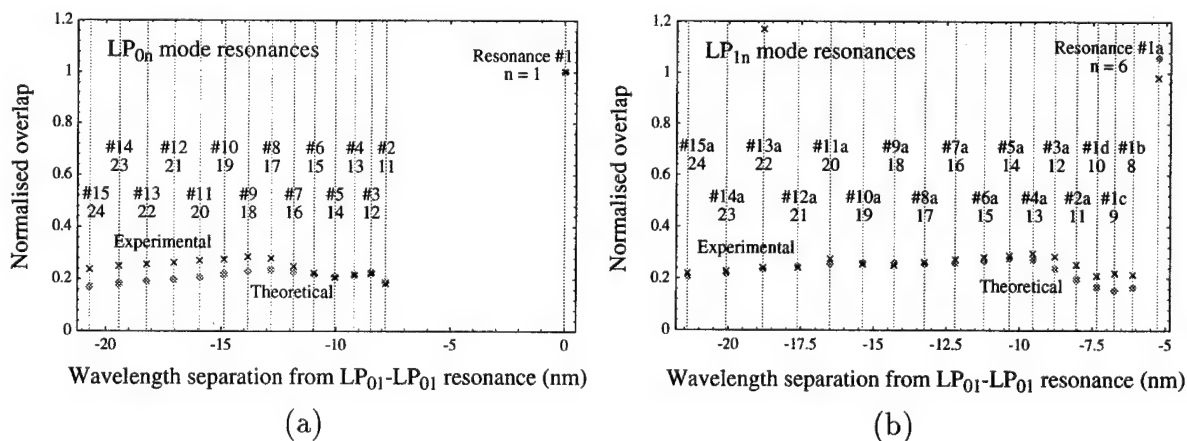


Figure 3: Experimental (crosses) and theoretical (circles) normalised overlap integrals for (a) the LP_{0n} and (b) the LP_{1n} mode set. The results are for the blazed ($\theta = 4.36^\circ$) grating in depressed-cladding fibre. Each resonance position is indicated by a light vertical line and is labelled with the notation used in Figure 1(b).

Discussion

The 'ghost'-grating line (resonance #1a) in Figures 1(b) and 3(b) is approximately equal in strength to the fundamental Bragg line (resonance #1). This implies that the LP_{01} - LP_{01} and LP_{01} - LP_{16} overlaps are comparable and, hence, that the LP_{16} mode has a significant amount of its power concentrated within the core of the fibre. Figure 4 confirms this fact and shows the radial field distribution of the resonant LP_{16} mode of the composite depressed-cladding structure (solid line), together with the LP_{11} mode of the central core region in isolation (broken line). The tightly confined higher-order mode gives rise to the pronounced 'ghost'-grating resonance in depressed-cladding fibres. Physical reasons for this behaviour, which is not observed in matched-cladding fibre, will be presented at the meeting.

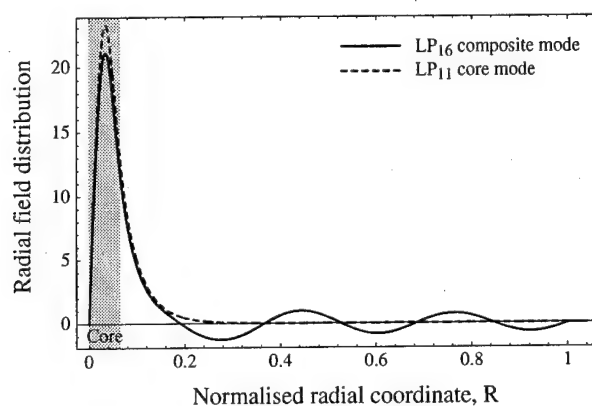


Figure 4: Radial field distributions of the resonant LP_{16} mode of the composite depressed-cladding fibre (solid line) and the LP_{11} mode of the central core region in isolation (broken line). In each case the fields are normalised such that $\int_0^\infty F^2(R)R dR = 1$ and the radial coordinate, R , is normalised to unity at the cladding-air interface. The extent of the fibre core is indicated by the shaded region.

References

- [1] S. J. Hewlett, J. D. Love, G. Meltz, T. J. Bailey and W. W. Morey. Cladding-mode coupling characteristics of Bragg gratings in depressed-cladding fibre. *Elect. Lett.* Submitted.
- [2] A. W. Snyder and J. D. Love. 1983. *Optical waveguide theory*. Chapman and Hall, London.
- [3] R. A. Sammut and C. Pask. 1981. Simplified numerical analysis of optical fibres and planar waveguides. *Elect. Lett.*, **17**, 105-106.

Fiber grating filters based on radiation- and cladding-mode coupling

T. Erdogan

The Institute of Optics, University of Rochester, Rochester, NY 14627
Tel: (716) 275-7227 Fax: (716) 244-4936 e-mail: turan@optics.rochester.edu

J. E. Sipe

Department of Physics, University of Toronto, Toronto, ON M5S1A7, Canada

Fiber Bragg gratings formed in germanosilicate optical fibers by ultraviolet (uv) irradiation [1] have developed rapidly in recent years. Numerous applications have been demonstrated that utilize fiber gratings as mirrors, in which a forward-propagating bound mode couples to a backward-propagating bound mode of the same type, and as mode converters, in which one type of bound mode couples to a different type. Fiber gratings can also function as effective loss filters by enabling the coupling of a bound mode to the radiation modes of the fiber [2]. Such filters have been demonstrated as spectrally selective loss elements for flattening the gain spectrum of an erbium-doped fiber amplifier [3]. Other potential applications of these filters for optical communications include filtering of amplified spontaneous emission (ASE) in optically amplified systems, and spectral clean-up filtering in wavelength-division multiplexed (WDM) systems. Furthermore, grating filters are desirable components for numerous other fiber-optic systems, such as fiber lasers and distributed sensor systems. The main advantages provided by fiber-grating filters for these applications include: low insertion loss, high spectral bandwidth, low back reflection, and potentially low cost.

In this paper we experimentally and theoretically demonstrate the effects of two fiber-grating features on the spectral properties of the filters described above. The first feature is the tilt or blaze angle of the grating fringes with respect to the fiber axis. We show how grating tilt can be used effectively both to control the loss spectrum and to nullify bound-mode Bragg reflection. The second feature is the presence or absence of the cladding-air interface in an actual fiber, which gives rise to a discrete set of cladding modes over a portion of the otherwise continuous spectrum of radiation modes. The existence of cladding modes transforms the otherwise smooth, broad-band loss spectrum arising from bound-mode to radiation-mode coupling into a transmission spectrum consisting of a quasi-periodic train of loss resonances.

To investigate the dependence of the radiation-mode coupling loss spectrum on tilt angle experimentally, a set of nominally identical gratings was written at various tilt angles. The grating periods are roughly $0.5\text{ }\mu\text{m}$, so that for wavelengths in the vicinity of $1.5\text{ }\mu\text{m}$ coupling of a forward-going bound mode to backward-going radiation modes is observed. Corning Flexcore fiber was used for these experiments because of its nearly step-index profile. The fiber had a core radius of approximately $a = 2.625\text{ }\mu\text{m}$ and $\Delta = 0.0055$. It was loaded with about 3.8 mole % of deuterium to enhance its photosensitivity [4]. Gratings were written by interfering two beams from a 242-nm, excimer-laser-pumped, frequency-doubled dye laser producing 15 ns pulses at a 30 Hz repetition rate. Exposures were done using 20 mW of average power, with the nearly gaussian beam focused to a spot size of about $5\text{ mm} \times 50\text{ }\mu\text{m}$ on the fiber. Exposure times varied from one to two minutes; the transmission spectrum was monitored in real time to achieve roughly the same uv-induced index change for all gratings. The index change is approximately $\Delta n/n_{\text{eff}} = 1.0 \times 10^{-3}$, where n_{eff} is the effective refractive index of the bound mode for which the grating is designed, and $2\Delta n$ is the peak-to-peak induced index change assuming perfect fringe visibility. It is important to note that due to variations in interferometer alignment and stability between the writing of each grating, there is noticeable variation in both grating fringe visibility and uv-induced index change among the gratings.

The grating tilt was achieved by rotating the fiber about the axis normal to the plane defined by the two intersecting uv beams. Using Snell's Law, a grating with a design Bragg wavelength of λ_B^0 and a grating tilt angle of θ (angle between the grating vector and the fiber axis) can be written using a uv beam intersection angle in air of $2\alpha_{ext}$ and an external tilt angle θ_{ext} (angle between the bisector of the uv beams and the normal to the fiber axis) given by

$$\begin{aligned} 2\alpha_{ext} &= \sin^{-1}[n_{cl} \sin(\alpha + \theta)] + \sin^{-1}[n_{cl} \sin(\alpha - \theta)] \\ \theta_{ext} &= \frac{1}{2} \sin^{-1}[n_{cl} \sin(\alpha + \theta)] - \frac{1}{2} \sin^{-1}[n_{cl} \sin(\alpha - \theta)]. \end{aligned} \quad (1)$$

Here 2α is the beam intersection angle inside the fiber, approximately determined by the equation

$$\alpha = \sin^{-1} \left(\frac{n_{eff}}{n_{cl}} \frac{\lambda_{uv}}{\lambda_B^0 \cos \theta} \right) \quad (2)$$

where n_{cl} is the cladding refractive index. Figure 1(a) shows a plot of the experimentally measured transmission loss spectra for gratings with tilt angles up to 15° . Here wavelength detuning is defined relative to the design Bragg wavelength. For these measurements the bare fiber was submerged in a suitable index-matching fluid to suppress effects associated with the cladding-air interface.

In order to more fully understand the spectra of Figure 1(a), a coupled-mode theory analysis was used to calculate the transmission loss spectra resulting from coupling of a forward-going LP_{01} bound mode to the continuum of backward-going LP_q radiation modes [5], where q is the azimuthal mode number. In Figure 1(b) the calculated transmission loss spectra corresponding to the measured spectra in Figure 1(a) are plotted. The calculations assume a design wavelength of $\lambda_B^0 = 1550$ nm. There is reasonably good agreement between the measured and the calculated spectra. The differences are mostly a result of approximations made in the calculation.

Another important effect of grating tilt is to reduce the bound-mode to bound-mode Bragg reflection. This result can be quite useful for devices designed to function only as loss filters, having low back reflection at all wavelengths [3]. Figure 2(a) shows a calculation of the peak grating reflectivity as a function of grating tilt angle for gratings similar to those described above, except with $\Delta n/n_{eff} = 0.5 \times 10^{-3}$. The reflectivity can be minimized either by choosing the tilt

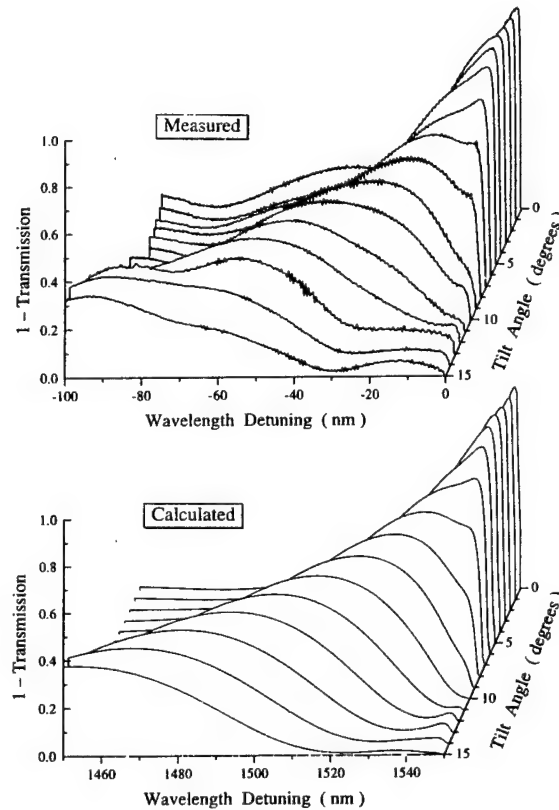


Figure 1: (a) Measured and (b) calculated transmission spectra through tilted fiber gratings.

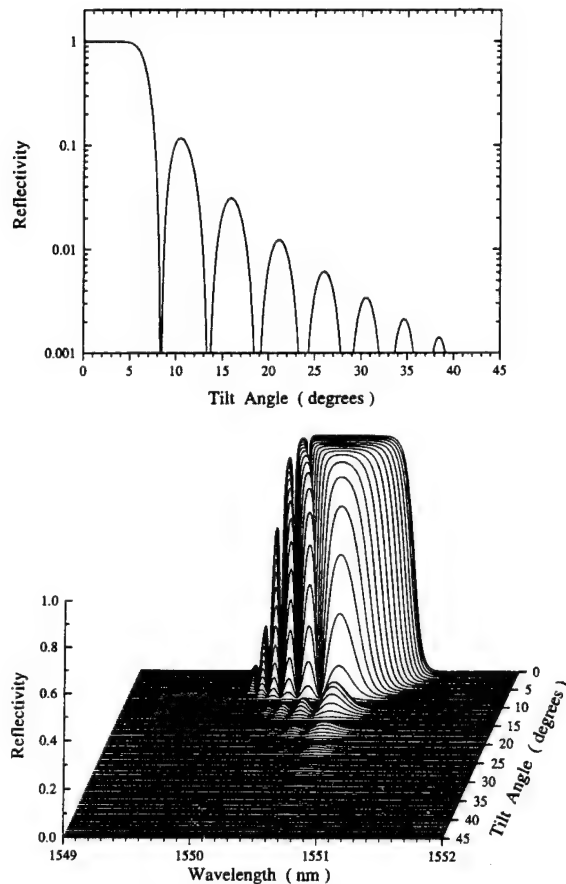


Figure 2: (a) Peak bound-mode to bound-mode reflectivity and (b) reflectivity spectra vs. grating tilt angle.

order to minimize its effect for applications requiring easily achieved with true radiation-mode coupling.

Figure 3(a) shows the transmission spectrum measured through a grating similar to those described above, except $\Delta n/n_{eff} = 3 \times 10^{-4}$ and $\lambda_B^0 = 1540$ nm. For this measurement the bare fiber was freely suspended in air, thus allowing cladding modes to propagate. For comparison, Figure 3(b) shows the calculated spectrum obtained using coupled-mode theory. Coupling coefficients were calculated between an LP_{01} bound mode and each of the exact (vector) cladding modes. The agreement between theory and experiment is quite good.

To conclude, we have demonstrated the dependence of spectral characteristics of fiber-grating filters on grating tilt and the existence of an extra dielectric interface at the cladding-air boundary. Both of these

carefully to be one of the zero-reflectivity values, or simply by choosing the tilt angle large enough to not exceed a specified maximum reflectivity. For instance, for all tilt angles greater than 40° in the example of Figure 2, the maximum reflectivity is less than -30 dB. Figure 2(b) shows a waterfall of the reflectivity spectra for such gratings.

As pointed out above, when the cladding-air interface is not index-matched with the appropriate fluid or polymer coating, the loss spectrum exhibits strong resonances associated with coupling between the bound mode and individual cladding modes of the fiber. The resulting filter characteristics are potentially quite useful for some applications. For short-period gratings, in which a forward-going bound mode couples to backward-going cladding modes, the loss spectrum forms a quasi-periodic train of loss peaks. For long-period gratings, in which the bound mode couples to forward-going cladding modes, the individual resonances are quite broad and spaced far apart, such that each resonance can function as a broad-band loss filter [6]. Sometimes these resonances are undesirable, and therefore it is useful to understand this coupling phenomenon in the smooth, broad-band loss spectra most

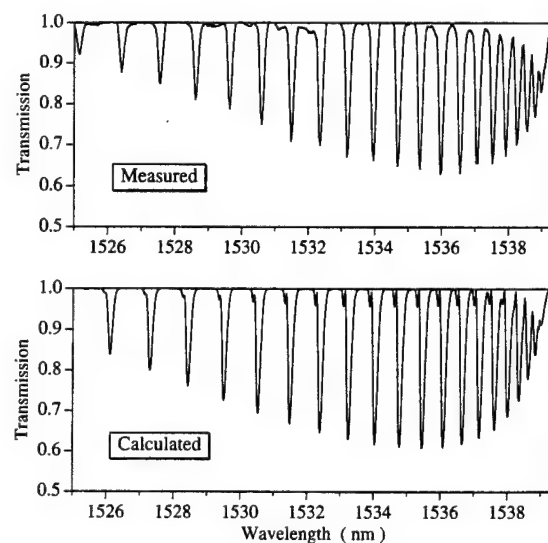


Figure 3: (a) Measured and (b) calculated transmission spectra through a fiber grating that supports cladding modes.

features markedly affect the spectra. Tilt provides a control knob to adjust the bandwidth, strength, and spectral location of loss, while the cladding-air interface transforms the smooth loss spectrum into a quasi-periodic train of loss resonances.

The authors are grateful to Victor Mizrahi for helpful insight, and to Paul J. Lemaire for the deuterium sensitization of the fibers used in the experiments. A portion of this work was conducted at and supported by AT&T Bell Laboratories, Murray Hill, NJ.

- [1] G. Meltz, W. W. Morey, and W. H. Glenn, *Opt. Lett.*, **14**, 823 (1989).
- [2] V. Mizrahi and J. E. Sipe, *J. Lightwave Tech.*, **11**, 1513 (1993).
- [3] R. Kashyap, R. Wyatt, and R. J. Campbell, *Electron. Lett.*, **29**, 154 (1993).
- [4] P. J. Lemaire, R. M. Atkins, V. Mizrahi, K. L. Walker, K. S. Kranz, and W. A. Reed, *Electron. Lett.*, **29**, 1191 (1993).
- [5] T. Erdogan and J. E. Sipe, submitted for publication, *J. Opt. Soc. Am. A*, (1995).
- [6] A. M. Vengsarkar, P. J. Lemaire, J. B. Judkins, V. Bhatia, T. Erdogan, and J. E. Sipe, paper PD4, Opt. Fiber Comm. Conf., San Diego, CA (1995).

Super coupled mode equations for periodic superstructure Bragg gratings

C. Martijn de Sterke and Neil G.R. Broderick

School of Physics and Optical Fibre Technology Centre, University of Sydney, New South Wales 2006, Australia. Phone: 61 2 351 2906, fax: 61 2 660 2903

(May 10, 1995)

I. INTRODUCTION

Periodic superstructure Bragg gratings are gratings in which at least one of the *grating parameters* vary periodically. They have been studied theoretically [1,2], as well as experimentally in both semiconductor [3-6], and in optical fibers geometries [7-9]. In particular, the recent work in fiber Bragg gratings has focused on sampled gratings in which the grating is made to vanish periodically, as illustrated in Fig. 1. This figure shows schematically the refractive index n as a function of position. Note that the superstructure period Λ is much larger than the period of the underlying grating, d .

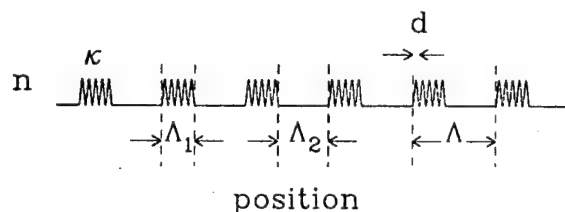


FIG. 1. Schematic of a periodic grating superstructure with grating period d , and superstructure period Λ .

As shown in Fig. 2, superstructure gratings have a reflection spectrum with discrete wavelength regions of high reflectivity; these extend over a much wider frequency interval than the reflection spectrum of uniform gratings [3-9]. Superstructure gratings have therefore found important applications such as in broadband tunable lasers, while uses in optical signal processing have been predicted [7].

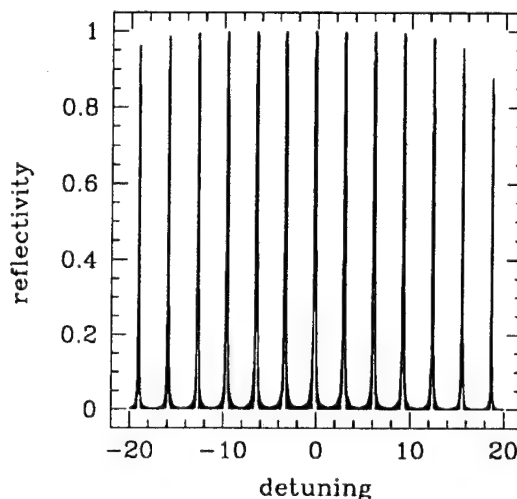


FIG. 2. Reflection spectrum for a periodic grating super structure with total length $L = 40$, $\Lambda = 1$, $\kappa = 1$, and $\Lambda_1 = 0.1$. If the units are taken to be millimeters, a single unit of detuning corresponds to a frequency of about 32 GHz.

The widening of the reflection spectrum can be understood as follows. For frequencies slightly detuned from a Bragg resonance the wavelets reflected off different grating rulings are not all in phase, and the grating thus reflects weakly. This is illustrated in Fig. 3, which, for a uniform grating, shows the sign of the phase of the reflected light as a function of position. Closer to the Bragg resonance the regions in Fig. 3 grow in size, until, very close to the Bragg resonance, they are as large as the grating itself. In this case the light reflected off all rulings is in phase, and the grating thus reflects strongly. Returning to the frequency in Fig. 3, we see that the grating can be made to reflect by removing the grating in regions where the phase of the

reflected light is, say, negative, as in *sampled gratings* (Fig. 1). Sampled gratings thus reflect light at frequencies where the associated uniform grating is not reflective at all.

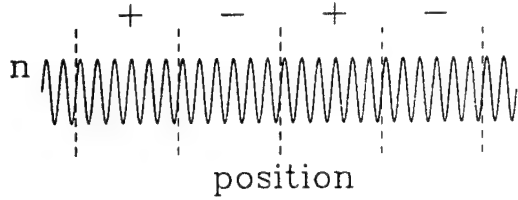


FIG. 3. Sign of the phase of the reflected light in a uniform grating away from the Bragg resonance. Contributions from adjacent regions almost cancel, thus the total reflectivity is small.

II. COUPLED MODE THEORY

Though the reflectivity of any fibre Bragg grating can be calculated by solving Maxwell's equations, often coupled mode theory is used, as it reduces the complexity of the problem, and because it allows insight into the nature of the solutions. When the grating is *shallow*, as is almost often true for fibre gratings, the procedure is particularly convenient to apply. For shallow gratings the electric field $E(z, t)$ is taken to be,

$$E(z, t) = \left[\mathcal{E}_+ e^{+ik_M z} + \mathcal{E}_- e^{-ik_M z} \right] e^{-i\omega_M t} + c.c., \quad (1)$$

where the functions $\mathcal{E}_\pm = \mathcal{E}_\pm(z, t)$ are slowly varying, and are thus envelope functions. In Eq. (1), $k_M = M\pi/d$, with M a positive integer labeling the Bragg order, and ω_M is the associated frequency. This choice for k ensures that the spectrum of the field is approximately matched to one of the Bragg resonances of the grating. It is well known that the \mathcal{E}_\pm satisfy the coupled mode equations

$$\begin{aligned} +i \frac{\partial \mathcal{E}_+}{\partial z} + \frac{i}{v_g} \frac{\partial \mathcal{E}_+}{\partial t} + \kappa_M(z) \mathcal{E}_- + \delta(z) \mathcal{E}_+ &= 0, \\ -i \frac{\partial \mathcal{E}_-}{\partial z} + \frac{i}{v_g} \frac{\partial \mathcal{E}_-}{\partial t} + \kappa_M(z) \mathcal{E}_+ + \delta(z) \mathcal{E}_- &= 0. \end{aligned} \quad (2)$$

Here v_g is the group velocity of the light in the absence of the grating, and

$$\begin{aligned} \kappa_M(z) &= \frac{\pi n_M(z)}{\lambda}, \\ \delta(z) &= \frac{2\pi[n_0(z) - \tilde{n}]}{\lambda}, \end{aligned} \quad (3)$$

where n_M is the M th Fourier component of the refractive index profile and \tilde{n} is a reference index. Thus κ_M and δ are the position-dependent grating strength and Bragg condition, respectively. For a superstructure κ_M and δ are periodic functions of position, while for a uniform grating they are constant.

Of course one can find the reflection spectrum of a sampled grating by solving the coupled mode equations (2). However, just as in coupled mode theory, where one considers the envelopes of the forward and backward propagating fields [Eq. (1)], one can formulate a *super coupled mode theory*, written in terms of the *super envelopes*, i.e. the envelopes of the usual envelope equations [1,2]. While in deriving the coupled mode equations for fibre gratings one can usually assume that the grating is shallow, in general this is not true for grating superstructures. The derivation of the super coupled mode equations is therefore more complicated. In particular, a simple *ansatz* like (1) is not sufficient.

III. ANALYSIS OF GRATING SUPERSTRUCTURES

Here we analyze the properties of grating superstructures in some detail. The results are then applied in Section 4 in the derivation of the super coupled mode equations.

To analyze grating superstructures systematically we set

$$\begin{aligned} \kappa(z) &= \sum_j \kappa_j e^{2\pi i j z / \Lambda}, \\ \delta(z) &= \sum_j \delta_j e^{2\pi i j z / \Lambda}, \end{aligned} \quad (4)$$

and use Bloch's theorem [10] to find the most general form of the continuous wave solutions

$$\mathcal{E}_{\pm}(z, t) = \sum_j \alpha_{\pm, j} e^{2\pi i j z / \Lambda} e^{i(kz - \Delta t)}. \quad (5)$$

Substituting Eqs. (4) and (5) into the coupled mode equations (2) leads to an infinite set of algebraic equations for the unknown parameters $\alpha_{\pm, j}$

$$\begin{aligned} \left(\Delta - k - j \frac{2\pi}{\Lambda}\right) \alpha_{+, j} + \sum_{\ell} \delta_{j-\ell} \alpha_{+, \ell} + \sum_j \kappa_{j-\ell} \alpha_{-, \ell} &= 0, \\ \left(\Delta + k - j \frac{2\pi}{\Lambda}\right) \alpha_{-, j} + \sum_{\ell} \delta_{j-\ell} \alpha_{-, \ell} + \sum_{\ell} \kappa_{j-\ell} \alpha_{+, \ell} &= 0. \end{aligned} \quad (6)$$

So for each value of k chosen within the first Brillouin zone (i.e. $-\pi/\Lambda < k \leq +\pi/\Lambda$) an eigenvalue problem in Δ ensues. The *eigenvalues* map out the photonic bands of the superstructure as illustrated in Fig. 4, while the *eigenvectors* correspond to the associated Bloch functions. Though in general it is necessary to solve Eqs. (6) exactly, approximate solutions can be found in the limit that

$$(\kappa_j \Lambda) \ll 1, \text{ and, } (\delta_j \Lambda) \ll 1. \quad (7)$$

In this limiting situation, in which the superstructure is *shallow*, the eigenvalues of matrix (6) at the centre and the edge of the Brillouin zone, are given by

$$v_g \Delta_j = -\delta_0 \pm \sqrt{\left(\frac{2\pi j}{\Lambda}\right)^2 + \kappa_0^2} \pm \kappa_j. \quad (8)$$

The solutions at the centre (edge) of the Brillouin zone correspond to even (odd) values of j ; Eq. (8) thus represent the positions of the photonic bandgaps (see Fig. 4), and thus the frequencies for which the superstructure is strongly reflective (Fig. 3). Note that in

the limits (7), Eqs. (8) predict that these frequencies occur periodically and that the size of gaps is proportional to the size of the associated Fourier component of the $\kappa(z)$, consistent with statements in Refs. [3-6].

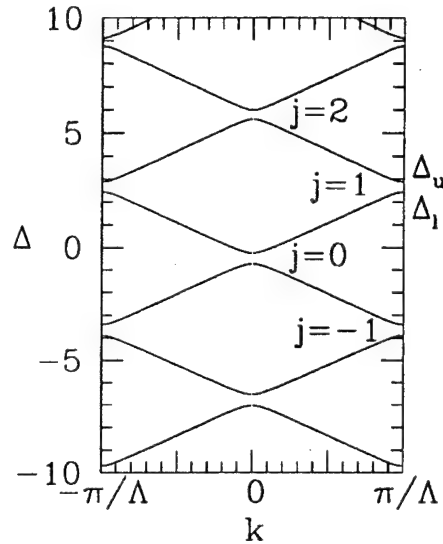


FIG. 4. Photonic band structure for a periodic grating super structure with $\Lambda = 1$, $\kappa = 2.5$, $\Lambda_1 = 0.1$. If the units are taken to be millimeters a single unit of detuning corresponds to a frequency of about 32 GHz.

In the more general, and physically realistic case where inequalities (7) are not satisfied these conclusions cannot be drawn. In general, therefore, the photonic band gaps are not periodic in frequency and the size of the j th gap is not proportional to the associated Fourier component.

IV. SUPER COUPLED MODE THEORY

To apply super coupled mode theory we choose an electric field with a spectrum concentrated around one of the photonic band gaps, $j = 1$, say (Fig. 4). Note that this is equivalent to choosing M in Eq. (1) in coupled mode theory. In addition, for deep su-

perstructures the inequalities (7) are not satisfied, and a simple *ansatz* like (1) is then not sufficient. Rather, we use

$$\hat{\mathcal{E}}(z, t) = \left[f_u(z, t)\varphi_u + f_l(z, t)\varphi_l \right] e^{-i\Delta_0 t}, \quad (9)$$

where $\hat{\mathcal{E}}$ is the column vector with elements \mathcal{E}_+ and \mathcal{E}_- . Further, $\Delta_0 = (\Delta_l + \Delta_u)/2$, where $\Delta_{u,l}$ are the frequencies at the edges of the photonic band gap under consideration, while $\varphi_u(z)$ and $\varphi_l(z)$ are the associated Bloch functions (Fig. 4). As in Eq. 1, the function $f_{u,l}$ are assumed to be varying slowly than the Bloch functions. Since they modulate the envelope functions \mathcal{E}_\pm we refer to them as super envelopes. Using a procedure very similar to that described in [11], it can be shown that the linear combinations

$$f_\pm = f_l \pm f_u \quad (10)$$

of the envelope functions $f_{u,l}$ in Eq. (9) satisfy the set of equations

$$\begin{aligned} +i\frac{\partial f_+}{\partial z} + \frac{i}{V}\frac{\partial f_+}{\partial t} + \tilde{\kappa} f_- &= 0, \\ -i\frac{\partial f_-}{\partial z} + \frac{i}{V}\frac{\partial f_-}{\partial t} + \tilde{\kappa} f_+ &= 0. \end{aligned} \quad (11)$$

Though these equations are very similar to the coupled mode equations (2), notice also the crucial differences: while in Eqs. (2) both κ and δ are periodic functions of position, in the super coupled mode equations Eqs. (11) $\tilde{\kappa}$ is constant and δ is absent. The super coupled mode equations for a superstructure Bragg grating are thus formally equivalent to the coupled mode equations for a *uniform* grating. Eqs. (11) are of course much easier to solve than Eqs. (2), leading to a significant reduction in the complexity of the problem. The only feature to be added is the application of the boundary conditions at the edges of the superstructure grating. While the envelope functions \mathcal{E}_\pm are continuous, the super envelopes f_\pm in general are not. The boundary conditions depend on the details of the

Bloch functions of the superstructure; but, once these have been established by solving Eqs. 6, the matching of the solutions at the interfaces is straightforward.

In conclusion we have shown that one can formulate a description of grating superstructures of any depth in terms of the superenvelopes, i.e. the envelopes of the usual envelope functions. Though the results are particularly simple for shallow structures [Eq. (7)] [1-6] we put these results in a wider context, making use of the superstructure Bloch functions.

The Optical Fibre Technology Centre is a partner in the APCRC.

-
- [1] P. St. J. Russell, Phys. Rev. Lett. **56**, 596-599 (1986).
 - [2] P. St. J. Russell, J. Appl. Phys. **59**, 3344-3355 (1986).
 - [3] V. Jayaraman *et al*, Appl. Phys. Lett. **60**, 2321-2323 (1992).
 - [4] V. Jayaraman *et al*, IEEE J. Quantum Electron. **29**, 1824-1834 (1993).
 - [5] Y. Tohmori *et al*, IEEE J. Quantum Electron. **29**, 1817-1823 (1993).
 - [6] H. Yasaka *et al*, Electron. Lett. **30**, 133-134 (1994).
 - [7] B.J. Eggleton *et al*, Electron. Lett. **30**, 1621-1622 (1994).
 - [8] M. Ibsen *et al* Electron. Lett. **31**, 37-38 (1995).
 - [9] J. Chow *et al*, Stable multiwavelength CW generation in an erbium-doped fibre laser using in-fibre comb filters, submitted to IOOC'95.
 - [10] C. Kittel, *Solid state physics*, 5th Ed. (Wiley, New York, 1976), Ch. 2.
 - [11] D.G. Salinas *et al* Opt. Comm. **111**, 105-110 (1994).

CHIRP, SELF-CHIRP AND META-CHIRP IN SAMPLED FIBRE GRATINGS

François Ouellette, Benjamin J. Eggleton, Peter C. Hill, Peter A. Krug
Optical Fibre Technology Centre, University of Sydney, Bldg. GO5, Maze Crescent,
NSW 2006, AUSTRALIA, tel. +61-2-335-0919, fax +61-2-335-0910

Sampled Bragg gratings consist of a periodic modulation of the amplitude and/or the phase of the Bragg grating. In the frequency domain, their reflectivity spectrum shows a number of equally spaced peaks, covering a range of wavelengths determined by the Fourier contents of the modulation, or "sampling" function. Sampled gratings have been used in DBR semiconductor lasers to extend their tuning range [1].

We have recently investigated the writing and applications of sampled Bragg gratings in photosensitive optical fibre. An initial demonstration of how such a grating can be fabricated [2] has been followed by a demonstration of a fibre laser with extended tunability, using two slightly mismatched sampled gratings as reflectors [3]. We have also demonstrated the use of chirped sampled gratings for broadband, or multi-wavelength dispersion compensation [4]. In this paper, we investigate in more detail the effects of chirp on the sampled gratings.

The effective index modulation in a sampled grating can be expressed as:

$$n(z) = n_0 + \frac{S(z) \delta n}{2} [1 + \gamma \cos(\beta_g z + \phi(z))] \quad (1)$$

where n_0 is the unirradiated core effective index, δn is the maximum index change, β_g is the fundamental wavenumber of the grating, $\phi(z)$ representing any modulation in the phase of the grating resulting in a chirp. $S(z)$ is a periodic sampling function affecting the grating amplitude. Periodic phase modulation can be included in $\phi(z)$. The effective index can also be expressed as:

$$n(z) = n_{av} + S_1(z) \frac{\delta n}{2} + S(z) \gamma \frac{\delta n}{2} \cos(\beta_g z + \phi(z)) \quad (2)$$

where:

$$n_{av} = n_0 + \frac{1}{P} \int_{-P/2}^{P/2} S(z) dz \quad (3)$$

$$S_1(z) = S(z) - \frac{1}{P} \int_{-P/2}^{P/2} S(z) dz \quad (4)$$

The electric field is described as:

$$E(z) = A_+(z) \exp[i\Phi(z)] + A_-(z) \exp[-i\Phi(z)] \quad (5)$$

where:

$$\Phi(z) = n_{av} k z + \frac{\delta n}{2} \int_0^z S_1(z) k dz \quad (6)$$

and $k=2\pi/\lambda$. A_+ and A_- are the forward and backward amplitudes, respectively. The coupled mode equations can then be derived using the usual procedure [5] and give:

$$\frac{dA_+}{dz} = i \frac{\kappa \gamma}{2} S(z) A_- \exp[-2i(\Delta z + \kappa S_p(z) - \Phi(z))] \quad (7)$$

$$\frac{dA_-}{dz} = -i \frac{\kappa \gamma}{2} S(z) A_+ \exp[2i(\Delta z + \kappa S_p(z) - \Phi(z))] \quad (8)$$

where:

$$\kappa = \frac{\pi \delta n}{\Lambda n_{av}}, \quad \Delta = n_{av} k - \frac{\pi}{\Lambda}$$

Λ being the grating period, and:

$$S_p(z) = \int S(z) dz \quad (10)$$

is the primitive of $S(z)$, provided that $S(z)=0$ at $z=0$. Since $S(z)$ is a periodic function, $S_p(z)$ is periodic with the same period. The product of the periodic functions $S(z)$ and $\exp(2i\kappa S_p(z))$ is itself a periodic function, and can be expanded as a Fourier series. Let P be the period of the sampled grating, then Eqs.(7-8) become:

$$\frac{dA_+}{dz} = i \frac{\kappa \gamma}{2} \sum_m S_m A_- \exp[-2i(\Delta z + \frac{\pi m z}{P} - \Phi(z))] \quad (11)$$

$$\frac{dA_-}{dz} = -i \frac{\kappa \gamma}{2} \sum_m S_m A_+ \exp[-2i(\Delta z + \frac{\pi m z}{P} - \Phi(z))] \quad (12)$$

where:

$$S_m = \frac{2}{P} \int_{-P/2}^{P/2} S(z) \exp \left[-2i \left(\kappa S_p(z) + \frac{\pi m z}{P} \right) \right] dz \quad (13)$$

Equations (11-12) are equivalent to those describing multiple gratings with wavenumbers separated by $2\pi/P$. Provided the gratings bandwidth is smaller than their separation, we first note that all these equivalent gratings have the same chirp function. Therefore a chirp applied to a sampled grating is applied to all the reflection peaks. This has been proposed as a way to achieve multi-wavelength dispersion compensation, or to alleviate the requirements to match the source to the grating for a dispersion compensating device [4].

The self-chirp can be described as the shift in Bragg wavelength due to the change in average refractive index in the UV-exposed region [5]. For the sampled grating, there is a first shift, due to the fact that n_{av} is not equal to n_0 , therefore the primary resonance ($m=0$) is not at the "nominal" wavelength $\lambda_0=2n_0\Lambda$, but rather at $2n_{av}\Lambda$. There is also a second self-chirp effect, that becomes apparent when one computes the coefficients S_m . Because of the presence of a z -dependent term in the exponential of eq.(13), the largest coefficient will not be S_0 . Thus the whole envelope of the sampled grating reflection spectrum is shifted to longer wavelengths. For example, for a square modulation of the grating, with length F , but period P (for a duty cycle F/P), the coefficients S_m are:

$$S_m = -2 i \frac{F}{P} \text{sinc} \left[\kappa F (1-F/P) + \frac{\pi F m}{P} \right] \quad (14)$$

The strongest peak is obtained for a value of m such that:

$$m = - \frac{\kappa}{\pi} (P-F) \quad (15)$$

or the closest integer. Thus the wavelength shift between the nominal Bragg wavelength and the strongest peak will be m times the wavelength separation between the peaks, plus the shift due to the change in average refractive index. In Fig. 1(a) is shown a sampled grating written with 100 samples, each about 100 nm long, separated by 1mm. The phase mask used to write this grating nominally gives a Bragg wavelength at 1530nm. the strongest peak is at 1538nm. This grating was subsequently chirped using our recently developed S-bend chirping technique. The result is shown in Fig. 1(b). The peaks all acquire the same broadening. The differences between the shape of the different peaks once the grating is chirped can possibly be explained by a non-uniformity along the sampled grating.

If the period of the sampled grating itself is not uniform, it can be shown that this generates a different chirp for the different peaks. In fact, it is possible, simply by chirping the sampled grating period, to get the strongest peak to be broadened and show a linear dispersion, without the grating to be actually chirped. Combined with a linear chirp, this would also allow to compensate the dispersion slope of a fibre in a multi-channel dispersion compensation device.

In conclusion, we have shown the effects of chirp, self-chirp, and meta-chirp on a fibre sampled grating. These must be taken into consideration when writing the gratings, but also have useful applications in multi-wavelength dispersion compensation.

Acknowledgments

The OFTC is a member of the Australian Photonics Cooperative Research Center.

References

- [1] V. Jayaraman, Z. M. Chuang, and L. A. Coldren, "Theory, design, and performance of extended tuning range semiconductor lasers with sampled gratings", *IEEE J. of Quantum Electron.* **29**, pp. 1824-1834 (1993).
- [2] B. J. Eggleton, P. A. Krug, L. Poladian and F. Ouellette, "Long superstructure Bragg gratings in optical fibres", *Electron. Lett.* **30**, pp. 1620-1622 (1994).
- [3] M. Ibsen, B. J. Eggleton, M. G. Sceats, and F. Ouellette, 'Broadly tunable DBR fibre laser using sampled fibre Bragg gratings', *Electron. Lett.* **31**, pp.37-38 (1995).
- [4] F. Ouellette, P. A. Krug, T. Stephens, G. Dhosi, B. Eggleton, 'Broadband and WDM dispersion compensation using sampled fibre Bragg gratings', to be publ. in *Electron. Lett.*, 1995.
- [5] L. Poladian, "Graphical and WKB analysis of nonuniform Bragg gratings", *Phys. Rev. E*, **48**, pp.4758-4767 (1993).

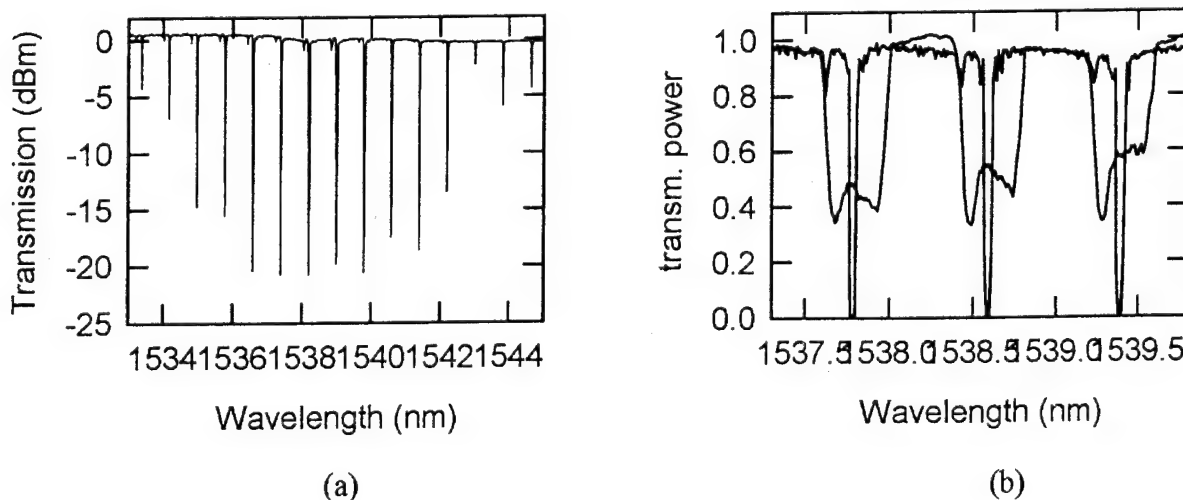


Fig.1 (a) Transmission spectrum of a sampled grating consisting of 100 samples, each 100 μ m long, separated by 1 mm. This grating was written with a phase mask giving a nominal Bragg wavelength of 1530 nm. (b) Close-up of the strongest peaks, showing their broadening when the grating is chirped.

Monday, September 11, 1995

Fiber Lasers

PMD 4:00–5:45pm
Multnomah Room

Gary A. Ball, *Presider*
3M Bragg Grating Technologies

Laser Applications of Fibre Gratings

Laurence Reekie

Optoelectronics Research Centre

Mountbatten Building

University of Southampton

Southampton, England SO17 1BJ.

Tel: (44) 1703 593186

Fax: (44) 1703 593149

E-mail: lr@orc.soton.ac.uk

In recent years, rare-earth doped fibre lasers have matured from a fledgling laboratory curiosity into a device capable of taking on other lasers at their own game, due in no small part to the invention of the photorefractive fibre grating. Single-handedly, this component has changed the way in which these lasers are perceived and used. It is no longer necessary to use bulk dielectric coated mirrors or fibre ring resonators to provide the optical feedback required for laser operation. Instead, by writing a grating into each end of a length of doped fibre, it is possible to make a robust device that can be readily spliced to other fibre components such as couplers and pigtailed diode lasers.

Photorefractive fibre gratings may be readily incorporated into a wide range of fibres using well-established techniques¹. By choosing a suitable glass host, fabrication of low loss gratings having a reflectivity in excess of 99% is routinely achievable. This, coupled with the intrinsic low loss of silica, allows highly efficient laser resonators to be formed such that the lasing performance is limited only by the efficiency of the rare-earth ion being used.

The first fibre laser to incorporate a fibre grating consisted of a Nd^{3+} -doped fibre spliced to an etched fibre grating². In marked contrast to photorefractive fibre gratings, these devices were polarisation sensitive and moreover were difficult to fabricate, requiring many individual steps over perhaps several days. Spectral line-narrowing of the laser output is a desirable side-effect of using fibre gratings. If the laser cavity is sufficiently long that many longitudinal modes lie within the linewidth of the fibre grating, then spectrally-narrowed, but multi-longitudinal mode operation of the laser will be obtained. The Nd^{3+} -doped fibre laser operated with a threshold of less than 2mW, a slope efficiency of 19% at $\lambda=1084\text{nm}$ and a linewidth of $\Delta\nu=16\text{GHz}$ ($\Delta\lambda=0.06\text{nm}$), demonstrating the potential of such a technique. Incorporating a similar device into an Er^{3+} -doped fibre laser operating at $\lambda=1551\text{nm}$ ³ gave a linewidth of $\Delta\nu=4.9\text{GHz}$ ($\Delta\lambda=0.04\text{nm}$).

Occasionally, it becomes necessary to improve the spectral purity of the laser by narrowing the linewidth down to a single longitudinal mode of the resonator. The laser linewidth is then limited only by environmental effects such as thermal drift, vibration and acoustic noise. In order to achieve this condition, two approaches may be followed. The first consists of providing sufficiently heavy spectral filtering that the laser is constrained to operate in a single longitudinal mode of the cavity. This method, essentially a 'brute-force' technique, was used in the first demonstration of a single frequency Nd^{3+} -doped fibre laser⁴. This was done by combining the

line-narrowing properties of a fibre grating with the large free spectral range of a short laser resonator. By using a fibre length of 50mm, single-mode operation with a linewidth of $\Delta\nu=1.3\text{MHz}$ at $\lambda=1082\text{nm}$ was obtained. This was in spite of the relatively broad linewidth of the grating ($\sim 200\text{GHz}$) compared to the 2GHz free spectral range of the resonator. This means of obtaining single mode operation has the advantage of being a simple technique which requires only the use of all-fibre components in the cavity. Heavy filtering is generally required however in order to provide robust single frequency performance. With the advent of high-reflectivity, low-loss photorefractive gratings which could be written directly into rare-earth doped fibres, it became possible to manufacture short cavity, single frequency Er^{3+} -doped fibre lasers operating in the region of $1.55\mu\text{m}$ ⁵. The inability to dope silica with high concentrations of Er^{3+} -ions meant that very low slope efficiencies were obtained using such lasers, as only a small fraction of the pump power could be absorbed in a short length. Two solutions to this problem were found. The first involved absorbing the residual pump power in a further length of Er^{3+} -doped fibre which acted as a power amplifier for the laser, thus making efficient use of the pump light - this was the master oscillator-power amplifier (MOPA) approach. The second solution was to co-dope the fibre with large quantities of Yb^{3+} -ions ⁶. This gave the fibre high absorption at the pump wavelength, in this case $\lambda=980\text{nm}$, and excellent slope efficiency if care was taken to maximise the transfer efficiency between the Yb^{3+} - and Er^{3+} -ions. In this case amplification of the laser was not necessary.

The second method used to obtain single frequency operation involves eliminating the condition which normally leads to multi-longitudinal mode lasing in a fibre laser *i.e.* spatial holeburning. This technique uses an optical isolator in the cavity in order to force unidirectional operation and, in general, very narrow linewidths ($\sim\text{kHz}$) can be achieved. Fibre gratings are not usually incorporated into such cavities, tuning and stabilisation being carried out using bulk optics, however gratings configured as filters may be employed ^{7,8}.

A recent variation on the first technique distributes the grating throughout the whole of the fibre cavity, giving a distributed feedback (DFB) laser ^{9,10}. Although first demonstrated using an interferometrically formed fibre grating, this type of laser is ideally suited to production by phase mask, as the $\lambda/4$ phase shift necessary for operation at the centre wavelength of the grating can then be written directly into the doped fibre. Highly efficient DFB fibre lasers up to 10cm in length have been fabricated using this technique.

An additional advantage to the fibre grating laser approach to single frequency operation is the ability to obtain continuous tunability of the laser over a broad bandwidth¹¹. This can be done by simply stretching or compressing the whole fibre laser cavity, including the grating reflectors, thus shifting the peak wavelength of the grating and simultaneously tracking the peak with a resonance of the cavity. Using this technique, it is possible to tune over most of the gain bandwidth of erbium.

In addition to their use as reflectors for rare-earth doped fibre lasers, fibre gratings can be written into the pigtail of a diode laser in order to provide wavelength selection and additional line-narrowing. This technique provides cost-effective alternatives to DFB semiconductor lasers for use in local area networks and as pump sources for solid-state lasers.

In conclusion, it can be seen that fibre gratings have revolutionised the field of rare-earth doped fibre lasers and are also impacting on the use of diode lasers. In addition, with their use in Er^{3+} -doped fibre amplifiers as filters and gain flattening elements, they are playing a major role in active fibre devices in general, changing the way that such devices are perceived and used.

REFERENCES

1. G. Meltz, W.W. Morey and W.H. Glenn: "Formation of Bragg gratings in optical fibres by a transverse holographic method", *Opt. Lett.*, 1989, **14**, pp.823-825.
2. I.M. Jauncey, L. Reekie, R.J. Mears, D.N. Payne, C.J. Rowe, D.C.J. Reid, I. Bennion and C. Edge: "Narrow-linewidth fibre laser with integral fibre grating", *Electron. Lett.*, 1986, **22**, pp.987-988.
3. I.M. Jauncey, L. Reekie, R.J. Mears and C.J. Rowe: "Narrow linewidth fibre laser operating at $1.55\mu\text{m}$ ", *Opt. Lett.*, 1987, **12**, pp.164-165.
4. I.M. Jauncey, L. Reekie, J.E. Townsend, D.N. Payne and C.J. Rowe: "Single longitudinal mode operation of a Nd^{3+} -doped fibre laser", *Electron. Lett.*, 1988, **24**, pp.24-26.
5. G.A. Ball, W.W. Morey and W.H. Glenn: "Standing wave monomode erbium fibre laser", *IEEE J. Photon. Tech. Lett.*, 1991, **3**, pp.613-615.

6. J.T. Kringlebotn, P.R. Morkel, L. Reekie and J.-L. Archambault: "Efficient diode-pumped single-frequency Erbium:Ytterbium fibre laser", *IEEE J. Photon. Tech. Lett.*, 1993, **5**, p.1162.
7. G.J. Cowle, D.N. Payne and D. Reid: "Single-frequency travelling wave erbium doped fibre loop laser", *Electron. Lett.*, 1991, **27**, pp.229-230.
8. M.C. Farries, D.C. Reid, L. Zhang and I. Bennion: "Fibre ring laser with fibre grating transmission filter", *Photosensitivity and Quadratic Nonlinearity in Glass Waveguides: Fundamentals and applications*, 1995, paper PMD4.
9. J.T. Kringlebotn, J.-L. Archambault, L. Reekie and D.N. Payne: " $\text{Er}^{3+}:\text{Yb}^{3+}$ co-doped fibre DFB laser", *Opt. Lett.*, 1994, **19**, p.2101.
10. A. Asseh, H. Storoy, J.T. Kringlebotn, W. Margulis, B. Sahlgren, S. Sandgren, R. Stubbe and G. Edwall: "10cm Yb^{3+} DFB fibre laser with permanent phase shifted grating", *Electron. Lett.*, 1995, **31**, p. 969.
11. G.A. Ball and W.W. Morey: "Compression-tuned single frequency Bragg grating fibre laser", *Opt. Lett.*, 1994, **19**, pp.1979-1981.

A Hamiltonian Approach to Propagation in Chirped and Non-Uniform Bragg Grating Structures

P.St.J. Russell and T.A. Birks

Optoelectronics Research Centre,
University of Southampton,
Southampton SO17 1BJ,
United Kingdom

One current and evolving use of fibre gratings is for chirped grating dispersion compensation[1]. Another is in the formation of effective $\lambda/4$ lasing cavities for DFB fibre lasers by imposing a slow local perturbation on the grating parameters[2]. In both cases the essential analytical problem is the same: How to treat the behaviour of light in spatially heterogeneous Bragg gratings? In this paper an approach is developed based on the Hamiltonian optics elegantly summarised by a number of authors, including notably Arnaud in his 1976 book *Beam and Fibre Optics*[3]. The Hamiltonian approach can be applied where the dispersion relation in the homogeneous structure is known, and where, in the heterogeneous real structure, parameters like average index vary slowly in space. It is essentially an analytical method for stepping through a non-uniform structure, matching phase velocities normal to the gradient of the heterogeneity at each step, and propagating along the local group velocity to the next point. This process is described by solutions of Hamilton's equations, which take the general form:

$$\frac{d\mathbf{x}}{d\sigma} = \nabla_{\mathbf{k}} H, \quad \frac{d\mathbf{k}}{d\sigma} = -\nabla H \quad (1)$$

where $\mathbf{x} = \{x, y, z, -t\}$ is the four-vector for space-time, $\mathbf{k} = \{k_x, k_y, k_z, \omega\}$ the generalised wavevector, σ an arbitrary parameter, and $H(\mathbf{x}, \mathbf{k})$ the Hamiltonian, which may be expressed directly from the dispersion relation for the waves. Note that in general \mathbf{k} depends on position. The Hamiltonian itself may be written in a number of equivalent ways, in all of which a phase front is given by the equation $H = 0$. In obtaining solutions to (1), it is important to distinguish total for partial differentiation. For a uniform weakly modulated 1-D grating H takes the special form[4]:

$$H \equiv \omega n_o/c - K/2 - \sqrt{(k - K/2)^2 + \kappa^2} = 0 \quad (2)$$

where κ is the usual grating coupling constant, $K=2\pi/\Lambda$ is the grating vector (Λ being the grating pitch), k the Bloch wavevector, and $k_o = \omega n_o/c$ the average wavevector in the grating. This Hamiltonian applies to any 1-D periodic structure (such as a fibre Bragg grating) whose effective index distribution is given by:

$$n^2(z) = n_o^2(z)[1 + M(z) \cos(K(z)z)] \quad (3)$$

where all the parameters are assumed to vary very slowly over many periods. Note that the Bloch

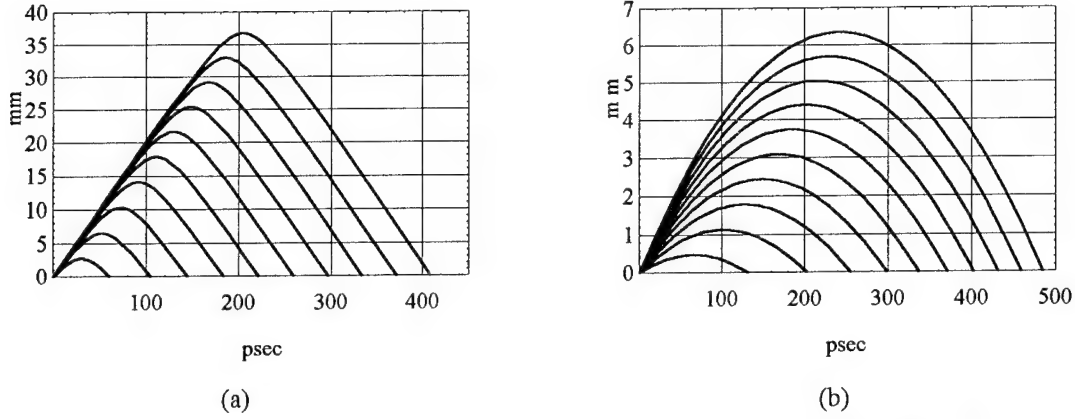


Figure 1: Space-time plots of ray paths in (a) weak and (b) strong grating (see text for parameters). The rays are spaced by 0.1 GHz. In (a), because the velocity at input and exit is close to the average value c/n_o , there will be only weak boundary reflections, eliminating Fabry-Perot effects. In (b), because the velocity is significantly less than c/n_o , there will be strong reflections at the boundary and strong Fabry-Perot effects.

waves are the normal modes of electromagnetic propagation in periodic media [4-6], just as plane waves are the modes of isotropic space. Their group velocities describe faithfully the ray paths taken by the light, and permit accurate and detailed explanations for the complex and often beautiful phenomena that can be seen in, for example, periodic planar waveguides[5-7].

The solution of (1) for the Hamiltonian (2) is particularly simple. Without loss of generality, it is given by:

$$\int_{z_o}^z \frac{n_o(z) dz}{\sqrt{1 - 1/\delta^2(z)}} = ct \quad (4)$$

where $\delta = \vartheta(z)/2\kappa(z)$ and $z = z_o$ at $t = 0$ (the dephasing parameter $\vartheta = 2k_o - K$). This expression relates time and position in the grating, allowing for example direct calculation of the time taken for light of a given wavelength to be reflected out again from a chirped grating, or the time taken for a complete cycle of oscillation in a heterogeneous DFB resonator. The integral in (4) may be evaluated analytically in a number of special cases. Let us now look at two examples.

The first is a linearly chirped grating. In this case, taking $\vartheta = \vartheta_o + az$, the solution is:

$$(\vartheta_o + az)^2 = (2\kappa)^2 + \left(-cta/n_o + \sqrt{\vartheta_o^2 - (2\kappa)^2} \right)^2. \quad (5)$$

Time/space plots of this solution for different incident conditions are given in Figure 1. The diagrams illustrate one of the limitations of the Hamiltonian approach as developed here; since it is classical, tunnelling effects are not included. Photons of course *do* tunnel through the potential barrier created by the grating stop-band; this process can be incorporated in the analysis by including an ad-hoc tunnelling probability near the stop-band edge. The case treated in Figure 1 corresponds to a pulse of bandwidth 10 GHz at 1.55 μm broadened by 350 psec in a fibre link. Notice that as the wavelength varies, the position where the Bloch waves are turned around shifts as expected. The time taken for

light at a given frequency to be reflected is:

$$\tau = \frac{2n_o \sqrt{\vartheta_o^2 - (2\kappa)^2}}{ca} \quad (6)$$

For a weak grating ($\kappa = 0.05/\text{mm}$ and $\vartheta_o = 0.15/\text{mm}$ for the first-reflected ray, Figure 1a) at $a = 0.018/\text{mm}^2$, the compensation is very linear, although the reflection efficiency will be low (strong tunnelling); the time-of-flight in the grating corresponds closely to a velocity of c/n_o , i.e., $(\vartheta_o/2\kappa)^2 \gg 1$. For a strong grating ($\kappa = 10/\text{mm}$ and $\vartheta_o = 20.05/\text{mm}$ for the first-reflected ray, Figure 1b) at $a = 0.1/\text{mm}^2$, on the other hand, the compensation is significantly nonlinear (owing to the proximity of the strong stop-band) although the efficiency will be much higher. This nonlinearity may be eliminated to a large degree by operating so that none of the frequencies in the pulse see Bragg reflection until they are already well into the grating; this of course implies the need for a longer grating. Notice however that, owing to the reduced group velocities near the stop-band edge, the grating length required is 7 times shorter than in the weak-grating case. The Hamiltonian solution as presented does not treat the reflection at the input boundary to the grating. This causes Fabry-Perot-like interference fringes in the cavity formed between itself and the turning point of the rays in the grating. If, however, the Bragg condition is not satisfied for any of the frequencies in the pulse in the initial few mm of the grating, the visibility of these fringes will be insignificant.

In the second example we consider a grating in which the square of the coupling constant varies quadratically with position:

$$\kappa^2 = \kappa_o^2 (1 + bz^2). \quad (7)$$

The solution in this case takes the form:

$$z = (v_o/\gamma) \sin(\gamma t + \arcsin(\gamma z_o/v_o)), \quad (8)$$

$$\gamma = 2c\kappa_o\sqrt{b}/(n_o\vartheta), \quad v_o = (c/n_o)\sqrt{1 - (2\kappa_o/\vartheta)^2}$$

where z_o is the initial position and, v_o is the initial group velocity if $z_o = 0$. These solutions are plotted in Figure 2 against t and $v_o n_o/c$ for $z_o = 0$ and $b = 0.15/\text{mm}^2$. As the launch velocity decreases (moving closer to the stop-band edge), the amplitude (in mm) of the oscillation and the cavity round trip time both decrease as expected. The absolute quantised frequencies of oscillation will be determined by the usual requirement that the round trip phase be a multiple of 2π , a matter we do not address here. The free spectral range of the resonances, however, is determined by the group time delay around the cavity and is given by $2\pi/\gamma$.

In conclusion, the Hamiltonian approach outlined in this paper provides an elegant alternative viewpoint from which to analyse and understand the behaviour of light in spatially heterogeneous 1-D grating structures. Its limitations are that the properties must vary slowly over many periods (well approximated in fibre Bragg gratings), and that tunnelling (not a classical concept) cannot be treated easily. More complicated spatial heterogeneities can be treated by numerical integration of (4).

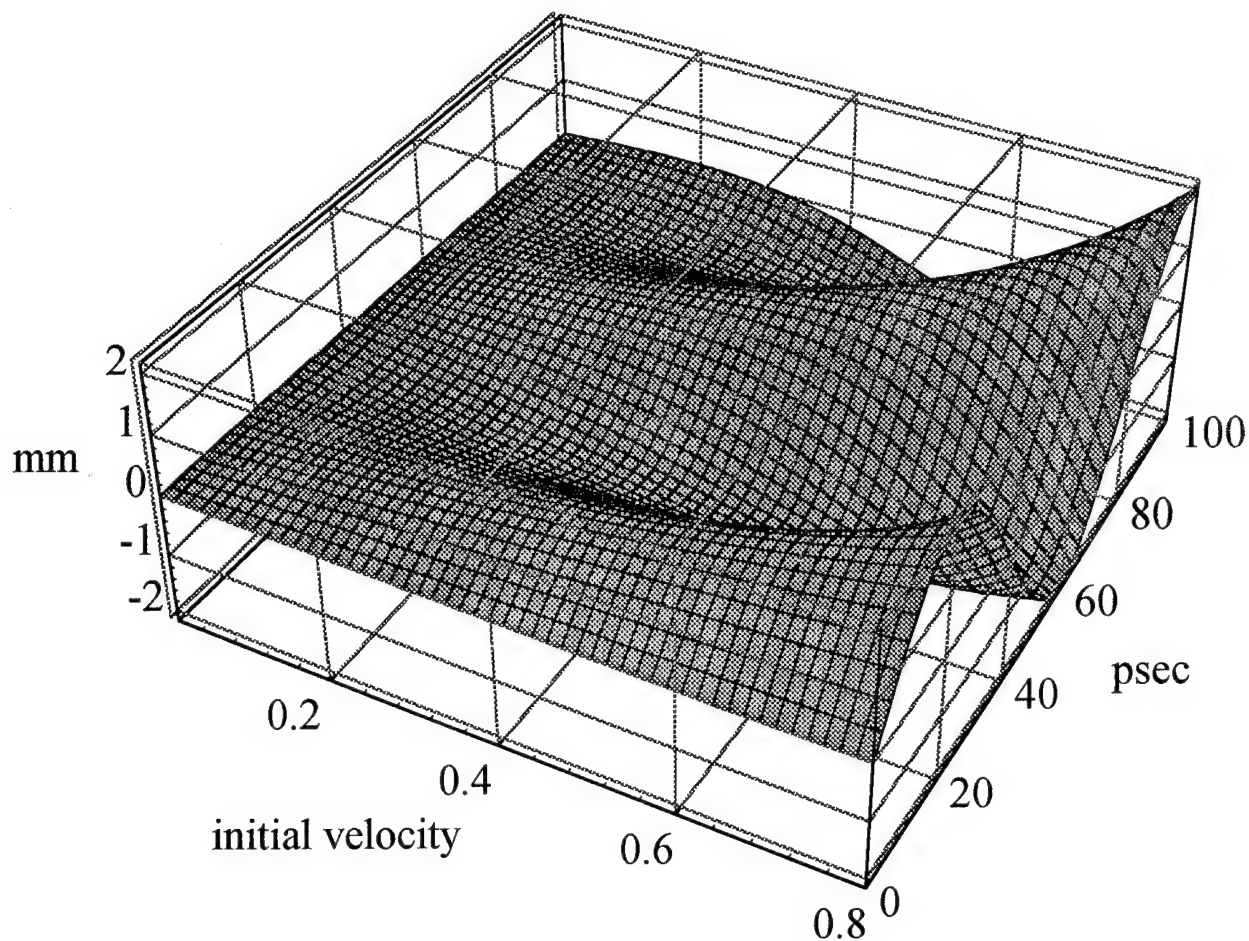


Figure 2: Plot of the motion of rays launched at different initial velocities at $z=0$ in a grating with a quadratic variation in grating strength with z . See the text for the parameters used.

References

- [1] See, e.g., J. Lauzon, S. Thibault, J. Martin and F. Ouellette, "Implementation and characterisation of fibre Bragg gratings linearly chirped by a temperature gradient," *Opt.Lett.* **19** (2027-2029) 1994.
- [2] J. T. Kringlebotn, J.-L. Archambault, L. Reekie and D.N. Payne, "Er³⁺:Yb³⁺ co-doped fiber distributed feedback laser," *Opt.Lett.* **24** (2101-2103) 1994.
- [3] J. A. Arnaud, *Beam and Fiber Optics*, (Academic Press, New York, San Francisco, London, 1976)
- [4] P.St.J. Russell, "Bloch wave analysis of dispersion and pulse propagation in pure distributed feedback structures", *J.Mod.Opt.*, **38** (1599-1619) 1991; Erratum: J. Capmany and P.St.J. Russell, *J.Mod.Opt.*, 1994.
- [5] P.St.J. Russell, T.A. Birks and F.D. Lloyd-Lucas, "Photonic Bloch Waves and Photonic Band Gaps," in *Confined Electrons and Photons: New Physics and Applications*, E. Burstein & C. Weisbuch (editors), Plenum Press, 1995
- [6] P.St.J. Russell, "Interference of integrated Floquet-Bloch waves," *Phys.Rev.*, **A33** (3232- 3242) 1986.
- [7] R. Zengerle, "Light propagation in single and doubly periodic planar waveguides," *J. Mod. Opt.* **34** (1589-1617) 1987.

Grating Michelson mirrors for optimised fibre laser performance.

Kate Sugden and Ian Bennion

Electronic Engineering and Applied Physics,
Aston University, Aston Triangle, Birmingham B4 7ET, UK.
Tel: 44 121 359 3611 ext 4972, Fax: 44 121 359 0156

Kevin Byron, Howard Rourke and Sandra Davies

BNR Europe Ltd, London Road, Harlow, Essex CM17 9NA, UK.
Tel: 44 1279 429531, Fax: 44 1279 441551

We report on the development of a novel use of a Michelson mirror based on fibre grating technology¹ which gives flexibility in optimising the output from fibre pigtailed semiconductor lasers and rare earth doped fibre lasers. The novel Michelson mirror schemes described here can be used to optimise the output power from lasers and to filter the broadband spontaneous noise. Furthermore, in the case of external cavity semiconductor lasers, by using a displacement between the two gratings in the Michelson arrangement, FM to AM conversion could be induced and used to stabilise frequency shifts in these devices.

An additional attraction of the grating Michelson mirror is that the optimisation may be carried out during operation of the laser without recourse to retro-fitting different reflectivity mirrors. This standard approach is costly in both time and resources and is limited by the step sizes between the reflectivities of the mirrors used. We will show how, by using a grating Michelson mirror, the power output of a fibre laser can be optimised by continuously tuning the reflectivity by the ultraviolet trimming one of the coupler arms. In addition to this, we will show how, as a consequence of the wavelength selectivity of the mirror, the sideband noise can be reduced by over 20 dB. Using the fibre grating Michelson mirror effectively combines the properties of a mirror and a bandstop filter in an all fibre device whilst causing no extra losses to the cavity.

Fibre lasers incorporating in-fibre grating mirrors were first reported in 1990 by Kashyap *et al.*² and Ball *et al.*³ and have since been frequently applied. In these situations, the grating provides a convenient integrated mirror which avoids the need to use bulk optical mirrors. However, in common with other laser systems the output of the laser has a broadband background of spontaneous emission and in sources used for optical communication this can lead to system penalties. By using the Michelson arrangement as the laser output coupler/reflector, as shown in figure 1a, the noise is filtered out. Only light with a wavelength that falls within the bandwidth of the two gratings will be reflected down either of ports 1 and 2. Everything else, including the background fluorescence noise of the fibre gain medium will be transmitted through ports 3 and 4.

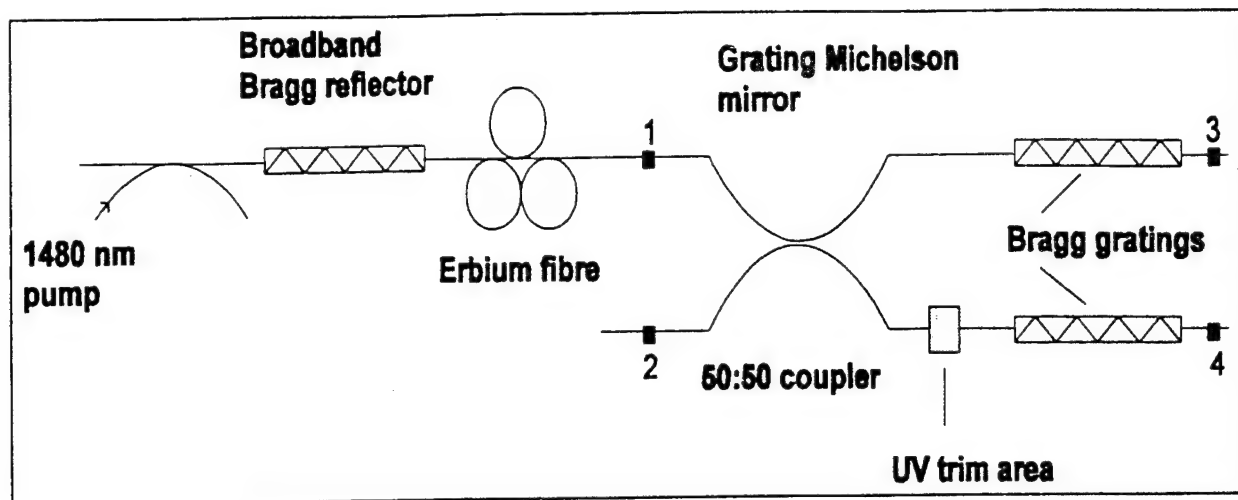


Figure 1(a). Laser cavity arrangement using a fibre grating Michelson mirror and a broadband Bragg reflector.

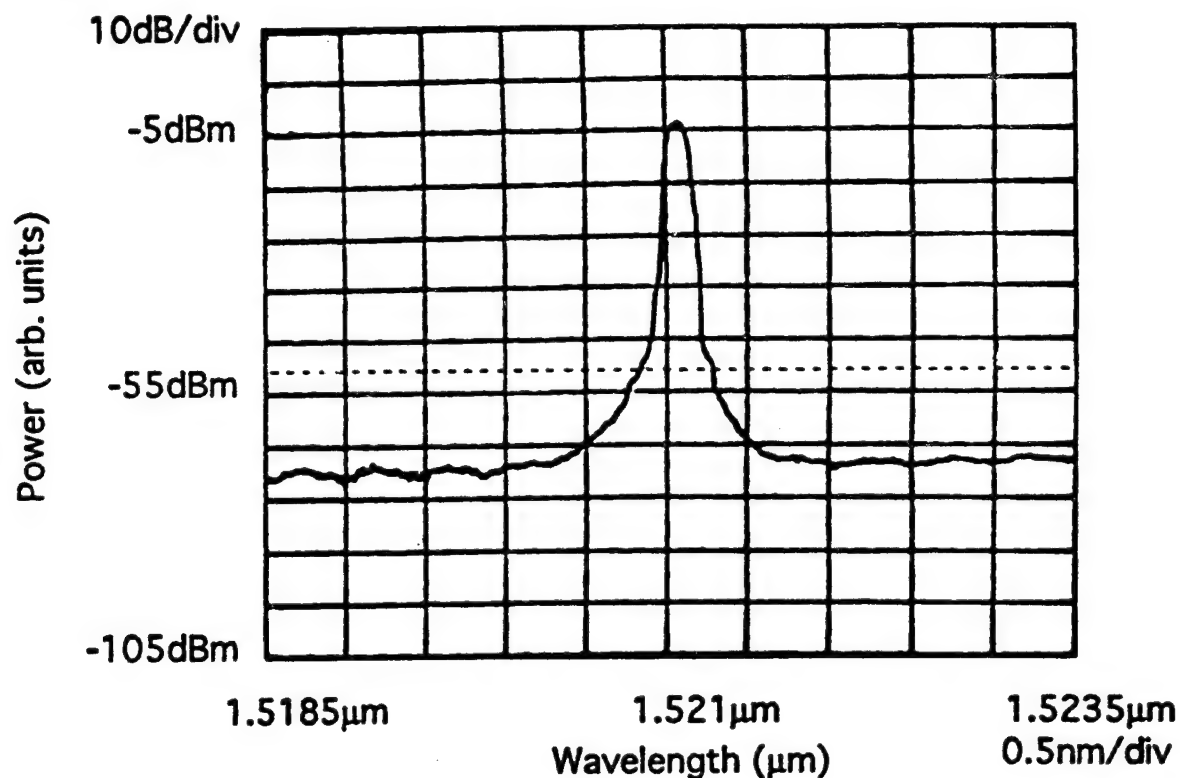


Figure 1(b). Laser output from port 2 with noise level from port 3 marked by the dashed line.

Figure 1(b) shows the output spectrum of an erbium fibre laser constructed in this way. Superimposed on the profile is the noise level that was measured for port 3 which is 3 dB less than would have been seen if the reflecting element was instead a single in-line Bragg grating. The total reduction in noise is therefore in excess of 20dB.

The reflectivity can be optimised either by trimming the path between the coupler and the gratings^{4,5} or by partial erasure of the grating using a fringeless beam. This is not only useful for application in laser cavities but could be applied to the technique of gain clamping⁶ erbium fibre amplifiers. Since in this situation the gain at which the amplifier is clamped depends on the lasing threshold of designated lasing line produced by feedback from the end reflector. If the reflectivity is then changed by the methods described above then the level at which the amplifier is clamped changes as a consequence.

The two gratings written on the two output ports of a fibre coupler reflect light at their Bragg wavelength back through the coupler. UV trimming, in the region illustrated, allows the output to be shifted from port 2 to port 1 by each $\lambda/2$ change in the optical path length of one arm. For a system operating at 1550 nm this would require a refractive index change of 1.3×10^{-4} for an exposure length of 3 mm and this is easily achievable with the modern high photosensitivity fibres.

The ability to introduce multiple $\lambda/2$ changes in the optical path length means that not only can this cycling of the power reflected from each port be used the power output of any given laser system with different output reflectors but also that there is enough photosensitivity in the fibre to then bias same device in order to give the optimum output. Results showing the cycling of laser power output as a function of UV induced refractive index change and the associated device reflectivity will be presented.

Another configuration for the grating Michelson mirror for producing FM to AM conversion is shown in figure 2. Here, the displacement between the gratings results in a reflectivity dependent the emission wavelength⁷. This device may be used in the first instance to measure chirp in semiconductor lasers and in external cavity semiconductor lasers in which the Michelson mirror forms the output mirror, the device may also be used to stabilise chirping effects. In the case of stabilisation, as the semiconductor laser changes frequency the feedback into the laser will be reduced due to the amplitude modulation of the device response.

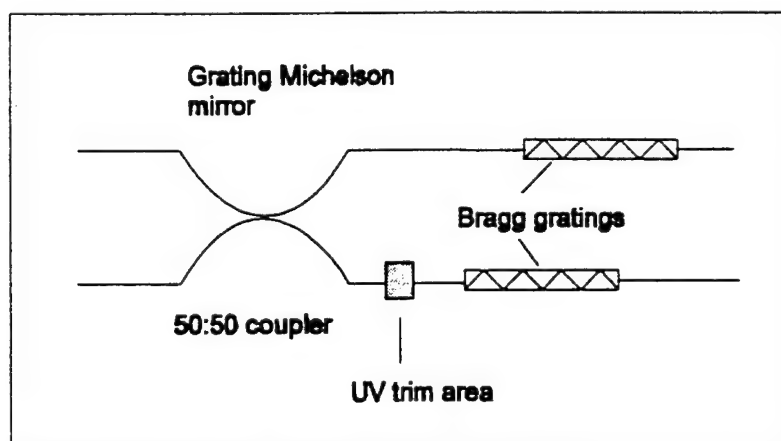


Figure 2. Asymmetric grating Michelson mirror.

In conclusion, a fibre laser has been optimised by varying the reflectivity of the back reflection/outcoupling ratio from a fibre grating Michelson mirror. The variation in power

distribution reflecting from the device can be achieved by changing the optical path length of one of the coupler arms; in this case by UV trimming. The fibre laser has been shown to exhibit reduced background noise outside of the bandwidth of the gratings used in the output coupler. This is due to the fibre grating Michelson mirror acting as a band stop type filter. This laser would therefore be useful in situations where low noise optical sources are required. It is also possible to use an asymmetrical grating Michelson mirror to measure the chirp of semiconductor lasers and to stabilise external cavity semiconductor lasers.

References

1. K O Hill, D C Johnson, F Bilodeau, S Faucher, 'Narrow-bandwidth optical waveguide transmission filters', *Electron Lett*, **23**, 1987, 465.
2. R Kashyap, J R Armitage, R Wyatt, S T Davey, D L Williams, 'All-fibre narrowband reflection gratings at 1500nm', *Electron Lett*, **26**, 1990, 730.
3. G A Ball, W W Morey, J P Walters, 'Nd³⁺ fibre laser utilising intra-core Bragg reflectors', *Electron Lett*, **26**, 1990, 1829-1830.
4. F Bilodeau, K O Hill, B Malo, D C Johnson, J Albert, 'High-return-loss narrowband all-fibre bandpass Bragg transmission filter', *IEEE Photon Technol Lett*, **6**, 1994, 80-82.
5. T J Cullen, H N Rourke, C P Chew, S R Baker, T Bricheno, K C Byron, A Fielding, 'Compact all-fibre wavelength drop and insert filter', *Electron Lett*, **30**, 1994, 2160-2161.
6. E Delevaque, T Georges, J F Bayon, M Monerie, P Niay, P Bernage, 'Gain control in erbium-doped fibre amplifiers by lasing at 1480nm with photoinduced Bragg gratings written on fibre ends', *Electron Lett*, **29**, 1993.
7. R A Saunders, J P King, I Hardcastle, 'Wide-band chirp measurement technique for high bit rate sources', *Electron Lett*, **30**, 1994, 1336-1338.

Fibre ring laser with fibre grating transmission filter.

M.C. Farries, D.C. Reid, L. Zhang*, I. Bennion *

GMMT, Caswell, Towcester, Northants, U.K., NN12 8EQ.

Tel 44 1327 356345 Fax 44 1327 356775

*Aston University, Aston Triangle, Birmingham, U.K. B4 7ET.

Introduction We report the first single mode fibre ring laser which uses a transmission fibre grating filter for selection of a single mode. Fibre gratings have been used in reflection mode in conjunction with a rare earth doped Sagnac loop to produce single mode operation ¹, but these are inefficient because a proportion of the internal laser power is reflected in the counter direction to the main lasing direction and this is absorbed in the isolator. The development of broad band chirped fibre gratings ² and transmission fibre gratings ^{3,4} has enabled a ring unidirectional ring laser to be built using all fibre components with the exception of a fibre coupled optical isolator. The advantage of a fibre ring laser is that it provides an efficient narrow linewidth source which can be tuned across the erbium fibre amplifier gain bandwidth. We also show that the laser can be used as a sensitive strain sensor.

Fibre grating transmission filter. The fibre grating filter is required to block transmission over the entire erbium gain band except for one narrow pass band. The filter is made by direct write two beam interference using curved wavefronts to produce a broad chirp reflection filter. A transmission band is produced in the fibre by either blocking part of the chirped fibre grating during writing ³ or by bleaching part of the chirped grating after writing ⁴. The filter used for the ring laser has a blocking reflection band from 1530 nm to 1565 nm and a pass band at 1554.7 nm which is 0.36 nm wide. The transmission of the pass band is 30%.

Fibre ring laser. Figure 1 shows the layout of the fibre ring laser which is pumped by an InGaAs pump diode via a fused taper coupler. A polarisation insensitive optical isolator is used in the ring to ensure unidirectional operation and prevent spatial hole burning due to standing waves. The isolator also prevents the laser operating as a

Fabry-Pérot laser with the fibre grating acting as two mirrors. The fibre ring does not contain any polarising components so there is no need to provide polarisation control in the ring. The output may therefore be in an elliptical polarisation state and can be set to a linear state by a polarisation controller at the output. The laser output is taken via a 50: 50 fused taper fibre coupler.

Results. Figure 2 shows the spectrum of the laser output which has a peak power in excess of 1 mW at a wavelength of 1554.5 nm. The laser linewidth was measured by the delayed self heterodyne method to be below the 10 kHz resolution limit of the measurement as shown in figure 3. Single mode operation was confirmed by a wideband self heterodyne measurement which shows the side modes to be 50 dB below the main mode (figure 3). Unidirectional operation is confirmed by measurement of the power at the spare port of the coupler, which is 30 dB below the power at the main output. The stability of the laser wavelength is limited by the temperature stability of the laboratory to 0.002 nm over a 10 minute period, which corresponds to a temperature change in the fibre grating of approximately 0.2 °C.

Strain sensitivity. The laser has been shown to provide a very sensitive strain monitor. A strain of 6.5 μS applied to the fibre grating produced a wavelength change of 0.01 nm when measured by a wavelength meter. A strain resolution of 1.3 μS is measurable with the laser in normal laboratory conditions and shielding the grating from temperature variations could provide sub-micro strain resolution.

Conclusions. We have demonstrated for the first time a single frequency ring fibre laser which uses a fibre grating transmission filter for mode selection. The line width of the laser is instrument resolution limited to less than 10 kHz. The fibre grating filter has the advantage of a low temperature sensitivity so that the laser wavelength is stable to 0.002 nm in laboratory conditions without active temperature control.

References

1. I.M. Jauncey, L. Reekie, R.J. Mears, C.J. Rowe, 'Narrow-linewidth fibre laser operating at 1.55 μm ', Opt. Lett. v22, p164, 1987
2. M.C. Farries, D.C. Reid, M. Goodwin, I. Bennion, K. Sugden, A. Malony, 'Broadband high reflectivity chirp fibre gratings in standard optical fibre', Electronics Letters, v 30, p891, 1994.
3. M.C. Farries, D.C. Reid, K. Sugden, N. Doran, 'Very broad bandwidth fibre gratings and transmission filters', paper CWF57 p230 CLEO Europe, Amsterdam 1994
4. L. Zhang, K. Sugden, J.A.R. Williams, I. Bennion, D.C.J. Reid, C.M. Ragdale, 'Post-fabrication exposure of gap-type bandpass filters in broadly chirped fibre gratings', Submitted to Topical meeting on Photosensitivity and quadratic nonlinearity in glass waveguides: fundamentals and applications, Portland, Oregon 1995.

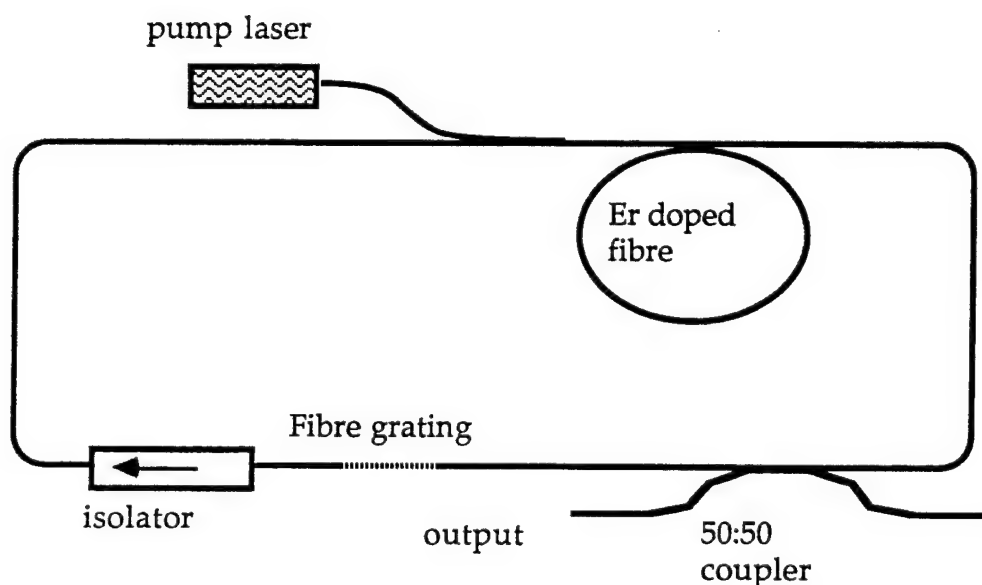


Figure 1. Schematic of fibre ring laser.

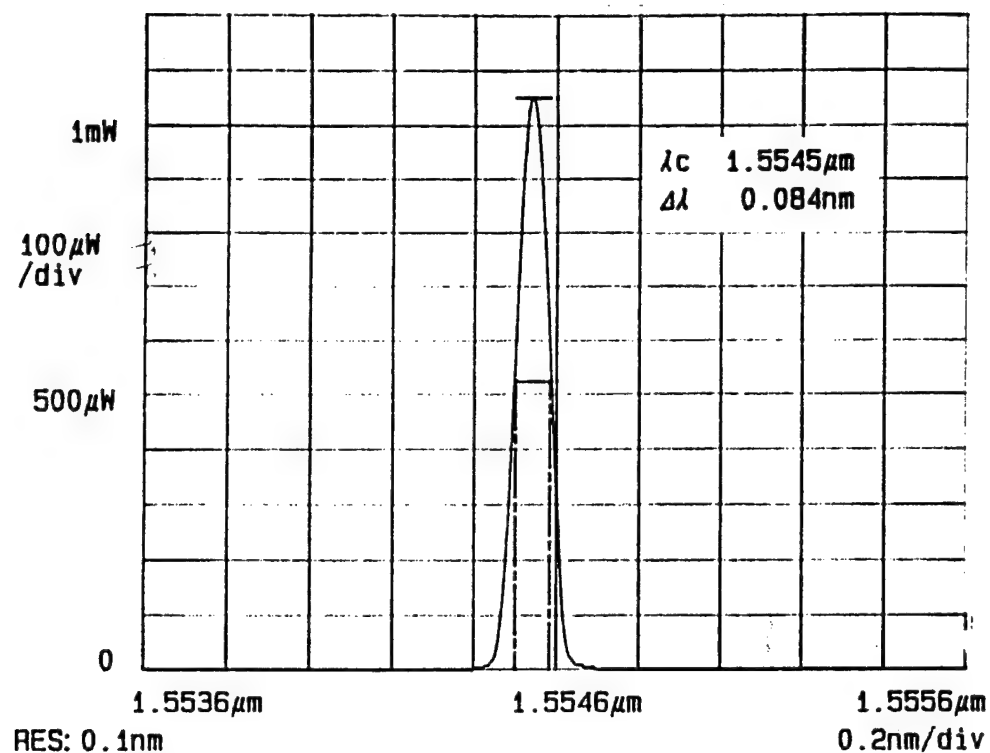


Figure 2. Lasing spectrum of ring laser.

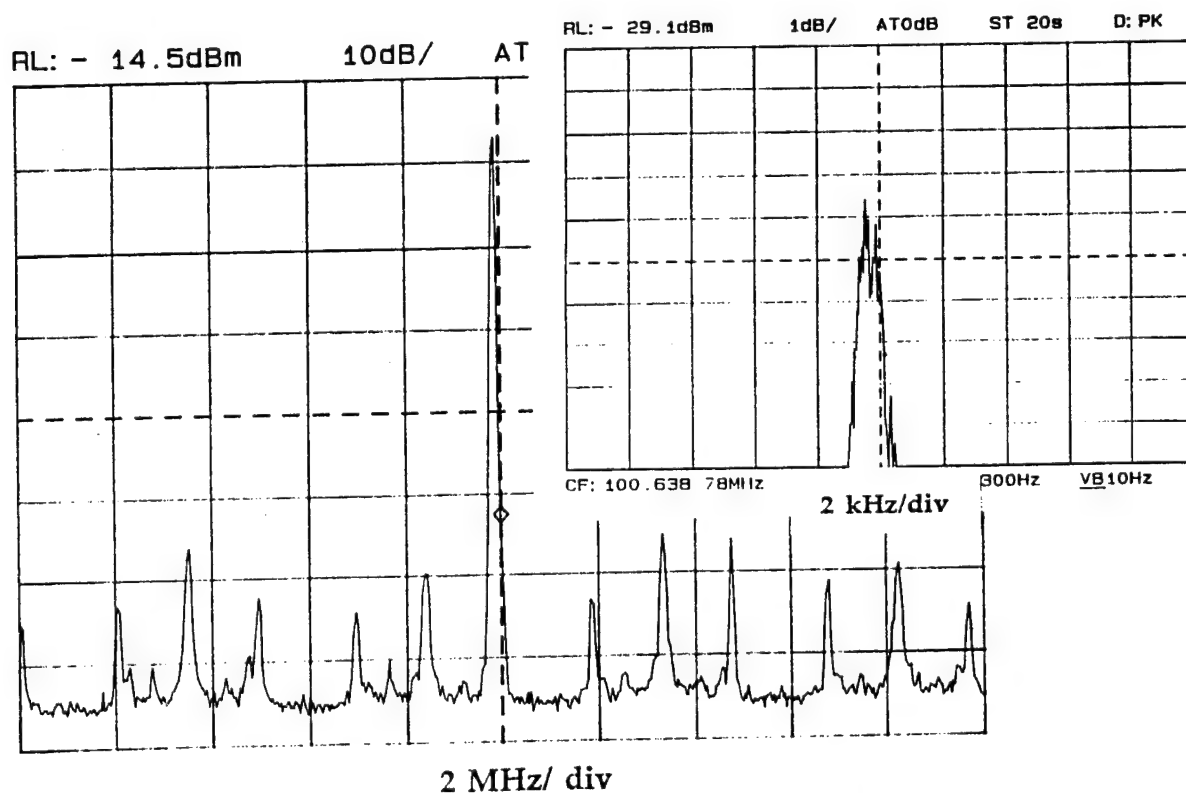


Figure 3. Delayed self heterodyne measurement of laser linewidth

Photoinduced absorption and photobleaching in thulium-doped fluorozirconate fibers

Pierre Laperle and Alain Chandonnet

National Optics Institute, 369 rue Franquet, Sainte-Foy, Québec, Canada, G1P 4N8

Tel: (418) 657-7006, FAX: (418) 657-7009

Réal Vallée

Département de physique, Centre d'optique, photonique et laser, Université Laval

Sainte Foy, Québec, Canada, G1K 7P4, Tel: (418) 656-2698, FAX: (418) 656-2623

Over the past few years, thulium-doped fluorozirconate fibers have been studied for application as blue fiber lasers. Blue upconversion fiber lasers at 480 nm [1] and 455 nm [2] in a thulium-doped fluorozirconate fiber have been demonstrated at room temperature. Recently, a potentially important application of these fibers for amplification near 800 nm in the first telecommunication window has been reviewed [3]. In our work, we have observed a strong photodarkening of thulium-doped fluorozirconate fibers when pumped at 1.12 μm [4]. A similar behavior was reported in thulium-doped aluminosilicate fibers exposed to 1064 nm light [5]. We have also observed that it is possible to bleach a fluorozirconate fiber by exposing it to 488 nm radiation. These results have stimulated the present study on the formation of photoinduced absorption which may limit the efficiency of blue fiber lasers and other devices using thulium-doped fluorozirconate fibers.

Three distinct experiments on thulium-doped fluorozirconate fibers were performed to determine: 1) the darkening rate of the fibers under pumping at 1.12 μm using a weak probe at 488 nm, 2) the induced absorption spectra of the fibers exposed to the pump beam, and 3) the bleaching rate of the fibers under pumping at 488 nm using a probe beam at 633 nm. Table 1 summarizes the characteristics of the four fibers tested.

Fiber	Tm ³⁺ concentration (ppm)	Core diameter (μm)	NA
A	500	3	0.21
B	1000	3	0.21
C	1000	3	0.39
D	20000	3	0.21

Table 1: Characteristics of the fluorozirconate fibers.

In the first experiment we used a CW Nd:YAG laser at $1.12\ \mu\text{m}$ to pump the fibers into the $^1\text{G}_4$ energy level of thulium [1]. The 488 nm line of an argon-ion laser was used as a probe to monitor the darkening evolution of 40-cm long samples. An unexposed length of fiber was used at each new power setting. The normalized probe transmission as a function of time for several pump powers is shown in Figure 1 for fiber B. The probe transmission of the four fibers exhibits a similar behavior and is found to follow a triple-exponential decay in time. The decay rates of the fibers calculated at the 90% transmission point indicate a fourth-power dependence on the pumping intensity (Figure 2). The slopes m are a best-fit to the measured data.

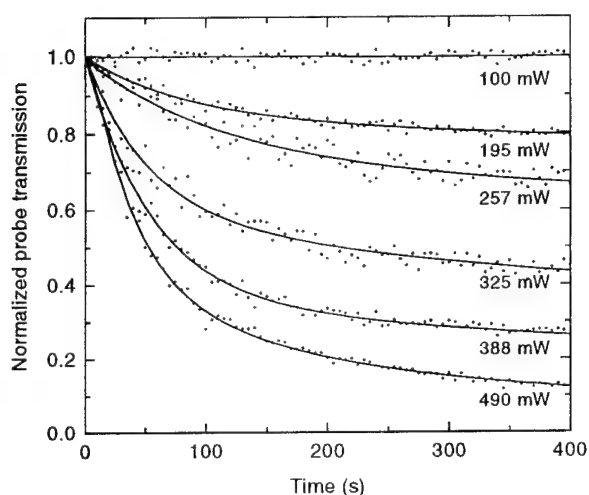


Figure 1: Normalized probe transmission for fiber B as a function of exposure time for several pump powers at $1.12\ \mu\text{m}$.

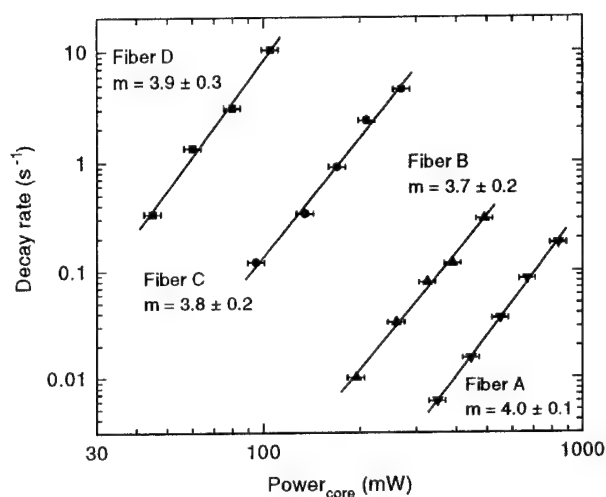


Figure 2: Decay rate of the probe at the 90% transmission point as a function of pump power at $1.12\ \mu\text{m}$ for fibers A to D.

We note that the darkening rate increases with the thulium concentration. We note also that fibers B and C with different numerical apertures do not exhibit the same darkening rate even when considering the different mode sizes in both fibers. This is probably due to the different chemicals used to modify the numerical aperture. This behavior suggests that other elements may play a role in the induced absorption. The fourth-power dependence of the darkening rate on the pump power suggests an excitation scheme of the $^1\text{D}_2$ level by nonradiative cross-relaxation of two excited thulium ions respectively in the $^1\text{G}_4$ and $^3\text{H}_4$ states [5].

In the second experiment we used a tungsten-halogen lamp to illuminate the fibers and a 0.5 m monochromator combined to a lock-in amplifier and a computer to filter and record the light. The absorption spectra of all four fibers have shown photoinduced absorption for wavelengths shorter than $1.1\ \mu\text{m}$. Figure 3 shows the losses induced in fiber B immediately

and one month after exposure to $1.12\ \mu\text{m}$. A small recovery of the probe transmission at $480\ \text{nm}$ ($\sim 5\ \text{dB/m}$) is observed. The other fibers exhibit a similar behavior except for fiber C which did not show any recovery.

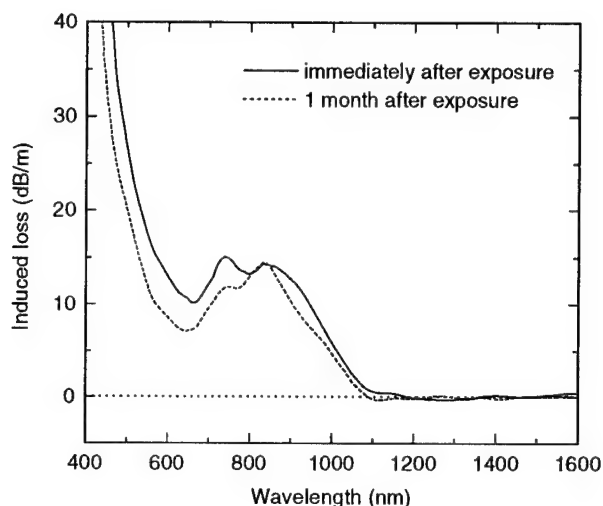


Figure 3: Spectrum of induced loss in fiber B measured immediately and one month after exposure to $1.12\ \mu\text{m}$.

In the third experiment we used the $488\ \text{nm}$ line of an argon-ion laser to pump previously darkened fibers. The low intensity radiation at $633\ \text{nm}$ of an helium-neon laser was used as a probe to monitor the fibers bleaching evolution. We have been able to restore the fibers to their original transmission even after many darkening/bleaching cycles. Figure 4 shows the normalized probe transmission of fiber B for several pump powers. As in the case of photodarkening, the probe transmission of all four fibers exhibits a similar behavior and follows a triple-exponential growth in time. The growth rates measured at the 30% transmission point indicate an almost linear dependence on pump power (Figure 5). This suggests that the photobleaching process involves one-photon absorption of the pump beam. No pump power threshold was observed for the onset of photobleaching. These observations set a limit to the activation energy of the colour centers at $2.55\ \text{eV}$.

The photoinduced absorption and photobleaching processes show that in the case of blue fiber lasers at $480\ \text{nm}$ involving a three-photon absorption cascade of $1.12\ \mu\text{m}$ radiation the pump power and the lasing (spontaneous) emission stimulate competing mechanisms inside the fiber. Efficient CW lasing showing no threshold degradation in time can be expected only when the bleaching rate overcomes the darkening rate.

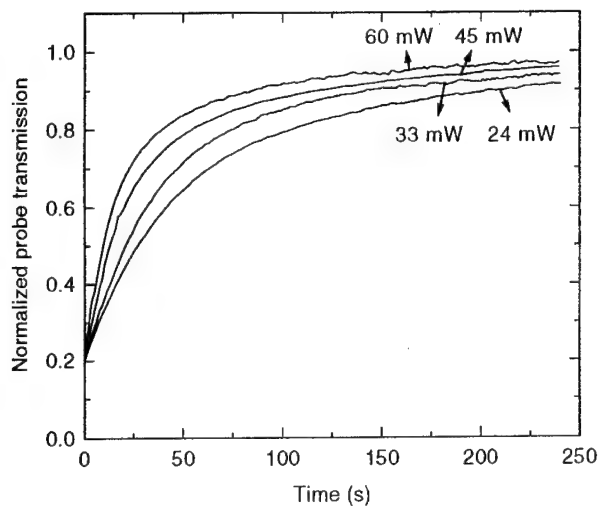


Figure 4: Normalized probe transmission for fiber B as a function of exposure time for several 488 nm pump powers.

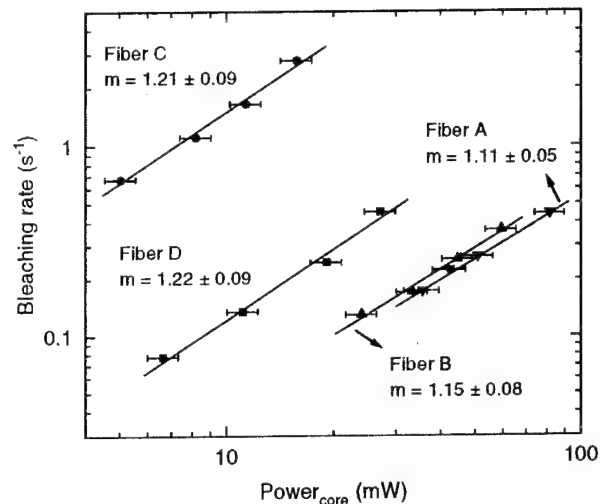


Figure 5: Bleaching rate at the 30% transmission point as a function of pump power at 488 nm for fibers B and C (probe at 633 nm).

In conclusion, we have observed a fourth-power dependence of the photodarkening rate on the pumping intensity at $1.12 \mu\text{m}$ in thulium-doped fluorozirconate fibers. The losses are induced mainly at UV-visible wavelengths and extend up to $1.1 \mu\text{m}$. We have also observed bleaching of the photoinduced absorption in the fibers exposed to 488 nm radiation. The bleaching rate follows a first-power dependence on the pumping intensity. The photobleaching powers needed to bring the fibers transmission back to their original value are much smaller than those required to induce the absorption. Further work is planned to identify the nature of the photoinduced absorption which is likely to have an impact on devices using thulium-doped fluorozirconate fibers.

- [1] S.G. Grubb, K.W. Bennett, R.S. Cannon, and W.F. Humer, *Electron. Lett.* **28**, 1243 (1992).
- [2] M.P. Le Flohic, J.Y. Allain, G.M. Stéphan, and G. Mazé, *Opt. Lett.* **19**, 1982 (1994).
- [3] R. Wyatt in *Optical Fiber Communications Conference*, **8**, 1995 OSA Technical Digest Series (Optical Society of America, Washington DC, 1995), paper WD3, 109.
- [4] P. Laperle, A. Chandonnet, and R. Vallée, "Photoinduced absorption in thulium-doped ZBLAN fibers", submitted to *Optics Letters*.
- [5] M.M. Broer, D.M. Krol, and D.J. DiGiovanni, *Opt. Lett.* **18**, 799 (1993).

Photodarkening in Upconversion Pumped Thulium Doped Fluorozirconate Fibre Lasers

I. J. Booth, J.-L. Archambault, B. F. Ventrudo
 Seastar Optics Inc.
 2045 Mills Road
 Sidney, B.C., Canada V8L 3S8
 Tel. (604) 656 9520 Fax. (604) 656 1927

Introduction

Upconversion pumped lasing in rare earth doped fluorozeirconate optical fibre offers the potential for compact blue green laser sources pumped by commercially available infrared laser diodes. A promising candidate for such a source is the thulium system first demonstrated by Steve Grubb and co-workers [1], which lases in the blue at 482 nm with a single pump source at about 1130 nm. Figure 1 illustrates the relevant energy levels of the trivalent thulium ion, and the upconversion mechanism. Ions excited to the short lived H_5 and $F_{2,3}$ levels decay rapidly by phonon emission to the metastable H_4 and F_4 levels from which further upconversion transitions occur. The centre wavelengths of the three transitions are respectively 1220 nm (H_6 to H_5), 1130 nm (H_4 to F_2), and 1150 nm (F_4 to G_4), but because of the broadening of the transitions in glass it is possible to excite all three with a single wavelength pump in the range 1110 nm to 1160 nm. The next energy level above G_4 in thulium is D_2 with a transition of 1480 nm separating the two, so that further upconversion above G_4 should not occur, or only very weakly. A low phonon energy host material such as ZBLAN fluorozeirconate glass is necessary so that the metastable levels do not decay rapidly by phonon emission.

A concern in any upconversion laser is the possibility of long term deterioration in the glass fibre. Photosensitivity and rapid darkening has been observed in thulium doped silica fibres pumped at 476 nm [2] and at 1064 nm [3]. In the case of 1064 pumping an upconversion process similar to Fig. 1 was proposed, but extending to higher excited levels of the thulium ion. The resulting ultraviolet photons were thought to cause ionization within the glass, producing colour centre defects. Our present results suggest that a similar process may occur in thulium doped fluorozeirconate glass, albeit more slowly.

Experimental Results

Thulium doped ZBLAN fibre was purchased from Le Verre Fluore with a core diameter of 3 microns and a numerical aperture of 0.21. Three levels of doping were obtained, 1000 ppm thulium, 2500 ppm thulium, and 1250 ppm thulium + 5000 ppm ytterbium. Upconversion lasing at 482 nm was successfully demonstrated in all three fibres with laser diode pumping at around 1130 nm. The pump sources for these measurements were 80 mW laser diodes of which approximately 50 mW could be launched into the fibre. Pump light absorption per unit length of fibre was consistent with the thulium concentration in each fibre. Multilayer dielectric mirrors reflective at 480 nm were butted to the cleaved fibre ends, with a high reflector at the pump input end, and a 90% reflector at the output to couple the blue laser power out of the fibre. Blue light outputs of up to 5 mW were obtained. with the 2500 ppm fibre exhibiting the highest efficiency, probably because the shorter fibre length has lower background loss associated with it. A 0.5

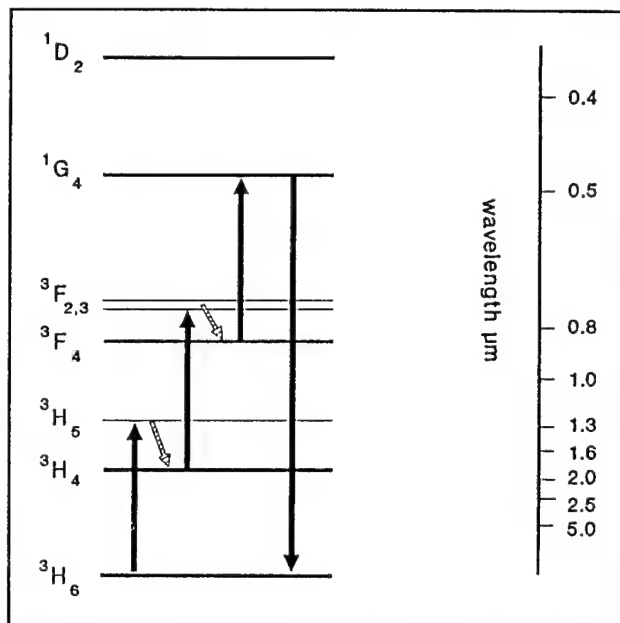


Figure 1 Energy Level Diagram for Tm^{3+} showing upconversion transitions and blue laser transition.

Watt MOPA diode laser was also used as a pump source in some experiments. Approximately 230 mW of infrared power at 1130 nm could be launched, producing outputs of up to 25 mW of blue light from a 1 meter, 1000 ppm fibre laser.

After a fibre was lased several times it was noticed that the threshold pump power required to start lasing would increase by 10-20%. Once lasing was established the threshold returned to normal levels. This transient increase in start up threshold was larger if the fibre had been left inactive for a longer time, hours or days. Turning the laser off and on again quickly produced no effect. This phenomenon was at first attributed to misalignment of the pump optics. When the high power MOPA laser was used as a pump source the effect in exposed fibres became much greater, with the transient threshold up to 5 or 10 times the normal operating threshold level. A decrease in blue output power was also observed after long periods of operation at high power. A 1000 ppm fibre which initially produced 25 mW of blue light decreased to 18 mW over eight hours of operation.

To explain these effects it was conjectured that colour centres were being produced in the core of the fibre. These centres must absorb only at shorter wavelengths, increasing the blue lasing threshold without affecting the infrared pump throughput, as observed. Under intense blue light the centres bleach, so that the threshold falls once lasing starts. The recovery time of the defects from bleaching must be slow. Attempts were made to measure the properties of these colour centres and the cause of their formation, with the following results.

The absorption spectrum of the colour centres was measured by comparing the white light transmission through a fibre with and without defects. As the defects appear to be bleached by lasing the spectrum was taken on the same piece of fibre just after lasing, and again some time later. A typical spectrum is shown in Figure 2. This was obtained with the 1000 ppm fibre which had been run at high power for eight hours with the MOPA laser. Similar spectra were obtained with 2500 ppm fibres.

The recovery time of the centres from bleaching was measured by leaving a fibre inactive for varying periods of time between lasing. The centres had no well defined time constant but appeared to follow a stretched exponential type of recovery. This suggests that the defects have a range of activation energies. Some fraction of the centres always unbleach quickly, producing a permanent increase in fibre loss, which explains the decrease in lasing power observed after several hours of operation at high power.

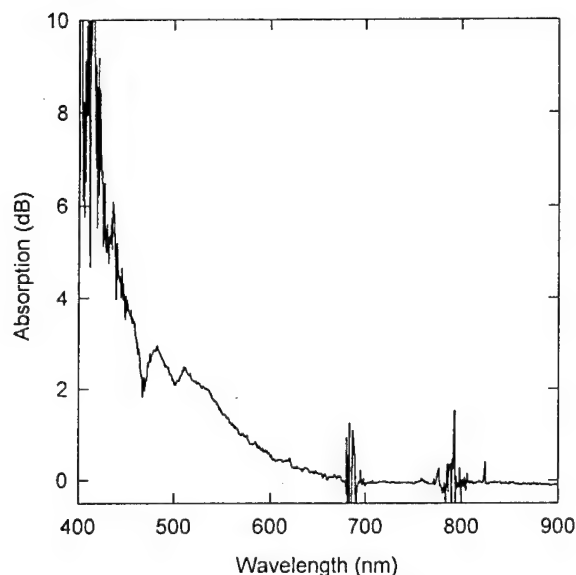


Figure 2 Absorption spectrum of defect centres.

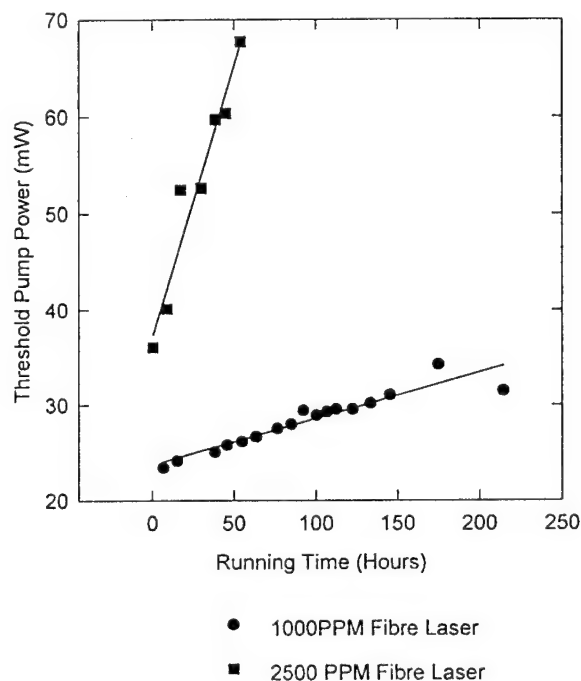


Figure 3 Transient threshold increase with time.

Further investigations showed that the defects were produced by the infrared pump light, rather than the blue lasing light as was initially supposed. Fibres pumped with 1130 nm light without allowing blue lasing subsequently demonstrated the transient threshold effect. Threshold hysteresis was not present in fresh fibres, and increased with exposure to pump light. The increase was much faster with high power levels, but the exact relation between pump power and deterioration rate has been difficult to measure, due to the transient nature of the phenomenon. Direct measurement of the white light absorption caused by the defects was only possible in heavily exposed fibres because of the poor signal to noise ratio.

Deterioration was observed to occur faster in fibre with 2500 ppm thulium doping, and in the ytterbium co-doped fibre, than in the 1000 ppm fibre. A systematic test was initiated using prototype blue laser pigtailed made with 1000 ppm and 2500 ppm fibre. The units were run for approximately 8 hours each day and turned off at night. The turn on threshold at the start of each day was monitored, as well as the running threshold. Figure 3 shows how the transient thresholds increase with use. The operating power level was only 26 mW of launched pump power in both units, due to poor launch efficiency in the 1000 ppm pigtail. It is expected that the deterioration would be faster at higher power levels. The turn-on threshold in the 2500 ppm pigtail increased approximately 12 times faster than the 1000 ppm unit, and soon exceeded the maximum available pump power. Lasing could still be started by pumping the fibre for several minutes, the fluorescence generated in the fibre being sufficient to cause some bleaching of the defects.

The effect of moderate heating was measured on fibres with colour centres. Temperatures of around 50°C speeded recovery of the centres from bleaching. However, baking at higher temperatures of 70 to 100° C for 24 hours appeared to remove some or most of the defects, as the subsequent threshold hysteresis was smaller, and in heavily deteriorated fibres the white light spectrum recovered to its bleached level.

In thulium doped silica glass fibre pumped at 1064 nm the cause of photodarkening was hypothesized to be an upconversion ladder leading to a highly excited state of the Tm ion, creating an electronic defect in the surrounding glass [3]. In the case of 1064 nm pumping the darkening rate followed approximately a 5th power dependence on the pump intensity, suggesting a 5 step upconversion, past the G_4 and D_2 levels to the P states of thulium. A similar process may be responsible for the defects observed in our lasers. If so there should be observable fluorescence from the Tm energy levels above G_4 , and a correlation between this fluorescence and the rate of fibre deterioration.

Pumping with an 1135 nm laser diode, and with no end mirrors on the fibre the fluorescence from the fibre end was measured with a spectrum analyzer. The fluorescence spectra from 71 cm of 1000 ppm fibre, and from 30.5 cm of 2500 ppm fibre are compared in Figure 4 for various launched pump power levels. The band at 480 nm is fluorescence from the G_4 level, while the small peaks at 360 nm, 455 nm and 515 nm are thought to be transitions from the D_2 level to H_6 , H_4 and H_3 respectively. The hump at about 390 nm is a spurious shadow of the 480 nm fluorescence. The presence of fluorescence from the D_2 level indicates that some upconversion is occurring past G_4 . It is not clear to what extent this is caused by direct pumping from G_4 to D_2 by the 1135 nm light, which is possible due to broadening of the transitions in glass. Energy transfer between thulium ions provides another upconversion path, and such ion-ion interactions become stronger with higher doping concentration. The fluorescence spectra from the 2500 ppm doped fibre show increased D_2 fluorescence relative to the 1000 ppm fibre, which strongly suggests that ion-ion interactions are indeed contributing to this upconversion. Spectra taken from the thulium-ytterbium co-doped fibre also exhibited enhanced D_2 fluorescence.

From the D_2 level, resonant pumping by 1135 nm is possible to the 3P_1 level, which relaxes to the 1I_6 state. This level is thought to be responsible for the severe photodarkening observed in thulium doped silica glass fibre. Fluorescence from the 1I_6 state is expected at 310 nm, which we cannot monitor with our equipment.

It is apparent that the D_2 fluorescence peaks increase faster than the 480 nm line with increasing pump power, however the dependence is less than the fourth power law expected for a 4 level upconversion, and tends to flatten out at higher powers indicating the saturation of some of the upconversion transitions. In fact the two upper transitions ($H_4 - F_{2,3}$ and $F_4 - G_4$) are expected to saturate at around 10 mW pump power.

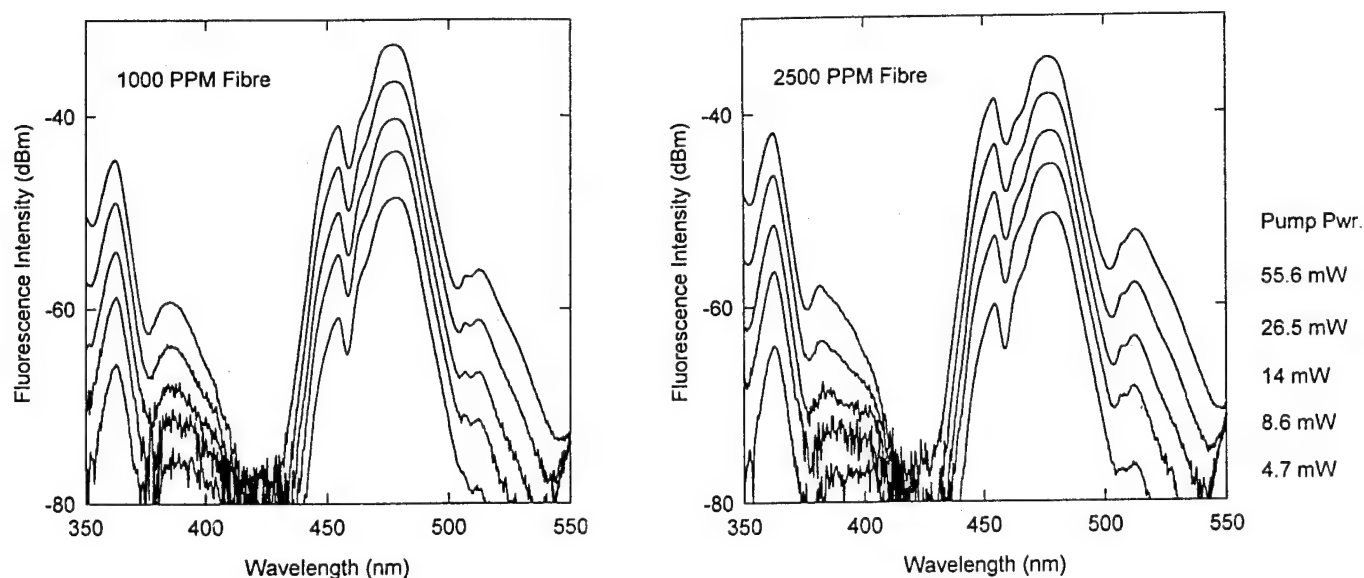


Figure 4 Fluorescence spectra from 1000 and 2500 ppm Tm-ZBLAN fibres.

Discussion and conclusions

Photodarkening has been observed in thulium doped ZBLAN fibre pumped at 1135 nm. This is probably an electronic defect caused by multi-step upconversion of thulium to a highly excited state. Such a damage process has been observed previously in thulium doped silica glass fibre. The rate of damage formation is strongly dependent on the pump power level and on thulium concentration. The centres absorb strongly only at wavelengths below about 650 nm, affecting the performance of blue upconversion lasing. The colour centres are bleached by intense blue light but recover with thermal excitation. They can be removed by thermal annealing at temperatures below 100°C.

In thulium-ZBLAN pumped at around 1135 nm, upconversion above the G_4 level seems to rely on energy transfer between thulium ions, as the G_4 - D_2 transition is not resonant with the pump light. We observe stronger D_2 fluorescence in fibres with higher levels of thulium doping, and in fibre with thulium-ytterbium co-doping. These fibres also develop photodarkening faster. An obvious step towards curing the problem is therefore to use fibre with lower levels of thulium doping. It is not clear how effective this will be in preventing damage since part of the G_4 - D_2 upconversion may be directly pumped due to broadening of the transition in glass. It is also possible that the susceptibility of the glass to damage depends on the composition and doping. Fibres with higher doping levels may provide more sites for colour centres to form. If this is true then the dopants used to modify the numerical aperture (NA) of the fibre core could be important. All three fibres used in our experiments were similar in core size and NA, so we have no way to tell if this is so.

References

- [1] S.G. Grubb, K.W. Bennett, R.S. Cannon, and W.H. Humer, "CW room-temperature blue upconversion fibre laser", *Electronics Letters*, **28**, p1243-4, (1992).
- [2] W.S. Brocklesby, A. Mathieu, R.S. Brown, and J.R. Lincoln, "Defect production in silica fibers doped with Tm^{3+} ", *Optics Letters*, **18**, p2105-7, (1993).
- [3] M.M. Broer, D.M. Krol, and D.J. DiGiovanni, "Highly nonlinear near-resonant photodarkening in a thulium-doped aluminosilicate glass fibre", *Optics Letters*, **18**, p799-801, (1993).

- Abe, M. — SaD1
 Albert, Jacques — SuB16, PMB5
 Alimpiev, S. S. — PMA4
 Allard, L. B. — SuB16
 Alley, Thomas G. — SaC5, SuD3
 Andersen, Lars-Ulrik Aaen — SuB2
 Archambault, J.-L. — PMD6
 Armes, D. J. — SaB5
 Askins, Charles G. — SuA5
 Atkins, Graham — PMA2
 Awazu, Koichi — PMA3
- Bagratashvili, Victor N. — PMA4
 Bailey, T. J. — PMC2
 Ball, Gary A. — PMC1, PMD
 Bayon, J. F. — SaD2, SuA1, SuB6
 Bazylenko, M. V. — SuB5
 Bennion, Ian — SuB11, SuB12, SuB13, PMD3, PMD4
 Berkovic, G. — SuC2
 Bernage, P. — SaD2, SuA1
 Bhatia, V. — SaB2
 Birks, T. A. — PMD2
 Booth, I. J. — PMD6
 Borne, S. — SaB4, SaD3
 Brebner, J. L. — SuB16
 Broderick, Neil G. R. — SuB9, PMC4
 Brueck, S. R. J. — SaA3
 Byron, Kevin — PMD3
- Campbell, R. J. — SaB5
 Canning, J. — SuA6
 Carvalho, I. C. S. — SaC1
 Chandonnet, Alain — PMD5
 Charra, F. — SaC2
 Chernov, Pavel V. — PMA4
 Chu, P. L. — SuB5
 Cochet, F. — SaD4
 Cohen, R. — SuC2
 Cole, M. J. — SuA3
 Cruz, J. L. — SuA2, PMB2
- Dacosta, A. — SaD2
 Dajani, Iyad — SaC5
 Davies, Sandra — PMD3
 de Lathouwer, M. — SaB5
 de Sterke, C. Martin — SuB9, SuB10, PMC4
 Delevaque, E. — SuA1
 Deslauriers, Jean — PMA2
 Dianov, E. M. — SaB3, SuB4
 Dong, Liang — SuA2, SuC1, PMA4, PMB2
 Donval, A. — SuC2
 Doran, N. J. — SuB13
 Douay, M. — SaD2, SuA, SuB6
 Duguay, Michel A. — PMA2
 Dunphy, J. R. — PMC1
- Eggleton, Benjamin J. — SuB9, PMC5
 Emplit, Ph. — SaB5
- Erdogan, Turan — SuA4, PMC3
 Essid, M. — SuB16
- Faith, M. — SuB8
 Farries, M. C. — PMD4
 Fiorini, C. — SaC2
 Fleming, S. C. — SuD1
 Fonjallaz, P. Y. — SaD4
 Friebele, E. Joseph — SuA5
 Fujiwara, Takumi — SuD1
- Garcia, F. C. — SaC1
 Gilbert, Sarah — SuB15
 Glass, A. M. — SaA1
 Gray, J. W. D. — SuB13
 Gross, M. — SuB5
- Haelterman, M. — SaB5
 Handerek, V. A. — PMB3
 Haugbølle, Søren — PMA5
 Henry, Leanne J. — SuD3
 Hering, E. N. — SaC1
 Hewlett, S. J. — PMB4, PMC2
 Hibino, Y. — SaD1
 Hill, Ken O. — SaA, SaB1
 Hill, Peter C. — PMC5
 Horinouchi, Suguru — SuC3
 Hosono, Hideo — SaD5, SuB1
 Huber, David R. — SaA2
 Hübner, Jörg — SuB2, PMA5
 Huston, Alan L. — SuD4
- Ibsen, M. — SuB8
- Jacobovitz-Veselka, Gloria R. — SaB2
 Judkins, J. B. — SaB2
 Justus, Brian L. — SuD4
- Kanellopoulos, E. — PMB3
 Karna, Shashi P. — SuB14
 Karpov, V. I. — SaB3
 Kashyap, Raman — SaB5, SaC
 Kawazoe, Hiroshi — SaD5, SuB1
 Kazansky, P. G. — SuC1, SuC4
 Kean, P. N. — SuB13
 Kemeny, P. — SuB8
 Kersey, Alan D. — PMB1, PMC1
 Kester, John J. — SaC5, SuB14, SuD3
 Kitagawa, T. — SaD1
 Kristensen, Martin — SuB2
 Krug, Peter A. — SuB7, PMC5
 Kurkov, A. S. — SaB3, SuB4
 Kyung, Jae H. — SaC4, SuD2
- Ladouceur, F. J. — SuB8
 Laming, R. I. — SuA3
 Laperle, Pierre — PMD5
 Laurell, F. — SaC1
 Lavi, B. — SuC2
 Lawandy, N. M. — SaC4, SuD2
 Leech, P. — SuB8
- Leistiko, O. — SuB8
 Lemaire, Paul J. — SaB, SaB2, SuA4
 Lesche, B. — SaC1
 Limberger, H. G. — SaD4
 Loh, W. H. — SuA3
 Love, J. D. — SuB8, PMB4, PMC2
- Magruder, Robert H., III — PMA1
 Marchenko, V. M. — SuB17
 Margulis, W. — SaC1, PMB
 Martin, Jean — PMA2
 Martinelli, G. — SuA1
 Mathieu, C. — SaD2
 Medvedkov, O. I. — SaB3, SuB4
 Meltz, Gerry — SaD, PMB4, PMC1, PMC2
 Morey, W. W. — PMB4, PMC1, PMC2
 Moss, D. — SuB5, SuB8
 Muta, Ken-ichi — PMA3
- Nageno, Y. — SaC4
 Niay, P. — SaD2, SuA1, SuB6, PMC
 Nishii, Junji — SaD5
 Nunzi, J. M. — SaC2
- Onuki, Hideo — PMA3
 Ouellette, François — SuB7, SuB8, SuB10, PMA, PMA2, PMC5
- Pasman, Remco — SuA6, SuB7
 Patrick, Heather — SuB15
 Pattison, D. A. — SuB13
 Payne, D. N. — SuA2
 Poignant, H. — SuA1
 Poulsen, Christian V. — SuB2, SuB3, SuB8, PMA5
 Poumellec, B. — SaD2, SaD3, SuB6
 Prokhorov, A.M. — SaB3
 Protopopov, V. N. — SaB3
 Pruneri, V. — SuC1
 Psaila, D. C. — SuB10
 Putnam, Martin A. — SuA5
- Ragdale, C. M. — SuB11
 Ramecourt, D. — SaD2
 Rand, Dennis S. — SuD3
 Ranon, Peter — SaC5
 Rasmussen, Thomas — SuB2
 Reekie, Laurence — SuA2, PMB2, PMD1
 Reid, D. C. J. — SuB11, PMD4
 Reigada, D. C. — SaC1
 Riant, I. — SaB4, SaD3
 Rourke, Howard — PMD3
 Russell, Philip St. J. — SuC1, SuC4, SuD, PMA4, PMD2
 Rybaltovskii, Aleksey O. — PMA4
- Salathé, R. P. — SaD4, PDP
 Sansonetti, P. — SaB4, SaD3
 Sasaki, Keisuke — SuC3

Sceats, M. G. — SuA6
 Sessler, G. M. — SuC4
 Simanovskii, Yaroslav O. — PMA4
 Sipe, J. E. — SaB2, PMC3
 Smith, A. R. — SuC1, SuC4
 Stolen, Roger H. — SuC
 Sugden, Kate — SuB11, SuB12, PMD3
 Sugihara, O. — SuC1
 Svalgaard, Mikael — SuB18

Takeshita, Naoyuki — SuB1
 Taunay, T. — SaD2, SuA1
 Têtu, Michel — PMA2

Tsai, Tsung-E. — SuA5
 Tsuchiya, Toshio — SuB1
 Tsykina, Svetlana I. — PMA4
 Tucknott, J. A. — PMB2

Vallée, Réal — PMD5
 Vasil'ev, S. A. — SaB3, SuB4
 Vengsarkar, A. M. — SaB2
 Ventrudo, B. F. — PMD6
 Verhaegen, M. — SuB16

Watanabe, Yuichi — SuB1
 Weeks, Robert A. — SuA

Williams, Glen M. — SuA5
 Williams, John A.R. — SuB11, SuB12
 Wong, D. — SuD1

Xie, W. X. — SuA1
 Xu, M. G. — SuA2, PMB2

Yam, R — SuC2
 Yang, G. M. — SuC4

Zavorotny, Yurly S. — PMA4
 Zervas, M. N. — SuA3
 Zhang, L. — SuB11, SuB12, PMD4

**PHOTOSENSITIVITY AND QUADRATIC NONLINEARITY IN
WAVEGUIDES: FUNDAMENTALS AND APPLICATIONS**

TECHNICAL PROGRAM COMMITTEE

Gerry Meltz, *United Technologies Research Center, General Chair*

Philip St. J. Russell, *University of Southampton, UK, General Chair*

Ken O. Hill, *Communications Research Center, Canada, Program Chair*

Dana Z. Anderson, *University of Colorado*

Charles G. Askins, *U. S. Naval Research Laboratory*

Victor N. Bagratashvili, *Russian Academy of Sciences, Russian Federation*

Gary A. Ball, *3M Bragg Grating Technologies*

Steven R. J. Brueck, *University of New Mexico*

Kevin K. Byron, *Bell Northern Research, Ltd., UK*

Eugenii M. Dianov, *Russian Academy of Sciences, Russia*

Marc Douay, *Université des Science Technique, France*

E. Joe Friebele, *U. S. Naval Research Laboratory*

David R. Huber, *Ciena Corporation*

Avais Kamal, *EME College NUST, Pakistan*

Raman Kashyap, *British Telecom Research Laboratories, UK*

Hiroshi Kawazoe, *Tokyo Institute of Technology, Japan*

John J. Kester, *Frank J. Sella Research Laboratory*

Nabil M. Lawandy, *Brown University*

Paul J. Lemaire, *AT&T Bell Laboratories*

Walter Margulis, *Imperial College, UK*

Ulf Österberg, *Dartmouth College*

François Ouellette, *University of Sydney, Australia*

Bertrand Poumellec, *Université de Paris Sud Orsay, France*

Laurence Reekie, *University of Southampton, UK*

R. P. Salathé, *Swiss Federal Institute of Technology, Switzerland*

* **Roger Stolen**, *AT&T Bell Laboratories*

Robert A. Weeks, *Vanderbilt University*

* OSA Technical Council Representative